Développement et caractérisation de matériaux à changement de phase à forme stabilisée pour la conception d'enveloppes du bâtiment durables et innovantes

Mohamed Sawadogo

▶ **To cite this version:**

Mohamed Sawadogo. Développement et caractérisation de matériaux à changement de phase à forme stabilisée pour la conception d'enveloppes du bâtiment durables et innovantes. Thermique [physics.class-ph]. Université de La Rochelle, 2023. Français. NNT : 2023LAROS042 . tel-04769235

HAL Id: tel-04769235

https://theses.hal.science/tel-04769235v1

Submitted on 6 Nov 2024

HAL is a multi-disciplinary open access archive for the deposit and dissemination of scientific research documents, whether they are published or not. The documents may come from teaching and research institutions in France or abroad, or from public or private research centers.

L'archive ouverte pluridisciplinaire **HAL**, est destinée au dépôt et à la diffusion de documents scientifiques de niveau recherche, publiés ou non, émanant des établissements d'enseignement et de recherche français ou étrangers, des laboratoires publics ou privés.

LA ROCHELLE UNIVERSITÉ
ÉCOLE DOCTORALE EUCLIDE

Institut du Littoral Urbain Durable et Intelligent

Laboratoire des Sciences de l'Ingénieur pour l'Environnement (LaSIE)

UMR CNRS 7356

THÈSE DE DOCTORAT

Présentée par

Mohamed SAWADOGO

Pour l'obtention du

Grade de Docteur de La Rochelle Université

Discipline : Energétique et Thermique

Développement et caractérisation de matériaux à changement de phase à forme stabilisée pour la conception d'enveloppes du bâtiment durables et innovantes

Thèse soutenue le 19/12/2023

Membres du jury :

Géraldine CASAUX-GINESTET, Professeure des Universités Bordeaux – ENSAP (Rapporteure)
Mahdia HATTAB, Professeure des Universités de l'Université de Lorraine – LEM3 (Examinatrice)
Delphine LACANETTE, Professeure des Universités de Bordeaux INP – I2M (Rapporteure)
Elena PALOMO DEL BARRIO, Directrice Scientifique au CICenergiGUNE (Examinatrice)
Ammar YAHIA, Professeure des Universités de l'Université de Sherbrooke (Examinateur)
Rafik BELARBI, Professeur des Universités de La Rochelle Université – LaSIE (Examinateur)
Marie DUQUESNE, Professeure des Universités de La Rochelle Université – LaSIE (Invitée)
Alexandre GODIN, Ingénieur de Recherche de La Rochelle Université – LaSIE (Examinateur)
Ameur HAMAMI, Maître de conférences de La Rochelle Université – LaSIE (Examinateur)

REMERCIEMENTS

Il y'a trois ans, quand je m'étais lancé dans ce projet de thèse, je n'aurai jamais imaginé toutes les rencontres, les émotions que j'allais vivre tout au long de cette aventure. Cet accomplissement n'aurait jamais été effectif sans le soutien et l'accompagnement de plusieurs personnes.

Je tiens tout d'abord à remercier Mahdia HATTAB pour avoir accepté présider ma soutenance de thèse. Je remercie également Delphine LACANETTE et Géraldine CASAUX-GINESTET pour avoir accepté rapporter mon manuscrit de thèse. Enfin, mes sincères remerciements à Amar YAHIA, Elena PALOMO DEL BARRIO et Alexandre GODIN pour avoir accepté examiner mon travail doctoral.

Je voudrais tout particulièrement remercier mes encadrants pour la confiance et l'accompagnement tout au long de ces trois derniers. Le mot famille choisi à la fin de la soutenance pour vous décrire n'était pas fortuit et traduit à dessein tout ce que vous représentez pour moi. A Rafik BELARBI, mon directeur de thèse tout d'abord, je te remercie d'avoir cru en moi et de m'avoir offert cette opportunité de faire de la recherche à tes côtés. Je te remercie également pour tes conseils avisés tant sur le plan scientifique que personnel.

A Marie DUQUESNE, ma co-encadrante, j'exprime également ma toute profonde gratitude pour ton encadrement et ta disponibilité tout au long de cette thèse. J'ai beaucoup appris à tes côtés et ta rigueur scientifique continuera de dépeindre sur moi dans chaque étape de ma vie professionnelle.

Merci à Ameur HAMAMI, mon co-encadrant pour ton accompagnement, ta disponibilité, tes conseils avisés et de m'avoir permis de réaliser l'une de mes plus grandes passions à savoir l'enseignement. Tes qualités humaines admirables m'auront beaucoup marqué.

J'adresse également mes remerciements à Alexandre GODIN pour son implication et son apport inestimable tout au long de ma thèse. Je garde en souvenir les nombreuses discussions scientifiques qu'on a menée qui m'ont été aussi bénéfique. Je n'oublie pas Mélissa, Naël et Mariya ces boules d'énergie qui ont su égayer nos fins de journée dans les bureaux.

A mes collègues et amis du laboratoire Fouad BOUKHELF, Rachid CHERIF, Achraf CHARAKA, Yara NASR, Hussein RAAD, Antoine MOREAU, Ali NEHME, Oscar COSSERAT, et Yassine BELARBI, merci pour tous les bons moments passés ensemble. Mes remerciements particuliers à Ferhat BENMAHIDDINE qui a contribué énormément à mon intégration au laboratoire. Merci à mes collègues et compagnons de foot Bassel HABEEB et Anis BAHAR pour tous ces fou rire et sorties partagées ensemble. Merci également à tous les membres de « Fuerza Latina » pour cette belle aventure footballistique.

Je remercie toute l'équipe du LaSIE et de l'école doctorale EUCLIDE pour leur accueil chaleureux. Mes remerciements à Armelle NOUVIAIRE, assistante ingénieur au LaSIE, pour son assistance lors de mes campagnes expérimentales des matériaux et Egle CONFORTO, responsable de la plateforme de microscopie au LaSIE.

Je tenais à remercier également tous mes partenaires de route depuis le Burkina jusqu'en France en passant par l'Algérie en particuliier Frédéric OUEDRAOGO et Lydie ZONGO, Assann OUEDRAOGO, Aboubacar TAMBOURA, Franck ZIDA et Sakina COMPAORE. D'une manière générale, je remercie tous ceux qui ont contribué de près ou de loin à ce voyage. Comme le dit un adage chez nous : « une seule main ne peut pas ramasser la farine ».

Enfin, je remercie mes deux parents Boureima SAWADOGO et Kouka Fati SAVADOGO pour leur affection, leur soutien, leurs prières au quotidien et leur encouragement. Papa, cette quête était plus la tienne que la mienne tant tu étais enthousiaste et fier à l'idée de voir ton fils docteur. Malheureusement, la vie t'a arraché prématurément à notre affection à mi-parcours. Je sais que de là ou tu es, tu es fier de ce que nous avons accompli ensemble. Merci à mes frères et sœurs Moussa, Aïcha, Afou et Ladji ainsi que mes neveux et nièces, pour leur soutient et amour inconditionnel.

MERCI

Mohamed SAWADOGO

RÉSUMÉ

Ces travaux de thèse s'inscrivent dans le cadre du projet BioMCP. L'innovation majeure de ces travaux de thèse réside dans le développement et la caractérisation de matériaux bio-composites. Ces matériaux, constitués de MCP biosourcés imprégnant la microporosité de matrices végétales, ont été élaborés dans le but de concevoir, caractériser et évaluer les performances d'enveloppes de bâtiment innovantes et durables. Pour mener à bien ces travaux de recherche, nous avons adopté une analyse multi-échelles allant de l'échelle du matériau à l'échelle du bâtiment en combinant des approches numériques et expérimentales.

Sur le plan expérimental, le potentiel des fibres naturelles en tant que matériaux support pour les matériaux à changement de phase (MCP) destinés aux bâtiments a été évalué. Quatre types de fibres naturelles (sapin, chanvre, chènevotte et paillis de lin) ont été présélectionnés pour la fabrication de composites MCP à forme stabilisée. La chènevotte a été retenue en raison de son taux d'imprégnation élevé (50% dans les acides caprique et laurique) et d'une application déjà effective dans les bâtiments (à travers le béton de chanvre). La chènevotte imprégnée de MCP a été utilisée pour fabriquer du béton de chanvre à base de MCP (bio-composite MCP). Les propriétés thermiques et hydriques des matériaux fabriqués sont investiguées pour mieux appréhender leurs comportements et créer une base de données d'entrée pour la modélisation. L'incorporation de MCP a conduit à une amélioration des propriétés thermiques du béton de chanvre de référence due à une augmentation de l'inertie thermique. De plus, le matériau composite a montré une excellente capacité de régulation de l'humidité. Ensuite, les performances hygrothermiques d'une paroi de référence (béton de chanvre) et d'une paroi intégrant le bio-composite ont été évaluées dans les conditions climatiques de La Rochelle. L'incorporation de MCP a permis de réduire de 2°C la température maximale pendant les canicules, réduisant les besoins de refroidissement. Cette réduction du pic de température s'explique par la forte inertie thermique des bio-composite développés. Le bio-composite ainsi développé a démontré une capacité à réguler à la fois la température et l'humidité relative.

Sur le volet numérique, un modèle hygrothermique basé sur les équations de conservation de l'énergie et de la masse a été développé pour simuler le comportement des matériaux de construction de référence et développés. Ce modèle a été validé avec succès à l'aide de données expérimentales du bio-composite et de celles de normes reconnues avec une bonne précision. Le modèle hygrothermique a été utilisé pour évaluer les performances de parois multicouches avec différents isolants, y compris le bio-composite, dans les conditions climatiques de Caracas et de New Delhi. Les parois intégrant le bio-composite se sont avérées très performantes. Leur inertie importante permet de limiter le recours à la climatisation, notamment, grâce au décalage temporel (plusieurs heures) des maximas de température. Une étude paramétrique a également été conduite afin d'analyser l'effet de l'épaisseur de la couche isolante et la fraction de MCP sur les performances du bio-composite MCP. Enfin, une approche de cosimulation a été proposée pour interfacer le modèle développé avec un modèle de simulation énergétique à l'échelle du bâtiment pour évaluer les performances de ces enveloppes innovantes et durables et leur impact sur les consommations énergétiques des bâtiments. Cette approche a été validée avec succès et a permis d'améliorer la prédiction du comportement hydrique des parois à travers une réduction de l'écart entre données expérimentales et la simulation de 2%. Elle a ainsi montré la necessité d'introduire une modélisation fine du comportement hygrothermique des enveloppes de bâtiments dans les logiciels de simultion dynamique.

Mots-clés : Fibres végétales, isolants biosourcés, matériaux à changement de phase, stabilisation en forme, inertie thermique, transferts hygrothermiques, performances energétiques des bâtiments, caractérisation expérimentale, modélisation, systèmes passifs de chauffage et de climatisation.

ABSTRACT

This thesis work is part of the BioMCP project. The major innovation of this thesis work lies in the development and characterization of bio-composite materials. These materials, made up of biosourced PCMs impregnating the microporosity of plant matrices, have been developed with the aim of designing, characterizing and assessing the performance of innovative, sustainable building envelopes. To carry out this research, we adopted a multi-scale analysis from the material scale to the building scale, combining numerical and experimental approaches.

On the experimental front, the potential of natural fibers as support materials for phase-change materials (PCMs) for buildings was assessed. Four types of natural fibers (fir pellets, hemp fibers, hemp shives and flax mulch) were shortlisted for the fabrication of form-stabilized PCM composites. Hemp shives was chosen because of its high impregnation rate (50 wt% in capric and lauric acid) and its effective application in buildings (through hemp concrete). The impregnated hemp shives were used to fabricate PCM-based hemp concrete (PCM bio-composite). The thermal and hydric properties of the manufactured materials has been assessed for better understanding of their behavior and create an input database for modeling. The incorporation of PCM has led to an improvement of the thermal properties of the reference concrete due to the increase in thermal inertia. In addition, the composite material showed excellent moisture regulation capacity. Moreover, the hygrothermal performance of the reference hemp concrete and PCM bio-composite were evaluated under La Rochelle climatic conditions in a bi-climatic chamber. The incorporation of PCM resulted in a 2°C reduction in peak temperature during heatwaves, reducing the need for cooling. This reduction in peak temperature can be explained by the high thermal inertia of the PCM bio-composites developed. The developed PCM bio-composite has demonstrated the ability to regulate both temperature and relative humidity.

On the numerical side, a hygrothermal model based on energy and mass conservation equations was developed to simulate the behavior of reference and developed building materials. This model has been successfully validated using experimental data from bio-composite and recognized standards with good accuracy. The hygrothermal model was used to assess the performance of multi-layer walls with different insulating materials, including bio-composite, under the climatic conditions of Caracas and New Delhi. The walls incorporating bio-composite proved to be highly efficient. Their high inertia reduces the need for air-conditioning, thanks in particular to the time lag (several hours) between temperature maxima. A parametric study was also carried out to analyze the effect of insulating layer thickness and PCM fraction on the performance of the PCM bio-composite. Finally, a co-simulation approach was proposed to interface the model developed with a building-scale energy simulation model to assess the performance of these innovative, sustainable envelopes and their impact on building energy consumption. This approach was successfully validated, and led to improved prediction of the hydric behavior of walls, with a reduction in the gap between experimental data and simulation of 2%. It also demonstrated the need to introduce fine modeling of the hygrothermal behavior of building envelopes into dynamic simulation software.

Keywords: Natural fibers, biosourced insulation, phase-change materials, shape stabilization, thermal inertia, hygrothermal transfers, energy performance of buildings, experimental characterization, modeling, passive heating and cooling techniques.

SOMMAIRE

Table des illustrations

Liste des tableaux

Nomenclature

Lettres latines

Notation	Description	Unité
C_p	Capacité calorifique massique	[J.kg^{-1}.K^{-1}]
T	Température	[°C ou K]
T_f	Température de fusion	[°C ou K]
f	Fraction de MCP	[%]
T_s	Température de solidification	[°C ou K]
u	Teneur en eau massique	[kg.kg^{-1}]
w	Teneur en eau volumique	[kg.m^{-3}]
C_m	Capacité de stockage d'humidité	[-]
p	Pression	[Pa]
k_T	Coefficient de diffusion de la phase liquide créé par un gradient de température	[kg.m^{-1}.s^{-1}.K^{-1}]
R	Constante des gaz parfaits	[J.mol^{-1}.K^{-1}]
M	Masse molaire de l'eau	[g.mol^{-1}]
C_p^*	Capacité calorifique massique effective	[J.kg^{-1}.K^{-1}]
h	Enthalpie spécifique	[J.kg^{-1}]
k_l	Coefficient de perméabilité liquide	[kg.s^{-1}.m^{-1}.Pa^{-1}]
D	Coefficient de diffusion d'humidité	[m^2.s^{-1}]
k_m	Coefficient de diffusion d'humidité totale	[kg.s^{-1}.m^{-1}.Pa^{-1}]
L_v	Chaleur latente de vaporisation de l'eau liquide	[J.kg^{-1}]
h_c	Coefficient d'échange de chaleur convectif	[W.m^{-2}.K^{-1}]
h_m	Coefficient d'échange de masse convectif	[s.m^{-1}]
j_l	Densité de flux massique de la phase liquide	[kg.m^{-2}.s^{-1}]
j_v	Densité de flux massique de la phase vapeur	[kg.m^{-2}.s^{-1}]
j_q	Densité de flux de chaleur	[W.m^{-2}]
j_{cond}	Densité de flux de chaleur conductif	[W.m^{-2}]

Lettres grecques

Notation	Description	Unité
φ	Humidité relative	[%]
ρ	Masse volumique	[kg.m^{-3}]
λ	Conductivité thermique	[W.m^{-1}.K^{-1}]
λ^*	Conductivité thermique effective	[W.m^{-1}.K^{-1}]
δ	Coefficient de perméabilité à la vapeur d'eau	[kg.s^{-1}.m^{-1}.Pa^{-1}]
γ	Coefficient de transfert de chaleur par convection dû au gradient de la pression de vapeur	[W.m^{-1}.Pa^{-1}]
σ	Rapport entre le flux de vapeur et le flux d'humidité totale	[-]

Indices

Notation	Description
φ	Humidité relative
ρ	Masse volumique
s	Solide
l	Liquide
v	Vapeur
sat	Saturation
ref	Référence
cond	Conductif

1 Introduction

Mes travaux de thèse sont réalisés dans le cadre du Projet BioMCP (« Étude des matériaux biosourcés à changement de phase pour le stockage d'énergie thermique dans les bâtiments et les réseaux de chaleur », Projet Région Nouvelle-Aquitaine n°2017-1R10209-00013023, 524 k€, 2020-2023). Ce projet est coordonné par le Laboratoire des Sciences de l'Ingénieur pour l'Environnement (LaSIE - UMR CNRS 7356, La Rochelle Université, axe Bâtiments et Villes Durables, coordinateur du Projet : R. Belarbi) en collaboration avec le département Transferts Fluides Energétique (TREFLE) de l'Institut de Mécanique et d'Ingénierie (I2M, UMR CNRS 5295, Université de Bordeaux). Mes activités s'inscrivent également dans celles du Laboratoire commun 4eVLab (Laboratoire pour l'Efficacité Energétique et Environnementale de l'Enveloppe et des Villes, Laboratoire commun EDF énergies nouvelles - La Rochelle Université CNRS - LaSIE).

1.1 Contexte

Le dernier rapport du groupe d'experts intergouvernemental sur l'évolution du climat (GIEC) dresse un tableau accablant. Dans le scénario le plus optimiste, les experts prévoient une hausse des températures de plus de 1,5°C dès 2030, contre un réchauffement de plus de 4°C selon le scénario le plus pessimiste [1]. Cette augmentation des températures est responsable des fréquentes vagues de chaleur et des records de température récemment observés dans plusieurs régions du monde. Malheureusement, ce dérèglement climatique ne se limite pas seulement à une augmentation de la température globale. En effet, des changements généralisés de l'atmosphère, des terres, de l'océan et des régions enneigées et englacées sont également attendus [1].

Les émissions anthropiques de gaz à effet de serre ont augmenté depuis l'ère préindustrielle en raison essentiellement de la croissance économique et démographique. Elles sont actuellement plus élevées que jamais, ce qui a entraîné des concentrations atmosphériques de dioxyde de carbone, de méthane et d'oxyde nitreux sans précédent depuis au moins 800 000 ans [2]. Leurs effets, associés à ceux d'autres facteurs anthropiques, ont été détectés dans tout le système climatique et il est très probable qu'ils aient été la cause principale du réchauffement observé depuis le milieu du XX^{e} siècle.

Face à cette situation, il est essentiel de prendre des mesures pour limiter les émissions de gaz à effet de serre afin d'atteindre un "bilan zéro carbone". Le secteur du bâtiment, qui représente un tiers de la consommation mondiale d'énergie et un quart des émissions de CO_2, reste l'un des premiers leviers d'action pour réduire la consommation d'énergie et limiter les émissions de gaz à effet de serre [3]. En effet, le bâtiment est un secteur particulièrement énergivore, avec un parc de bâtiments vieillissant qui nécessite une amélioration des enveloppes pour diminuer les besoins de chauffage et de climatisation.

Sur le plan régional, la Région Nouvelle-Aquitaine a l'ambition d'être la première Région française de la transition énergétique et du climat. Elle s'est fixée trois objectifs : la réduction des émissions de gaz à effet de serre, la réduction des consommations d'énergie et l'utilisation/valorisation des énergies renouvelables. La ville de La Rochelle est pionnière dans la mise en place de solutions pour faire face aux enjeux environnementaux et se veut être une agglomération sobre et durable. En effet, la ville de la Rochelle se donne comme objectif de ne plus émettre de carbone sur le territoire d'ici 2040 et met en place des solutions pour atteindre

cet objectif. Elle bénéficie déjà d'un mix énergétique avec 20% d'énergies renouvelables [4] : auto-consommation dans les bâtiments publics adaptés, centrale de cogénération issue de la méthanisation à Rochefort (157 MWh), 250 bâtiments de la collectivité de la ville de La Rochelle bénéficient déjà d'un mix énergétique à haute valeur ajoutée (part d'énergies renouvelables produites localement) [5].

Le Projet BioMCP dans lequel s'inscrivent les travaux de ma thèse, vise à développer et évaluer de nouveaux matériaux à changement de phase (MCP) biosourcés, susceptibles de rivaliser voire de surpasser les performances des MCP traditionnellement utilisés. Cette initiative s'inscrit dans une démarche de développement durable et d'économie circulaire, contribuant ainsi aux Objectifs de Développement Durable (ODD) 11, 12 et 13[1]. L'objectif ultime est de contribuer à améliorer les performances énergétiques des systèmes, des bâtiments existants et d'autres installations (réseaux de chaleur, centrales de cogénération) dans les quartiers et les villes. Ces axes sont fondamentaux pour décarboner le chauffage et le rafraîchissement, réhabiliter les bâtiments, réduire les îlots de chaleur urbains et réussir la transition énergétique.

Les MCP qui retiennent notre attention dans cette étude sont ceux à transition solide-liquide. Le principe clé du stockage d'énergie par chaleur latente consiste à emmagasiner l'excès d'énergie thermique provenant de l'environnement sous forme de chaleur latente pendant le processus de fusion puis à le restituer lorsque la température descend en dessous de la température de solidification des MCP. Cette alternance de fusion et de solidification permet aux MCP de réguler la température à l'intérieur des bâtiments. Les performances de bâtiments incorporant des MCP dépendent non seulement de ces derniers mais aussi des conditions climatiques et des configurations des bâtiments. Il est à noter que malgré de nombreuses études sur les MCP, peu de recherches portent sur l'échelle de l'enveloppe du bâtiment, la plupart se concentrant sur le développement des matériaux composites sans explorer pleinement l'échelle du bâtiment.

1.2 Règlementation

A l'échelle européenne, le parlement a adopté des projets de mesures visant à augmenter le taux de rénovation et à réduire la consommation énergétique des bâtiments ainsi que les émissions de gaz à effet de serre. Avec 40 % de la consommation d'énergie et générant 36 % des émissions de gaz à effet de serre, le secteur du bâtiment est le premier consommateur d'énergie en Europe [6]. Cela s'explique par le fait que la plupart des bâtiments dans l'UE ne sont pas économes en énergie et sont encore principalement alimentés par des combustibles fossiles. La Commission propose qu'à partir de 2030, tous les bâtiments neufs soient à émissions nulles. Cela signifie que les bâtiments devront consommer peu d'énergie, être alimentés par des énergies renouvelables dans la mesure du possible et ne produire aucune émission de carbone sur site provenant de combustibles fossiles [6].

Les classes d'efficacité énergétique des bâtiments sont des catégories ou des niveaux de performance énergétique attribués à un bâtiment en fonction de sa consommation d'énergie annuelle, de son efficacité énergétique et de ses émissions de gaz à effet de serre. Elles

[1] De nombreux appels à projets inscrivent les actions à mener dans le contexte d'objectifs de développement durable (ODD). Les ODD (17 au total) ont été adoptés par les Nations Unies en 2015. Ils répondent aux défis mondiaux auxquels nous sommes confrontés et nous donnent la marche à suivre pour parvenir à un avenir meilleur et plus durable pour tous (ODD 11 : Faire en sorte que les villes et les établissements humains soient ouverts à tous, sûrs, résilients et durables ; ODD 12 : Établir des modes de consommation et de production durables ; ODD 13 : Prendre d'urgence des mesures pour lutter contre les changements climatiques et leurs répercussions).

permettent de classer les bâtiments en fonction de leur impact environnemental et de leur efficacité énergétique, allant généralement de A, représentant la meilleure classe en termes de performance énergétique à G, la moins performante. Cette classification vise à encourager l'amélioration de l'efficacité énergétique des bâtiments et à informer les propriétaires et les occupants sur leur performance énergétique globale. En ce qui concerne les rénovations, de nouvelles normes minimales au niveau de l'UE en matière de performance énergétique sont proposées. Elles exigent que les 15 % les moins performants du parc immobilier de chaque État membre soient modernisés pour passer de la classe d'efficacité énergétique G à au moins la classe F, d'ici à 2027 pour les bâtiments non résidentiels et d'ici à 2030 pour les bâtiments résidentiels [6].

En complément de la stratégie européenne, des initiatives à l'échelle nationale ont été entreprises pour réduire l'impact environnemental. Ainsi, en France le Grenelle de l'Environnement avait déjà fixé un objectif ambitieux de réduction des consommations d'énergie pour les bâtiments neufs construits après 2012. Cet objectif s'est traduit par la réglementation thermique 2012 (RT 2012) [7], en vigueur jusqu'à son remplacement par la réglementation environnementale 2020 (RE 2020) [8]. La RT 2012 a également introduit une exigence de recours aux énergies renouvelables pour les maisons individuelles. La RE 2020 répond à la loi de transition énergétique pour la croissance verte (LTECV 2015) et à la loi évolution du logement, de l'aménagement et du numérique (ELAN 2018) à travers la poursuite des objectifs d'amélioration de la performance énergétique des bâtiments neufs, de réduction de leur impact sur le climat (prise en compte des émissions de gaz à effet de serre sur l'ensemble du cycle de vie des bâtiments) et de leur adaptation aux conditions climatiques futures (renforcement du confort d'été).

1.3 Objectifs et défis d'actualité

Les systèmes de stockage d'énergie thermique par chaleur latente intègrent des MCP comme matériaux de stockage. La densité énergétique élevée des MCP, leur capacité à stocker à température quasi constante et la diversité des matériaux disponibles font des systèmes de stockage à chaleur latente des technologies particulièrement compétitives pour de nombreuses applications dont le secteur du bâtiment. Les cycles de charge/décharge et les performances des systèmes les intégrant sont fortement influencés par la nature des MCP et leurs propriétés, notamment celle de surfusion. La surfusion est un état métastable dans lequel un liquide demeure à l'état liquide à une température inférieure à sa température de fusion. Pour le chauffage et le rafraichissement, le MCP peut être intégré dans les parois du bâtiment (système de stockage d'énergie passif à court terme) afin d'augmenter l'inertie de celles-ci. Cela permet de gérer la variation diurne de l'ensoleillement. Pour ce type de stockage, le phénomène de surfusion doit être le plus faible possible de manière à décharger l'énergie thermique rapidement dans la plage de températures souhaitée pour faciliter les cycles de charge/décharge.

Ce type de systèmes passifs à base de MCP constitue une solution pour la diminution des besoins de rafraichissement assurés par les systèmes de climatisation traditionnels répandus dans le secteur du bâtiment. En effet, de nombreuses études ont mis en évidence le potentiel des MCP dans la régulation de la température dans l'ambiance des bâtiments [9–14]. L'intégration des MCP dans l'enveloppe des bâtiments améliore le confort thermique grâce à une inertie augmentée à travers le phénomène de changement de phase. L'inertie thermique se réfère à la capacité de ces matériaux à retarder et à modérer les variations de température intérieure des bâtiments en réponse aux variations de la température extérieure. Elle est le

résultat de la capacité des matériaux de construction à emmagasiner et à diffuser la chaleur. L'inertie thermique des bâtiments permet de maintenir une température plus stable et de réduire les fluctuations de température, contribuant ainsi à l'efficacité énergétique et au confort thermique. Les enveloppes de bâtiment intégrant les MCP possèdent une densité de stockage 5 à 10 fois supérieure à celle des murs standards [15].

L'apport innovant de mes travaux de thèse est le développement et la caractérisation de matériaux bio-composites (MCP biosourcés imprégnant la microporosité de matrices supports végétales), pour la conception, la caractérisation et l'évaluation des performances d'enveloppes du bâtiment durables et innovantes. Ces travaux numériques et expérimentaux, à différentes échelles, ont pour objectifs ultimes :

- D'améliorer la gestion de l'énergie thermique des bâtiments en intégrant les besoins bâtiments/usagers (maintien du confort des habitants),
- De diminuer les consommations énergétiques,
- De participer à la décarbonation du chauffage et du rafraîchissement en favorisant la valorisation de l'énergie thermique disponible ainsi que le développement d'enveloppes durables et innovantes de bâtiment.

1.4 Structure de la thèse

Ce manuscrit est rédigé sous forme de thèse par articles. Mes travaux de thèse ont, à ce jour, donné lieu à **7 articles publiés** et **01 article soumi** (voir Annexe).

- **Article 1 :** M. Sawadogo, M. Duquesne**,** R. Belarbi, A. Hamami, A. Godin, "Review on the Integration of Phase Change Materials in Building Envelopes for Passive Latent Heat Storage", Applied Sciences (Impact Factor: 2.7), 11, 9305, 2021; doi : 10.3390/app11199305.

- **Article 2 :** M. Sawadogo, A. Godin, A. Hamami, M. Duquesne, R. Belarbi, "A review on numerical modelling of the hygrothermal behavior of building envelopes incorporating phase change materials", Buildings 2023, 13(12), doi : 10.3390/buildings13123086.

- **Article 3 :** M. Sawadogo, A. Godin, M. Duquesne, E. Lacroix, A. Veillère, A.E.A. Hamami, R. Belarbi, "Investigation of eco-friendly and economic shape-stabilized composites for building walls and thermal comfort", Building and Environment (Impact Factor : 7.4), 2023, 231, 110026; doi : 10.1016/j.buildenv.2023.110026.

- **Article 4 :** M. Sawadogo, F. Benmahiddine, A. Hamami, R. Belarbi, A. Godin, M. Duquesne, "Investigation of a novel bio-based PCM hemp concrete for passive energy storage in buildings", Applied Thermal Engineering (Impact Factor : 6.4), 212, 2022, doi : 10.1016/j.applthermaleng.2022.118620.

- **Article 5 :** M. Sawadogo, F. Benmahiddine, A. Godin, M. Duquesne, R. Belarbi, A. Hamami, "Development and hygrothermal performance analysis of a novel eco-friendly

insulating wall under various climatic conditions", Building and Environment (Impact Factor : 7.4), 110841, 2023; doi : 10.1016/j.buildenv.2023.110841.

- **Article 6 :** M. Sawadogo, A. Godin, M. Duquesne, R. Belarbi, A. Hamami, "An inverse method for the estimation of the vapor and liquid diffusivity coefficient of conventional and innovative building materials", Construction and Building Material, 2024, Volume 422,2024,135804, ISSN 0950-0618, https://doi.org/10.1016/j.conbuildmat.2024.135804. (Impact Factor : 7.4).

- **Article 7 :** Y. Belarbi, M. Sawadogo, P. Poullain, N. Issaadi, A. Hamami, S. Bonnet and R. Belarbi, "Experimental Characterization of Raw Earth Properties for Modeling Their Hygrothermal Behavior", Buildings, 2022, 12(5), 648; doi : 10.3390/buildings12050648.

- **Article 8 :** M. Sawadogo, A. Godin, R. Belarbi, A. Hamami, A. Perro, M. Duquesne**,** "Numerical investigation of the hygrothermal behavior of innovative eco-friendly multilayer building walls with increased thermal inertia using phase change materials", soumis dans le Journal Energy and Buildings (Impact Factor : 6.7).

Mon manuscrit est organisé en trois chapitres :

- Le premier chapitre a fait l'objet de **deux articles de review** (**article 1**, publié dans le journal Applied Sciences et **article 2**, soumis dans le journal Buildings). Ce chapitre recense les travaux et résultats existant dans la littérature afin :
  - d'identifier les verrous à lever concernant l'incorporation de MCP dans les enveloppes de bâtiment et la modélisation de ce type d'enveloppes,
  - de positionner mes travaux de thèse dans l'état de l'art,
  - de proposer une contribution originale, en phase avec les enjeux d'actualité, basée sur le développement d'enveloppes de bâtiments durables intégrant une solution de stockage d'énergie thermique.

- Le deuxième chapitre a fait l'objet de **quatre articles** (**articles 3** et **4** publiés dans Building and Environment, **article 5** publié dans Applied Thermal Engineering, **article 6** publié dans Construction and Building Materials). Ce chapitre décrit les activités expérimentales à différentes échelles permettant :
  - la sélection des matériaux composant les bio-composites,
  - le développement d'un protocole de synthèse de ces bio-composites,
  - la caractérisation des propriétés thermiques et hydriques des matériaux composant les bio-composites et des bio-composites eux-mêmes,
  - la caractérisation du comportement hygrothermique des parois intégrant ces bio-composites permettant d'une part l'évaluation des parois développées, d'autre part de valider les modèles proposés dans la section suivante.

- Le troisième chapitre a donné lieu à **deux articles** (**article 7** publié dans Buildings et **article 8** soumis dans Energy and Buildings). Ce chapitre présente le développement d'un modèle de transferts couplés pour atteindre les objectifs suivants :
  - contribuer à la compréhension du fonctionnement des matériaux développés et guider leur amélioration (les propriétés des matériaux sont utilisées comme données d'entrée du modèle développé),

- disposer d’outils de simulation permettant de tester différents types d’enveloppes (enveloppes de référence, enveloppes innovantes et durables développées, enveloppes monocouches ou multicouches, d’autres types d’enveloppes) soumises à différentes conditions climatiques,
- mettre en place une cosimulation, donc interfacer ce modèle avec un modèle de simulation énergétique à l’échelle du bâtiment pour évaluer les performances de ces enveloppes innovantes et durables et leur impact sur les consommations énergétiques des bâtiments. Un article est en cours de rédaction sur cette dernière partie.

2 Synthèse bibliographique

2.1 Techniques d'incorporation des MCP dans les enveloppes des bâtiments

L'utilisation des MCP dans le secteur des bâtiments offre un potentiel significatif pour améliorer la performance thermique de ces derniers tout en réduisant leur impact environnemental. Dans l'**article 1**, nous avons passé en revue les études expérimentales et numériques récentes sur l'intégration des MCP dans l'enveloppe des bâtiments pour le stockage passif de l'énergie. Les résultats des différentes études montrent que l'utilisation de MCP permet d'assurer le confort thermique dans les bâtiments en réduisant l'amplitude et les fluctuations de température des ambiances habitables. Cela est principalement dû à une augmentation de l'inertie thermique des bâtiments due à l'incorporation des MCP. Ces derniers peuvent être incorporés dans l'ensemble de l'enveloppe du bâtiment : murs, toits, fenêtres et planchers.

Quatre techniques d'incorporation des MCP dans l'enveloppe des bâtiments sont présentées dans la littérature : l'incorporation directe, l'imprégnation, l'encapsulation et la stabilisation de la forme.

- L'incorporation directe consiste à mélanger directement les MCP dans les enveloppes de bâtiments. Elle est considérée comme la technique la plus simple et économique, mais présente des inconvénients tels que le risque de fuite du MCP avec le temps et la dégradation des propriétés mécaniques du matériau de construction.

- L'imprégnation, qui consiste à immerger le matériau de construction poreux dans le MCP fondu, est plus efficace que l'incorporation directe, mais comporte toujours les mêmes risques de fuite et de dégradation des propriétés mécaniques.

- L'encapsulation implique de confiner le MCP dans une capsule pour éviter les fuites de la phase liquide. Les capsules sont classées en fonction de leur taille et de leur forme, qui sont influencées par le processus de synthèse et le type de matériau de capsule utilisé. On parle de nano-capsules ou de nano-sphères si le diamètre des capsules est compris entre 0 et 1000 nm, de microcapsules si le diamètre des capsules est inférieur à 1 mm ou 1 cm et de macro-capsules lorsque les capsules ont un diamètre supérieur à 1 mm ou 1 cm [16].

- Enfin, les MCP à forme stabilisée sont obtenus en imprégnant la porosité des matériaux de construction avec des MCP pour éviter les problèmes de fuite pendant le changement de phase. Deux techniques principales sont utilisées : la méthode d'imprégnation en deux étapes et la méthode de synthèse in situ en une étape. La première implique d'imprégner les MCP liquides dans les nanopores du support poreux, tandis que la seconde consiste à encapsuler les MCP in situ pendant la formation d'un réseau poreux. Différents matériaux, tels que des polymères, des matériaux poreux et des nanomatériaux, sont utilisés pour la fabrication de MCP à forme stabilisée.

En raison des techniques de fabrication simples et peu coûteuses, du taux d'imprégnation élevé par rapport aux autres techniques et de la grande variété de matériaux de support disponibles, la stabilisation de la forme a été choisie pour imprégner les MCP dans les études menées dans

ce travail. Parmi ces matériaux de support, les matériaux biosourcés, en particulier les matériaux isolants fibreux, offrent des perspectives prometteuses pour la fabrication de composites à forme stabilisée.

En effet, en plus de leur origine biologique, la structure poreuse de ces matériaux permet des valeurs élevées de taux d'imprégnation (approchant les 100 %). La liste des matériaux biosourcés pouvant être utilisés pour la stabilisation de forme des MCP est très vaste mais nous nous concentrons sur les matériaux isolants déjà en usage ou prometteurs pour une application dans les bâtiments (Tableau 1). Il s'agit de fibres végétales telles que le lin ou le chanvre. Un autre avantage de ces matériaux est leur capacité à réguler l'humidité, garantissant ainsi une bonne qualité de l'air intérieur. Enfin, le coût de ces isolants biosourcés est très attractif.

Tableau 1. Isolants biosourcés envisagés comme matériaux de support potentiels pour la fabrication de composites à forme stabilisée.

Isolant	**Masse volumique ($kg.m^{-3}$)**	**Conductivité thermique ($mW.m^{-1}.K^{-1}$)**	**Prix (€/kg)**	**Références**
Fibres de Bambou	431-538	77-88	-	[17]
Fibres de chanvre	25-100	40-49	2-5	[18]
Fibres de lin	20-100	35-45	5-25	[18]
Fibres de tiges de coton	150-450	58-82	-	[19]
Chènevotte	100-140	80-122	0,8-1	[20]
Kapok	17,24	30-48,6	-	[21–23]
Fibres de coco	40-90	50,09-57,58	63	[24]

Les acides gras et leurs mélanges eutectiques ont des températures de fusion dans la gamme de variation de la température des ambiances habitables (15-45°C) et sont couramment utilisés. De plus, ils sont renouvelables et présentent des caractéristiques similaires ou meilleures que les cires de paraffine utilisées dans les systèmes actuels. Les acides gras d'intérêt pour l'application ciblée sont répertoriés dans le Tableau 2.

Tableau 2. Acides gras d'intérêt et leurs mélanges eutectiques pour l'application visée, CA : acide caprique, LA: acide laurique, MA: acide myristique, PA: acide palmitique, SA: acide stéarique [25,26].

MCP	**Température de fusion (°C)**
CA	29,6 – 33,2
LA	41 – 45,3
MA	49 – 56,1
PA	58,9 - 64
SA	53,8 – 70,8
CA (72%)-LA (28%)	21,14
CA (84%)-MA (16%)	24,24
CA (87%)-PA (13%)	27,95
CA (93%)-SA (28%)	26,91
LA (71%)-MA (29%)	33,07
LA (79%)-PA (21%)	35,46
LA (87%)-SA(13%)	40,2

Sur la base de cette revue, nous avons identifié des contributions possibles pour améliorer l'efficacité des systèmes passifs incorporant des MCP. Ainsi, les acides gras et leurs mélanges eutectiques, MCP biosourcés, combinés à des isolants naturels, tels que les fibres végétales, ont été choisis pour fabriquer des bio-composites de MCP stabilisés. Ces composites peuvent être intégrés dans les bâtiments en tant que matériau de stockage passif de l'énergie thermique.

Au niveau expérimental, on constate que la majorité des études se concentrent sur le développement de matériaux composites et leur caractérisation. Différents matériaux et méthodes d'incorporation ont été utilisés et l'effet positif des MCP sur la régulation de la température à l'intérieur des bâtiments a été démontré. Cependant, parmi les articles analysés, très peu ont franchi l'étape de l'application des MCP à l'échelle du bâtiment ou de la paroi. Cette dernière étape est essentielle pour évaluer l'effet des MCP à une échelle réelle. Certaines zones d'incertitude subsistent, notamment le positionnement des MCP dans l'enveloppe du bâtiment et la température de fusion du MCP à choisir en fonction des conditions climatiques, même si de nombreuses études ont été menées sur cet aspect.

La littérature manque également d'études sur la stabilité des MCP dans les enveloppes de bâtiment à long terme et sur l'effet du vieillissement. Un aspect très important qui reste à investiguer est l'analyse du comportement hydrique des bâtiments incorporant des MCP, nécessaire pour l'évaluation de la qualité de l'air. Enfin, comme l'ont souligné Lamrani et al. [11], aucune étude ne prend en compte les charges internes et la présence des occupants ou leur comportement (utilisation réelle du bâtiment).

2.2 Modélisation et simulation numérique du comportement hygrothermique des enveloppes de bâtiments avec MCP

Les bâtiments sont soumis à diverses sollicitations externes et internes susceptibles d'affecter leurs performances énergétiques. Parmi ces sollicitations, la température et l'humidité jouent un rôle crucial et peuvent irrémédiablement affecter le confort des occupants et la qualité des ambiances. Pour évaluer l'impact des sollicitations sur les performances des bâtiments, une modélisation fine des phénomènes de transferts de chaleur, d'air et d'humidité est nécessaire. Pour comprendre et prédire ces comportements, les chercheurs ont développé plusieurs modèles, chacun adapté à des scénarios et des hypothèses spécifiques. Deux approches différentes sont utilisées pour décrire les transferts couplés de chaleur, d'air et d'humidité dans les matériaux poreux : les modèles nodaux et les modèles HAM (*Heat, Air and Moisture* en anglais).

L'approche nodale est une approche unidimensionnelle, employée dans les logiciels de simulation énergétique des bâtiments les plus courants, tels que TRNSYS, EnergyPlus [27]. Ces logiciels permettent la description des changements dynamiques de l'humidité relative et de la température intérieure qui se produisent en raison des variations du climat extérieur, des charges hygrothermiques internes et externes. À l'exception de Wufi, qui intègre un modèle d'humidité complet, la plupart des logiciels de simulation énergétique des bâtiments se concentrent principalement sur la simulation des variations de température et des besoins énergétiques dans les bâtiments. Par conséquent, dans ces outils, les modèles de transferts d'humidité à l'échelle des murs reposent sur une approche simplifiée qui ne tient pas compte du couplage des phénomènes de transferts de chaleur et d'humidité à travers l'enveloppe du bâtiment. Ainsi, aucun transfert d'humidité avec l'extérieur n'est modélisé dans ces logiciels. Par conséquent, le climat extérieur n'a aucun effet sur le transfert d'humidité à l'intérieur de

l'enveloppe du bâtiment dans les simulations numériques [28,29]. Cette limitation a conduit la communauté scientifique à développer des modèles entièrement couplés basés sur le principe de conservation (chaleur et masse).

Les modèles HAM offrent une approche plus complexe pour comprendre les transferts couplés de chaleur, d'air et d'humidité. Contrairement à l'approche nodale, les modèles HAM prennent en compte le transfert simultané de la chaleur, de l'air et de l'humidité dans les matériaux poreux. Ces modèles intègrent divers processus physiques tels que la conduction, la convection, la capillarité et la diffusion de la vapeur. L'un des principaux facteurs de différenciation de ces modèles est le choix des moteurs de transfert qu'ils prennent en compte. Le Tableau 3 présente un résumé des différents modèles en fonction du moteur de transport d'humidité utilisé.

Tableau 3. Synthèse des différents moteurs utilisés dans les modèles HAM.

Moteur de transport d'humidité	**Références**
Teneur en eau	[30], [31], [32], [33] [34] [35] [36,37] [38] [39] [40] [41] [42–44]
Humidité relative	[45], [46–51], [52–57], [58,59], [60]
Pression capillaire	[61,62], [63], [64], [65,66], [67]
Pression de vapeur	[68], [69], [70,71]

La validation des modèles de simulation des transferts hygrothermiques au sein d'éléments de parois peut se faire de différentes manières. Afin de s'assurer que les erreurs du modèle ne sont pas masquées par les incertitudes des données d'entrée ou des résultats des essais, une validation rigoureuse doit comporter trois étapes.

- La première étape est la confirmation de la mise en œuvre correcte des principes physiques fondamentaux par comparaison avec les solutions analytiques lorsque cela est possible. Pour l'absorption d'humidité dans une région semi-infinie, il existe un exemple de référence dans la norme BS EN 15026 (2007).

- La deuxième étape consiste à comparer les résultats des calculs à des essais en laboratoire avec des conditions limites et des données sur les matériaux bien définies.

- La troisième étape doit être proche de la réalité, par exemple en simulant le comportement hygrothermique transitoire d'un composant de l'enveloppe d'un bâtiment exposé au climat naturel.

Les MCP, du fait de leurs propriétés thermiques, améliorent significativement l'efficacité énergétique des bâtiments comme indiqué dans la section précédente. La modélisation des MCP est un axe de recherche clé. Il existe plusieurs approches pour étudier le changement de phase solide-liquide. Il s'agit notamment des méthodes basées sur l'enthalpie, de la méthode de la capacité thermique effective, des méthodes de suivi du front et des méthodes de maillages adaptatifs [72]. Les méthodes basées sur l'enthalpie et la capacité thermique sont les plus utilisées dans la littérature. De nombreuses études ont montré que les performances des bâtiments peuvent être améliorées en combinant les propriétés thermiques des MCP et l'aptitude de régulation de l'humidité des matériaux dits hygroscopiques.

En fonction de la technique d'incorporation, différentes méthodes sont utilisées dans la littérature pour intégrer numériquement les MCP dans les modèles de transfert de chaleur. La plupart des études dans la littérature ne considèrent pas les transferts couplés mais se concentrent uniquement sur les transferts de chaleur [73–78]. Seules quelques études sont rapportées sur les aspects de transfert de chaleur et de masse [79–83]. Bien que la littérature soit riche en caractérisations expérimentales du comportement hygrothermique des composites MCP/matériaux hygroscopiques, seules quelques-unes de ces solutions sont évaluées numériquement.

Cette deuxième analyse bibliographique (**article 2**) a mis en évidence le besoin de modèles numériques qui traitent du changement de phase et du comportement de l'humidité dans ces matériaux composites, capables de contrôler la température et l'humidité, car les études antérieures ignorent souvent les caractéristiques hygroscopiques. Il est donc nécessaire de développer des modèles numériques afin de simuler le comportement réel de ces matériaux prometteurs capables de contrôler à la fois la température et l'humidité.

2.3 Bilan

Suite à l’étude bibliographique nous avons identifié deux principaux verrous. Le premier porte sur l'absence d'application concrète des matériaux à changement de phase (MCP) à l'échelle du bâtiment ou d’une paroi, malgré des preuves expérimentales positives de leur efficacité dans la régulation thermique. Une piste envisagée pour lever ce verrou est le recours aux MCP à forme stabilisée utilisant des fibres végétales pour fabriquer des enveloppes du bâtiment durables et innovantes.

Le second, d’ordre numérique concerne le manque de modèles numériques spécifiques capables de traiter à la fois le changement de phase et le comportement hygroscopique des matériaux composites. Un des apports innovants de cette thèse serait donc de proposer un modèle numérique afin de simuler le comportement réel de ces matériaux prometteurs capables de contrôler à la fois la température et l'humidité.

3 Synthèse et caractérisation de bio-composites innovants

Cette partie est dédiée à la synthèse et la caractérisation de matériaux composites. Elle est divisée en quatre sections. La première est consacrée à la sélection du MCP et du matériau de support (fibres végétales) pour la fabrication de composites à formes stabilisées. La deuxième section décrit l'incorporation des formes stabilisées dans les matériaux de construction pour fabriquer du béton de chanvre à base de MCP. Les propriétés hygrothermiques de ce dernier ont été caractérisées grâce à une campagne expérimentale afin d'appréhender son comportement. La troisième section traite du développement de méthodes inverses pour estimer le coefficient de diffusion liquide du béton de chanvre à base de MCP. Dans la quatrième section, un spécimen à l'échelle de la paroi est fabriqué afin d'évaluer les performances hygrothermiques en conditions dynamiques réelles dans une chambre biclimatique.

3.1 Sélection des matériaux pour la fabrication de composites

La revue bibliographique expérimentale sur les techniques d'incorporation des MCP dans les enveloppes a permis d'identifier les fibres végétales qui serviront de matériaux de support pour la fabrication de composites à forme stabilisée. Dans cette section nous étayons la procédure suivie pour sélectionner les fibres végétales et MCP qui seront utilisés pour la fabrication de ces composites.

Pour ce faire, deux séries d'expériences sont menées successivement : la première vise à sélectionner le matériau support, ce qui permet d'étudier plusieurs types de fibres ; la seconde vise à sélectionner le MCP pour imprégner la microporosité de la fibre retenue après la première série d'expériences.

3.1.1 Sélection des fibres

Le logiciel de sélection des matériaux Ansys Granta® a été utilisé pour la sélection des fibres végétales. Ce logiciel est basé sur un ensemble de critères tels que les propriétés physico-chimiques, thermo-mécaniques et environnementales, les processus de fabrication et les coûts des matières premières. Le grand nombre de matériaux disponibles dans sa large base de données est un avantage considérable dans le processus de sélection. Dans cette étude, les fibres naturelles (Tableau 1) sont sélectionnées sur la base de quatre critères : (i) biosourcés, (ii) produits sur le continent européen, (iii) avec une forte absorption d'eau, une structure poreuse permettant un bon taux d'imprégnation et une bonne capacité de régulation de l'humidité et (iv) avec une faible conductivité thermique pour remplacer l'isolation conventionnelle dans les murs des bâtiments. Sur la base de ces critères, quatre fibres naturelles ont été présélectionnées (fibres de sapin, fibres de chanvre, chènevotte et paillis de lin, voir **article 3**).

Les fibres sélectionnées sont imprégnées de deux acides gras purs, l'acide caprique (CA) et l'acide laurique (LA), afin de comparer le taux d'imprégnation, un critère important dans la sélection du matériau support. Les deux acides gras sont choisis parce que leurs températures de fusion se situent dans la gamme de variation de la température des ambiances habitables (15-45°C). Ensuite, les fibres présentant les meilleurs taux d'imprégnation font l'objet d'une analyse de calorimétrie différentielle à balayage (*differential scanning calorimetry* – DSC) et thermogravimétrique afin de s'assurer qu'elles ne subissent pas de dégradation dans la plage de température des bâtiments.

Le processus d'imprégnation est utilisé et un protocole a été développé pour fabriquer des formes stabilisées fibres naturelles/MCP (**article 3**). Tout d'abord, les fibres végétales sélectionnées sont pesées et mélangées au MCP fondu. Le mélange est placé dans une étuve sous vide dont la température est fixée à 10°C au-dessus de la température de fusion la plus élevée de tous les MCP (i.e. 50°C pour la sélection des fibres et 80°C pour la sélection du MCP). Le MCP fondu est absorbé dans les micropores des fibres naturelles sous l'effet des forces de tension capillaire et superficielle. Après l'imprégnation, l'excès de MCP liquide est éliminé par filtration. La fraction massique d'incorporation du MCP dans les fibres naturelles est alors calculé. Un schéma synthétique du protocole d'imprégnation est présenté en Figure 1.

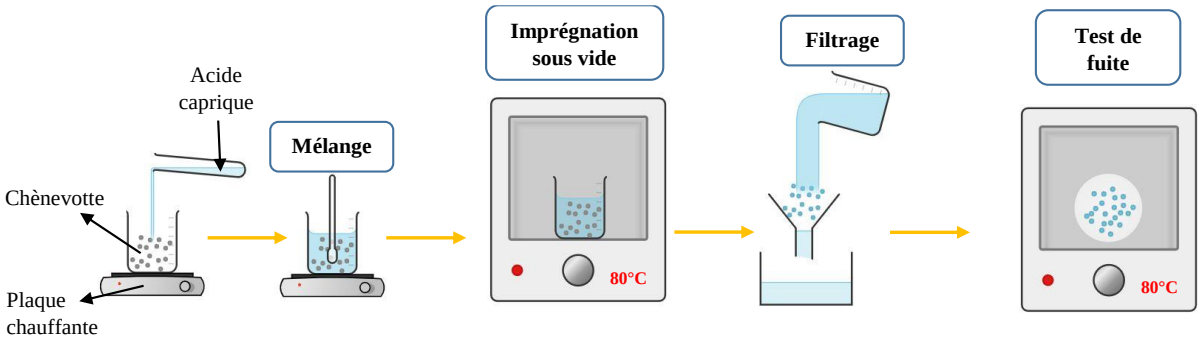

Figure 1. Protocole d'imprégnation sous vide de fibres végétales avec des MCP.

Le processus d'imprégnation dépend de plusieurs critères tels que le temps de séjour (durée du processus d'imprégnation) et les conditions d'imprégnation (sous vide ou pression atmosphérique). Afin de mettre en place un processus de sélection efficace, ces deux paramètres ont fait l'objet d'une étude visant à optimiser le protocole de synthèse des formes stabilisées.

Tout d'abord, les échantillons obtenus via les deux modes d'imprégnation (sous vide ou pression atmosphérique) sont soumis à 50 cycles thermiques réalisés en DSC dans une plage de températures entre 20 et 70°C (Figure 2). En effet, le bio-composite doit stocker et libérer de l'énergie sur une longue période sans fuite ni diminution des performances thermiques. Le test de cyclage thermique est important pour évaluer la stabilité à long terme du bio-composite, l'objectif étant qu'il soit intégré aux enveloppes de bâtiment et que sa durabilité soit assurée sur la durée de vie du bâtiment.

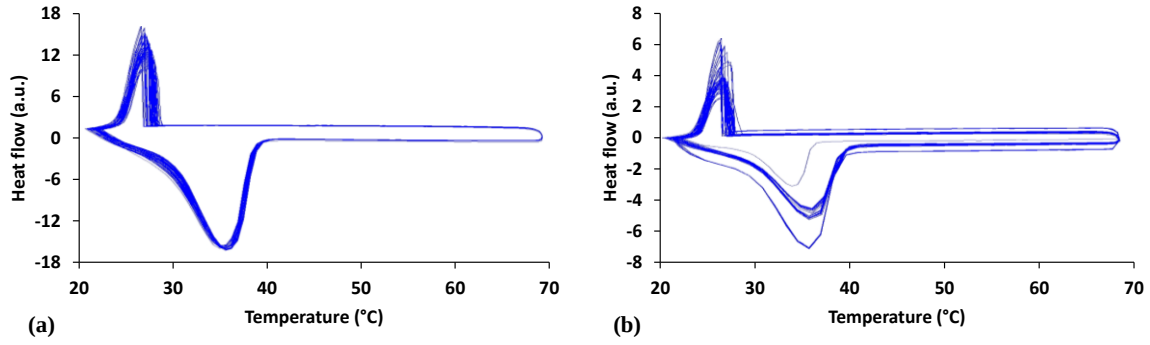

Figure 2. Thermogrammes obtenus par DSC obtenus pour les formes stabilisées chènevotte/acide caprique imprégnées sous-vide (a) et à pression atmosphérique (b) soumises à 50 cycles thermiques (plage de températures entre 20 et 70 °C)

Lorsque l'imprégnation est réalisée à pression atmosphérique (Figure 2.b), le MCP n'est pas absorbé à l'intérieur des nanopores. Par conséquent, il y a une fuite pendant la phase de chauffage, ce qui affecte les températures et enthalpies de changement de phase. Les thermogrammes obtenus par DSC avec les formes stabilisées imprégnées sous vide (Figure 2.a) présentent une quasi-parfaite superposition des 50 cycles, ce qui met en évidence leur stabilité au cours des cycles. Sur la base de ce résultat, tous les bio-composites dans la suite de cette étude ont été imprégnés sous vide avec un temps de séjour de 5 jours (temps de séjour optimal).

Afin de s'assurer de l'efficacité du processus d'imprégnation, les échantillons chènevotte/acide caprique à formes stabilisées ont été observés par microscopie électronique à balayage (MEB). Les images de la section transversale des formes stabilisées chènevotte/acide caprique obtenues par MEB sont présentées sur la Figure 3. D'après ces observations, nous constatons que l'acide caprique s'incorpore efficacement dans la microporosité des particules de chènevotte lors du processus d'imprégnation. Le protocole expérimental est donc validé et appliqué à tous les bio-composites, composés de fibres naturelles et de MCP biosourcés, étudiés par la suite.

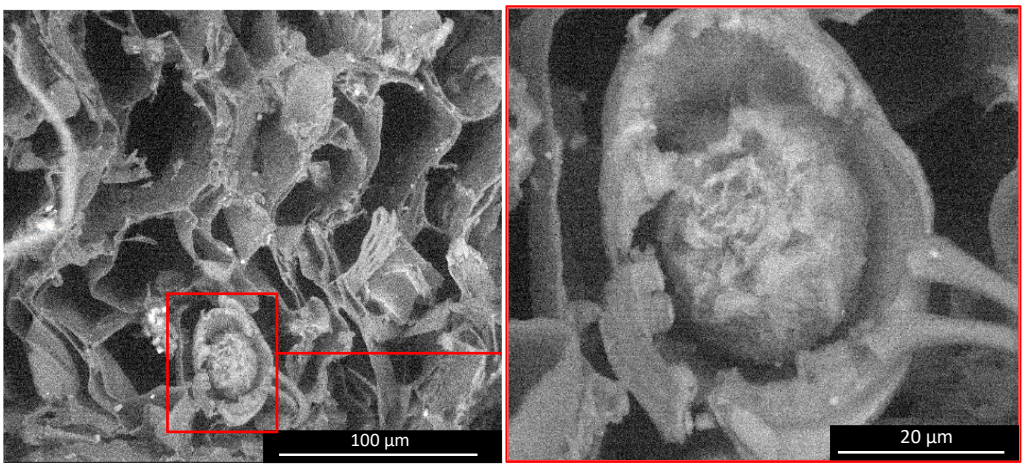

Figure 3. Observations MEB du composite chènevotte/acide caprique. Les images ont été réalisées par le Dr. Egle CONFORTO, responsable de la plateforme de microscopie électronique du laboratoire LaSIE La Rochelle Université.

Les meilleurs taux massique d'imprégnation sont obtenus pour la chènevotte et le paillis de lin avec un maximum de 50 wt% et 51 wt% respectivement pour les bio-composites chènevotte/acide laurique et paillis de lin/acide caprique alors que le taux d'imprégnation pour les fibres de chanvre et le sapin est beaucoup plus faible (entre 1 et 8 wt%). Ceci s'explique par la microstructure du matériau de support [84]. En effet, la porosité des matériaux tels que la chènevotte est très importante. Elle permet donc une meilleure imprégnation par rapport aux fibres dont la porosité est relativement faible. Cette dernière est sélectionnée comme matériau support en raison d'une application déjà effective dans les bâtiments (à travers le béton de chanvre), de sa masse volumique et de sa conductivité thermique (similaires à celles du paillis de lin même si légèrement plus élevées).

La chènevotte ou paille de chanvre est la partie bois de la tige du chanvre, essentiellement composée de cellulose. Elle est composée de canaux transportant la sève et l'air lorsque la tige est sèche. Elle a une densité très faible (environ 110 $kg.m^{-3}$), ce qui la rend très efficace en

thermique et en phonique. Elle s'utilise comme isolant, soit en vrac par déversement ou mélangée à de la chaux pour réaliser des bétons isolants notamment le béton de chanvre.

Une fois que nous avons choisi les fibres, démontré la faisabilité et validité du protocole, nous allons désormais procéder à des tests avec divers matériaux à changement de phase (MCP) pour déterminer celui qui offrira les meilleures performances dans le composite final pour l'application spécifique que nous visons.

3.1.2 Sélection du MCP

Après la sélection du matériau support, celui-ci (la chènevotte) a été imprégné avec 5 acides gras purs (acides caprique, laurique, palmitique, myristique et stéarique) et de 7 mélanges eutectiques (Tableau 2) afin de sélectionner le MCP approprié pour la fabrication d'un composite aux performances optimisées. Ces matériaux à changement de phase ont été choisis sur la base de deux critères : ils doivent être de nature biosourcée et posséder une température de fusion dans la gamme de variation de la température des ambiances habitables (15-45°C).

La valeur maximale du taux d'incorporation de MCP dans la chènevotte (50 wt%) est obtenue pour l'acide laurique et les mélanges eutectiques à base d'acide laurique. Ceci montre que la chènevotte a une meilleure affinité avec l'acide laurique qu'avec les autres acides gras. L'acide caprique, myristique et palmitique ont montré des comportements similaires avec des taux d'imprégnation de 48, 48 et 45 wt% respectivement. Le taux d'imprégnation le plus faible est obtenu pour l'acide stéarique avec une valeur de 40 wt%.

Les analyses thermogravimétriques des MCP seuls sont illustrées sur la Figure 4.a et celles des formes stabilisées chènevotte/MCP, sur la Figure 4.b. Cette dernière montre deux points d'inflexion correspondant à la température de dégradation de chaque composant du bio-composite (chènevotte et MCP). Les courbes de la Figure 4.a quant à elles présentent une seule chute de masse correspondant à la dégradation du MCP seul. Ce résultat indique que les MCP ont été imprégnés avec succès dans la chènevotte. De plus, la température de dégradation la plus basse est de 125°C, on peut affirmer que tous les bio-composites chènevotte/MCP sont stables jusqu'à 125°C et conviennent donc à une application dans les bâtiments.

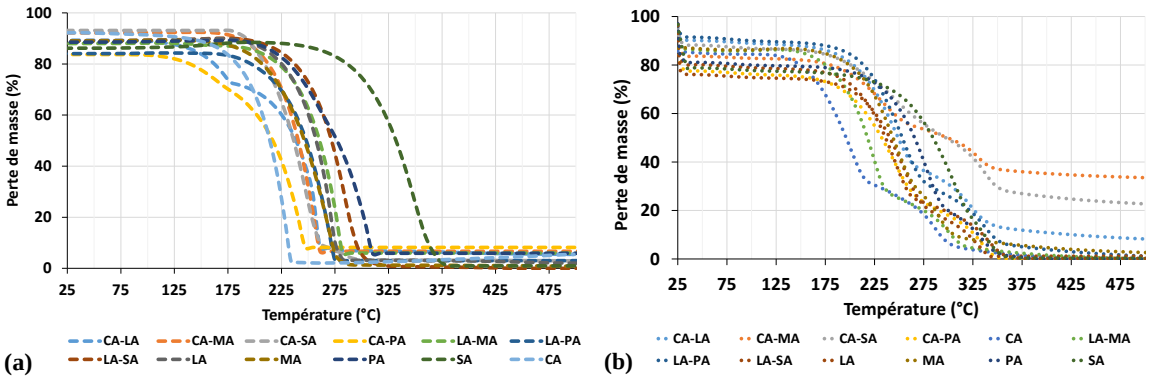

Figure 4. Courbes d'analyse thermogravimétrique des MCP seuls (a), et des composites chènevotte/MCP (b).

Outre le taux d'imprégnation, les propriétés de fusion et de solidification du bio-composite présentent un réel intérêt. Ces propriétés détermineront les performances thermiques de l'ensemble du système passif de stockage de l'énergie thermique, à savoir l'enveloppe du

bâtiment dans notre cas. Si un composite possède un taux d'imprégnation élevé mais une faible chaleur latente de fusion, il est clair qu'un autre composite avec un taux d'imprégnation plus faible mais une chaleur de fusion plus élevée sera préféré puisque nous nous intéressons aux propriétés thermiques des bio-composites. Par conséquent, les chaleurs latentes de fusion et de solidification des bio-composites sont représentées sur la Figure 5. Les enthalpies de fusion des bio-composites se situent entre 33,64 et 94,3 $J.g^{-1}$. Les enthalpies de solidification sont légèrement inférieures à celle de la fusion et se situent entre 24,5 et 93,7 $J.g^{-1}$. Les valeurs les plus élevées pour les deux quantités sont obtenues pour l'acide stéarique avec 94,29 et 93,7 $J.g^{-1}$ pour les chaleurs latentes de fusion et de solidification respectivement. Au contraire, les valeurs les plus basses sont obtenues pour l'eutectique acide caprique-acide stéarique avec 33,6 et 24,5 $J.g^{-1}$ pour la chaleur de fusion et la solidification respectivement. Comme on peut le constater, l'enthalpie de fusion et de solidification de tous les bio-composites est inférieure à celle des mélanges d'acides gras purs ou eutectiques. Cette diminution s'explique par la réduction de la part de masse du MCP au sein du bio-composite, ainsi qu'une baisse de la cristallinité du MCP.

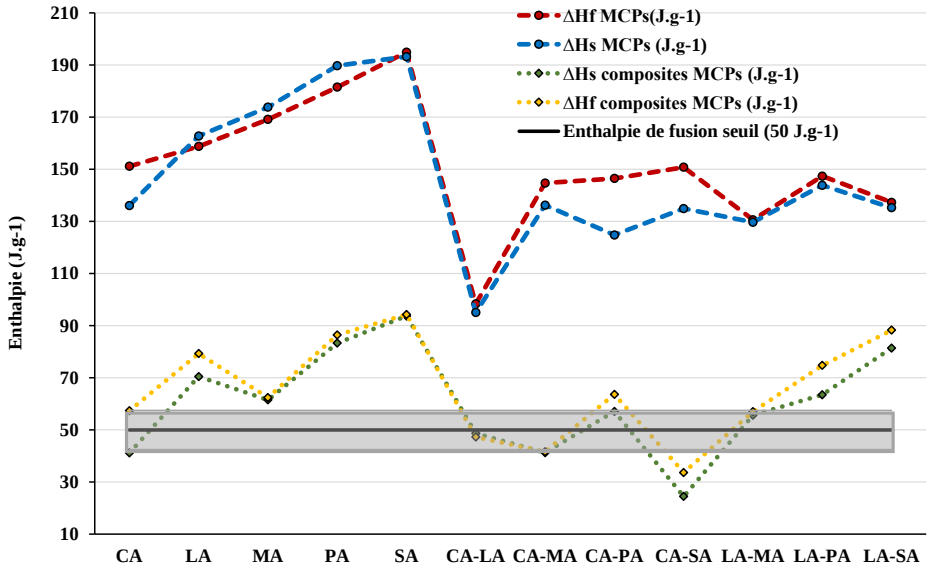

Figure 5. Enthalpies de fusion et de solidification des MCP purs et des bio-composites chènevotte/MCP.

Parmi les bio-composites, les formes stabilisées chènevotte/acide laurique et chènevotte/acide caprique constituent les meilleurs compromis en raison d'un taux d'imprégnation plus élevé (50 wt %) et d'enthalpies de fusion (79,3 et 57,37 $J.g^{-1}$ respectivement) et de solidification prometteuses (70,4 et 41,15 $J.g^{-1}$ respectivement). De plus, la température de fusion de ces composites se situe dans la gamme de température ciblée (entre 15 et 45°C) (Figure 6). Les températures de fusion/solidification et l'enthalpie de ces deux bio-composites sont très prometteuses pour le stockage passif de l'énergie thermique dans les bâtiments par rapport aux MCP composites à formes stabilisées étudiés dans la littérature (**article 3**).

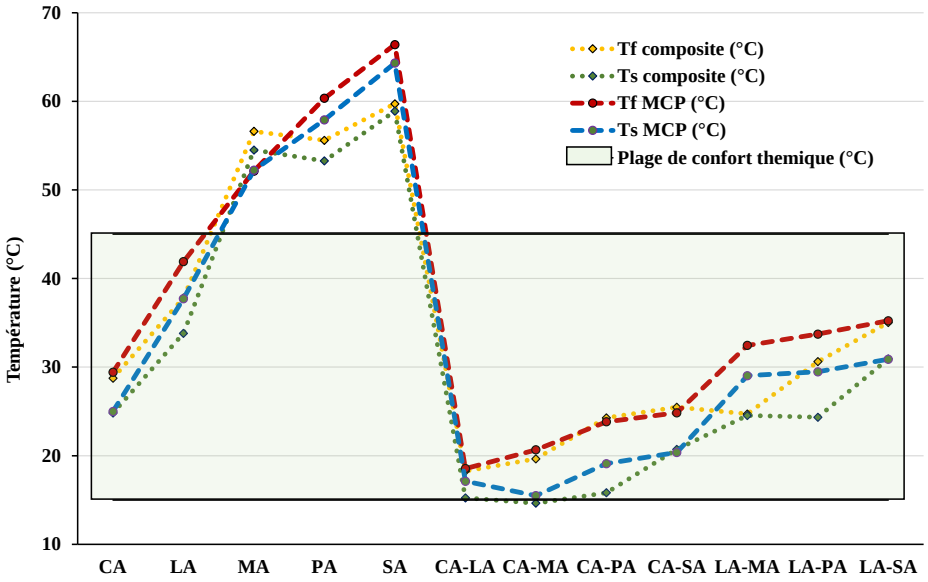

Figure 6. Températures de fusion et de solidification des MCP purs et des bio-composites chènevotte/MCP.

A l'issue de l'étape de sélection du matériau support et des MCP imprégnant la microporosité de ce dernier, les matériaux retenus doivent être caractérisés et comparés à un matériau de référence, matériau de construction conventionnel.

3.2 Caractérisation des matériaux

Du fait des performances intéressantes du bio-composite chènevotte/acide caprique à forme stabilisée pour une application dans les bâtiments et de la température de fusion de l'acide caprique inférieure à celle de l'acide laurique, ce bio-composite est utilisé pour fabriquer un béton de chanvre à base de MCP. La formulation du béton de chanvre consiste à mélanger 16 wt% de chènevotte, 34 wt% de chaux (Tradical® PF70) utilisée comme liant et 50 wt% d'eau. La chènevotte utilisée est le Chanvribat fourni par Ecohabitat (Matériaux Ecologiques pour l'Habitat, masse volumique moyenne d'environ 100 kg/m^3). En se référant à cette formulation, taux d'incorporation de 50 wt% dans la chènevotte correspond à une fraction massique de 14 wt% de MCP dans le bio-composite.

Une fois la synthèse de ce matériau réalisée, il est important d'évaluer ses performances thermiques et hydriques pour étudier la faisabilité d'une telle paroi et ses performances en tant qu'enveloppe du bâtiment. Des échantillons de béton de chanvre de référence (sans MCP) et intégrant des MCP (bio-composite avec de l'acide caprique piégé dans la microporosité de la chènevotte) ont été fabriqués afin d'évaluer et de comparer leurs propriétés hygrothermiques.

3.2.1 Conductivité thermique

La conductivité thermique des matériaux, notée λ, est mesurée à l'aide de l'appareil λ-Meter Ep500e® (Figure 7) à trois températures différentes : 10, 23 et 40°C. Son principe de mesure repose sur la méthode de la plaque chaude gardée selon la norme NFEN12664 [85] et NFEN12667 [86]. Les dimensions des échantillons sont de 15×15×5 cm^3 et les mesures sont effectuées pour le béton de chanvre de référence et le bio-composite. Pour chaque échantillon, les mesures sont effectuées trois fois pour vérifier leur répétabilité.

Figure 7. Dispositif λ-Meter Ep500e® utilisé pour la mesure de la conductivité thermique - LaSIE.

La conductivité thermique, est de 0,084, 0,088 et 0,094 $W.m^{-1}.K^{-1}$ pour le bio-composite contre 0,066, 0,07 et 0,075 $W.m^{-1}.K^{-1}$ pour le béton de chanvre de référence à 10, 23 et 40°C respectivement. Selon Arnaud et al [87], la conductivité thermique du béton de chanvre varie entre 0,06 et 0,18 $W.m^{-1}.K^{-1}$ pour une masse volumique sèche allant de 200 à 800 $kg.m^{-3}$, ce qui est en accord avec les valeurs mesurées dans cette étude. Comme on peut le constater, la conductivité thermique du béton de chanvre augmente avec l'ajout du MCP. En effet, des augmentations de conductivité thermique de 27%, 26% et 25% sont observées pour le bio-composite par rapport à la référence à 10, 23 et 40°C, respectivement. Ce résultat était attendu d'après l'état de l'art sur les MCP à forme stabilisée [88–92]. Cela s'explique par le fait que l'acide caprique a remplacé l'air dans la chènevotte (la conductivité thermique de l'acide caprique est 10 fois supérieure à celle de l'air). Malgré cette augmentation de la conductivité thermique due à l'incorporation du MCP, ces valeurs restent globalement basses et dans la gamme de celles des matériaux isolants biosourcés comme le béton de chanvre.

3.2.2 Capacité calorifique massique

La capacité calorifique massique, notée C_p, est une propriété exprimant la capacité d'un matériau à stocker de la chaleur. La connaissance de la capacité calorifique massique des matériaux est indispensable pour compléter la caractérisation thermique. Pour cela, le calorimètre Calvet a été utilisé conformément à la norme NF EN 821-3 [93]. Le calorimètre Calvet représenté sur la Figure 8 est un appareil différentiel. Il est équipé de deux thermopiles 3D qui entourent respectivement une cellule de mesure dans laquelle est placé un échantillon du matériau testé et une cellule de référence contenant un produit thermiquement inerte. Un échantillon plus grand donne des résultats plus précis, ce qui rend la méthode Calvet plus précise par rapport à l'équipement DSC traditionnel en raison d'un volume (8 cm^3) plus représentatif du matériau.

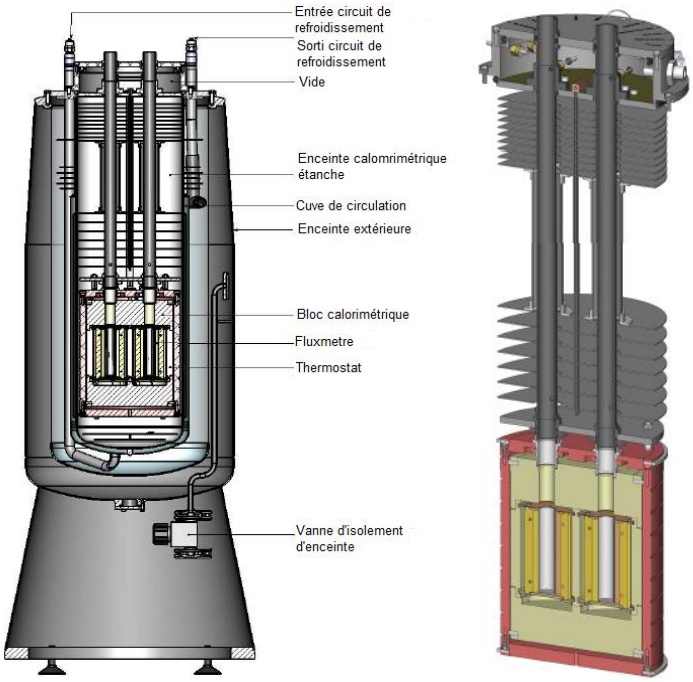

Figure 8. Calorimètre Calvet® utilisé pour la mesure de la capacité calorifique des matériaux - LaSIE.

Les mesures de capacité calorifique massique sont effectuées uniquement pour le béton de chanvre de référence et le MCP. La capacité calorifique massique du béton de chanvre varie entre 1000 et 1100 J.kg^{-1}.K^{-1} dans la plage de température considérée (0-45 °C). La capacité calorifique massique solide et liquide du MCP varient entre 2000 et 2500 J.kg^{-1}.K^{-1}. La capacité thermique du bio-composite est obtenue en combinant la capacité thermique du béton de chanvre et du MCP pur à l'aide de la méthode de la capacité thermique équivalente.

3.2.3 Masse volumique sèche

La masse volumique sèche apparente, notée ρ_s,du bio-composite et de la référence est mesurée sur des échantillons de dimensions 15x15x3 cm^3 à l'état sec (conditionnement pendant 14 jours dans étuve sous vide à 45 °C afin d'accélérer le processus de séchage). La masse et le volume des échantillons sont mesurés après la période de conditionnement et la masse volumique sèche est obtenue en divisant la masse de l'échantillon sec par le volume total (ρ_s=m/V). Les masses volumiques apparentes, de la référence et du bio-composite sont de 507,1±15,5 kg.m^{-3} et 582,2±15,5 kg.m^{-3} respectivement.

3.2.4 Capacité de tampon hydrique

Les propriétés hygroscopiques du béton de chanvre sont étudiées en mesurant la valeur tampon de l'humidité (MBV). Ce dernier est défini comme la capacité du matériau à réguler l'humidité. Par conséquent, le MBV quantifie la quantité d'humidité qu'un matériau peut stocker et libérer lorsqu'il est soumis à des variations cycliques de l'humidité relative environnante [94]. La mesure du MBV a été effectuée selon le protocole du projet Nordtest [95] : les échantillons de béton de chanvre de dimension 10×10×5 cm^3 sont initialement pré-conditionnés à 50% d'humidité relative et 23°C, puis exposés à des variations cycliques de l'humidité relative entre des valeurs élevées (75%) et basses (33%) pendant 8 et 16 heures respectivement jusqu'à stabilisation.

Les valeurs du MBV sont de 3,05 et 2,23 $g.m^{-2}.\%RH^{-1}$ pour la référence et le bio-composite respectivement, ce qui permet de les considérer comme d'excellents régulateurs d'humidité selon la classification du projet Nordtest.

3.2.5 Isothermes de sorption

L'isotherme de sorption détermine la capacité du matériau à stocker ou à libérer de l'eau en fonction de l'humidité relative de l'environnement extérieur à température constante. La détermination expérimentale de cette courbe est essentielle pour la prédiction du comportement hydrique des matériaux de construction poreux. Ce test indique la teneur en eau massique d'un matériau, notée w, en fonction de l'humidité relative. La mesure des isothermes de sorption du béton de chanvre de référence et du bio-composite a été effectuée à l'aide de l'analyseur de sorption de vapeur SPS de ProUmid GmbH (Figure 9), basé sur une méthode gravimétrique.

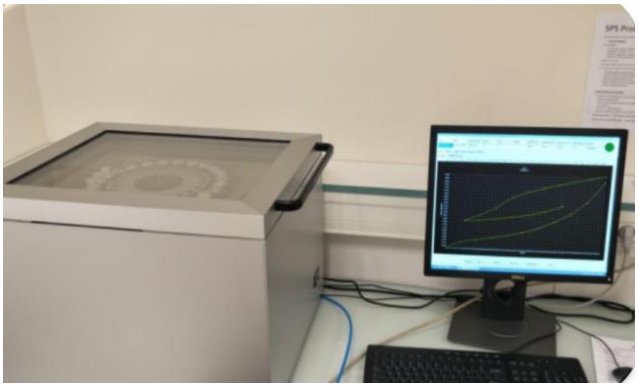

Figure 9. SPS ProUmid GmbH pour la mesure des isothermes de sorption - LaSIE.

Les isothermes de sorption du bio-composite MCP et de la référence sont mesurées entre 0 et 90% d'humidité relative. Le matériau de référence possède une teneur en eau plus élevée par rapport au bio-composite avec une valeur maximale de 14%. Cette diminution de la capacité d'adsorption est due à l'incorporation des MCP dans la chènevotte qui limite la disponibilité dans les pores pour l'adsorption de l'eau. Par la suite, les isothermes de sorption ont été modélisées par le modèle Guggenheim-Anderson-de Boer (GAB). Ce type de modélisation permet de construire des fonctions utilisées comme entrées dans les modèles hygrothermiques.

3.2.6 Capacité de stockage d'humidité

Les résultats des isothermes de sorption sont utilisés pour calculer la capacité de stockage de l'humidité, définie comme la pente des courbes d'isothermes de sorption ($C_m = \frac{\partial w}{\partial \varphi}$) obtenues avec la modélisation GAB. Cette dernière est un paramètre d'entrée important pour les modèles de transferts couplés de chaleur, d'air et d'humidité. Elle représente la capacité du matériau à adsorber et à libérer de l'humidité lorsque les conditions d'humidité de l'environnement changent. Sur la Figure 10, on observe que la capacité de stockage d'humidité de la référence est plus élevée que celle du bio-composite, ce qui est une conséquence directe des courbes isothermes. La diminution observée de la capacité d'adsorption de la vapeur d'eau du matériau composite peut réduire ses propriétés hydriques (pouvoir tampon hydrique et perméabilité à la vapeur d'eau) ainsi que ses propriétés thermiques (conductivité thermique et Capacité calorifique massique). Cette diminution de la capacité d'absorption pour le bio-composite MCP entraine une réduction de la capacité de régulation d'humidité par rapport au matériau de

référence. Malgré cette réduction, le bio-composite MCP demeure toujours un excellent régulateur d'humidité (selon la classification du protocole Nordtest).

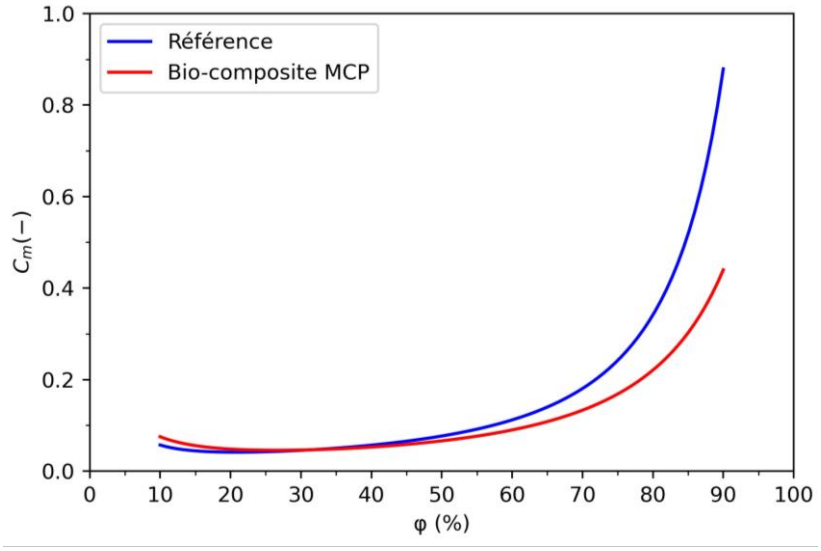

Figure 10. Capacité de stockage d'humidité du bio-composite MCP et du béton de chanvre de référence.

3.2.7 Perméabilité à la vapeur

Le coefficient de perméabilité à la vapeur d'eau, notée δ_v, est déterminé par la méthode des coupelles décrite dans la norme NF EN ISO 12572 [96] à l'aide du GINTRONIC® Gravitest 6400 (Figure 11). Cet appareil est constitué d'une chambre climatique avec 6 coupelles et d'une pesée automatique. Un gradient de pression de vapeur est appliqué entre les deux faces de l'échantillon. Ce gradient est assuré en appliquant deux humidités différentes (φ=3% à l'intérieur de la coupelle et φ=50% dans l'ambiance de la chambre climatique). La variation de la masse de l'échantillon (m) est surveillée jusqu'à l'état d'équilibre (flux de vapeur constant à travers l'échantillon et équilibre de masse). Une fois stabilisé, le flux de vapeur d'eau est calculé. Le test est effectué sur trois échantillons cylindriques de 8 cm de diamètre et de 2 cm d'épaisseur.

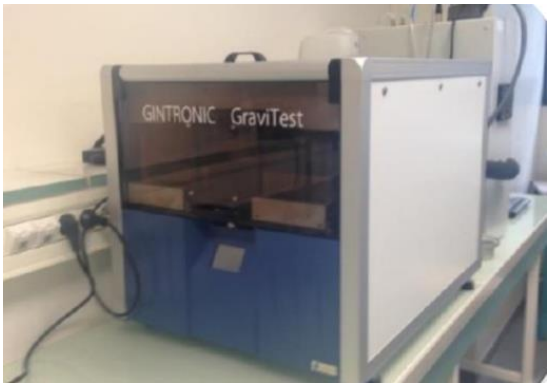

Figure 11. Dispositif GINTRONIC® Gravitest 6400 pour la mesure de la perméabilité à la vapeur - LaSIE.

La perméabilité à la vapeur d'eau du bio-composite et de la référence sont respectivement de $(1{,}8\pm0{,}2)\cdot10^{-11}$ [$Kg.m^{-1}.Pa^{-1}.s^{-1}$] et de $(2{,}7\pm0{,}062)\cdot10^{-11}$ [$Kg.m^{-1}.Pa^{-1}.s^{-1}$]. On observe une diminution de la perméabilité à la vapeur d'eau du matériau avec l'incorporation du MCP dans la microporosité de chènevotte. Ce résultat, similaire à celui observé avec la mesure du MBV,

est dû à la réduction de l'absorption d'eau dans la chènevotte avec l'incorporation de MCP. La valeur de la perméabilité à la vapeur d'eau de la référence est cohérente avec celle trouvée dans la littérature. Cependant, la perméabilité liquide dont la détermination expérimentale est délicate fera l'objet d'une estimation par méthodes inverses.

3.3 Estimation des propriétés hydriques à l'aide de méthodes inverses

Lorsque toutes les propriétés hygrothermiques d'un matériau et les conditions aux limites sont connues et utilisées comme données d'entrée d'un modèle dont les équations permettent de simuler le comportement hygrothermique du matériau, le problème étudié est dit problème direct.

A l'inverse, dans le cas où certaines propriétés ne sont pas connues en amont de la modélisation, autrement dit quand certaines données d'entrées sont manquantes, des méthodes inverses dont la formulation classique est un problème de minimisation entre des données expérimentales (profil d'humidité relative pour estimer les propriétés hydriques inconnues du matériau) et une loi de comportement permettent d'estimer ces données manquantes. Dans ce cas, le problème est dit inverse.

Le coefficient de diffusion de l'eau liquide est une grandeur qui exprime la capacité d'un milieu poreux à transmettre un fluide sous l'effet d'un gradient de pression capillaire (loi de Darcy). Dans les équations couplées de transfert de chaleur et de masse, cette grandeur est à l'origine du couplage entre flux de chaleur et flux d'humidité. Pour les matériaux de construction poreux, il n'existe pas de dispositif permettant de mesurer le coefficient de diffusivité de l'eau liquide. Cette dernière est généralement estimée par des méthodes inverses [97–99]. La détermination de cette propriété hydrique est un verrou important à lever pour améliorer la prédiction des modèles hygrothermiques. A cet effet, une méthode inverse a été développée afin d'identifier le coefficient de diffusion de l'eau liquide du bio-composite et du béton de chanvre de référence (**article 6**). En plus de cette propriété, il faut également souligner que le coefficient de diffusion de la vapeur d'eau est mesurée pour une humidité relative donnée. La méthode inverse développée permet également de déterminer l'évolution de cette propriété en fonction de l'humidité relative. En rappel, il est possible de lier les coefficients de diffusion de l'eau liquide et de la vapeur aux coefficients de perméabilités correspondants grâce aux équations 1 et 2.

$$D_v = \delta_v \, p_{v,sat} \tag{1}$$

$$D_l = k_l \frac{RT\rho_l}{M\varphi} \tag{2}$$

avec δ_v et k_l la perméabilité à la vapeur et à l'eau liquide en kg.m^{-1}.s^{-1}.Pa^{-1}, respectivement. D_v et D_l les coefficients de diffusion de la vapeur et du liquide en kg.m^{-1}.s^{-1}, respectivement. R [J.mol^{-1}.K^{-1}] la constante des gaz parfaits, ρ_l [kg.m^{-3}] la masse volumique de l'eau liquide et M [g.mol^{-1}] la masse molaire de l'eau.

3.3.1 Problème direct

Les coefficients de diffusivité liquide et vapeur étant des propriétés purement hydriques nous considérons un problème direct simplifié ne considérant que les transferts hydriques. Pour se placer dans cette configuration, les essais sont réalisés en conditions isothermes (T=23°C) afin de s'affranchir de l'effet de la température.

Le problème direct (équation 1) est décrit par l'équation de transfert de masse unidirectionnel (1D) isotherme définie par la loi de Fick pour la diffusion de la vapeur et la loi de Darcy pour la diffusion du liquide (équation 3). L'humidité relative est considérée comme le moteur du transfert.

$$\rho_s C_m(\varphi)\frac{\partial \varphi}{\partial t} = div((D_v(\varphi) + D_l(\varphi))\nabla\varphi) \quad (3)$$

Afin de résoudre le problème direct, l'équation 1 est discrétisée (différences finies pour la discrétisation spatiale et schéma implicite pour le terme temporel). Le système d'équations algébriques obtenu est résolu à l'aide d'un code que j'ai développé sous python. Ce code est basé sur l'algorithme de matrice tri diagonale de Thomas "TDMA" afin de réaliser l'intégration temporelle.

Afin de s'assurer de la validité du code avant de l'utiliser pour estimer les paramètres, ses résultats sont comparés à ceux obtenus de la solution analytique du HAMSTAD Benchmark [100]. L'écart maximal entre la solution analytique et simulée est de l'ordre de 4%, ce qui a permis de valider le code numérique pour la résolution du problème direct et de mettre en place la méthode inverse proposée.

3.3.2 Problème inverse

Le problème inverse consiste à identifier les paramètres $\boldsymbol{p^{est}}$, à partir des paramètres a priori $\boldsymbol{p^0}$, en minimisant la différence entre les données expérimentales $\boldsymbol{\varphi}^{\boldsymbol{obs}}$ et les valeurs numériques estimées grâce au problème direct.

Le problème d'optimisation à résoudre s'écrit selon l'équation 4 :

$$\min_{p \in \Omega_p} J(x,t,p) \quad (4)$$

avec $J(x,t,p) = \left\|\varphi(x,t,p) - \varphi^{obs}\right\|^2$ est la fonction objectif à minimiser, définie comme la somme des erreurs quadratiques entre les mesures expérimentales et les valeurs estimées. Les paramètres de minimisation sont ajustés de manière à ce que l'écart entre les résultats expérimentaux et simulés soit le plus faible possible (équation 5) :

$$p^{est} = \arg\min_{p \in \Omega_p} J(x,t,p) \quad (5)$$

L'optimisation de la fonction objectif est réalisée sous python à l'aide d'un algorithme basé sur la méthode Nelder-Mead [101]. La stratégie d'estimation de paramètres est illustrée sur la Figure 12.

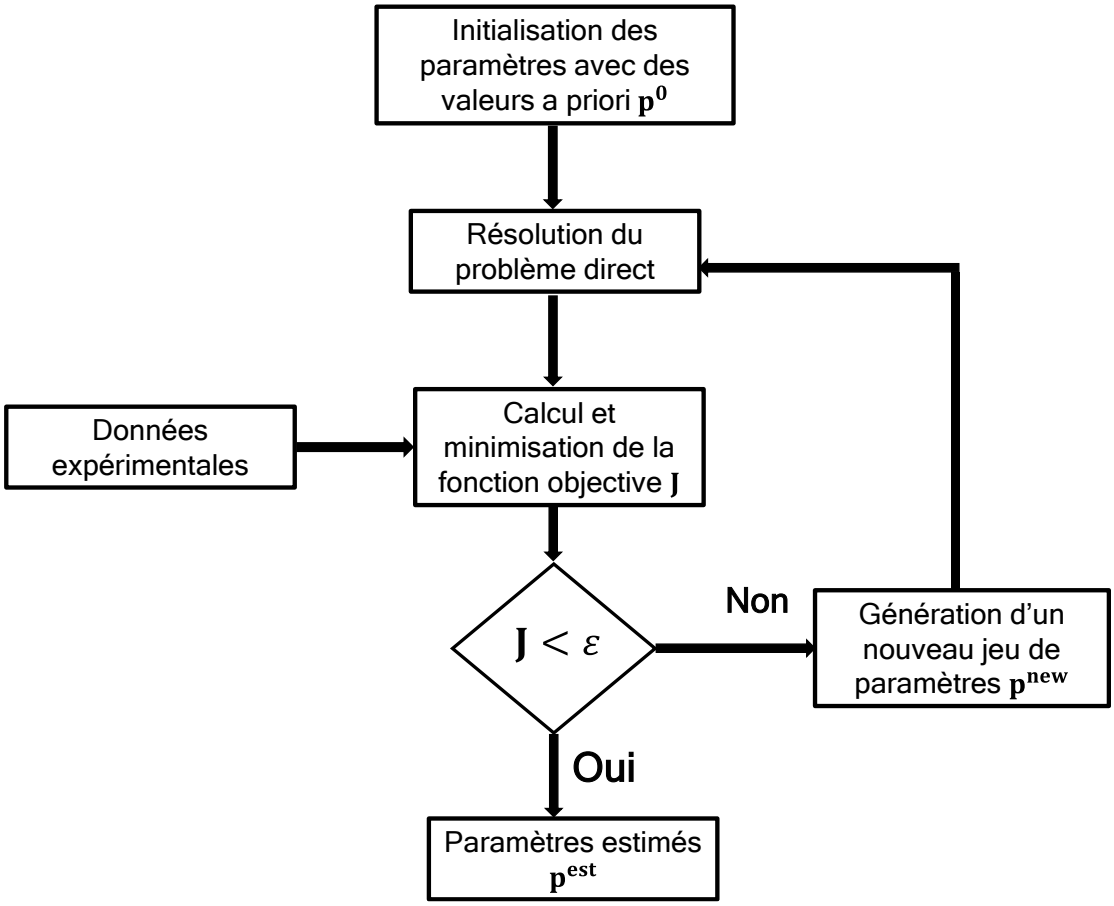

Figure 12. Stratégie de minimisation pour l'estimation des paramètres.

Les coefficients de diffusion de l'eau liquide et de la vapeur d'eau sont modélisés comme des fonctions exponentielles avec quatre paramètres **p** {D_{v0}, D_{l0}, a et b}. Cette hypothèse d'évolution exponentielle se base sur les travaux de la littérature qui montrent une tendance exponentielle pour ces deux propriétés [97,98,102,103].

$$\begin{cases} D_v(\varphi) = D_{v0} * e^{a*\varphi} \\ D_l(\varphi) = D_{l0} * e^{b*\varphi} \end{cases} \quad (6)$$

avec D_{v0} [kg.m^{-1}.s^{-1}], D_{l0} [kg.m^{-1}.s^{-1}], a, b (sans unités) les paramètres à estimer par minimisation de la fonction objectif.

Les valeurs de la perméabilité à la vapeur mesurée pour le matériau de référence et le bio-composite dans la section 3.2.7 par la méthode de la coupelle sont utilisées pour initialisation des paramètres à estimer. De plus nous faisons l'hypothèse que les coefficients de diffusion liquide et vapeur sont du même ordre de grandeur. Ainsi, les valeurs a priori sont : $\mathrm{D_{v0}} = 10^{-6}\ \mathrm{kg.m^{-1}.s^{-1}}$, $D_{l0} = 10^{-6}\ \mathrm{kg.m^{-1}.s^{-1}}$, a et b sont choisis de manière arbitraire (a = 1, b = 1).

3.3.3 Campagne expérimentale

Pour chaque matériau, deux échantillons cylindriques de 8 cm de diamètre et 20 cm de hauteur sont fabriqués. Les échantillons sont entourés d'une feuille d'aluminium étanche à l'humidité afin de les isoler. Une face circulaire est laissée libre afin d'obtenir des conditions de transfert de masse unidirectionnel. Afin d'éviter les contraintes liées aux conditions aux limites, l'ensemble

du domaine ne sera pas pris en compte dans les simulations. Un retrait de 2,5 cm sera effectué sur chaque bord. Le domaine considéré dans les simulations fait 15 cm de long. Par conséquent, quatre capteurs de température et d'humidité relative, de la marque Ahlborn et de type FHA 646 R (±2% d'incertitude sur la mesure de l'humidité relative), sont placés à l'intérieur de chaque échantillon à différentes positions : 0 cm, 5 cm, 10 cm et 15 cm. Les capteurs placés à 0 cm et 15 cm seront considérés comme les conditions limites gauche et droite.

Les échantillons sont placés dans une chambre climatique Excal 2211-HA de Climats (Figure 13) soumise à un programme d'humidité variant de 10 % à 90 % et à une température constante de 23 °C. La durée totale du test est de 18 jours. Ce cas est présenté comme une étude de cas des transferts hydriques en régime instationnaire et permettra l'identification des paramètres des coefficients de diffusivité liquide et vapeur.

(a) (b)

Figure 13. Dispositif expérimental pour l'étude de cas de transferts hydriques en régime instationnaire : (a) enceinte climatique Excal 2211-HA de climats, (b) échantillons (référence et bio-composite MCP) cylindriques (8 cm de diamètre et 20 cm de hauteur) avec faces isolées et emplacement des capteurs.

La comparaison des courbes expérimentales, incluant les incertitudes de mesure, avec les simulations numériques réalisées avec les paramètres optimisés (Tableau 4) montre un bon accord qui justifie l'efficacité de la procédure d'estimation (Figure 14.a-b)). En effet, pour une profondeur de 5 cm, l'erreur quadratique moyenne est de 2.64% et 0.016% pour le matériau de référence et le bio-composite MCP, respectivement. A 10 cm de profondeur, l'erreur quadratique moyenne entre données expérimentales et simulées est de 3,47% et 0.035% pour le matériau de référence et le bio-composite MCP, respectivement.

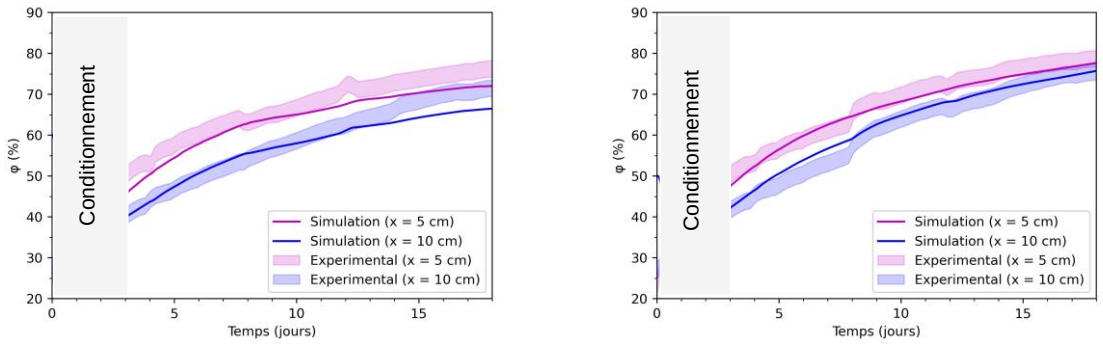

(a) (b)

Figure 14. Comparaison entre les courbes expérimentales et numériques pour chaque matériau à x= 5 cm et x=10 cm : échantillon de référence (béton de chanvre) (a) et échantillon testé (bio-composite) (b).

En général, l'estimation est plus précise sur le capteur placé à x = 5 cm que sur celui placé à x = 10 cm, comme en témoignent par les valeurs plus faible d'erreur quadratique moyenne. De plus, la précision est meilleure pour le bio-composite. Cela peut s'expliquer par le fait que le profil d'humidité à l'intérieur est mieux décrit par une loi exponentielle.

Tableau 4. Paramètres de la diffusivité vapeur et liquide issus de la minimisation.

	D_{v0} [kg.m^{-1}.s^{-1}]	a	D_{l0} [kg.m^{-1}.s^{-1}]	b
Référence	1,2733·10^{-6}	-4,1899	5,7893·10^{-9}	8,1002
Bio-composite	1,2998·10^{-6}	-4,3631	7,5511·10^{-8}	4,7225

Les Figure 15.a et Figure 15b présentent les courbes de diffusivité de la vapeur et du liquide obtenues par les méthodes inverses. On remarque que la courbe de diffusivité de la vapeur diminue avec l'humidité relative alors que la courbe de diffusivité du liquide augmente avec l'humidité (a<0). Les coefficients de diffusivité de vapeur des deux matériaux sont très proches. La valeur maximale, de l'ordre de 10^{-6}, est atteinte pour les faibles humidités avant de diminuer lorsque l'humidité augmente.

La tendance inverse est observée pour le coefficient de diffusion liquide, qui augmente avec l'humidité relative (b>0). La valeur du coefficient de diffusivité liquide est plus élevée pour la référence par rapport aux bio-composites.

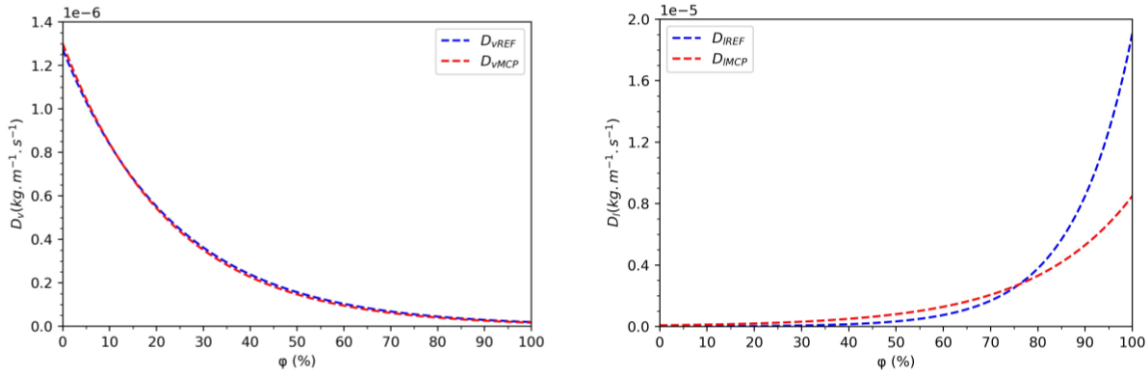

(a) (b)

Figure 15. Coefficients de diffusivité de la vapeur d'eau (a) et de l'eau liquide (b) pour chaque matériau, obtenus à partir des paramètres estimés.

Enfin, la courbe de diffusivité de la vapeur est comparée aux données extraites de la littérature sur la caractérisation du béton de chanvre (Figure 16). La courbe obtenue par la méthode inverse reproduit assez bien les résultats de la littérature.

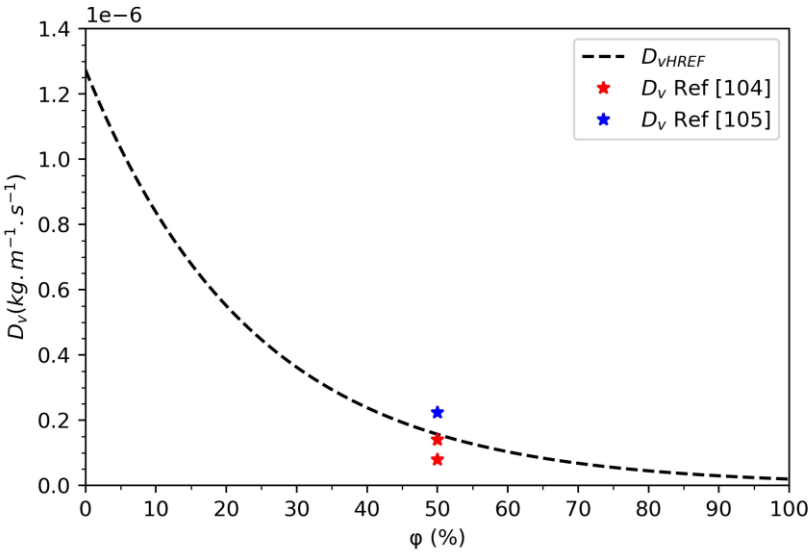

Figure 16. Comparaison entre la diffusivité de la vapeur estimée et la littérature [104,105].

La méthode développée dans cette section a permis d'estimer les coefficients de diffusion liquide et vapeur afin de compléter la campagne de caractérisation. Toutes les propriétés hygrothermiques du matériau de référence et du bio-composite MCP sont récapitulées dans le Tableau 5 (**articles 4 et 5**).

Tableau 5. Expression des propriétés hygrothermiques du bio-composite et du béton de chanvre de référence.

Paramètres	Expressions
u [%]	$\frac{m \cdot C \cdot K \cdot \varphi}{(1-K\varphi) * (1-K\phi+KC\varphi)}$ où : $\begin{cases} m = 0{,}02245, C = 54{,}0309 \text{ et } K = 0{,}93899 \text{ (REF)} \\ m = 0{,}02227, C = 20{,}9271 \text{ et } K = 0{,}87663 \text{ (Bio}-\text{composite)} \end{cases}$
C_m [−]	$\frac{\partial w}{\partial \varphi}$
λ [W.m^{-1}.K^{-1}]	$\begin{cases} 0{,}0003 \cdot T + 0{,}063 \ (REF) \\ 0{,}0004 \cdot T + 0{,}0805 \text{ (Bio}-\text{composite MCP)} \end{cases}$
D_v [Kg.m^{-1}.s^{-1}]	$D_{v0} * e^{a*\varphi}$ où : $\begin{cases} D_{v0} = 1{,}2733 \cdot 10^{-6}\ ;\ a = -4{,}1899 \text{ (REF)} \\ D_{v0} = 1{,}2998 \cdot 10^{-6}\ ;\ a = -4{,}3631 \text{ (Bio}-\text{composite)} \end{cases}$
$C_{p,s}$ [J. kg^{-1}.K^{-1}]	$\begin{cases} 1000 - 1100 \text{ (REF)} \\ 1200 - 4500 \text{ (Bio}-\text{composite MCP)} \end{cases}$
ρ_s [kg.m^{-3}]	507,1 (REF) 582.2 (Bio − composite MCP)
L_v [J.kg^{-1}]	$2{,}44 \cdot 10^6$
D_l [Kg.m^{-1}.s^{-1}]	$D_{l0} * e^{b*\varphi}$ où : $\begin{cases} K_{l0} = 5{,}7893 \cdot 10^{-9}\ ;\ b = 8{,}1002 \text{ (REF)} \\ K_{l0} = 7{,}5511 \cdot 10^{-8}\ ;\ b = 4{,}7225 \text{ (Bio}-\text{composite)} \end{cases}$

La masse volumique et la capacité thermique du bio-composite sont plus élevées que celles du matériau de référence. Par conséquent, le bio-composite a une inertie thermique plus élevée que la référence. Il est également important de souligner l'inertie supplémentaire apportée par le changement de phase. Ainsi, les enveloppes incorporant le bio-composite présenteraient une

inertie thermique plus importante que celles avec le matériau de référence. Cette comparaison approfondie des propriétés et des performances entre le matériau de référence et le bio-composite MCP proposé révèle que ce dernier est compétitif et prometteur une application effective dans les bâtiments.

Les matériaux étant complètement caractérisés, il est essentiel d'évaluer leurs performances hygrothermiques à une échelle plus grande, notamment l'échelle de la paroi.

3.4 Evaluation des performances hygrothermiques à l'échelle de la paroi

Dans la section précédente, le bio-composite développé a montré des propriétés prometteuses pour une application dans les enveloppes des bâtiments. Afin de poursuivre l'étude, nous proposons dans cette sous-section d'évaluer et de comparer les performances hygrothermiques du bio-composite avec celles de la référence à l'échelle de la paroi. Une paroi en béton de chanvre (Figure 17.a), construite dans le cadre d'une étude précédente portant sur l'effet d'hystérésis dans le béton de chanvre ([106]), est utilisée comme paroi de référence dans cette étude. Le protocole de fabrication de la paroi ayant fait ses preuves ([106]), il sera appliqué pour la fabrication de la paroi à tester, intégrant le bio-composite (Figure 17.b). Les dimensions de ces deux parois sont identiques et ajustées (90 x 90 x 10 cm^3) pour qu'elles puissent être insérées dans une enceinte biclimatique composée d'une chambre C-40/1000/S et d'une chambre C-20/1000/S de CTS GmbH. Les performances hygrothermiques de ces deux parois, soumises à des conditions climatiques dynamiques identiques grâce à l'utilisation de l'enceinte biclimatique, sont investiguées et comparées.

(a) (b)

Figure 17. Parois isolantes de 90 x 90 x 10 cm^3 : Paroi de référence (Béton de chanvre) (a) et Paroi testée (bio-composite) (b).

La conception de l'enceinte climatique permet de réaliser des parois dans des conditions de transfert de chaleur et de masse unidirectionnel. A cet effet, afin d'assurer un transfert unidirectionnel de chaleur et d'humidité, les faces latérales des deux parois sont recouvertes d'une feuille d'aluminium. Afin d'évaluer et de comparer leurs performances thermiques et hydriques respectives, des capteurs de température et d'humidité relative de type Ahlborn FHA 646 R ont été placés à différentes profondeurs dans les parois : 2,5, 5 et 7,5 cm et sur les deux faces (interne et externe) en suivant la même configuration (proposée dans ([106]). Un capteur de flux de chaleur est également placé sur les deux faces de la paroi. Douze capteurs sont

placés à quatre endroits différents (Figure 18) afin de vérifier l'hypothèse d'un transfert unidirectionnel et de calculer l'incertitude des mesures.

Après instrumentation, les parois sont placées entre les deux compartiments de l'enceinte biclimatique afin d'évaluer les performances hygrothermiques. Les deux chambres de l'enceinte ont un volume d'essai d'environ 1 m^3.

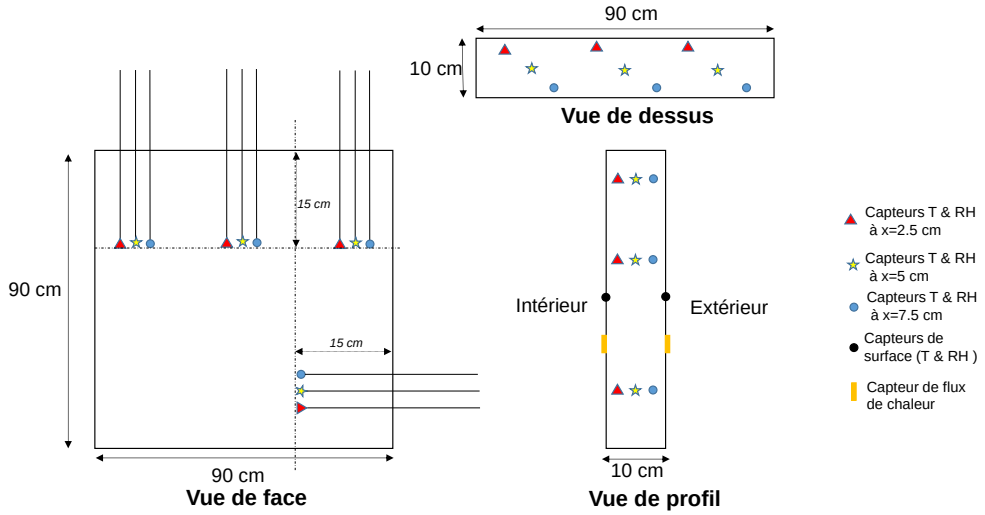

Figure 18. Position des capteurs de température, des capteurs d'humidité relative et des capteurs de flux de chaleur.

Le comportement hygrothermique des deux matériaux est évalué dans différentes conditions climatiques selon quatre scenarii (Figure 19) après une phase de conditionnement [0-3 jours] : conditions statiques estivales (40°C, 10% d'humidité relative [3-10 jours]) et hivernale (10°C, 90% d'humidité relative [10-17 jours]), journée d'été typique (température allant de 18 à 40°C et une humidité relative variant de 80 à 40% [17-24 jours]) et journée d'hiver typique (température allant de -2 à 12°C et une humidité relative en entre 50% et une condition libre 24-31 jours]).

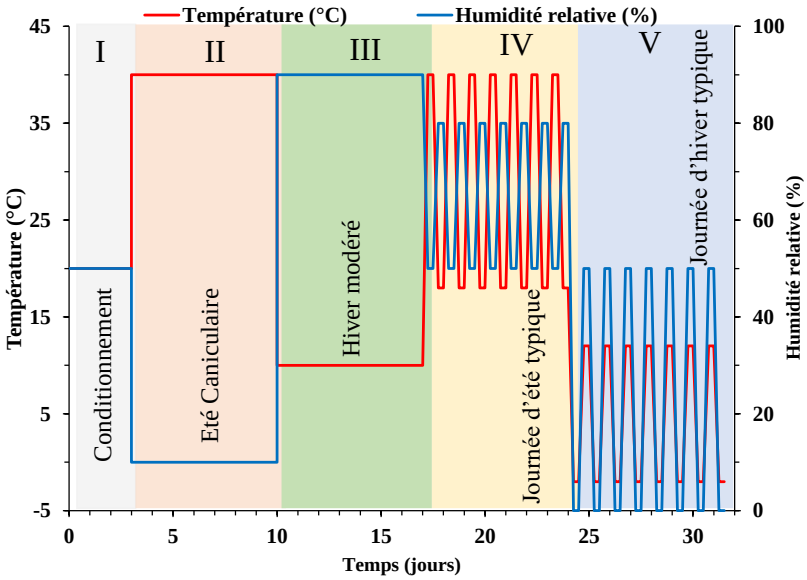

Figure 19. Programme de température et d'humidité relative pour le test hygrothermique en enceinte climatique.

Les Figure 20 et Figure 21 représentent l'évolution de la température et de l'humidité relative à l'intérieur du bio-composite et de la référence à des profondeurs de 2,5 (a), 5 (b) et 7,5 (c) cm, respectivement.

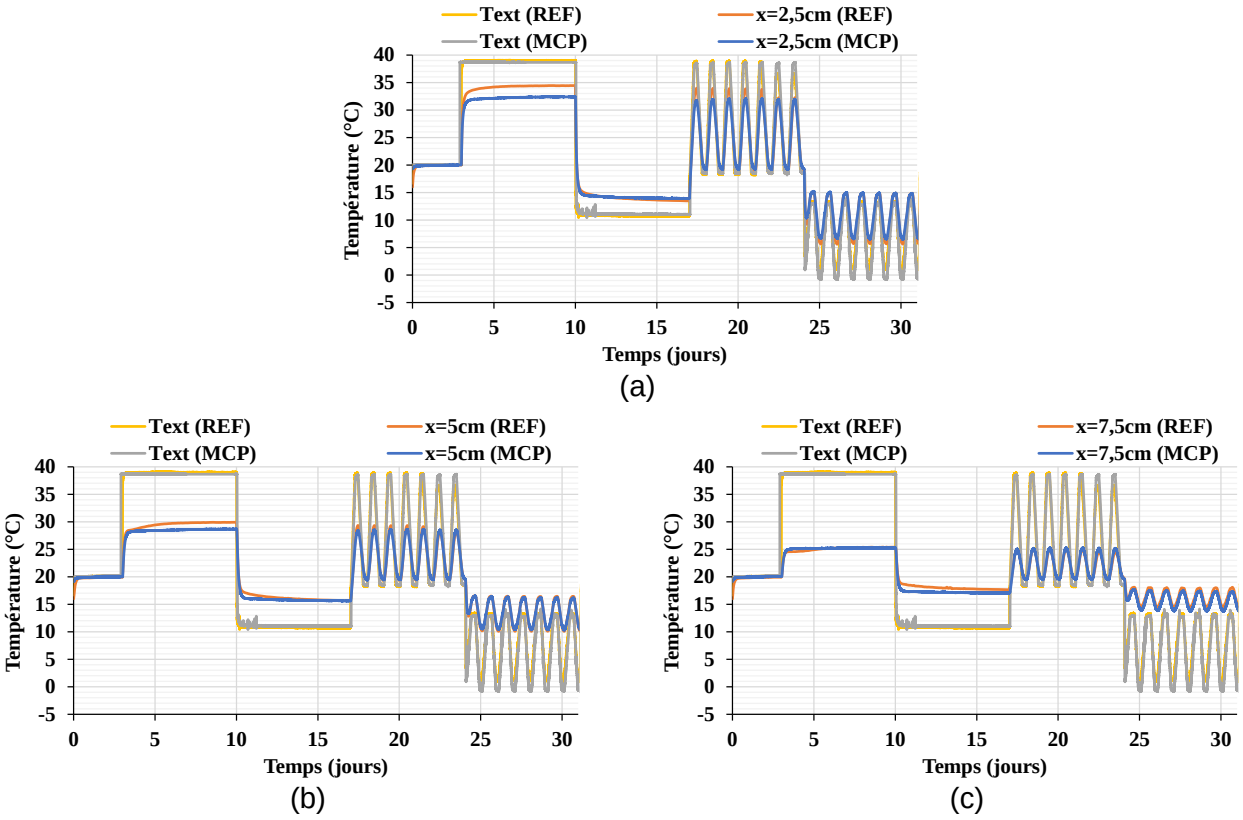

Figure 20. Évolution de la température pour le matériau de référence et le bio-composite MCP à x=2,5 cm (a), 5 cm (b), 7,5 cm (c).

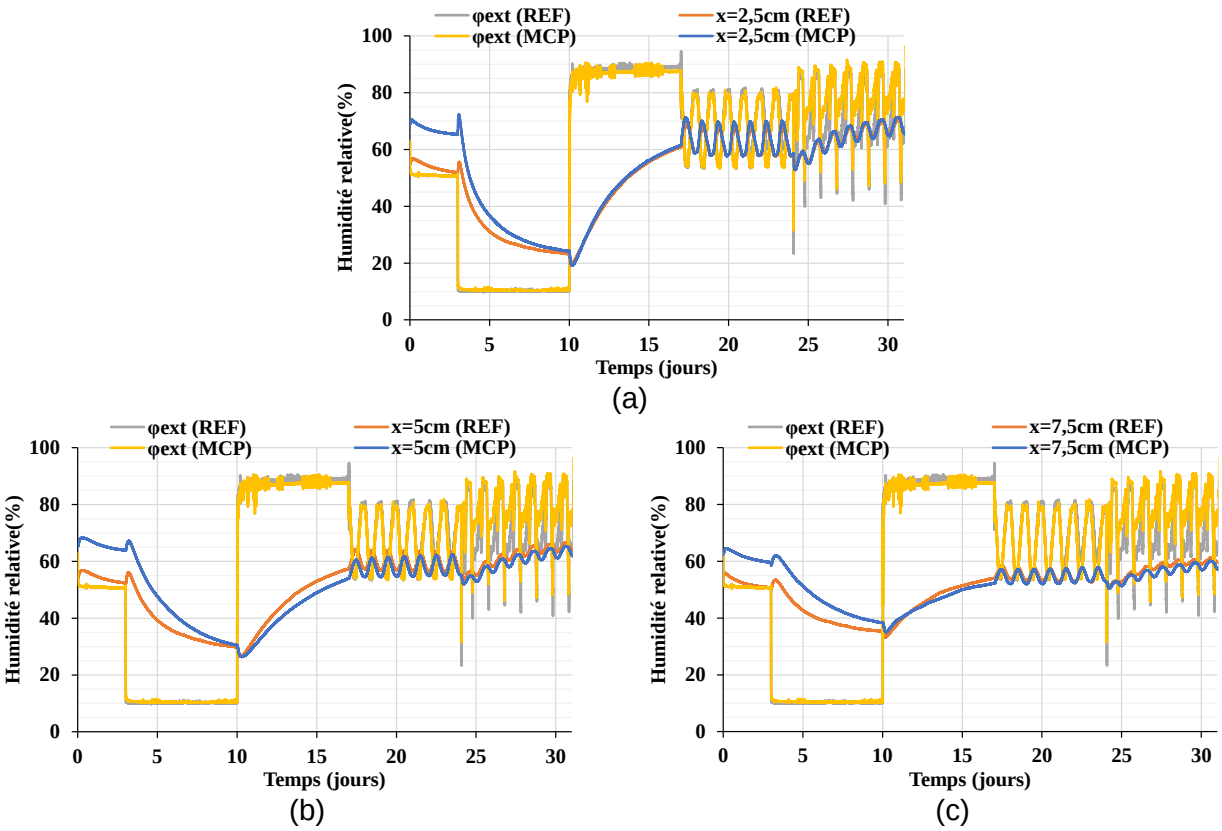

Figure 21. Évolution de la température pour le matériau de référence et le bio-composite MCP à x=2,5 cm (a), 5 cm (b), 7,5 cm (c).

Les évolutions de la température et de l'humidité relative seront divisées en trois zones pour les besoins de l'analyse. Une région de conditions statiques pendant 17 jours, une région de journées d'été typiques entre le 17e et le 24e jour, et enfin une journée d'hiver typique entre le 24e et le 31e jour.

3.4.1 Conditions estivales et hivernales statiques

Lorsque la température extérieure est fixée à 40 °C (3 à 10 jours, Figure 20) la température maximale à l'intérieur du mur est réduite de 2 °C et 1°C avec l'incorporation du MCP à des profondeurs de 2,5 cm et 5 cm, respectivement. Cependant, pour le capteur à 7,5 cm, qui est proche des conditions intérieures, aucune réduction de température dans le mur à cette profondeur n'est observée. Cela s'explique par le fait que ce point n'atteint pas la température de fusion du bio-composite (environ 30°C) donc que le dégagement de chaleur (changement de phase du MCP) n'est pas activé à cette profondeur (7,5 cm).

Lorsque la température extérieure est fixée à 10°C (10 à 17 jours, Figure 20), les deux matériaux présentent le même comportement, avec un léger avantage pour le béton de chanvre de référence qui affiche de meilleures performances thermiques (meilleure isolation thermique) à des températures plus basses. La différence entre la température du bio-composite MCP et la référence est significative à 7,5 cm (environ 1°C). Cela s'explique par la conductivité thermique plus élevée du bio-composite par rapport à la référence (Tableau 5), compte tenu du fait que les deux matériaux agissent comme des matériaux de stockage sensible (Tableau 5) dans cette plage de température.

En ce qui concerne l'humidité relative, initialement, le matériau de référence, plus sec que le bio-composite, atteint plus rapidement (3 premiers jours) un taux d'humidité relative de 50%, principalement en raison de conditions initiales différentes. Cette différence est perceptible pendant la phase de séchage (humidité maintenue à 10%, 3 à 10 jours, Figure 21). Cependant, lorsque l'humidité est augmentée à 90%, les différences entre les deux matériaux diminuent et deviennent négligeables, notamment près la surface externe (à 2,5 cm, 10 à 17 jours, Figure 21). Pour les positions plus profondes (5 cm et 7,5 cm), les écarts initiaux persistent mais sont amoindris du fait du profil hydrique initial non constant à l'intérieur du matériau. Globalement, le matériau de référence montre une cinétique d'humidité plus rapide que le bio-composite, en grande partie en raison de sa perméabilité liquide et vapeur légèrement plus grande (Voir Tableau 5) (3 à 17 jours, Figure 21). Cette différence affecte très peu les performances hygroscopiques des deux matériaux qui ont un comportement similaire.

3.4.2 Conditions hivernales dynamiques

Dans les conditions hivernales (24-31 jours, Figure 20), le profil de température des deux parois montre une tendance similaire avec une température légèrement plus élevée pour la paroi de référence, meilleur isolant que le bio-composite donc plus adapté pour les climats froids. En effet, pour la gamme de températures subies par les deux parois en hiver, la conductivité et la diffusivité thermiques de la paroi de référence sont inférieures à celles du bio-composite (Tableau 5). Cela pourrait expliquer la meilleure isolation de la paroi référence pour les climats froids. Ce résultat était attendu en raison de la température de fusion de l'acide caprique choisi comme MCP (environ 30°C) qui convient aux climats chauds. En dessous de cette température de fusion, le dégagement de chaleur (changement de phase) n'est pas activé.

Les deux parois ont montré presque le même comportement à x=2,5 cm, avec une différence maximale d'environ 2% d'humidité relative (24-31 jours, Figure 21). Cependant, aux autres positions (5 cm et 7,5 cm), la cinétique est plus rapide pour la référence par rapport au bio-composite MCP.

3.4.3 Conditions estivales dynamiques

Sous des conditions cycliques typiques d'une journée d'été (17-24 jours, Figure 20), le bio-composite MPC présente de meilleures performances en termes de réduction de la température maximale. En effet, la température maximale est réduite de 2°C pour le capteur proche de la condition extérieure. La réduction est d'environ 1°C pour le capteur à 5 cm et négligeable pour le capteur à 7,5 cm. Ces résultats indiquent que les performances du bio-composite MCP dépendent des conditions extérieures, qui doivent être supérieures à la température de fusion du MCP, qui est d'environ 30°C. Cette condition est atteinte pour le capteur proche des conditions extérieures, ce qui justifie la réduction de température à 2,5 et 5 cm.

Concernant l'humidité, la cinétique est plus rapide pour le matériau de référence par rapport au bio-composite MCP d'une façon générale (17-24 jours, Figure 21). Cette observation a été expliquée précédemment par la valeur des perméabilités liquides et vapeur, ainsi que par la capacité de stockage d'humidité de la référence, qui sont plus élevées que celles du bio-composite MCP en raison de l'incorporation de l'acide caprique dans les fibres de chanvre. La différence maximale est d'environ 4% et est obtenue au centre du mur (capteur à 5 cm). Cette différence est plus faible pour les capteurs près des conditions aux limites (capteurs à 2,5 cm et 7,5 cm) avec une différence maximale d'environ 2%.

3.5 Bilan

Les conclusions de la revue bibliographique ont permis d'identifier les fibres végétales comme matériaux support pour la fabrication de MCP à forme stabilisée. Ainsi, quatre types de fibres naturelles (sapin, chanvre, chènevotte et paillis de lin) ont été présélectionnées en tant que matériaux support pour les bio-composites. Suite à une étape de sélection, les fibres de chènevotte ont été retenues comme matériau support en raison de leur faible coût, leurs bonnes propriétés thermiques et de leur taux d'imprégnation élevé (50%). La microporosité de ces fibres a été imprégnée avec cinq acides gras purs (acide caprique, laurique, palmitique, myristique et stéarique) et sept mélanges eutectiques grâce au protocole de synthèse mis en place et validé. Des matériaux composites biosourcés à changement de phase adaptés à la plage de température ciblée (15-45°C) ont ainsi été synthétisés et investigués. Les formes stabilisées {chènevotte + acide caprique} ont été retenues en raison de l'imprégnation efficace de l'acide caprique dans la microporosité des fibres de chènevotte, de son coût raisonnable et de sa température de fusion (30°C).

Ensuite, les formes stabilisées retenues ont été utilisées pour fabriquer du béton de chanvre à base de MCP. Les propriétés thermiques et hydriques du matériau bio-composite ont été évaluées et comparées à celle du matériau de référence (béton de chanvre). Les propriétés estimées pour ce dernier sont en adéquation avec les données de la littérature. L'incorporation de MCP a conduit à une augmentation de la conductivité thermique du matériau de référence de 25,7% à 23°C. De plus, le matériau composite a montré une excellente capacité de régulation de l'humidité. L'isotherme de sorption a été mesurée pour évaluer la capacité du matériau à stocker ou libérer de l'eau en fonction de l'humidité relative. La perméabilité à la vapeur d'eau a également été mesurée, montrant une réduction due à la présence de MCP, en raison de la réduction de l'adsorption par la chènevotte (les pores étant moins disponibles car occupés par le MCP). Afin de compléter la campagne expérimentale, une méthode inverse a été développée pour estimer le coefficient de diffusivité du liquide et de la vapeur à travers les matériaux bio-composites ainsi que le béton de chanvre de référence. Les propriétés estimées pour le matériau de référence sont en adéquation avec les données de la littérature ce qui témoigne de la robustesse de la méthode inverse développée.

Une étude comparative des performances hygrothermiques a été réalisée en soumettant des parois de référence (béton de chanvre) et des parois contenant le bio-composite aux conditions climatiques de la ville de La Rochelle. Les résultats ont montré que par temps froid, la paroi de référence en béton de chanvre a présenté une température légèrement plus élevée que la paroi innovante proposée, indiquant une meilleure isolation thermique. Les deux parois ont démontré une bonne capacité de régulation de l'humidité, mais la cinétique d'humidité a été plus rapide pour celle de référence en raison de sa perméabilité supérieure. Les résultats ont également montré que l'incorporation de MCP réduit la température maximale lors des canicules d'environ 2°C, ce qui peut réduire les besoins de rafraichissement dans les bâtiments. Pour conclure, la paroi contenant le bio-composite démontre une capacité à réguler efficacement à la fois la température et l'humidité relative.

4 Modélisation des transferts couplés dans les enveloppes des bâtiments

Ce chapitre s'articule autour du développement d'un modèle de transferts couplés de chaleur et d'humidité dans les enveloppes des bâtiments, avec trois sous-sections distinctes. La première décrit le développement d'un modèle permettant de simuler le comportement hygrothermique de parois, modèle validé grâce aux mesures expérimentales réalisées sur la paroi de référence (béton de chanvre) et sur la paroi innovante proposée (bio-composite). Ensuite, ce modèle est utilisé pour évaluer diverses parois dans des conditions climatiques de Caracas et New Delhi, avec une étude paramétrique sur l'épaisseur de la paroi et la proportion de MCP dans le bio-composite. La dernière section présente une cosimulation entre un modèle thermique dynamique à l'échelle du bâtiment (TRNSYS) et le modèle hygrothermique développé (COMSOL Multiphysics), validé grâce à la littérature (données de l'Agence Internationale de l'Énergie, Annexe 41 [107]). Cette approche est utilisée pour évaluer les performances hygrothermiques du bio-composite MCP à l'échelle du bâtiment, y compris les économies d'énergie potentielles par rapport aux isolants classiques.

4.1 Modèle de transferts couplés pour l'évaluation des performances hygrothermiques

4.1.1 Formulation mathématique du modèle

Les études expérimentales permettent d'évaluer les performances des matériaux de construction dans des conditions climatiques réelles. De telles études sont essentielles pour prédire le comportement hygrothermique de ces matériaux une fois intégrés dans les bâtiments. Cependant, les études expérimentales sont chronophages et limitent le champ d'investigation. Pour remédier à cela, un modèle hygrothermique a été développé permettant plus de flexibilité que l'expérience et le test de différentes configurations soumises à diverses conditions climatiques.

Après avoir développé (sous les hypothèses formulées dans **l'article 5**) les équations de conservation de l'énergie et de la masse, en considérant la température (T [K]) et la pression de vapeur (p_v [Pa]) comme moteurs de transfert, le système d'équations non-linéaires de transferts couplés de chaleur et d'humidité est obtenu (équations 7 et 8) :

$$\rho_s \frac{C_m}{p_{v,sat}} \frac{\partial p_v}{\partial t} = div(k_T \nabla T + k_m \nabla p_v) \tag{7}$$

$$\rho_s C_p^* \frac{\partial T}{\partial t} = div(\lambda^* \nabla T + \gamma \nabla p_v) + \rho_s C_m \sigma L_v \frac{\partial p_v}{\partial t} \tag{8}$$

avec k_T [kg.m^{-1}.s^{-1}.K^{-1}] le coefficient de transfert d'humidité dû à un gradient de température, k_m [kg.m^{-1}.s^{-1}.Pa^{-1}] le coefficient de diffusion d'humidité totale, λ^* [W.m^{-1}.K^{-1}] la conductivité thermique effective, γ [W.m^{-1}.Pa^{-1}] le coefficient transfert de chaleur par convection dû à un gradient de pression de vapeur, σ [-] le rapport entre flux de vapeur et le flux d'humidité total, L_v [J.kg^{-1}] la chaleur latente de vaporisation de l'eau liquide, C_m [-] la capacité de stockage d'humidité, C_p^* [J.kg^{-1}.K^{-1}] la capacité thermique effective, ρ_s [kg.m^{-3}] la masse volumique sèche du matériau, $p_{v,sat}$ [Pa] la pression de vapeur saturante.

Les propriétés hygrothermiques des matériaux (caractérisation des matériaux, sous-sections 3.2 et 3.3) sont les paramètres d'entrée du modèle et permettent le calcul de certains coefficients du modèle (Tableau 5).

4.1.2 Application au cas du bio-composite MCP

Les mesures expérimentales réalisées pour caractériser le bio-composite (sous-sections 3.2 et 3.3) sont utilisées pour valider le modèle proposé (**article 5**). Les simulations sont réalisées avec le logiciel COMSOL Multiphysics et utilisent un solveur temporel avec couplage fort basé sur la méthode de Newton. L'hypothèse de condition limite de Dirichlet est considérée. La température et l'humidité relative de la surface interne et externe de la paroi sont utilisées comme conditions limites intérieures et extérieures pour le modèle numérique 1D.

La Figure 22 montre l'évolution des températures expérimentales et simulées à l'intérieur de la paroi bio-composite. La simulation numérique a montré un bon accord avec les données expérimentales et l'évolution de la température est reproduite avec une bonne précision. La différence de température est maximale dans la zone de transition entre les deux zones statiques (3-17 jours) (40 et 10 °C) et atteint 2,5°C. En dehors de cette zone de transition, la différence de température entre les températures expérimentales et simulées fluctue entre ±1°C. C'est une bonne approximation compte tenu de l'hypothèse du modèle de transfert unidirectionnel (1D). Cependant, l'erreur quadratique moyenne (EQM, équation 9) entre les températures expérimentales et simulées est de 0,6 °C, 0,4 °C et 0,3 °C pour 2,5, 5 et 7,5 cm respectivement.

$$\mathrm{EQM} = \sqrt{\sum_{i=1}^{n} \frac{\left(y_{sim,i} - y_{exp,i}\right)}{n}} \qquad (9)$$

avec y_{sim} les données simulées, y_{exp} les données expérimentales et n le nombre de données.

La précision augmente avec la profondeur et les meilleures estimations sont obtenues pour 7,5 cm qui est moins sensible aux conditions extérieures cycliques. Ces incertitudes sont essentiellement dues à l'hypothèse 1D, à l'incertitude dans la caractérisation des propriétés des matériaux, à l'incertitude des mesures et à l'incertitude sur la position du capteur. Malgré les divergences, le modèle numérique décrit avec une bonne précision le comportement thermique du bio-composite.

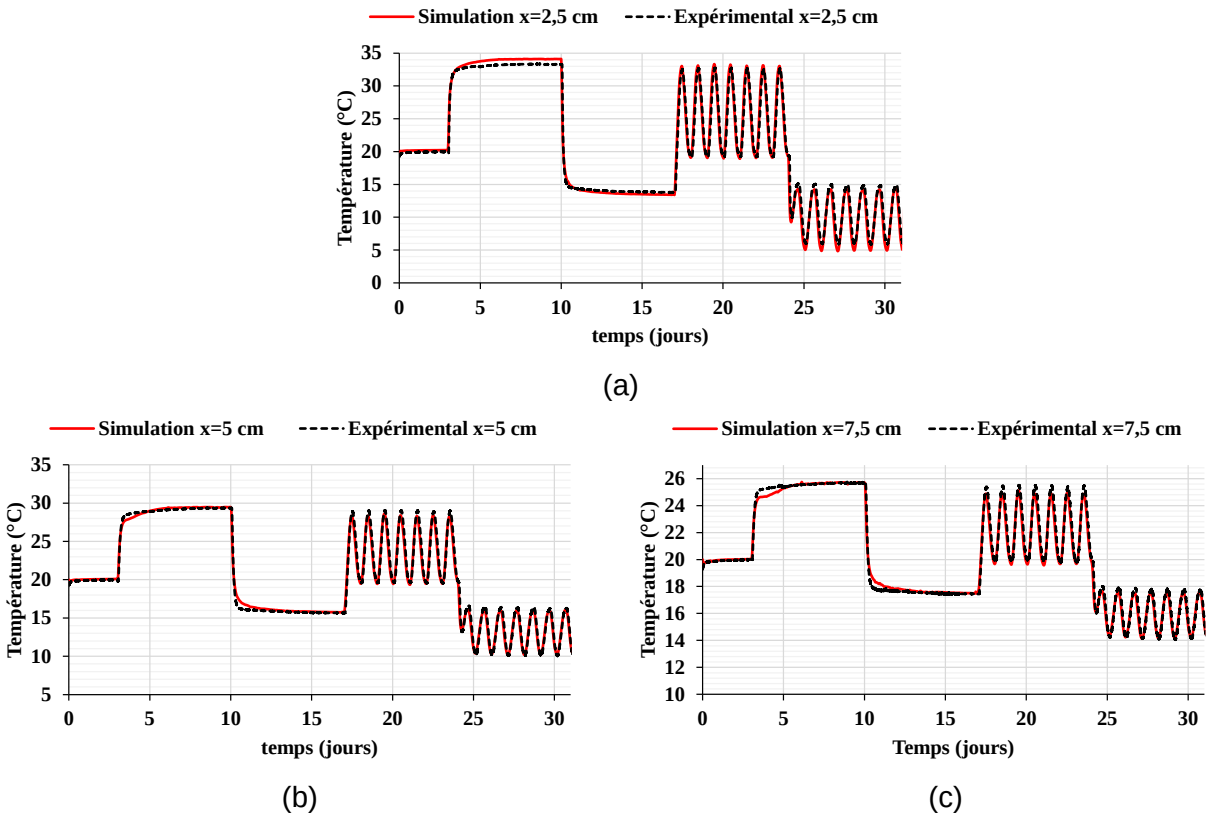

Figure 22. Comparaison entre la température expérimentale et simulée (COMSOL) dans le bio-composite à x=2,5 cm (a), x=5 cm (b) et x=7,5 cm (c).

La Figure 23 montre l'évolution de l'humidité relative expérimentale et simulée à l'intérieur du bio-composite MCP. La concordance entre les valeurs expérimentales et numériques est bonne. En effet, l'erreur quadratique moyenne est d'environ 6%, 5% et 4% pour 2,5, 5 et 7,5 cm respectivement.

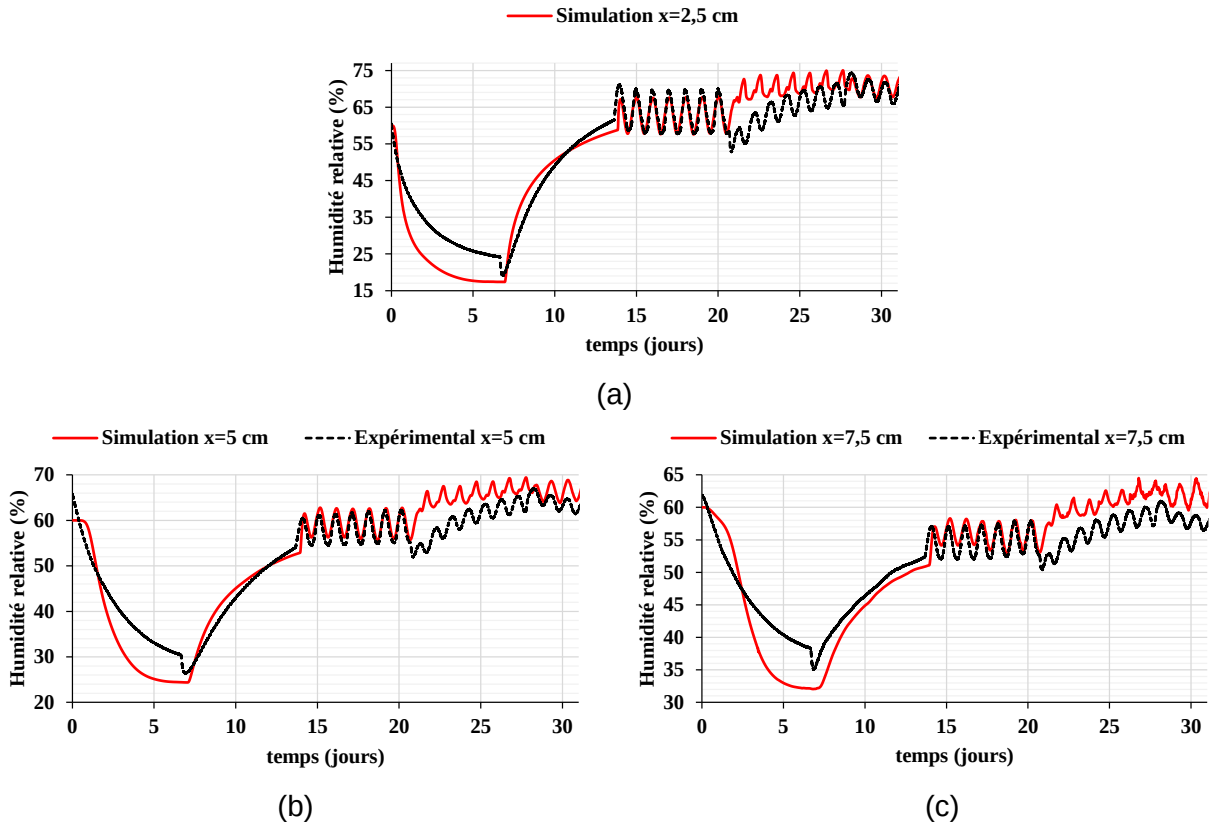

Figure 23. Comparaison entre l'humidité relative expérimentale et simulée (COMSOL) dans le bio-composite MCP à x=2,5 cm, x=5 cm (b) et x=7,5 cm (c).

Comme pour le profil de température, la précision de la simulation augmente avec la profondeur. En outre, la meilleure concordance est observée pour la phase d'humidification (condition statique avec humidité fixée à 90%) et pour une journée d'été typique. Le manque de précision pour le scénario de la journée d'hiver typique pourrait être attribué à la chute drastique de l'humidité dans l'enceinte climatique au début du cycle que le modèle n'arrive pas à reproduire. Dans les perspectives, ce scénario sera testé seul afin de vérifier cette affirmation. Cependant, la précision est jugée satisfaisante et le modèle numérique est utilisé pour simuler le comportement hygrothermique de différentes parois soumises à diverses conditions climatiques.

4.1.3 Application du modèle à d'autres matériaux

Pour évaluer la robustesse du modèle, deux autres cas de validation ont été employés (différents matériaux, différentes conditions aux limites et initiales), en se basant sur des données issues de la littérature. Le premier cas de validation repose sur les résultats de l'essai expérimental mené par Olutimayin et al. [108]. Dans cette expérience, un isolant en cellulose d'une épaisseur de 30 cm est utilisé, avec une température initiale et une humidité relative dans le matériau de 21 °C et 13 %, respectivement. Un écoulement laminaire (Re = 1900) à une température de 38 °C et une humidité relative de 70 % circule d'un côté du matériau, tandis que l'autre côté est maintenu dans des conditions adiabatiques. La vitesse de l'écoulement d'air est réglée à 0,68 m/s. Les configurations expérimentales et les processus expérimentaux peuvent être consultés dans [108]. Des conditions au limites de Neumann sont fixées sur la face supérieur de l'échantillon. Le coefficient de transfert de chaleur convectif en surface est de 3,4 $W.m^{-2}.K^{-1}$, et le coefficient de transfert de masse convectif est de $2,06 \cdot 10^{-8}$ $s.m^{-1}$. Les propriétés

hygrothermiques de l'isolation en cellulose sont extraites des références [108,109]. Les variations d'humidité relative et de température du matériau à x = 6, 12, 18 et 24 cm ont été mesurées et comparées. Les Figure 24.a et b montrent l'évolution des températures et des humidités relatives simulées et expérimentales à l'intérieur de l'isolation en cellulose. Les résultats présentent de très bonnes concordances avec une erreur relative maximale de 3 % pour la température et de 5 % pour l'humidité relative.

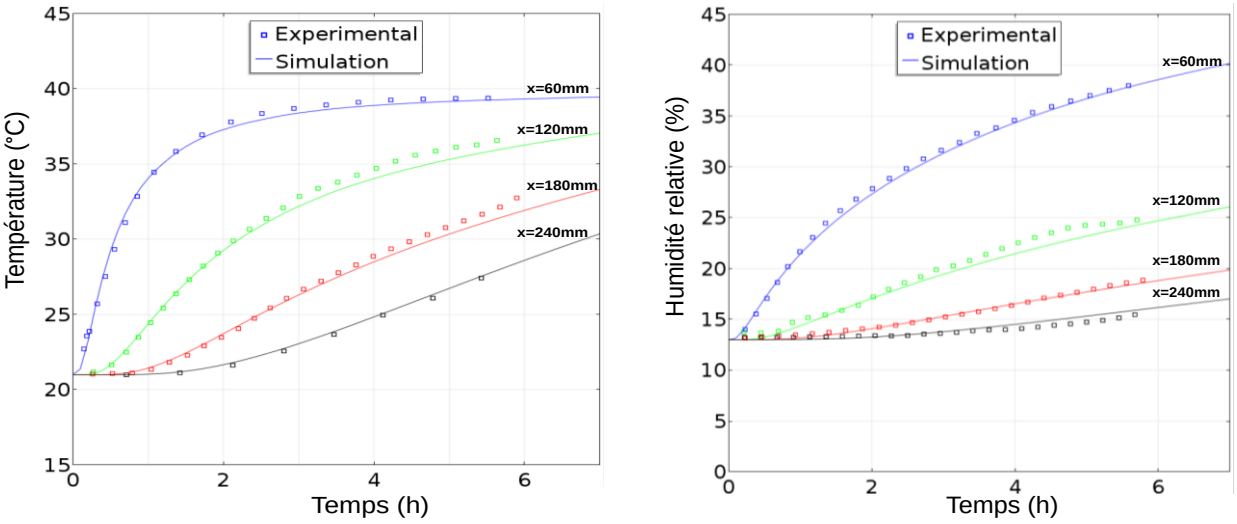

(a) (b)

Figure 24. Comparaison entre les résultats expérimentaux et numérique de la température (a) et de l'humidité relative (b) dans l'isolation en cellulose.

Le test de référence défini dans la norme EN 15026 [110] pour la validation d'un logiciel calculant le transfert d'humidité par simulation numérique est utilisé pour le second cas de validation. La géométrie du modèle consiste en un seul segment pour l'élément de construction. Sa taille est suffisamment grande pour représenter une région semi-infinie à l'échelle de temps de la simulation (2 m). Une humidité relative de 50 % et une température de 20 °C sont fixées comme conditions initiales, tandis que sur la limite gauche, l'humidité relative est fixée à 95 % et la température à 30°C. Une condition de flux nul est imposée sur la limite droite. L'étude temporelle est réalisée sur une année, les distributions de température et d'humidité relative sont vérifiées à 7, 30 et 365 jours. Les profils de température et de teneur en eau simulées et expérimentales à 7, 40 et 365 jours sont présentés (Figure 25.a et b). Les résultats ont montré une bonne concordance entre la simulation numérique et les expériences.

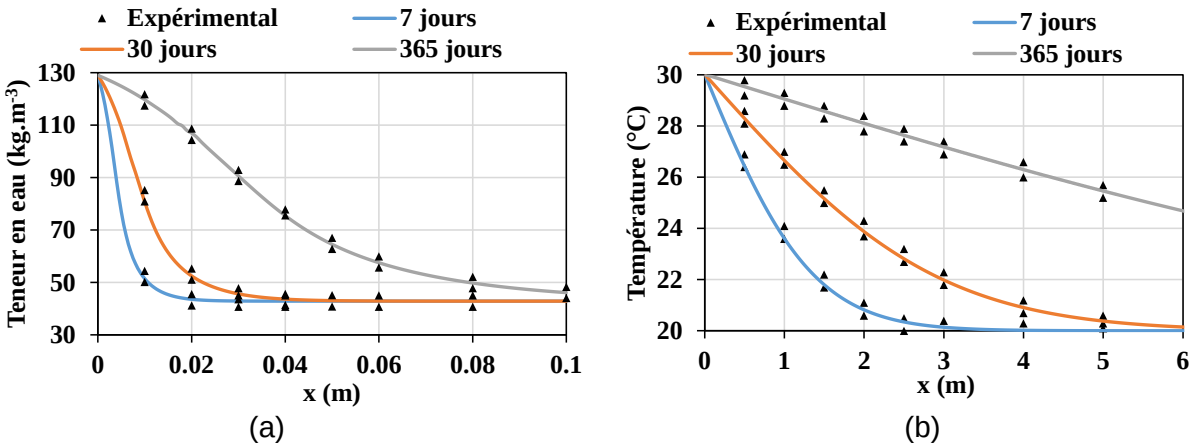

Figure 25. Comparaison des profils de teneur en eau (a) et de température (b) obtenus numériquement (lignes continues) avec ceux expérimentaux de la norme EN 15026 (triangles).

Enfin, le modèle a été utilisé pour comparer les performances hygrothermiques de quatre matériaux de 20 cm d'épaisseur à savoir la terre crue, le béton de chanvre, la brique d'argile et le béton de poudre de verre (**article 7**). Initialement, le matériau est en équilibre avec un environnement extérieur à une température constante de 20 °C et une humidité relative constante de 50%. Les conditions climatiques externes sont T = 35 °C et HR = 90% sur la face extérieure (x = 0 cm) et l'autre face est supposée être adiabatique et imperméable (condition de flux nul).

En raison de la difficulté de mesurer la conductivité hydraulique des liquides, la méthode du critère de changement de phase (PCC) a été utilisée [109]. Ce paramètre représente le rapport entre le flux de vapeur et le flux total. Il s'exprime selon l'équation 10:

$$PCC = \frac{\delta_v * P_v}{k_l \frac{R\rho_l}{M} T + \delta_v * P_{v,sat}} \tag{10}$$

On remarque que pour des valeurs de PCC inférieures à 0,6, l'influence du PCC n'est pas très importante. Le transfert de masse est essentiellement un transfert de vapeur et le transfert de liquide est négligeable. Pour les parois cellulosiques, Wang et al [109] ont trouvé que si l'humidité relative est inférieure à 60%, le PCC peut être fixé à 1. Dans cette étude, il a été fixé arbitrairement à 0,8 afin de prendre en compte la diffusivité du liquide qui disparaît lorsque le PCC est égal à 1.

Afin de mieux décrire la dynamique à l'intérieur des matériaux, l'évolution de l'humidité relative et la température à x=5 cm (à proximité des conditions aux limites extérieures) est présentée en fonction du temps (Figure 26.a et b) pour quatre matériaux de construction, à savoir, un béton de chanvre, un béton de poudre de verre, une terre crue et une brique d'argile. Comme on peut le voir sur la courbe de température, l'équilibre thermique est atteint après 24h pour la poudre de verre et 72h, pour le béton de chanvre, après 144h pour la terre crue et la brique d'argile. La réponse aux sollicitations thermiques extérieures est très faible pour la terre crue par rapport aux deux autres matériaux, ce qui indique que la terre crue est le plus isolant des trois matériaux.

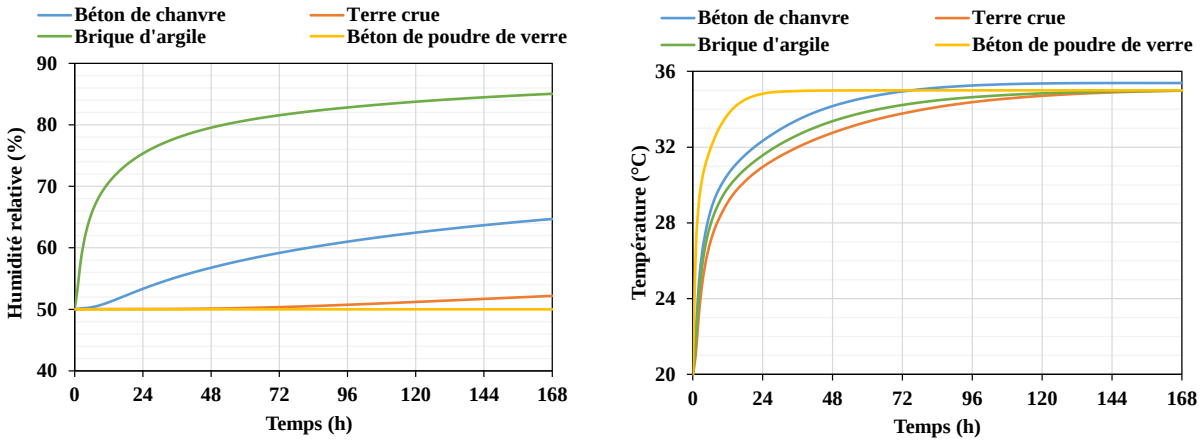

Figure 26. Evolution temporelle de l'humidité relative (a) et de la température (b) à x=5 cm pour le béton de chanvre, la terre crue, la brique d'argile et le béton de poudre de verre.

Après 168 heures, l'équilibre hydrique n'est atteint pour aucun des quatre matériaux. Les simulations ont donc été étendues à un an afin d'obtenir des effets plus représentatifs (Figure 27). Au bout de trois mois, l'équilibre hydrique est atteint pour la brique d'argile. Cependant, pour le béton de chanvre, la terre crue et le béton de poudre de verre, l'équilibre est loin d'être atteint avec une valeur relativement plus élevée pour le béton de chanvre et la terre crue par rapport au béton de poudre de verre. En effet, ces derniers possèdent une capacité de stockage d'humidité supérieure à celle de la brique d'argile, ce qui leur confère une plus grande inertie hydrique. Cette inertie hydrique est à l'origine de la cinétique de transfert hydrique lente pour ces trois matériaux par rapport à la brique d'argile. Ainsi, ces matériaux permettent de réguler efficacement l'humidité interne dans les bâtiments en réduisant le transfert d'humidité de l'extérieur vers l'intérieur.

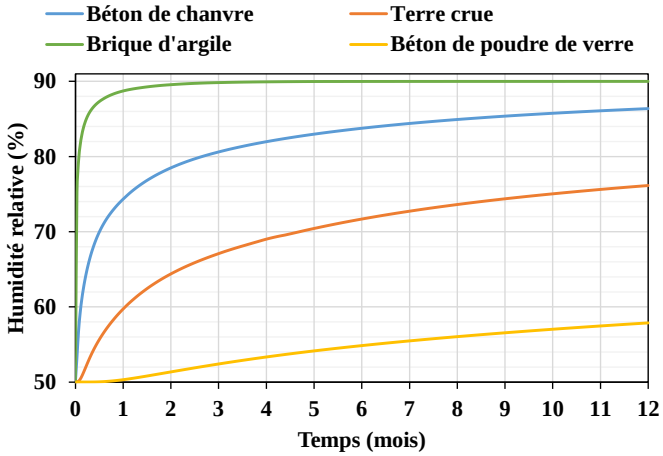

Figure 27. Evolution annuelle de l'humidité relative à x=5 cm pour le béton de chanvre, la terre crue, la brique d'argile et le béton de poudre de verre.

Le modèle est validé pour différentes parois monocouches et différentes sollicitations climatiques internes et extérieures. Nous allons à présent le tester dans le cadre d'enveloppes de bâtiments multicouches.

4.2 Étude numérique du comportement hygrothermique d'enveloppes de bâtiments multicouches

Les transferts hydriques impactent la détérioration des matériaux donc la durabilité des ouvrages. Prédire finement le comportement hygrothermique des enveloppes de bâtiments et caractériser les propriétés des matériaux (hydriques, thermiques, microstructurales) permet d'évaluer les risques liés à l'humidité. Par ailleurs, leur prise en compte pourrait réduire la demande énergétique des bâtiments jusqu'à 30 %. Dans cette sous-section, nous allons présenter l'adaptation du modèle de paroi monocouche proposé à une paroi multicouche et étudier son comportement hygrothermique dans des climats humides (cas défavorables).

Les performances hygrothermiques de cinq matériaux isolants ont été investiguées : le béton de chanvre, la laine de verre, le polystyrène expansé, l'isolant cellulosique et le bio-composite. Les propriétés de ces cinq matériaux sont recensées dans l'**article 8**.

Les cas d'étude analysés sont des configurations de parois multicouches constituées de 10 cm de matériau isolant extérieur, 20 cm de brique, matériau de construction conventionnel, et 2 cm de plâtre pour la couche de finition (Figure 28). Plusieurs isolants sont testés et leurs performances comparées. Par contre, les couches de brique et de plâtre restent inchangées, quel que soit l'isolant testé.

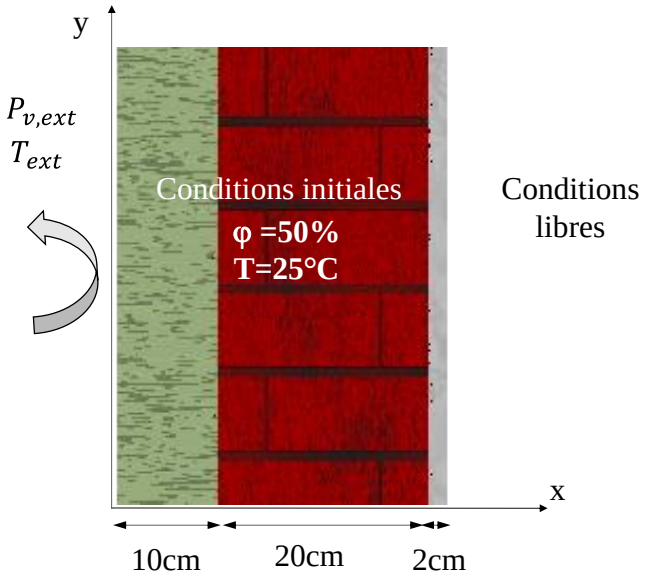

Figure 28. Configurations de murs multicouches étudiées. La couleur verte représente l'isolation, l'orange la brique et la grise le plâtre.

Les parois multicouches étudiées sont soumises aux conditions climatiques réelles (température et humidité relative) de deux villes : New Delhi pour un temps très chaud et humide et Caracas pour un temps modérément chaud et très humide. Ces villes au climat chaud permettent (température le plus souvent supérieure à 30°C) d'exposer pleinement l'intérêt du bio-composite et du changement de phase des MCP (transition de phase autour de 30°C).

4.2.1 Performances hygrothermiques des isolants

La Figure 29.a illustre l'évolution de la température intérieure au cours de l'année pour les cinq matériaux étudiés dans les conditions climatiques de Caracas. Pour des températures

relativement basses (inférieures à 28 °C), l'isolation en laine de verre montre les meilleures performances avec une température intérieure plus basse. En revanche les températures intérieures les plus élevées sont relevées pour la cellulose. Les parois constituées de bio-composite, de béton de chanvre et de polystyrène expansé ont exhibé un comportement similaire avec des températures de surface intérieures, variant entre 25 et 30 °C. Cependant, parmi ces trois derniers matériaux, les températures les plus basses sont obtenues pour le bio-composite, suivi par le polystyrène et le béton de chanvre. Ces résultats montrent l'intérêt de l'incorporation des MCP pour la régulation de la température intérieure des bâtiments.

Dans le climat très chaud et humide de New Delhi, lorsque les niveaux d'humidité sont inférieurs à 65% (avant 180 jours) les matériaux isolants en cellulose et laine de verre sont les plus efficaces, avec des températures de surface interne inférieures à celles des autres matériaux isolants (Figure 29.b). Cependant, lorsque l'humidité relative est élevée, l'efficacité de ces isolants diminue considérablement au profit du béton de chanvre, du bio-composite et du polystyrène. L'effet de l'incorporation de MCP dans le béton de chanvre est à peine perceptible, en raison des températures extérieures bien supérieures à la température de fusion du MCP (environ 30°C). Ces résultats laissent supposer que l'utilisation de MCP à température de fusion plus élevée, notamment le composite acide laurique/chènevotte pourrait être plus efficace dans un tel climat. En se basant sur les propriétés des matériaux, on constate que les propriétés hydriques de la cellulose et la laine de verre sont très élevées par rapport aux autres matériaux en raison d'une forte porosité. Cela explique la dépendance de leurs performances en fonction des conditions de l'humidité. Ainsi, le couplage est plus important pour ces deux matériaux ce qui justifie les résultats observés.

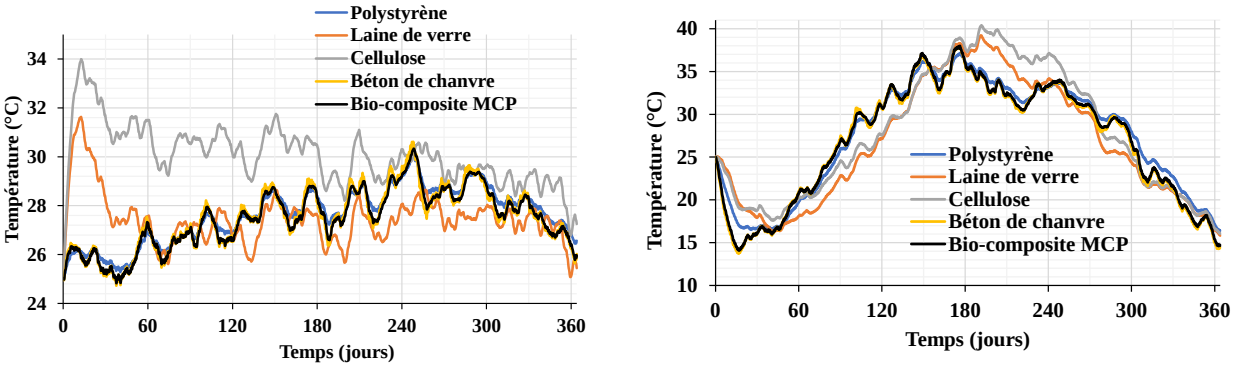

Figure 29. Evolution annuelle de la température intérieure des ambiances pour des conditions de la ville de Caracas (a) et New Delhi (b) dans les parois multicouches contenant les différents matériaux isolants.

En ce qui concerne l'humidité relative, le béton de chanvre, le bio-composite et la laine de verre répondent de manière similaire aux sollicitations externes de la ville de Caracas (Figure 30.a). En raison de la capacité de stockage d'humidité et de la perméabilité à l'eau liquide et à la vapeur de ces matériaux (tableau de propriétés en annexe de l'**article 8**), le transfert d'humidité est plus rapide et se stabilise à environ 85 % d'humidité relative. La cinétique est légèrement plus lente pour le polystyrène expansé et l'isolation cellulosique, se stabilisant à environ 80% correspondant à la moyenne de l'humidité relative extérieure.

La Figure 30.b montre l'évolution de l'humidité intérieure au cours de l'année pour chacun des cinq matériaux isolants dans la ville de New Delhi. L'humidité relative intérieure varie entre 40% et 75% pour tous les isolants, à l'exception de l'isolant cellulosique, où l'humidité maximale est

légèrement inférieure à 70%, en raison de sa plus faible perméabilité à la vapeur d'eau par rapport aux autres isolants, ce qui se traduit par une cinétique beaucoup plus faible.

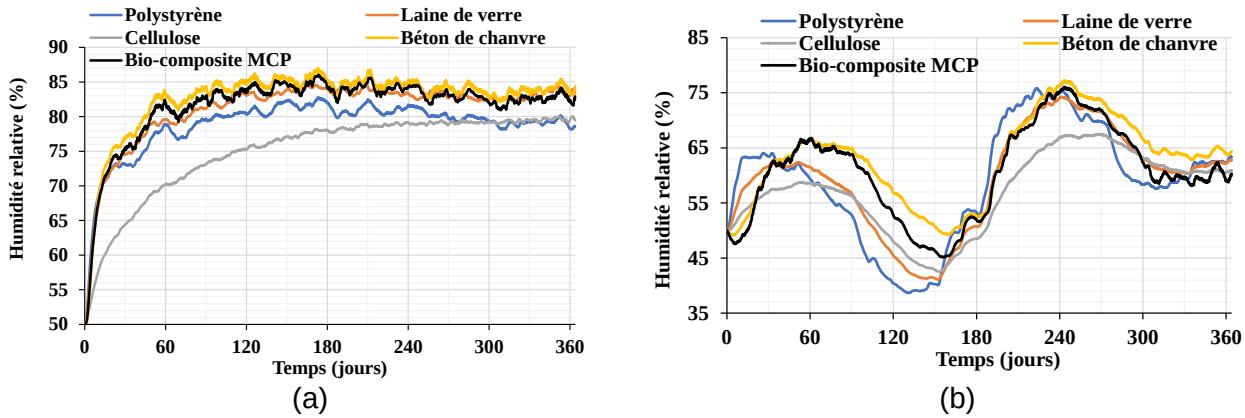

Figure 30. Evolution annuelle de l'humidité relative pour la ville de Caracas (a) et New Delhi (b) dans les parois multicouches contenant les différents matériaux isolants.

Afin d'évaluer et de comparer de manière précise les performances globales de différents types d'isolants, la charge de transmission de chaleur, qui indique la quantité de chaleur transmise à l'environnement intérieur, a été calculée. Plus l'isolation est efficace, moins de chaleur est transmise. Les charges de transmission de climatisation et de chauffage ont été calculées pour une plage de confort thermique entre 20 et 25 °C (équation 11). Une température supérieure à 25 °C correspond donc à des besoins en climatisation et une température inférieure à 20°C, à des besoins en chauffage. L'intégration est effectuée tout au long de l'année.

$$Q_{cool/heat} = \sum_i h_{m,int} * \Delta T_i \tag{11}$$

avec $\Delta T = T - 25$ [°C] pour les besoins en climatisation et $\Delta T = 20 - T$ [°C] pour les besoins en chauffage, i est l'indice du pas de temps.

La Figure 31 présente les charges de transmission de chaleur pour les cinq types d'isolants dans les conditions climatiques de Caracas et de New Delhi. L'isolation en laine de verre est la plus performante, quelle que soit la condition climatique. À New Delhi, où le climat est chaud et humide, le béton de chanvre et le bio-composite offrent des performances presque identiques. En revanche, le polystyrène et l'isolant en cellulose ont des charges de transfert de chaleur plus élevées en raison de leur faible inertie thermique (par rapport au bio-composite et au béton de chanvre) et de leur conductivité thermique relativement plus élevée (par rapport à la laine de verre).

À Caracas, où le climat est chaud et très humide, l'isolation en cellulose se révèle inefficace avec une charge de transmission de chaleur très élevée. L'isolation en laine de verre reste la plus efficace, avec une charge de transmission de chaleur inférieure à 800 kW.m^{-2}. La paroi intégrant le bio-composite est plus efficace à Caracas, montrant une amélioration par rapport au béton de chanvre, principalement en raison des températures proches de la température de fusion du MCP. Le polystyrène présente des charges de transmission de chaleur légèrement plus élevées que celles des autres isolants.

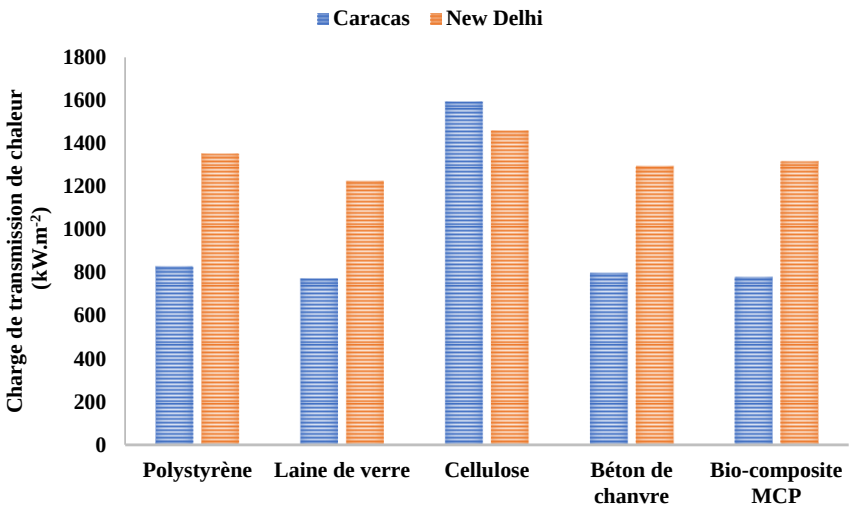

Figure 31. Charge de transmission thermique des différents matériaux isolants dans les conditions climatiques de New Delhi et de Caracas.

4.2.2 Etude paramétrique

Afin d'évaluer l'effet de la fraction massique de MCP et de l'épaisseur, des indicateurs de performances différents sont utilisés : la réduction de la température maximale, le décalage temporel, la différence de température mensuelle et le potentiel maximal d'économies d'énergie. En plus du bio-composite testé jusqu'à présent, qui contient 14 wt% de MCP, deux autres formulations avec des pourcentages de MCP de 20 % et 30 %, désignées MCP20 et MCP30, ont été évaluées. Pour chaque fraction massique, trois épaisseurs d'isolation sont investiguées : 10 cm, 20 cm et 30 cm.

Pour la ville de Caracas, à épaisseur de paroi constante, l'augmentation de la fraction de MCP entraîne une réduction de la température maximale par rapport à la paroi de référence (béton de chanvre). Ainsi, pour 10 cm d'isolation, on observe une réduction de la température de surface interne tout au long de l'année, avec des valeurs maximales de 0,4, 0,5 et 0,7°C pour le bio-composite, le bio-composite MCP20 et le bio-composite MCP30, respectivement (Tableau 6), à environ 230 jours.

Tableau 6. Réduction maximale de la température de surface interne et décalage dans le temps de chaque fraction de MCP et de l'épaisseur de l'isolation (10 cm, 20 cm et 30 cm) pour les conditions climatiques de Caracas.

Epaisseur (cm)	Fraction de MCP (%)	Réduction de température maximale (°C)	Délai (h)
10	14	0,4	28,5
	20	0,5	31
	30	0.6	36
20	14	0,6	70
	20	0.7	76,5
	30	0,9	111
30	14	0,7	118
	20	0,8	151,5
	30	1	198

Sous le climat très chaud et humide de New Delhi, les résultats montrent que l'utilisation du MCP comme isolation réduit significativement les températures maximales par rapport à

l'isolation de référence. Cette réduction augmente proportionnellement avec l'épaisseur de l'isolation. Pour une épaisseur d'isolation de 10 cm, les températures maximales sont réduites de 0,5°C, 0,7°C et 0,9°C pour le bio-composite, le MCP20 et le MCP30 respectivement, par rapport au béton de chanvre de référence (Tableau 7). Ces réductions de température s'accompagnent de décalages temporels de 73, 76,5 et 84 heures pour chaque fraction de MCP, respectivement.

Tableau 7. Réduction maximale de la température et décalage dans le temps de chaque fraction de MCP et de l'épaisseur de l'isolation (10 cm, 20 cm et 30 cm) pour les conditions climatiques de New Delhi.

Epaisseur (cm)	Fraction de MCP (%)	Réduction de température maximale (°C)	Délai (h)
10	14	0,5	73
	20	0,7	76,5
	30	0,9	84
20	14	0,9	33,5
	20	1,3	57
	30	1,7	69.5
30	14	1	72
	20	1,5	80
	30	2,5	137,5

L'augmentation de la fraction de MCP a un impact significatif sur la réduction de la charge de transfert de chaleur, bien plus que l'augmentation de l'épaisseur de l'isolant, ce qui permet d'obtenir des matériaux d'isolation plus compacts et plus performants. En effet, le bio-composite MCP30 démontre une réduction substantielle de la charge de transfert de chaleur à New Delhi (Figure 32.a), avec une diminution allant jusqu'à 40 % pour une épaisseur de 30 cm, soulignant le rôle important de la fraction de MCP par rapport à l'épaisseur pour la conception de matériaux d'isolation efficaces. Les résultats pour la ville de Caracas (Figure 32.b) montrent des tendances similaires, avec des réductions allant jusqu'à 25 % de la charge de transfert de chaleur pour le bio-composite MCP30 à une épaisseur de 30 cm. Les bio-composites à base de MCP démontrent des performances prometteuses dans diverses conditions climatiques, en particulier pour les climats qui correspondent aux points de fusion des MCP.

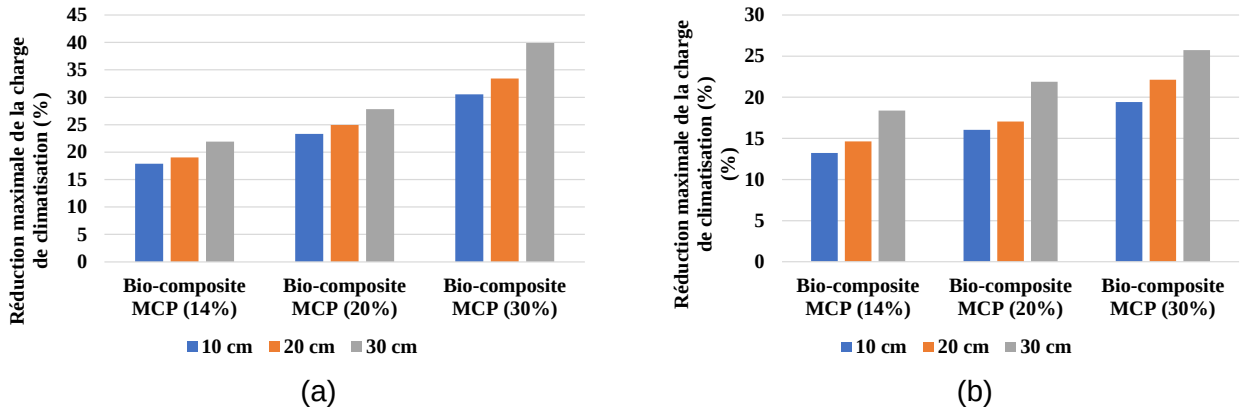

Figure 32. Effet de la fraction de MCP et de l'épaisseur de l'isolation sur la réduction maximale de la charge de climatisation pour New Delhi (a) et Caracas (b).

Le modèle développé permet donc la simulation du comportement hygrothermique de différents types de parois (monocouches, multicouches, conventionnelles, innovantes etc.). Ce modèle a

été validé, testé pour différentes parois soumises à diverses conditions climatiques et peut à présent être utilisé pour une étude à l'échelle du bâtiment.

4.3 Développement d'une approche de couplage COMSOL-TRNSYS

4.3.1 Introduction

Le modèle développé nous a permis de simuler le comportement hygroscopique de différentes parois soumises à diverses conditions climatiques réelles. Cependant, sa principale limite, outre le fait qu'il s'agit d'un modèle unidimensionnel, réside dans sa prise en compte des conditions aux limites internes. En effet, le modèle suppose que la température de l'air est égale à la température de la surface du mur à l'itération précédente et ne prend pas en compte le renouvellement de l'air ou la production d'humidité.

Afin de surmonter cette limitation et d'obtenir une évaluation plus complète et réaliste des performances hygrothermiques des enveloppes de bâtiments, nous proposons dans cette partie une approche novatrice de cosimulation entre COMSOL Multiphysics et TRNSYS. En effet, TRNSYS est un logiciel de simulation thermique dynamique spécialement conçu pour analyser le comportement thermique des bâtiments en prenant en compte une gamme complète de paramètres, tels que l'emplacement, les matériaux de construction, la conception architecturale, le concept énergétique ainsi que les systèmes de chauffage et de climatisation. Il permet une étude approfondie de la performance thermique d'un bâtiment en intégrant tous ces éléments. Cependant, les modèles de transfert d'humidité de TRNSYS reposent sur une approche simplifiée qui ne tient pas compte du couplage des phénomènes de transfert de chaleur et d'humidité à travers l'enveloppe du bâtiment.

Cette dernière limitation constitue une autre motivation du développement d'une approche de cosimulation couplant TRNSYS avec un modèle hygrothermique élaboré à l'échelle de la paroi. Cette approche est conçue pour pouvoir prendre en compte et étudier l'influence du couplage des transferts de chaleur et d'humidité au sein de différentes parois sur les performances énergétiques du bâtiment. Dans la suite de cette section, nous présenterons la stratégie d'implémentation de cette cosimulation, sa validation, ainsi qu'un exemple concret d'application.

4.3.2 Stratégie d'implémentation

Zhai et al. [111] ont classé les méthodes de cosimulation en deux groupes : le couplage statique et le couplage dynamique. Dans le couplage statique, l'interaction entre les deux outils de simulation est unidirectionnelle, les informations circulant d'un logiciel à l'autre sans retour d'information ni échange itératif pendant la simulation. En revanche, le couplage dynamique implique une interaction bidirectionnelle entre les outils, permettant un échange continu d'informations et un retour d'information au cours du processus de simulation. Le couplage dynamique permet une représentation plus complète et plus précise du comportement hygrothermique des bâtiments. En effet, il tient compte de l'influence mutuelle des phénomènes de transferts couplés de chaleur et d'humidité, ce qui permet des simulations prédictives plus réalistes et de mieux évaluer les performances du bâtiment.

Dans une première tentative, nous avons opté pour le couplage statique encore appelé méthode par chainage. L'approche de cosimulation consiste à coupler un outil de simulation dynamique de bâtiment (TRNSYS) avec un modèle de transfert couplé de chaleur, d'air et d'humidité implémenté dans COMSOL Multiphysics (Figure 33).

Tout d'abord le bâtiment et les différentes zones sont modélisés sur TRNSYS. Les propriétés des matériaux constituants les enveloppes du bâtiment, sa localisation, les différents systèmes de chauffage et de climatisation sont également définis. Une première simulation est alors lancée sur TRNSYS (pas de temps utilisé : 1h) afin de générer des fichiers de sortie qui constituent les données d'entrée (conditions aux limites) du modèle hygrothermique (humidités et températures intérieures et extérieures). Cette génération de données est gérée par l'outil *Printegretor* de TRNSYS.

Ensuite, le comportement hygrothermique de l'enveloppe du bâtiment est modélisé sur COMSOL Multiphysics grâce au modèle précédemment développé. Une étude de convergence du modèle hygrothermique a été réalisée, le meilleur compromis est un pas de temps plus fin (15 minutes). Les données de sortie de cette deuxième simulation sont utilisées pour calculer les flux d'humidité (J_{moist} [kg.m^{-2}.s^{-1}]) et de chaleur (J_{heat} [W.m^{-2}]) afin de corriger la simulation effectuée par TRNSYS. Le calcul de ces flux est réalisé grâce aux équations 12 et 13.

$$J_{moist} = -k_T \nabla T - k_m \nabla P_v \tag{12}$$

$$J_{heat} = \lambda^* \nabla T + \gamma \nabla P_v - j_{cond} \tag{13}$$

On notera que le terme de transfert par conduction (j_{cond}) dans l'équation 13 n'est pas pris en compte puisque déjà pris en compte par le code de calcul de TRNSYS. Ces flux de chaleurs et d'humidité sont intégrés dans TRNSYS en les considérant comme gain de chaleur et d'humidité respectivement. Cette approche permet de corriger au premier ordre le calcul effectué par TRNSYS en prenant en compte les transferts couplés de chaleur et de masse de manière plus précise.

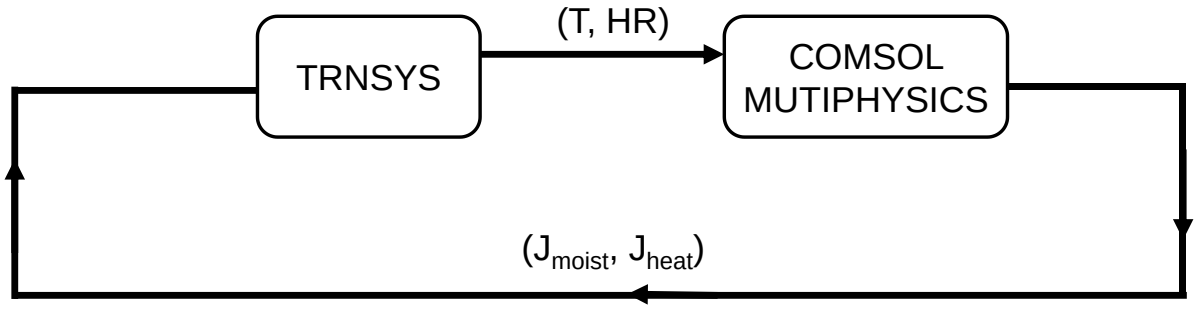

Figure 33. Stratégie d'implémentation de la cosimulation par chainage TRNSYS-COMSOL Multiphysics.

4.3.3 Validation de la méthodologie

Afin de valider l'approche de cosimulation, une validation expérimentale a été entreprise en confrontant le modèle couplé TRSYS-COMSOL Multiphysics à des résultats expérimentaux de tests publiés par l'agence internationale de l'énergie IEA dans le cadre de l'annexe 41 [107].

Ce test a été réalisé sur le site d'essai extérieur de l'Institut Fraunhofer de physique du bâtiment à Holzkirchen dans l'objectif de comparer les mesures avec les modèles développés dans le cadre de l'annexe 41. Le test a été réalisé sur une chambre d'un volume de 50 m^3 et d'une surface de paroi de 67 m^2 (sans plancher, porte et fenêtre) (Figure 34). La paroi est constituée de 24 cm de brique avec une isolation extérieure de 7 cm de polystyrène intercalée entre deux enduits à base de plâtre minéral de 0,5 cm (vers l'extérieur) et 15 cm (vers l'intérieur). Un enduit en plâtre de 3 cm (dont 2 cm vieux plâtre et 1 cm plâtre de gypse) assure la finition intérieure.

Les propriétés hygrothermiques des matériaux constituant la paroi ainsi que leurs épaisseurs sont présentées dans le Tableau 8. Une fenêtre à double vitrage de dimensions égales à 1,41 × 1,94 m² a été incluse dans la paroi sud.

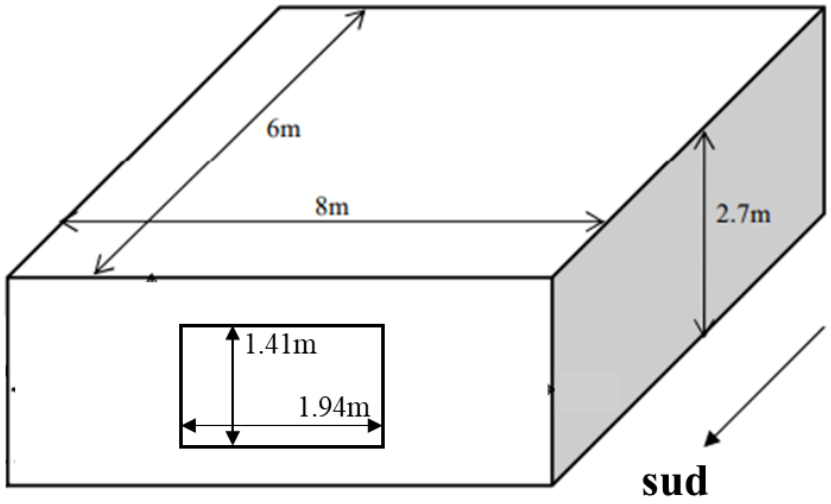

Figure 34. Dimensions du bâtiment étudié.

Tableau 8. Propriétés hygrothermiques et géométriques des matériaux constituant l'enveloppe du bâtiment étudié.

Matériaux	e [m]	ρ_s [kg.m^{-3}]	ε [m^3.m^{-3}]	C_p [J.kg^{-1}.K^{-1}]	λ [W.m^{-1}.K^{-1}]	μ [-]
Extérieur						
Plâtre minéral	0,005	1900	0,24	850	0,8	25
Polystyrène	0,07	30	0,95	1500	0,04	50
Plâtre minéral	0,015	1900	0,24	850	0,8	25
Brique	0,24	1650	0,4	850	0,6	9,5
Vieux plâtre intérieur	0,02	1721	0,31	850	0,2	13
Plâtre de gypse	0,01	850	0,65	850	0,2	8,3
Intérieur						

La chambre est équipée d'un système de régulation thermique, d'une ventilation permettant de maintenir une température constante de 20°C et un taux d'échange d'air constant de 0.6 h^{-1}. Pour simuler une production d'humidité par trois personnes dans la chambre, un scénario d'apport d'humidité a été imposé avec une production journalière de 2.4 kg. Cette production d'humidité est répartie comme mentionnée sur la Figure 35 en considérant une moyenne de 25 g.h^{-1} avec des pics de 400 g.h^{-1} entre 6 h et 8 h et de 200 g.h^{-1} entre 16 h et 22 h.

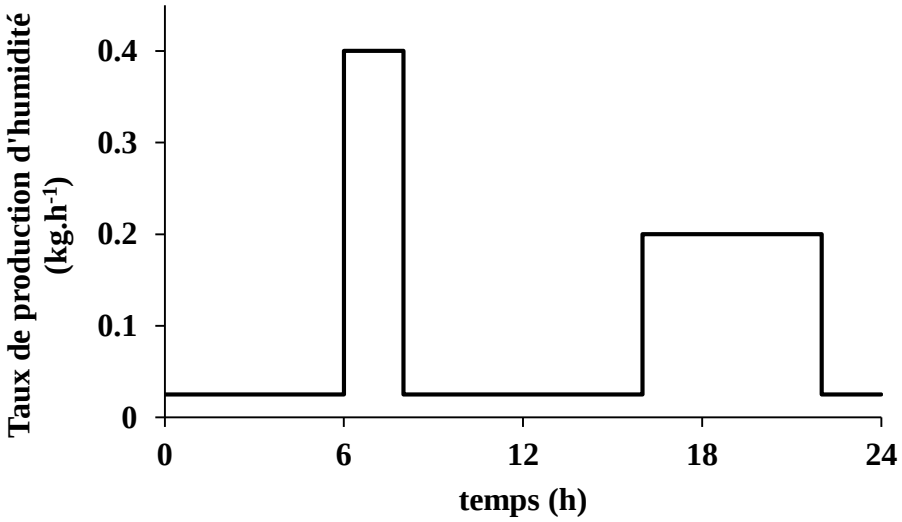

Figure 35. Profil de production d'humidité journalière.

La Figure 36 montre l'évolution de la densité de flux d'humidité sur une période de 48h, calculée sur COMSOL Multiphysics en utilisant les données météo issues de la première simulation de TRNSYS. La densité de flux d'humidité varie entre -1,5 et 3,5 x10^{-7} [kg.m^{-2}.s^{-1}] et suit la même allure que le profil imposé pour la production d'humidité. Elle est renseignée dans le logiciel TRNSYS afin de corriger le calcul hydrique effectué dans ce dernier.

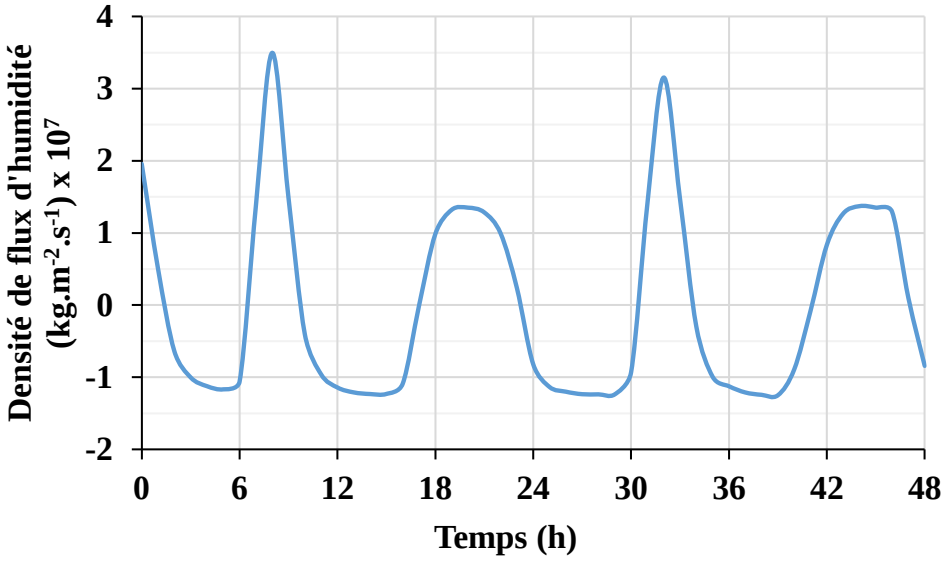

Figure 36. Densité de flux d'humidité à la surface intérieure de l'enveloppe du bâtiment.

La Figure 37.a présente l'évolution de l'humidité intérieure comparée à des simulations conduites en considérant le modèle TRNSYS seul, d'une part et la cosimulation TRNSYS-COMSOL Multiphysics, d'autre part. De prime abord, on note une amélioration de la prédiction du comportement hydrique en prenant en compte les transferts hygrothermiques dans les parois grâce à la cosimulation. En effet, l'écart maximal d'humidité par rapport aux données expérimentales est de 6.3% pour la simulation TRNSYS seul et de 4.4% pour la cosimulation

TRNSYS-COMSOL, respectivement (Figure 37.b). Ce cas de validation montre l'efficacité de la stratégie de cosimulation implémentée.

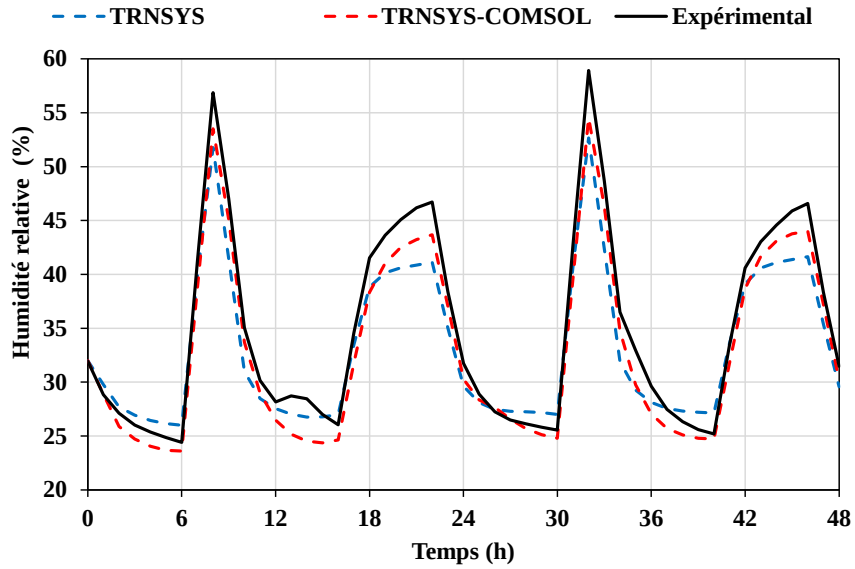

(a)

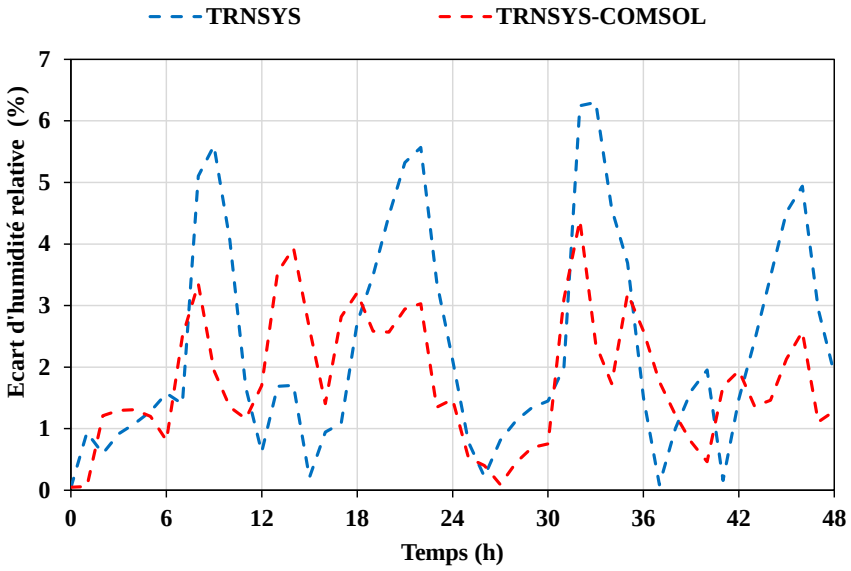

(b)

Figure 37. (a) Comparaison entre la simulation TRNSYS et la cosimulation TRNSYS-COMSOL avec les données expérimentales de la littérature [107], (b) Ecart d'humidité relative entre la simulation TRNSYS et la cosimulation TRNSYS-COMSOL par rapport aux données expérimentales..

4.3.4 Présentation du cas d'étude

Le cas d'étude choisi concerne une chambre de dimensions identiques à celles utilisées pour valider la stratégie de cosimulation. L'enveloppe du bâtiment est composée des parois multicouches élaborées dans la sous-section 4.2, permettant une évaluation plus précise de leur comportement hygrothermique à l'échelle du bâtiment. Pour cette étude, nous considérons uniquement trois isolants à savoir le béton de chanvre, la laine de verre et le polystyrène expansé. L'étude du bio-composite fera l'objet d'une étude ultérieure du fait du phénomène de changement de phase non pris en charge par TRNSYS.

L'épaisseur de l'isolation en laine de verre et polystyrène est de 10 cm tandis qu'une épaisseur de 20 cm est considérée pour le béton de chanvre de référence afin d'avoir la même résistance thermique sachant que le béton de chanvre est deux fois moins isolant que les deux autres. Les performances du bâtiment sont toujours évaluées dans les climats chauds et humides de Caracas et New Delhi. Le même profil quotidien de production d'humidité illustré dans la Figure 35 est également supposé dans cette investigation.

La chambre est équipée d'un système de régulation thermique, d'une ventilation permettant de maintenir une température entre 20 et 25°C et un taux d'échange d'air constant de 0.6 h^{-1} à une humidité de 30%. Les puissances de climatisation et de chauffage nécessaires pour maintenir cette plage de confort sont calculées afin d'évaluer les performances de chaque isolant.

Les Figure 38.a et b montrent l'évolution de l'humidité relative de l'ambiance interne obtenue en utilisant le modèle TRNSYS seul et la cosimulation TRNSYS-COMSOL Multiphysics pour les villes de New Delhi et Caracas, respectivement. On observe une différence notoire entre les profils d'humidité obtenus avec les deux approches indépendamment des conditions climatiques. Pour la ville de New Delhi, l'effet du couplage entre les transferts thermiques et hydriques est mis en évidence. Cet effet, encore appelé thermodiffusion est plus prononcé pendant l'été lorsque la température extérieure est supérieure à 30°C (amplitude des fluctuations de température élevée). Pendant cette période, le flux d'humidité induit par la thermodiffusion atteint une valeur maximale de 8.10^{-5} $kg.m^{-2}.s^{-1}$ (Figure 38.c). Ainsi, pour un climat chaud et humide, la non prise en compte du couplage entre les deux mécanismes de transfert entraine une surestimation de l'humidité relative. Pour la ville de Caracas, l'effet de la thermodiffusion est quasiment négligeable. Cela s'explique par de faibles gradients de température du fait de la température quasi-constante tout au long de l'année. En effet, lorsqu'on observe l'évolution du flux d'humidité induit par la thermodiffusion, on constate qu'il fluctue autour d'une valeur moyenne proche de zéro tout au long de l'année. Ces résultats laissent supposer que pour un climat type de Caracas, la simulation avec le logiciel TRNSYS est suffisante pour décrire les profils d'humidité avec une bonne estimation.

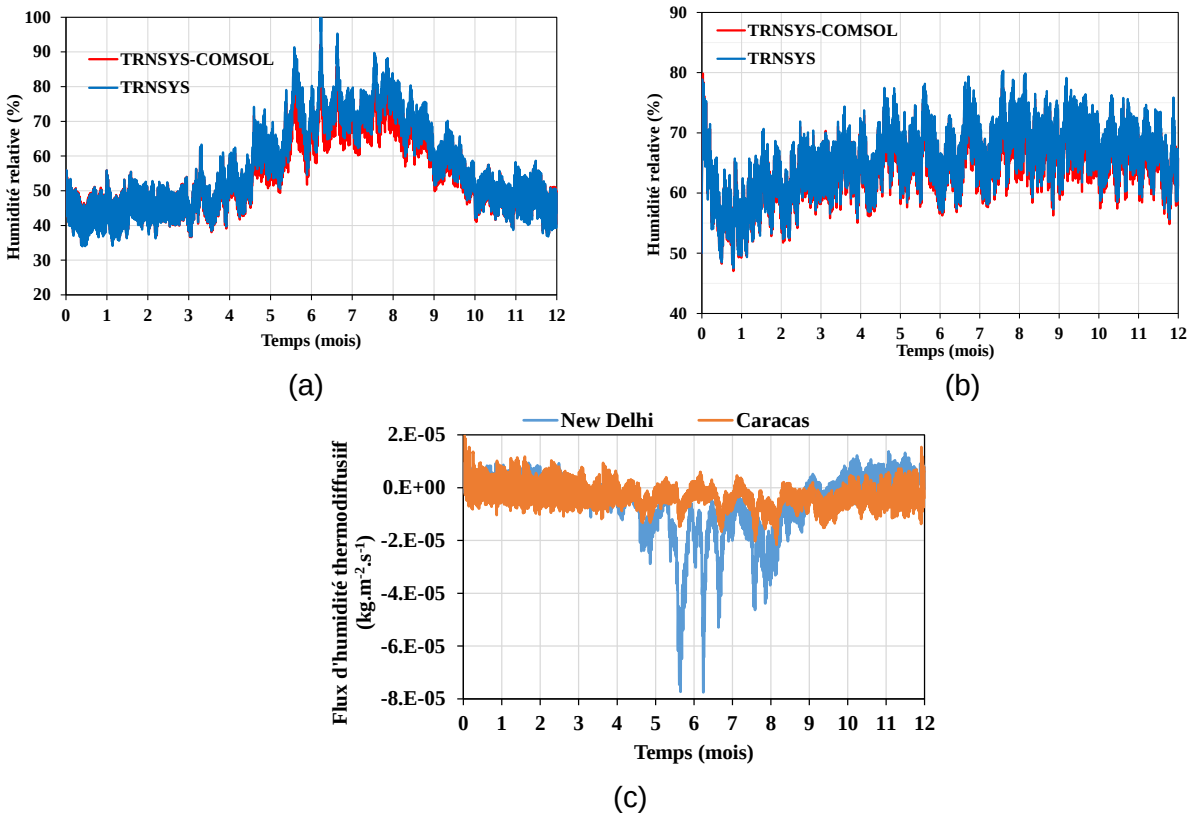

Figure 38. Evolution de l'humidité relative de l'ambiance interne obtenue en utilisant la simulation TRNSYS seule et la cosimulation TRNSYS-COMSOL Multiphysics pour les villes de New Delhi (a), Caracas (b) et évolution du flux d'humidité dû à la thermodiffusion dans les deux villes (c).

En utilisant l'approche de cosimulation, l'évolution de l'humidité de l'ambiance interne au cours de l'année est simulée pour les trois isolants considérés dans les conditions climatiques de la ville de New Delhi et Caracas. Pour la ville de New Delhi (Figure 39.a), on observe des pics d'humidité plus élevés avec des valeurs avoisinant les 100% pour les isolants à base de polystyrène et de laine de verre. L'utilisation du béton de chanvre permet de lisser ces fluctuations et de réduire les pics. En effet, le béton de chanvre est un excellent moyen d'amortir passivement les variations quotidiennes de l'humidité relative. Il serait intéressant d'analyser également la réponse des deux autres matériaux à épaisseur équivalente pour vérifier si le même lissage est observé.

Pour la ville de Caracas (Figure 39.b), l'humidité interne varie sur une plage relativement étroite contrairement aux résultats observés pour la ville de New Delhi. En effet, l'humidité interne fluctue entre 50 et 80% avec une moyenne atour de 65%, contre 30 à 100% pour la ville de New Delhi. Dans ces conditions, les trois isolants réagissent de la même manière et l'effet de régulateur du béton de chanvre est moins prépondérant. Cela peut s'expliquer par la faible présence de la thermodiffusion dans cette configuration climatique (Figure 38.c).

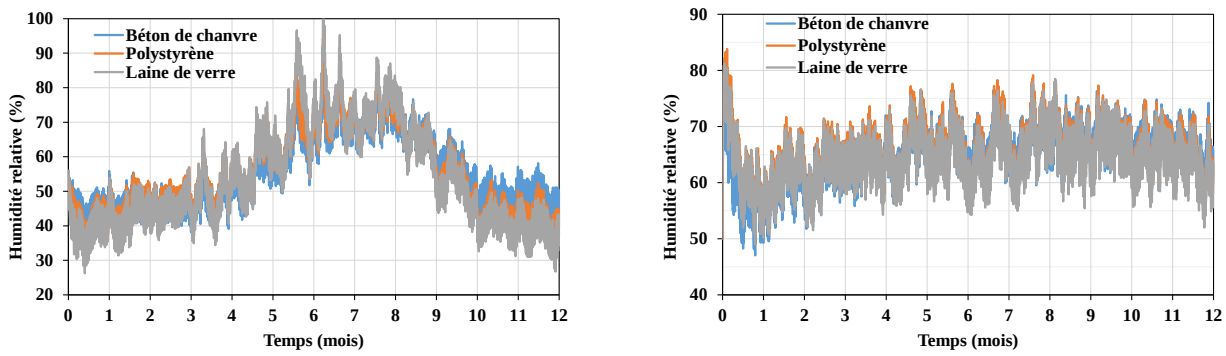

Figure 39. Evolution de l'humidité relative avec trois matériaux d'isolation (béton de chanvre, polystyrène et laine de verre) dans la ville de New Delhi (a) et Caracas (b).

Les puissances de chauffage et de climatisation nécessaires pour maintenir une température interne entre 20 et 25°C pour chacune des configurations d'enveloppes et de conditions climatiques ont été calculées afin d'évaluer l'efficacité de chaque isolant. Les Figure 40.a et b montrent l'évolution de la puissance de climatisation pour chaque isolant dans la ville de New Delhi et Caracas, respectivement. On constate une meilleure efficacité pour la laine de verre suivie du polystyrène, le béton de chanvre possédant l'efficacité la plus faible. Ce résultat est en rapport avec les valeurs de la conductivité thermique des isolants : la laine de verre possède la conductivité thermique la plus faible, suivie du polystyrène et enfin le béton de chanvre. Pour la ville de New Delhi, le maximum de la consommation énergétique est obtenu pour le mois de juin avec des valeurs de 297,53 kWh, 281,62 kWh et 265,14 kWh pour le béton de chanvre, le polystyrène et la laine de verre, respectivement. Par contre, pour la ville de Caracas, cette consommation de climatisation est maximale pour le mois d'octobre avec des valeurs de 138,61 kWh, 133,18 kWh et 126,54 kWh pour le béton de chanvre, le polystyrène et la laine de verre, respectivement. Cependant, pour deux mois en l'occurance mars et novembre, le béton de chanvre montre des performances similaires et voire même meilleures que les autres isolants.

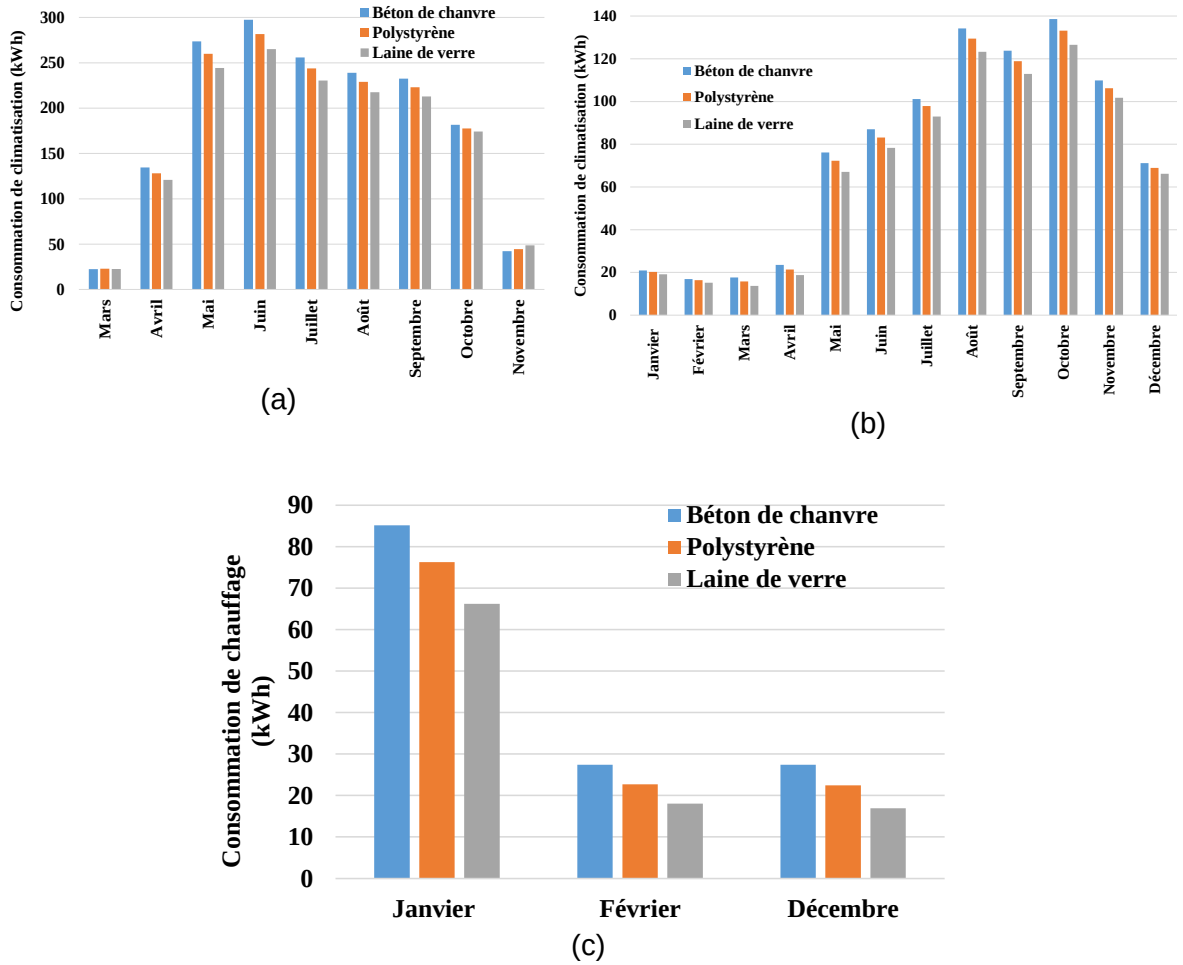

Figure 40. Evolution de la puissance de climatisation mensuelle pour chaque isolant dans la ville de New Delhi (a) et Caracas (b) et évolution de la puissance de chauffage mensuelle pour la ville de New Delhi (c).

En raison de températures toujours supérieures à 20°C pour la ville de Caracas, il n'y a pas de besoin en chauffage. Pour la ville de New Delhi (Figure 40.c), cette consommation de chauffage est maximale pour le mois de janvier avec des valeurs de 85,16 kWh, 76,23 kWh et 66,19 kWh pour le béton de chanvre, le polystyrène et la laine de verre, respectivement. En abaissant la température seuil pour l'activation du chauffage à 18°C, les besoins en chauffage s'annulent.

4.3.5 Conclusion

Dans cette étude, nous avons proposé une approche de cosimulation basée sur la méthode de chainage. La méthode a été confrontée aux données expérimentales extraites des résultats de la littérature. Deux approches ont été utilisées, notamment une simulation avec le logiciel TRNSYS seul et une seconde avec la cosimulation TRNSYS-COMSOL. Les résultats ont montré une amélioration de la prédiction avec la prise en compte de couplage hygrothermique réduisant l'écart entre données expérimentales et la simulation de 2%.

La plateforme de cosimulation développée a été utilisée pour évaluer les performances hygrothermiques de trois isolants à l'échelle du bâtiment dans les conditions climatiques des villes de New Delhi et Caracas. Les résultats ont montré que pour la ville de New Delhi, le maximum de la consommation énergétique est obtenue pour le mois de juin avec des valeurs de 297,53 kWh, 281,62 kWh et 265.14 kWh pour le béton de chanvre, le polystyrène et la laine

de verre, respectivement. En revanche, pour la ville de Caracas, cette consommation de cliamtisation est maximale pour le mois d'octobre avec des valeurs de 138,61 kWh, 133,18 kWh et 126,54 kWh pour le béton de chanvre, le polystyrène et la laine de verre, respectivement.

Cette étude est une introduction à la cosimulation. Dans les futurs travaux, nous envisageons développer une approche de cosimulation dynamique avec une interaction à chaque pas de temps entre les deux logiciels. De plus, il n'a pas été possible d'étudier le bio-composite developpé dans cette thèse du fait du phénomène de changement phase non pris en charge par TRNSYS. Cependant, certains auteurs comme Al-saadi et al. [112] ont développé un type (module) qui permet de prendre en compte le changement de phase sur TRNSYS. D'autres auteurs ont développé des modèles capables de simuler le comportement des MCP dans un modèle hygrothemique [82]. Néanmoins, dans ces études, le comportement hygrothermique est décrit par le modèle de Künzel qui néglige la thermodiffusion qui, comme demontré dans cette étude ne peut être négligé dans les climats très chauds et humides. Ainsi, dans la continuité de ces travaux, nous nous attèlerons à implémenter un modèle de changement de phase dans le modèle TRNSYS en parallèle avec la stratégie de cosimulation dynamique qui prend en compte tous les phénomènes liés au couplage hygrothermique.

4.4 Bilan

Dans cette partie, nous nous sommes intéressés au développement d'un modèle de transfert couplé de chaleur et d'humidité dans les enveloppes des bâtiments. Un modèle hygrothermique, basé sur les équations de conservation de l'énergie et de la masse, a été développé pour simuler le comportement de matériaux de construction. Ce modèle est alimenté par les données expérimentales issues d'une campagne expérimentale. Les données expérimentales du bio-composite sont utilisées pour valider le modèle numérique (développé grâce au logiciel COMSOL Multiphysics). Le modèle numérique développé a montré une bonne concordance avec les résultats expérimentaux, avec une erreur quadratique moyenne maximale entre les résultats expérimentaux et numériques d'environ 0,6°C et 6% pour la température et l'humidité relative, respectivement. En plus de cette validation, le modèle numérique a été validé avec succès en utilisant des données expérimentales et celles des normes reconnues pour différents types de matériaux. Il constitue donc un outil robuste pour évaluer et comparer les performances de divers matériaux de construction dans des conditions climatiques réelles.

Ensuite, le modèle hygrothermique a été utilisé pour évaluer les performances et le comportement hygrothermique de parois multicouches dans des conditions météorologiques réalistes. Cinq types de parois, y compris une paroi hybride innovante intégrant une couche isolante à base de formes stabilisées (béton de chanvre + MCP) soumises à des conditions climatiques réelles de Caracas et de New Delhi ont été investiguées. Les parois hybrides innovantes se sont avérées prometteuses. À New Delhi, elles ont montré des performances similaires au béton de chanvre mais avec la capacité de retarder les pics de température de 28,5 h. À Caracas, ces parois hybrides étaient plus efficaces, réduisant la charge de transfert de chaleur de 20 $kW.m^{-2}$. La fraction de MCP dans le matériau a un impact significatif. Une paroi hybride avec une fraction élevée de MCP peut réduire la charge de transfert de chaleur de 40 % pour une épaisseur de 30 cm. En résumé, ces parois hybrides à base de MCP sont prometteuses pour améliorer l'efficacité énergétique des bâtiments dans des climats chauds et humides.

Enfin, une approche de cosimulation entre COMSOL Multiphysics et TRNSYS est proposée pour mieux prendre en compte le couplage entre les transferts de chaleur et d'humidité dans les enveloppes de bâtiments. Cela permet d'obtenir une évaluation plus complète et réaliste des performances hygrothermiques des matériaux isolants. L'approche a été validée en utilisant les données expérimentales de la littérature. On dénote une amélioration significative de la prédiction du comportement hydrique des parois, réduisant l'écart entre données expérimentales et la simulation de 2%. L'approche de cosimulation a été utilisée pour évaluer les performances hygrothermiques d'enveloppes intégrant trois isolants d'épaisseurs différentes (20 cm pour le béton de chanvre et 10 cm pour la laine de verre et le polystyrène) à savoir le béton de chanvre, le polystyrène et la laine de verre dans les villes de New Delhi et Caracas. Ce cas d'étude a permis de montrer que pour un climat chaud et humide, la non prise en compte du couplage entre les deux mécanismes de transfert entraine une surestimation de l'humidité relative. Cette approche originalé, bien qu'introductive a montré la necessité d'introduire une modélisation fine du comportement hygrothermique des enveloppes de bâtiments dans les logiciels de simulation dynamique. Dans la suite de mes travaux de thèse, l'approche de cosimulation sera améliorée notamment à travers la prise en compte du phénomène de changement de phase afin de pouvoir évaluer les performances hygrothermiques du bio-composite à l'échelle du bâtiment.

5 Conclusion et perspectives

Le contexte climatique régional et mondial impose de revoir les stratégies de consommation d'énergie et d'émissions des gaz à effet de serre. Le secteur du bâtiment représente une grande part des consommations énergétiques et des émissions de gaz à effet de serre. Le développement d'enveloppes durables et innovantes contribuerait à la stratégie bas carbone, à la diminution des consommations énergétiques et à la valorisation des énergies disponibles. C'est dans ce contexte que s'inscrivent mes travaux de thèse. Ils visent à développer, caractériser et simuler le comportement hygrothermique des enveloppes innovantes à base de matériaux à changement de phase biosourcés pour optimiser le confort thermique estival dans les bâtiments de manière durable. La littérature fait état de nombreuses études portant sur l'incorporation des MCP dans les enveloppes des bâtiments. Malgré les nombreuses avancées de nombreux verrous restent en suspens, notamment le manque d'études à l'échelle de l'enveloppe du bâtiment, la majorité des études se limitant au développement du matériau composite. De plus, le comportement hygrothermique des enveloppes incorporant les MCP demeurait un enjeu majeur qu'il restait à élucider. Pour mener à bien ces travaux de recherche, nous avons adopté une approche multi-échelles allant de l'échelle du matériau à l'échelle du bâtiment combinant des études numériques et expérimentales.

Tout d'abord, une étude bibliographique a été menée afin de dégager les principales pistes de contribution. Il existe quatre techniques d'incorporation des MCP dans les enveloppes des bâtiments à savoir : l'incorporation directe, la micro et macroencapsulation, l'imprégnation et les formes stabilisées. Indépendamment de la technique utilisée, le MCP doit être encapsulé afin de contenir la phase liquide lors du changement de phase. L'étude bibliographique a ainsi permis d'identifier les fibres végétales comme matériaux de support potentiels pour la fabrication de MCP à formes stabilisées. Outre leur origine biologique, ces matériaux ont une très bonne structure poreuse, ce qui constitue un atout majeur dans le processus d'imprégnation. Quant aux MCP, les acides gras et leurs eutectiques ont retenu notre attention en raison de leur nature renouvelable et de leurs propriétés thermo-physiques intéressantes.

Le logiciel de sélection de matériaux Ansys Granta a permis une sélection préliminaire de quatre fibres naturelles, à savoir les fibres de sapin, les fibres de chanvre, la chènevotte et le paillis de lin, sur la base de critères physiques, thermiques, géographiques et économiques. Les fibres sélectionnées sont imprégnées dans deux MCP purs (acides caprique et laurique) et comparées en termes de taux d'imprégnation afin de sélectionner le meilleur matériau support pour la stabilisation de la forme d'acides gras. Les fibres de sapin et de chanvre ont montré de faibles taux d'imprégnation (entre 1 et 8 wt%) tandis que la chènevotte et le paillis de lin ont obtenu de bien meilleurs résultats avec des taux d'incorporation de 50 % et 51 %, respectivement. Le choix du matériau support final s'est porté sur chènevotte qui a le principal avantage d'être déjà utilisée dans le secteur de la construction grâce au béton de chanvre, un matériau isolant standardisé. Après la sélection du matériau support, celui-ci a été imprégné avec cinq acides gras purs et sept mélanges eutectiques pour choisir le MCP approprié en vue de la fabrication d'un composite aux performances optimisées. La chaleur latente de fusion est supérieure à 50 J/g pour la plupart des composites, répondant ainsi aux exigences thermiques, notamment une chaleur latente élevée, une faible surfusion, des températures de fusion entre 15 et 45 °C, et une facilité de fabrication. Les bio-composites chènevotte/acide laurique (enthalpie de fusion de 79,3 $J.g^{-1}$ à un taux d'imprégnation de 50 wt%) et chènevotte/acide caprique (57,37 $J.g^{-1}$ à un

taux d'imprégnation de 50 wt%) ont été sélectionnés comme matériaux potentiels pour les applications dans le domaine de la construction.

Ensuite, la chènevotte dont la microporosité a été imprégnée de MCP a été utilisée pour fabriquer du béton de chanvre à base de MCP. Les propriétés thermiques et hydriques du matériau composite ont été évaluées. L'incorporation de MCP a conduit à une augmentation de la conductivité thermique du matériau de référence de 25,7% à 23°C. De plus, le matériau composite a montré une excellente capacité de régulation de l'humidité. L'isotherme de sorption a été mesurée pour évaluer la capacité du matériau à stocker ou libérer de l'eau en fonction de l'humidité relative. La perméabilité à la vapeur d'eau a également été mesurée, montrant une réduction due à la présence de MCP, en raison de la réduction de l'adsorption par la chènevotte. La capacité calorifique massique du bio-composite MCP est obtenue en combinant la capacité thermique du béton de chanvre et du MCP pur à l'aide de la méthode de la capacité thermique équivalente. Afin de compléter la campagne expérimentale, une méthode inverse a été développée pour estimer la diffusivité du liquide et de la vapeur à travers les matériaux composites MCP ainsi que le béton de chanvre de référence. La méthode d'identification est basée sur la minimisation de la différence quadratique entre les valeurs numériques et expérimentales de l'humidité relative. Les coefficients de diffusion de liquide et de vapeur obtenus à partir de l'ensemble des paramètres estimés montrent une bonne concordance avec les résultats de la littérature. Comparé au matériau de référence, le bio-composite possède une inertie thermique plus élevée du fait du changement de phase. Cette inertie thermique augmentée permet non seulement de réduire les pics de température mais aussi ces derniers sont retardés dans le temps. Ainsi, les enveloppes incorporant le bio-composite présenteraient une inertie thermique plus importante que celles avec le matériau de référence. De plus il constitue un bon régulateur d'humidité ce qui permet de résoudre les problèmes de condensation. Le bio-composite constitue une solution prometteuse pour une application dans les bâtiments au regard de toutes ces propriétés hygrothermiques.

A l'échelle de la paroi, une étude comparative des performances hygrothermiques a été réalisée en exposant des parois de béton de chanvre de référence et des parois intégrant le bio-composite (MCP) aux conditions climatiques de la ville de La Rochelle. Ces essais ont été conduits dans une enceinte biclimatique permettant de réguler la température et l'humidité. Le comportement hygrothermique des deux matériaux est évalué dans différentes conditions climatiques : conditions statiques, journée d'hiver typique et journée d'été typique. Les résultats ont montré que l'incorporation de MCP réduit la température maximale lors des canicules d'environ 2°C, ce qui peut réduire les besoins de refroidissement dans les bâtiments. Cette réduction de la température maximale pendant les vagues de chaleur estivales est due à l'augmentation de l'inertie thermique résultant de l'incorporation du MCP. Ce résultat est prometteur pour la réduction des besoins de climatisation dans les bâtiments. Toutefois, par temps froid, la paroi de référence en béton de chanvre a présenté une température légèrement plus élevée que la paroi bio-composite, indiquant une meilleure isolation thermique. Les deux matériaux ont démontré une bonne capacité de régulation de l'humidité mais la cinétique d'humidité a été plus rapide pour le béton de chanvre de référence en raison de sa perméabilité supérieure. En somme, la paroi en bio-composite ainsi développée démontre une capacité à réguler à la fois la température et l'humidité relative.

Sur le volet numérique, un modèle hygrothermique, basé sur les équations de conservation de l'énergie et de la masse, a été développé pour simuler le comportement des matériaux de construction. Ce modèle est alimenté par les données expérimentales issues de la campagne

expérimentale. Les données expérimentales de l'évaluation des performances hygrothermiques de la paroi bio-composite dans l'enceinte biclimatique sont utilisées pour valider le modèle numérique développé grâce au logiciel COMSOL Multiphysics. Le modèle numérique développé a montré une bonne concordance avec les résultats expérimentaux, avec une erreur quadratique moyenne maximale entre les résultats expérimentaux et numériques d'environ 0,6°C et 6% pour la température et l'humidité relative, respectivement. En plus de cette validation, le modèle numérique a été validé par comparaison avec des données expérimentales et des normes reconnues. Il constitue donc un outil robuste pour évaluer et comparer les performances de divers matériaux de construction dans des conditions climatiques réelles.

Par la suite, le modèle hygrothermique a été utilisé pour évaluer les performances et le comportement hygrothermique des parois multicouches dans des conditions météorologiques réalistes. Cinq types de parois, y compris une paroi hybride innovante intégrant le bio-composite, ont été évaluées dans les conditions climatiques de Caracas et de New Delhi. Les parois hybrides, intégrant le bio-composite, se sont avérées très performantes. À New Delhi, elles ont montré des performances similaires au béton de chanvre, mais avec la capacité de retarder les pics de température de 28,5 heures. À Caracas, ces parois hybrides étaient plus efficaces, réduisant la charge de transfert de chaleur de 20 $kW.m^{-2}$. La fraction massique de MCP dans le matériau a un impact significatif. Ainsi, il a été montré qu'une paroi hybride avec une fraction massique de MCP élevée peut réduire la charge de transfert de chaleur de 40 % pour une épaisseur de 30 cm. En résumé, ces parois hybrides à base de MCP sont prometteuses pour améliorer l'efficacité énergétique des bâtiments dans les climats chauds et humiques.

Enfin, une approche de cosimulation entre le logiciel COMSOL Multiphysics et TRNSYS est proposée pour mieux prendre en compte le couplage entre les transferts de chaleur et d'humidité dans les enveloppes de bâtiments. Cela permet d'obtenir une évaluation plus complète et réaliste des performances hygrothermiques des matériaux isolants. L'approche a été validée en utilisant les données expérimentales de la littérature. On dénote une amélioration significative de la prédiction du comportement hydrique des parois avec une réduction de l'écart entre données expérimentales et la simulation de 2%. La stratégie de cosimulation a ensuite été utilisée pour évaluer les performances hygrothermiques d'enveloppes intégrant trois isolants différents à savoir le béton de chanvre, le polystyrène et la laine de verre dans la ville de New Delhi et Caracas. Cette étude de cas a révélé que, dans un climat chaud et humide, négliger le couplage entre les deux mécanismes de transfert entraîne une surestimation de l'humidité relative. L'approche innovante développée dans le cadre ces travaux de thèse servira de base pour des travaux futurs, notamment en intégrant le phénomène de changement de phase, dans le but d'évaluer les performances hygrothermiques du bio-composite à une échelle plus large, celle du bâtiment.

Les résultats de ces travaux de thèse permettent d'entrevoir plusieurs perspectives, notamment concernant le développement de nouveaux matériaux composites à base de MCP via d'autres techniques et la caractérisation de leurs propriétés ainsi que le développement d'approches numériques pour évaluer leur performances à toutes les échelles. Tout d'abord, à l'échelle du composite fibre + MCP, les acides gras ont montré une bonne affinité avec la chènevotte. Cette affinité pourrait venir de la rugosité de la chènevotte qui améliore la probabilité de nucléation. Cette rugosité peut avoir un impact positif sur les cycles de fusion/solidification du composite. Cette hypothèse doit être correctement étudiée, en particulier à l'interface chènevotte/acide laurique, afin de mieux comprendre le phénomène sous-jacent et la manière dont il affecte les

propriétés thermiques des composites. La caractérisation de l'interface chènevotte/acide laurique peut être réalisée par microscopie et analyse chimique XPS et fera l'objet d'investigations ultérieures. En outre, une analyse quantitative de la nucléation hétérogène des acides gras à la surface de la chènevotte, basée sur la thermographie infrarouge, peut être effectuée pour évaluer l'influence de la rugosité de la surface des pores de la chènevotte sur la nucléation.

Sur le plan expérimental, les propriétes thermiques ont été mesurées uniquement en fonction de la température sans tenir compte de leur état hydrique. Or, de nombreuses études ont montré que ces propriétés dépendent de l'état hydrique du matériau. Une amélioration possible de ce travail serait de caractériser les propriétés thermiques des matériaux developpés en fonction de la teneur en eau. Cela pourrait également avoir un impact positif sur la précision du modèle hygrothermique developpé. A l'échelle de la paroi, malgré de nombreuses améliorations, des études supplémentaires sont nécessaires sur la stabilité à long terme du bio-composite. En effet, au cours des cycles de charge et de décharge, les propriétés du MCP et de l'enveloppe sont amenées à changer ce qui pourrait avoir une incidence sur les performances. Il serait donc intéressant de faire subir aux matériaux developées des cycles de vieillissement accélérés ou en conditions réelles pour évaluer leurs performances sur le long terme.

Dans cette thèse, nous avons utilisé le béton de chanvre pour incorporer les MCP dans les enveloppes des bâtiments. L'inconvenient principal est la fraction maximale de MCP qu'il est possible d'incorporer dans le béton de chanvre. Pour le bio-composite, cette fraction est de 14 wt%. Pour contourner cette limitation, d'autres pistes peuvent être envisagées, notamment la fabrication de panneaux avec la chènevotte imprégnée de MCP en utilisant un bio-liant comme la fécule de maïs. Cela permettrait d'augmenter le pourcentage de MCP dans le mélange mais aussi d'améliorer les propriétés d'isolation. Une autre piste constite à avoir recours à la fabrication additive pour créer soit des macrocapsules incorporant des MCP ou des filaments fabriqués à base de MCP pour la conception d'éléments de paroi à transition solide-solide.

Sur le plan numérique, le modèle a été développé en négligeant l'hystérésis hydrique qui pourrait avoir une incidence non négligeable sur la prédiction du comportement hygrothermique. Ainsi, le modèle développé sera amélioré en prénant en compte le phénomène d'hystérésis. De plus, le modèle suppose un gradient de pression totale négligeable dans les transferts hygrothermiques. Les futurs travaux pourraient s'atteler à l'introduction du transfert d'air sec dans les enveloppes du bâtiment. Ce modèle permettrait d'évaluer la contribution du gradient de pression totale et statuer sur la limite de validité de l'hypothèse formulée dans le modèle developpé. De plus, une étude paramétrique peut être entreprise pour évaluer l'impact de paramètres tels que la température de fusion du MCP, les enthalpies de fusion/solidification et la position de la couche de MCP dans la paroi afin de trouver des paramètres optimaux spécifique à des conditions climatiques données afin d'élargir le domaine d'application des solutions proposées. Enfin, comme dernière perspective, nous envisageons de développer une approche de cosimulation dynamique avec une interaction à chaque pas de temps entre les deux logiciels. Le logiel MATLAB est envisagé comme outil intégrateur pour faire le lien entre TRNSYS et COMSOL Multiphysics. Une telle approche aura pour but d'améliorer la méthode par chainage developpée dans ces travaux. De plus, il n'a pas été possible d'étudier le bio-composite developpé dans cette thèse du fait du phénomène de changement phase non pris en charge par TRNSYS. Ainsi, dans la continuité de ces travaux, nous nous attèlerons à implémenter un modèle de changement de phase dans TRNSYS en parallèle avec la strategie de cosimulation dynamique.

6 Références bibliographiques

[1] V. Masson-Delmotte, P. Zhai, A. Pirani, S.L. Connors, C. Péan, S. Berger, N. Caud, Y. Chen, L. Goldfarb, M.I. Gomis, M. Huang, K. Leitzell, E. Lonnoy, J.B.R. Matthews, T.K. Maycock, T. Waterfield, Ö. Yelekçi, R. Yu, B. Zhou, eds., Climate Change 2021: The Physical Science Basis. Contribution of Working Group I to the Sixth Assessment Report of the Intergovernmental Panel on Climate Change, Cambridge University Press, 2021.

[2] AR5 Synthesis Report: Climate Change 2014 — IPCC, (n.d.). https://www.ipcc.ch/report/ar5/syr/ (accessed October 21, 2023).

[3] Buildings - Energy System, IEA. (n.d.). https://www.iea.org/energy-system/buildings (accessed October 25, 2023).

[4] Stratégie énergétique de la ville, (n.d.). https://www.larochelle.fr/action-municipale/ville-durable/agir-contre-le-changement-climatique/gestion-energetique/strategie-energetique-de-la-ville (accessed October 21, 2023).

[5] Un rapport de développement, pour quoi faire ?, Rapport du développement durable. (n.d.). https://dev-durable.agglo-larochelle.fr/2022/ (accessed October 21, 2023).

[6] Rénovation et décarbonation des bâtiments, European Commission - European Commission. (n.d.). https://ec.europa.eu/commission/presscorner/detail/fr/ip_21_6683 (accessed October 21, 2023).

[7] Réglementation thermique RT2012, Ministères Écologie Énergie Territoires. (n.d.). https://www.ecologie.gouv.fr/reglementation-thermique-rt2012 (accessed October 21, 2023).

[8] Réglementation environnementale RE2020, Ministères Écologie Énergie Territoires. (n.d.). https://www.ecologie.gouv.fr/reglementation-environnementale-re2020 (accessed June 13, 2022).

[9] V. Basecq, G. Michaux, P. Blondeau, C. Inard, Short term storage systems of the thermal energy for buildings: a review, Advances in Building Energy Research. 7 (2013) 66–119. https://hal.archives-ouvertes.fr/hal-01052828 (accessed May 5, 2021).

[10] S. Ben Romdhane, A. Amamou, R. Ben Khalifa, N.M. Saïd, Z. Younsi, A. Jemni, A review on thermal energy storage using phase change materials in passive building applications, Journal of Building Engineering. 32 (2020) 101563. https://doi.org/10.1016/j.jobe.2020.101563.

[11] B. Lamrani, K. Johannes, F. Kuznik, Phase change materials integrated into building walls: An updated review, Renewable and Sustainable Energy Reviews. 140 (2021) 110751. https://doi.org/10.1016/j.rser.2021.110751.

[12] A.A.A.A. Al-Rashed, A.A. Alnaqi, J. Alsarraf, Energy-saving of building envelope using passive PCM technique: A case study of Kuwait City climate conditions, Sustainable Energy Technologies and Assessments. 46 (2021) 101254. https://doi.org/10.1016/j.seta.2021.101254.

[13] J. Bohórquez-Órdenes, A. Tapia-Calderón, D.A. Vasco, O. Estuardo-Flores, A.N. Haddad, Methodology to reduce cooling energy consumption by incorporating PCM envelopes: A case study of a dwelling in Chile, Building and Environment. 206 (2021) 108373. https://doi.org/10.1016/j.buildenv.2021.108373.

[14] Y.K. Yang, I.S. Kang, M.H. Chung, S. Kim, J.C. Park, Effect of PCM cool roof system on the reduction in urban heat island phenomenon, Building and Environment. 122 (2017) 411–421. https://doi.org/10.1016/j.buildenv.2017.06.015.

[15] B. Lamrani, K. Johannes, F. Kuznik, Phase change materials integrated into building walls: An updated review, Renewable and Sustainable Energy Reviews. 140 (2021) 110751. https://doi.org/10.1016/j.rser.2021.110751.

[16] E. Alehosseini, S.M. Jafari, Micro/nano-encapsulated phase change materials (PCMs) as emerging materials for the food industry, Trends in Food Science & Technology. 91 (2019) 116–128. https://doi.org/10.1016/j.tifs.2019.07.003.

[17] D. Kumar, M. Alam, P.X.W. Zou, J.G. Sanjayan, R.A. Memon, Comparative analysis of building insulation material properties and performance, Renewable and Sustainable Energy Reviews. 131 (2020) 110038. https://doi.org/10.1016/j.rser.2020.110038.
[18] S. Vaitkus, R. Karpavičiūtė, S. Vėjelis, L. Lekūnaitė, Development and Research of Thermal Insulation Materials from Natural Fibres, Key Engineering Materials. 604 (2014) 285–288. https://doi.org/10.4028/www.scientific.net/KEM.604.285.
[19] X. -y. Zhou, F. Zheng, H. -g. Li, C. -l. Lu, An environment-friendly thermal insulation material from cotton stalk fibers, Energy and Buildings. 42 (2010) 1070–1074. https://doi.org/10.1016/j.enbuild.2010.01.020.
[20] A.D. Tran-Le, S.-T. Nguyen, T. Langlet, A novel anisotropic analytical model for effective thermal conductivity tensor of dry lime-hemp concrete with preferred spatial distributions, Energy and Buildings. 182 (2019) 75–87. https://doi.org/10.1016/j.enbuild.2018.09.043.
[21] J.C. Damfeu, P. Meukam, Y. Jannot, Modeling and measuring of the thermal properties of insulating vegetable fibers by the asymmetrical hot plate method and the radial flux method: Kapok, coconut, groundnut shell fiber and rattan, Thermochimica Acta. 630 (2016) 64–77. https://doi.org/10.1016/j.tca.2016.02.007.
[22] M.L. Voumbo, A. Wereme, S. Gaye, M. Adj, G. Sissoko, Characterization of the thermophysical properties of kapok, Research Journal of Applied Sciences, Engineering and Technology. 2 (2010) 143–148.
[23] C. Pend, W. Fumei, An investigation of heat flow through kapok insulating material, Fibres Textiles. 2 (2009) 88–92.
[24] K. Manohar, D. Ramlakhan, G. Kochhar, S. Haldar, Biodegradable fibrous thermal insulation, Journal of the Brazilian Society of Mechanical Sciences and Engineering. 28 (2006) 45–47. https://doi.org/10.1590/S1678-58782006000100005.
[25] M. Duquesne, C. Mailhé, K. Ruiz-Onofre, F. Achchaq, Biosourced organic materials for latent heat storage: An economic and eco-friendly alternative, Energy. 188 (2019) 116067. https://doi.org/10.1016/j.energy.2019.116067.
[26] M. Duquesne, C. Mailhé, S. Doppiu, J.-L. Dauvergne, S. Santos-Moreno, A. Godin, G. Fleury, F. Rouault, E. Palomo del Barrio, Characterization of Fatty Acids as Biobased Organic Materials for Latent Heat Storage, Materials. 14 (2021) 4707. https://doi.org/10.3390/ma14164707.
[27] M.-A. Hamdaoui, M.-H. Benzaama, Y. El Mendili, D. Chateigner, A review on physical and data-driven modeling of buildings hygrothermal behavior: Models, approaches and simulation tools, Energy and Buildings. 251 (2021) 111343. https://doi.org/10.1016/j.enbuild.2021.111343.
[28] K. A, K. A, Theoretical and computational investigation of simultaneous heat and moisture transfer in buildings: “Effective penetration depth” theory., (1989). https://www.aivc.org/resource/theoretical-and-computational-investigation-simultaneous-heat-and-moisture-transfer (accessed August 2, 2023).
[29] M. Abadie, N. Mendes, Comparative Analysis of Response-factor and Finite-volume based Methods for predicting Heat and Moisture Transfer through Porous Building Materials, Journal of Building Physics. 30 (2006) 7–37. https://doi.org/10.1177/1744259106064599.
[30] J.R. Philip, Flow in Porous Media, Annu. Rev. Fluid Mech. 2 (1970) 177–204. https://doi.org/10.1146/annurev.fl.02.010170.001141.
[31] A.V. Luikov, Heat and Mass Transfer in Capillary-Porous Bodies, in: Advances in Heat Transfer, Elsevier, 1964: pp. 123–184. https://doi.org/10.1016/S0065-2717(08)70098-4.
[32] J. Irudayaraj, Y. Wu, Analysis and Application OF Luikov’s Heat, Mass, and Pressure Transfer Model to a Capillary Porous Media, Drying Technology. 14 (1996) 803–824. https://doi.org/10.1080/07373939608917125.
[33] M. Qin, R. Belarbi, A. Aït-Mokhtar, L.-O. Nilsson, Coupled heat and moisture transfer in multi-layer building materials, Construction and Building Materials. 23 (2009) 967–975. https://doi.org/10.1016/j.conbuildmat.2008.05.015.

[34] R.W. Lewis, W.J. Ferguson, The effect of temperature and total gas pressure on the moisture content in a capillary porous body, International Journal for Numerical Methods in Engineering. 29 (1990) 357–369. https://doi.org/10.1002/nme.1620290210.
[35] C.R. Pedersen, Prediction of moisture transfer in building constructions, Building and Environment. 27 (1992) 387–397. https://doi.org/10.1016/0360-1323(92)90038-Q.
[36] N. Mendes, I. Ridley, R. Lamberts, P. C. Philippi, and K. Budag. Umidus: A PC program for the Prediction of Heat and Mass Transfer in Porous Building Elements. In IBPSA 99, pages 277–283, Japan, 1999. International Conference on Building Performance Simulation.
[37] N. Mendes, P.C. Philippi, R. Lamberts, A new mathematical method to solve highly coupled equations of heat and mass transfer in porous media, International Journal of Heat and Mass Transfer. 45 (2002) 509–518. https://doi.org/10.1016/S0017-9310(01)00172-7.
[38] S. Whitaker, Simultaneous Heat, Mass, and Momentum Transfer in Porous Media: A Theory of Drying, in: J.P. Hartnett, T.F. Irvine (Eds.), Advances in Heat Transfer, Elsevier, 1977: pp. 119–203. https://doi.org/10.1016/S0065-2717(08)70223-5.
[39] P.C.D. Milly, The coupled transport of water and heat in a vertical soil column under atmospheric excitation, Thesis, Massachusetts Institute of Technology, 1980. https://dspace.mit.edu/handle/1721.1/16085 (accessed July 24, 2023).
[40] K. Abahri, Modélisation des transferts couplés de chaleur, d'air et d'humidité dans les matériaux poreux de construction, These de doctorat, La Rochelle, 2012. https://www.theses.fr/2012LAROS384 (accessed July 25, 2023).
[41] M. Qin, R. Belarbi, A. Aït-Mokhtar, A. Seigneurin, An analytical method to calculate the coupled heat and moisture transfer in building materials, International Communications in Heat and Mass Transfer. 33 (2006) 39–48. https://doi.org/10.1016/j.icheatmasstransfer.2005.08.001.
[42] M. Steeman, M. Van Belleghem, M. De Paepe, A. Janssens, Experimental validation and sensitivity analysis of a coupled BES–HAM model, Building and Environment. 45 (2010) 2202–2217. https://doi.org/10.1016/j.buildenv.2010.04.003.
[43] M.Y. Ferroukhi, R. Djedjig, R. Belarbi, K. Limam, K. Abahri, Effect of Coupled Heat, Air and Moisture Transfers Modeling in the Wall on the Hygrothermal Behavior of Buildings, Energy Procedia. 78 (2015) 2584–2589. https://doi.org/10.1016/j.egypro.2015.11.293.
[44] Y. Liu, Y. Wang, D. Wang, J. Liu, Effect of moisture transfer on internal surface temperature, Energy and Buildings. 60 (2013) 83–91. https://doi.org/10.1016/j.enbuild.2013.01.019.
[45] Künzel, Hartwig. (1995). Simultaneous heat and moisture transport in building components. One- and two-dimensional calculation using simple parameters. Fraunhofer IBP.
[46] T. Alioua, B. Agoudjil, A. Boudenne, K. Benzarti, Sensitivity analysis of transient heat and moisture transfer in a bio-based date palm concrete wall, Building and Environment. 202 (2021) 108019. https://doi.org/10.1016/j.buildenv.2021.108019.
[47] Y.A. Oumeziane, Evaluation des performances hygrothermiques d'une paroi par simulation numérique : application aux parois en béton de chanvre, phdthesis, INSA de Rennes, 2013. https://theses.hal.science/tel-00871004 (accessed July 17, 2023).
[48] N. Reuge, F. Collet, S. Pretot, S. Moisette, M. Bart, O. Style, A. Shea, C. Lanos, Hygrothermal effects and moisture kinetics in a bio-based multi-layered wall: Experimental and numerical studies, Construction and Building Materials. 240 (2020) 117928. https://doi.org/10.1016/j.conbuildmat.2019.117928.
[49] D. Zirkelbach, S.-R. Mehra, K.-P. Sedlbauer, H.-M. Künzel, B. Stöckl, A hygrothermal green roof model to simulate moisture and energy performance of building components, Energy and Buildings. 145 (2017) 79–91. https://doi.org/10.1016/j.enbuild.2017.04.001.
[50] T. Krejčí, J. Kruis, M. Šejnoha, T. Koudelka, Numerical analysis of coupled heat and moisture transport in masonry, Computers & Mathematics with Applications. 74 (2017) 229–248. https://doi.org/10.1016/j.camwa.2017.03.022.
[51] D. Medjelekh, L. Ulmet, F. Gouny, F. Fouchal, B. Nait-Ali, P. Maillard, F. Dubois, Characterization of the coupled hygrothermal behavior of unfired clay masonries:

Numerical and experimental aspects, Building and Environment. 110 (2016) 89–103. https://doi.org/10.1016/j.buildenv.2016.09.037.
[52] L. Nespoli, M.B. Janetti, F. Ochs, Comparing Different Approaches for Moisture Transfer inside Constructions with Air Gaps, in: COMSOL Conference Rotterdam, 2013.
[53] Y. Xu, Z. Zeng, D. Sun, Experimental and numerical investigation on the effect of heat and moisture coupling migration of unsaturated lateritic clay for the soil thermal storage system, Energy and Buildings. 276 (2022) 112499. https://doi.org/10.1016/j.enbuild.2022.112499.
[54] G. Promis, O. Douzane, A.D. Tran Le, T. Langlet,Moisture hysteresis influence on mass transfer through bio-based building materials in dynamic state, Energy and Buildings, Volume 166, 2018, Pages 450-459, ISSN 0378-7788, https://doi.org/10.1016/j.enbuild.2018.01.067.
[55] Colinart, Thibaut & lelièvre, dylan & Glouannec, Patrick. (2014). Hygrothermal behavior of bio-based building materials including hysteresis effects: Experimental and numerical analyses. Energy and Buildings. 84. 10.1016/j.enbuild.2014.09.013.
[56] D. Lelièvre, Simulation numérique des transferts de chaleur et d'humidité dans une paroi multicouche de bâtiment en matériaux biosourcés, PhD Thesis, Lorient, 2015.
[57] Janetti, M. Bianchi, Fabian Ochs, and W. Feist. "3D Simulation of Heat and Moisture Diffusion in Constructions." Comsol Conference Stuttgart. 2011.
[58] L. Rong, H. Yuewu, Heat and Moisture Transfer Characteristics of Multilayer Walls, Energy Procedia. 152 (2018) 324–329. https://doi.org/10.1016/j.egypro.2018.09.142.
[59] F. Liu, B. Jia, B. Chen, W. Geng, Moisture transfer in building envelope and influence on heat transfer, Procedia Engineering. 205 (2017) 3654–3661. https://doi.org/10.1016/j.proeng.2017.10.229.
[60] X. Wang, X. Jin, Y. Yin, X. Shi, X. Zhou, A transient heat and moisture transfer model for building materials based on phase change criterion under isothermal and non-isothermal conditions, Energy. 224 (2021) 120112. https://doi.org/10.1016/j.energy.2021.120112.
[61] CEN/TC 89/WG 10 - Moisture, iTeh Standards Store. (n.d.). https://standards.iteh.ai/catalog/tc/cen/827dd119-af0f-4d12-a371-3d0f0008b295/cen-tc-89-wg-10 (accessed July 31, 2023).
[62] Hagentoft, Carl-Eric & Adan, Olaf & Adl-Zarrabi, Bijan & Becker, Rachel & Brocken, Harold & Carmeliet, Jan & Djebbar, Reda & Funk, Max & Grunewald, John & Hens, Hugo & Kumaran, M. & Roels, Staf & Sasic Kalagasidis, Angela & Shamir, Dina. (2004). Assessment Method of Numerical Prediction Models for Combined Heat, Air and Moisture Transfer in Building Components : Benchmarks for One-Dimensional Cases. Journal of Thermal Envelope and Building Science. 27. 10.1177/1097196304042436.
[63] H. Janssen, B. Blocken, J. Carmeliet, Conservative modelling of the moisture and heat transfer in building components under atmospheric excitation, International Journal of Heat and Mass Transfer. 50 (2007) 1128–1140. https://doi.org/10.1016/j.ijheatmasstransfer.2006.06.048.
[64] Q. Li, J. Rao, P. Fazio, Development of HAM tool for building envelope analysis, Building and Environment. 44 (2009) 1065–1073. https://doi.org/10.1016/j.buildenv.2008.07.017.
[65] A. Fang, Y. Chen, L. Wu, Modeling and numerical investigation for hygrothermal behavior of porous building envelope subjected to the wind driven rain, Energy and Buildings. 231 (2021) 110572. https://doi.org/10.1016/j.enbuild.2020.110572.
[66] A. Fang, Y. Chen, L. Wu, Transient simulation of coupled heat and moisture transfer through multi-layer walls exposed to future climate in the hot and humid southern China area, Sustainable Cities and Society. 52 (2020) 101812. https://doi.org/10.1016/j.scs.2019.101812.
[67] T. Odgaard, S.P. Bjarløv, C. Rode, Influence of hydrophobation and deliberate thermal bridge on hygrothermal conditions of internally insulated historic solid masonry walls with built-in wood, Energy and Buildings. 173 (2018) 530–546. https://doi.org/10.1016/j.enbuild.2018.05.053.
[68] B. Remki, K. Abahri, M. Tahlaiti, R. Belarbi, Hygrothermal transfer in wood drying under the atmospheric pressure gradient, International Journal of Thermal Sciences. 57 (2012) 135–141. https://doi.org/10.1016/j.ijthermalsci.2012.02.005.

[69] J. Berger, D. Dutykh, N. Mendes, B. Rysbaiuly, A new model for simulating heat, air and moisture transport in porous building materials, International Journal of Heat and Mass Transfer. 134 (2019) 1041–1060. https://doi.org/10.1016/j.ijheatmasstransfer.2019.01.025.
[70] L. Ayres de Mello, L.M. Moura, N. Mendes, A model for predicting heat, air and moisture transfer through fibrous materials, International Journal of Thermal Sciences. 145 (2019) 106036. https://doi.org/10.1016/j.ijthermalsci.2019.106036.
[71] L. Ayres de Mello, L.M. Moura, N. Mendes, A model for assessment of heat and moisture transfer through hollow porous buildings elements, Case Studies in Thermal Engineering. 14 (2019) 100446. https://doi.org/10.1016/j.csite.2019.100446.
[72] S.N. AL-Saadi, Z. (John) Zhai, Modeling phase change materials embedded in building enclosure: A review, Renewable and Sustainable Energy Reviews. 21 (2013) 659–673. https://doi.org/10.1016/j.rser.2013.01.024.
[73] A. Frazzica, V. Brancato, V. Palomba, D. La Rosa, F. Grungo, L. Calabrese, E. Proverbio, Thermal performance of hybrid cement mortar-PCMs for warm climates application, Solar Energy Materials and Solar Cells. 193 (2019) 270–280. https://doi.org/10.1016/j.solmat.2019.01.022.
[74] D. Zhou, G.S.F. Shire, Y. Tian, Parametric analysis of influencing factors in Phase Change Material Wallboard (PCMW), Applied Energy. 119 (2014) 33–42. https://doi.org/10.1016/j.apenergy.2013.12.059.
[75] A.M. Thiele, G. Sant, L. Pilon, Diurnal thermal analysis of microencapsulated PCM-concrete composite walls, Energy Conversion and Management. 93 (2015) 215–227. https://doi.org/10.1016/j.enconman.2014.12.078.
[76] J. Jia, B. Liu, L. Ma, H. Wang, D. Li, Y. Wang, Energy saving performance optimization and regional adaptability of prefabricated buildings with PCM in different climates, Case Studies in Thermal Engineering. 26 (2021) 101164. https://doi.org/10.1016/j.csite.2021.101164.
[77] Z.A. Al-Absi, M.H. Mohd Isa, M. Ismail, Phase Change Materials (PCMs) and Their Optimum Position in Building Walls, Sustainability. 12 (2020) 1294. https://doi.org/10.3390/su12041294.
[78] S. Wi, S.J. Chang, S. Kim, Improvement of thermal inertia effect in buildings using shape stabilized PCM wallboard based on the enthalpy-temperature function, Sustainable Cities and Society. 56 (2020) 102067. https://doi.org/10.1016/j.scs.2020.102067.
[79] Y. Fraine, C. Seladji, A. Aït-Mokhtar, Effect of microencapsulation phase change material and diatomite composite filling on hygrothermal performance of sintered hollow bricks, Building and Environment. 154 (2019) 145–154. https://doi.org/10.1016/j.buildenv.2019.02.036.
[80] D. Wu, M. Rahim, M. El Ganaoui, R. Bennacer, B. Liu, Multilayer assembly of phase change material and bio-based concrete: A passive envelope to improve the energy and hygrothermal performance of buildings, Energy Conversion and Management. 257 (2022) 115454. https://doi.org/10.1016/j.enconman.2022.115454.
[81] S.J. Chang, Y. Kang, S. Wi, S.-G. Jeong, S. Kim, Hygrothermal performance improvement of the Korean wood frame walls using macro-packed phase change materials (MPPCM), Applied Thermal Engineering. 114 (2017) 457–465. https://doi.org/10.1016/j.applthermaleng.2016.11.188.
[82] N. Zhu, X. Li, P. Hu, F. Lei, S. Wei, W. Wang, An exploration on the performance of using phase change humidity control material wallboards in office buildings, Energy. 239 (2022) 122433. https://doi.org/10.1016/j.energy.2021.122433.
[83] Z. Wu, M. Qin, M. Zhang, Phase change humidity control material and its impact on building energy consumption, Energy and Buildings. 174 (2018) 254–261. https://doi.org/10.1016/j.enbuild.2018.06.036.
[84] Y. Jiang, M. Lawrence, A. Hussain, M. Ansell, P. Walker, Comparative moisture and heat sorption properties of fibre and shiv derived from hemp and flax, Cellulose. 26 (2019) 823–843. https://doi.org/10.1007/s10570-018-2145-0.

[85] NF EN 12664, Afnor EDITIONS. (n.d.). https://www.boutique.afnor.org/fr-fr/norme/nf-en-12664/performance-thermique-des-materiaux-et-produits-pour-le-batiment-determinat/fa045168/18797 (accessed November 10, 2021).
[86] Norme NF EN 12667 Performance thermique des matériaux et produits pour le bâtiment. Détermination de la résistance thermique par la méthode de la plaque chaude gardée et la méthode fluxmétrique - Produits de haute et moyenne résistance thermique - AFNOR, n.d. https://www.decitre.fr/livres/norme-nf-en-12667-performance-thermique-des-materiaux-et-produits-pour-le-batiment-5552120005762.html (accessed November 10, 2021).
[87] P. Bouloc, S. Allegret, L. Arnaud, Hemp: industrial production and uses, CABI, Wallingford, 2013.
[88] P.K.S. Rathore, S.K. Shukla, Enhanced thermophysical properties of organic PCM through shape stabilization for thermal energy storage in buildings: A state of the art review, Energy and Buildings. 236 (2021) 110799. https://doi.org/10.1016/j.enbuild.2021.110799.
[89] M.M. Umair, Y. Zhang, K. Iqbal, S. Zhang, B. Tang, Novel strategies and supporting materials applied to shape-stabilize organic phase change materials for thermal energy storage–A review, Applied Energy. 235 (2019) 846–873. https://doi.org/10.1016/j.apenergy.2018.11.017.
[90] L. Boussaba, G. Lefebvre, S. Makhlouf, A. Grados, L. Royon, Investigation and properties of a novel composite bio-PCM to reduce summer energy consumptions in buildings of hot and dry climates, Solar Energy. 214 (2021) 119–130. https://doi.org/10.1016/j.solener.2020.11.060.
[91] M. Dehmous, E. Franquet, N. Lamrous, Mechanical and thermal characterizations of various thermal energy storage concretes including low-cost bio-sourced PCM, Energy and Buildings. 241 (2021) 110878. https://doi.org/10.1016/j.enbuild.2021.110878.
[92] D.G. Atinafu, W. Dong, X. Huang, H. Gao, G. Wang, Introduction of organic-organic eutectic PCM in mesoporous N-doped carbons for enhanced thermal conductivity and energy storage capacity, Applied Energy. 211 (2018) 1203–1215. https://doi.org/10.1016/j.apenergy.2017.12.025.
[93] NF EN 821-3, Afnor EDITIONS. (n.d.). https://m.boutique.afnor.org/fr-fr/norme/nf-en-8213/ceramiques-techniques-avancees-ceramiques-monolithiques-proprietes-thermoph/fa113314/24983 (accessed March 31, 2022).
[94] I. Gómez-Arriaran, I. Sellens-Fernández, M. Odriozola-Maritorena, A. Erkoreka-González, A PC-tool to calculate the Moisture Buffer Value, Energy Procedia. 133 (2017) 68–75. https://doi.org/10.1016/j.egypro.2017.09.373.
[95] C. Rode, R. Peuhkuri, B. Time, K. Svennberg, T. Ojanen, Moisture Buffer Value of Building Materials, Heat-Air-Moisture Transport: Measurements on Building Materials. (2007). https://doi.org/10.1520/STP45403S.
[96] NF EN 12572-2, Afnor EDITIONS. (n.d.). https://www.boutique.afnor.org/fr-fr/norme/nf-en-125722/structures-artificielles-descalade-partie-2-exigences-de-securite-et-method/fa182518/58638 (accessed March 31, 2022).
[97] F. Boukhelf, Proposition d'une nouvelle formulation mathématique pour l'analyse du comportement hydro thermo mécanique des structures fonctionnellement graduées, These de doctorat, La Rochelle, 2020. https://www.theses.fr/2020LAROS030 (accessed May 29, 2023).
[98] A. Zaknoune, P. Glouannec, P. Salagnac, Identification of the Liquid and Vapour Transport Parameters of an Ecological Building Material in Its Early Stages, Transp Porous Med. 98 (2013) 589–613. https://doi.org/10.1007/s11242-013-0162-x.
[99] A. Challansonnex, F. Pierre, J. Casalinho, P. Lv, P. Perré, Mass diffusivity determination of various building materials based on inverse analysis of relative humidity evolution at the back face of a sample, Construction and Building Materials. 193 (2018) 539–546. https://doi.org/10.1016/j.conbuildmat.2018.10.219.
[100] Assessment Method of Numerical Prediction Models for Combined Heat, Air and Moisture Transfer in Building Components: Benchmarks for One-dimensional Cases - Carl-Eric Hagentoft, Angela Sasic Kalagasidis, Bijan Adl-Zarrabi, Staf Roels, Jan

Carmeliet, Hugo Hens, John Grunewald, Max Funk, Rachel Becker, Dina Shamir, Olaf Adan, Harold Brocken, Kumar Kumaran, Reda Djebbar, 2004, (n.d.). https://journals.sagepub.com/doi/10.1177/1097196304042436 (accessed July 31, 2023).
[101] J.A. Nelder, R. Mead, A Simplex Method for Function Minimization, The Computer Journal. 7 (1965) 308–313. https://doi.org/10.1093/comjnl/7.4.308.
[102] A.A.J. Ketelaars, L. Pel, W.J. Coumans, P.J.A.M. Kerkhof, Drying kinetics: A comparison of diffusion coefficients from moisture concentration profiles and drying curves, Chemical Engineering Science. 50 (1995) 1187–1191. https://doi.org/10.1016/0009-2509(94)00494-C.
[103] K. Koumbogle, F. Gitzhofer, N. Abatzoglou, Moisture Transport Coefficients Determination on a Model Pharmaceutical Tablet, Processes. 10 (2022) 254. https://doi.org/10.3390/pr10020254.
[104] F. Collet, J. Chamoin, S. Prétot, C. Lanos, Comparison of the hygric behaviour of three hemp concretes, Energy and Buildings. 62 (2013) 294–303. https://doi.org/10.1016/j.enbuild.2013.03.010.
[105] F. Bennai, M.Y. Ferroukhi, F. Benmahiddine, R. Belarbi, A. Nouviaire, Assessment of hygrothermal performance of hemp concrete compared to conventional building materials at overall building scale, Construction and Building Materials. 316 (2022) 126007. https://doi.org/10.1016/j.conbuildmat.2021.126007.
[106] F. Benmahiddine, Études des transferts couplés de chaleur, d'air et d'humidité par des techniques de changement d'échelle (microscopique-macroscopique) : Application à l'évaluation de la performance énergétique et la durabilité des matériaux de construction, phdthesis, Université de La Rochelle ; Université Abderrahmane Mira - Bejaïa (Bejaïa, Algérie), 2020. https://theses.hal.science/tel-03516072 (accessed August 15, 2023).
[107] Annex 41, (n.d.). https://bwk.kuleuven.be/bwf/projects/annex41/ (accessed October 16, 2023).
[108] S.O. Olutimayin, C.J. Simonson, Measuring and modeling vapor boundary layer growth during transient diffusion heat and moisture transfer in cellulose insulation, International Journal of Heat and Mass Transfer. 48 (2005) 3319–3330. https://doi.org/10.1016/j.ijheatmasstransfer.2005.02.024.
[109] X. Wang, X. Jin, Y. Yin, X. Shi, X. Zhou, A transient heat and moisture transfer model for building materials based on phase change criterion under isothermal and non-isothermal conditions, Energy. 224 (2021) 120112. https://doi.org/10.1016/j.energy.2021.120112.
[110] NF EN 15026, Afnor EDITIONS. (n.d.). https://www.boutique.afnor.org/fr-fr/norme/nf-en-15026/performance-hygrothermique-des-composants-et-parois-de-batiments-evaluation/fa119083/31029 (accessed March 31, 2023).
[111] Z. Zhai, Q. Chen, P. Haves, J.H. Klems, On approaches to couple energy simulation and computational fluid dynamics programs, Building and Environment. 37 (2002) 857–864. https://doi.org/10.1016/S0360-1323(02)00054-9.
[112] S.N. Al-Saadi, Z. Zhai, A new validated TRNSYS module for simulating latent heat storage walls, Energy and Buildings. 109 (2015) 274–290. https://doi.org/10.1016/j.enbuild.2015.10.013.

Annexes

Article 1

applied sciences

MDPI

Review

Review on the Integration of Phase Change Materials in Building Envelopes for Passive Latent Heat Storage

Mohamed Sawadogo [1,2], Marie Duquesne [2,*], Rafik Belarbi [1], Ameur El Amine Hamami [1] and Alexandre Godin [3]

[1] La Rochelle Université, LaSIE UMR CNRS 7356, Avenue Michel Crépeau, CEDEX 1, 17042 La Rochelle, France; mohamed.sawadogo@univ-lr.fr (M.S.); rafik.belarbi@univ-lr.fr (R.B.); ameur_el_amine.hamami@univ-lr.fr (A.E.A.H.)
[2] Bordeaux INP, CNRS, Université de Bordeaux I2M, Bât A11, 351 Cours de la Libération, 33400 Talence, France
[3] Amplitude, 11 Avenue de Canteranne, Cité de la Photonique, Bâtiment MEROPA, 33600 Pessac, France; alexandre.godin@amplitude-laser.com
* Correspondence: marie.duquesne@u-bordeaux.fr

Featured Application: Passive latent heat storage for building applications, thermal comfort.

Abstract: Latent heat thermal energy storage systems incorporate phase change materials (PCMs) as storage materials. The high energy density of PCMs, their ability to store at nearly constant temperature, and the diversity of available materials make latent heat storage systems particularly competitive technologies for reducing energy consumption in buildings. This work reviews recent experimental and numerical studies on the integration of PCMs in building envelopes for passive energy storage. The results of the different studies show that the use of PCMs can reduce the peak temperature and smooth the thermal load. The integration of PCMs can be done on the entire building envelope (walls, roofs, windows). Despite many advances, some aspects remain to be studied, notably the long-term stability of buildings incorporating PCMs, the issues of moisture and mass transfer, and the consideration of the actual use of the building. Based on this review, we have identified possible contributions to improve the efficiency of passive systems incorporating PCMs. Thus, fatty acids and their eutectic mixtures, combined with natural insulators, such as vegetable fibers, were chosen to make shape-stabilized PCMs composites. These composites can be integrated in buildings as a passive thermal energy storage material.

Keywords: passive energy storage; buildings; phase change materials; energy efficiency

check for updates

Citation: Sawadogo, M.; Duquesne, M.; Belarbi, R.; Hamami, A.E.A.; Godin, A. Review on the Integration of Phase Change Materials in Building Envelopes for Passive Latent Heat Storage. *Appl. Sci.* **2021**, *11*, 9305. https://doi.org/10.3390/app11199305

Academic Editor: Adrián Mota Babiloni

Received: 8 September 2021
Accepted: 1 October 2021
Published: 7 October 2021

Publisher's Note: MDPI stays neutral with regard to jurisdictional claims in published maps and institutional affiliations.

Copyright: © 2021 by the authors. Licensee MDPI, Basel, Switzerland. This article is an open access article distributed under the terms and conditions of the Creative Commons Attribution (CC BY) license (https://creativecommons.org/licenses/by/4.0/).

1. Introduction

The latest report of the Intergovernmental Panel on Climate Change (IPCC) paints a very damning picture. In the most optimistic scenario, the experts predict a temperature rise of more than 1.5 °C as early as 2030, against a warming of more than 4 °C according to the most pessimistic scenario [1]. It is clear that the ambitious objective set by the COP21 and the Paris Agreement to limit global warming to 1.5 °C will not be met. This increase in temperature is responsible for the frequent heat waves and temperature records recently observed in several regions of the world.

Faced with this situation, it is essential to take actions to limit greenhouse gas emissions in order to achieve a zero carbon footprint. The building sector, which accounts for 40% of greenhouse gas emissions, remains one of the first sectors of action to reduce energy consumption and thus limit greenhouse gas emissions [2].

To reduce this energy consumption, mainly used for heating and cooling, it is essential to improve the energy efficiency of buildings by insulation and by taking advantage of renewable energies, such as solar energy.

Thermal energy storage is an effective solution to achieve these objectives through its many advantages:

- the correction of the phase shift between demand and off-peak periods during which prices are more favorable,
- the time shift between production and consumption which allows the reduction of the dependence on fossil fuels by using renewable energies and the limitation of heat losses through storage.

The basic principle of thermal energy storage is the same regardless of the application. A thermal energy storage cycle is divided into three parts: charging, storage and discharging. During the production period, energy is used to charge the storage system. The stored energy can later be returned to the environment as a supplement or substitute for the heating or cooling system, thus reducing energy consumption. The different thermal energy storage techniques are classified according to the scale, the method used and the duration of the storage.

Depending on the duration of the storage, we distinguish short-term and long-term (seasonal) storage. Short-term storage is used on the scale of a few hours, whereas long-term storage is used for longer periods (weeks and months). In addition, short-term storage is used to correct daily (diurnal) or hourly temperature variations, while long-term storage is used to smooth out seasonal temperature fluctuations.

Thermal energy storage can also be classified according to the storage mechanism. Thermal storage can be done in essentially three ways: sensible heat storage, latent heat storage, and thermochemical storage. The difference between these three methods lies in the material used, the operating temperature and many other parameters.

Historically, sensible heat energy storage is the most used in buildings [3–6]. However, it requires large volumes of materials due to the low energy density. The use of phase change materials (PCMs) overcomes this constraint through the contribution of latent heat of phase change, which allows the design of more compact systems [7]. Due to the latent heat involved in the phase change processes, PCMs offer high thermal capacity, and more energy can be stored in the building envelope compared to traditional sensible materials.

The main advantages of latent heat storage over sensible heat are higher energy density (up to 14 times higher), nearly constant storage temperature and the wide variety of materials available.

However, PCMs are subjected to many problems due to their low thermal conductivity, supercooling, phase segregation, etc. [7].

Numerous experimental and numerical studies have shown that the integration of PCMs into building envelopes can improve thermal comfort (maintaining the temperature inside a building room between 15 and 35 °C) by reducing peaks and fluctuations in indoor temperature [6–11].

The objective of this work is to review the recent advances on passive latent heat energy storage and, more specifically, on numerical and experimental studies of different techniques for the integration of PCMs in buildings. To do so, the review is structured as follows: first, a brief description of thermal energy storage systems and different techniques for integrating PCMs into buildings are presented in Section 2. Section 4 is dedicated to the presentation of experimental and numerical studies of buildings incorporating PCMs. The experimental studies are divided into two groups: studies at the composite scale and studies at the wall and building scale. This part is ended by a discussion of the conclusions of the different studies in order to select the techniques and materials that will be studied further in the context of passive thermal energy storage in buildings.

2. Thermal Energy Storage Systems in Buildings

Thermal energy storage systems in buildings are classified into three categories: passive, active or hybrid. Generally, an energy storage system consists of a storage unit and a heat transfer fluid. In passive systems, the heat transfer fluid does not contribute significantly to the storage because of its low heat capacity (usually air) and the storage is done at

low temperatures between 20–60 °C. In contrast, in active systems, the heat transfer fluid contributes to the storage and the heat can be stored at both low and medium temperatures (between 40 and 95 °C) [11]. Another singular difference between passive and active storage is the system used to circulate the heat transfer fluid. In passive systems, the heat transfer fluid circulates naturally while a mechanical device (fan, pump) is used to circulate the heat transfer fluid in an active system. Hybrid systems combine the two previous storage modes.

Passive storage systems have been shown to effectively improve thermal comfort while minimizing the need for mechanical heating or cooling systems.

2.1. Materials for Passive Thermal Energy Storage

Capacity, charge and discharge rate, storage period, charge and discharge time, and cost are the most important criteria for the selection of storage materials [12]. As mentioned in the introduction, heat can be stored in a material by three mechanisms: sensible, latent, and thermochemical heat.

Sensible heat storage is the easiest way to store energy and involves applying a temperature gradient to a material for storing heat or cold. The amount of heat stored depends on three parameters: the mass of the material, the heat capacity of the material at constant pressure, and the range of temperature variation. The materials generally used for sensible storage are clay, hollow bricks, concrete or stone, which are widely used in the building industry.

Latent heat storage stores energy by taking advantage of phase change. The materials used for latent storage are known as PCMs. PCMs are classified according to several criteria, such as their nature (organic or inorganic), their origin (renewable or non-renewable), and their phase change temperature (low, medium, and high) or according to the nature of the phase change involved in the process (solid-solid, solid-liquid, liquid-gas). The solid-liquid phase change is, to date, the most widely used because of its high enthalpy and the absence of problems related to pressure [13]. Abhat et al. [14] proposed a classification of solid-liquid PCMs into three groups according to their nature: organic, inorganic, and eutectic. Organic PCMs include paraffin, fatty acids, sugar alcohol, and polyethylene glycol (PEG). Inorganic PCMs are salt hydrates, nitrates, and metallics having a high heat of fusion. Eutectic PCMs are mixtures of two or more PCMs and are classified as organic-organic, inorganic-inorganic or organic-inorganic.

Finally, the last storage mode uses thermochemical materials that store energy through an endothermic/exothermic reaction/process by generating easily separable reaction products [15].

The advantages and disadvantages of the different storage modes are presented in Table 1.

Table 1. Advantages and disadvantages of the different storage modes [8,16,17].

Storage Modes	Advantages	Disadvantages
Sensible	- Low price - Availability - Non-toxic - Simple and already commercialized technologies	- Incompatibility to corrosion - Thermal instability during cycles - Low energy density
Latent	- High energy density - Quasi-constant storage temperature - No overheating	- Low thermal conductivity - Presence of overpressure and phase segregation

Table 1. *Cont.*

Storage Modes	Advantages	Disadvantages
Thermochemical	- Efficiency	- Corrosion
	- Suitable for seasonal storage	- Risk of exhaustion of solid-gas chemical reactions
	- Large storage capacity	- Complex and not mature technology

Recently, PCMs have been studied extensively in order to lift the locks and allow a massive deployment of this technology in buildings. Thus, the systems that will be presented in this study will be those incorporating PCMs only. Table 2 provides a comparative summary of the advantages and disadvantages of the different types of PCMs.

Table 2. Advantages and disadvantages of the different types of PCMs [9,18–20].

PCM Types	Advantages	Disadvantages
Organic	- High enthalpy of fusion - Long-term thermal and chemical stability - Compatibility with most building materials	- Incompatibility with some container materials, e.g., plastic - Flammability - Low thermal conductivity (about 0.2 W m^{-1} K^{-1})
Inorganic	- High storage density compared to organic PCMs - High thermal conductivity (almost double that of organic PCMs) - Low cost availability - Compatibility with plastic containers - Non-flammability	- Corrosion - Significant volume expansion - Phase segregation
Eutectic	- Appropriate and adjustable transition temperature - High enthalpy of fusion - Congruence of phase change	- High cost - Limited thermo-physical properties

Organic PCMs are the most widely used for thermal energy storage due to their suitable melting/solidification temperature, high storage density, chemical stability, and storage capacity [17].

2.2. Passive Storage Systems Incorporating PCMs

Basecq et al. [11] have identified three techniques for passive energy storage. The first method is to use the structural elements of the building, such as walls, roofs, and floor, to capture and store energy. The second method is to increase the storage capacity of the building by adding an additional storage system, such as a water tank or pebble bed system. The last method is to use the thermal capacity of the ground or the exterior envelope of the building. Only the systems of the first method are presented in this section.

2.2.1. Building Envelopes

Firstly, we will present the conventional building envelopes and the efforts put in place to limit the energy consumption of buildings. Then we will compare these systems with those integrating PCMs in order to discuss the interest of this integration in terms of energy performance of the building.

2.2.2. Conventional Building Envelopes

The building can be considered as a thermodynamic system with the building envelope as its boundary. The balance between energy production, consumption, and storage in buildings is influenced by internal and external loads, as well as the thermal resistance and thermal capacity of the envelope [20]. Therefore, improving the thermal performance of the building envelope is crucial to reduce energy consumption for heating and cooling.

Conventionally, the building structure itself is a means of energy storage. Thus, many passive storage systems rely on structural elements of the building such as walls, roofs, windows, and floors. This type of system can be accomplished on the surface of the structure, which is called surface activation. In this configuration, no specific storage system is used; rather, the intrinsic storage capacity of the building is exploited. It is possible to improve the surface activation system by inserting ducts or pipes in the materials composing the structure to allow a more efficient circulation of the heat transfer fluid [11].

It is also possible to improve the thermal performance of conventional buildings through suitable insulation. The purpose of this insulation layer is to limit heat loss. Building insulation materials can be classified into three categories: conventional, state-of-the-art, and natural. Conventional insulation materials like mineral wool, polystyrene, cellulose, and cork are produced by both chemical and mechanical processes and are commercially available. State-of-the-art insulators are mostly in the research and development stage, such as aerogel, vacuum insulation board, etc. Natural insulators are obtained from agriculture and forest residues, sheep wools [21], and biochar that is obtained from the pyrolysis of agricultural residues.

In most cases, the replacement of part of the conventional building materials by waste materials, such as coffee grounds, natural fibers, wood aggregates, and rubber waste particles, enable to decrease the thermal conductivity and density of the building composites leading to better insulators. Building materials and cement composites have thermal conductivities in the range of 0.120–0.975 W m^{-1} K^{-1} [22].

However, the main disadvantage of insulation materials is the reduction of mechanical properties, such as compressive and tensile strength, which limits their percentage in building materials (between 2.5% and 10%) [23,24].

Lastly, the thermal capacity, energy efficiency, and comfort impact of the thermal storage unit (building, structure or storage unit) can be increased by using PCMs.

2.2.3. Building Envelopes Integrating PCMs

PCMs have the advantage to be easily incorporated into the building structure. PCM-based gypsum boards have been used in many studies to incorporate PCMs into building envelopes [25–27]. In fact, gypsum boards are cheap and widely used in many applications, making them very suitable for encapsulating PCMs [28].

Window shutters can also be used to embed PCMs in buildings [29–31]. Thus, the shutter containing the PCMs is placed on the outside of the windows. During the day, they are open and exposed to solar irradiation, heat is absorbed, and the PCM melts. At night, the shutter is closed and the heat from the PCM is released into the rooms.

Finally, another possibility is to incorporate the PCMs into concrete blocks or other building materials, which results in a structure with high thermal inertia. This technique allows the incorporation of PCMs throughout the building envelope (walls, roofs, floors) to store energy [32–36].

2.2.4. Trombe Walls

Originally developed by Edward Morse in 1881, this passive wall system is named after the French architect Felix Trombe who began applying it in the late 1950s [37]. Standard Trombe walls consist of a high thermal mass wall made of concrete, stone, brick, or earth, covered with glass, resulting in an air channel between the two components.

New Trombe wall configurations incorporating PCMs have been developed in recent years to boost their performance [38–41]. The PCM layer is usually placed on the wall

surface but can also be located inside the wall [42]. The use of PCMs in the Trombe wall reduces the annual energy consumption by 10–30%, depending on the climatic conditions [43,44]. This is because PCMs can increase the amount of stored thermal energy. Therefore, the Trombe wall will be able to heat the room much longer with PCMs than without PCMs.

In the next section, we will discuss the different techniques for incorporating PCMs into passive systems.

2.2.5. Incorporation of PCMs into Building Envelopes

The integration of PCMs into building envelopes improves thermal comfort by reducing peak and fluctuating indoor temperatures due to a storage density 5–10 times higher than that of standard walls [17]. Moreover, thanks to this high thermal inertia, the temperature peak is delayed in time, resulting in a reduction in peak temperature, which allows taking advantage of lower electricity costs.

PCMs can be incorporated into the entire building envelope: walls, roofs, windows, and floors. Four techniques for incorporating PCMs into building envelopes are presented in the literature: direct incorporation, impregnation, encapsulation, and shape-stabilized.

The distinction between the last two methods is not clear in the literature. Some authors [9,18,45] distinguish between encapsulation and shape stabilization, while Umair et al. [46] classify encapsulation in shape stabilization. In this section, we will distinguish between encapsulation and shape stabilization.

2.2.6. Direct Incorporation

This technique involves the direct incorporation of PCMs into building materials. Direct incorporation is considered the simplest and most economical way to incorporate PCMs into building walls [17]. The main disadvantage of this technique is the risk of leakage of the PCM over time and degradation of the mechanical properties of the building material [45].

2.2.7. Impregnation

In this method, the porous building material, such as gypsum board, brick or concrete block, is immersed in the molten PCM and absorbs it by capillarity [20]. Although more effective than the direct incorporation technique, it is still subject to the same risks of leakage and degradation of the mechanical properties of the building material.

2.2.8. Encapsulation

In this technique, the PCM is encapsulated before incorporation into the building materials to contain the liquid phase. The encapsulation material must meet certain criteria to be compatible with the materials of construction: (1) formation of a shell surrounding the PCM called the core; (2) prevention from the leakage of molten PCM; (3) no incorporation of impurities into the core/shell system, and (4) resistance to mechanical and thermal stresses [47]. Capsules are classified based on their size and shape, which are influenced by the synthesis process and the type of shell material used. They are referred to as nano-capsules or nano-spheres if the diameter of the capsules is between 0 and 1000 nm, micro-capsules if the diameter of the capsules is less than 1 mm or 1 cm, and macro-capsules when the capsules are larger than 1 mm or 1 cm [48].

2.2.9. Shape-Stabilized

Shape-Stabilized PCMs are obtained by impregnating PCMs into porous building materials. This technique stabilizes the PCMs and prevents leakage problems during the phase change process due to capillary force, surface tension, hydrogen bonding interaction, and other interactions between the porous matrix and the PCMs confined in the nanopores of the building materials [49].

In general, two main techniques are used to infiltrate liquid or solid PCMs into a porous support to fabricate shape-stabilized PCMs composites: the two-step impregnation method and the one-step in situ synthesis method.

The two-step technique involves impregnating liquid PCMs into the nanopores of the porous support. Various impregnation methods have been used to synthesize shape-stabilized PCMs. The preparation processes generally involve the following steps: (1) design and synthesis of the porous supports; (2) addition of the porous support to the PCM solution, which is absorbed into the porous supports, and (3) obtaining the final composite PCMs after complete evaporation of the solvent [49]. Depending on the impregnation process, this method can be divided into direct impregnation and vacuum impregnation. Jeong et al. [50] analyzed the impregnation rate of a PCM in vacuum and non-vacuum processing. It was found that the impregnation rate was close to 50% in the vacuum treatment compared to only 30% in the non-vacuum conditions.

In the one-step method, the PCMs are encapsulated in situ during the formation of an interconnected network of porous supports [49].

There are a wide variety of materials used for shape stabilization of PCMs, including polymers, porous materials, and nanomaterials. Umair et al. [46] classified these materials into five major groups: micro-encapsulation, polymer matrices, nanomaterials, porous materials, and solid-solid PCMs.

Table 3 summarizes the advantages and disadvantages of the different techniques for incorporating PCMs into buildings. Due to the simple and inexpensive manufacturing techniques, the very high impregnation rate compared to other techniques as well as the wide variety of support materials available, shape stabilization was chosen to impregnate PCMs in our future studies.

Table 3. Advantages and disadvantages of the different techniques for incorporating PCMs into buildings [9,18,47,49].

Techniques	Advantages	Disadvantages
Direct incorporation	- Easy technique - Economical technique	- Reduction of mechanical properties - Impact on the hydration process - Leakage of PCM
Impregnation	- Easy technique - Economical technique	- Long-term leakage of PCM - Incompatibility with building materials - Corrosion of reinforced steel when incorporated into concrete elements
Micro-encapsulation	- Improvement heat transfer - Reduction of volume variation of PCM - Possibility of incorporation into various materials - Reduction of phase separation and improvement cycle stability - Improvement of thermal reliability	- Limitation of the volume of PCM that can be used - Complex and costly manufacturing process - Requirement for a non-permeable capsule to prevent leakage - Some production methods may have harmful by-products
Macro-encapsulation	- Improved environmental compatibility of materials - Improved handling of PCMs during production - Increase in the amount of PCMs used	- Moisture transfer problem since the PCM is macro-encapsulated - More work to integrate into the building envelope. - Low thermal conductivity

Table 3. *Cont.*

Techniques	Advantages	Disadvantages
Shape-stabilized	- Simple and inexpensive techniques - Containment of the liquid phase - Wide variety of support materials - Increased thermal conductivity - Possibility to encapsulate a large fraction of PCMs (10–100%)	- PCMs can diffuse to the surface and be progressively lost if the process is not optimized - More contact between the PCM and the environment, which can lead to corrosion or adverse reactions

3. Studies of PCMs Incorporated in Passive Systems

3.1. Experimental Studies

In recent years, many experimental studies have been carried out to evaluate the performance of buildings incorporating building materials/PCMs composites. In this section, these studies are divided into two categories according to the scale involved (material or system).

3.1.1. At the Composite Scale

Cunha et al. [19] incorporated a paraffin PCM (RT22HC) into a mortar made from Portland cement. Four different compositions were tested from the fresh to the 28-day aged state: the reference mortar (0 wt% PCM) and three other mortars composed of 5 wt%, 10 wt% and 15 wt% PCM. The different mortar formulations were tested in terms of physical properties (workability, density, water absorption by capillarity and immersion), mechanical properties (compressive and tensile strength) and thermal behavior. The thermal test was conducted in a climatic chamber of 0.008 m^3 simulating the summer (11–44 °C) and winter (12–29 °C) climatic conditions of a region in Portugal. The results show an improvement of the liquid binder ratio but a reduction for superplasticizer with the PCM fraction was observed. Moreover, the incorporation of 5 wt% of PCM leads to a reduction of the water absorption coefficient by capillarity of 34%. The mechanical properties varied little with the addition of PCM up to 20 wt% where reductions of 8% and 19% were observed for the compressive and tensile properties. On the other hand, the mortar with 20 wt% PCM exhibited the best thermal performance due to a reduced peak temperature of 5 °C and was delayed by 48 min in time.

In a similar study, Kulkarni and Muthadhi [51] analyzed and compared the thermal performance of direct incorporation of PCMs into mortar. Five different PCMs with phase change temperatures in the range of 17–33 °C were used in this study: two inorganic PCMs, HS24 and HS29, and three organic PCMs, OM29, which is a commercially available organic PCM, n-Butyl stearate (n-BS) and polyethylene glycol-600 (PEG-600). The cement in the mortar is partially replaced by the PCMs in proportions of 5 wt% to 15 wt%. To ensure proper retention of the liquid phase of the PCM in the mortar, a leakage test was conducted. The compression test showed a reduction in compressive strength with the addition of PCM. For inorganic PCMs, there was no effect on the mechanical strength at all ages up to 10 wt% incorporation rate compared to organic PCMs where a drastic reduction in mechanical properties is observed at all incorporation levels regardless of ages. All PCM compositions showed high thermal stability after 750 and 1000 cycles. Thermal conductivity measurement performed by the guarded hot plate method for several days shows an increase in thermal conductivity with age and a decrease with the addition of PCM. The formulation of 10 wt% inorganic PCM in the mortar was selected as optimal because it

does not affect the mechanical strength properties and has good thermal performance with a reduction in peak temperature of 3–5°C.

Boussaba et al. [52] conducted an experimental and numerical study of the characteristics of a bio-sourced composite material by direct impregnation of a vegetable non-cocoa oil in an insulating material made of clay and cellulose fibers with an incorporation rate of 56% by volume of PCM. The temperatures, heat of fusion, and solidification of the composite material are measured by differential scanning calorimetry (DSC) and have values of 34.83 °C, 22.34 °C, and 60.41 J g^{-1}, 62.39 J g^{-1}, respectively. The results of chemical and thermal analysis showed good thermochemical stability of the composite material after more than 2000 cycles. However, the PCM impregnation reduces the mechanical properties of the composite material by a factor of two, which remain acceptable for non-building applications. The addition of recycled graphite increased the thermal conductivity by 415% (from 0.2 to 0.83 W m^{-1} K^{-1}).

Dehmous et al. [33] developed a new thermal energy storage concrete consisting of lightweight aggregates impregnated with vegetable oil PCMs, of melting temperature between 23 and 26 °C, mixed in a cement mortar. Three types of mineral aggregates were used (bentonite, sepiolite and silica gel), as well as two impregnation methods, namely direct incorporation and vacuum impregnation. The best impregnation rates were obtained with silica gel (56%), but sepiolite (32%) should be preferred for regulatory reasons according to the mechanical tests. In fact, the regulations for masonry elements stipulate that the value of compressive strength should not be less than 15 MPa [53]. Despite a loss of mechanical strength, the authors demonstrated that composite mortars with a compressive strength greater than 7–10 MPa are feasible. In addition, the results showed an improvement of 24.4% and more than 13.5% for energy storage capacity and thermal conductivity, respectively.

Bake et al. [54] studied the effect of incorporating micro-encapsulated PCMs (MICRONAL® DS 5040X) with temperature between 22 and 23 °C with a heat of fusion of 95 J/g into gypsum board. The proportion of PCM is chosen lower than 30 wt% in order to guarantee the mechanical properties of the composites. Thus, four different compositions of gypsum boards are manufactured: reference gypsum board (0 wt% of PCM), gypsum with 5 wt% of PCM, gypsum with 10 wt% of PCM, and gypsum board with 15% of PCM. The incorporation of PCMs leads to a reduction in compressive strength but the value is still permissible given the recommendation for gypsum board in the building structure, which suggests a compressive strength greater than or equal to 2 MPa [55]. In addition, the thermal conductivity decreases with the addition of PCM that increases the insulation properties of the gypsum boards.

Li et al. [56] conducted an experimental study on the thermal performance of wall-boards containing a micro-encapsulated PCM (MPCM for micro-encapsulated PCM), PH-31, using two methods: DSC and a home-made experimental device. Three different techniques were used to obtain the enthalpy-temperature (H-T) curve: theoretical calculation from DSC data, a dynamic method, and the stepwise method. The sample analyzed is composed of gypsum with 20 wt% microencapsulated kerosene having a phase change temperature of 31 °C. The addition of MPCM decreases the thermal conductivity of the gypsum board due to the lower density and thermal conductivity of PCM, but increases the apparent heat capacity up to 2.71 times for a temperature range of 26–32 °C.

Renewable materials, such as natural fibers, are considered as promising carbon sequestration resources with beneficial effects on the planet's ecosystems, living environment and energy efficiency [57–59]. Kirilovs et al. [60] investigated the specific heat capacity and thermal conductivity of a wallboard made from hemp shives mixed with a commercial organic PCM, S50 at 5 wt%. The addition of nano-capsules increased the heat capacity by 62% to 2.369 J g^{-1} K^{-1}. The thermal conductivity of the samples is in the range of 64–74 mW m^{-1} K^{-1}, which is consistent with the class of commercially available hemp insulation products.

To improve the thermal conductivity of building envelopes incorporating PCMs, additives, such as expanded graphite (EG for "expanded graphite"), montmorillonite, pen-

taerythritol, and melamine polyphosphate can be used [61]. Karaipekli and Sari [62] found that the thermal conductivities of fatty acid/expanded vermiculite composite PCMs were increased by 104–150% by the addition of 10 wt% expanded graphite. Wang et al. [63] have suggested that dopamine modification can solve the problem related to the measurement of the latent heat of expanded vermiculite (EVM)-based composite PCMs. Indeed, the measured latent heat were significantly lower than the calculated values during the phase change process. This mismatch is reduced by increasing the concentration of dopamine. The effect of the dopamine is the modification of the surface of EVM leading to an increase of the latent heat and the encapsulation capacity.

Rathore and Shukla [64] investigated the combined effect of loading expanded graphite (EG) and expanded vermiculite (EV for "expanded vermiculite") on the thermo-physical and thermal regulator properties of commercially available low-cost PCM (OM37). Four samples with different compositions of EG, PCM and EV were prepared with 0, 3, 5, and 7% expanded graphite, respectively. The heat of fusion of the composite was reduced from 50% to 57% compared to pure PCM due to the increase in the mass percentage of expanded vermiculite and expanded graphite in the composite, which do not contribute to latent energy storage. Increases of 33.1%, 79.3%, and 114.4% in the thermal conductivity were observed for the composites containing 3%, 5%, and 7% EG compared to pure PCM. The prepared composites exhibited the same thermal characteristics after 1000 heating and cooling cycles. In addition, when incorporated into the wall panel, the composite containing 7% EG showed excellent ability to regulate the interior temperature.

Biochar has been used to fabricate stabilized shapes due to its interesting porous structure [65–67]. Zhang et al. [68] prepared a shape-stabilized composite material by impregnating a eutectic mixture of lauric-stearic acid (LA-SA) into carbonized corn cobs (CNCC). The latter, thanks to its porous structure, constitutes an excellent support material allowing the LA-SA eutectic mixture to be suitably encapsulated with a maximum impregnation rate of 77.9 wt%. DSC analysis showed that the LA-SA/CNCC composite melts at 35.1 °C with a heat of fusion of 148.3 J/g and solidifies at 29.7 °C with a heat of solidification of 144.2 J g^{-1}. Moreover, its stability after 200 cycles makes it a good candidate for an application in energy storage in buildings.

To minimize the degradation of the thermal regulation performance of PCMs composites, Liu et al. [69] proposed the multi-layer sandwich structure of $Na_2SO_4.10H_2O$, expanded vermiculite and magnesium oxychloride cement (MOC) with a melting temperature in the range of 20–40 °C. Compared with the MOC house-like model and ambient condition, the multi-layer sandwich PCM composite exhibited better results with time shift of 93 min and 84 min for heating and cooling, respectively.

Different techniques are available to integrate PCMs into building envelopes. However, between the high cost of micro-encapsulation and the leakage problems of impregnation and direct incorporation techniques, shape-stabilized PCMs are a good compromise. Moreover, the availability and the wide range of support materials considerably increase the field of application of shape-stabilized PCMs.

Numerous experimental studies have shown that it is possible to increase the thermal conductivity of PCMs by shape stabilization with suitable support materials [70]. Table 4 summarizes some studies using materials of natural origin to shape-stabilize PCMs. It appears that bio-sourced materials, in particular, insulating materials, are promising for the future.

Table 4. Various experimental studies using naturally occurring support materials for the fabrication of shape-stabilized PCMs.

Composites		Temperature of Fusion (°C)	Heat of Fusion (J g^{-1})	References
Support materials	PCM (wt%)			
Diatomite	Paraffin (47.4)	41.11	70.51	[71]
	PEG (50)	27.7	87.09	[72]
	Capric-lauric acid (CA-LA)	23.61	87.33	[73]
Kaolin	Lauric alcohol (24)	19.14	48.08	[74]
	Capric acid (17.5)	30.71	27.23	[75]
	PEG600 (21)	5.16	32.80	[75]
	Heptadecane (16.5)	22.08	34.63	[75]
	Stearic acid (75)	60.1	149.5	[76]
Expanded Vermiculite	n-octadecane (80)	26.1	142	[77]
	Lauric acid (70)	41.88	126.8	[78]
	CA-PA-SA (70)	19.3	117.6	[79]
	CA-LA (40) CA-PA (40) CA-SA (40)	19.09 23.51 25.64	61.03 72.05 71.53	[62]
Expanded Graphite	Heptadecane (94.5)	13.8	195.9	[80]
	LA-MA-SA (92.3)	29.05	137.1	[81]
	PEG (90)	18.89	98.59	[82]
	SA (90)	52.74	169.9	[83]
Biochar	Heptadecane (25.7)	13.9	53,3	[80]
	Paraffin (60)	57.67	179.4	[84]
	LA-SA (77.9)	35.1	148.3	[68]
	Methyl palmitate (43-55)	26–27	108–138	[85]

Table 4. *Cont.*

Composites		Temperature of Fusion (°C)	Heat of Fusion (J g^{-1})	References
Wood flour	LA-SA (60.3)	33.1	98.2	[86]
	Paraffin (29.9)	26.18	20.62	[87]
	CA-PA (80)	22.30	28.16	[88]
Wood fibers	CA-SA (52)	23.38	92.1	[89]
Wood (other forms)	CA-PA (61.2)	23.4	94.4	[90]
	1-tetradecanol (65)	36.87	119.2	[91]
	PEG (45.58)	25.5	46.7	[92]
	MA (83.9)	55.7	179.1	[93]
	Paraffin (84)	60.3	181.9	[93]
	PEG (74.1)	55.8	132.6	[93]
	1-tetradecanol (60.04)	36.24	125.6	[94]
Vegetable fibers	Paraffin (87.2–91.3)	22.1–22.5	192.2–201.6	[95]
	MA-TD (40.5)	28.5–42.5	192	[96]

In addition to their biological origin, these materials have a very good porous structure, which justifies the very high value of the impregnation rate approaching 100%. Shape stabilization is therefore considered as a promising way to take advantage of the latent storage capacity of PCMs. The list of bio-sourced materials that can be used to shape-stabilize PCMs is very large, so we focus on insulating materials that are already in use or are promising for application in buildings (Table 5). These are vegetable fibers, such as flax or hemp. Another advantage of these materials is their ability to regulate humidity, which ensures good indoor air quality. Finally, the cost of these bio-sourced insulators is very attractive.

Fatty acids and their eutectic mixtures have melting temperatures suitable for thermal comfort application (15 to 30 °C, T) and are commonly used. In addition, they are renewable and have similar or better characteristics than paraffin waxes used in actual systems. Fatty acids of interest for the targeted application are reported in Table 6.

Table 5. Bio-sourced insulators considered in a future study as support materials for the fabrication of shape-stabilized PCMs.

Insulator	Density (kg m^{-3})	Thermal Conductivity (W m^{-1} K^{-1})	Cost (€/kg)	References
Bamboo fibers	431–538	77–88	–	[21]
Hemp fibers	25–100	40–49	2–5	[97]
Flax fibers	20–100	35–45	5–25	[97]
Cotton stalk fibers	150–450	58–82	–	[98]
Chènevotte	100–140	80–122	0.8–1	[99]
Kapok	17.24	30–48.6	–	[96,100,101]
Fibres de coco	40–90	501.09–57.58	63	[102]

Table 6. Fatty acids of interest for the targeted application, CA: capric acid, LA: lauric acid, MA: myristic acid, PA: palmitic acid, SA: stearic acid [103,104].

PCM	Temperature of Fusion (°C)
CA	29.87
CA (72%)-LA (28%)	21.14
CA (84%)-MA (16%)	24.24
CA (87%)-PA (13%)	27.95
CA (93%)-SA (28%)	26.91
LA (71%)-MA (29%)	33.07
LA (79%)-PA (21%)	35.46

3.1.2. At the System Scale (Envelopes and Buildings)

PCMs can also be integrated into existing building envelopes through the insulation layers. Lee et al. [105] integrated paraffin with a melting temperature of 28–30 °C into cellulose wall insulation. Two experimental cells of quasi-cubic shape (5.09 m^3) with a window size of 0.32 m^2 were constructed to evaluate the energy performance of insulation with PCMs. Molten PCM is sprayed on the cellulose insulation and the mixture is blown into the wall cavities. Only summer data was studied, as the objective was to reduce space cooling and shift the thermal load over time by measuring the indoor air temperatures on the inside and outside of each wall. The incorporation of paraffin in the insulation reduced the heat flux from 16.1% to 38.5%. The maximum heat flow is delayed from 1.5 to 3 h, which reduces the electricity bill. Analysis of the results for each wall individually showed that only the west-facing wall exhibited a significant reduction in maximum heat flow.

Erlbeck et al. [106] studied different forms of hydrated salt-based PCM macro-encapsulated in aluminum foil to test the influence on the convective heat transfer during phase change. The PCM used is a mixture of 50 wt% $MgCl_2$-$6H_2O$ and 50 wt% $CaCl_2$-$6H_2O$ with a melting temperature of about 21 °C. Several brick block samples containing four different shapes of PCM macro-capsules were fabricated: cubic, cylindrical, spherical and plate shapes, and then compared to reference brick blocks. The results showed that changing the design of a set of PCMs can adjust the thermal behavior without changing the mass of the PCM. The best results were obtained for the plate and cylindrical shape but the complex production process required outweighs the positive thermal effects obtained.

Vicente et Silva [107] conducted a study on three types of wall: a horizontally hollowed-out clay wall taken as reference, a wall with macro-capsules of PCM and a wall with macro-capsules of PCM plus an insulation layer (XPS) named M1, M2, and M3, respectively. The walls are made of horizontally hollowed-out clay bricks (0.009 cm^3) with insertion of parallelepiped steel macro-capsules of two different thicknesses (2.8 cm and 0.75 mm) filled with RT18, an organic PCM with a melting temperature of 18 °C. The tests were

conducted in a climate chamber simulating the equivalent temperature profile for different cities in Portugal. The results showed a strong reduction of the temperature peak for M2 and M3 compared to the reference (M1), up to 50% and 80%, respectively. In addition to the reduction of the temperature maximum, the peak is delayed in time by 3 h for M3. These results provide clear evidence of the thermal regulation effect of macro-encapsulated PCM and the value of combining PCM with well-managed insulation layers to achieve energy savings.

Al-Yasiri and Szabó [108] conducted an experimental study to determine the optimal thickness of a roof incorporating PCM macro-capsules containing paraffin wax of melting temperature 44 °C under the hot climate of Iraq. Three different thicknesses of 10, 15, and 20 mm were studied based on energy indicators, such as ambient temperature, interior surface temperature, and average exterior surface temperature. The values obtained were compared to a reference roof without PCM. The roofs with PCM showed a reduction in maximum room temperature between 7.25 and 9 °C compared to the reference roof. Increasing the thickness from 10 to 15 mm reduced the room temperature by 2.3% compared to only 0.4% when the thickness was increased from 15 to 20 mm. The average decrease in room temperature fluctuation during the day and night is defined as the sum of the average decrease in room temperature during the day and the average increase in room temperature during the night. This parameter allows comparison of different storage devices. The best value is obtained for 15 mm of macro-encapsulated PCM. The reason is that the 20 mm is too thick to solidify passively during the night, which reduces its performance.

To solve the moisture transfer problem caused by macro-encapsulation, Sun et al. [109] proposed a method for encapsulating PCMs in pipes. The tests were conducted in a cubic dynamic wall simulator. n-Octadecane with a melting temperature between 27.5 and 38 °C is used as the PCM. The PCM is melted and then poured into a copper pipe and placed inside the wall cavity by using a wooden frame. Two pipes of different diameters, 1.9 cm and 1.27 cm, are used and placed at two different locations: medium depth and next to the wall. The maximum reduction in peak heat flux was 36.5% for a mass fraction of PCM of about 25% when the maximum wall surface temperature was 55 °C. When the PCM is encapsulated in the 1.27 cm pipes and placed next to the wallboard, the maximum reduction in peak heat flux was 22.45%. Based on these results, the authors conclude that the optimal position should be between the middle depth and the wallboard to complete the daily melting/solidification, and that the PCM should be encapsulated in smaller tubes with a larger surface/volume ratio so that the phase transition process can proceed easily.

In order to increase the apparent thermal capacity of buildings, it is possible to incorporate PCMs not only in the building envelope but also in the partition walls and windows. Bontemps et al. [110] conducted an experimental study in two small rooms separated by a hollow glass brick wall and filled with three different PCMs: fatty acid, paraffin, and salt hydrates with melting temperatures of 21.4 °C, 25 °C, and 27.5 °C, respectively, and compared with an identical cell without PCM. The maximum temperature of the test cell with PCM is lower than that without PCM. The temperature decrease varies between 3.5 and 4 °C for fatty acid, 2 and 3 °C for paraffin, and between 3.5 and 5 °C for salt hydrate. These results are difficult to compare because of the varying boundary conditions. For this reason, a 1D model based on the Kondo method [111] was developed with TRNSYS. The simulated PCM temperature follows the same dynamics as the experimental temperature. In fact, the result of the simulation compared with the experiences showed that the assumption of a plane liquid-solid interface of the model is not valid because the PCM melts mainly at the center.

Silva et al. [29] conducted an experimental campaign during summer on a south-facing window shutter containing PCMs. The test cell was located in Aveiro, Portugal, a region with a Mediterranean climate. The south-facing orientation is chosen because it is subjected to discomfort problems, such as indoor temperature asymmetry in winter and overheating in summer. The cell is divided into two internal compartments (of equal dimensions) by an internal partition. The front facade consists of four double-glazed

windows. The reference compartment is equipped with an aluminum shutter; the PCM compartment is equipped with the same shutter filled with paraffin (RT28HC®). The results showed a thermal regulation capacity of the internal temperature of about 18–22% for the compartment equipped with the PCM shutter. The maximum and minimum temperature peaks decreased by 6% and 11%, respectively. In addition, the minimum and maximum temperature peaks are delayed by 45 min and one hour, respectively, compared to the reference compartment.

The majority of studies in the literature focus on the short-term thermal stability of PCMs incorporated into buildings. In order to provide reliable data and to go beyond the development stage, it is essential to investigate the stability of building envelopes with integrated PCMs over longer periods in real environmental conditions of a building. To this end, Cabeza et al. [112] evaluated the thermal performance of a cubic concrete enclosure containing encapsulated PCMs ten years after its construction in a previous study by the same authors [113]. In this previous study, two cubic enclosures were constructed, one serving as a reference made with conventional concrete and the other containing 5 wt% of encapsulated PCMs. The results showed a more stable temperature and a delay in maximum heat flux for the enclosure containing PCMs. Although the experiments in 2005 and ten years later were both performed in summer, the weather conditions were not identical. Indeed, the solar radiation was similar, but the outdoor temperature was higher in 2016 than in 2005. As a result, the indoor temperature was also higher in 2016 than in 2005, which explains a difference in temperatures between conventional concrete and concrete incorporating with and without PCMs (between 1–3 °C in 2005 and 5–7 °C in 2016). These results showed that concrete with PCMs is much more effective under extreme conditions (very high temperatures). The compressive strength test performed in 2016 in the same way as in 2005 showed no significant variation, which allows to affirm that the concrete with PCMs shows no change or mechanical degradation.

3.1.3. Dynamic Numerical Simulations of Buildings Incorporating PCMs

Numerical modeling and simulation of PCMs embedded in building envelopes are very useful for building design and optimization. In most numerical studies, commercial software, such as EnergyPlus, TRNSYS, MATLAB, COMSOL, and ANSYS Fluent, are used to solve the energy equations and to perform numerical simulations under varying weather conditions [17]. The main objective of these simulations is to study and optimize the effect of the integration of PCMs in the walls of buildings, their position in the walls, their thermo-physical properties, such as melting temperature, thermal conductivity, and the effect of their thickness.

Frazzica et al. [114] studied composites based on standard mortar and two commercial micro-encapsulated paraffin PCMs with melting temperatures of 23 and 26 °C, respectively. Several percentages of PCMs were used and the performance of the resulting composites was experimentally tested. These experimental data were used to validate a numerical model developed on COMSOL Multiphysics. The numerical model is based on a one temperature formulation and considers that the PCM and the mortar constitute a homogeneous medium. A parametric study was conducted to propose a method to optimize the choice of the melting temperature of the PCM. Using the climatic conditions of Messina in Italy, the authors obtained an optimal temperature of 27 °C. The results also showed that the addition of 15 wt% of PCMs increases the thermal comfort conditions by about 15% compared to the reference case composed of pure mortar (without PCM) based on the American standard ASHRAE 2017 [115].

Zhou et al. [116] conducted a parametric study on the factors influencing the performance of PCM-based wallboard applied on the interior and exterior faces using the effective heat capacity method to describe the phase change. The exterior wall is subjected to a periodic boundary condition and solar radiation. Thermal properties, such as melting temperature, phase change range, enthalpy of fusion, thermal conductivity, and heat exchange coefficient, were optimized based on two criteria: interior surface temperature and

diurnal thermal energy storage. The optimal melting temperature of the PCM embedded in the interior wall is equal to the interior ambient temperature without taking into account the internal heat gains. The melting temperature of the exterior PCM wall depends on both the interior and exterior environments, although the impact of the exterior environment is reduced due to the exterior insulation. Walls containing PCM show the best results if the PCM melts completely over a full daily cycle. Moreover, the parametric study showed that the thermal conductivity of the PCM has a low impact on the results.

Thiele et al. [117] examined, through a numerical study, the effects of adding micro-encapsulated PCMs to concrete based on four criteria: PCM mass fraction, enthalpy of melting, phase change temperature, phase change range, and external temperature. The simulations were performed considering two walls: one heterogeneous and one homogeneous. The difference between the simulation of the heterogeneous and homogeneous walls is less than 2%, which shows that the heterogeneous composite can be treated as a homogeneous material with a volumetric thermal capacity and an effective thermal conductivity. The rest of the simulation was therefore performed with a homogeneous model. The main results are as follows:

- the addition of micro-encapsulated PCM and/or the increase of the PCM melting enthalpy reduced and delayed the thermal load of the building,
- the melting temperature of the PCM should be close to the indoor temperature regardless of the climatic conditions,
- the phase-change temperature range had limited effect on energy flux reduction and time shift.

The thermal performance and energy consumption of a prefabricated building with PCM was investigated using EnergyPlus software in five different climate regions in China: severe cold area, cold area, mild area, hot summer and warm winter area, hot summer and cold winter area [118]. The study focused on the optimization of the thermal properties of the PCM, its position in the building structure, and the orientation of the PCM added to the building envelope using the direct incorporation technique. The results showed that adding the PCM to the building envelope on the East or West side is more energy efficient compared to the other orientations. For different regions, based on a comprehensive evaluation of the relationship between energy savings rate and cost, increasing the thickness of PCM has a limited effect on improving the energy savings rate of buildings. The authors suggested to place the PCM on the interior side of the building regardless of the area, as the energy saving rate is 77.11% and 32.53% when PCM is located on the interior and exterior sides of the wall, respectively.

Al-Absi [119] reviewed the related literature that examines the application of PCMs in different positions inside the walls of buildings to determine their optimal position and influential parameters. It was found that the optimal positions of PCMs are highly dependent on parameters, such as climatic and weather conditions, and the purpose of the application, melting temperature and melting enthalpy of PCMs, amount of PCMs, thermal properties of wall materials, and wall orientation.

In order to improve the thermal inertia effect in buildings using shape-stabilized PCM wall panels, Wi, Chang et al. [120] analyzed the enthalpy-temperature function based on the thermal properties of 22 types of shape-stabilized PCMs and applied it to a dynamic energy simulation program. The modeled building has a wooden structure and is south-facing. Then, the PCMs were integrated into the internal and external face of a 20 mm thick wall. A preliminary study was carried out to determine where the PCM should be integrated. During cooling periods, the PCM should be placed on the outer layer of the wall and on the inner layer during heating periods because it is effective in storing and releasing the heat generated in the room during this period. On average, total energy consumption was reduced by 5% per year.

Recently, Li et al. [36] conducted an optimization process with COMSOL Multiphysics to find the best value for critical parameters such as: the location of the PCM layer, its thickness, the melting temperature of the PCM, and different loading conditions (month

and city). The authors used two performance indicators to evaluate the performance of the wall: the instantaneous fluctuation of the indoor temperature and the intensity of thermal discomfort, which is defined as the period during which the temperature is outside the chosen thermal comfort range between 22 and 28 °C. The optimal position is obtained for PCMs placed close to the inner layer of the wall. The analysis of several thicknesses ranging from 2.5 to 15 mm showed better results obtained for thicker layers due to the comparatively larger amount of PCMs. It was also found that the selection of the melting temperature of PCMs is highly dependent on the loading condition. Indeed, the authors recommend PCMs with a melting temperature between 26–30 °C for cooling and 20–24 °C for heating.

3.1.4. Discussion

At the experimental level, it can be seen that the majority of studies are focused on the development of composite materials and their characterization. Different materials and methods of incorporation have been used and the positive effect of PCMs on temperature regulation inside buildings has been demonstrated. However, among the analyzed articles, very few have moved to the application of PCMs at the building or wall scale. This last step is essential to evaluate the effect of PCMs at real scale. Some areas of uncertainty remain, namely the positioning of the PCM in the building envelope, and the melting temperature of the PCM to be chosen according to the climatic conditions, even if many studies have been carried out in this direction.

The literature also lacks studies on the stability of PCMs in building envelopes over the long term and the effect of aging. A very important aspect that remains to be investigated is the analysis of the hydric behavior of buildings incorporating PCMs necessary for the evaluation of air quality. Finally, as pointed out by Lamrani et al. [17], no study takes into consideration the internal loads and the existence of the occupant or his behavior (real use of the building).

Numerical studies carried out under different climatic conditions established criteria for the selection of PCMs as well as their location in the building envelopes. The conclusions of these studies showed that the PCM should be placed near the heat source. Thus, in hot climates, the PCM should be located next to the exterior envelope while in cooler climates, a location near the interior envelope is recommended.

The findings of the various numerical studies indicated the need to conduct an optimization study on the properties of the PCM to select its location as well as its quantity under various weather conditions.

4. Conclusions

In this work, recent experimental and numerical advances on the incorporation of PCMs in building envelopes have been reviewed. Passive thermal energy storage systems in buildings incorporating PCMs are presented as a promising solution for improving the energy efficiency of buildings. The various studies have shown the potential of PCMs to reduce peak temperature, temperature fluctuations, and improve thermal comfort. The PCMs targeted for passive storage must have a melting temperature in the comfort range (15 to 35 °C). Fatty acids and paraffinic compounds have been used in the majority of experimental studies. Techniques for incorporating PCMs into passive systems are classified into four categories: direct incorporation, impregnation, encapsulation, and shape-stabilized PCMs. Shape-stabilized PCMs are promising because of the high impregnation rate compared to other techniques and the wide variety of support materials. Most of the studies were devoted to the optimization of the selection of the PCM and its position in the building envelope according to the climatic conditions.

Despite numerous improvement, more studies are required regarding the mass and moisture transfer problem, the long-term stability of passive systems incorporating PCMs, the optimization of the properties of the PCMs and their location, and the consideration of the real use of the building in numerical simulations.

This literature review allowed us to screen the different PCMs, support materials, the different techniques of incorporation of PCMs in building envelopes, and the challenges to be taken up for a future study. In terms of PCMs, fatty acids and their eutectics have retained our attention because of their renewable nature and their interesting thermophysical properties. These PCMs can be stabilized in shape by using natural insulators, such as vegetable fibers, already used in building insulation.

Author Contributions: Conceptualization, all authors; methodology, all authors; formal analysis, all authors; investigation, all authors; resources, all authors; data curation, all authors; writing—original draft preparation, M.S.; writing—review and editing, all authors; visualization, all authors; supervision, R.B., M.D., and A.E.A.H.; project administration, R.B. and M.D.; funding acquisition, R.B., M.D. All authors have read and agreed to the published version of the manuscript.

Funding: This research work was developed in the framework of SUDOKET project (Interreg Sudoe SOE2/P1/E0677). The authors are grateful to the European Regional Development Fund (ERDF) to co-fund the project through the Interreg Sudoe Programme, the Region Nouvelle Aquitaine for subsidizing BioMCP project (Project-2017-1R10209-13023), and Energy Saving Certificate Program of the Ministry of Ecological and Solidarity Transition 'SmartReno support' 2019–2021 (PRO-INNO-13).

Institutional Review Board Statement: Not applicable.

Informed Consent Statement: Not applicable.

Data Availability Statement: The data presented in this study are available on request from the corresponding author.

Acknowledgments: The authors would also like to thank Valérie Thouard for the administrative and financial management over SUDOKET.

Conflicts of Interest: The authors declare no conflict of interest.

References

1. Masson-Delmotte, V.; Zhai, P.; Pirani, A.; Connors, S.L.; Péan, C.; Berger, S.; Caud, N.; Chen, Y.; Goldfarb, L.; Gomis, M.I.; et al. *Global Warming of 1.5 °C—Climate Change 2021: The Physical Science Basis. Contribution of Working Group I to the Sixth Assessment Report of the Intergovernmental Panel on Climate Change*; Cambridge University Press: Cambridge, UK, 2021.
2. Buildings—Topics—International Energy Agency (IEA). Available online: https://www.iea.org/topics/buildings (accessed on 30 April 2021).
3. Asan, H.; Sancaktar, Y.S. Effects of Wall's Thermophysical Properties on Time Lag and Decrement Factor. *Energy Build.* **1998**, *28*, 159–166. [CrossRef]
4. Zhuang, Z.; Li, Y.; Chen, B.; Guo, J. Chinese Kang as a Domestic Heating System in Rural Northern China—A Review. *Energy Build.* **2009**, *41*, 111–119. [CrossRef]
5. Saadatian, O.; Sopian, K.; Lim, C.H.; Asim, N.; Sulaiman, M.Y. Trombe Walls: A Review of Opportunities and Challenges in Research and Development. *Renew. Sustain. Energy Rev.* **2012**, *16*, 6340–6351. [CrossRef]
6. Ståhl, F. *Influence of Thermal Mass on the Heating and Cooling Demands of a Building Unit*; Chalmers Tekniska: Hogskola, Sweden, 2009.
7. Delgado, J.M.P.Q.; Martinho, J.C.; Vaz Sá, A.; Guimarães, A.S.; Abrantes, V. *Thermal Energy Storage with Phase Change Materials: A Literature Review of Applications for Buildings Materials*; SpringerBriefs in Applied Sciences and Technology; Springer International Publishing: Cham, Switzerland, 2019; ISBN 978-3-319-97498-9.
8. Ben Romdhane, S.; Amamou, A.; Ben Khalifa, R.; Saïd, N.M.; Younsi, Z.; Jemni, A. A Review on Thermal Energy Storage Using Phase Change Materials in Passive Building Applications. *J. Build. Eng.* **2020**, *32*, 101563. [CrossRef]
9. Akeiber, H.; Nejat, P.; Majid, M.Z.A.; Wahid, M.A.; Jomehzadeh, F.; Famileh, I.Z.; Calautit, J.K.; Hughes, B.R.; Zaki, S.A. A Review on Phase Change Material (PCM) for Sustainable Passive Cooling in Building Envelopes. *Renew. Sustain. Energy Rev.* **2016**, *60*, 1470–1497. [CrossRef]
10. Al-Yasiri, Q.; Szabó, M. Incorporation of Phase Change Materials into Building Envelope for Thermal Comfort and Energy Saving: A Comprehensive Analysis. *J. Build. Eng.* **2021**, *36*, 102122. [CrossRef]
11. Basecq, V.; Michaux, G.; Blondeau, P.; Inard, C. Short Term Storage Systems of the Thermal Energy for Buildings: A Review. *Adv. Build. Energy Res.* **2013**, *7*, 66–119. [CrossRef]
12. Thermal Energy Storage: Technology Brief. Available online: /publications/2013/Jan/Thermal-energy-storage (accessed on 3 May 2021).
13. Navarro, L.; de Gracia, A.; Colclough, S.; Browne, M.; McCormack, S.J.; Griffiths, P.; Cabeza, L.F. Thermal Energy Storage in Building Integrated Thermal Systems: A Review. Part 1. Active Storage Systems. *Renew. Energy* **2016**, *88*, 526–547. [CrossRef]

14. Abhat, A. Low Temperature Latent Heat Thermal Energy Storage: Heat Storage Materials. *Sol. Energy* **1983**, *30*, 313–332. [CrossRef]
15. Desai, F.; Sunku Prasad, J.; Muthukumar, P.; Rahman, M.M. Thermochemical Energy Storage System for Cooling and Process Heating Applications: A Review. *Energy Convers. Manag.* **2021**, *229*, 113617. [CrossRef]
16. Cabeza, L.F.; Castell, A.; Barreneche, C.; de Gracia, A.; Fernández, A.I. Materials Used as PCM in Thermal Energy Storage in Buildings: A Review. *Renew. Sustain. Energy Rev.* **2011**, *15*, 1675–1695. [CrossRef]
17. Lamrani, B.; Johannes, K.; Kuznik, F. Phase Change Materials Integrated into Building Walls: An Updated Review. *Renew. Sustain. Energy Rev.* **2021**, *140*, 110751. [CrossRef]
18. Baetens, R.; Jelle, B.P.; Gustavsen, A. Phase Change Materials for Building Applications: A State-of-the-Art Review. *Energy Build.* **2010**, *42*, 1361–1368. [CrossRef]
19. Cunha, S.; Leite, P.; Aguiar, J. Characterization of Innovative Mortars with Direct Incorporation of Phase Change Materials. *J. Energy Storage* **2020**, *30*, 101439. [CrossRef]
20. Soares, N.; Costa, J.J.; Gaspar, A.R.; Santos, P. Review of Passive PCM Latent Heat Thermal Energy Storage Systems towards Buildings' Energy Efficiency. *Energy Build.* **2013**, *59*, 82–103. [CrossRef]
21. Kumar, D.; Alam, M.; Zou, P.X.W.; Sanjayan, J.G.; Memon, R.A. Comparative Analysis of Building Insulation Material Properties and Performance. *Renew. Sustain. Energy Rev.* **2020**, *131*, 110038. [CrossRef]
22. Abu-Jdayil, B.; Mourad, A.-H.; Hittini, W.; Hassan, M.; Hameedi, S. Traditional, State-of-the-Art and Renewable Thermal Building Insulation Materials: An Overview. *Constr. Build. Mater.* **2019**, *214*, 709–735. [CrossRef]
23. Asim, M.; Uddin, G.M.; Jamshaid, H.; Raza, A.; Hussain, U.; Satti, A.N.; Hayat, N.; Arafat, S.M. Comparative Experimental Investigation of Natural Fibers Reinforced Light Weight Concrete as Thermally Efficient Building Materials. *J. Build. Eng.* **2020**, *31*, 101411. [CrossRef]
24. Jami, T.; Karade, S.R.; Singh, L.P. A Review of the Properties of Hemp Concrete for Green Building Applications. *J. Clean. Prod.* **2019**, *239*, 117852. [CrossRef]
25. Jeong, S.-G.; Wi, S.; Chang, S.J.; Lee, J.; Kim, S. An Experimental Study on Applying Organic PCMs to Gypsum-Cement Board for Improving Thermal Performance of Buildings in Different Climates. *Energy Build.* **2019**, *190*, 183–194. [CrossRef]
26. Errebai, F.B.; Chikh, S.; Derradji, L.; Amara, M.; Younsi, Z. Optimum Mass Percentage of Microencapsulated PCM Mixed with Gypsum for Improved Latent Heat Storage. *J. Energy Storage* **2021**, *33*, 101910. [CrossRef]
27. Paranjothi, G.; Odukomaiya, A.; Cui, S.; Bulk, A. Evaluation of Phase Change Plaster/Paste Composites for Building Envelopes. *Energy Build.* **2021**, *253*, 111372. [CrossRef]
28. Tyagi, V.V.; Buddhi, D. PCM Thermal Storage in Buildings: A State of Art. *Renew. Sustain. Energy Rev.* **2007**, *11*, 1146–1166. [CrossRef]
29. Silva, T.; Vicente, R.; Rodrigues, F.; Samagaio, A.; Cardoso, C. Performance of a Window Shutter with Phase Change Material under Summer Mediterranean Climate Conditions. *Appl. Therm. Eng.* **2015**, *84*, 246–256. [CrossRef]
30. Gao, Y.; Zheng, Q.; Jonsson, J.C.; Lubner, S.; Curcija, C.; Fernandes, L.; Kaur, S.; Kohler, C. Parametric Study of Solid-Solid Translucent Phase Change Materials in Building Windows. *Appl. Energy* **2021**, *301*, 117467. [CrossRef]
31. Alawadhi, E.M. Using Phase Change Materials in Window Shutter to Reduce the Solar Heat Gain. *Energy Build.* **2012**, *47*, 421–429. [CrossRef]
32. Shen, Y.; Liu, S.; Zeng, C.; Zhang, Y.; Li, Y.; Han, X.; Yang, L.; Yang, X. Experimental Thermal Study of a New PCM-Concrete Thermal Storage Block (PCM-CTSB). *Constr. Build. Mater.* **2021**, *293*, 123540. [CrossRef]
33. Dehmous, M.; Franquet, E.; Lamrous, N. Mechanical and Thermal Characterizations of Various Thermal Energy Storage Concretes Including Low-Cost Bio-Sourced PCM. *Energy Build.* **2021**, *241*, 110878. [CrossRef]
34. Jia, C.; Geng, X.; Liu, F.; Gao, Y. Thermal Behavior Improvement of Hollow Sintered Bricks Integrated with Both Thermal Insulation Material (TIM) and Phase-Change Material (PCM). *Case Stud. Therm. Eng.* **2021**, *25*, 100938. [CrossRef]
35. Hamidi, Y.; Aketouane, Z.; Malha, M.; Bruneau, D.; Bah, A.; Goiffon, R. Integrating PCM into Hollow Brick Walls: Toward Energy Conservation in Mediterranean Regions. *Energy Build.* **2021**, *248*, 111214. [CrossRef]
36. Li, M.; Cao, Q.; Pan, H.; Wang, X.; Lin, Z. Effect of Melting Point on Thermodynamics of Thin PCM Reinforced Residential Frame Walls in Different Climate Zones. *Appl. Therm. Eng.* **2021**, *188*, 116615. [CrossRef]
37. Navarro, L.; de Gracia, A.; Niall, D.; Castell, A.; Browne, M.; McCormack, S.J.; Griffiths, P.; Cabeza, L.F. Thermal Energy Storage in Building Integrated Thermal Systems: A Review. Part 2. Integration as Passive System. *Renew. Energy* **2016**, *85*, 1334–1356. [CrossRef]
38. Bevilacqua, P.; Benevento, F.; Bruno, R.; Arcuri, N. Are Trombe Walls Suitable Passive Systems for the Reduction of the Yearly Building Energy Requirements? *Energy* **2019**, *185*, 554–566. [CrossRef]
39. Duan, S.; Wang, L.; Zhao, Z.; Zhang, C. Experimental Study on Thermal Performance of an Integrated PCM Trombe Wall. *Renew. Energy* **2021**, *163*, 1932–1941. [CrossRef]
40. Oluah, C.; Akinlabi, E.T.; Njoku, H.O. Selection of Phase Change Material for Improved Performance of Trombe Wall Systems Using the Entropy Weight and TOPSIS Methodology. *Energy Build.* **2020**, *217*, 109967. [CrossRef]
41. Li, S.; Zhu, N.; Hu, P.; Lei, F.; Deng, R. Numerical Study on Thermal Performance of PCM Trombe Wall. *Energy Procedia* **2019**, *158*, 2441–2447. [CrossRef]

42. Sergei, K.; Shen, C.; Jiang, Y. A Review of the Current Work Potential of a Trombe Wall. *Renew. Sustain. Energy Rev.* **2020**, *130*, 109947. [CrossRef]
43. Al-Saadi, S.N.; Zhai, Z. A New Validated TRNSYS Module for Simulating Latent Heat Storage Walls. *Energy Build.* **2015**, *109*, 274–290. [CrossRef]
44. Guarino, F.; Athienitis, A.; Cellura, M.; Bastien, D. PCM Thermal Storage Design in Buildings: Experimental Studies and Applications to Solaria in Cold Climates. *Appl. Energy* **2017**, *185*, 95–106. [CrossRef]
45. Memon, S.A. Phase Change Materials Integrated in Building Walls: A State of the Art Review. *Renew. Sustain. Energy Rev.* **2014**, *31*, 870–906. [CrossRef]
46. Umair, M.M.; Zhang, Y.; Iqbal, K.; Zhang, S.; Tang, B. Novel Strategies and Supporting Materials Applied to Shape-Stabilize Organic Phase Change Materials for Thermal Energy Storage–A Review. *Appl. Energy* **2019**, *235*, 846–873. [CrossRef]
47. Sivanathan, A.; Dou, Q.; Wang, Y.; Li, Y.; Corker, J.; Zhou, Y.; Fan, M. Phase Change Materials for Building Construction: An Overview of Nano-/Micro-Encapsulation. *Nanotechnol. Rev.* **2020**, *9*, 896–921. [CrossRef]
48. Alehosseini, E.; Jafari, S.M. Micro/Nano-Encapsulated Phase Change Materials (PCMs) as Emerging Materials for the Food Industry. *Trends Food Sci. Technol.* **2019**, *91*, 116–128. [CrossRef]
49. Gao, H.; Wang, J.; Chen, X.; Wang, G.; Huang, X.; Li, A.; Dong, W. Nanoconfinement Effects on Thermal Properties of Nanoporous Shape-Stabilized Composite PCMs: A Review. *Nano Energy* **2018**, *53*, 769–797. [CrossRef]
50. Jeong, S.-G.; Jeon, J.; Lee, J.-H.; Kim, S. Optimal Preparation of PCM/Diatomite Composites for Enhancing Thermal Properties. *Int. J. Heat Mass Transf.* **2013**, *62*, 711–717. [CrossRef]
51. Kulkarni, P.; Muthadhi, A. Thermal Energy Storage Cement Mortar with Direct Incorporation of Organic and Inorganic Phase Change Materials. *Innov. Infrastruct. Solut.* **2021**, *6*, 30. [CrossRef]
52. Boussaba, L.; Lefebvre, G.; Makhlouf, S.; Grados, A.; Royon, L. Investigation and Properties of a Novel Composite Bio-PCM to Reduce Summer Energy Consumptions in Buildings of Hot and Dry Climates. *Sol. Energy* **2021**, *214*, 119–130. [CrossRef]
53. JO RAPD, DTR BC 2.41: Design and Calculation Rules for Reinforced Concrete Structures Reinforced Concrete Structures—C.B.A. 93—Regulatory Technical Document, Ministry of and Urbanism of the People's Democratic Republic of Algeria People (2013). Available online: https://pdfcoffee.com/cba-93-pdf-free.html (accessed on 20 August 2021).
54. Bake, M.; Shukla, A.; Liu, S. Development of Gypsum Plasterboard Embodied with Microencapsulated Phase Change Material for Energy Efficient Buildings. *Mater. Sci. Energy Technol.* **2021**, *4*, 166–176. [CrossRef]
55. Standard E.N. 13279-2, Gypsum Binders and Gypsum Plasters. Part 2: *Test methods*. 2004.
56. Li, C.; Yu, H.; Song, Y. Experimental Investigation of Thermal Performance of Microencapsulated PCM-Contained Wallboard by Two Measurement Modes. *Energy Build.* **2019**, *184*, 34–43. [CrossRef]
57. Elfordy, S.; Lucas, F.; Tancret, F.; Scudeller, Y.; Goudet, L. Mechanical and Thermal Properties of Lime and Hemp Concrete ("Hempcrete") Manufactured by a Projection Process. *Constr. Build. Mater.* **2008**, *22*, 2116–2123. [CrossRef]
58. Kymäläinen, H.-R.; Sjöberg, A.-M. Flax and Hemp Fibres as Raw Materials for Thermal Insulations. *Build. Environ.* **2008**, *43*, 1261–1269. [CrossRef]
59. Murphy, D.P.; Behring, H.; Wieland, H. The Use of Flax and Hemp Materials for Insulating Buildings. *Proc. Flax Other Bast Plants Symp.* **1997**, *30*, 79–84.
60. Kirilovs, E.; Zotova, I.; Gendelis, S.; Jörg-Gusovius, H.; Kukle, S.; Stramkale, V. Experimental Study of Using Micro-Encapsulated Phase-Change Material Integrated into Hemp Shive Wallboard. *Buildings* **2020**, *10*, 228. [CrossRef]
61. Zhu, N.; Li, S.; Hu, P.; Wei, S.; Deng, R.; Lei, F. A Review on Applications of Shape-Stabilized Phase Change Materials Embedded in Building Enclosure in Recent Ten Years. *Sustain. Cities Soc.* **2018**, *43*, 251–264. [CrossRef]
62. Karaipekli, A.; Sari, A. Preparation, Thermal Properties and Thermal Reliability of Eutectic Mixtures of Fatty Acids/Expanded Vermiculite as Novel Form-Stable Composites for Energy Storage. *J. Ind. Eng. Chem.* **2010**, *16*, 767–773. [CrossRef]
63. Wang, H.; Deng, Y.; Wu, F.; Dai, X.; Wang, W.; Mai, Y.; Gu, Y.; Liu, Y. Effect of Dopamine-Modified Expanded Vermiculite on Phase Change Behavior and Heat Storage Characteristic of Polyethylene Glycol. *Chem. Eng. J.* **2021**, *415*, 128992. [CrossRef]
64. Rathore, P.K.S.; Shukla, S.K. Improvement in Thermal Properties of PCM/Expanded Vermiculite/Expanded Graphite Shape Stabilized Composite PCM for Building Energy Applications. *Renew. Energy* **2021**, *176*, 295–304. [CrossRef]
65. Chen, Y.; Cui, Z.; Ding, H.; Wan, Y.; Tang, Z.; Gao, J. Cost-Effective Biochar Produced from Agricultural Residues and Its Application for Preparation of High Performance Form-Stable Phase Change Material via Simple Method. *Int. J. Mol. Sci.* **2018**, *19*, 3055. [CrossRef]
66. Jeon, J.; Park, J.H.; Wi, S.; Yang, S.; Ok, Y.S.; Kim, S. Characterization of Biocomposite Using Coconut Oil Impregnated Biochar as Latent Heat Storage Insulation. *Chemosphere* **2019**, *236*, 124269. [CrossRef]
67. Wan, Y.-C.; Chen, Y.; Cui, Z.-X.; Ding, H.; Gao, S.-F.; Han, Z.; Gao, J.-K. A Promising Form-Stable Phase Change Material Prepared Using Cost Effective Pinecone Biochar as the Matrix of Palmitic Acid for Thermal Energy Storage. *Sci. Rep.* **2019**, *9*, 1–10. [CrossRef]
68. Zhang, W.; Zhang, X.; Zhang, X.; Yin, Z.; Liu, Y.; Fang, M.; Wu, X.; Min, X.; Huang, Z. Lauric-Stearic Acid Eutectic Mixture/Carbonized Biomass Waste Corn Cob Composite Phase Change Materials: Preparation and Thermal Characterization. *Thermochim. Acta* **2019**, *674*, 21–27. [CrossRef]

69. Liu, L.; Li, J.; Deng, Y.; Yang, Z.; Huang, K.; Zhao, S. Optimal Design of Multi-Layer Structure Composite Containing Inorganic Hydrated Salt Phase Change Materials and Cement: Lab-Scale Tests for Buildings. *Constr. Build. Mater.* **2021**, *275*, 122125. [CrossRef]
70. Rathore, P.K.S.; Shukla, S.K. Enhanced Thermophysical Properties of Organic PCM through Shape Stabilization for Thermal Energy Storage in Buildings: A State of the Art Review. *Energy Build.* **2021**, *236*, 110799. [CrossRef]
71. Xu, B.; Li, Z. Paraffin/Diatomite Composite Phase Change Material Incorporated Cement-Based Composite for Thermal Energy Storage. *Appl. Energy* **2013**, *105*, 229–237. [CrossRef]
72. Karaman, S.; Karaipekli, A.; Sar, A.; Biçer, A. Polyethylene Glycol (PEG)/Diatomite Composite as a Novel Form-Stable Phase Change Material for Thermal Energy Storage. *Sol. Energy Mater. Sol. Cells* **2011**, *95*, 1647–1653. [CrossRef]
73. Wen, R.; Zhang, X.; Huang, Z.; Fang, M.; Liu, Y.; Wu, X.; Min, X.; Gao, W.; Huang, S. Preparation and Thermal Properties of Fatty Acid/Diatomite Form-Stable Composite Phase Change Material for Thermal Energy Storage. *Sol. Energy Mater. Sol. Cells* **2018**, *178*, 273–279. [CrossRef]
74. Ali Memon, S.; Yiu Lo, T.; Shi, X.; Barbhuiya, S.; Cui, H. Preparation, Characterization and Thermal Properties of Lauryl Alcohol/Kaolin as Novel Form-Stable Composite Phase Change Material for Thermal Energy Storage in Buildings. *Appl. Therm. Eng.* **2013**, *59*, 336–347. [CrossRef]
75. Sari, A. Fabrication and Thermal Characterization of Kaolin-Based Composite Phase Change Materials for Latent Heat Storage in Buildings. *Energy Build.* **2015**, *96*, 193–200. [CrossRef]
76. Jafaripour, M.; Sadrameli, S.M.; Pahlavanzadeh, H.; Mousavi, S.A.H.S. Fabrication and Optimization of Kaolin/Stearic Acid Composite as a Form-Stable Phase Change Material for Application in the Thermal Energy Storage Systems. *J. Energy Storage* **2021**, *33*, 102155. [CrossRef]
77. Chung, O.; Jeong, S.-G.; Kim, S. Preparation of Energy Efficient Paraffinic PCMs/Expanded Vermiculite and Perlite Composites for Energy Saving in Buildings. *Sol. Energy Mater. Sol. Cells* **2015**, *137*, 107–112. [CrossRef]
78. Wen, R.; Huang, Z.; Huang, Y.; Zhang, X.; Min, X.; Fang, M.; Liu, Y.; Wu, X. Synthesis and Characterization of Lauric Acid/Expanded Vermiculite as Form-Stabilized Thermal Energy Storage Materials. *Energy Build.* **2016**, *116*, 677–683. [CrossRef]
79. Zhang, W.; Zhang, X.; Huang, Z.; Yin, Z.; Wen, R.; Huang, Y.; Wu, X.; Min, X. Preparation and Characterization of Capric-Palmitic-Stearic Acid Ternary Eutectic Mixture/Expanded Vermiculite Composites as Form-Stabilized Thermal Energy Storage Materials. *J. Mater. Sci. Technol.* **2018**, *34*, 379–386. [CrossRef]
80. Atinafu, D.G.; Yun, B.Y.; Wi, S.; Kang, Y.; Kim, S. A Comparative Analysis of Biochar, Activated Carbon, Expanded Graphite, and Multi-Walled Carbon Nanotubes with Respect to PCM Loading and Energy-Storage Capacities. *Environ. Res.* **2021**, *195*, 110853. [CrossRef]
81. Liu, C.; Yuan, Y.; Zhang, N.; Cao, X.; Yang, X. A Novel PCM of Lauric–Myristic–Stearic Acid/Expanded Graphite Composite for Thermal Energy Storage. *Mater. Lett.* **2014**, *120*, 43–46. [CrossRef]
82. Yang, Y.; Pang, Y.; Liu, Y.; Guo, H. Preparation and Thermal Properties of Polyethylene Glycol/Expanded Graphite as Novel Form-Stable Phase Change Material for Indoor Energy Saving. *Mater. Lett.* **2018**, *216*, 220–223. [CrossRef]
83. Yu, H.; Gao, J.; Chen, Y.; Zhao, Y. Preparation and Properties of Stearic Acid/Expanded Graphite Composite Phase Change Material for Low-Temperature Solar Thermal Application. *J. Therm. Anal. Calorim.* **2016**, *124*, 87–92. [CrossRef]
84. Das, D.; Bordoloi, U.; Muigai, H.H.; Kalita, P. A Novel Form Stable PCM Based Bio Composite Material for Solar Thermal Energy Storage Applications. *J. Energy Storage* **2020**, *30*, 101403. [CrossRef]
85. Hekimoğlu, G.; Sarı, A.; Kar, T.; Keleş, S.; Kaygusuz, K.; Tyagi, V.V.; Sharma, R.K.; Al-Ahmed, A.; Al-Sulaiman, F.A.; Saleh, T.A. Walnut Shell Derived Bio-Carbon/Methyl Palmitate as Novel Composite Phase Change Material with Enhanced Thermal Energy Storage Properties. *J. Energy Storage* **2021**, *35*, 102288. [CrossRef]
86. Ma, L.; Guo, C.; Ou, R.; Sun, L.; Wang, Q.; Li, L. Preparation and Characterization of Modified Porous Wood Flour/Lauric-Myristic Acid Eutectic Mixture as a Form-Stable Phase Change Material. *Energy Fuels* **2018**, *32*, 5453–5461. [CrossRef]
87. Barreneche, C.; Vecstaudza, J.; Bajare, D.; Fernandez, A.I. *PCM/Wood Composite to Store Thermal Energy in Passive Building Envelopes*; IOP Publishing: Bristol, UK, 2017; Volume 251.
88. Jingchen, X.; Keyan, Y.; Yucheng, Z.; Yuxiang, Y.; Jianmin, C.; Liping, C.; Sheldon, S.Q. Form-Stable Phase Change Material Based on Fatty Acid/Wood Flour Composite and PVC Used for Thermal Energy Storage. *Energy Build.* **2020**, *209*, 109663. [CrossRef]
89. Sarı, A.; Hekimoğlu, G.; Tyagi, V.V. Low Cost and Eco-Friendly Wood Fiber-Based Composite Phase Change Material: Development, Characterization and Lab-Scale Thermoregulation Performance for Thermal Energy Storage. *Energy* **2020**, *195*, 116983. [CrossRef]
90. Ma, L.; Wang, Q.; Li, L. Delignified Wood/Capric Acid-Palmitic Acid Mixture Stable-Form Phase Change Material for Thermal Storage. *Sol. Energy Mater. Sol. Cells* **2019**, *194*, 215–221. [CrossRef]
91. Yang, H.; Wang, Y.; Yu, Q.; Cao, G.; Yang, R.; Ke, J.; Di, X.; Liu, F.; Zhang, W.; Wang, C. Composite Phase Change Materials with Good Reversible Thermochromic Ability in Delignified Wood Substrate for Thermal Energy Storage. *Appl. Energy* **2018**, *212*, 455–464. [CrossRef]
92. Xu, J.; Yang, T.; Xu, X.; Guo, X.; Cao, J. Processing Solid Wood into a Composite Phase Change Material for Thermal Energy Storage by Introducing Silica-Stabilized Polyethylene Glycol. *Compos. Part A Appl. Sci. Manuf.* **2020**, *139*, 106098. [CrossRef]
93. Liu, S.; Wu, H.; Du, Y.; Lu, X.; Qu, J. Shape-Stable Composite Phase Change Materials Encapsulated by Bio-Based Balsa Wood for Thermal Energy Storage. *Sol. Energy Mater. Sol. Cells* **2021**, *230*, 111187. [CrossRef]

94. Yang, H.; Wang, S.; Wang, X.; Chao, W.; Wang, N.; Ding, X.; Liu, F.; Yu, Q.; Yang, T.; Yang, Z.; et al. Wood-Based Composite Phase Change Materials with Self-Cleaning Superhydrophobic Surface for Thermal Energy Storage. *Appl. Energy* **2020**, *261*, 114481. [CrossRef]
95. Sheng, N.; Rao, Z.; Zhu, C.; Habazaki, H. Honeycomb Carbon Fibers Strengthened Composite Phase Change Materials for Superior Thermal Energy Storage. *Appl. Therm. Eng.* **2020**, *164*, 114493. [CrossRef]
96. Damfeu, J.C.; Meukam, P.; Jannot, Y. Modeling and Measuring of the Thermal Properties of Insulating Vegetable Fibers by the Asymmetrical Hot Plate Method and the Radial Flux Method: Kapok, Coconut, Groundnut Shell Fiber and Rattan. *Thermochim. Acta* **2016**, *630*, 64–77. [CrossRef]
97. Vaitkus, S.; Karpavičiūtė, R.; Vėjelis, S.; Lekūnaitė, L. Development and Research of Thermal Insulation Materials from Natural Fibres. *Key Eng. Mater.* **2014**, *604*, 285–288. [CrossRef]
98. Zhou, X.Y.; Zheng, F.; Li, H.G.; Lu, C.L. An Environment-Friendly Thermal Insulation Material from Cotton Stalk Fibers. *Energy Build.* **2010**, *42*, 1070–1074. [CrossRef]
99. Tran-Le, A.D.; Nguyen, S.-T.; Langlet, T. A Novel Anisotropic Analytical Model for Effective Thermal Conductivity Tensor of Dry Lime-Hemp Concrete with Preferred Spatial Distributions. *Energy Build.* **2019**, *182*, 75–87. [CrossRef]
100. Voumbo, M.L.; Wereme, A.; Gaye, S.; Adj, M.; Sissoko, G. Characterization of the Thermophysical Properties of Kapok. *Res. J. Appl. Sci. Eng. Technol.* **2010**, *2*, 143–148.
101. Pend, C.; Fumei, W. An investigation of heat flow through kapok insulating material. *Fibres Text.* **2009**, *2*, 88–92.
102. Manohar, K.; Ramlakhan, D.; Kochhar, G.; Haldar, S. Biodegradable Fibrous Thermal Insulation. *J. Braz. Soc. Mech. Sci. Eng.* **2006**, *28*, 45–47. [CrossRef]
103. Duquesne, M.; Mailhé, C.; Ruiz-Onofre, K.; Achchaq, F. Biosourced Organic Materials for Latent Heat Storage: An Economic and Eco-Friendly Alternative. *Energy* **2019**, *188*, 116067. [CrossRef]
104. Duquesne, M.; Mailhé, C.; Doppiu, S.; Dauvergne, J.-L.; Santos-Moreno, S.; Godin, A.; Fleury, G.; Rouault, F.; Palomo del Barrio, E. Characterization of Fatty Acids as Biobased Organic Materials for Latent Heat Storage. *Materials* **2021**, *14*, 4707. [CrossRef]
105. Lee, K.O.; Medina, M.A.; Sun, X.; Jin, X. Thermal Performance of Phase Change Materials (PCM)-Enhanced Cellulose Insulation in Passive Solar Residential Building Walls. *Solar Energy* **2018**, *163*, 113–121. [CrossRef]
106. Erlbeck, L.; Schreiner, P.; Schlachter, K.; Dörnhofer, P.; Fasel, F.; Methner, F.-J.; Rädle, M. Adjustment of Thermal Behavior by Changing the Shape of PCM Inclusions in Concrete Blocks. *Energy Convers. Manag.* **2018**, *158*, 256–265. [CrossRef]
107. Vicente, R.; Silva, T. Brick Masonry Walls with PCM Macrocapsules: An Experimental Approach. *Appl. Therm. Eng.* **2014**, *67*, 24–34. [CrossRef]
108. Al-Yasiri, Q.; Szabó, M. Case Study on the Optimal Thickness of Phase Change Material Incorporated Composite Roof under Hot Climate Conditions. *Case Stud. Constr. Mater.* **2021**, *14*, e00522. [CrossRef]
109. Sun, X.; Medina, M.A.; Lee, K.O.; Jin, X. Laboratory Assessment of Residential Building Walls Containing Pipe-Encapsulated Phase Change Materials for Thermal Management. *Energy* **2018**, *163*, 383–391. [CrossRef]
110. Bontemps, A.; Ahmad, M.; Johannès, K.; Sallée, H. Experimental and Modelling Study of Twin Cells with Latent Heat Storage Walls. *Energy Build.* **2011**, *43*, 2456–2461. [CrossRef]
111. Kondo, T.; Ibamoto, T. Research on Thermal Storage Using Rock Wool Phase-Change Material Ceiling Board. *ASHRAE Trans.* **2006**, *112*, 526.
112. Cabeza, L.F.; Navarro, L.; Pisello, A.L.; Olivieri, L.; Bartolomé, C.; Sánchez, J.; Álvarez, S.; Tenorio, J.A. Behaviour of a Concrete Wall Containing Micro-Encapsulated PCM after a Decade of Its Construction. *Sol. Energy* **2020**, *200*, 108–113. [CrossRef]
113. Cabeza, L.F.; Castellón, C.; Nogués, M.; Medrano, M.; Leppers, R.; Zubillaga, O. Use of Microencapsulated PCM in Concrete Walls for Energy Savings. *Energy Build.* **2007**, *39*, 113–119. [CrossRef]
114. Frazzica, A.; Brancato, V.; Palomba, V.; La Rosa, D.; Grungo, F.; Calabrese, L.; Proverbio, E. Thermal Performance of Hybrid Cement Mortar-PCMs for Warm Climates Application. *Sol. Energy Mater. Sol. Cells* **2019**, *193*, 270–280. [CrossRef]
115. ASHRAE Publishes 2017 Version of Thermal Comfort Standard. Available online: https://www.ashrae.org/about/news/2017/ashrae-publishes-2017-version-of-thermal-comfort-standard (accessed on 21 August 2021).
116. Zhou, D.; Shire, G.S.F.; Tian, Y. Parametric Analysis of Influencing Factors in Phase Change Material Wallboard (PCMW). *Appl. Energy* **2014**, *119*, 33–42. [CrossRef]
117. Thiele, A.M.; Sant, G.; Pilon, L. Diurnal Thermal Analysis of Microencapsulated PCM-Concrete Composite Walls. *Energy Convers. Manag.* **2015**, *93*, 215–227. [CrossRef]
118. Jia, J.; Liu, B.; Ma, L.; Wang, H.; Li, D.; Wang, Y. Energy Saving Performance Optimization and Regional Adaptability of Prefabricated Buildings with PCM in Different Climates. *Case Stud. Therm. Eng.* **2021**, *26*, 101164. [CrossRef]
119. Al-Absi, Z.A.; Mohd Isa, M.H.; Ismail, M. Phase Change Materials (PCMs) and Their Optimum Position in Building Walls. *Sustainability* **2020**, *12*, 1294. [CrossRef]
120. Wi, S.; Chang, S.J.; Kim, S. Improvement of Thermal Inertia Effect in Buildings Using Shape Stabilized PCM Wallboard Based on the Enthalpy-Temperature Function. *Sustain. Cities Soc.* **2020**, *56*, 102067. [CrossRef]

Article 2

buildings

MDPI

Review

A review on numerical modelling of the hygrothermal behavior of building envelopes incorporating phase change materials

Mohamed Sawadogo [1,2], Alexandre Godin [1,2], Marie Duquesne [1], Ameur Hamami [1] and Rafik Belarbi [1,3,*]

[1] La Rochelle Université, LaSIE UMR CNRS 7356, Avenue Michel Crépeau, 17042 La Rochelle Cedex 1, France; mohamed.sawadogo@univ-lr.fr (M.S.); alexandre.godin@univ-lr.fr (A.G.); marie.duquesne.@univ-lr.fr (M.D.); ameur_el_amine.hamami@univ-lr.fr (A.H.); rafik.belarbi@univ-lr.fr (R.B.);
[2] 4ev Lab, EDF R&D, CNRS, LaSIE, La Rochelle University, Avenue Michel Crépeau, CEDEX 1, 17042 La Rochelle, France
[3] Canadian University Dubaï, city walk Dubaï, UAE
* Correspondence: rafik.belarbi@univ-lr.fr

Abstract: Buildings are submitted to various external and internal solicitations that could affect its energy performances. Among these solicitations, temperature and moisture play a crutial role and could irrevocably affect the comfort of the occupants and the indoor air quality of the living environment. To assess the impact of the solicitation on buildings performances, a fine modelling of the heat, air and moisture transfer phenomenon is necessary. This work proposes an extensive review of the hygrothermal models for building envelopes. The different models are divided in nodal and HAM techniques for Heat, Air, and Moisture (HAM) transfer models. The HAM approaches has been classified based on four driving potential: moisture content, relative humidity, capillary pressure and vapor pressure. PCMs, alongside hygroscopic materials, enhance building thermal capacity and energy efficiency. There are various approaches to studying phase changes, with enthalpy-based and heat capacity approaches being the most popular. Building performance can be improved by combining PCM thermal inertia with hygroscopic moisture management. This review has exhibited the need for numerical models that address phase change and moisture behavior in these hybrid materials, capable of controlling temperature and humidity.

Keywords: Heat, air and moisture transfer, Phase change materials, modelling, humidity and temperature control materials.

Citation: To be added by editorial staff during production.

Academic Editor: Firstname Lastname

Received: date
Revised: date
Accepted: date
Published: date

Copyright: © 2023 by the authors. Submitted for possible open access publication under the terms and conditions of the Creative Commons Attribution (CC BY) license (https://creativecommons.org/licenses/by/4.0/).

1. Introduction

Energy conservation and environmental sustainability are major social concerns. They are linked to climate change phenomena, which, at building level, result in uncomfortable conditions during the different seasons. Indeed, buildings are subjected to a various of internal and external solicitation that have an effect on their hygrothermal behavior. The inhabitant comfort and the indoor air quality are both significantly impacted by these requests, and temperature and moisture play a crucial role [1,2]. This has led to the development of humidity control materials such as geo-based material [3–7] (rammed earth, cob earth material), bio-based material [8–11] (natural fiber components, straw, hemp) and generally the innovative ecofriendly materials. A better understanding of the properties of these materials and their response to dynamic climatic conditions constitute a major challenge in order to improve their energy and environmental performance. Indeed, the relative humidity of the air can be automatically regulated by humidity control materials that rely on their own features and the induction of changes in the surrounding temperature and humidity. Therefore, a precise modelling of the heat, air and moisture transport phenomenon is required to determine the effect of the solicitation on building performances [12–20]. The mathematical model for expressing the quantity of moisture

held in the material is a decisive issue among all the physical phenomena involved in heat and mass transfer processes through porous building materials.

To this end, the exploration of simultaneous heat and moisture transfer in porous building materials and envelopes has been a subject of research for over seven decades, resulting in the development of numerous theoretical models. The driving potentials and assumptions of each theoretical model are different and there is no unified theoretical model to describe the heat transfer and moisture migration in building envelopes [21]. The most used and accepted macroscopic models for studying heat and moisture transfer through porous media are the Luikov model [22] and Phillip and de Vries model [23], which use the temperature and moisture content as driving potentials. However, the major limitation of using the moisture content profile as driving potential is its discontinuity at the interface between two porous media [24]. In order to address this limitation, several models has been developed based on alternative driving potential such as relative humidity [25], capillary pressure [26], vapor pressure [22] and porous matrix potential [27].

In addition, phase change materials (PCMs) has been identified as an efficient technique to increase the thermal capacity, energy performance and comfort impact of buildings [28–33]. During the phase change process, PCMs absorb or release large amounts of latent heat from or to the indoor air. In this way, PCMs can smooth the temperature fluctuation and increase the thermal inertia of buildings. The variety of materials available, material liability and safety, cost and economic viability, design configurations, integration with other sustainable energy technologies and impact on thermal and energy performance are just a few of the challenges associated with using PCMs in buildings [34]. To address these challenges, numerical simulation is seen as an effective solution and has been used in numerous studies. There are several different approaches available for studying solid-liquid phase change. These include enthalpy-based methods, effective heat capacity methods, front tracking methods and adaptive grid methods [35]. However, a particular numerical strategy should be carefully chosen in order to evaluate accurately the performances of building incorporating PCMs.

PCMs and hygroscopic materials can be combined to improve the performance of building envelopes as a whole [36,37]. Energy efficiency, temperature regulation and moisture control can all be improved at once by combining the thermal inertia of PCMs with the moisture inertia of hygroscopic materials. Nevertheless, research in this field has primarily focused on thermal and energy factors, frequently ignoring the equally important hydric performance, despite the potential advantages of such integrated materials. Only a few number of researchers have thus thoroughly investigated both thermal and hygroscopic behavior inside these integrated systems.

This last concern has motivated the present study that aims at reviewing the hygrothermal model to evaluate the performances of building materials incorporating PCMs. First, the different models of Heat, air and moisture (HAM) transfer in buildings are presented. These models are divided in two groups namely the nodal and HAM approach. In the HAM, the models are divided based on four driving potential: moisture content, relative humidity, capillary pressure and vapor pressure. Afterwards, the numerical models of PCMs in buildings are presented with a focus on the so-called fixed domain method that are widely used in the literature. Finally, models that integrate both hygrothermal and phase change models are presented and the limitation as well as the challenges of the different models are discussed.

2. Physical phenomena of heat, air and moisture transfer

Heat, air and moisture transfer remains a highly complex phenomenon, requiring detailed modelling that takes into account not only each individual phenomenon but also all the interactions between the different phenomena. All these equations are based on the fundamental principle of heat and mass conservation. In this section, the equations describing each phenomenon are presented separately, before introducing the various models reported in the literature that translate the coupling between different phenomena.

2.1. Moisture transfer

Moisture refers to the transfer of water in liquid and vapor forms. This moisture (water and vapor) comes from several sources: rainwater running down walls, water vapor present in the material's ambient air etc [24]. It can be absorbed by porous building envelopes, depending on the equilibrium sorption moisture content.

2.1.1. Liquid water transfer

The transfer of the liquid phase is described by Darcy's law and is induced by a capillary suction gradient [23,38]. The mass flow density of liquid water is obtained by applying Darcy's law as follows:

$$J_{lc} = -\rho_l K_l \nabla \psi \quad (1)$$

where K_l is the hydraulic conductivity [m.s^{-1}] , ρ_l the liquid density [kg.m^{-3}] and ψ [m] the capillary suction. Liquid water can also migrate under the effect of gravity [25], which leads to consider an additional J_{lg} [kg.m^{-2}.s^{-1}] flow term on top of the previous term:

$$J_{lg} = -\rho_l K_l \vec{k} \quad (1)$$

where $\vec{k}$ is the vertical unit vector oriented positively upwards.

It is also possible to use other transfer motors to express liquid water flow, such as water content, relative humidity and vapor pressure. For example, Crausse et al. [38] defined a flux expression as a function of water content (θ [kg.m^{-3}]) as follows:

$$J_{lc} = -\rho_l (D_{\theta l} \nabla \theta + D_{Tl} \nabla T) \quad (1)$$

where $D_{\theta l}$ [m^2.s^{-1}] and D_{Tl} [m^2.s^{-1}.K^{-1}] represent the diffusion coefficients of liquid water under the effect of a water content gradient and a temperature gradient, respectively. These water diffusivities are related to hydraulic conductivity by:

$$D_{\theta l} = K_l \left(\frac{\partial \psi}{\partial \theta}\right)_T \quad (1)$$

$$D_{Tl} = K_l \left(\frac{\partial \psi}{\partial T}\right)_\theta \quad (1)$$

2.1.2. Water vapor transfer

Water vapor is transported by diffusion under the influence of a concentration gradient. The molecular diffusion process of water vapor in air is given as a function of the vapor concentration gradient by FICK's law [39] as follows:

$$J_v = -D_v \nabla \rho_v \quad (1)$$

J_v: Water vapor mass flux density [kg.m^{-2}.s^{-1}];

D_v: Coefficient of vapor diffusion in air [m^2.s^{-1}], characterizes the movement resulting from diffusion.

$\nabla \rho_v$: Water vapor concentration gradient;

If we consider water vapor pressure as the driving force for moisture transfer, Fick's law can be written as a function of the vapor pressure gradient:

$$p_v = \rho_v r_v T \quad \leftrightarrow \quad \rho_v = \frac{p_v}{r_v T} \quad (1)$$

$$J_v = \frac{D_v}{r_v T} \nabla p_v \quad (1)$$

Where p_v [Pa] is the water vapor pressure and r_v [J.kg^{-1}.K^{-1}] is the ideal gas constant.

2.2. Air transfer

In the presence of a total pressure gradient, a transfer of dry and humid air through an infiltration process occurs and must be taken into account in the total balance. This phenomenon, which is governed by a total pressure gradient, is expressed as follows:

$$J_a + J_v = -k_f \nabla P \quad (1)$$

J_a: dry and humid air mass flux density [kg.m^{-2}.s^{-1}];
k_f: is the total infiltration coefficient [kg.m^{-1}.s^{-1}.Pa^{-1}];
P : is the total pressure [Pa].

Some others as Tariku et al [40] used Poiseuille's law of proportionality [41], which relates the pressure gradient to flow velocity to express the airflow through a porous media. Under the assumption of incompressible air due to the very low airflow speeds and low pressure and temperature changes that are encountered in practice, the conservation equation for air mass balance is given by:

$$\nabla(\delta_a \nabla P) = 0 \quad (1)$$

δ_a: is the air permeability [s].

2.3. Heat transfer

In a porous material partially saturated with water, heat transfer can take place in three forms: purely conductive transfer according to Fourier's law [42], convective transfer of sensible heat by liquid and vapor flows and, finally, transfer of latent heat carried by the vapor. Considering all these phenomena, the heat flux density can be written as follows:

$$J_q = -\lambda \nabla \mathrm{T} + h_l\left(J_{lc} + J_{lg}\right) + h_v J_v \quad (1)$$

with λ [W.m-1.K-1] the heat conductivity of the material h_l and h_v [J.kg-1] the enthalpy of mass of liquid water and vapor, respectively. Remember that at a given temperature T [K] and with respect to a reference temperature T_0, these two quantities can be written as:

$$h_l = C_l(T - T_0) \quad (1)$$

$$h_l = C_l(T - T_0) + h_{lv} \quad (1)$$

with C_l [J.kg^{-1}.K^{-1}] the liquid water heat capacity and h_{lv} [J.kg^{-1}] the latent heat of vaporization of water.

3. Coupled heat, air and moisture transfer

The study of coupled heat, air and moisture transfer in porous materials is of key importance in a variety of fields, including building science, materials engineering and environmental science. Porous materials, such as building components and soils, often undergo complex interactions between heat, air and moisture, resulting in complex hygrothermal behaviors. To understand and predict these behaviors, researchers have developed a plethora of models, each tailored to specific scenarios and assumptions. Two different approaches are used to predict coupled heat, air and moisture transfer in porous materials: nodal models and HAM models.

3.1. Nodal approach

In the nodal approach, each node represents volumes of material or components, while inter-node connections represent the flow paths of thermal and mass fluxes (walls, doors, windows, etc.). The graphic representation of the model has the same appearance as an electrical diagram, hence the analogue method were used, where:

- the temperature and density of water vapor are represented by electrical potentials;
- energy flows and mass transfers are represented by current intensities;

- thermal and moisture resistances are represented by electrical resistances;
- the thermal and moisture retention capacities are represented by capacitors.

The nodal approach is a one-dimensional approach that is currently employed in the most common Building Energy Simulation (BES) software, such as TRNSYS, EnergyPlus [43]. They all focus on describing the dynamic changes in indoor relative humidity and temperature, which occur due to variations in outdoor climate, hygrothermal loads and the moisture buffering effect of indoor condition loads.

Boyer et al. [44] described a physical model of the building that is obtained by assembling thermal models of each element such as walls and glass windows. The thermo-convective balance equation of the dry-bulb air node and the radiative balance equation of the inside mean radiant temperature node are considered in the proposed model. The mathematical formulation of the thermal model of the building is a linear system of 4 equations expressed as follow:

$$C_{si}\frac{dT_{si}}{dt} = h_{ci}(T_{ai} - T_{si}) + h_{ri}(T_{rm} - T_{si}) + K(T_{se} - T_{si}) + q_{swi} \quad (1)$$

$$C_{se}\frac{dT_{se}}{dt} = h_{ce}(T_{ai} - T_{si}) + h_{re}\left(T_{sky} - T_{se}\right) + K(T_{se} - T_{si}) + q_{swe} \quad (1)$$

$$C_{ai}\frac{dT_{ai}}{dt} = \sum_{j=1}^{N_w} h_{ci}\left(T_{ai} - T_{si}(j)\right) + c\dot{Q}(T_{ae} - T_{ai}) \quad (1)$$

$$0 = \sum_{j=1}^{N_w} h_{ci}A_j(T_{si}(j) - T_{rm}) \quad (1)$$

where C [J.K^{-1}.m^{-2}] is the thermal capacity, c [J.kg^{-1}.K^{-1}.m^{-2}] is the specific heat, h [W.m^{-2}.K^{-1}] is the heat transfer coefficient, K [W.m^{-2}.K^{-1}] is the thermal conductivity per unit of length, q [W.m^{-2}] the radiation flux density, $\dot{Q}$ [kg.s^{-1}] is the mass flow rate and A [m^2] is the area.

The subscripts $ae, ai, se, si, ce, ci, lwe, re, ri, rm, swe, swi, w$ stand for air outside, air inside, surface outside, surface inside, outside convection, inside convection, long wave outside, outside radiation, inside radiation, inside radiant mean, short wave outside, short wave inside and wall, respectively.

Except Wufi that integrates a full moisture model, most of the building energy simulation software's such as TRNSYS and EnergyPlus primarily focuses on simulating temperature variations and energy requirements in specific spaces on a large scale. As a consequence, in these tools, the moisture exchange models at the wall scale rely on a simplified approach that does not account for the coupling of heat and moisture transfer phenomena through the building envelope.

One can distinguish two simplified models for simulating surface moisture adsorption and desorption: Effective Capacitance Moisture (ECM) model and Effective Moisture Penetration Depth (EMPD) model [45].

An effective moisture capacitance, defined as the product of the zone air mass and a moisture capacitance ratio, is used in the first model to account for the buffer effect of adsorptive and desorptive materials, soil areas, or plants [45]. A moisture balance for any zone results in the following differential equation:

$$M_{air,i}W_{cap}\frac{d\omega_i}{dt} = \dot{m}_{inf,i}(\omega_a - \omega_i) + \sum_{k}^{nvent} \dot{m}_{v,k,i}(\omega_{v,k,i} - \omega_i) + \dot{W}_{g,i} + \sum_{i-j}^{surfaces} \dot{m}_{cp\ lg,s}(\omega_j - \omega_i) \quad (1)$$

where $M_{air,i}$ [kg] effective moisture capacitance of the zone;
W_{cap} is humidity capacitance of the air and ranges from 1 to 10;
ω_i [%] the humidity ratio of the zone;
ω_a [%] the ambient humidity ratio;
$\omega_{v,k,i}$ [%] the humidity ratio of the ventilation air from ventilation type k;
$\dot{W}_{g,i}$ [kg.s^{-1}] internal moisture gains;
ω_j [%] the humidity ratio of an adjacent zone j;
$\dot{m}_{inf,i}$ [kg.s^{-1}] mass flow rate of infiltration air;
$\dot{m}_{v,k,i}$ [kg.s^{-1}] mass flow rate of ventilation air of ventilation type k;
$\dot{m}_{cp\ lg,s}$ [kg.s^{-1}] is the mass flow rate of air entering zone i across walls or windows.

The buffer storage humidity model describes a separate humidity buffer divided into a surface and deep storage . Each buffer is defined by three parameters: the gradient of the sorptive isothermal line of the material (κ), the mass of the material (M) and the moisture exchange coefficient between the two regions (β) and the zone air (Equation 19).

$$M_{air,i}\frac{d\omega_i}{dt} = \dot{m}_{inf,i}(\omega_a - \omega_i) + \sum_{k}^{nvent} \dot{m}_{v,k,i}(\omega_{v,k,i} - \omega_i) + \dot{W}_{g,i} + \sum_{i-j}^{surfaces} \dot{m}_{cp\ lg,s}(\omega_j - \omega_i) + \beta_{surf}(\omega_{surf} - \omega_i) \quad (1)$$

Additionally, two new differential equations were introduced to describe the dynamics of the water content of the surface and the deep storage.

$$M_{surf}\kappa_{surf}f(\varphi,\omega)\frac{d\omega_{surf}}{dt} = \beta_{surf}(\omega_i - \omega_{surf}) + \beta_{deep}(\omega_{deep} - \omega_{surf}) \quad (1)$$

$$M_{deep}\kappa_{deep}f(\varphi,\omega)\frac{d\omega_{deep}}{dt} = \beta_{deep}(\omega_{surf} - \omega_{deep}) \quad (1)$$

κ_{surf} [kg water /kg material /rel. humidity] gradient of sorptive isothermal line of surface buffer;
κ_{deep} [kg water /kg material /rel. humidity] gradient of sorptive isothermal line of deep buffer;
$f(\varphi,\omega)$ conversion factor from relative humidity to humidity ratio;
β_{surf} [kg.s^{-1}] the exchange coefficient between zone and surface storage;
β_{deep} [kg.s^{-1}]he exchange coefficient surface between storage and deep storage.

It should be noticed that this model allows taking into account the moisture transfer between external walls, internal walls or furniture and the zone air only. No moisture transfer with the exterior is modelled; as a result, the outdoor climate has no effect on the moisture transfer within the building envelope [46,47]. This limitation has conducted authors to develop fully coupled models based on the conservation principle (heat and mass).

3.2. Heat, air and moisture conservation based models

HAM models offer a more complex approach to understand the coupled transfer of heat, air and moisture. Unlike the nodal approach, HAM models take into account the simultaneous movement of heat, air and moisture within porous materials. These models integrate various physical processes such as conduction, convection, capillarity and vapor diffusion. One of the key factors differentiating these models is the choice of transfer motors they take into account. Heat, air and moisture can move through porous materials by different mechanisms, such as conduction, convection and capillarity. A summary of the different models based on their driving potential is presented in Table 1.

Table 1. Summary of the different models based on their driving potential

Driving potential	References
Moisture content	[23], [48], [49], [24] [50] [26] [51,52] [53] [54] [55] [56] [15,91,92]
Relative humidity	[25], [57–62], [63–68], [69,70], [71]
Capillary pressure	[72,73], [74], [75], [76,77], [78]
Vapor pressure	[79], [80], [81,82]

3.2.1. Models using moisture content as driving potential

The first coupled heat and moisture models were developed in 1957 by Philip and De Vries [23]. This model was based on the hypothesis of temperature-dependent soil moisture transport. Volumetric water content θ [$m^3.m^{-3}$] and temperature T [K] are the main driving forces of transport for heat and moisture transfer. The general differential equations describing coupled heat and moisture transfer in porous materials are:

$$\frac{\partial \theta}{\partial t} = \nabla(D_\theta \nabla\theta) + \nabla(D_T \nabla T) + \frac{\partial K}{\partial z} \quad (1)$$

$$\rho_s C_p \frac{\partial T}{\partial t} = \nabla(\lambda \nabla T) + h_{lv} \nabla(D_{v\theta} \nabla\theta) \quad (1)$$

Where ρ_s [$kg.m^{-3}$] is the density of the material, C_p [$J.kg^{-1}.K^{-1}$] is the specific heat of the dry material, λ [$W.m^{-1}.K^{-1}$] is the thermal conductivity of material, h_{lv} [$J.kg^{-1}$] is the latent heat of evaporation and $D_{v\theta}$ [$m^2.s^{-1}$] is the isothermal water vapor diffusion coefficient, K [$m.s^{-1}$] is the hydraulic conductivity, D_θ [$m^2.s^{-1}$] and D_T [$kg.m^{-1}.s^{-1}.K^{-1}$] are respectively the moisture diffusion coefficient related to temperature and moisture content gradients.

Luikov et al [48], was one of the first researchers to develop a mathematical model of thermo-hydric transfer in porous building materials. In this model, moisture in either vapor or liquid phase is transported under the influence of gradients in temperature, mass water content (u [$kg.kg^{-1}$]) and total pressure. However, it proposes to separate liquid (j_l) and vapor flow (j_v), since a concentration gradient and the latter induce the former by a thermal gradient.

$$j_v = -D_v \rho_s \nabla u - D_{vT} \rho_s \nabla T \quad (1)$$

$$j_l = -D_l \rho_s \nabla u - D_{lT} \rho_s \nabla T \quad (1)$$

Where D_v and D_l are the diffusion coefficients for water vapor and liquid water due to water content gradient respectively.

D_{vT} and D_{lT} are the diffusion coefficients for water vapor and liquid water due to temperature gradient, respectively.

Luikov introduced the concept of phase change criterion (PCC) ε that is defined as the ratio of the water vapor flux divergence to the total moisture flux divergence, as shown in Equation 26.

$$\varepsilon = \frac{div(j_v)}{div(j_v) + div(j_l)} \quad (1)$$

In addition to the heat and mass conservation equation, Luikov proposed an additional equation to describe the total pressure variation. The system of heat, air and moisture equation becomes:

$$\frac{\partial u}{\partial t} = \nabla\left(D_m\left(\nabla u + \delta_T \nabla T + \delta_f \nabla p\right)\right) \quad (1)$$

$$\rho_s C_p \frac{\partial T}{\partial t} = \nabla(\varepsilon h_{lv} D_m \nabla u + (\lambda + \varepsilon h_{lv} D_m \delta_T)\nabla T + \varepsilon h_{lv} D_m \rho_a \nabla p) \quad (1)$$

$$\rho C_f \frac{\partial p}{\partial t} = \nabla\left(\varepsilon D_m \nabla u - \varepsilon D_m \delta_T \nabla T + \left(k_f - \varepsilon D_m \rho_a\right)\nabla p\right) \quad (1)$$

where D_m [m².s^{-1}] is the moisture diffusion coefficient (water vapor and liquid water), δ_T [kg.m^{-3}.K^{-1}] is the thermogradient coefficient, C_f [Pa^{-1}] is the humid air capacity, k_f [kg.m^{-1}.s^{-1}.Pa^{-1}] is the filtration permeability coefficient, ρ_a [kg.m^{-3}] is the air density.

The disadvantage of this model is that the parameter ε is not derived from experimental tests, and its empirical determination is complex. Irudayaraj and Wu [49] and Lewis and Ferguson [50] were the first who have numerically investigated the solution of Luikov's partial differential equations. This model has been used intensively by authors in the literature and has inspired many other models.

The moisture content is discontinuous at the interface between two materials due to their different hygroscopic properties, which brought problems when the model of multilayer materials was numerically solved. In order to solve the problem of moisture content discontinuity, the Luikov model and Phillip-De Vries model had been modified by using other moisture driving potentials instead of the moisture content [26].

Mendes et al [51,52] proposed a new hygrothermal model based on Philip and De Vries' equations, but instead of the volumetric water content, he preferred the volumetric moisture content θ and the temperature gradient T as the principle driving forces for the coupled heat and moisture transfer. The governing partial differential equations to model the hygrothermal behavior are therefore given by:

$$\frac{\partial \theta}{\partial t} = -\nabla(D_\theta \nabla\theta + D_T \nabla T) \quad (1)$$

$$\rho_s C_p \frac{\partial T}{\partial t} = \nabla(\lambda \nabla T) - h_{lv} \nabla(D_{v\theta} \nabla\theta + D_{vT} \nabla T) \quad (1)$$

Whitaker [53] proposed a detailed theory based on local mean volume behavior, in which the transport equations are described for each phase (solid, liquid and gas) at macroscopic and microscopic levels.

$$\rho_s \frac{\partial u}{\partial t} = -\nabla(\rho_s f D_v \nabla u_v + D_b \nabla \rho_v - \rho_l \bar{V}_l) \quad (1)$$

$$\frac{\partial\left(\varepsilon_l \rho_l h_l + \varepsilon_g \rho_v h_v + \varepsilon_s \rho_s h_s + \bar{\rho}_b \bar{h}_b\right)}{\partial t} = \nabla(\lambda \nabla T) + h_v \rho_g f D_v \nabla u_v + h_b D_b \nabla \rho_v - h_l \rho_l \bar{V}_l \quad (1)$$

ρ_l, ρ_v and ρ_s are respectively the density of water vapor, liquid phase and the solid phase, f is the dimensionless diffusivity tensor, u_v is the vapor mass fraction.

D_v [m².s⁻¹] and D_b [m².s⁻¹] are respectively the water vapor and bound water diffusivity and $\bar{V}_l$ [m.s⁻¹] is the liquid phase velocity [43,83].

Where h_l, h_v, h_s and h_b are respectively the enthalpy of the liquid phase, vapor phase, solid phase of water and enthalpy of bound water. $\varepsilon_l, \varepsilon_v$ and ε_s are respectively the volume fraction of liquid, vapor and solid.

Milly [54] have reformulated the Philip and de Vries equations for coupled heat and moisture transfer to obtain a ''porous matrix potential" rather than moisture content as independent variable.

Abahri et al [55] proposed a more detailed model of coupled HAM transfer in building envelopes. For moisture transfer, in addition to diffusion, the contribution of the total pressure gradient, expressed by a coefficient, is taken into account, as is the contribution of the thermal gradient expressed by a thermogradient coefficient. Both coefficients have been evaluated experimentally using laboratory tests [84]. The mass and energy balances are presented in the following system of equations:

$$\frac{\partial u}{\partial t} = \nabla\left(D_m\left(\nabla u + \delta_T \nabla T + \alpha_p \nabla p\right)\right) \quad (1)$$

$$C_p \rho_s \frac{\partial T}{\partial t} = \nabla(a_T \nabla T + \delta_u \nabla u + \alpha_T \nabla p) + \rho_s h_{lv} \varepsilon \frac{\partial u}{\partial t} \quad (1)$$

$$C_f \rho_s \frac{\partial p}{\partial t} = \nabla\left(k_f \nabla p\right) + \rho_s \varepsilon \frac{\partial u}{\partial t} \quad (1)$$

where a_T [W.m⁻¹.K⁻¹] is the modified thermal conductivity ; δ_u [W.m⁻¹] and α_T [W.m⁻¹.Pa⁻¹] are coefficients reflecting thermal advection due to moisture and total pressure gradients respectively.

Similarly, Trabelsi et al [15,91,92] proposed another macroscopic model based on Luikov's work, with temperature and vapor content as transfer drivers. The results of this model showed good agreement between numerical and analytical resolutions. In the same work, they studied the sensitivity of this model to the thermal gradient coefficient. This study showed the need to take thermo-diffusion into account, as its impact on overall mass transfer is non-negligible.

Qin et al [24] proposed a dynamic mathematical model for simulating the coupled heat and moisture migration through multilayer porous building materials. Vapor content (v [kg.m-3]) and temperature were chosen as the principal driving potentials. The phase change occurring within porous materials acts as a heat source or sink, which results in the coupled relationship between moisture and heat transfer. The heat of absorption or desorption is generally one of the sources or sinks as well. Both phenomena are considered in the developed model. A local thermodynamic equilibrium between the fluid and the porous matrix is assumed. The set of differential equations for coupled heat and mass transfer are as follows:

$$\rho_s \xi \frac{\partial v}{\partial t} = \nabla(D_m \nabla v) + \nabla(\varepsilon D_m \nabla T) \quad (1)$$

$$\rho_s C_p \frac{\partial T}{\partial t} = \nabla(\lambda \nabla T) + \rho_s \xi (\varepsilon h_{lv} + \gamma) \frac{\partial v}{\partial t} \quad (1)$$

where ξ [m³.kg⁻¹] is the specific moisture storage capacity, γ [J.kg⁻¹] is the heat of absorption or desorption.

In addition, the authors proposed an analytical method [56] to calculate the coupled heat and moisture transfer process in building materials. The coupled system was first subjected to Laplace transformation, and then the equations were solved by introducing

the Transfer Function Method. The transient temperature and moisture content distribution across the material can thus be easily obtained from the solutions. A new experimental methodology for determining the temperature gradient coefficient for building materials was also proposed [85]. Both the moisture diffusion coefficient and the temperature gradient coefficient for building material were experimentally evaluated.

3.2.2. Models using relative humidity as driving potential

In 1995, Künzel introduced a new model that was based on Kieβl's theorem [25]. In this model, Künzel attempted to use the terms of relative humidity φ and temperature T as the primary driving forces to describe the coupled heat and moisture transfer in building components.

$$\frac{dw}{d\varphi}\frac{d\varphi}{dt} = \nabla\left(D_\varphi \nabla\varphi + \delta_v \nabla(\varphi p_{sat})\right) \quad (1)$$

$$\frac{dH}{dT}\frac{dT}{dt} = \nabla(\lambda \nabla T) + h_{lv}\nabla\left(\delta_v \nabla(\varphi p_{sat})\right) \quad (1)$$

where $\frac{dw}{d\varphi} = C_m$ [kg.m^{-3}] is the moisture storage capacity of the porous material, D_φ [kg.m^{-1}.s^{-1}] is the liquid conduction coefficient, δ_v [kg.m^{-1}.s^{-1}.Pa^{-1}] is the water vapor permeability of the porous material, φ [%] is the relative humidity and p_{sat} [Pa] is the water vapor saturation pressure and $\frac{dH}{dT} = C$ [J. m^{-3}.K^{-1}] is the heat storage capacity of the porous material.

This model belongs to Fraunhofer Institut Für BauphysiK IBP. It was then integrated into the WUFI (Wärme Und Feuchte Instationär) software package, one of the most widely used commercial tools for modelling heat and moisture transfer. This software is used to model the hygrothermal behavior of multi-layered building elements exposed to the natural climate. This model has been used by several researchers [57–62], with generally satisfactory results.

As shown by many authors, it is possible to explicitly present the temperature by modifying the saturation pressure term as it can be expressed as a function of temperature. The novel system of coupled heat and mass transfer equation becomes [63,64,67,68,86,87]:

$$\frac{dw}{d\varphi}\frac{d\varphi}{dt} = \nabla\left(D_w^\varphi \nabla\varphi + D_w^T \nabla T\right) \quad (1)$$

$$\frac{dH}{dT}\frac{dT}{dt} + \frac{dH}{d\varphi}\frac{dT}{d\varphi} = \nabla\left(D_e^T \nabla T + D_e^\varphi \nabla\varphi\right) \quad (1)$$

Where D_e^T [W.m^{-1}.K^{-1}], D_e^φ [W.m^{-1}], D_w^T [kg.m^{-1}.s^{-1}] and D_w^φ [kg.m^{-1}.s^{-1}.K^{-1}] are the material specific transport coefficients defined by the following expressions:

$$D_e^T = \lambda + (h_v + C_{p,v}T)\delta_v \cdot \varphi \frac{dp_{sat}}{dT} \quad (1)$$

$$D_e^\varphi = (h_v + C_{p,v}T)p_{sat} \cdot \delta_v \quad (1)$$

$$D_w^T = \varphi \cdot \delta_v \frac{dp_{sat}}{dT} \quad (1)$$

$$D_w^\varphi = p_{sat}\delta_v + K^* \quad (1)$$

A more detailed model has been proposed with additional terms on the material specific transport coefficient [69,70] and a source term to the mass transfer equation. The new system of equations becomes:

$$\frac{dw}{d\varphi}\frac{d\varphi}{dt} = \Delta\left(\left(\delta_v\ p_{sat} + K_l\rho_l R_D\frac{T}{\varphi}\right)\nabla\varphi + \left(\varphi\cdot\delta_v\frac{dp_{sat}}{dT} + K_l\rho_l r_v\ln(\varphi)\right)\nabla T\right) - \nabla\left(j_a\frac{0.622}{p_{atm}}\varphi p_{sat}\right) \quad (1)$$

$$\frac{dH}{dT}\frac{dT}{dt} = \Delta\left(D_e^T\nabla\varphi + D_e^\varphi\nabla\varphi\right) - \nabla\left(C_{p,a}j_a T + \frac{0.622}{p_{atm}}j_a h_v\varphi p_{sat}\right) \quad (1)$$

K_l [kg.m^{-1}.s^{-1}.Pa^{-1}] is liquid water permeability, p_{atm} [Pa] is atmospheric pressure, $C_{p,a}$ [J.kg^{-1}.K^{-1}] is the air heat capacity.

Wang et al. [71] developed a transient model for the coupled heat and moisture transfer in building materials based on the PCC introduced by Luikov. The temperature and relative humidity were used as the driving potentials. At the exception of the other PCC-based models, the PCC was introduced in both the energy conservation equation and the moisture conservation equation to simplify the model not only in the energy conservation equation.

$$(1-\varepsilon)C_m\frac{\partial\varphi}{\partial t} = \nabla\left(D_{\varphi,l}\nabla\varphi\right) \quad (1)$$

$$\left(\rho_s C_{p,s} + wC_{p,l}\right)\frac{\partial T}{\partial t} = \nabla(\lambda\nabla T) + C_m(\varepsilon h_{lv} + \gamma)\frac{\partial\varphi}{\partial t} \quad (1)$$

The expression of the PCC in isothermal and non-isothermal conditions is as follow:

$$\varepsilon = \frac{D_{m,v}}{D_m} = \frac{\delta_v p_v}{K_l\rho_l r_v T + \delta_v p_v} \quad (1)$$

$$\varepsilon = \frac{\left|\delta_v\varphi\frac{dp_s}{dT}\nabla T + \delta_v p_s\nabla\varphi\right|}{\left|\delta_v\varphi\frac{dp_s}{dT}\nabla T + \delta_v p_s\nabla\varphi\right| + \left|K_l\rho_l r_v ln\varphi\nabla T + K_l\rho_l r_v\frac{T}{\varphi}\nabla\varphi\right|} \quad (1)$$

3.2.3. Models using capillary pressure as driving potential

Moisture transfer is often considered to be driven by capillary pressure gradients, as this quantity is an actual potential [72,73]. Capillary pressure p_c [pa] is defined as the pressure difference between the liquid and gas phases:

$$p_c = p_l - p_{v+a} \quad (1)$$

Janssen et al [74] proposed a numerical model for simulations of moisture and heat transfer in building components under atmospheric excitation based on the model. Temperature and capillary pressure are used as driving potential. The set of heat and mass transfer equations are:

$$\frac{\partial w}{\partial p_c}\frac{\partial p_c}{\partial t} = -\nabla\left(j_{m,l} + j_{m,v}\right) \quad (1)$$

$$\left(\rho_s C_{p,s} + wC_{p,l}\right)\frac{\partial T}{\partial t} + \left(C_{p,l}T\frac{\partial w}{\partial p_c}\right)\frac{\partial p_c}{\partial t} = \nabla\left(j_{h,c} + j_{h,a}\right) \quad (1)$$

$$j_{m,l} = -K_l\nabla p_c \quad (1)$$

$$j_{m,v} = -\frac{\delta_v p_v}{\rho_l r_v T}\nabla p_c - \frac{\delta_v p_v}{\rho_l r_v T^2}\left(\rho_l h_{lv} + p_c(T\gamma - 1)\right)\nabla T \quad (1)$$

$$j_{h,c} = -\lambda\nabla T \quad (1)$$

$$j_{h,a} = C_{p,l} T j_l + \left(C_{p,v} T + h_{lv}\right) j_v \quad (1)$$

Li et al. [75] also used capillary pressure as driven potential for the moisture transfer and temperature gradient for the heat transfer. The governing equations for the heat, air and moisture transport in building materials are based on conservation of the combined heat and moisture transport of the representative elementary volume and expressed in the coefficient term as:

$$\boldsymbol{d_a} \begin{bmatrix} \frac{\partial T}{\partial t} \\ \frac{\partial p_c}{\partial t} \end{bmatrix} = \nabla \left(\boldsymbol{b} \nabla \begin{bmatrix} T \\ p_c \end{bmatrix} \right) + \boldsymbol{\varepsilon} \nabla \begin{bmatrix} T \\ p_c \end{bmatrix} + \begin{bmatrix} Q_h \\ Q_m \end{bmatrix} \quad (1)$$

d_a is the damping coefficient matrix and written as:

$$\boldsymbol{d_a} = \begin{bmatrix} \rho_s C_{p,s} + w C_{p,l} & 0 \\ 0 & \frac{\partial w}{\partial p_c} \end{bmatrix} \quad (1)$$

b is the diffusive coefficient matrix and written as

$$\boldsymbol{b} = \begin{bmatrix} \lambda + \delta_v h_{lv} \varphi \frac{dp_s}{dT} & -\frac{\delta_v h_{lv} \varphi p_s}{\rho_l R_v T} \\ -\delta_v \varphi \frac{dp_s}{dT} & k_l + \frac{\delta_v \varphi p_s}{\rho_l R_v T} \end{bmatrix} \quad (1)$$

ε is the convective coefficient matrix and written as

$$\boldsymbol{\varepsilon} = \nu \begin{bmatrix} -\left(\rho_a C_{p,a} + h_{lv} \frac{d\rho_v}{dT}\right) & \frac{h_{lv} \varphi}{\rho_l R_v T} \frac{d\rho_v}{d\varphi} \\ \frac{d\rho_v}{dT} & -\left(\frac{\varphi}{\rho_l R_v T} \frac{d\rho_v}{d\varphi}\right) \end{bmatrix} \quad (1)$$

The model is validated through inter-model comparisons with benchmarking cases of the HAMSTAD project and with experimental results of full-scale wall panels.

Fang et al. [76,77] developed a model similar to the model of Li et al with capillary pressure and temperature as driven potential. The validation of the model was accomplished by comparing the simulation results with the experiment results in the study of Odgaard et al. [78].

3.2.4. Models using pressure vapor as driving potential

Berger et al. [80] developed a detailed mathematical model combined with an innovative efficient numerical model to predict heat, air and moisture transfer through porous building materials. The model is based on Luikov's work and uses Whitaker volume averaging method to link the microscopic and macroscopic approaches. The model considers the transient effects of air transport and its impact on the heat and moisture transfer. Temperature, partial vapor pressure an total pressure are used as driving potential. The system of coupled heat, air and mass transfer differential equation is as follow:

$$c_m \frac{\partial p_v}{\partial t} = \nabla(k_m \nabla p_v - a_v p_v) \quad (1)$$

$$C_q \frac{\partial T}{\partial t} = \nabla\left(k_q \nabla T + a_q T\right) + h_v \nabla(\delta_v \nabla p_v - a_v p_v) - \sum_{i=1}^{3} \nabla(c_i T) j_{c,i} - C_{p,v} h_v \frac{\partial p}{\partial t} + C_{p,s} h_v \frac{\partial \sigma}{\partial t} \quad (1)$$

$$C_a \frac{\partial p}{\partial t} = \nabla(\delta_a \nabla p) - \nabla(\delta_v \nabla p_v - a_v p_v) + C_{av} \frac{\partial p_v}{\partial t} + C_{at} \frac{\partial T}{\partial t} + C_{as} \frac{\partial \sigma}{\partial t} \quad (1)$$

where a_v [s.m^{-1}] and a_q [W.m^{-2}.K^{-1}] are the advection coefficients. C_q [J.m^{-3}.K^{-1}], c_m [Kg.m^{-3}.Pa^{-1}], C_a [Kg.J^{-1}], C_{as} [Kg.Pa.J^{-1}], C_{av} [Kg.J^{-1}], C_{at} [Kg.Pa.J^{-1}.K^{-1}], C_{qv} [Kg.J^{-1}] and C_{qs} [Kg.Pa.J^{-1}] the storage coefficients.

Ayres de Mello et al [81,82] proposed a new mathematical model, called CAR-HAM (Conductive, Advective, and Radiative Heat, Air and Moisture) that includes the radiative transfer equation to calculate the thermal radiation effects within the porous materials to be taken into account in the energy balance. The formulation is based on the model presented in the HAMSTAD (Heat, air and moisture standard development) project, adding the contribution related to radiation. The moisture and the energy conservation equations are simultaneously solved using a fully implicit scheme and the MTDMA (MultiTridiagonal-MatrixAlgorithm) algorithm. The system of moisture and energy balance equations including the radiation contribution is presented as follow:

$$\frac{\partial w}{\partial t} = -\nabla j_{tot} \quad (1)$$

$$j_{tot} = j_v + j_l \quad (1)$$

$$j_v = -\delta_v \nabla p_v + \boldsymbol{u}\rho_v \quad (1)$$

$$j_l = -k_l(\nabla p_{suc} - \rho_l \boldsymbol{g}) \quad (1)$$

$$\frac{\partial H}{\partial t} = -\nabla j_q \quad (1)$$

$$j_{tot} = \lambda \nabla T + \boldsymbol{u}\rho_c c_a T + j_v h_{lv} + j_l c_l T + \boldsymbol{q}_{rad} \quad (1)$$

The radiative flux is calculated using the Equation 70:

$$\nabla \boldsymbol{q}_{rad} = \kappa \left(4\pi I_b - \int_0^{4\pi} I d\Omega \right) \quad (1)$$

3.3. Co-simulation approach

The building simulation program such as TRNSYS and EnergyPlus does not accurately include hygrothermal interactions with the building envelope. Therefore, it is essential to integrate a non-isothermal combined heat and mass transfer model into the simulation environment. To overcome this problem and better stimulate the hygrothermal behavior of buildings, several approaches have been proposed in recent years. One of these is co-simulation, which consists in using two existing software packages, one for dynamic building simulation, the other for precise modeling of hygrothermal behavior at the envelope level.

Zhai et al [88] classified the co-simulation methods in two groups as either static or dynamic coupling. In static coupling, the interaction between the two simulation tools is one-way, with information flowing from one software to the other without any feedback or iterative exchange during the simulation. On the other hand, dynamic coupling involves a two-way interaction between the tools, allowing a continuous exchange of information and feedback during the simulation process. Dynamic coupling enables a more comprehensive and accurate representation of the hygrothermal behavior of buildings, as it accounts for the mutual influence of heat and moisture transfer phenomena, leading to improved predictions and a better understanding of the building's performance.

In order to investigate the effects of sorption isotherm hysteresis on indoor climate and energy demand, Kwiatkowski et al [89] developed and implemented in the energy performance simulation tool, TRNSYS a new module for precise representation of mass transfer in materials in contact with indoor air, called Humi-mur.

Steeman et al. [90,91] developed a coupled TRNSYS-HAM model which allows to account for the response of a multizone building on moisture buffering effects in a more detailed way. The HAM model describes one dimensional transient coupled heat and mass transfer in porous materials. To illustrate the applicability of the integrated TRNSYS-HAM model for the design and evaluation of numerous building applications, the model was used to predict the surface relative humidity in an office space equipped with a gypsum cooled ceiling. Results show that a simplified model overpredicts the surface relative humidity because non-isothermal vapor diffusion in the hygroscopic gypsum layer is neglected.

Ferroukhi et al. [92–94] have extended their work by developing a co-simulation platform HAM-BES (BES: Building Energy Simulation) in order to accurately predict the hygrothermal behavior of the wall and living environment in buildings. This has enabled to highlight the impact of hygrothermal transfer on the prediction of energy consumption and to study the effectiveness of different ventilation methods (extraction or insufflation) in controlling and reducing the risk of disorders caused by humidity.

Frasca et al. [95] proposed a multi-step methodology to investigate the capability of a BES software coupled with a HAM model (HAM-BES) as a technique for diagnostics and conservation in complex settings. The methodology was thus applied to the historical church of the 17th century Chiesa di Santa Rosalia (Italy), allowing to explore climate-induced conservation risks based on simulations.

3.4. Boundary condition

In addition to the physical modeling of heat and moisture transfer coupled equations, boundary conditions such as ambient conditions and climatic data are necessary for accurate simulations and assessments. The boundary conditions are classified as interior and exterior conditions and expressed simultaneous for heat and moisture transfer.

The outside boundary condition is governed by several parameters including the ambient air temperature, the relative humidity, solar radiation, rain load, wind velocity and direction. The outer and inner surface boundary conditions are given by [21,43,96]:

$$j_{v,ext} = \beta_{m,ext}\left(p_{v,ext} - p_{v,surf,ext}\right) \quad (1)$$

$$j_{q,ext} = h_{c,ext}\left(T_{ext} - T_{surf,ext}\right) + h_{lv}j_{v,ext} + \alpha q_{solar} \quad (1)$$

$$j_{m,int} = \beta_{m,int}\left(p_{v,int} - p_{v,surf,int}\right) \quad (1)$$

$$j_{q,int} = h_{c,int}\left(T_{air,int} - T_{surf,int}\right) + h_{lv}j_{v,int} \quad (1)$$

It should be noticed that the liquid flux is not considered in both interior and exterior surfaces. In fact, it is reasonable to assume that there is no liquid water penetrating the indoor boundary surface (interior surface of the wall). This is because the interior of a building is generally designed to be dry and measures are taken to prevent water intrusion from the outside. In the absence of wind-driven rain, the same assumption holds true for the outer boundary surface. However, when wind-driven rain is present, it can lead to rainwater accumulation on the exterior wall, ultimately resulting in surface saturation [97–99].

3.5. Models validation

The validation of hygrothermal simulation models can be done in various ways. In order to make sure that model errors are not hidden by any uncertainties of input data or test results, a rigorous validation should comprise three steps. The first step is the confirmation of correct implementation of physical fundamentals by comparison with analytical solutions when it is possible. For moisture uptake in a semi-infinite region, there is a benchmark example in BS EN 15026 (2007). As second step, it is useful to compare the calculation results to laboratory tests with well-defined boundary conditions and material

data. The third step should be close to the real thing, e.g. simulating the transient hygrothermal behavior of a building envelope component exposed to natural climate.

Dong et al. [21] and Judkoff et al [100] highlighted three commonly used methods for model validation: theoretical, intermodel and experimental validation. A summary of the model validation methods is presented in Table 2.

Table 2. Summary of the model validation methods

Validation methods		**References**
Theoretical validation		[101], [71,102–105], [56,106,107]
Intermodel validation		[102,108,109], [110–113], [114,115]
Experimental validation	Material scale	[16,17,21,66,116–118], [119–122]
	Wall scale	[96,123–127], [128–131]

3.5.1. Theoretical validation

In the theoretical validation, the model's predictions are compared with analytical solutions or well-established theoretical equations. HAMSTAD Benchmark case #2 [101] is an efficient theoretical validation case study for moisture transfer models. It describes the moisture redistribution in a homogeneous single layer wall under isothermal conditions. Since the temperature difference through the interior and exterior of the wall is eliminated, an analytical solution can be obtained. Several authors has used this analytical to validate their modelling [71,102–105]. In addition to the Benchmark, some authors developed analytical tools to solve heat and mass transfer problems [56,106,107]. Qin et al [56] proposed an analytical method to calculate the coupled heat and moisture transfer process in building materials based on Laplace transformation and Transfer Function Method. The transient temperature and moisture content distribution across the material can thus be easily obtained from the solutions. The results were compared with the experimental data and other analytical solutions available in the literature; a good agreement was obtained.

3.5.2. Intermodel validation

The intermodel validation method involves comparing the results of the model in question with those obtained from other independently developed models that aim to simulate similar phenomena. By comparing the outcomes, researchers can assess the consistency and accuracy of the model's predictions against other established models. This method can be divided into two categories: comparison with the numerical results of previous research literature and comparison with the simulated results of hygrothermal simulation software, such as COMSOL Multiphysics [102,108,109], Wufi [110–113], Delphin [114,115]. In addition, the HAMSTAD Benchmark case #3-5 [101] are often used for intermodel validation for numerous model.

3.5.3. Experimental validation

In the experimental validation method, the model's predictions are compared with real-world experimental data obtained from physical tests or measurements. This approach is crucial as it enables researchers to verify how well the model replicates the actual behavior observed in experiments.

Busser et al. [20] reviewed the recent experimental studies to validate the hygrothermal models for building materials and envelopes and divided the experimental facilities into two scales: material and wall. At the material scale, two types of experimental facilities were distinguished: the climatic chamber [16,17,21,66,116–118] and the wind air tunnel [119–122]. These facilities differ only in the way convective boundary conditions were

controlled. The wall scale can be divided into exposure to controlled conditions in the climate chamber (including one-sided and doubled-sided responses) 96,123–127] or natural outdoor conditions on one side (including single-layer and multilayer walls) [128–131].

4. Integration of phase change materials in HAM models

4.1. Modelling of PCMs

Solid-liquid phase change is generally described by the classic Stefan problem, named after the Slovenian physicist Joseph Stefan, who studied the solidification of soil and the formation of ice in the oceans around 1890 [132]. The Stefan problem describes the evolution of the boundary between two phases of a material undergoing a process of phase change. This problem is treated by solving the heat equations in the two regions (solid and liquid) with associated initial and boundary conditions. The temperature at the solid-liquid interface is the phase-change temperature. As the equations for the two phases are not valid at the interface, also known as the melting or solidification front, a final equation is introduced to close the mathematical system: the Stefan condition. This condition is obtained by performing an energy balance, which makes it possible to determine the position of the phase-change front:

Solid phase:

$$\rho C_{p,sol} \frac{\partial T_{sol}}{\partial t} = \frac{\partial}{\partial x}\left(\lambda_{sol} \frac{\partial T_{sol}}{\partial x}\right) \quad (1)$$

Liquid phase:

$$\rho C_{p,liq} \frac{\partial T_{liq}}{\partial t} = \frac{\partial}{\partial x}\left(\lambda_{liq} \frac{\partial T_{liq}}{\partial x}\right) \quad (1)$$

Stefan's condition for energy conservation at the boundary:

$$\frac{\partial}{\partial x}\left(\lambda_{sol} \frac{\partial T_{sol}}{\partial x}\right) - \frac{\partial}{\partial x}\left(\lambda_{liq} \frac{\partial T_{liq}}{\partial x}\right) = \rho L_f v \quad (1)$$

Analytical solutions of Stefan's problem can be found in advanced heat transfer books [34]. However, numerical methods are generally used to solve this system of equations. These numerical methods can be divided into three groups [35]: fixed-grid methods, interface tracking methods and hybrid methods.

In fixed-domain methods, Stefan's condition is taken into account implicitly by reformulating the conservation equations and the position of the boundary is known a posteriori, i.e. once the solution has converged. Fixed-domain methods are characterized by their ease of implementation, convenience, adaptability and versatility compared with other methods [133]. Latent heat can be taken into account using the enthalpy method, the apparent heat capacity method, the temperature transformation model and the heat source method. Al-Saadi and Zhai [134] have carried out a review of all these methods, the synthesis of which will be presented in this section.

4.1.1. The enthalpy method

The enthalpy method was proposed by Eyres [135] to deal with thermal properties whose evolution depends on temperature. In this method, the sensible and latent heat terms are combined into an enthalpy term in the energy conservation equation. For heat transfers governed mainly by conduction, the conservation equation is described by Equation 78.

$$\rho \frac{\partial h(T)}{\partial t} = \frac{\partial}{\partial x}\left(\lambda \frac{\partial T}{\partial x}\right) \quad (1)$$

The enthalpy term represents the sum of two contributions: a sensible part (liquid and solid) and a latent part, whose respective expressions are described in the Equations 79-81:

$$h(T) = h_{sensible}(T) + h_{latent}(T) \quad (1)$$

$$h_{sensible}(T) = \int_{T_{intiale}}^{T_{fusion}} C_{p,sol}(T)dT + \int_{T_{fusion}}^{T_{fusion}} C_{p,liq}(T)dT \quad (1)$$

$$h_{latent}(T) = f(T)L_f \quad (1)$$

where L_f [J.kg-1] is the latent heat of fusion and $f(T)$ the liquid fraction as function of temperature.

The variation of enthalpy as a function of H-T temperature is obtained experimentally by calorimetry or by integrating the apparent heat capacity curve obtained by Differential Scanning Calorimetry (DSC), which improves the accuracy of simulations.

This equation is non-linear in the sense that enthalpy and thermal conductivity are temperature-dependent. It can be solved either using a non-linear solver (Newton's method) or by linearizing the equation.

The enthalpy method has a number of advantages: i) it is valid over a wide range of cases, from isothermal phase change to phase change over a temperature range, ii) it is independent of the discretization scheme chosen (Finite Volume, Finite Difference, Finite Elements ...), iii) no conditions have to be imposed on the change front, which is automatically taken into account [35]. The method is also simple and the agreement with experimental data is good, making it one of the most widely used methods for modeling solidification/melting problems.

However, this method still faces two problems: it is difficult to take into account undercooling problems and the temperature in a mesh can oscillate over time.

4.1.2. The heat capacity method

In this method, the heat capacity is modified around the phase-change temperature to include latent heat. Two approaches are proposed in the literature to take this latent heat into account: the apparent heat capacity method and the effective heat capacity method. These two methods differ only in the approximation made to the heat capacity.

The apparent heat capacity method was introduced by Hashemi and Spielcevich [136] to solve a heat transfer problem with a phase change. The unsteady one-way conduction equation can be rewritten using the apparent heat capacity method as follows:

$$\rho C^{app}(T)\frac{\partial T}{\partial t} = \frac{\partial}{\partial x}\left(\lambda \frac{\partial T}{\partial x}\right) \quad (1)$$

where $C^{app}(T)$ represents the apparent heat capacity, which can be calculated in two different ways: either using analytical/experimental relationships or using numerical approximations.

Analytical/experimental relationships are obtained using thermo-physical characterization techniques such as DSC or the T-history method [137]. These characterization techniques provide material properties such as melting temperature, enthalpy of phase change and heat capacities of the liquid and solid phases. These data are used to estimate the heat capacity of PCM using a simple direct relationship by introducing a fictitious phase change range (2ϵ):

$$C^{app} = \begin{cases} C_{p,sol} \ \ if \ \ T < T_f - \varepsilon \\ \dfrac{C_{p,sol} + C_{p,liq}}{2} + \dfrac{L_f}{2\varepsilon} \quad if \ \ T_f - \varepsilon \le T \le T_f + \varepsilon \\ C_{p,sol} \ \ if \ \ T > T_f + \varepsilon \end{cases} \quad (1)$$

The choice of phase change range is a very important parameter when modeling with the apparent heat capacity method, as it can lead to convergence problems. If the range is too small, or the time step too large, there is a risk of missing the latent heat contribution. It is therefore essential to carry out a parameter study to estimate the optimum values for these parameters.

Moreover, the accuracy of the method depends on the approximation made to the apparent heat capacity curve used in the simulation. Several shapes are proposed in the literature: rectangular, triangular, Gaussian, trapezoidal. Triangular and Gaussian profiles give better results than the other two [134].

To solve the convergence problem associated with analytical/experimental relationships, some authors have proposed an approach based on a numerical approximation of the heat capacity. Thus, Comini [138] expressed the heat capacity as a temperature derivative of enthalpy in a numerical resolution using the finite element method. Morgan et al [139] improved this method by using an iterative scheme in which the heat capacity is approximated using successive temperature and enthalpy solutions.

$$C^{app} = \frac{\Delta h}{\Delta T} = \frac{h^n - h^{n-1}}{T^n - T^{n-1}} \quad (1)$$

Another alternative is to use the effective heat capacity method proposed by Poirier et al [140]. In this method, a temperature profile is considered between nodes and instead of calculating the apparent heat capacity from the nodal point temperature, an effective heat capacity is calculated by integrating heat capacity across the nodal volume and the assumed temperature profile as follows:

$$C_{eff} = {[\int C_a dV]}/{V} \quad (1)$$

Despite being more accurate than the apparent heat capacity method, this method faces the same problems as the latter, due to the discontinuity around the phase change. This problem arises mainly for materials with isothermal phase change, where temperature jumps around the change are avoided and mainly for materials with phase change, where latent heat is not taken into account,

Although this method is more efficient than the apparent heat capacity method, its calculation and implementation costs are still higher.

4.1.3. The heat source or enthalpy-porosity method

In the heat source or enthalpy-porosity method, the enthalpy term is divided into sensible and latent heats, which is considered as a heat source. The energy conservation equation thus deviates:

$$\rho C_{avg}(T)\frac{\partial T}{\partial t} = \frac{\partial}{\partial x}\left(\lambda \frac{\partial T}{\partial x}\right) - \rho L_f \frac{\partial f}{\partial t} \quad (1)$$

The phase change front is known by evaluating the liquid fraction field at each node. The value of the liquid fraction is 0 for the solid phase, 1 for the liquid phase and varies between]0 ;1[for the phase change range. It is generally approximated by the linear auxiliary function shown in the equation where $T_{solidus}$ is the highest temperature at which the material is completely solid and $T_{liquidus}$ the lowest temperature at which the material is completely liquid:

$$f(T) = \begin{cases} 0 \;\; if \;\; T < T_{solidus} \\ \dfrac{T - T_{solidus}}{T_{liquidus} - T_{solidus}} \quad if \;\; T_{solidus} \le T \le T_{liquidus} \\ 1 \;\; if \;\; T > T_{liquidus} \end{cases} \quad (1)$$

Material properties are thus written as a function of the liquid fraction to consider the transition between the two phases:

$$C_{avg} = \big(1 - f(T)\big)C_{p,sol}(T) + f(T)C_{p,liq}(T) \quad (1)$$

$$\lambda = \big(1 - f(T)\big)\lambda_{sol}(T) + f(T)\lambda_{liq}(T) \quad (1)$$

$$\rho = \big(1 - f(T)\big)\rho_{sol}(T) + f(T)\rho_{liq}(T) \quad (1)$$

The enthalpy porosity method is very intuitive, converges quickly with good accuracy and is widely used when convection plays a very important role. One of the constraints of this method is its dependence on the mesh size. Indeed, depending on the mesh size chosen, numerical diffusion may occur at the solid/liquid interface. This problem can be solved by coupling the method with advanced numerical techniques such as adaptive meshing.

4.1.4. Phase-field model

The phase-field model, mainly used to study crystal growth during solidification, consists in using an auxiliary field to characterize the phase of the medium as a function of position and time. The transition between the different phases is tracked using the values of the phase parameter, enabling, in a similar way to the enthalpy model, to obtain an intermediate zone between the different phases. The equation for the evolution of the phase parameter for a pure material is described by Equation 91 and its value is between -1 and 1 [141]. It is possible to write a modified heat transfer equation as a function of the parameter.

$$\alpha\varepsilon^2\frac{\partial\phi}{\partial t} = \varepsilon^2\frac{d^2\phi}{dx^2} - \frac{1}{2}(\phi^3 - \phi) + \frac{\varepsilon s}{2\sigma}\big(T - T_f\big)(1 - \phi^2) \quad (1)$$

α is the relaxation scale coefficient, σ [J.m^{-2}] is the surface tension, s [J.m^{-3}.K^{-1}] is the entropic density difference between the phases and ε [m] is the thickness of the solid/liquid interface.

$$\alpha\rho C_p\frac{\partial T}{\partial t} = \frac{\partial}{\partial x}\left(\lambda\frac{\partial T}{\partial x}\right) - \frac{1}{2}\rho L_f\frac{\partial\phi}{\partial t} \quad (1)$$

The relationship between the phase parameter and the liquid fraction gives the following system of equations:

$$\begin{cases}\rho C_p\dfrac{\partial T}{\partial t} = \dfrac{\partial}{\partial x}\left(\lambda\dfrac{\partial T}{\partial x}\right) - \rho L_f\dfrac{\partial f}{\partial t}\\ \dfrac{\partial f}{\partial t} = \dfrac{s}{\alpha\varepsilon\sigma}\big(T - T_f\big)f(1 - f)\end{cases} \quad (1)$$

This method has gained considerable popularity in the modeling of phase transformation and multiphase flow due to its ability to directly incorporate phase transition thermodynamics into the formulation [142].

4.2. PCMs in HAM models

PCMs can be incorporated into the entire building envelope: walls, roofs, windows and floors [143–147]. Four experimental techniques for incorporating PCMs into building envelopes are presented in the literature: direct incorporation, impregnation, encapsulation and shape-stabilized. Depending on the incorporation technique, different methods are used in the literature to numerically integrate PCMs in heat transfer models. Most of the studies in the literature concerned only the heat transfer aspect [148–153] and only few studies are reported on both heat and mass transfer aspects. Despite the literature is full of experimental characterization of the hygrothermal behavior of PCM composites ,only few of these solutions are evaluated numerically. In this section, we propose to evaluate the different studies addressing the hygrothermal numerical behavior of building materials incorporating PCMs.

The first way is to consider the PCM as a different layer of the building envelope. Therefore, the whole building wall is modelled as a multilayer material with each layer defined by its set of characteristics equations. Fraine et al [36] proposed a MPCM (Micro-encapsulated PCM)/diatomite composite as an alternative solution for the substitution of EPS (Expanded polystyrene), for adjusting indoor temperature and relative humidity. The MPCM/diatomite composite was modeled using the coupled heat and moisture transfer model of Kunzel et al. [25]. The PCM was incorporated into the porosity of the diatomite and modelled using modified heat capacity method. The effective thermal properties of the media assuming a parallel configuration are:

$$\left(\rho C_p\right)_{eff} = \rho_d C_{pd} \theta_d + \rho_{PCM} C_{pPCM} (1 - \theta_d) \quad (1)$$

Comparable outcomes were observed by Shi et al [154], where macro-encapsulated PCM was integrated into concrete walls. This integration demonstrated analogous effects in terms of enhancing temperature and humidity regulation.

Recently, Wu et al. [37] proposed a passive envelope solution that integrates a hydrocarbon-based PCM and hemp concrete to improve buildings' energy, thermal and hydric performances simultaneously. The relative humidity and temperature are chosen as driving potentials of moisture and heat transfer, respectively. The effective heat capacity model was chosen to describe the heat transfer of the PCM. Four integrated scenarios were considered and compared with a reference scenario (hemp concrete only). The performance of the integrated envelope was studied numerically based on the impact of the PCM's properties and its location in the envelope. As the PCM moves toward the interior, the energy and hygrothermal performances improve. Thus, it is recommended to place the PCM close to the interior as the total heat load, temperature amplitude and partial water vapor pressure amplitude are reduced by 8.2%, 46.3%, and 43.7%, respectively, in summer and 1.3%, 9.1%, and 8.2%, respectively, in winter, compared to the reference scenario.

Chang et al. [155] assessed the hygrothermal performance of building components, including wood frame walls made of a macro-packed PCM (MPPCM) containing noctadecane, using the WUFI PRO 5.3 program. The results showed that the hygrothermal performance of the wood-frame structures applied to the MPPCM, which replaced the use of the vapor retarder, is improved. Also, the results of analysis of mold growth risk showed that it is possible to solve the problems of mold growth risk using MPPCM.

Zhu et al [156] studied the effects of Phase Change Humidity Controlling Materials (PCHCM) wallboards on building energy consumption and indoor hygrothermal environment for Wuhan city in China, which has hot summers and cold winters. The PCM effect was integrated using the effective heat capacity method that allows the relationship between the specific heat capacity of dry materials and the temperature. The phase change temperature range was set to 1°C and Kunzel's model is used to describe the hygrothermal behavior. The simulation results based on TRNSYS showed that the PCHCM wallboard was able to both reduce energy consumption and improve indoor hygrothermal environment for the case study building significantly.

The second way is to model the PCM and hygrothermal material as a homogeneous material with unique properties. There is few works reported in the literature using this method. A novel model for analyzing the hygrothermal performance of a PCHCM in built environment is developed and validated using experimental data [157]. The model consists in a combined model of the heat and moisture transfer with phase change process using the enthalpy method and Kunzel method. The numerical results indicate that PCHCM is suitable for the areas that simultaneously manifest a wide amplitude of hygrothermal (temperature and humidity) difference.

5. Assessment of material properties

The input parameters of each model including hygrothermal and phase change models are summarized in **Table 3**. These parameters are obtained from the experimental characterization of the material properties and can classified as thermal and hydric properties. In the following, the techniques of characterization of each group of properties will be presented.

Table 3. Material hygrothermal properties and characterization techniques.

	PROPERTIES	MEASUREMENT TECHNIQUES
HYDRIC PROPERTIES	Moisture content	- Gravimetric method: cup methods, DVS - Volumetric method
	Liquid permeability	- Direct methods - Inverse techniques
	Vapor permeability	Cup method
	Moisture storage capacity ($C_m = \frac{\partial w}{\partial \varphi}$)	Retrieve from the sorption isotherm
THERMAL PROPERTIES	Thermal conductivity (λ)	Hot plate method, guarded hotbox method, hot wire method, hot Disk method, Flash method
	Heat capacity (C_p) Melting/fusion temperature Latent heat of fusion/crystallization	- DSC (dynamic and isothermal step method) - T-history method

5.1. Hydric properties

The sorption isotherm w(φ) establishes how much water a material can either absorb or release based on the relative humidity of the surrounding environment while maintaining a constant temperature. Typically, the measurement of adsorption/desorption isotherms is carried out using two distinct methods: gravimetric methods and volumetric methods [158]. The principle involves regularly monitoring the change in the apparent mass of the studied material over time at various relative humidity levels. The humidity is controlled either by salt solutions (silica gel, magnesium nitrate, barium chloride) or by designed devices using water vapor such as Dynamic Vapor Sorption (DVA) and Vapor Sorption Analyzer (VSA). At the contrary, the volumetric methods consist in measuring the change in volume of water vapor adsorbed or released by the material. By placing a sample in a controlled volume, a specific amount of water vapor is injected until the targeted pressure is reached. Once equilibrium is achieved, the volume of vapor adsorbed by the material is determined. These approaches significantly reduce the testing time but involve working with small-sized samples combined with a dynamic flow of water vapor.

The moisture storage capacity is defined as the slope of the sorption isotherm curves ($C_m = \frac{\partial w}{\partial \varphi}$). The latter is an important input parameter for coupled heat, air and moisture models. It represents the ability of the material to adsorb and release moisture when environmental moisture conditions change [8].

The general method to measure the liquid, vapor or air diffusivities and permeabilities is to expose the material to a pressure gradient (vapor pressure, liquid pressure or total pressure) and to measure to resulting flow. Each property has to be measured separately by avoiding the other pressure gradients or making them negligible. As for the sorption isotherm, this method is a steady-state method.

In the case of vapor permeability (δ_v), the most commonly used measurement technique is the cup method, which adheres to the ISO 12572, 2013 standard. This method establishes a vapor pressure gradient by maintaining a difference in relative humidity between the two sides of the sample, while keeping the temperature constant. The change in mass is measured to determine the mass flow rate. The fundamental concept behind

this method is to measure a consistent change in mass while controlling the flow of vapor, which is driven by the contrast in relative humidity between the two sides of the sample, all while maintaining a constant temperature.

Liquid water permeability (K_l) is a hygrothermal characteristic that describes the transfer of liquid water through porous materials and depends on the moisture content of the porous material. This property is assessed experimentally by measuring the liquid permeability at various moisture levels in the porous medium. Methods for determining this property can be classified into two categories: direct and inverse methods [159]. The direct method consists in applying a liquid pressure gradient between the two ends of a sample to create a flow of liquid water through the porous material. The flow rate of the water passing through the sample is then measured. The values of the flow rate and the liquid pressure gradient are subsequently used in conjunction with Darcy's law to calculate the permeability. The principle of indirectly determining liquid permeability as a function of moisture content involves inducing the transfer of liquid water through a sample (typically through imbibition or drying) and measuring the change in relative humidity within the material. This test is then modelled within a hygrothermal transfer simulation tool, which calculates the evolution of relative humidity within the porous material. Permeability is then the optimized value that minimizes the difference between the simulated and measured relative humidities.

5.2. Thermal properties

The thermal conductivity represents the ease with which heat spreads within a material based on a given temperature difference. It is one of the most important intrinsic properties on the hygrothermal behavior of a building. There are two types of measurement: steady state, where the medium is subjected to a flow that is independent of time (stationary). These include the guarded hot plate method and the guarded hotbox method, and transient measurements such as the hot wire method, the Hot Disk method, the Flash method and the shock probe method [160]. These last two methods are the most widely used.

Specific heat C_P [J.K-1.g-1], also known as mass heat capacity or mass heat, defines the amount of energy required to raise one gram of material by one degree Celsius. This property can be measured by differential scanning calorimetry (DSC), a technique that measures the heat flux absorbed or released by the sample as a function of time for a specific temperature change in a controlled atmosphere. DSC is also used to measure the melting/solidification temperatures and enthalpies that are important properties for PCMs [161–164].

For some PCMs models, it is important to know the shape of enthalpy-temperature curve with a temperature uncertainty $\delta T<1K$. The h-T curve is obtained using classical DSC under dynamic mode or isothermal step mode [137]. Due to its small sample size, DSC in general is not suitable for heterogeneous materials. For these PCMs, the T-history method can be used to determine h(T) data with sufficient precision.

6. Conclusion

The present study reviewed the hygrothermal models of PCMs integrated in building envelopes to evaluate the performances. First, the different models of HAM transfer in buildings are presented. These models have been divided in two groups: the nodal and HAM approaches.

Nodal models are suitable for steady-state analyses as well as quick assessments and are currently employed in the most common BES software, such as TRNSYS. They predominantly focus on simulating temperature variations and energy requirements in specific spaces on a larger scale. However, their moisture exchange models at the wall scale often rely on simplified approaches that do not consider the coupling of heat and moisture transfer phenomena through building envelopes. Two simplified models for surface moisture adsorption and desorption, namely the Effective Capacitance Moisture model and

the Effective Moisture Penetration Depth model, are distinguished within the nodal framework.

Unlike the nodal approach, HAM models take into account the simultaneous movement of heat, air and moisture within porous materials and offers a more comprehensive perspective on dynamic behavior and interactions. These models integrate various physical processes such as conduction, convection, capillarity and vapor diffusion. Several HAM approaches are presented in the literature. One of the key factors differentiating these models is the choice of transfer motors they take into account. Based on an extensive literature review, the different HAM models has been classified according to four driving potentials that are relative humidity, vapor pressure and moisture content. The latter being discontinuous at the interface between two materials due to their different hygroscopic properties, it is not suitable for multilayer simulations. Several validations techniques exist for these models to test their accuracy including theoretical, intermodel and experimental validations.

Alongside with hygroscopic materials, PCMs has been identified as an efficient technique to increase the thermal capacity, energy efficiency and comfort impact of buildings. There are several different approaches available for studying solid-liquid phase change. These include enthalpy-based methods, effective heat capacity methods, front tracking methods and adaptive grid methods. The enthalpy-based and heat capacity methods are the most widely used in the literature.

Consequently, it is valuable to integrate the thermal inertia of PCMs with the moisture inertia of hygroscopic materials, making it possible to improve the energy, thermal and hydric performances of the envelope simultaneously. However, when it comes to the integration of these two types of materials, most studies have focused only on their thermal and energy performances while neglecting their hydric performance. The literature is lacking of numerical methods to describe both phase change and hygroscopic behavior. It is therefore necessary to development numerical models in order to fully assess the behavior of these hybrid materials capable to control both temperature and humidity.

Author Contributions: Declaration of Competing Interest: The authors declare that they have no known competing financial interests or personal relationships that could have appeared to influence the work reported in this paper.

Acknowledgments:

Author Contributions: Conceptualization, all authors; methodology, all authors; formal analysis, all authors; investigation, all authors; resources, all authors; data curation, all authors; writing—original draft preparation, M.S.; writing—review and editing, all authors; visualization, all authors; supervision, R.B., M.D., A.H. and A.G.; project administration, R.B. and M.D.; funding acquisition, R.B., M.D. All authors read and agreed to the published version of the manuscript.

Funding: This work is carried out in the frame of Region Nouvelle Aquitaine for subsidizing BioMCP pro-ject (Project-2017-1R10209-13023) and in the frame of the Laboratory for Energy and Environ-mental Efficiency of Envelopes and Cities, 4ev Lab, the joint Laboratory between EDF R&D, CNRS, LaSIE conducting research to improve the energy and environmental performance of buildings and the quality of life of the inhabitants of urban spaces.

Data Availability Statement: We encourage all authors of articles published in MDPI journals to share their research data. In this section, please provide details regarding where data supporting reported results can be found, including links to publicly archived datasets analyzed or generated during the study. Where no new data were created, or where data is unavailable due to privacy or ethical restrictions, a statement is still required. Suggested Data Availability Statements are available in section "MDPI Research Data Policies" at https://www.mdpi.com/ethics.

Conflicts of Interest: The authors declare that they have no known competing financial interests or personal relationships that could have appeared to influence the work reported in this paper.

References

1. Liu, S.; Kwok, Y.-T.; Lau, K.; Ng, E. Applicability of Different Extreme Weather Datasets for Assessing Indoor Overheating Risks of Residential Buildings in a Subtropical High-Density City. *Building and Environment* **2021**, *194*, 107711, doi:10.1016/j.buildenv.2021.107711.
2. Xia, D.; Zhong, Z.; Huang, Y.; Zou, Y.; Lou, S.; Zhan, Q.; Guo, J.; Yang, J.; Guo, T. Impact of Coupled Heat and Moisture Transfer on Indoor Comfort and Energy Demand for Residential Buildings in Hot-Humid Regions. *Energy and Buildings* **2023**, *288*, 113029, doi:10.1016/j.enbuild.2023.113029.
3. Hamard, E.; Cazacliu, B.; RAZAKAMANANTSOA, A.; MOREL, J.C. Cob, a Vernacular Earth Construction Process in the Context of Modern Sustainable Building. *Building and Environment* **2016**, *106*, 17p, doi:10.1016/j.buildenv.2016.06.009.
4. Various Types of Earth Buildings - ScienceDirect Available online: https://www.sciencedirect.com/science/article/pii/S1877042813029704 (accessed on 31 March 2022).
5. Evans, I.; Smiley, L.; Smith, M.G. *The Hand-Sculpted House: A Philosophical and Practical Guide to Building a Cob Cottage*; Chelsea Green Publishing, 2002;
6. Ben-Alon, L.; Loftness, V.; Harries, K.A.; Hameen, E.C.; Bridges, M. INTEGRATING EARTHEN BUILDING MATERIALS AND METHODS INTO MAINSTREAM CONSTRUCTION. *Journal of Green Building* **2020**, *15*, 87–106, doi:10.3992/1943-4618.15.1.87.
7. Watson, L. The Cob Building Technique. Past, Present and Future.
8. Benmahiddine, F.; Cherif, R.; Bennai, F.; Belarbi, R.; Tahakourt, A.; Abahri, K. Effect of Flax Shives Content and Size on the Hygrothermal and Mechanical Properties of Flax Concrete. *Construction and Building Materials* **2020**, *262*, 120077, doi:10.1016/j.conbuildmat.2020.120077.
9. Delannoy, G.; Marceau, S.; Glé, P.; Gourlay, E.; Guéguen-Minerbe, M.; Diafi, D.; Nour, I.; Amziane, S.; Farcas, F. Aging of Hemp Shiv Used for Concrete. *Materials and Design* **2018**, *160*, 752–762, doi:10.1016/j.matdes.2018.10.016.
10. Seng, B.; Lorente, S.; Magniont, C. Scale Analysis of Heat and Moisture Transfer through Bio-Based Materials — Application to Hemp Concrete. *Energy and Buildings* **2017**, *155*, 546–558, doi:10.1016/j.enbuild.2017.09.026.
11. Abahri, K.; El Hachem, C.; Bennai, F.; Toan, N.; Belarbi, R. Prediction of Hemp Concrete Morphological Deformation by X-Ray Tomography.; 2017; Vol. 2017-January, pp. 616–625.
12. Recart, C.; Sturts Dossick, C. Hygrothermal Behavior of Post-Retrofit Housing: A Review of the Impacts of the Energy Efficiency Upgrade Strategies. *Energy and Buildings* **2022**, *262*, 112001, doi:10.1016/j.enbuild.2022.112001.
13. Wang, R.; Ge, H.; Baril, D. Moisture-Safe Attic Design in Extremely Cold Climate: Hygrothermal Simulations. *Building and Environment* **2020**, *182*, 107166, doi:10.1016/j.buildenv.2020.107166.
14. Bastien, D.; Winther-Gaasvig, M. Influence of Driving Rain and Vapour Diffusion on the Hygrothermal Performance of a Hygroscopic and Permeable Building Envelope. *Energy* **2018**, *164*, 288–297, doi:10.1016/j.energy.2018.07.195.
15. Liu, Y.; Wang, Y.; Wang, D.; Liu, J. Effect of Moisture Transfer on Internal Surface Temperature. *Energy and Buildings* **2013**, *60*, 83–91, doi:10.1016/j.enbuild.2013.01.019.
16. Belarbi, R.; Qin, M.; Aït-Mokhtar, A.; Nilsson, L.-O. Experimental and Theoretical Investigation of Non-Isothermal Transfer in Hygroscopic Building Materials. *Building and Environment* **2008**, *43*, 2154–2162, doi:10.1016/j.buildenv.2007.12.014.
17. Qin, M.; Aït-Mokhtar, A.; Belarbi, R. Two-Dimensional Hygrothermal Transfer in Porous Building Materials. *Applied Thermal Engineering* **2010**, *30*, 2555–2562, doi:10.1016/j.applthermaleng.2010.07.006.
18. Bennai, F.; Ferroukhi, M.Y.; Benmahiddine, F.; Belarbi, R.; Nouviaire, A. Assessment of Hygrothermal Performance of Hemp Concrete Compared to Conventional Building Materials at Overall Building Scale. *Construction and Building Materials* **2022**, *316*, 126007, doi:10.1016/j.conbuildmat.2021.126007.

19. Trabelsi, A.; Belarbi, R.; Abahri, K.; Qin, M. Assessment of Temperature Gradient Effects on Moisture Transfer through Thermogradient Coefficient. *Build. Simul.* **2012**, *5*, 107–115, doi:10.1007/s12273-012-0063-x.
20. Busser, T.; Berger, J.; Piot, A.; Pailha, M.; Woloszyn, M. Comparison of Model Numerical Predictions of Heat and Moisture Transfer in Porous Media with Experimental Observations at Material and Wall Scales: An Analysis of Recent Trends. *Drying Technology* **2019**, *37*, 1363–1395, doi:10.1080/07373937.2018.1502195.
21. Dong, W.; Chen, Y.; Bao, Y.; Fang, A. A Validation of Dynamic Hygrothermal Model with Coupled Heat and Moisture Transfer in Porous Building Materials and Envelopes. *Journal of Building Engineering* **2020**, *32*, 101484, doi:10.1016/j.jobe.2020.101484.
22. Luikov, A.V. HEAT AND MASS TRANSFER IN CAPILLARY-POROUS BODIES. In *Heat and Mass Transfer in Capillary-Porous Bodies*; Elsevier, 1966; pp. 233–303 ISBN 978-1-4832-0065-1.
23. Philip, J.R. Flow in Porous Media. *Annu. Rev. Fluid Mech.* **1970**, *2*, 177–204, doi:10.1146/annurev.fl.02.010170.001141.
24. Qin, M.; Belarbi, R.; Aït-Mokhtar, A.; Nilsson, L.-O. Coupled Heat and Moisture Transfer in Multi-Layer Building Materials. *Construction and Building Materials* **2009**, *23*, 967–975, doi:10.1016/j.conbuildmat.2008.05.015.
25. Kuenzel, Hartwig. (1995). Simultaneous heat and moisture transport in building components. One- and two-dimensional calculation using simple parameters. Fraunhofer IBP.
26. Pedersen, C.R. Prediction of Moisture Transfer in Building Constructions. *Building and Environment* **1992**, *27*, 387–397, doi:10.1016/0360-1323(92)90038-Q.
27. Janssen, H.; Carmeliet, J.; Hens, H. The Influence of Soil Moisture in the Unsaturated Zone on the Heat Loss from Buildings via the Ground. *Journal of Thermal Envelope and Building Science* **2002**, *25*, 275–298, doi:10.1177/0075424202025004683.
28. Basecq, V.; Michaux, G.; Blondeau, P.; Inard, C. Short Term Storage Systems of the Thermal Energy for Buildings: A Review. *Advances in Building Energy Research* **2013**, *7*, 66–119.
29. Ben Romdhane, S.; Amamou, A.; Ben Khalifa, R.; Saïd, N.M.; Younsi, Z.; Jemni, A. A Review on Thermal Energy Storage Using Phase Change Materials in Passive Building Applications. *Journal of Building Engineering* **2020**, *32*, 101563, doi:10.1016/j.jobe.2020.101563.
30. Lamrani, B.; Johannes, K.; Kuznik, F. Phase Change Materials Integrated into Building Walls: An Updated Review. *Renewable and Sustainable Energy Reviews* **2021**, *140*, 110751, doi:10.1016/j.rser.2021.110751.
31. Al-Rashed, A.A.A.A.; Alnaqi, A.A.; Alsarraf, J. Energy-Saving of Building Envelope Using Passive PCM Technique: A Case Study of Kuwait City Climate Conditions. *Sustainable Energy Technologies and Assessments* **2021**, *46*, 101254, doi:10.1016/j.seta.2021.101254.
32. Bohórquez-Órdenes, J.; Tapia-Calderón, A.; Vasco, D.A.; Estuardo-Flores, O.; Haddad, A.N. Methodology to Reduce Cooling Energy Consumption by Incorporating PCM Envelopes: A Case Study of a Dwelling in Chile. *Building and Environment* **2021**, *206*, 108373, doi:10.1016/j.buildenv.2021.108373.
33. Yang, Y.K.; Kang, I.S.; Chung, M.H.; Kim, S.; Park, J.C. Effect of PCM Cool Roof System on the Reduction in Urban Heat Island Phenomenon. *Building and Environment* **2017**, *122*, 411–421, doi:10.1016/j.buildenv.2017.06.015.
34. AL-Saadi, S.N.; Zhai, Z. (John) Modeling Phase Change Materials Embedded in Building Enclosure: A Review. *Renewable and Sustainable Energy Reviews* **2013**, *21*, 659–673, doi:10.1016/j.rser.2013.01.024.
35. Zeneli, M.; Nikolopoulos, A.; Karellas, S.; Nikolopoulos, N. Chapter 7 - Numerical Methods for Solid-Liquid Phase-Change Problems. In *Ultra-High Temperature Thermal Energy Storage, Transfer and Conversion*; Datas, A., Ed.; Woodhead Publishing Series in Energy; Woodhead Publishing, 2021; pp. 165–199 ISBN 978-0-12-819955-8.
36. Fraine, Y.; Seladji, C.; Aït-Mokhtar, A. Effect of Microencapsulation Phase Change Material and Diatomite Composite Filling on Hygrothermal Performance of Sintered Hollow Bricks. *Building and Environment* **2019**, *154*, 145–154, doi:10.1016/j.buildenv.2019.02.036.

37. Wu, D.; Rahim, M.; El Ganaoui, M.; Bennacer, R.; Liu, B. Multilayer Assembly of Phase Change Material and Bio-Based Concrete: A Passive Envelope to Improve the Energy and Hygrothermal Performance of Buildings. *Energy Conversion and Management* **2022**, *257*, 115454, doi:10.1016/j.enconman.2022.115454.
38. Crausse, P.; Laurent, J.P.; Perrin, B. Influence des phénomènes d'hystérésis sur les propriétés hydriques de matériaux poreux: Comparaison de deux modèles de simulation du comportement thermohydrique de parois de bâtiment. *Revue Générale de Thermique* **1996**, *35*, 95–106, doi:10.1016/S0035-3159(96)80002-X.
39. Fick, A. V. On Liquid Diffusion. *The London, Edinburgh, and Dublin Philosophical Magazine and Journal of Science* **1855**, *10*, 30–39, doi:10.1080/14786445508641925.
40. Tariku, F.; Kumaran, K.; Fazio, P. Transient Model for Coupled Heat, Air and Moisture Transfer through Multilayered Porous Media. *International Journal of Heat and Mass Transfer* **2010**, *53*, 3035–3044, doi:10.1016/j.ijheatmasstransfer.2010.03.024.
41. Hens H. Heat transfer. Build Phys - Heat, Air Moisture 2017:15–124.https://doi.org/doi:10.1002/9783433608548.ch1.
42. Fourier, J.B.J. (1822) Theorie analytique de la chaleur. Didot, Paris, 499-508.
43. Hamdaoui, M.-A.; Benzaama, M.-H.; El Mendili, Y.; Chateigner, D. A Review on Physical and Data-Driven Modeling of Buildings Hygrothermal Behavior: Models, Approaches and Simulation Tools. *Energy and Buildings* **2021**, *251*, 111343, doi:10.1016/j.enbuild.2021.111343.
44. Boyer, H.; Chabriat, J.P.; Grondin-Perez, B.; Tourrand, C.; Brau, J. Thermal Building Simulation and Computer Generation of Nodal Models. *Building and Environment* **1996**, *31*, 207–214, doi:10.1016/0360-1323(96)00001-7.
45. Welcome | TRNSYS : Transient System Simulation Tool Available online: https://www.trnsys.com/ (accessed on 8 August 2023).
46. A, K.; A, K. Theoretical and Computational Investigation of Simultaneous Heat and Moisture Transfer in Buildings: "Effective Penetration Depth" Theory. **1989**.
47. Abadie, M.; Mendes, N. Comparative Analysis of Response-Factor and Finite-Volume Based Methods for Predicting Heat and Moisture Transfer through Porous Building Materials. *Journal of Building Physics* **2006**, *30*, 7–37, doi:10.1177/1744259106064599.
48. Luikov, A.V. Heat and Mass Transfer in Capillary-Porous Bodies. In *Advances in Heat Transfer*; Elsevier, 1964; Vol. 1, pp. 123–184 ISBN 978-0-12-020001-6.
49. lrudayaraj, J.; Wu, Y. Analysis and Application OF Luikov's Heat, Mass, and Pressure Transfer Model to a Capillary Porous Media. *Drying Technology* **1996**, *14*, 803–824, doi:10.1080/07373939608917125.
50. Lewis, R.W.; Ferguson, W.J. The Effect of Temperature and Total Gas Pressure on the Moisture Content in a Capillary Porous Body. *International Journal for Numerical Methods in Engineering* **1990**, *29*, 357–369, doi:10.1002/nme.1620290210.
51. N. Mendes, I. Ridley, R. Lamberts, P. C. Philippi, and K. Budag. Umidus: A PC program for the Prediction of Heat and Mass Transfer in Porous Building Elements. In IBPSA 99, pages 277–283, Japan, 1999. International Conference on Building Performance Simulation.
52. Mendes, N.; Philippi, P.C.; Lamberts, R. A New Mathematical Method to Solve Highly Coupled Equations of Heat and Mass Transfer in Porous Media. *International Journal of Heat and Mass Transfer* **2002**, *45*, 509–518, doi:10.1016/S0017-9310(01)00172-7.
53. Whitaker, S. Simultaneous Heat, Mass, and Momentum Transfer in Porous Media: A Theory of Drying. In *Advances in Heat Transfer*; Hartnett, J.P., Irvine, T.F., Eds.; Elsevier, 1977; Vol. 13, pp. 119–203.
54. Milly, P.C.D. The Coupled Transport of Water and Heat in a Vertical Soil Column under Atmospheric Excitation. Thesis, Massachusetts Institute of Technology, 1980.
55. Abahri, K. Modélisation Des Transferts Couplés de Chaleur, d'air et d'humidité Dans Les Matériaux Poreux de Construction. These de doctorat, La Rochelle, 2012.

56. Qin, M.; Belarbi, R.; Aït-Mokhtar, A.; Seigneurin, A. An Analytical Method to Calculate the Coupled Heat and Moisture Transfer in Building Materials. *International Communications in Heat and Mass Transfer* **2006**, *33*, 39–48, doi:10.1016/j.icheatmasstransfer.2005.08.001.
57. Alioua, T.; Agoudjil, B.; Boudenne, A.; Benzarti, K. Sensitivity Analysis of Transient Heat and Moisture Transfer in a Bio-Based Date Palm Concrete Wall. *Building and Environment* **2021**, *202*, 108019, doi:10.1016/j.buildenv.2021.108019.
58. Oumeziane, Y.A. Evaluation des performances hygrothermiques d'une paroi par simulation numérique : application aux parois en béton de chanvre. phdthesis, INSA de Rennes, 2013.
59. Reuge, N.; Collet, F.; Pretot, S.; Moisette, S.; Bart, M.; Style, O.; Shea, A.; Lanos, C. Hygrothermal Effects and Moisture Kinetics in a Bio-Based Multi-Layered Wall: Experimental and Numerical Studies. *Construction and Building Materials* **2020**, *240*, 117928, doi:10.1016/j.conbuildmat.2019.117928.
60. Zirkelbach, D.; Mehra, S.-R.; Sedlbauer, K.-P.; Künzel, H.-M.; Stöckl, B. A Hygrothermal Green Roof Model to Simulate Moisture and Energy Performance of Building Components. *Energy and Buildings* **2017**, *145*, 79–91, doi:10.1016/j.enbuild.2017.04.001.
61. Krejčí, T.; Kruis, J.; Šejnoha, M.; Koudelka, T. Numerical Analysis of Coupled Heat and Moisture Transport in Masonry. *Computers & Mathematics with Applications* **2017**, *74*, 229–248, doi:10.1016/j.camwa.2017.03.022.
62. Medjelekh, D.; Ulmet, L.; Gouny, F.; Fouchal, F.; Nait-Ali, B.; Maillard, P.; Dubois, F. Characterization of the Coupled Hygrothermal Behavior of Unfired Clay Masonries: Numerical and Experimental Aspects. *Building and Environment* **2016**, *110*, 89–103, doi:10.1016/j.buildenv.2016.09.037.
63. Nespoli, L.; Janetti, M.B.; Ochs, F. Comparing Different Approaches for Moisture Transfer inside Constructions with Air Gaps. In Proceedings of the COMSOL Conference Rotterdam; 2013; Vol. 61.
64. Xu, Y.; Zeng, Z.; Sun, D. Experimental and Numerical Investigation on the Effect of Heat and Moisture Coupling Migration of Unsaturated Lateritic Clay for the Soil Thermal Storage System. *Energy and Buildings* **2022**, *276*, 112499, doi:10.1016/j.enbuild.2022.112499.
65. G. Promis, O. Douzane, A.D. Tran Le, T. Langlet,Moisture hysteresis influence on mass transfer through bio-based building materials in dynamic state, Energy and Buildings, Volume 166, 2018, Pages 450-459, ISSN 0378-7788, https://doi.org/10.1016/j.enbuild.2018.01.067.
66. Colinart, Thibaut & lelièvre, dylan & Glouannec, Patrick. (2014). Hygrothermal behavior of bio-based building materials including hysteresis effects: Experimental and numerical analyses. Energy and Buildings. 84. 10.1016/j.enbuild.2014.09.013..
67. Lelièvre, D. Simulation Numérique Des Transferts de Chaleur et d'humidité Dans Une Paroi Multicouche de Bâtiment En Matériaux Biosourcés. PhD Thesis, Lorient, 2015.
68. Janetti, M. Bianchi, Fabian Ochs, and W. Feist. "3D Simulation of Heat and Moisture Diffusion in Constructions." Comsol Conference Stuttgart. 2011.
69. Rong, L.; Yuewu, H. Heat and Moisture Transfer Characteristics of Multilayer Walls. *Energy Procedia* **2018**, *152*, 324–329, doi:10.1016/j.egypro.2018.09.142.
70. Liu, F.; Jia, B.; Chen, B.; Geng, W. Moisture Transfer in Building Envelope and Influence on Heat Transfer. *Procedia Engineering* **2017**, *205*, 3654–3661, doi:10.1016/j.proeng.2017.10.229.
71. Wang, X.; Jin, X.; Yin, Y.; Shi, X.; Zhou, X. A Transient Heat and Moisture Transfer Model for Building Materials Based on Phase Change Criterion under Isothermal and Non-Isothermal Conditions. *Energy* **2021**, *224*, 120112, doi:10.1016/j.energy.2021.120112.
72. CEN/TC 89/WG 10 - Moisture Available online: https://standards.iteh.ai/catalog/tc/cen/827dd119-af0f-4d12-a371-3d0f0008b295/cen-tc-89-wg-10 (accessed on 31 July 2023).

73. Hagentoft, Carl-Eric & Adan, Olaf & Adl-Zarrabi, Bijan & Becker, Rachel & Brocken, Harold & Carmeliet, Jan & Djebbar, Reda & Funk, Max & Grunewald, John & Hens, Hugo & Kumaran, M. & Roels, Staf & Sasic Kalagasidis, Angela & Shamir, Dina. (2004). Assessment Method of Numerical Prediction Models for Combined Heat, Air and Moisture Transfer in Building Components : Benchmarks for One-Dimensional Cases. Journal of Thermal Envelope and Building Science. 27. 10.1177/1097196304042436.
74. Janssen, H.; Blocken, B.; Carmeliet, J. Conservative Modelling of the Moisture and Heat Transfer in Building Components under Atmospheric Excitation. *International Journal of Heat and Mass Transfer* **2007**, *50*, 1128–1140, doi:10.1016/j.ijheatmasstransfer.2006.06.048.
75. Li, Q.; Rao, J.; Fazio, P. Development of HAM Tool for Building Envelope Analysis. *Building and Environment* **2009**, *44*, 1065–1073, doi:10.1016/j.buildenv.2008.07.017.
76. Fang, A.; Chen, Y.; Wu, L. Modeling and Numerical Investigation for Hygrothermal Behavior of Porous Building Envelope Subjected to the Wind Driven Rain. *Energy and Buildings* **2021**, *231*, 110572, doi:10.1016/j.enbuild.2020.110572.
77. Fang, A.; Chen, Y.; Wu, L. Transient Simulation of Coupled Heat and Moisture Transfer through Multi-Layer Walls Exposed to Future Climate in the Hot and Humid Southern China Area. *Sustainable Cities and Society* **2020**, *52*, 101812, doi:10.1016/j.scs.2019.101812.
78. Odgaard, T.; Bjarløv, S.P.; Rode, C. Influence of Hydrophobation and Deliberate Thermal Bridge on Hygrothermal Conditions of Internally Insulated Historic Solid Masonry Walls with Built-in Wood. *Energy and Buildings* **2018**, *173*, 530–546, doi:10.1016/j.enbuild.2018.05.053.
79. Remki, B.; Abahri, K.; Tahlaiti, M.; Belarbi, R. Hygrothermal Transfer in Wood Drying under the Atmospheric Pressure Gradient. *International Journal of Thermal Sciences* **2012**, *57*, 135–141, doi:10.1016/j.ijthermalsci.2012.02.005.
80. Berger, J.; Dutykh, D.; Mendes, N.; Rysbaiuly, B. A New Model for Simulating Heat, Air and Moisture Transport in Porous Building Materials. *International Journal of Heat and Mass Transfer* **2019**, *134*, 1041–1060, doi:10.1016/j.ijheatmasstransfer.2019.01.025.
81. Ayres de Mello, L.; Moura, L.M.; Mendes, N. A Model for Predicting Heat, Air and Moisture Transfer through Fibrous Materials. *International Journal of Thermal Sciences* **2019**, *145*, 106036, doi:10.1016/j.ijthermalsci.2019.106036.
82. Ayres de Mello, L.; Moura, L.M.; Mendes, N. A Model for Assessment of Heat and Moisture Transfer through Hollow Porous Buildings Elements. *Case Studies in Thermal Engineering* **2019**, *14*, 100446, doi:10.1016/j.csite.2019.100446.
83. Nagata, G.A.; Costa, T.V.; Perazzini, M.T.B.; Perazzini, H. Coupled Heat and Mass Transfer Modelling in Convective Drying of Biomass at Particle-Level: Model Validation with Experimental Data. *Renewable Energy* **2020**, *149*, 1290–1299, doi:10.1016/j.renene.2019.10.123.
84. Remki, B.; Abahri, K.; Tahlaiti, M.; Belarbi, R. Hygrothermal Transfer in Wood Drying under the Atmospheric Pressure Gradient. *International Journal of Thermal Sciences* **2012**, *57*, 135–141, doi:10.1016/j.ijthermalsci.2012.02.005.
85. Qin, M.; Belarbi, R.; Ait-Mokhtar, A.; Nilsson, L.-O. Nonisothermal Moisture Transport in Hygroscopic Building Materials: Modeling for the Determination of Moisture Transport Coefficients. *Transp Porous Med* **2008**, *72*, 255–271, doi:10.1007/s11242-007-9148-x.
86. Promis, G.; Douzane, O.; Tran Le, A.D.; Langlet, T. Moisture Hysteresis Influence on Mass Transfer through Bio-Based Building Materials in Dynamic State. *Energy and Buildings* **2018**, *166*, 450–459, doi:10.1016/j.enbuild.2018.01.067.
87. Lelievre, D.; Colinart, T.; Glouannec, P. Hygrothermal Behavior of Bio-Based Building Materials Including Hysteresis Effects: Experimental and Numerical Analyses. *Energy and Buildings* **2014**, *84*, 617–627, doi:10.1016/j.enbuild.2014.09.013.
88. Zhai, Z.; Chen, Q.; Haves, P.; Klems, J.H. On Approaches to Couple Energy Simulation and Computational Fluid Dynamics Programs. *Building and Environment* **2002**, *37*, 857–864, doi:10.1016/S0360-1323(02)00054-9.

89. Kwiatkowski, J.; Woloszyn, M.; Roux, J.-J. Influence of Sorption Isotherm Hysteresis Effect on Indoor Climate and Energy Demand for Heating. *Applied Thermal Engineering* **2011**, *31*, 1050–1057, doi:10.1016/j.applthermaleng.2010.11.030.
90. Steeman, M.; Janssens, A.; Steeman, H.-J.; Van Belleghem, M.; De Paepe, M. On Coupling 1D Non-Isothermal Heat and Mass Transfer in Porous Materials with a Multizone Building Energy Simulation Model. *Building and Environment* **2010**, *45*, 865–877.
91. Steeman, M.; Van Belleghem, M.; De Paepe, M.; Janssens, A. Experimental Validation and Sensitivity Analysis of a Coupled BES–HAM Model. *Building and Environment* **2010**, *45*, 2202–2217, doi:10.1016/j.buildenv.2010.04.003.
92. Ferroukhi, M.Y.; Djedjig, R.; Limam, K.; Belarbi, R. Hygrothermal Behavior Modeling of the Hygroscopic Envelopes of Buildings: A Dynamic Co-Simulation Approach. *Build. Simul.* **2016**, *9*, 501–512, doi:10.1007/s12273-016-0292-5.
93. Ferroukhi, M.Y.; Djedjig, R.; Belarbi, R.; Limam, K.; Abahri, K. Effect of Coupled Heat, Air and Moisture Transfers Modeling in the Wall on the Hygrothermal Behavior of Buildings. *Energy Procedia* **2015**, *78*, 2584–2589, doi:10.1016/j.egypro.2015.11.293.
94. Ferroukhi, M.Y.; Abahri, K.; Belarbi, R.; Limam, K. Integration of a Hygrothermal Transfer Model for Envelope in a Building Energy Simulation Model: Experimental Validation of a HAM–BES Co-Simulation Approach. *Heat Mass Transfer* **2017**, *53*, 1851–1861, doi:10.1007/s00231-016-1944-9.
95. Frasca, F.; Verticchio, E.; Cornaro, C.; Siani, A.M. Performance Assessment of Hygrothermal Modelling for Diagnostics and Conservation in an Italian Historical Church. *Building and Environment* **2021**, *193*, 107672, doi:10.1016/j.buildenv.2021.107672.
96. Alvarado-Alvarado, A.A.; De Bock, A.; Ysebaert, T.; Belmans, B.; Denys, S. Modeling the Hygrothermal Behavior of Green Walls in Comsol Multiphysics®: Validation against Measurements in a Climate Chamber. *Building and Environment* **2023**, *238*, 110377, doi:10.1016/j.buildenv.2023.110377.
97. Janssen, H.; Blocken, B.; Carmeliet, J. Conservative Modelling of the Moisture and Heat Transfer in Building Components under Atmospheric Excitation. *International Journal of Heat and Mass Transfer* **2007**, *50*, 1128–1140, doi:10.1016/j.ijheatmasstransfer.2006.06.048.
98. Blocken, B.; Carmeliet, J. Spatial and Temporal Distribution of Driving Rain on a Low-Rise Building. *Wind and Structures, An International Journal* **2002**, *5*, 441–462, doi:10.12989/was.2002.5.5.441.
99. Yu, S.; Liu, X.; Li, Y.; He, S.; Yao, Y.; Sun, S. Experimental and Numerical Simulation Study on Hygrothermal Migration of Damaged Envelope Walls during Wind-Driven Rain. *Building and Environment* **2023**, *243*, 110653, doi:10.1016/j.buildenv.2023.110653.
100. Judkoff, R.; Neymark, J. *International Energy Agency Building Energy Simulation Test (BESTEST) and Diagnostic Method*; National Renewable Energy Lab.(NREL), Golden, CO (United States), 1995;
101. Assessment Method of Numerical Prediction Models for Combined Heat, Air and Moisture Transfer in Building Components: Benchmarks for One-Dimensional Cases - Carl-Eric Hagentoft, Angela Sasic Kalagasidis, Bijan Adl-Zarrabi, Staf Roels, Jan Carmeliet, Hugo Hens, John Grunewald, Max Funk, Rachel Becker, Dina Shamir, Olaf Adan, Harold Brocken, Kumar Kumaran, Reda Djebbar, 2004 Available online: https://journals.sagepub.com/doi/10.1177/1097196304042436 (accessed on 31 July 2023).
102. van Schijndel, A.W.M.; Goesten, S.; Schellen, H.L. Simulating the Complete HAMSTAD Benchmark Using a Single Model Implemented in Comsol. *Energy Procedia* **2017**, *132*, 429–434, doi:10.1016/j.egypro.2017.09.651.
103. Shen, X.; Li, L.; Cui, W.; Feng, Y. Coupled Heat and Moisture Transfer in Building Material with Freezing and Thawing Process. *Journal of Building Engineering* **2018**, *20*, 609–615, doi:10.1016/j.jobe.2018.07.026.
104. Chen, G.; Luo, Q.; Guo, X.; Liu, X.; Tu, M.; He, Y. Study on Mould Germination Risk in Hydroscopic Building Wall. *Procedia Engineering* **2017**, *205*, 2712–2719, doi:10.1016/j.proeng.2017.10.193.
105. Knarud, J.I.; Geving, S. Implementation and Benchmarking of a 3D Hygrothermal Model in the COMSOL Multiphysics Software. *Energy Procedia* **2015**, *78*, 3440–3445, doi:10.1016/j.egypro.2015.12.327.

106. Wan, H.; Huang, G.; Xu, X. Development of a Moisture Transfer Calculation Method of Hygroscopic Material Plate in Buildings. *Building and Environment* **2018**, *142*, 398–413, doi:10.1016/j.buildenv.2018.06.032.
107. Korjenic, A.; Bednar, T. An Analytical Solution of a Moisture Transfer Problem for Coupled Room and Building Component. *Energy and Buildings* **2012**, *47*, 254–259, doi:10.1016/j.enbuild.2011.11.045.
108. COMSOL: Multiphysics Software for Optimizing Designs Available online: https://www.comsol.com/ (accessed on 4 August 2023).
109. Liu, X.; Chen, Y.; Ge, H.; Fazio, P.; Chen, G. Numerical Investigation for Thermal Performance of Exterior Walls of Residential Buildings with Moisture Transfer in Hot Summer and Cold Winter Zone of China. *Energy and Buildings* **2015**, *93*, 259–268, doi:10.1016/j.enbuild.2015.02.016.
110. WUFI (de).
111. Huang, Z.; Sun, Y.; Musso, F. Hygrothermal Performance Optimization on Bamboo Building Envelope in Hot-Humid Climate Region. *Construction and Building Materials* **2019**, *202*, 223–245, doi:10.1016/j.conbuildmat.2019.01.039.
112. Park, J.H.; Kang, Y.; Lee, J.; Chang, S.J.; Wi, S.; Kim, S. Development of Wood-Lime Boards as Building Materials Improving Thermal and Moisture Performance Based on Hygrothermal Behavior Evaluation. *Construction and Building Materials* **2019**, *204*, 576–585, doi:10.1016/j.conbuildmat.2019.01.139.
113. López, O.; Torres, I.; Guimarães, A.S.; Delgado, J.M.P.Q.; de Freitas, V.P. Inter-Laboratory Variability Results of Porous Building Materials Hygrothermal Properties. *Construction and Building Materials* **2017**, *156*, 412–423, doi:10.1016/j.conbuildmat.2017.08.184.
114. Sontag: Validierung Der Solverimplementierung Des... - Google Scholar Available online: https://scholar.google.com/scholar_lookup?title=Validierung%20der%20Solverimplementierung%20des%20hygrothermischen%20Simulationsprogramms%20Delphin&publication_year=2013&author=L.%20Sontag&author=A.%20Nicolai&author=S.%20Vogelsang (accessed on 4 August 2023).
115. Ruiz, M.; Masson, V.; Bonhomme, M.; Ginestet, S. Numerical Method for Solving Coupled Heat and Mass Transfer through Walls for Future Integration into an Urban Climate Model. *Building and Environment* **2023**, *231*, 110028, doi:10.1016/j.buildenv.2023.110028.
116. Gonçalves, M.; Simões, N.; Serra, C.; Flores-Colen, I. Laboratory Assessment of the Hygrothermal Performance of an External Vacuum-Insulation Composite System. *Energy and Buildings* **2022**, *254*, 111549, doi:10.1016/j.enbuild.2021.111549.
117. Pavlík, Z.; Černý, R. Experimental Assessment of Hygrothermal Performance of an Interior Thermal Insulation System Using a Laboratory Technique Simulating On-Site Conditions. *Energy and Buildings* **2008**, *40*, 673–678, doi:10.1016/j.enbuild.2007.04.019.
118. Wu, D.; Rahim, M.; El Ganaoui, M.; Bennacer, R.; Djedjig, R.; Liu, B. Dynamic Hygrothermal Behavior and Energy Performance Analysis of a Novel Multilayer Building Envelope Based on PCM and Hemp Concrete. *Construction and Building Materials* **2022**, *341*, 127739, doi:10.1016/j.conbuildmat.2022.127739.
119. Talukdar, P.; Olutmayin, S.O.; Osanyintola, O.F.; Simonson, C.J. An Experimental Data Set for Benchmarking 1-D, Transient Heat and Moisture Transfer Models of Hygroscopic Building Materials. Part I: Experimental Facility and Material Property Data. *International Journal of Heat and Mass Transfer* **2007**, *50*, 4527–4539, doi:10.1016/j.ijheatmasstransfer.2007.03.026.
120. Talukdar, P.; Olutmayin, S.O.; Osanyintola, O.F.; Simonson, C.J. An Experimental Data Set for Benchmarking 1-D, Transient Heat and Moisture Transfer Models of Hygroscopic Building Materials. Part I: Experimental Facility and Material Property Data. *International Journal of Heat and Mass Transfer* **2007**, *50*, 4527–4539, doi:10.1016/j.ijheatmasstransfer.2007.03.026.
121. Olutimayin, S.O.; Simonson, C.J. Measuring and Modeling Vapor Boundary Layer Growth during Transient Diffusion Heat and Moisture Transfer in Cellulose Insulation. *International Journal of Heat and Mass Transfer* **2005**, *48*, 3319–3330, doi:10.1016/j.ijheatmasstransfer.2005.02.024.

122. Van Belleghem, M.; Steeman, M.; Willockx, A.; Janssens, A.; De Paepe, M. Benchmark Experiments for Moisture Transfer Modelling in Air and Porous Materials. *Building and Environment* **2011**, *46*, 884–898, doi:10.1016/j.buildenv.2010.10.018.
123. Evrard, A.; De Herde, A. Hygrothermal Performance of Lime-Hemp Wall Assemblies. *Journal of Building Physics* **2010**, *34*, 5–25, doi:10.1177/1744259109355730.
124. Colinart, T.; Lelievre, D.; Glouannec, P. Experimental and Numerical Analysis of the Transient Hygrothermal Behavior of Multilayered Hemp Concrete Wall. *Energy and Buildings* **2016**, *112*, 1–11, doi:10.1016/j.enbuild.2015.11.027.
125. Boukhelf, F.; Trabelsi, A.; Belarbi, R.; Bachir Bouiadjra, M. Experimental and Numerical Modelling of Hygrothermal Transfer: Application on Building Energy Performance. *Energy and Buildings* **2022**, *254*, 111633, doi:10.1016/j.enbuild.2021.111633.
126. Belloum, R.; Agoudjil, B.; Chennouf, N.; Boudenne, A. Hygrothermal Performance Assessment of a Bio-Based Building Made with Date Palm Concrete Walls. *Building and Environment* **2022**, *223*, 109467, doi:10.1016/j.buildenv.2022.109467.
127. Chennouf, N.; Agoudjil, B.; Alioua, T.; Boudenne, A.; Benzarti, K. Experimental Investigation on Hygrothermal Performance of a Bio-Based Wall Made of Cement Mortar Filled with Date Palm Fibers. *Energy and Buildings* **2019**, *202*, 109413, doi:10.1016/j.enbuild.2019.109413.
128. Rahim, M.; Djedjig, R.; Wu, D.; Bennacer, R.; Ganaoui, M.E. Experimental Investigation of Hygrothermal Behavior of Wooden-Frame House under Real Climate Conditions. *Energy and Built Environment* **2023**, *4*, 122–129, doi:10.1016/j.enbenv.2021.09.002.
129. Xia, D.; Zhong, Z.; Huang, Y.; Zou, Y.; Lou, S.; Zhan, Q.; Guo, J.; Yang, J.; Guo, T. Impact of Coupled Heat and Moisture Transfer on Indoor Comfort and Energy Demand for Residential Buildings in Hot-Humid Regions. *Energy and Buildings* **2023**, *288*, 113029, doi:10.1016/j.enbuild.2023.113029.
130. Zhan, Q.; Pungercar, V.; Musso, F.; Ni, H.; Xiao, Y. Hygrothermal Investigation of Lightweight Steel-Framed Wall Assemblies in Hot-Humid Climates: Measurement and Simulation Validation. *Journal of Building Engineering* **2021**, *42*, 103044, doi:10.1016/j.jobe.2021.103044.
131. Friis, N.K.; Møller, E.B.; Lading, T. Hygrothermal Assessment of External Walls in Arctic Climates: Field Measurements and Simulations of a Test Facility. *Building and Environment* **2023**, *238*, 110347, doi:10.1016/j.buildenv.2023.110347.
132. Stefan: Über Einige Probleme Der Theorie Der Wärmeleitung - Google Scholar Available online: https://scholar.google.com/scholar_lookup?title=Uber%20einige%20probleme%20der%20theorie%20der%20warmeleitung&publication_year=1889&author=J.%20Stefan (accessed on 8 August 2023).
133. Alexiades, V. *Mathematical Modeling Of Melting And Freezing Processes*; CRC Press, 1992; ISBN 978-1-56032-125-5.
134. AL-Saadi, S.N.; Zhai, Z. (John) Modeling Phase Change Materials Embedded in Building Enclosure: A Review. *Renewable and Sustainable Energy Reviews* **2013**, *21*, 659–673, doi:10.1016/j.rser.2013.01.024.
135. Eyres, N.R.; Hartree, D.R.; Ingham, J.; Sarjant, R.J.; Wagstaff, J.B. The Calculation of Variable Heat Flow in Solids. *Philosophical Transactions of the Royal Society of London. Series A, Mathematical and Physical Sciences* **1946**, *240*, 1–57, doi:10.1098/rsta.1946.0002.
136. Hashemi, H.T.; Sliepcevich, C.M. A Numerical Method for Solving Two-Dimensional Problems of Heat Conduction with Change of Phase. *Chem. Eng. Prog. Symp. Series* **1967**, *63*, 34–41.
137. Günther, E.; Hiebler, S.; Mehling, H.; Redlich, R. Enthalpy of Phase Change Materials as a Function of Temperature: Required Accuracy and Suitable Measurement Methods. *Int J Thermophys* **2009**, *30*, 1257–1269, doi:10.1007/s10765-009-0641-z.
138. Bonacina, C.; Comini, G.; Fasano, A.; Primicerio, M. Numerical Solution of Phase-Change Problems. *International Journal of Heat and Mass Transfer* **1973**, *16*, 1825–1832, doi:10.1016/0017-9310(73)90202-0.
139. Morgan, K.; Lewis, R.W.; Zienkiewicz, O.C. An improved algrorithm for heat conduction problems with phase change. *International Journal for Numerical Methods in Engineering* **1978**, *12*, 1191–1195, doi:10.1002/nme.1620120710.
140. Poirier, D.; Salcudean, M. On Numerical Methods Used in Mathematical Modeling of Phase Change in Liquid Metals. *Journal of Heat Transfer* **1988**, *110*, 562–570, doi:10.1115/1.3250529.

141. Han, X.X.; Tian, Y.; Zhao, C.Y. An Effectiveness Study of Enhanced Heat Transfer in Phase Change Materials (PCMs). *International Journal of Heat and Mass Transfer* **2013**, *60*, 459–468, doi:10.1016/j.ijheatmasstransfer.2013.01.013.
142. Ghoneim, A.Y. A Smoothed Particle Hydrodynamics-Phase Field Method with Radial Basis Functions and Moving Least Squares for Meshfree Simulation of Dendritic Solidification. *Applied Mathematical Modelling* **2020**, *77*, 1704–1741, doi:10.1016/j.apm.2019.09.017.
143. Shen, Y.; Liu, S.; Zeng, C.; Zhang, Y.; Li, Y.; Han, X.; Yang, L.; Yang, X. Experimental Thermal Study of a New PCM-Concrete Thermal Storage Block (PCM-CTSB). *Construction and Building Materials* **2021**, *293*, 123540, doi:10.1016/j.conbuildmat.2021.123540.
144. Dehmous, M.; Franquet, E.; Lamrous, N. Mechanical and Thermal Characterizations of Various Thermal Energy Storage Concretes Including Low-Cost Bio-Sourced PCM. *Energy and Buildings* **2021**, *241*, 110878, doi:10.1016/j.enbuild.2021.110878.
145. Jia, C.; Geng, X.; Liu, F.; Gao, Y. Thermal Behavior Improvement of Hollow Sintered Bricks Integrated with Both Thermal Insulation Material (TIM) and Phase-Change Material (PCM). *Case Studies in Thermal Engineering* **2021**, *25*, 100938, doi:10.1016/j.csite.2021.100938.
146. Hamidi, Y.; Aketouane, Z.; Malha, M.; Bruneau, D.; Bah, A.; Goiffon, R. Integrating PCM into Hollow Brick Walls: Toward Energy Conservation in Mediterranean Regions. *Energy and Buildings* **2021**, *248*, 111214, doi:10.1016/j.enbuild.2021.111214.
147. Li, M.; Cao, Q.; Pan, H.; Wang, X.; Lin, Z. Effect of Melting Point on Thermodynamics of Thin PCM Reinforced Residential Frame Walls in Different Climate Zones. *Applied Thermal Engineering* **2021**, *188*, 116615, doi:10.1016/j.applthermaleng.2021.116615.
148. Frazzica, A.; Brancato, V.; Palomba, V.; La Rosa, D.; Grungo, F.; Calabrese, L.; Proverbio, E. Thermal Performance of Hybrid Cement Mortar-PCMs for Warm Climates Application. *Solar Energy Materials and Solar Cells* **2019**, *193*, 270–280, doi:10.1016/j.solmat.2019.01.022.
149. Zhou, D.; Shire, G.S.F.; Tian, Y. Parametric Analysis of Influencing Factors in Phase Change Material Wallboard (PCMW). *Applied Energy* **2014**, *119*, 33–42, doi:10.1016/j.apenergy.2013.12.059.
150. Thiele, A.M.; Sant, G.; Pilon, L. Diurnal Thermal Analysis of Microencapsulated PCM-Concrete Composite Walls. *Energy Conversion and Management* **2015**, *93*, 215–227, doi:10.1016/j.enconman.2014.12.078.
151. Jia, J.; Liu, B.; Ma, L.; Wang, H.; Li, D.; Wang, Y. Energy Saving Performance Optimization and Regional Adaptability of Prefabricated Buildings with PCM in Different Climates. *Case Studies in Thermal Engineering* **2021**, *26*, 101164, doi:10.1016/j.csite.2021.101164.
152. Al-Absi, Z.A.; Mohd Isa, M.H.; Ismail, M. Phase Change Materials (PCMs) and Their Optimum Position in Building Walls. *Sustainability* **2020**, *12*, 1294, doi:10.3390/su12041294.
153. Wi, S.; Chang, S.J.; Kim, S. Improvement of Thermal Inertia Effect in Buildings Using Shape Stabilized PCM Wallboard Based on the Enthalpy-Temperature Function. *Sustainable Cities and Society* **2020**, *56*, 102067, doi:10.1016/j.scs.2020.102067.
154. Shi, X.; Memon, S.A.; Tang, W.; Cui, H.; Xing, F. Experimental Assessment of Position of Macro Encapsulated Phase Change Material in Concrete Walls on Indoor Temperatures and Humidity Levels. *Energy and Buildings* **2014**, *71*, 80–87, doi:10.1016/j.enbuild.2013.12.001.
155. Chang, S.J.; Kang, Y.; Wi, S.; Jeong, S.-G.; Kim, S. Hygrothermal Performance Improvement of the Korean Wood Frame Walls Using Macro-Packed Phase Change Materials (MPPCM). *Applied Thermal Engineering* **2017**, *114*, 457–465, doi:10.1016/j.applthermaleng.2016.11.188.
156. Zhu, N.; Li, X.; Hu, P.; Lei, F.; Wei, S.; Wang, W. An Exploration on the Performance of Using Phase Change Humidity Control Material Wallboards in Office Buildings. *Energy* **2022**, *239*, 122433, doi:10.1016/j.energy.2021.122433.
157. Wu, Z.; Qin, M.; Zhang, M. Phase Change Humidity Control Material and Its Impact on Building Energy Consumption. *Energy and Buildings* **2018**, *174*, 254–261, doi:10.1016/j.enbuild.2018.06.036.

158. Benmahiddine, F. Études des transferts couplés de chaleur, d'air et d'humidité par des techniques de changement d'échelle (microscopique-macroscopique) : Application à l'évaluation de la performance énergétique et la durabilité des matériaux de construction. phdthesis, Université de La Rochelle ; Université Abderrahmane Mira - Bejaïa (Bejaïa, Algérie), 2020.
159. Oubrahim, I. Fiabilisation des approches théoriques pour la caractérisation des matériaux et la modélisation hygrothermique des enveloppes du bâtiment.
160. Kaemmerlen, A. Transfert de Chaleur à Travers Les Isolants Thermiques Du Bâtiment. thesis, Nancy 1, 2009.
161. Sawadogo, M.; Godin, A.; Duquesne, M.; Lacroix, E.; Veillère, A.; Hamami, A.E.A.; Belarbi, R. Investigation of Eco-Friendly and Economic Shape-Stabilized Composites for Building Walls and Thermal Comfort. *Building and Environment* **2023**, *231*, 110026, doi:10.1016/j.buildenv.2023.110026.
162. Sawadogo, M.; Benmahiddine, F.; Hamami, A.E.A.; Belarbi, R.; Godin, A.; Duquesne, M. Investigation of a Novel Bio-Based Phase Change Material Hemp Concrete for Passive Energy Storage in Buildings. *Applied Thermal Engineering* **2022**, *212*, 118620, doi:10.1016/j.applthermaleng.2022.118620.
163. Duquesne, M.; Mailhé, C.; Doppiu, S.; Dauvergne, J.-L.; Santos-Moreno, S.; Godin, A.; Fleury, G.; Rouault, F.; Palomo del Barrio, E. Characterization of Fatty Acids as Biobased Organic Materials for Latent Heat Storage. *Materials* **2021**, *14*, 4707, doi:10.3390/ma14164707.
164. Mailhé, C.; Duquesne, M.; Palomo del Barrio, E.; Azaiez, M.; Achchaq, F. Phase Diagrams of Fatty Acids as Biosourced Phase Change Materials for Thermal Energy Storage. *Applied Sciences* **2019**, *9*, 1067, doi:10.3390/app9061067.

Disclaimer/Publisher's Note: The statements, opinions and data contained in all publications are solely those of the individual author(s) and contributor(s) and not of MDPI and/or the editor(s). MDPI and/or the editor(s) disclaim responsibility for any injury to people or property resulting from any ideas, methods, instructions or products referred to in the content.

Article 3

Building and Environment 231 (2023) 110026

Contents lists available at ScienceDirect

Building and Environment

journal homepage: www.elsevier.com/locate/buildenv

Investigation of eco-friendly and economic shape-stabilized composites for building walls and thermal comfort

Mohamed Sawadogo [a,b,*], Alexandre Godin [a,c], Marie Duquesne [a], Elodie Lacroix [d], Amélie Veillère [e], Ameur El Amine Hamami [a], Rafik Belarbi [a,f]

[a] La Rochelle Université, LaSIE UMR CNRS 7356, Avenue Michel Crépeau, CEDEX 1, 17042, La Rochelle, France
[b] Université de Bordeaux, Bordeaux INP, CNRS, I2M, Bâtiment A11, 351 cours de la Libération, 33400, Talence, France
[c] 4ev Lab, EDF R&D, CNRS, LaSIE, La Rochelle University, Avenue Michel Crépeau, CEDEX 1, 17042, La Rochelle, France
[d] Bordeaux INP, ENSCBP, 6 avenue Pey Berland, 33600, Pessac, France
[e] CNRS, Université de Bordeaux, Bordeaux INP, ICMCB, UMR 5026, 33600, Pessac, France
[f] Canadian University Dubaï, city walk Dubaï, UAE

A B S T R A C T

The objective of this study is to investigate the potential of natural fibers as support materials for PCMs for buildings application using shape-stabilization. The material selection software Ansys Granta has allowed a preliminary selection of four natural fibers (fir fibers, hemp fibers, hemp shives and flax mulch) based on physical, thermal, geographical and economic criteria. The candidates fibers are impregnated with capric acid and lauric acid and their performances are compared, allowing the selection of the fiber with the highest impregnation rate. Hemp shives with maximum impregnation rate of about 50 wt% with LA and a good thermal stability under 150 °C has shown the best performances and has been selected as support material. Afterwards, it has been impregnated with 5 different pure fatty acids and 7 eutectic mixtures in order to identify the best composite. Most of the composites developed have latent heat higher than 50 J g^{-1}, which is very promising for energy storage in buildings application. Taking into account the thermal requirements, which are high latent heat, low undercooling and temperature of fusion ranging from 15 to 45 °C, lauric acid hemp shives composites has been selected as potential materials for buildings application with promising performances (enthalpy of fusion of 79.31 J g^{-1} at 50 wt% of impregnation rate).

1. Introduction

Building is one of the most energy-intensive sector in the world, accounting for 40% of the total energy consumption and 33% of greenhouse gas emissions [1]. A large part of the energy demand in buildings is used to prevent temperature changes in the indoor space, or to regulate the thermal conditions of the indoor space within the comfort range. In order to reduce the environmental impact of buildings, a new regulation for buildings namely RE2020 in replacement of the RT2012 has been set by the French government [2]. The RE2020 has three main objectives: to prioritize energy sobriety and decarbonization; to reduce the carbon impact of building construction; to guarantee the comfort in hot weather, as heat waves are expected to become increasingly frequent.

Latent heat thermal energy storage (LHTES) is an efficient technique to increase the thermal capacity, energy efficiency and comfort impact of buildings due to the integration of phase change materials (PCMs) [3–8] and could contribute to the previous objectives. Shape-stabilized PCMs are presented as a promising technique to incorporate PCMs in buildings envelopes [9,10]. This technique consists in impregnating a porous support with a PCM in order to stabilize the PCM and limit the risk of leakage. The shape-stabilization technique is simple, inexpensive, possesses high impregnation rates compared to other techniques and is compatible with a wide variety of support materials including polymers, porous materials and nanomaterials. These shape-stabilized composites would ensure insulation like the conventional insulating construction materials but would also contribute to keep indoor temperature for thermal comfort.

Depending on the building user, the comfort temperature may be different (currently ranging from 18 to 25 °C according to the relative humidity, sunlight etc.). The composites considered in this study should be integrated into an insulating wall, itself in building envelopes. The latters, having low conductivities, are unfavorable to thermal transfers. In addition, thermal losses can occur in building walls. Thus, we have

* Corresponding author. La Rochelle Université, LaSIE UMR CNRS 7356, Avenue Michel Crépeau, CEDEX 1, 17042, La Rochelle, France.
E-mail addresses: mohamed.sawadogo@univ-lr.fr (M. Sawadogo), alexandregodin1@hotmail.com (A. Godin), marie.duquesne@univ-lr.fr (M. Duquesne), elacroix002@enscbp.fr (E. Lacroix), amelie.veillere@icmcb.cnrs.fr (A. Veillère), ameur_el_amine.hamami@univ-lr.fr (A.E.A. Hamami), rafik.belarbi@univ-lr.fr (R. Belarbi).

https://doi.org/10.1016/j.buildenv.2023.110026
Received 10 October 2022; Received in revised form 13 December 2022; Accepted 16 January 2023
Available online 18 January 2023
0360-1323/© 2023 Elsevier Ltd. All rights reserved.

voluntarily increased the maximum melting temperature of the PCMs that will be integrated in these walls to overcome these drawbacks (PCMs melting temperature should therefore be between 15 °C and 45 °C).

Renewable materials, such as natural fibers, are considered as promising carbon sequestration resources with beneficial effects on the planet's ecosystems, living environment and energy efficiency [11–13]. In addition, their porous structure is suitable for shape-stabilization. They are also compatible with the construction materials and several formulation of concrete has been proposed in the literature [14–17]. Ma et al. [18] impregnated capric-palmitic acid (CA-PA) eutectic mixture in delignified wood to create a form stable PCM using vacuum impregnation method with an impregnation rate of 61.2 wt% without leakage. The composite presented high thermal stability and reliability, a phase transition temperature of 23.4 °C and a high latent heat of 94.4 J g^{-1}. Sheng et al. [19] fabricated a composite PCMs as-supported by carbon fiber bundles by a simple vacuum impregnation. The porous and honeycomb-shaped carbon fibers were prepared by the direct carbonization of biomass sisal fibers and impregnated with a petroleum derivative (paraffin) with two fusion (25 °C and 60 °C) and solidification pics (25 °C and 57.6 °C). The composite PCMs showed very high latent heat (192.2 J g^{-1} at a carbon ratio of 12.8 wt%), good shape stability, favourable thermal reliability and cyclability.

Despite the mentioned studies, natural fibers PCM composites especially fatty acids and their eutectic mixtures have been poorly studied considering the wide variety of natural fibers. A literature review conducted by Sawadogo et al. [20] has allowed the establishment of a list of potential candidates for shape-stabilization (Table 1). The novelty of this study is an extensive investigation and the fabrication of eco-friendly and economic shape-stabilized PCMs, impregnated within natural fibers, for building application.

To achieve that, a first investigation using Ansys Granta, a material selection software, with selection criteria such as availability, cost and renewable nature has allowed the identification of four natural fibers as potential candidates for shape-stabilization: fir fibers, hemp fibers, hemp shives and flax mulch. In addition, these fibers fulfil physical requirements such as high water absorbency, porous structure and low thermal conductivity. In fact, the low thermal conductivity will allow a continuous release of heat from the PCMs over a long period whereas high water absorbency and porous structure would ensure good impregnation rate. The impregnation technique depends on several criteria such as the residence time and the condition of the impregnation (under vacuum or atmospheric pressure). For this reason, a preliminary study has been conducted with hemp shives impregnated with capric acid in order to establish a suitable experimental protocol for this study. Afterwards, the natural fibers selected as potential candidates are impregnated with capric acid and lauric acid following the experimental protocol set up and their performances are compared allowing the selection of an adequate natural support material. The criteria of comparison are impregnation rate and mass degradation. After this first step, hemp shives showed the best results and has been selected as support material. The second step of the study is dedicated to the selection of the PCM for the fabrication of the final composite. Therefore, hemp shives have been impregnated with 5 pure fatty acids and 7 eutectic mixtures. The resulting hemp shives/PCM composites are compared in terms of impregnation rate, energy storage capacity and temperature of fusion in order to select the best composite for buildings walls.

Table 1
Natural fibers as potential candidate support materials for the fabrication of shape-stabilized PCMs.

Natural fibers	**Density ($kg.m^{-3}$)**	**Thermal conductivity ($W.m^{-1}.K^{-1}$)**	**Cost (€/kg)**	References
Bamboo fibers	431–538	0.077–0.088	–	[21]
Hemp fibers	25–100	0.040–0.049	2–5	[22]
Flax fibers	20–100	0.035–0.045	5–25	[22]
Cotton stalk fibers	150–450	0.058–0.082	–	[23]
Hemp shives	100–140	0.080–0.012	0.8–1	[24]
Kapok	17	0.030–0.049	–	[25–27]
Coco fibers	40–90	0.050–0.058	63	[28]

2. Preliminary selection of the materials

Two series of experiments are carried out successively: the first one aims at selecting the support material, thus several types of fibers are investigated, the second one aims at selecting the PCM to impregnate the fiber retained after the first experimental series.

2.1. Selection of the fibers

The material selection software Ansys Granta has been used for the selection of the natural fibers. Ansys Granta is a material selection software based on a set of criteria such as physical-chemical, thermo-mechanical and environmental properties, manufacturing processes and raw material costs. The large number of materials available in its huge database is an important feature in the selection process. In this study, the natural fibers are selected based on physical, thermal, economic and geographical criteria of several families of materials. The materials are selected based on four criteria: i. bio-based, ii. produced in European continent, iii. with high water absorption and porous structure to obtain good impregnation rate and moisture regulation capability and iv. with low thermal conductivity to replace converenntional insulation in building walls.

The material category "natural fibers" in Ansys Granta allowed the accomplishment of the first selection criterion. The natural fibers within the database of the software and their location are presented in Fig. 1 (see the geographical origins of all the fibers selected in red and green in Fig. 1). The second criterion lead to the elimination of the majority of the natural fibers in the software (see red color in Fig. 1). At this stage, only hemp fibers, hemp shives, flax mulch and fir pellets are satisfying the first two criteria.

The water absorbency of the selected fibers are presented in Table 2. All the selected fibers possessed a water absorbency higher than 200 wt % meaning that they can absorb more water than twice the weight of the dry fibers making them suitable for the impregnation process with expected high impregnation rates with fatty acids. The microporosity and the pores diameters of the fibers are also indicators of the absorption capacity of a material and necessary to make the composite, so that the fibers encapsulate the PCM and prevent its leakage during fusion. Scanning electron microscopy (SEM) images of flax mulch and hemp shives in the literature justify their use in PCM impregnation process [29] due to their very porous structure. Indeed, the pores diameters of hemp shives are between 15 and 40 μm and those of flax mulch between 5 and 20 μm. For fir pellets and hemp fibers, there are no information on their microstructure in the literature.

Finally, in view of application of the composite in a building wall concrete, fibers with low thermal conductivity are sought. This would allow a continuous release of heat from the PCMs over a long period. On the other hand, the fibers should not be completely insulating, otherwise they would not transmit the heat generated by the solidification of the PCM. The thermal conductivity of each material was therefore checked and presented in Table 2. As it can be seen, all the natural fibers can be considered as insulators with thermal conductivity in the range 0.04–0.14 W m^{-1} K^{-1}. Therefore, all four materials are selected for this study (Fig. 2).

The selected fibers are impregnated with two pure fatty acids, capric acid and lauric acid, in order to compare the impregnation rate, an important criterion in the selection of the support material. The two fatty acids are chosen because their temperatures of fusion fit the

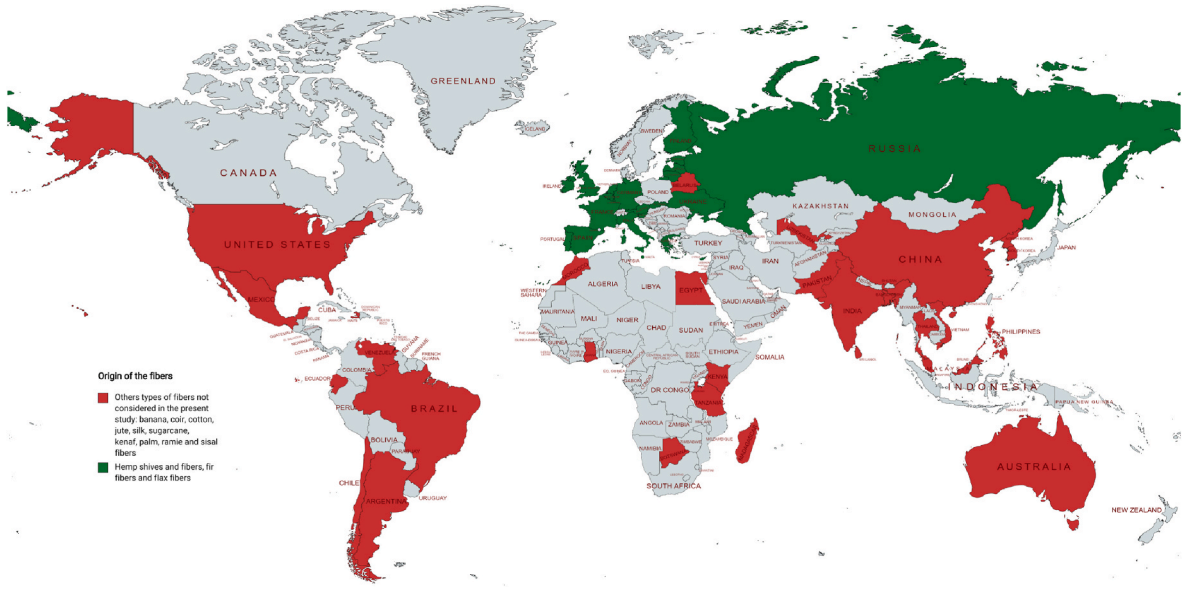

Fig. 1. Type of fibers and their origin provided by Ansys Granta Software.

Table 2
Properties, origin and cost of the selected fibers for this study.

	Fir pellets	Hemp fibers	Hemp shives	Flax mulch
Water absorbency (wt%)	200[a]	230 [29]	300-400 [30]	300[a]
Density (kg. m^{-3})	250	50	100	80
Thermal conductivity (W.m^{-1}.K^{-1})	0.14	0.05	0.11	0.04
Origin	Denmark, France, Belgium, Germany, UK	France, Hungary, Italy, Russia, Ukraine	France, Hungary, Italy, Russia, Ukraine	Belgium, France, Russia, UK

[a] Datas from Ansys Granta.

thermal requirements for thermal comfort temperature. Next, the fibers with the best impregnation rates will undergo a mass degradation assessment to ensure that they do not suffer from any degradation within the temperature range of the buildings.

2.2. Selection of the PCM

After the selection of the best support materials, the panel of PCMs has been extended in order to select the best composite (natural fiber and PCM). Fatty acids such as capric acid (CA), lauric acid (LA), myristic acid (MA), palmitic acid (PA) and stearic acid (SA) have been extensively studied in recent years and their potential in passive latent heat storage systems was demonstrated [18,31–33]. Therefore, in addition with CA and LA already considered in the first part, MA, PA and SA has been added to the list of potential PCM of interest. General information of the pure fatty acids are presented in Table 3. However, among the fatty acids, only few possess a temperature of fusion in the aimed temperature range (15–45 °C, Table 4). This condition is necessary to ensure efficient and rapid passive charge and discharge of the PCM in a diurnal cycle. Fortunately, it is possible to tune the temperature of fusion of the PCMs to meet this climatic requirement by fabricating eutectics mixtures. Fatty acid eutectic mixture is a composition of two or more fatty acids with eutectic mass ratio [34], each of which melts and solidifies at

Table 3
General information about the studied pure PCMs.

PCMs	Acronym	CAS Number	Formula	Supplier	Purity*
Capric acid	CA	334-48-5	$C_{10}H_{20}O_2$	Sigma aldrich	99 wt%
Lauric acid	LA	143-07-7	$C_{12}H_{24}O_2$	Sigma aldrich	≥98 wt %
Myristic acid	MA	544-63-8	$C_{14}H_{28}O_2$	Sigma aldrich	99 wt%
Palmitic acid	PA	57-10-3	$C_{16}H_{32}O_2$	Sigma aldrich	99 wt%
Stearic acid	SA	57-11-4	$C_{18}H_{36}O_2$	Sigma aldrich	99 wt%

Table 4
Thermal conductivity and temperature of fusion of pure fatty acids acids [33].

Acronym	Fusion Temperature (°C)	Thermal Conductivity (W.m^{-1}.K^{-1})
CA	29.6–33.2	0.21
LA	41–45.3	0.15–0.37
MA	49–56.1	0.17–0.39
PA	58.9–64	0.3
SA	53.8–70.8	0.159–0.35

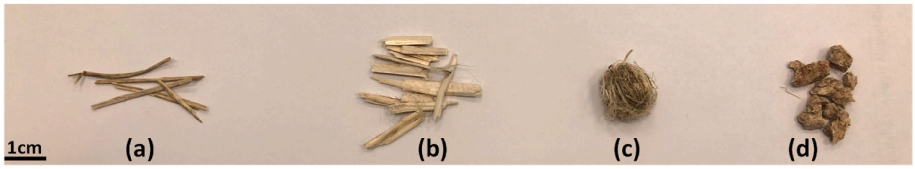

Fig. 2. Natural fibers considered in the study: flax mulch (a), hemp shives (b), hemp fibers (c) and fir pellets (d).

the same eutectic temperature, being always inferior to the temperature of fusion of the pure PCMs constituting the mixture [35,36]. Fatty acid mixture with eutectic mass ratio has the lowest temperature of fusion and the best thermal reliability compared to the other mixtures combined by the same fatty acids with different proportions.

Therefore, six eutectic mixtures made of a combination of the aforementioned pure fatty acids have been fabricated. The eutectic mixtures of the fatty acids, their mass composition and temperature of fusion are gathered in Table 5. As can be seen, the temperature of fusion of all the selected eutectic mixtures falls in the thermal comfort temperature range.

3. Experimental protocol

3.1. Techniques of characterization

3.1.1. Scanning electron microscopy (SEM)

The characterization of the morphology and microstructure of the samples is essential to understand the impregnation mechanism. The microstructure of hemp shives and hemp shives/CA composites was successively observed by scanning electron microscope (SEM) (QUANTA 200 environmental field effect gun, FEI, FRANCE) in environmental mode. This mode avoids any preliminary treatment of the samples and is very adapted to non-conductive samples such as hemp shives. The observations were performed at low pressure (typically 2 mbar), a voltage of 15 KV.

3.1.2. Differential scanning calorimetry (DSC) and Thermogravimetry analysis (TGA)

A DSC3+/TGA differential scanning calorimeter/thermogravimetric analyser device provided by METTLER TOLEDO is used to measure the heat flow released by the materials tested as well as the mass change during the tests. TGA is performed to verify the mass degradation and the thermal stability of the composite-PCM in the building application's temperature range.

The DSC allows the estimation of the fusion/solidification temperatures and enthalpies of the different samples: PCMs and PCMs/natural fibers composites. The DSC was calibrated using four calibration standards (gold, zinc, aluminium and indium) to ensure precise certainty on the temperature range considered. The purity of all the calibration standards is about 99.999 wt%. Prior to the measurements, a blank run is performed to correct the baseline. The measurements are performed over a cycle with a heating/cooling rate of 0.5 °C.min^{-1} in a range of temperatures from 10 to 80 °C (superior to the highest temperature of fusion of the sample) for the heating phase, and from 80 to 10 °C for the cooling phase. The low heating/cooling rate is selected in order to avoid thermal gradient inside the sample and because of the insulating behaviour of the fibers that may cause a slow down of the heat transfer.

Table 5
Fatty acids eutectic mixtures.

Eutectic mixture	Acronym	Mass composition (wt%)	**Temperature of fusion (°C)**
Capric acid-lauric acid	CA-LA	73–27	21.7
Capric acid-myristic acid	CA-MA	83–17	24.1
Capric acid-stearic acid	CA-SA	91–9	26.0
Capric acid-palmitic acid	CA-PA	88–12	26.1
Lauric acid-myristic acid	LA-MA	73–27	33.6
Lauric acid-palmitic acid	LA-PA	79–21	34.6
Lauric acid-stearic acid	LA-SA	87–13	40.2

For the same reasons, the isothermal steps are hold for 15 min to reach an eliquibrium. For each sample (PCMs and natural fibers), a mass between 10 and 20 mg are weighed and placed in 70 μL alumina crucibles. The experiment was carried out by purging the sample cell with Argon at a flow rate of 25 mL min^{-1}. The integrated software of METTLER TOLEDO is used to calculate the latent heats of fusion and solidification by numerical integration of the area under the peaks that represent the solid-liquid and the liquid-solid phase transitions. The onset temperature is chosen as temperature of fusion for the fusion peak whereas the endset is selected as solidification temperature for the solidification peak. These two values are chosen because they are not influenced by the heating rate unlike the peak temperature. The maximum uncertainty for the enthalpy calculation is 15% and 1.5 °C for the temperature. In addition, for all measurements (DSC and TGA), the tests are repeated three times for each sample to verify repeatability and reproducibility.

The thermogravimetric analysis (TGA) is performed with the same device. TGA allows analyzing the mass degradation of the composite in the building temperature's range by quantifying the mass variation of the material according to the temperature. CA, hemp shives only and hemp shives/CA composites samples are analyzed in a temperature range of 25–500 °C with a heating rate of 10 °C.min^{-1}.

The thermal cycling test is conducted only on the hemp shives/CA samples. The vacuum and non-vacuum impregnation techniques are compared in terms of stability over 50 cycles between the temperature range 20–70 °C.

3.2. Impregnation process

The impregnation process is used to fabricate the natural fiber/PCM composites. First, the selected natural fibers are weighed (m_1) and mixed with PCM. The precision (Δm) of the balance is about 10^{-4} g. The mixture is placed in an oven at 10 °C above the highest temperature of fusion of all the PCMs (80 °C). The molten PCM is absorbed into the pores of the natural fibers by mean of capillary and surface tension forces [31]. The amount of liquid PCM is chosen to recover the fibers to ensure effective impregnation. The weight ratio depends on the nature of the fibers but in general, a ratio was 1:10 chosen for the majority of fibers. After impregnation, the excess liquid PCM was removed by filtration. The impregnated natural fibers were placed on a filter paper and kept in the oven at 80 °C to remove the PCM on the surface of the fibers. The filter paper is changed continuously until no leakage is observed (after 3 days). The final mass of the composite (m_2) is weighed and the mass ratio of PCM in the composite is calculated using equation (1). The uncertainty (ΔR) on the mass ratio is calculated by the error propagation law (equation (2)).

$$R = \frac{m_2 - m_1}{m_2} * 100 \quad (1)$$

$$\frac{\Delta R}{R} = \left(\frac{2}{m_2 - m_1} + \frac{1}{m_2}\right) * \Delta m \quad (2)$$

The impregnation process depends on several criteria such as the residence time and the conditions of the impregnation (under vacuum or atmospheric pressure). Jeong et al. [37] analyzed the impregnation rate of a PCM in vacuum and non-vacuum processing and found that the impregnation rate was close to 50 wt% in the vacuum treatment compared to only 30 wt% in the non-vacuum conditions.

3.2.1. Vacuum vs non-vacuum impregnation

To establish the experimental protocol, first the vacuum and non-vacuum impregnation techniques are compared. The vacuum level is set at 100 mbar [38] in order to remove the air inside the fibers and enabled the liquid PCMs to diffuse into the fibers. The impregnation is governed by the capillary force and therefore, the vacuum level depends on the surface tension, the radius and the wettability of the fiber [39]. For this first study, we selected hemp shives as support material and CA

as PCM to set the adequate operating conditions for the impregnation process. The two impregnation modes are compared in terms of long-term stability over thermal cycling (DSC). In fact, the composite should store and release energy over a long period without any leakage or decrease in thermal performances. The thermal cycling test is important to evaluate the long-term stability of the PCM composite. This test investigates the thermal reliability of the bio-composite PCM after several repetitive phase change cycles. The samples obtained by the two methods are thermally cycled over 50 cycles in a temperature range between 20 and 70 °C (Fig. 3).

When the impregnation is performed at atmospheric pressure, the PCM is not absorbed inside the nanopores. Therefore, there is leakage during the heating phase, affecting thermal properties (phase change temperatures and enthalpies). The thermograms obtained in DSC with hemp shives/CA composites impregnated under vacuum show a quasi-perfect superposition of the 50 cycles that allows visualizing their stability under cycles. The final protocol had to consider this result and all other composites were vacuum impregnated.

This proves that the composite reacts in the same way to all the cycles, so it does not degrade with cycling, and there does not seem to be any leakage of the PCM from the fibers. All the thermograms obtained for the remaining composites show similar quasi-perfect superpositions.

3.2.2. Residence time

The residence time is one of the factors that influences the impregnation rate of PCMs in a support material. In this part, the effect of residence time on the impregnation rate of CA within hemp shives has been investigated. The hemp shives are impregnated with CA and filtered after 1, 4, 5, 6, 7 and 10 days. The impregnation rate at each time is measured and presented in Fig. 4. After 1 day, the impregnation rate was 30 wt% and increased by 50 wt% after 5 days to reach a value of 48 wt%. After 5 days, the impregnation rate does not increase a lot and a plateau of about 50 wt% is reached. At the end of the 10 days, the maximum impregnation rate was 53 wt%. Since the impregnation rate increased only by less than 10 wt% between day 5 and day 10, it can be stated that an impregnation rate of 5 days is a good compromise.

Based on the preliminary study, all the remaining tests are conducted under vacuum with a residence time of 5 days.

In order to ensure the effectiveness of the impregnation process, the impregnated hemp shives/CA has been observed by SEM. The cross section images of hemp shives/CA composite obtained by SEM is presented in Fig. 5. The interior of the pores is more visible in the cross-section of the fiber, which allows the observation of PCM in hemp shives. From the SEM observations, we observe that CA successfully occupies the pores of the hemp shives after the impregnation process. The experimental protocol is thus validated and applied for all subsequent investigated composites made of natural fibers and bio-based PCMs.

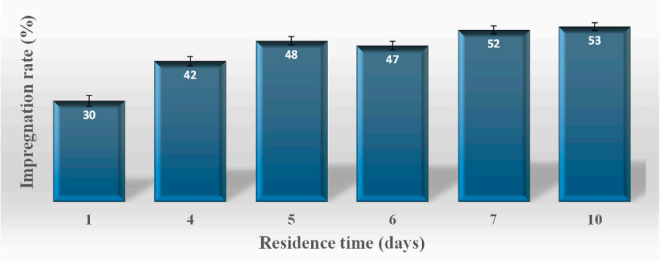

Fig. 4. Impregnation rate of hemp shives in CA as a function of time.

4. Results and selection of PCMs natural fibers composites

4.1. Selection of the support material

4.1.1. Impregnation rate

The impregnation rate of capric acid and lauric acid in the selected natural fibers are presented in Table 6. The best impregnation rates are obtained for hemp shives and flax mulch with a maximum of 50 wt% and 51 wt% respectively for hemp shives/LA and flax mulch/CA whereas the impregnation rate for hemp fibers and fir is much lower (about 8 wt%). This is explained by the microstructure of the material [40]. In fact, the porosity of materials such as hemp shives is very large and allows then better impregnation compared to fibers with relatively poor porosity, pore size and density. This porosity affects the absorption capacity of the material. This is consistent with the absorption capacity values of about 200 wt%, 300 wt% and 400 wt% for fir, flax mulch and hemp shives respectively given in Table 2. Based on these results, hemp fibers and fir are eliminated from the list of potential natural support materials impregnation rate. The rest of the study is conducted for the two remaining materials: hemp shives and flax mulch.

4.1.2. Mass degradation

The results of the TGA performed for hemp shives and flax mulch are presented in Fig. 6. The mass degradation of the pure fatty acids (CA and LA) are also illustrated in order to allow comparison. The degradation of CA started at 150 °C against 200 °C for LA. The mass degradation curve of the hemp shives and flax mulch are almost similar. The degradation of flax much occurs between 200 and 350 °C with 60 wt% of mass loss. For hemp shives, 60 wt% of the initial mass is lost between 200 and 325 °C. The TGA curve of the composites is a combination of the TGA curve of each component (natural fiber and PCM) represented by two inflexions in the TGA curve. The results showed that the composite is stable up to 150 °C and therefore suitable for application in buildings.

Finally, both, flax mulch and hemp shives could satisfy the requirements. As hemp shives have a slightly higher density and thermal conductivity and as they are already used in buildings through hemp concrete, they are selected as natural support material for the rest of the study.

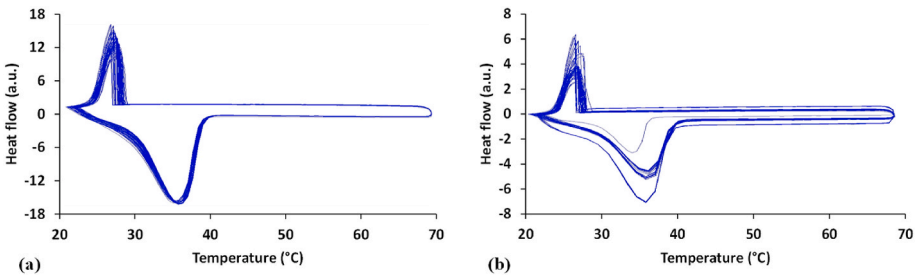

Fig. 3. 50 cycles DSC of CA/hemp shives composites impregnated under vacuum (a) and under atmospheric pressure (b).

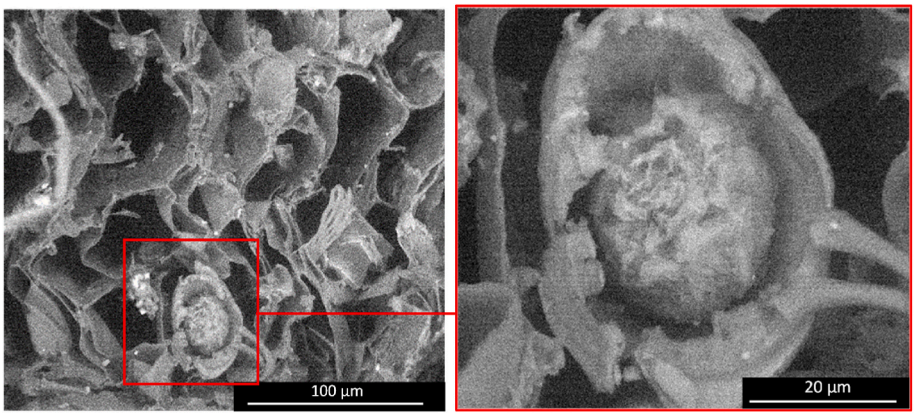

Fig. 5. SEM observations of hemp shives/CA composite.

Table 6
Impregnation rate of the studied natural fibers.

Impregnation rate (wt%)	Capric acid	Lauric acid
Hemp fibers	5	0
Hemp shives	48	50
Fir pellets	1	8
Flax mulch	51	43

4.2. Selection of the PCM

The results of the previous section have shown that hemp shives are efficient natural support materials. The impregnation performances of hemp shives being only investigated for two PCMs, the impregnation rate of hemp shives in different fatty acids and their eutectic mixtures have been experimentally assessed. Five pure fatty acids (CA, LA, MA, PA, SA) and seven eutectic mixtures (CA-LA, CA-MA, CA-PA, CA-SA, LA-MA, LA-PA and LA-SA) are tested.

4.2.1. Impregnation rate

The impregnation rates of hemp shives with the PCMs are presented in Fig. 7. As observed, the maximum impregnation rate is about 50 wt%. This maximum value is obtained for LA and LA eutectic mixtures showing that hemp shives have better affinity with LA compared to the other fatty acids. CA, MA and PA have similar behaviors with impregnation rates of 48, 48 and 45 wt% respectively. The lowest impregnation rate is obtained for SA with a value of 40%.

The impregnation rate of eutectic mixtures is a combination of that of the components. This explains the relatively high impregnation rate of LA eutectic mixtures and especially when the amount of LA in the mixture is high. Another illustration is the lowest impregnation rate value of CA-SA, which is made of a pure fatty acid (SA) with the lowest

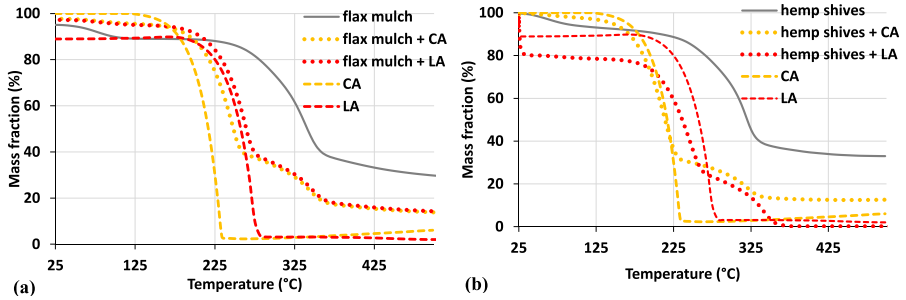

Fig. 6. TGA of CA, LA/flax mulch (a) and hemp shives (b) composites.

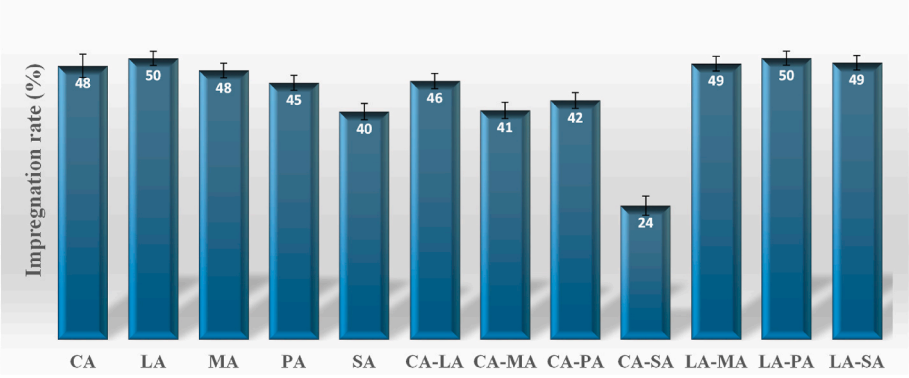

Fig. 7. Impregnation rate of hemp shives in fatty acids and their eutectic mixtures.

impregnation rates. The resulting eutectic compound possesses the lowest impregnation of all the studied PCMs.

4.2.2. Mass degradation

TGA analysis has been conducted in order to study the mass degradation of all composites selected and also allows ensuring the presence of PCMs in hemp shives. Fig. 8 (a) presents the mass degradation curve of pure fatty acids and the eutectic mixtures used in this study. The temperature of degradation of the materials increases with the temperature of fusion. In other words, the higher the temperature of fusion, the higher is the temperature degradation. Therefore, the lowest and highest temperatures of degradation are obtained for CA-LA and the LA-SA with values of 150 °C and 230 °C respectively.

The TGA curves of PCMs/hemp shives composites are plotted in Fig. 8 (b) and showed two inflexions points corresponding to the degradation temperature of each component of the composite (natural fiber and PCM). This result indicated that the PCMs are successfully impregnated with hemp shives. In addition, the lowest degradation temperature being 150 °C, it can be stated that all the PCMs hemp shives composites are stable up to 150 °C and therefore suitable for application in buildings.

4.2.3. Energy storage performances

In addition to the impregnation rate, the fusion and solidification properties of the composite are of real interest. These properties will govern the thermal performances of the overall thermal energy storage system that is the building envelope in our case. If a composite possesses a high impregnation rate but a low heat of fusion, it is clear that another composite with low impregnation rate but a higher heat of fusion will be preferred since we are interested in the thermal properties of the composites. Therefore, the heat of fusion and solidification of the composites are plotted in Fig. 9 (a). The heat of fusion of the composites are between 33.64 and 94.3 J g^{-1}. The heats of solidification are slightly lower than that of fusion and are between 24.5 and 93.7 J g^{-1}. The highest values for both quantities are obtained for SA with 94.29 and 93.7 J g^{-1} for heat of fusion and solidification respectively. In contrary, the lowest are obtained for CA-SA with values of 33.6 and 24.5 J g^{-1} for heat of fusion and solidification respectively.

As can be seen, the enthalpy of fusion and solidification for all composites are lower compared to that of pure or eutectic fatty acid eutectic mixtures. This reduction is caused by the reduction of the mass ratio of PCM in the composite and the reduction of the crystallinity of the PCM. It is possible to assess that by comparing the theoretical enthalpy and the measured one. The theoretical enthalpy is calculated by multiplying the enthalpy of the fatty acid alone by the impregnation rate (R) as presented in equation (3).

$$\Delta H_{calculated} = R^{*}\Delta H_{calculated} \quad (3)$$

Fig. 9 (b) compares the calculated and measured enthalpies of fusion/solidification. In general, the two values are close but the calculated values are higher than the measured one. In order to better represent the discrepancies, the absolute and relative differences between calculated and measured enthalpies are plotted in Fig. 10. The differences ranges from 0.26 to 21 J g^{-1}, and 2.93–21.3 J g^{-1} for heat of fusion and solidification respectively. These differences correspond to relative errors between 0.31-41% and 3.51–34% for enthalpies of fusion and solidification respectively. The maximum relative difference are obtained for MA and CA-MA composites. For the remaining composites, the differences for the enthalpy of fusion is between 0 and 15%, which is within the uncertainty range of the DSC device (15% for enthalpy calculation). However, the difference is still very large especially for the solidification enthalpy that exceeds the uncertainty of the device for some composites. This difference may be explained by the statistical behaviour of the impregnation process (all the particles will not absorb the same amount of PCM) and the error induced by the sampling. In fact, the impregnation rate is measured on a sample of few grams whereas the DSC measurements are obtained on samples of 10–20 mg. The mismatch between calculated and measured enthalpy could be considerably improved by the utilization of DSC with high size samples.

Except from CA-SA, CA-LA and CA-MA, all the composites have a latent heat of fusion superior to 50 J g^{-1}, which is higher than most of the composites with natural fibers [38,41–43]. These latent heat values are very promising for energy storage in buildings.

In addition to a high value of latent heat, the temperature of fusion of the composites should be in the temperature range (15–45 °C) in order to be eligible to building application and thermal comfort. The temperatures of fusion of the composites are presented in Fig. 11. Except from pure MA PA and SA, all the pure PCMs and the fabricated composites possess a temperature of fusion corresponding to the aimed thermal requirements.

Fig. 12 shows the absolute and relative differences between the PCMs and PCMs/composites fusion and solidification temperatures. The differences range from 0.045 to 8 °C corresponding to a relative difference between 0.14 and 25%. The fusion and solidification temperatures of the composites are lower than that of the PCMs alone. This difference is explained by the insulating nature of the hemp shives that can induce a delay in the heat conduction resulting to lower temperature compared to those of pure PCMs. In addition, this decrease in phase change temperatures can be due to weak attractive interactions between fatty acid molecules and inner surface wall of the porous material [44].

4.2.4. Undercooling

The performance of energy storage systems incorporating PCMs is typically evaluated in terms of charge/discharge cycles. The latter and the associated performances are strongly influenced by the nature of the PCMs and their properties as previously mentioned but also by their undercooling.

Undercooling is a metastable state in which a liquid remains in a liquid state at a temperature inferior to its melting temperature. The integration of composites in buildings walls will allow for an increase in thermal inertia and short term passive energy storage. The latter allows managing the diurnal sunshine variation. For this type of storage, the phenomenon of undercooling must be as low as possible (5 °C maximum) in order to discharge the thermal energy fastly in the desired

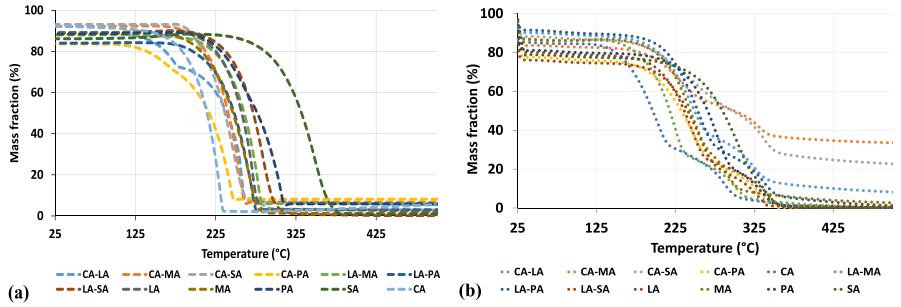

Fig. 8. TGA of PCMs (a) and PCMs/hemp shives composites (b).

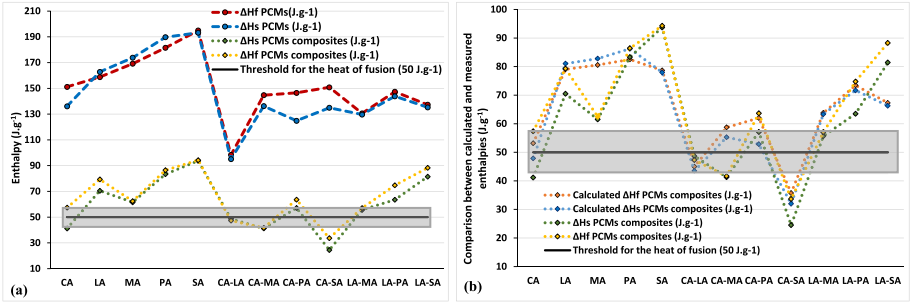

Fig. 9. (a) Enthalpy of fusion and solidification of PCMs and PCM hemp shives composites, (b) Comparison between calculated and measured enthalpies. The gray box represents the uncertainty on the threshold enthalpy (50 J g^{-1}) based on the precision of the device (15%).

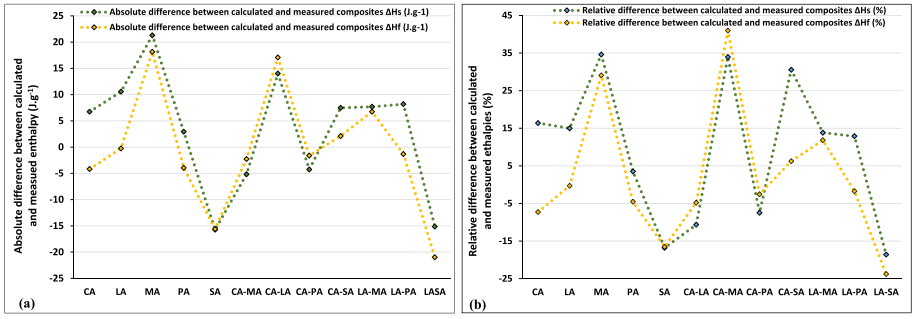

Fig. 10. (a) Absolute and (b) relative differences between measured and calculated enthalpies.

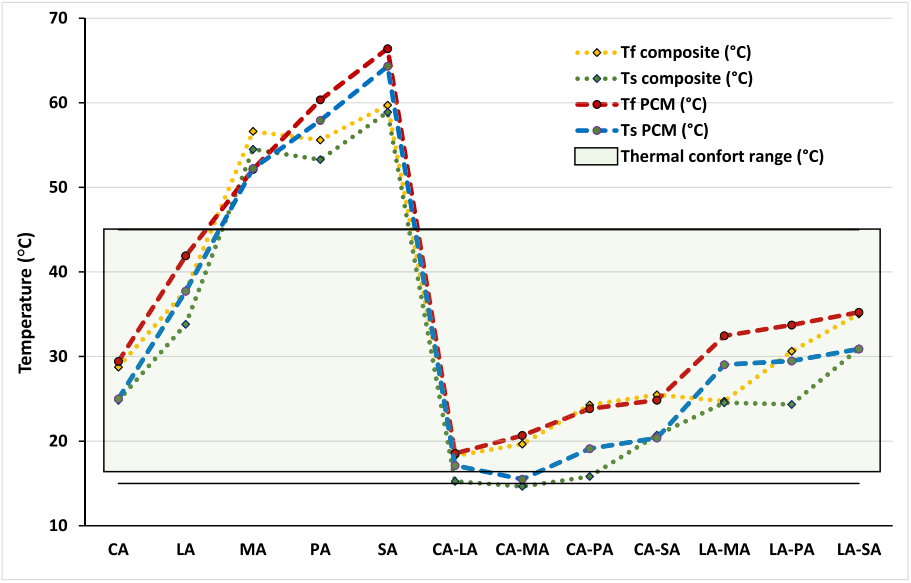

Fig. 11. Temperature of fusion/solidification of PCMs and hemp shives PCMs composites.

temperature range and to facilitate the charge/discharge cycles.

The undercooling level of PCMs and hemp shives PCMs composites are presented in Fig. 13. Apart from CA-PA, all the PCMs possess an undercooling degree below 5 °C making them suitable for thermal energy storage. The same tendency is observed for hemp shives PCMs composites at the exception of CA-MA, CA-PA, CA-SA and LA-PA. The latter are eliminated from the list of potential candidates because of high undercooling. CA-SA is also eliminated because of its undercooling degree close to 5 °C but mainly because of its low impregnation rate (24%, Fig. 7).

Finally, taking into account the thermal requirements, which are a high latent heat, undercooling below 5 °C and temperature of fusion between 15 and 45 °C, only CA, LA, LA-MA and LA-SA composites are selected as potential materials for buildings application. However due to the complexity of fabrication of eutectic mixtures for large scale applications, LA-MA and LA-SA are also eliminated and the final composites selected are CA and LA hemp shives composites.

5. Discussion

The selection process has allowed the selection of hemp shives as support material for the fabrication of shape-stabilized composites. In addition to his high impregnation rate, this support material is very cheap (less than 1€.kg^{-1}) and possesses a relatively low thermal

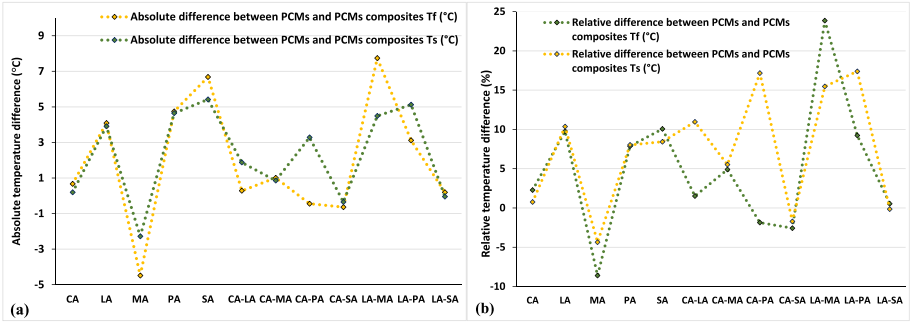

Fig. 12. (a) Absolute and (b) relative differences between the PCM and PCMs/composites fusion and solidification temperatures.

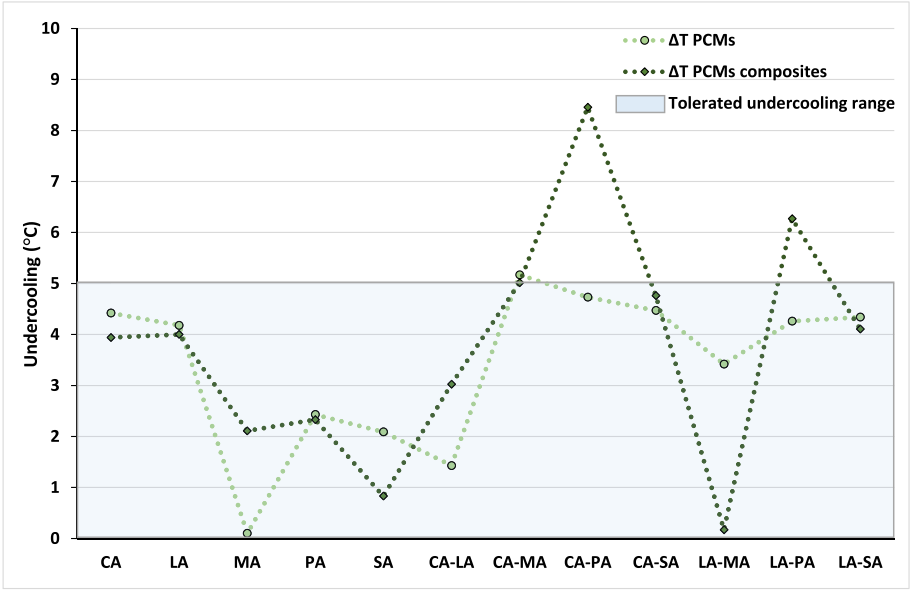

Fig. 13. Undercooling level of PCMs and PCMs composites.

conductivity. The thermal conductivity of hemp shives is compared with some natural insulators in buildings (Table 1). Despite a higher conductivity compared with conventional insulators, hemp shives impregnated with PCMs can be an interesting alternative due to expected higher energy density and acceptable thermal conductivity. Another advantage of hemp shives is their hygroscopic behaviour, which can help to regulate the humidity in buildings.

Regarding the composites selection, CA and LA hemp shives composites have been selected as potential composites for building applications because they fulfil all physical, thermal, geographical and economic criteria. In addition, the composites made with pure fatty acid are easy to manufacture compared to those made with eutectic mixtures. This is of great importance for building scale applications.

Among the two composites, hemp shives/LA is the best compromise because of higher impregnation rate (50 wt%) and higher enthalpy of fusion and solidification (79.3 and 70.4 J g^{-1} respectively) compare to CA. In addition, LA is more than two times cheaper than CA respectively 36.4 and 75.1 €.kg^{-1} at a purity of 99% [33]. The fusion/solidification temperatures and enthalpy of LA hemp shives composites are still very promising for energy storage in buildings compared to shape-stabilized PCMs studied by other references (Table 7). The composite exhibits competitive latent heats of fusion and solidification with low undercooling.

Fatty acids in general and LA in particular have shown a good affinity with hemp shives. The reason is probably due to the roughness of the hemp shives as presented in Fig. 1 that improve the probability of nucleation [45]. This roughness may have a positive impact on the fusion/solidification cycles of composite. This hypothesis should be properly studied, especially at the hemp shives/LA interface for better understanding of the underlying phenomenon and how it affects the thermal properties of the composites. The characterization of the LA/hemp shives interface can be done using microscopy and chemical analysis XPS and will be the purpose of further investigations. In addition, a quantitative analysis of the heteregeneous nucleation of fatty acids at the surface of the hemp shives, based on infrared thermography, will be conducted to assess the influence of the roughness of the hemp

Table 7
Comparison of the phase change properties of the prepared hemp shives/LA composite with some bio-based PCM composites.

PCM composites	Temperature of fusion (°C)	Solidification temperature (°C)	**Heat of fusion (J.g^{-1})**	Heat of solidification (J.g^{-1})	Reference
Delignified wood/CA-PA	23.4 ± 0.3	14.5 ± 0.2	94.4 ± 1.0	91.4 ± 0.6	[18]
Carbon fibers/paraffin	22.5–60	22.5–57.6	192.2	191.1	[19]
Kapok fibers/MA-Tetradecanol	24–42.3	10.5–29.7	76.8	77.4	[38]
Hemp shives/LA	37.8	33.8	79.3	70.4	**This study**

shives in the nucleation process.

The mismatch between calculated and measured heat of fusion has been explained by the statistical behaviour of the impregnation and the limitation of the size of sample for DSC measurement. This limitation can be alleviated by using a large volume calorimeter like Calvet that allow samples of few grams and possesses 3D heat and temperature sensors. Another possibility is to reduce the heating and cooling rate because fibers slow down heat transfer due to their insulating nature.

Finally, the fabricated PCMs hemp shives composites could be easily integrated in buildings through hemp concrete. In fact, hemp concrete is very wide spread in France and has a regulatory frame work for its use and formulation in the construction sector [46]. Therefore, the fabricated CA and LA hemps shives composite could be mixed with lime and water in various proportions to fabricate a PCM hemp concrete. The new PCM hemp concrete material is expected to possess excellent hygrothermal properties and suitable for LHTES application in building envelopes.

6. Conclusion

In this study, the potential of natural fibers as support materials for PCMs for buildings application was investigated. The material selection software Ansys Granta has allowed the a preliminary selection of four natural fibers namely fir fibers, hemp fibers, hemp shives and flax mulch based on physical, thermal, geographical and economic criteria. First, the selected fibers are impregnated with two pure PCMs (CA and LA) and compared in terms of impregnation rate in order to selected the best support material for shape-stabilization. The results indicated poor performances for fir and hemp fibers with impregnation rates of 1 and 8 wt% respectively. In contrast, hemp shives and flax mulch presented better results with impregnation rate of 50 wt% and 51 wt% respectively. Therefore, only hemp shives and flax mulch are selected for the rest of the study and two others (hemp and fir fibers) were eliminated. TGA curves of PCMs/hemp shives and flax mulch composites showed a no mass degradation under 150 °C, thus suitable for buildings application. As hemp shives are already used in buildings through hemp concrete, which is a normalized insulating material and presently slighltly higher density and thermal conductivity, they have been selected as natural support material since they presented highest impregnation rates with good thermal stability.

After the selection of the support material, it has been impregnated with 5 pure fatty acids and 7 eutectics mixtures in order to select the suitable PCM for the fabrication of a composite with optimized performances. The comparison of the different impregnation rates has shown that hemp shives are more compatible with LA and LA eutectic mixtures. The lowest impregnation rate are obtained for CA-SA. In addition, the lowest degradation temperature being 150 °C, it can be stated that all the PCMs hemp shives composites are stable below 150 °C and therefore suitable for application in buildings. Except from CA-SA, CA-MA and CA-LA, all the composites have latent heat higher than 50 J/g, which is higher than most of the composites with natural fibers. Taking into account the thermal requirements, which are high latent heat, low undercooling temperature of fusion between 15 and 45 °C, and facility to manufacture, LA hemp shives composite (enthalpy of fusion of 79.3 J g^{-1} at 50 wt% of impregnation rate) has been selected as potential materials for buildings application.

In order to develop competitive and efficient envelopes with good insulation, hygroscopic, energy storage capacity with the incorporation of PCMs, it is necessary to conduct a multiscale analysis. First, at the material level in order to characterize and select a suitable composite. Then, once the composite selected, it must be integrated in envelopes and compared to conventional walls. Finally, the solution must be tested at the building scale and its performances in terms of energy saving must be evaluated. This investigation was a part of the first step. It has allowed the selection of hemp shives/LA composite that showed a highpotential for building application. Future works will be emphasized on the development of hemp concrete incorporating PCM. The hygrothermal properties of the material will be characterized and its thermal performances evaluated under various climatic conditions at different scales (from the material to the envelope one).

CRediT authorship contribution statement

Mohamed Sawadogo: Writing – review & editing, Writing – original draft, Visualization, Validation, Methodology, Investigation, Data curation, Conceptualization. **Alexandre Godin:** Writing – review & editing, Writing – original draft, Visualization, Validation, Supervision, Methodology, Data curation. **Marie Duquesne:** Writing – original draft, Visualization, Validation, Supervision, Resources, Project administration, Methodology, Investigation, Funding acquisition, Formal analysis, Data curation, Conceptualization. **Elodie Lacroix:** Data curation, Investigation, Methodology, Writing – original draft. **Amélie Veillère:** Writing – original draft, Visualization, Validation, Supervision, Formal analysis. **Ameur El Amine Hamami:** Writing – original draft, Visualization, Validation, Supervision, Resources, Data curation. **Rafik Belarbi:** Writing – original draft, Visualization, Validation, Supervision, Resources, Project administration, Funding acquisition.

Declaration of competing interest

The authors declare that they have no known competing financial interests or personal relationships that could have appeared to influence the work reported in this paper.

Data availability

Data will be made available on request.

Acknowledgment

The authors acknowledge the financial support of Region Nouvelle Aquitaine for subsidizing BioMCP project (Project-2017-1R10209–13023). The authors would also like to thank Bordeaux INP for the funding of this project. We would also like to thank ENSCBP, MPI 4.0 specialization that has allowed the accomplishment of this project. A special thanks to Livie Ducasse, Emma Baptiste, Méyanne Hurtault and Elodie Lacroix for their precious help and implication in the project Ecowall. The authors are also grateful to Dr. Egle CONFORTO, responsible of the electron microscopy platform of the LaSIE laboratory of La Rochelle University.

References

[1] Buildings – Topics, IEA. (n.d.). https://www.iea.org/topics/buildings(accessed April 30, 2021).
[2] Réglementation environnementale RE2020, Ministères Écologie Énergie Territoires. (n.d.). https://www.ecologie.gouv.fr/reglementation-environnementale-re2020(accessed June 13, 2022).
[3] V. Basecq, G. Michaux, P. Blondeau, C. Inard, Short term storage systems of the thermal energy for buildings: a review, Adv. Build. Energy Res. 7 (2013) 66–119. https://hal.archives-ouvertes.fr/hal-01052828. (Accessed 5 May 2021). accessed.
[4] S. Ben Romdhane, A. Amamou, R. Ben Khalifa, N.M. Saïd, Z. Younsi, A. Jemni, A review on thermal energy storage using phase change materials in passive building applications, J. Build. Eng. 32 (2020), 101563, https://doi.org/10.1016/j.jobe.2020.101563.
[5] B. Lamrani, K. Johannes, F. Kuznik, Phase change materials integrated into building walls: an updated review, Renew. Sustain. Energy Rev. 140 (2021), 110751, https://doi.org/10.1016/j.rser.2021.110751.
[6] A.A.A.A. Al-Rashed, A.A. Alnaqi, J. Alsarraf, Energy-saving of building envelope using passive PCM technique: a case study of Kuwait City climate conditions, Sustain. Energy Technol. Assessments 46 (2021), 101254, https://doi.org/10.1016/j.seta.2021.101254.
[7] J. Bohórquez-Órdenes, A. Tapia-Calderón, D.A. Vasco, O. Estuardo-Flores, A. N. Haddad, Methodology to reduce cooling energy consumption by incorporating PCM envelopes: a case study of a dwelling in Chile, Build. Environ. 206 (2021), 108373, https://doi.org/10.1016/j.buildenv.2021.108373.

[8] Y.K. Yang, I.S. Kang, M.H. Chung, S. Kim, J.C. Park, Effect of PCM cool roof system on the reduction in urban heat island phenomenon, Build. Environ. 122 (2017) 411–421, https://doi.org/10.1016/j.buildenv.2017.06.015.
[9] S. Wi, S.J. Chang, S. Kim, Improvement of thermal inertia effect in buildings using shape stabilized PCM wallboard based on the enthalpy-temperature function, Sustain. Cities Soc. 56 (2020), 102067, https://doi.org/10.1016/j.scs.2020.102067.
[10] N. Zhu, S. Li, P. Hu, S. Wei, R. Deng, F. Lei, A review on applications of shape-stabilized phase change materials embedded in building enclosure in recent ten years, Sustain. Cities Soc. 43 (2018) 251–264, https://doi.org/10.1016/j.scs.2018.08.028.
[11] S. Elfordy, F. Lucas, F. Tancret, Y. Scudeller, L. Goudet, Mechanical and thermal properties of lime and hemp concrete ("hempcrete") manufactured by a projection process, Construct. Build. Mater. 22 (2008) 2116–2123, https://doi.org/10.1016/j.conbuildmat.2007.07.016.
[12] H.-R. Kymäläinen, A.-M. Sjöberg, Flax and hemp fibres as raw materials for thermal insulations, Build. Environ. 43 (2008) 1261–1269, https://doi.org/10.1016/j.buildenv.2007.03.006.
[13] D.P. Murphy, H. Behring, H. Wieland, The Use of Flax and Hemp Materials for Insulating Buildings, 1997, pp. 79–84. https://www.openagrar.de/receive/timport_mods_00042620. (Accessed 26 May 2021). accessed.
[14] A.D. Tran Le, J.S. Zhang, Z. Liu, D. Samri, T. Langlet, Modeling the similarity and the potential of toluene and moisture buffering capacities of hemp concrete on IAQ and thermal comfort, Build. Environ. 188 (2021), 107455, https://doi.org/10.1016/j.buildenv.2020.107455.
[15] V.S. Parameswaran, Fibre-reinforced concrete: a versatile construction material, Build. Environ. 26 (1991) 301–305, https://doi.org/10.1016/0360-1323(91)90054-F.
[16] E.A. Olanipekun, K.O. Olusola, O. Ata, A comparative study of concrete properties using coconut shell and palm kernel shell as coarse aggregates, Build. Environ. 41 (2006) 297–301, https://doi.org/10.1016/j.buildenv.2005.01.029.
[17] F. Benmahiddine, F. Bennai, R. Cherif, R. Belarbi, A. Tahakourt, K. Abahri, Experimental investigation on the influence of immersion/drying cycles on the hygrothermal and mechanical properties of hemp concrete, J. Build. Eng. 32 (2020), 101758, https://doi.org/10.1016/j.jobe.2020.101758.
[18] L. Ma, Q. Wang, L. Li, Delignified wood/capric acid-palmitic acid mixture stable-form phase change material for thermal storage, Sol. Energy Mater. Sol. Cell. 194 (2019) 215–221, https://doi.org/10.1016/j.solmat.2019.02.026.
[19] N. Sheng, Z. Rao, C. Zhu, H. Habazaki, Honeycomb carbon fibers strengthened composite phase change materials for superior thermal energy storage, Appl. Therm. Eng. 164 (2020), 114493, https://doi.org/10.1016/j.applthermaleng.2019.114493.
[20] M. Sawadogo, M. Duquesne, R. Belarbi, A.E.A. Hamami, A. Godin, Review on the integration of phase change materials in building envelopes for passive latent heat storage, Appl. Sci. 11 (2021) 9305, https://doi.org/10.3390/app11199305.
[21] B. Abu-Jdayil, A.-H. Mourad, W. Hittini, M. Hassan, S. Hameedi, Traditional, state-of-the-art and renewable thermal building insulation materials: an overview, Construct. Build. Mater. 214 (2019) 709–735, https://doi.org/10.1016/j.conbuildmat.2019.04.102.
[22] S. Vaitkus, R. Karpavičiūtė, S. Vėjelis, L. Lekūnaitė, Development and research of thermal insulation materials from natural fibres, Key Eng. Mater. 604 (2014) 285–288. https://doi.org/10.4028/www.scientific.net/KEM.604.285.
[23] X. -y. Zhou, F. Zheng, H. -g. Li, C. -l. Lu, An environment-friendly thermal insulation material from cotton stalk fibers, Energy Build. 42 (2010) 1070–1074, https://doi.org/10.1016/j.enbuild.2010.01.020.
[24] A.D. Tran-Le, S.-T. Nguyen, T. Langlet, A novel anisotropic analytical model for effective thermal conductivity tensor of dry lime-hemp concrete with preferred spatial distributions, Energy Build. 182 (2019) 75–87, https://doi.org/10.1016/j.enbuild.2018.09.043.
[25] J.C. Damfeu, P. Meukam, Y. Jannot, Modeling and measuring of the thermal properties of insulating vegetable fibers by the asymmetrical hot plate method and the radial flux method: kapok, coconut, groundnut shell fiber and rattan, Thermochim. Acta 630 (2016) 64–77, https://doi.org/10.1016/j.tca.2016.02.007.
[26] M.L. Voumbo, A. Wereme, S. Gaye, M. Adj, G. Sissoko, Characterization of the thermophysical properties of kapok, Res. J. Appl. Sci. Eng. Technol. 2 (2010) 143–148.
[27] C. Pend, W. Fumei, An investigation of heat flow through kapok insulating material, Fibres Textiles 2 (2009) 88–92.
[28] K. Manohar, D. Ramlakhan, G. Kochhar, S. Haldar, Biodegradable fibrous thermal insulation, J. Braz. Soc. Mech. Sci. Eng. 28 (2006) 45–47, https://doi.org/10.1590/S1678-58782006000100005.
[29] B. Poletanovic, I. Janotka, M. Janek, M. Bacuvcik, I. Merta, Influence of the NaOH-treated hemp fibres on the properties of fly-ash based alkali-activated mortars prior and after wet/dry cycles, Construct. Build. Mater. 309 (2021), 125072, https://doi.org/10.1016/j.conbuildmat.2021.125072.
[30] J. Cigasova, N. Stevulova, I. Schwarzova, Innovative use of plant wastes - hemp hurds slices, Chemical Eng. Transact. 50 (2016) 373–378, https://doi.org/10.3303/CET1650063.
[31] W. Zhang, X. Zhang, X. Zhang, Z. Yin, Y. Liu, M. Fang, X. Wu, X. Min, Z. Huang, Lauric-stearic acid eutectic mixture/carbonized biomass waste corn cob composite phase change materials: preparation and thermal characterization, Thermochim. Acta 674 (2019) 21–27, https://doi.org/10.1016/j.tca.2019.01.022.
[32] M. Duquesne, C. Mailhé, S. Doppiu, J.-L. Dauvergne, S. Santos-Moreno, A. Godin, G. Fleury, F. Rouault, E. Palomo del Barrio, Characterization of fatty acids as biobased organic materials for latent heat storage, Materials 14 (2021) 4707, https://doi.org/10.3390/ma14164707.
[33] M. Duquesne, C. Mailhé, K. Ruiz-Onofre, F. Achchaq, Biosourced organic materials for latent heat storage: an economic and eco-friendly alternative, Energy 188 (2019), 116067, https://doi.org/10.1016/j.energy.2019.116067.
[34] C. Mailhé, S. Gorsse, B. Thirion, E. Palomo, M. Duquesne, High-throughput experiment for the rapid screening of organic phase change materials, J. Therm. Anal. Calorim. 147 (2022) 8137–8143, https://doi.org/10.1007/s10973-021-11091-9.
[35] H. Ke, Phase diagrams, eutectic mass ratios and thermal energy storage properties of multiple fatty acid eutectics as novel solid-liquid phase change materials for storage and retrieval of thermal energy, Appl. Therm. Eng. 113 (2017) 1319–1331, https://doi.org/10.1016/j.applthermaleng.2016.11.158.
[36] C. Mailhé, M. Duquesne, E. Palomo del Barrio, M. Azaiez, F. Achchaq, Phase diagrams of fatty acids as biosourced phase change materials for thermal energy storage, Appl. Sci. 9 (2019) 1067, https://doi.org/10.3390/app9061067.
[37] S.-G. Jeong, J. Jeon, J.-H. Lee, S. Kim, Optimal preparation of PCM/diatomite composites for enhancing thermal properties, Int. J. Heat Mass Tran. 62 (2013) 711–717, https://doi.org/10.1016/j.ijheatmasstransfer.2013.03.043.
[38] T. Dong, W. jiang, Y. liu, Y. Wu, Y. Qi, J. Li, Y. Ma, H. Ben, G. Han, A phase change material embedded composite consisting of kapok and hollow PET fibers for dynamic thermal comfort regulation, Ind. Crop. Prod. 158 (2020), 112945, https://doi.org/10.1016/j.indcrop.2020.112945.
[39] M. Connor, S. Toll, J.-A.E. Månson, On surface energy effects in composite impregnation and consolidation, Compos. Manuf. 6 (1995) 289–295, https://doi.org/10.1016/0956-7143(95)95022-Q.
[40] Y. Jiang, M. Lawrence, A. Hussain, M. Ansell, P. Walker, Comparative moisture and heat sorption properties of fibre and shiv derived from hemp and flax, Cellulose 26 (2019) 823–843, https://doi.org/10.1007/s10570-018-2145-0.
[41] C. Barreneche, J. Vecstaudza, D. Bajare, A.I. Fernandez, PCM/wood Composite to Store Thermal Energy in Passive Building Envelopes, 2017, https://doi.org/10.1088/1757-899X/251/1/012111.
[42] X. Jingchen, Y. Keyan, Z. Yucheng, Y. Yuxiang, C. Jianmin, C. Liping, S.Q. Sheldon, Form-stable phase change material based on fatty acid/wood flour composite and PVC used for thermal energy storage, Energy Build. 209 (2020), 109663, https://doi.org/10.1016/j.enbuild.2019.109663.
[43] A. Sarı, G. Hekimoğlu, V.V. Tyagi, Low cost and eco-friendly wood fiber-based composite phase change material: development, characterization and lab-scale thermoregulation performance for thermal energy storage, Energy 195 (2020), 116983, https://doi.org/10.1016/j.energy.2020.116983.
[44] A. Karaipekli, A. Sari, Preparation, thermal properties and thermal reliability of eutectic mixtures of fatty acids/expanded vermiculite as novel form-stable composites for energy storage, J. Ind. Eng. Chem. 16 (2010) 767–773, https://doi.org/10.1016/j.jiec.2010.07.003.
[45] M. Duquesne, A. Godin, E. Palomo del Barrio, J. Daranlot, Experimental analysis of heterogeneous nucleation in undercooled melts by infrared thermography, Quantitative InfraRed Thermography Journal 12 (2015) 112–126, https://doi.org/10.1080/17686733.2015.1031987.
[46] Publication semestrielle C2P - Édition Janvier 2018, Agence Qualité Construction. (n.d.), https://qualiteconstruction.com/publication/janvier-2018-publication-semestrielle/. (Accessed 12 December 2022). accessed.

Article 4

Applied Thermal Engineering 212 (2022) 118620

Contents lists available at ScienceDirect

Applied Thermal Engineering

journal homepage: www.elsevier.com/locate/apthermeng

Investigation of a novel bio-based phase change material hemp concrete for passive energy storage in buildings

Mohamed Sawadogo [a,c], Ferhat Benmahiddine [a], Ameur El Amine Hamami [a], Rafik Belarbi [a,*], Alexandre Godin [b], Marie Duquesne [c]

[a] La Rochelle Université, LaSIE UMR CNRS 7356, Avenue Michel Crépeau, CEDEX 1, 17042 La Rochelle, France
[b] Amplitude, 11 Avenue de Canteranne, Cité de la Photonique, Bâtiment MEROPA, 33600 Pessac, France
[c] Bordeaux INP, CNRS, Université de Bordeaux I2M, Bât A11, 351 Cours de la Libération, 33400 Talence, France

ARTICLE INFO

Keywords:
Bio-based shape-stabilized phase change material composite
Latent heat thermal energy storage
Hemp concrete
Thermal performances

ABSTRACT

In latent heat storage, energy is stored through the change of state of a material and then released when the material returns to its original phase. Latent heat thermal energy storage systems incorporate phase change materials (PCMs) as storage materials. The objective of this study is the fabrication and characterization of a biosourced PCM hemp concrete. Hemp shives are vacuum impregnated with CA with an incorporation rate of 53%. The resulting shape-stabilized hemp shives/CA composite is used to fabricate PCM hemp concrete. The morphology and thermophysical properties of the materials at all stages (from pure CA to hemp concrete PCMs) are characterized using differential scanning calorimetry (DSC), scanning electron microscopy (SEM) and compared to the reference state (hemp concrete without PCMs). Results of the DSC measurement indicated melting and solidification temperatures of hemp shives/CA composite of 28.9 °C and 23 °C, respectively and enthalpy of melting and solidification calculated as 78.7 and 76.4 $J.g^{-1}$, respectively. The TGA/dTG results showed that the form stable composite exhibits good thermal stability under 170 °C, making it suitable for building application. The thermal performances of PCM hemp concrete are evaluated in a climatic chamber and compared to those of a reference hemp concrete. Results showed a good thermoregulation capacity of the PCM hemp concrete with a maximum time shift of 30 min and a temperature difference between reference and PCM hemp concrete of about 4.6 °C.

Featured Application: Passive latent heat storage for building applications, thermal comfort.

1. Introduction

The building sector is the biggest energy consumer accounting for 40% in the total world energy consumption [1]. In the context of climate change [2], it is necessary to reduce the energy consumption at the worldwide level. The building sector is one of the key factor to achieve this goal. In order to reduce the energy consumption of buildings, essentially used for heating and cooling, it is important to decrease their energy consumption by better insulation or thermal energy storage. The latter consists in capturing the thermal energy from internal heat gains or renewables, such as solar, at one time to use it later. The main advantages of thermal energy storage are: reduction of the energy consumption, limitation of heat losses, shift of electricity consumption from peak to off-peak periods and development of the use of intermittent renewable energy sources [3].

Numerous studies have shown that latent heat thermal energy storage (LHTES) which incorporates phase change materials (PCMs) is an efficient technique to increase the thermal capacity, energy efficiency and comfort impact of buildings [4-10]. The PCMs of interest in this work are solid-liquid ones. The basic principle of the LHTES based on solid-liquid transition is the following: during the melting process, the excess of thermal energy from the ambient is stored as latent heat in the PCMs and restored to the environment when the temperature drops below the temperature of solidification of the PCMs. In this study, the targeted application is the passive LHTES. In passive systems, the heat transfer fluid does not contribute to the storage and circulates naturally without any mechanical device. Silva et al. [11] studied the thermal performances of a south facing window shutter containing PCMs in a test

* Corresponding author.
E-mail addresses: mohamed.sawadogo@univ-lr.fr (M. Sawadogo), ferhat.benmahiddine1@univ-lr.fr (F. Benmahiddine), ameur_el_amine.hamami@univ-lr.fr (A.E.A. Hamami), rafik.belarbi@univ-lr.fr (R. Belarbi), alexandre.godin@amplitude-laser.com (A. Godin), marie.duquesne@u-bordeaux.fr (M. Duquesne).

https://doi.org/10.1016/j.applthermaleng.2022.118620
Received 30 November 2021; Received in revised form 1 March 2022; Accepted 3 May 2022
Available online 6 May 2022
1359-4311/© 2022 Elsevier Ltd. All rights reserved.

Table 1
General information about capric acid (CA).

Fatty Acid	Acronym	CAS Number	Formula	Supplier	Purity * (%)	Melting Temperature
Capric acid (Decanoic acid)	CA	334–48-5	$C_{10}H_{20}O_2$	Alfa Aesar	99	29–33 °C [24,29]

* Purity as given by the supplier.

cell located in Aveiro, Portugal, during summer. The results showed a thermal regulation capacity of the internal temperature of about 18–22% and temperature peaks delayed by 45 min to one hour compared to the reference compartment. Lee et al. [12] integrated paraffin with a melting temperature of 28–30 °C into cellulose wall insulation. The incorporation of paraffin in the insulation reduced the heat flux from 16.1% to 38.5%. The maximum heat flow was delayed from 1.5 to 3 h, which would allow reducing the electricity bill. Umberto et al. [13] investigated the thermal performances of two test cells, one as a reference and the other one containing a composite PCM system, comprised of two PCMs products with melting temperatures of 21.7 °C and 25 °C. The results indicated improved performances of the test cell containing the PCM composite system in lowering the maximum interior and surface temperatures by up to 6 °C.

Many studies has been conducted in order to select the suitable PCM for a specific application. Jinghua et al. [14] investigated numerically the effects of the phase transition temperature, layer thickness and phase transition temperature radius of PCM on the performances of a roof with outer-layer shape-stabilized PCM. The optimal phase change temperature were 31–33 °C, 34–36 °C, 36–38 °C, 34–36 °C, and 29–31 °C respectively in severe cold region, cold region, hot summer and cold winter region, hot summer and warm winter region and mild region. Al-Rashed et al. [15] compared three PCMs (RT-31, RT-35 and RT-42) with different melting temperatures in terms of reduction of the heat gains in the Kuwaiti hot climate region. The best results (energy saving as well as CO_2 saving) were obtained for RT-31, a PCM with phase change temperature of 27–33 °C compared to other PCM. Meng et al. [16] suggested a combined PCM with low (17–19 °C) and high (28–30 °C) melting temperatures allowing both energy storage in winter and summer.

These studies have shown the interest of incorporating PCMs in buildings envelopes. For this purpose, four different techniques have been used to integrate PCMs into building envelopes: direct incorporation, immersion, encapsulation and shape-stabilization [9,17-19]. A recent literature review [20] allowed the identification of shape-stabilized PCMs as a promising technique to incorporate PCMs in buildings. Shape-stabilized PCMs are obtained by impregnating PCMs into porous building materials preventing leakage problems during the phase change process. This technique is simple, inexpensive, possesses a high impregnation rate compared to other techniques and is compatible with a wide variety of support materials. Biosourced materials, in particular, insulating materials such as hemp, flax and bamboo with their good porous structure are promising for the fabrication of shape-stabilized PCMs. This will allow the fabrication of a 100% bio-based PCMs composites.

The solid-liquid PCMs are classified in three groups: organics, inorganics and eutectic mixtures [21]. Organic PCMs are the most widely used for thermal energy storage due to their suitable melting/solidification temperature, high energy storage density, chemical stability and storage capacity [10]. Recently, fatty acids has gained of interest due to their suitable thermophysical properties such as high-energy capacity, congruent melting, solidification behaviour as well as good chemical and thermal stability [6,10,22-27]. Additionally, they have no toxicity, no corrosivity, small or no undercooling, small volume change during phase change and easy production from vegetable and animal oils [22].

Only few of these fatty acids possess a melting temperature in the range of the thermal comfort (15 to 30 °C,T) [8,10]. However, the melting temperature of the PCMs can be adjusted to this climatic requirement by preparation of fatty acids eutectic mixtures. Duquesne et al. [24,28] have prepared two eutectics mixtures of capric and myristic acid, capric and palmitic acid with melting temperature of 24.29 °C and 26.25 °C. Ke et al. [29] have prepared a series of binary and multiple fatty acid eutectics by using five fatty acids (i.e. capric acid (CA), lauric acid (LA), myristic acid (MA), palmitic acid (PA), and stearic acid (SA), respectively). The melting temperature of the tested materials were found between 15 and 53 °C.

The objective of this work is to fabricate a new composite PCM hemp concrete. Many researchers have identified hemp concrete as a good insulation material with promising physical and hygrothermal properties [30-33]. Coupled with the aforementioned PCMs excellent properties, the composite material is expected to possess excellent properties and suitable for LHTES application in building envelopes. The novelty of this study is the development of a bio-based PCM hemp concrete followed by a troughout properties characterization and thermal performances test of the developed materials. The PCM hemp concrete is intended to be used as an insulating element in building envelopes. For this purpose, hemp shives with a high porous structure are impregnated with CA, a pure fatty acid with melting temperature within the thermal comfort range. Vacuum impregnation method is used to fabricate shape-stabilized PCMs composites with improved thermal properties and without leakage. The novel 100% bio-based PCM composite is then used to fabricate PCM hemp concrete. The morphology and thermophysical properties of the materials at all stages (from pure CA to PCM hemp concrete) are characterized using differential scanning calorimetry (DSC), scanning electron microscopy (SEM) and compared to the reference state (hemp concrete without PCMs). Finally, the thermal performances of the novel PCM hemp concrete are studied in a climatic chamber and compared to the reference hemp concrete.

2. Materials and methods

2.1. Materials

2.1.1. Selection of the PCM

The PCM must meet several selection criteria in order to be used effectively as a thermal energy storage material. Schröder and Gawron [34] developed a list summarizing the selection criteria for PCMs:

- High latent heat of phase change per unit volume and mass and heat capacity in order to allow the most compact system possible.
- Transition temperatures in the temperature range of the target application. For thermal comfort, this range is between 15 °C and 30 °C [10]. This temperature can be chosen considering the average day and night temperature and other weather conditions [17,35].
- High thermal conductivity to accelerate the charge and discharge of the storage system.
- Low vapour pressure to avoid evaporation that could affect the integrity of the system and reduce its efficiency.
- Low undercooling degree and high crystallization rate to facilitate the charge and discharge of the storage system.
- Low volume expansion during melting which implies very close solid and liquid densities.
- Chemical and thermal stabilities over a high number of charge and discharge cycles without altering the material properties and safely (i.e. non-toxic, non-corrosive, non-flammable and non-explosive).
- Use of an abundant and less expensive material to make the technology attractive for widespread use.

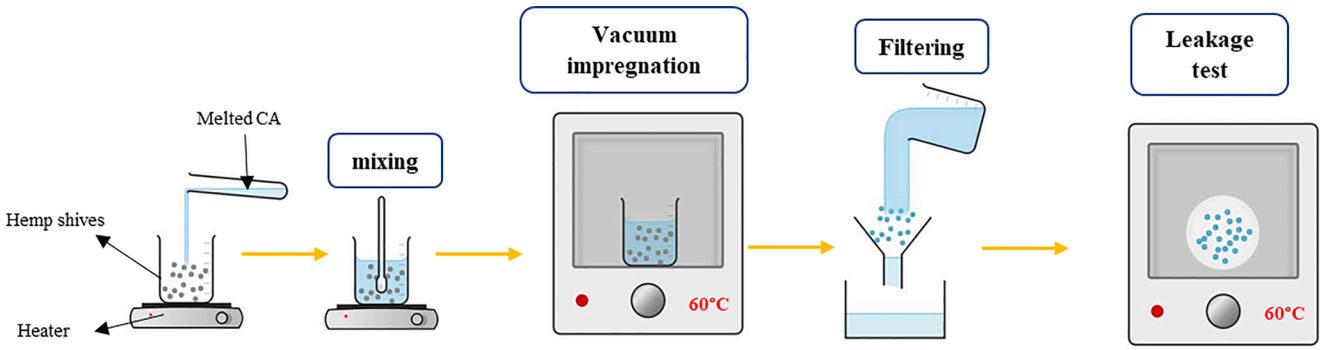

Fig. 1. Fabrication of the hemp shives/CA by vacuum impregnation method.

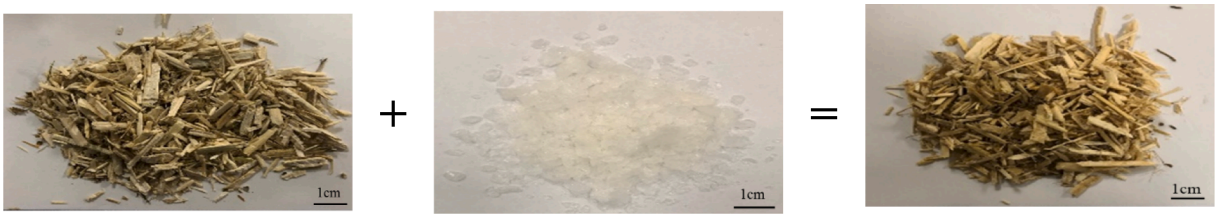

Fig. 2. Images of: (a) hemp shives, (b) CA and (c) form-stable hemp shives/CA composite.

Based on these recommendations, capric acid (CA), a fatty acid, supplied from Alfa Aesar with a purity of 99% has been chosen as PCM in this study. The general information of the CA are presented in Table 1.

2.1.2. Preparation of shape-stabilized hemp shives/CA composites

The hemp shives used in this study are the Chanvribat provided by Ecohabitat (Ecological Materials for Habitat) with an average density of about 100 kg/m^3. The choice of hemp shives is governed by their high porous structure with a total accessible porosity of 76.67% [36] which is suitable for impregnation process.

To fabricate the form stable hemp shives/CA composite, the vacuum impregnation technique has been used (Fig. 1).

Hemp shives (Fig. 2.a) are weighed (m_1) and mixed with the pre-weighed liquid CA (Fig. 2.b).

The mixture is put in a vacuum oven at a temperature superior to the melting temperature of the PCM (60 °C). The melted CA is absorbed in the pores of the hemp shives by capillarity and surface tension forces [37]. The quantity of liquid CA is chosen to recover the hemp shives in order to ensure effective impregnation. The mixture is kept alternatively under vacuum (100 mbar [38]) and non-vacuum conditions to push out the remaining air in the pores of the hemp shives and enhance the diffusion of CA. After the impregnation, the excess of liquid CA is removed by filtration. The impregnated hemp shives are placed on a filter paper and kept on the oven at 60 °C to remove the CA at the surface of the hemp shives. The filter paper was changed continually until no leakage was observed. The final mass of the composite (m_2) is weighed and the mass ratio of CA in the composite is calculated using equation (1) according to [37]. The final mass ratio without leakage is 53%. This value is comparable with the value reported in the literature for vegetable fibers: 52% for wood fibers/CA-SA [39], 43–54% for biochar/methylpalmitate [40] and 40.5% for kapok fibers/MA-TD (1-Tetradecanol) [38].

$$R = \frac{m_2 - m_1}{m_2} * 100 \quad (1)$$

2.1.3. Fabrication of hemp concrete PCM

The formulation, which will be used as reference concrete (REF) in the following, has been set in accordance with the professional rules for the execution of hemp products that were definitively validated in 2012. The formulation of hemp concrete consists in mixing 16% hemp shives, 34% tradical® PF40 used as a binder and 50% water.

The manufactured hemp concrete samples (PCM and REF) were conserved for four days in their moulds in a climatic chamber regulated at a temperature (T) of 20 °C and a relative humidity (RH) of 50%. Then, the moulds were disassembled to allow the drying of samples.

For each characterization, two different samples has been fabricated: one acting as a reference (without PCM) and the other one made of shape-stabilized hemp shives/CA with 53% of impregnation rate. Thus, two samples of each (with and without PCM) with dimensions of 15 × 15 × 5 cm^3, 10 × 10 × 6 cm^3, 5 × 5 × 5 cm^3 and 10 × 10 × 8 cm^3 are made for thermal conductivity, MBV and thermal performances test respectively.

2.2. Characterization

2.2.1. Morphology and micro-structure

The characterization of the morphology and the microstructure of the samples is essential to understand the impregnation mechanism. The microstructure of the CA, hemp shives and the shape-stabilized hemp shives/CA has been observed successively by scanning electron microscope (SEM) (QUANTA 200 Environmental Field Effect Gun apparatus, FEI, FRANCE) in the environmental mode. This mode avoids any previous treatment of the samples like gold deposit, which could considerably alter the observations. In addition, this mode is very adequate for non-conductive samples like hemp shives. The observations were performed at low pressure (typically 2 mbar), two different voltages (5 for CA and 15 KV for hemp shives) and at different magnifications (70, 500, 600, 2000 and 2400x).

2.2.2. Hygrothermal properties

2.2.2.1. Hygroscopic properties. The hygroscopic properties of the hemp concrete are investigated by measuring the Moisture Buffer Value (MBV). The moisture buffering is the ability to naturally regulate

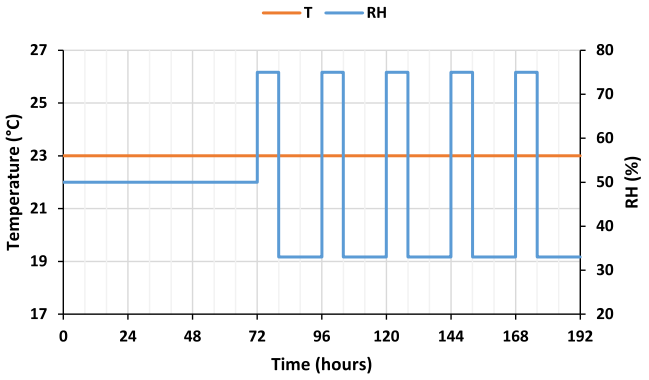

Fig. 3. Nordtest Project protocol for the measurement of the MBV.

relative humidity through their moisture capacity. Therefore, the MBV quantifies the amount of moisture that a material can store and release when it is subjected to cyclic variations of the surrounding relative humidity (RH) [41]. In this study, the measurement of the MBV has been performed according to the Nordtest Project protocol [42]. Based on this protocol, the hemp concrete samples of dimension 10 × 10 × 5 cm^3 are initially preconditioned at 50% RH and 23 °C, then exposed to cyclic step-changes in RH between high (75%) and low (33%) values for 8 and 16 h respectively (Fig. 3). The mass of the sample is recorded at each step and used to calculate the MBV according to equation (2):

$$MBV = \frac{\Delta m}{A^*(RH_{max} - RH_{min})} \quad (2)$$

Where MBV [g/(%RH.m^2)] is the Moisture Buffer Value, Δm [g] is the mass variation during the absorption/desorption phase, A [m^2] is the exposed sample surface area and RH_{max}, RH_{max}[%] is the maximum and minimum relative humidity applied during the humidification and drying cycle, respectively.

2.2.2.2. Thermal conductivity. Thermal conductivity of the hemp concrete is measured using the λ-Meter Ep500e® device based on the guarded hot plate method under stationary conditions at three different temperatures: 10, 23 and 40 °C according to the standard NFEN12664 [43] and NFEN12667 [44]. The dimensions of the hemp concrete samples are 15 × 15 × 5 cm^3 and the measurements are performed for both REF and PCM hemp concrete (Fig. 4). For each sample, the measurements are conducted three times to verify the repeatability. Since the measurement were conducted three times, the average thermal conductivity ($\bar{k}$) is used and the uncertainty is calculated by using the standard deviation (σ) expressed by the equation (3):

$$\sigma = \sqrt{\frac{\sum_{i=1}^{n}(k_i - \bar{k})^2}{n-1}} \quad (3)$$

where n is the number of measurement and $\bar{k}$ the average thermal conductivity.

2.2.2.3. Phase change properties and thermal stability. A DSC3+/TGA differential scanning calorimeter / thermo-gravimetric analyser device provided by METTLER TOLEDO is used to measure the heat flow released by the materials tested as well as the mass change during the tests. TGA is performed to verify the thermal stability of the composite-PCM in the building application temperature range. The long term stability of the composite will be investigated in a future work.

The DSC gives the melting/solidification temperatures and enthalpies of the different samples: CA and hemp shives/CA composites. The DSC was calibrated using four calibration standards (gold, zinc,

Table 2
Melting properties and specifications of the calibration standards, provided by METTLER TOLEDO. T: temperature, H_f: heat of fusion, ΔT_s: uncertainty on sample temperature, ΔT_r: uncertainty on reference temperature, ΔH_f: uncertainty on heat of fusion.

	Literature values		Standards specifications		
Material	T (°C)	$\Delta H_m (Jg^{-1})$	ΔT_s(°C)	ΔT_r(°C)	$\Delta(\Delta H_m)$(%)
Indium	156.6	28.45	1.5	2.5	15
Zinc	419.5	107.5	2	3	15
Aluminium	660.3	397	2.5	3.5	20
Gold	1064.2	63.7	3	4	20

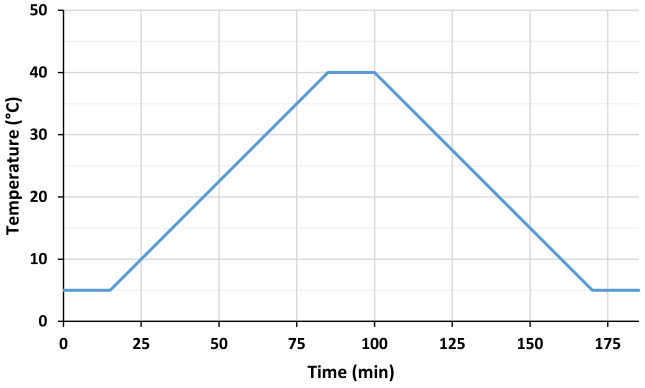

Fig. 5. Heating/cooling program for the DSC measurement.

Fig. 4. (a) REF and (b) PCM hemp concrete samples for the thermal conductivity measurement.

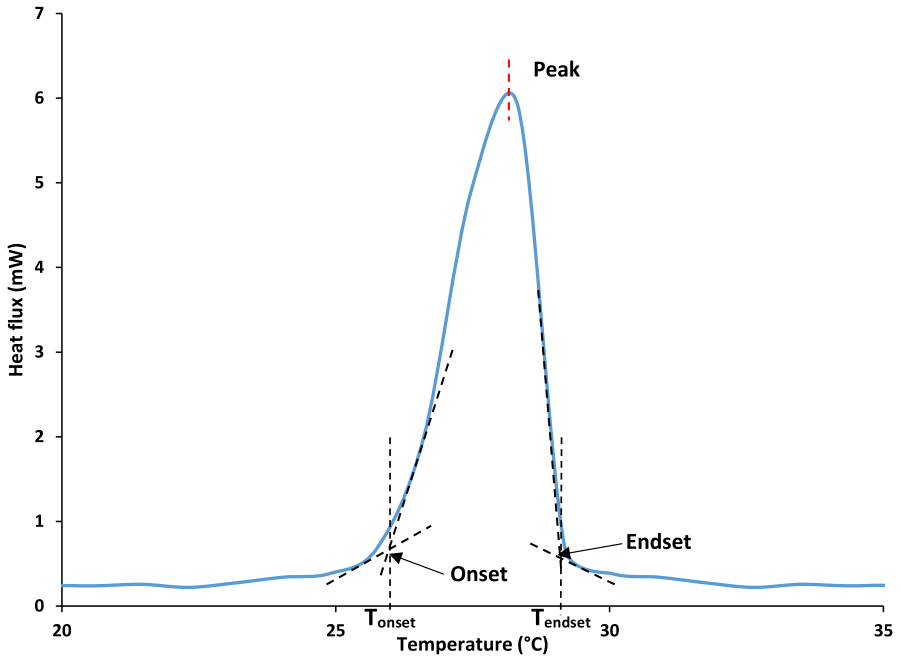

Fig. 6. Determination of the onset, endset and peak temperature for exothermic process DSC measurements.

Table 3
Temperature, heating rate and RH ranges of the climatic chamber.

Temperature range (°C)	Heating rate range (°C.min^{-1})	RH range (%)
−70 to 180	0.5 to 35	+10 to +90

aluminium and indium) to ensure precise certainty on the temperature range considered. The purity of all the calibration standards is about 99.999%. The melting properties and the uncertainty range of the calibration standards are presented in Table 2. Prior to the measurements, a blank run is performed to correct the baseline. The measurements are performed over a cycle with a heating/cooling rate of 0.5 °C.min^{-1} in a range of temperatures from 5 to 40 °C for the heating phase, and from 40 to 5 °C for the cooling phase (Fig. 5). The isothermal steps are hold for 15 min in order to avoid the thermal gradient inside the sample [45]. For each sample (CA and hemp shives), a mass between 5 and 20 mg is weighed and placed in 70 μL alumina crucibles. The experiment was carried out by purging the sample cell with Argon at a flow rate of 20 ml.min^{-1}.

The tests are repeated three times for each sample to ensure accuracy and calculate the standard deviation. The integrated software of METTLER TOLEDO is used to calculate the latent heats of fusion and solidification by numerical integration of the area under the peaks that represent the solid-liquid and the liquid-solid phase transitions. The onset temperature is chosen as melting temperature for the fusion peak whereas the endset is selected as solidification temperature for the crystallization peak (Fig. 6). These two values are chosen because they are not influenced by the heating rate unlike the peak temperature.

The thermogravimetric analysis (TGA) is performed simultaneously with DSC tests on the same device. TGA allows analysing the thermal stability of the composite in the building temperature's range by quantifying the mass variation of the material according to temperature. CA, hemp shives only and hemp shives/CA composites samples are

Fig. 7. REF and PCM hemp concrete samples for the thermal performances test and the position of the RH and T sensors.

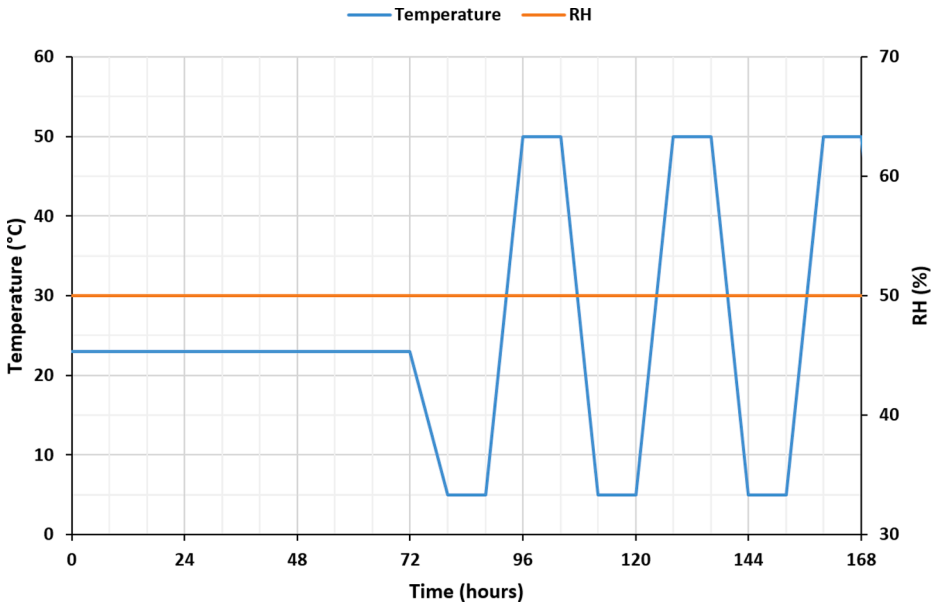

Fig. 8. Temperature program for the thermal performances test in the climatic chamber.

Table 4
Technical specifications of the RH and T sensors.

RH accuracy	±2%
T accuracy	−20 to 0 °C: ±0.4 °C; 0 to 70 °C: ±0.2 °C: 70 to 100 °C: ±0.6 °C
RH measurement range	0 to 100% RH
T measurement range	−20 to 100 °C
Maximum response time	10 s

analysed in a temperature range of 25–500 °C with a heating rate of 5 °C. min^{-1}. As for the DSC measurements, the tests are also repeated three times for each sample to verify repeatability and reproducibility.

2.2.3. Thermal performances

The thermal performances test are performed in a climatic chamber. This climatic chamber allows the regulation of the temperature and the RH in the working range specified in Table 3.

REF and PCM hemp concrete of dimension 10 × 10 × 8 cm^3 are placed in the climatic chamber and subjected to temperature variations between 5 and 50 °C at 50% of relative humidity. In order to ensure a unidirectional moisture flow from only one side of the cube, the tested samples are covered by aluminium foil on 5 sides (Fig. 7). As the targeted application is passive latent heat storage, diurnal temperature variation is applied. The latter means that the temperature varies between minimum and maximum values within 24 h (Fig. 8). Measurements are performed for 7 days, including a 3-day preconditioning at 23 °C and 50% relative humidity to ensure testing under fixed humidity conditions.

In order to record the temperature inside the hemp concrete, the temperature and RH sensors (Ahlborn FHA 646 R) are used and placed at three different positions (2.5, 5 and 7.5 cm) and at the same depth (5 cm) as presented in Fig. 7. The RH measurement circuit is capacitive, while an N-type thermistor is used to measure temperature. The advantages of these captors is their small size and the measurement of both temperature and RH. The sensors were pre-calibrated by the manufacturer. They are connected to the ALMEMO data acquisition system that records the data every minute. The technical specifications of the sensors are presented in Table 4.

3. Results and discussion

3.1. Characterization of form-stable hemp shives/CA composites

3.1.1. Morphology and microstructure

Fig. 9 and Fig. 11 shows the SEM images of pure CA (Fig. 9.(a,b)), melted and recrystallized CA (Fig. 9.(c,d)), hemp shives only (Fig. 11.a) and hemp shives/CA composite (Fig. 11.(b,c,d)) at different magnifications and voltage. For CA it was impossible to work at high voltage because the sample melts instantaneously. This phenomenon is inherent to the relative low melting temperature of CA (approximately 30 °C).

The pure CA presents a regular shaped-crystal structure as observed by [39] (Fig. 9.a). The size of the crystals is increased after melting and solidification and the structure is more regular, indeed, a paste-like texture is observed (Fig. 9.d). At first sight, we can notice that the melting/crystallization process increases the crystallinity of the capric acid. Morover, the CA was more electron conductor and easier to study by SEM due to increased crystallinity [46,47]. The energy dispersive spectroscopy (EDS) spectra obtained for CA (Fig. 10) is in adequation with the results based on the chemical composition of CA. From the EDS spectrum of CA, we observed that the mass fraction of O is 19.8% against 80.1% for C and H. It should be recalled that EDS does not detect the transitions of H and their contribution is reported in that of C.

The cross section images of the pure hemp shives (Fig. 9.a) shows a very porous structure. As stated in the literature, the pores are approximately 50–80 μm in diameter and are surrounded by relatively thick cell walls which are mainly composed of cellulose, hemicellulose, lignin and pectin [36]. Fig. 11.(b,c,d) show the form stable hem shives/CA and that the pores of the hemp shives are successfully occupied by CA after the vacuum impregnation process by means of physical absorption. The CA is trapped without leakage in the microstructure of hemp shives thanks to hydrogen bond attraction, capillary and surface tension forces [39].

3.1.2. Phase change and thermal properties

3.1.2.1. DSC. DSC is used to measure thermal energy storage capacity through investigation of the melting/solidification properties of the prepared PCM composite. Fig. 12 shows the DSC curve of the CA, hemp shives and hemp shives/CA composite. The melting and solidification temperatures and the enthalpies of the different materials are presented

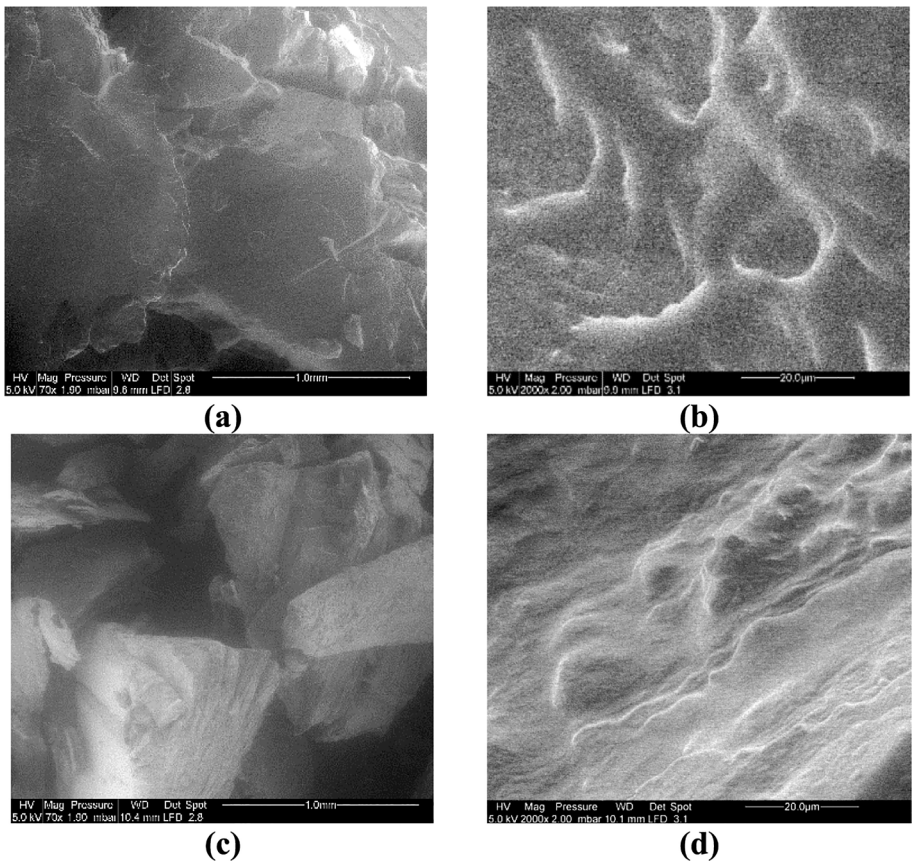

Fig. 9. SEM images of: (a,b) pure CA, (c,d) melted and recrystallized CA at 70 and 2000x magnifications.

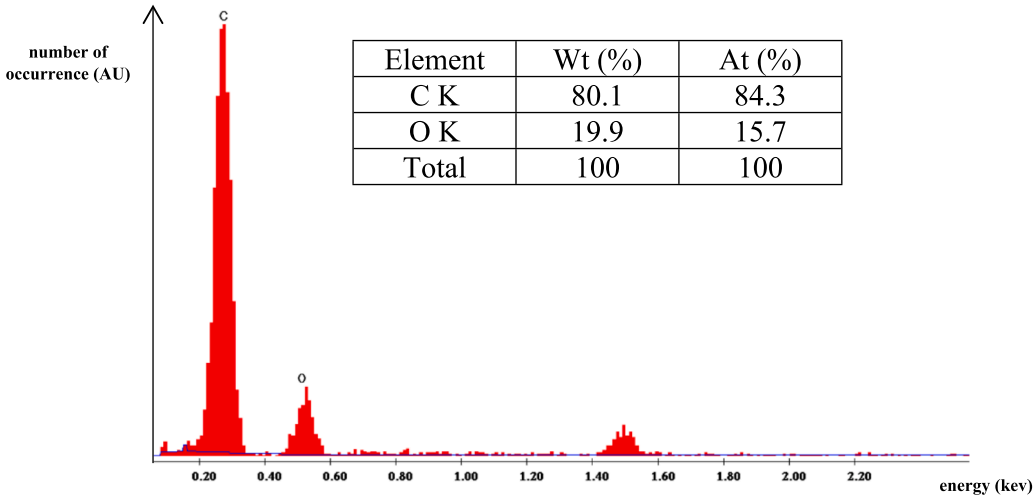

Element	Wt (%)	At (%)
C K	80.1	84.3
O K	19.9	15.7
Total	100	100

Fig. 10. EDS spectra and composition of CA.

in Table 5 with the uncertainty associated. As mentioned in section 2.2, the onset temperature is chosen for endothermic processes whereas the endset temperature is used for exothermic processes. The melting and solidification temperatures of CA and hemp shives/CA composite were obtained as 29.8 ± 0.1 °C and 25 ± 1 °C, 28.9 ± 0.4 °C and 23 ± 1 °C, respectively. The enthalpies of melting and solidification were calculated as 140.7 ± 3.1 and 135.6 ± 2.6 J.g^{-1}, 78.7 ± 4.6 and 76.4 ± 3.1 J.g^{-1}, respectively.

As can be seen, the measured melting and solidification temperatures and enthalpies for CA are consistent with the values provided by the literature [24]. Both melting/solidification enthalpies are reduced after the fabrication of the shape-stabilized hemp shives/CA composite. This reduction is caused by the reduction of the mass ratio of CA in the composite and the reduction of the crystallinity of the CA. Additionally, the melting/solidification temperatures are lower compared to pure CA before impregnation. This decrease in phase change temperatures can be due to weak attractive interaction between fatty acid molecules and inner surface wall of the porous material [25].

The measured latent heats of melting and solidification of the composite PCMs were close to the values calculated by multiplying the mass

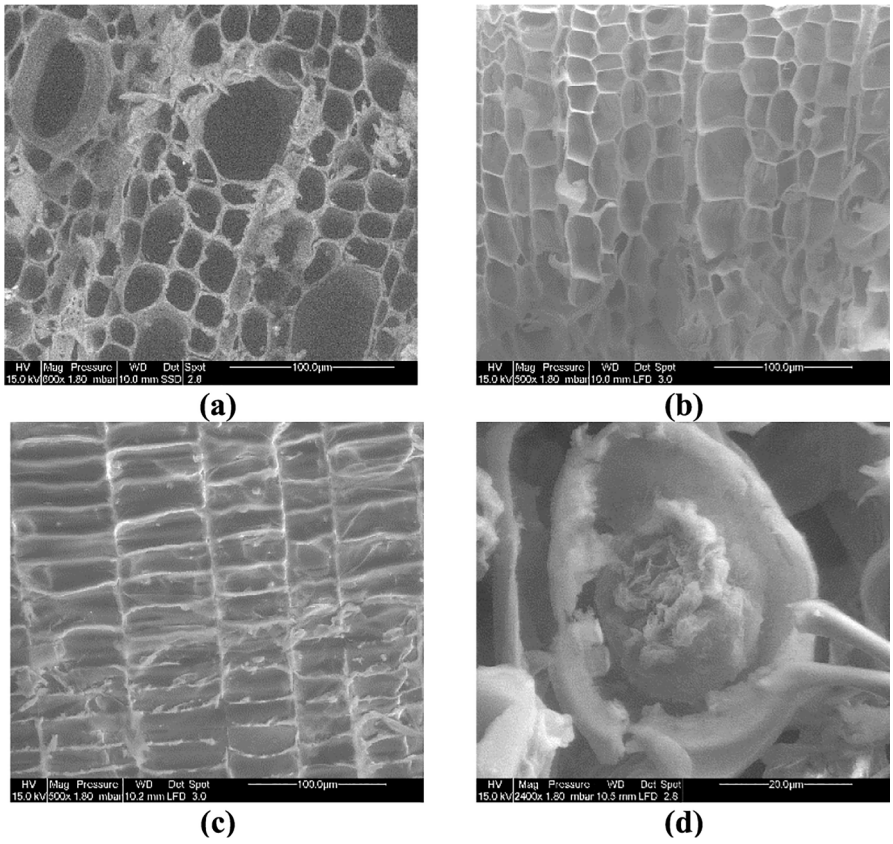

Fig. 11. SEM images of: (a) hemp shives, (b,c,d) form stable hemp shives/CA at respectively 500x and 2400x magnifications.

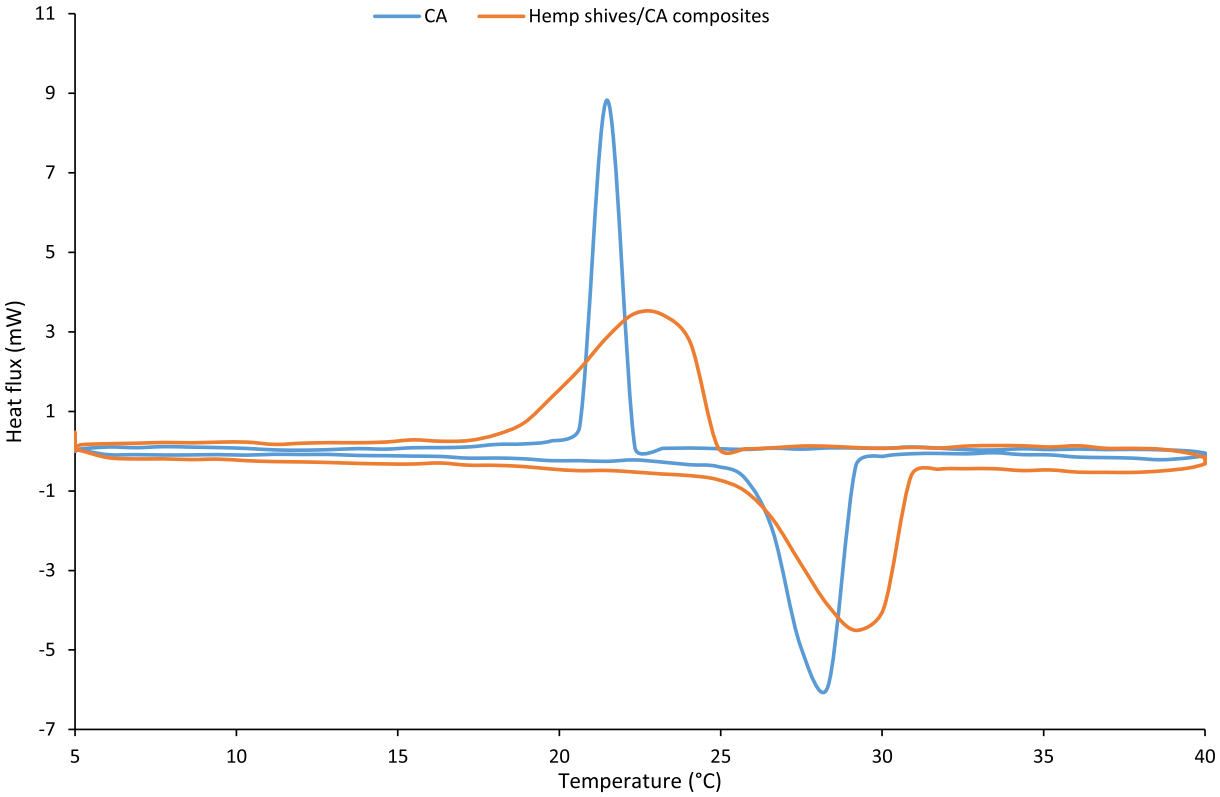

Fig. 12. DSC curves of CA, hemp shives only and hemp shives/CA composite.

Table 5
Melting/solidification temperatures and enthalpies of CA and hemp shives/CA composite.

Samples	Melting process			Solidification process		
	T_m(°C)	T_{peak}(°C)	ΔH_m(J.g^{-1})	T_s(°C)	T_{peak}(°C)	ΔH_s(J.g^{-1})
CA	29.8 ± 0.1	30.4 ± 0.1	140.7 ± 3.1	25 ± 1	26.8 ± 0.9	135.6 ± 2.6
Hemp shives/CA	28.9 ± 0.4	31.6 ± 0.2	78.7 ± 4.6	23 ± 1	27.3 ± 0.4	76.4 ± 3.1

ratio of the CA in the composites, and their phase change enthalpies as stated by [48]. In fact, the ratio of the heat of fusion of pure CA and hemp shives/CA is 56% that is very close to the theoretical value of the impregnation rate (53%).

Although the latent heats of the prepared hemp shives/CA composite decreased significantly due to shape stabilization, these latent heat values are still very promising for energy storage in buildings compared to shape-stabilized PCMs studied by other references, as listed in Table 6.

3.1.2.2. TGA/DTG. TGA/DTG is essential in order to ensure the stability of the materials on the temperature range of buildings. The TGA measures mass changes in a material as a function of temperature (or time) under a controlled atmosphere. The first derivative of the TGA curve (the DTG curve) helps to determine inflection points, useful for further interpretation as well as for differential thermal analysis. Fig. 13 and Fig. 14 show respectively the weight loss and derivated thermogravimetry (DTG) curve of CA, hemp shives only and hemp shives/CA form-stable composite from room temperature (25 °C) to 500 °C.

From the different curves, it can be seen that CA is mainly degraded between 150 and 240 °C with degradation starting at around 125 °C. This observation is in adequation with the results obtained by Kar et al. [51].

Concerning hemp shives only, the DTG curve shows a first peak between 50 and 150 °C attributed to the evaporation of free water in the hemp shives. A second degradation shoulder peak at about 250–335 °C is attributed to thermal depolymerisation of hemicelluloses or pectin. The final decomposition peak occurring between 300 and 380 °C is attributed to the decomposition of cellulose [52].

The TGA curve of the form stable hemp shives/CA is a superposition of the weight loss curve of CA and hemp shives. The same phenomena are observed at the same temperature. From the DTG curve that allows detecting the temperature at which transformations occur, it is found that the form stable composite exhibits good thermal stability under 170 °C with less than 10% of mass loss making it suitable for building application for which the temperature rarely exceeds 60 °C. TGA is also a way to obtain the impregnation rate of the hemp shives/composite and correct the theoretical value if needed. From the TGA curve, the impregnation rate is approximately 53.97%, which is in accordance with the theoretical value found (53%). The discrepancies are explained by the statistical behaviour of the impregnation process (all the particles will not absorb the same amount of CA) and the error induced by the sampling.

3.2. Hygrothermal properties of hemp concrete PCM

3.2.1. Thermal conductivity

Thermal conductivity is one of the key parameters that is considered in the selection of materials for building application. Thermal conductivity measures the rate at which temperature gradient transmits through a material. It allows classifying materials as isulators or conductors and thus to select a material for a specific application. The results of the thermal conductivity of REF and PCM hemp concrete composite and the uncertainty associated are presented at three

Table 6
Comparison of the phase change properties of the prepared hemp shives/CA composite with that of some bio-based PCM composites.

PCM composites	Melting temperature (°C)	Solidification temperature (°C)	Heat of fusion (J.g^{-1})	Heat of solidification (J.g^{-1})	Reference
Wood flour/paraffin	26.18	–	20.62	–	[49]
Wood flour/CA-PA	22.03	20.06	28.16	29.77	[50]
Wood fiber/CA-SA	23.38	21.87	92.1	91.9	[39]
Kapok fibers/MA-TD	24–42.3	10.5–29.7	76.8	77.4	[38]
Hemp shives/CA	**28.9 ± 0.4**	**23 ± 1**	**78.7 ± 4.6**	**76.4 ± 3.1**	**This study**

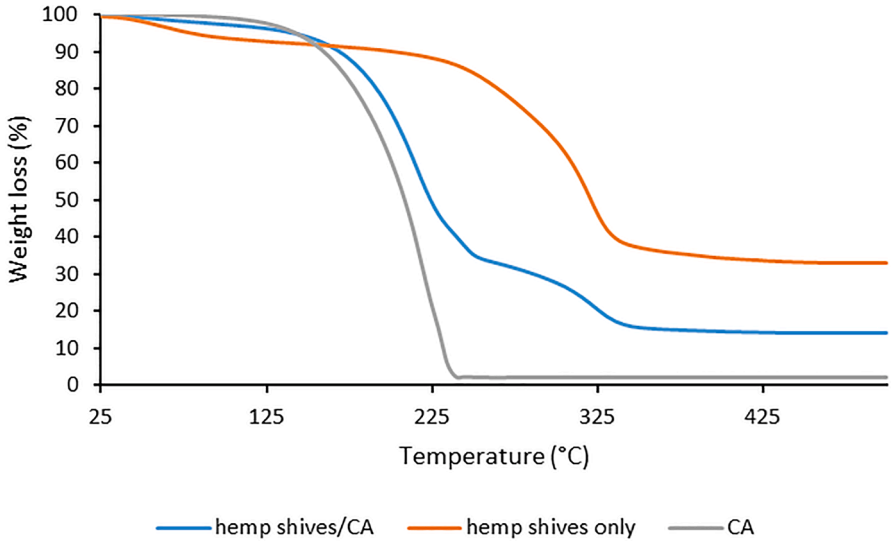

Fig. 13. TGA curves of CA, hemp shives only and the fabricated form stable hemp shives/CA.

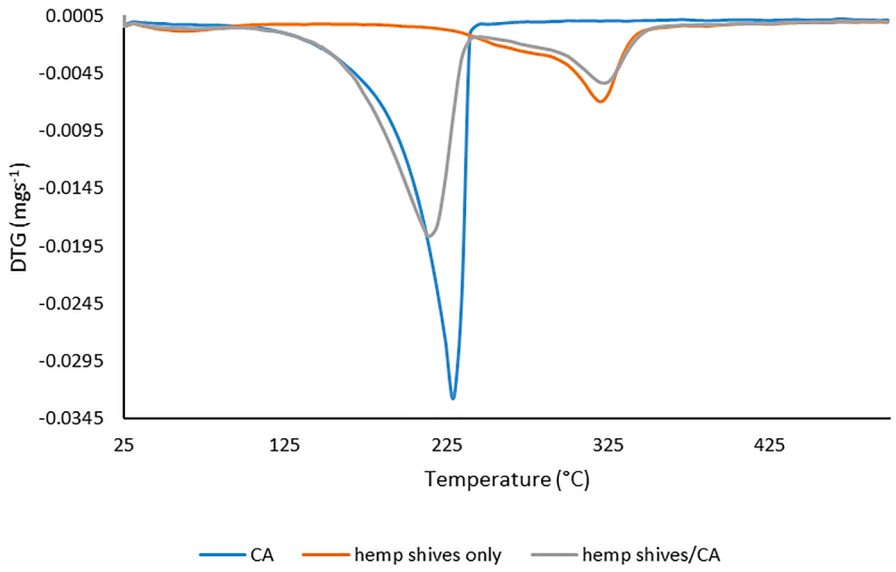

Fig. 14. DTG curves of CA, hemp shives only and the fabricated form stable hemp shives/CA.

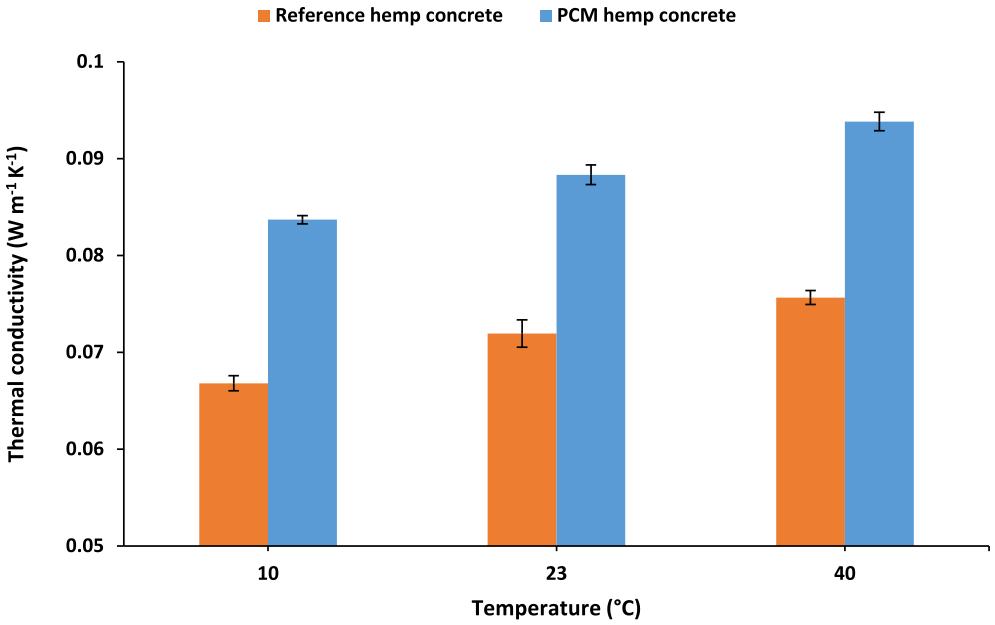

Fig. 15. Thermal conductivity of reference and PCM hemp concrete at 10, 23 and 40 °C.

different temperatures (10, 23 and 40 °C) in Fig. 15. For each sample, the thermal conductivity was 0.084, 0.088 and 0.094 $Wm^{-1}K^{-1}$ for PCM hemp concrete compared to 0.066, 0.07 and 0.075 $Wm^{-1}K^{-1}$ for the REF at 10, 23 and 40 °C respectively. According to Arnaud et al. [53], the thermal conductivity of hemp concrete varies between 0.06 and 0.18 $Wm^{-1}K^{-1}$ for a dry density ranging from 200 to 800 $kg.m^{-3}$, which is in accordance with the values measured in this study.

As noted, the thermal conductivity of hemp concrete increases with the addition of CA. Indeed, increases in thermal conductivity of 27%, 26% and 25% are observed for PCM hemp concrete compared to REF at 10, 23 and 40 °C respectively. This result was expected according to the literature of shape-stabilized PCMs where the thermal conductivity of the porous support is enhanced by the impregnation with PCMs [7,19,54-56]. The thermal conductivity of the composite PCM is higher than that of the corresponding support matrix, because CA has replaced air in the hemp shives/CA composites. The thermal conductivity of CA (about 0.21 $Wm^{-1}K^{-1}$ at ambient temperature [24]) is 10 times higher than that of air (about 0.02 $Wm^{-1}K^{-1}$).

3.2.2. *MBV*

MBV is used to estimate the dynamic hygrothermal behavior of the material when exposed to an indoor environment. It indicates the average amount of water that is exchanged by sorption or desorption when the material surfaces are subjected to relative humidity variations over a given time. The MBV values were calculated as 3.05 ± 0.34 and 2.23 ± 0.23 $g.m^{-2}.\%RH^{-1}$ for REF and PCM hemp concrete respectively, according to the Nordtest program protocol. The MBV of REF is in agreement with the results of [57] where the average MBV for a hemp concrete varied between 1.82 $g.m^{-2}.\%RH^{-1}$ and 3.02 $g.m^{-2}.\%RH^{-1}$. The results show a reduction of the MBV with the incorporation of the PCM. This is due to the reduction of the absorption of the hemp shives with the incorporation of the PCM. Despite the decrease in the MBV, both REF and PCM hemp concrete are classified as excellent humidity regulator regarding the classification of Nordtest Project (Fig. 16).

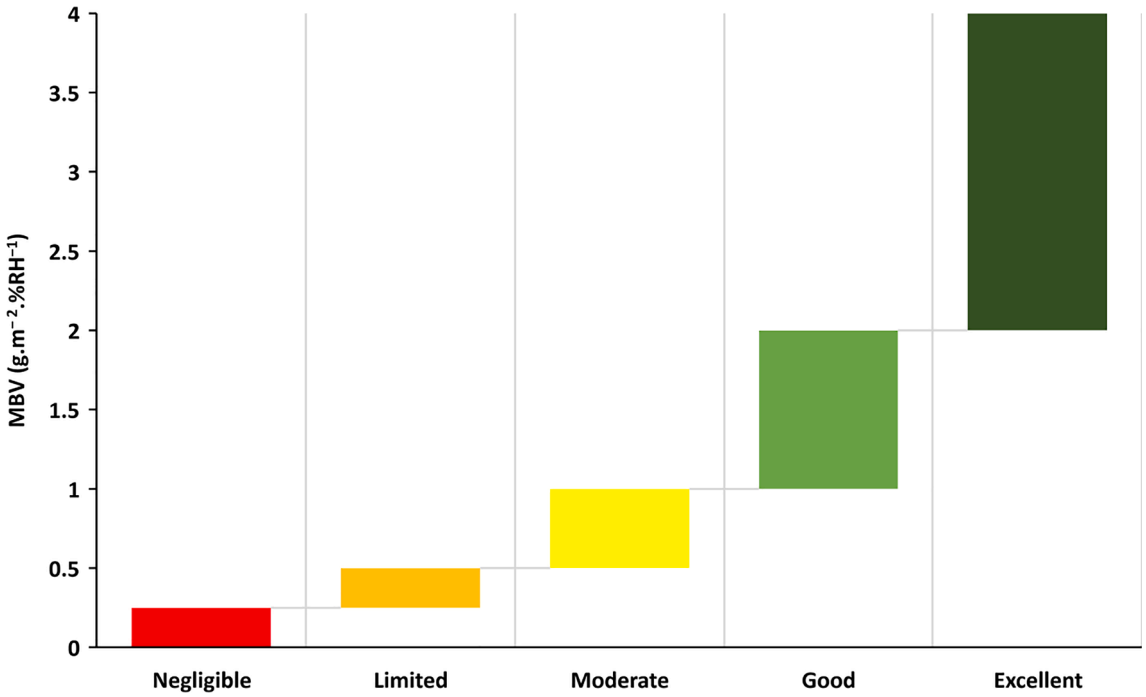

Fig. 16. Classification of the MBV according to Nordtest project.

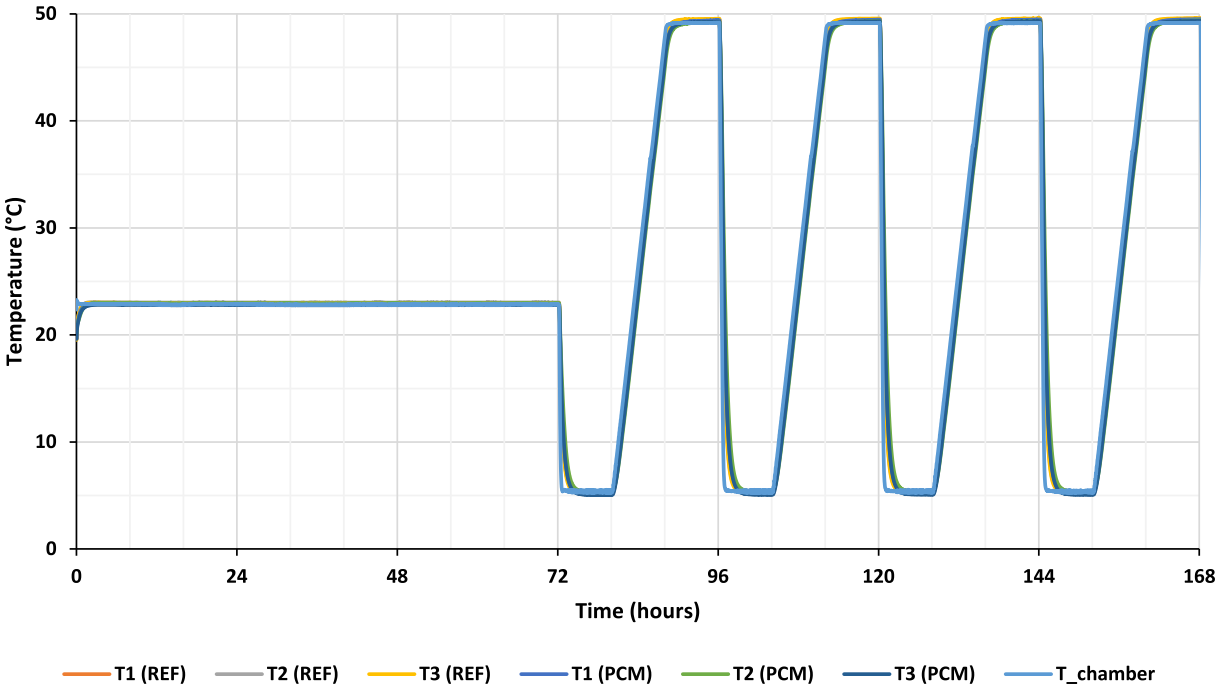

Fig. 17. Evolution of the temperature of the reference and PCM hemp concrete for the different T sensors.

3.3. Thermal performances of hemp concrete PCM

The thermal performances of REF and PCM hemp concrete submitted to cyclic temperature variations between 5 and 50 °C have been investigated in a climatic chamber for 7 days. Fig. 17 shows the temperature evolution in REF and PCM hemp concrete composite as well as the temperature in the climatic chamber. It can be seen that the temperature recorded by the three sensors in each sample are almost identical. The standard deviation is about 0.1 °C and 0.2 °C for REF and PCM hemp concrete, which is in the uncertainty range of the sensor (0.2 °C).

Fig. 18 shows the evolution of the average temperature of the three sensors placed in each sample (REF and PCM hemp concrete) over a 24-hour cycle. Three phases can be distinguished: an ascending phase, a stabilization phase and a descending phase. During the ascending phase, the temperature of the PCM hemp concrete is slightly lower than for REF. The trend is reversed during the descending phase over which the temperature of the PCM hemp concrete remains slightly higher than REF. This difference is explained by the LHTES effect of PCM hemp concrete as well as the sensible heat absorption that delays the increase or decrease in the temperature in the sample [58].

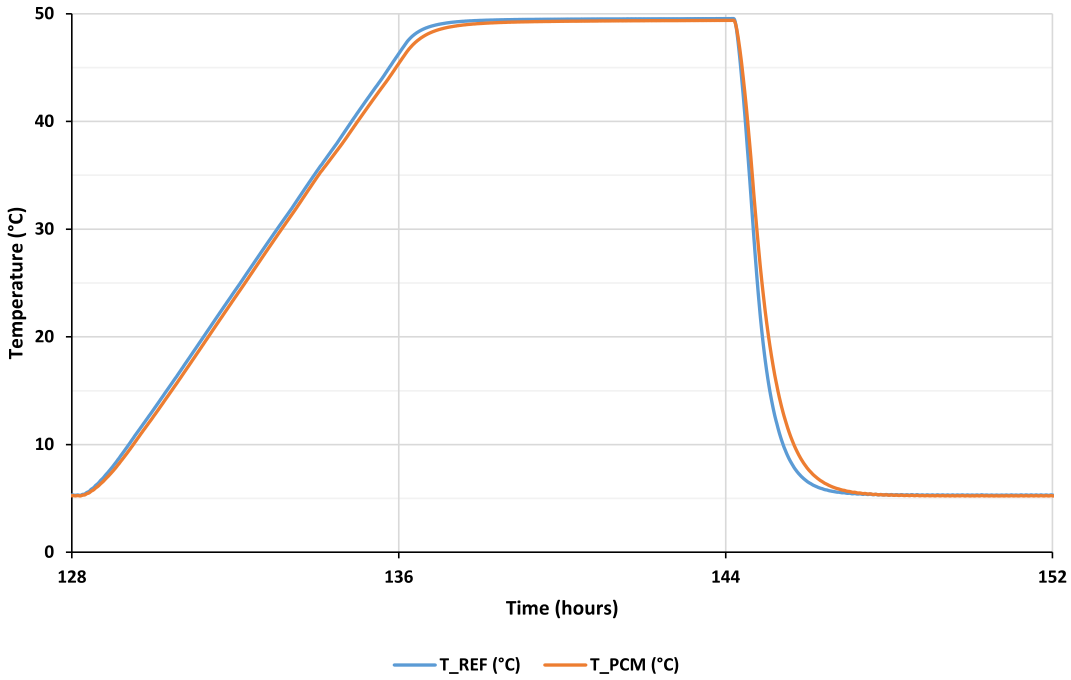

Fig. 18. Evolution of the aerage temperature of the reference and PCM hemp concrete within a 24-hour cycle.

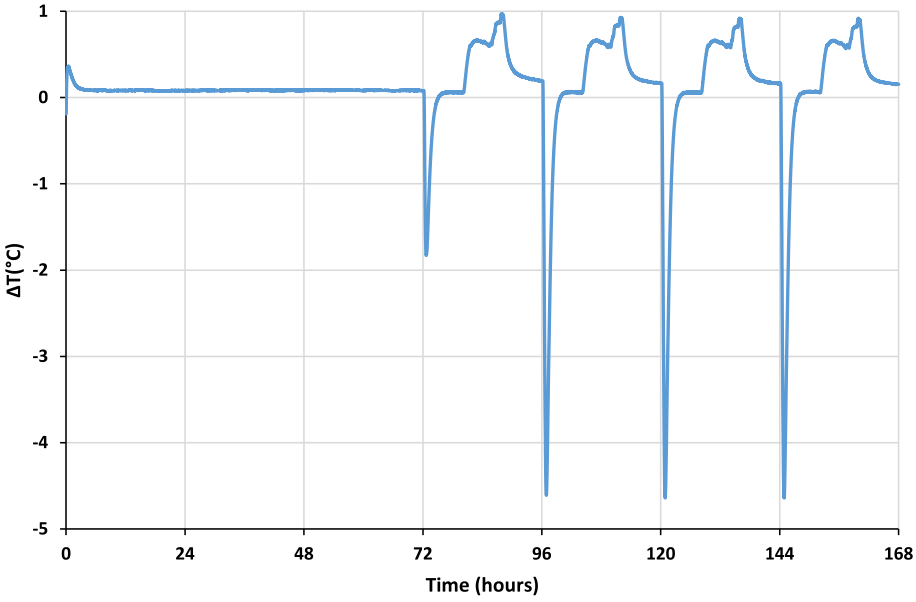

Fig. 19. Evolution of the temperature difference between the reference and PCM hemp concrete.

To further quantify the temperature difference between REF and the PCM hemp concrete, we have plotted the evolution of the temperature difference (ΔT) between REF and PCM hemp concrete over time (Fig. 19). The maximum difference is about 1 °C during the heating phase against 4.6 °C for the cooling phase. The difference for the cooling phase is particularly pronounced in the temperature range 5–30 °C. This result indicates that the PCM hemp concrete is more efficient during cooling periods. This is due to the fact that PCM discharges and releases its latent heat stored during heating periods inside the PCM hemp concrete sample preventing the temperature of the hemp concrete to drop immediately. The maximum time shift for the heating and the cooling period are 30 min and 20 min, respectively. These experimental results showed the good thermoregulation capacity of the PCM hemp concrete.

4. Conclusion

This study investigated the hygrothermal performances of a novel PCM hemp concrete for passive thermal energy storage in buildings. CA for his suitable melting properties and renewable origin has been used to fabricate shape-stabilized hemp shives/CA composite using vacuum impregnation technique. The principal findings of this study are presented as follow:

- CA was successfully impregnated in hemp shives with 53% incorporation rate without any leakage. This observation was confirmed by SEM results, which showed that the CA was efficiently retained in the porous structure of the hemp shives.

- DSC results showed that the hemp shives PCM composite possess promising melting and solidification properties. The melting and solidification temperatures of CA and hemp shives/CA composite were obtained as 29.8 °C and 25 °C, 28.9 °C and 23 ± 1 °C, respectively. The enthalpies of melting and solidification were calculated as 140.7 and 135.6 J.g^{-1}, 78.7 and 76.4 J.g^{-1}, respectively. These results indicated a reduction of the latent heat of the PCM composite compared to the pure PCM. However, these values are still very promising for energy storage in buildings compared to shape-stabilized PCMs studied by other references. The TGA/dTG results indicated that the form stable composite exhibits promising thermal stability under 170 °C making it suitable for building application.
- The shape-stabilized hemp shives/CA composite is used to fabricate PCM hemp concrete. The hygrothermal properties of the PCM hemp concrete are assessed and compared to REF. The thermal conductivity measurement conducted at three temperatures (10, 23, 40 °C) indicated an increase in the thermal conductivity (of about 25.7% at 23 °C) of the PCM hemp concrete compared to REF.
- The moisture buffer value (MBV) is defined as the capacity of the material to regulate the humidity. The MBV of the PCM hemp concrete and REF are measured following the Nordtest protocol. The MBV values were 3.05 and 2.23 g.m^{-2}.%RH^{-1} for REF and the PCM hemp concrete respectively which allow classifying them as excellent humidity regulator regarding the classification of Nordtest Project.
- The thermal performances test conducted in a climatic chamber showed that the PCM hemp concrete present promising thermoregulation capacity. The maximum temperature difference between REF and PCM hemp concrete and time shift were about 1 °C and 30 min during the heating phase against 4.6 °C and 20 min for the cooling phase.

Further study should be conducted to determine the long-term stability and cyclability of the hemp shives/CA and the PCM hemp concrete. Different temperature programs with realistic weather can be tested in order to investigate the behaviour of the PCM hemp concrete under various conditions. Finally, a real scale-cycling thermal performance at the building envelope scale should be also investigated.

CRediT authorship contribution statement

Mohamed Sawadogo: Conceptualization, Methodology, Formal analysis, Investigation, Resources, Data curation, Writing – original draft, Writing – review & editing, Visualization. **Ferhat Benmahiddine:** Conceptualization, Methodology, Formal analysis, Investigation, Resources, Data curation, Writing – review & editing, Visualization. **Ameur El Amine Hamami:** Conceptualization, Methodology, Formal analysis, Investigation, Resources, Data curation, Writing – review & editing, Visualization, Supervision. **Rafik Belarbi:** Conceptualization, Methodology, Formal analysis, Investigation, Resources, Data curation, Writing – review & editing, Visualization, Supervision, Project administration, Funding acquisition. **Alexandre Godin:** Conceptualization, Methodology, Formal analysis, Investigation, Resources, Data curation, Writing – review & editing, Visualization. **Marie Duquesne:** Conceptualization, Methodology, Formal analysis, Investigation, Resources, Data curation, Writing – review & editing, Visualization, Supervision, Project administration, Funding acquisition.

Declaration of Competing Interest

The authors declare that they have no known competing financial interests or personal relationships that could have appeared to influence the work reported in this paper.

Acknowledgments

The authors are grateful to the Region Nouvelle Aquitaine for subsidizing BioMCP project (Project-2017-1R10209-13023) and Energy saving certificate program of the Ministry of Ecological and Solidarity Transition 'SmartReno support'' 2019–2021. The authors would like also to thank Dr. Egle CONFORTO, responsible of the electron microscopy platform of the LaSIE laboratory of La Rochelle University for the technical assistance in SEM acquisition.

References

[1] Buildings – Topics, IEA. (n.d.). https://www.iea.org/topics/buildings (accessed April 30, 2021).
[2] V. Masson-Delmotte, P. Zhai, A. Pirani, S.L. Connors, C. Péan, S. Berger, N. Caud, Y. Chen, L. Goldfarb, M.I. Gomis, M. Huang, K. Leitzell, E. Lonnoy, J.B.R. Matthews, T.K. Maycock, T. Waterfield, Ö. Yelekçi, R. Yu, B. Zhou (Eds.), Climate Change 2021: The Physical Science Basis. Contribution of Working Group I to the Sixth Assessment Report of the Intergovernmental Panel on Climate Change, Cambridge University Press, 2021.
[3] V. Basecq, G. Michaux, P. Blondeau, C. Inard, Short term storage systems of the thermal energy for buildings: a review, accessed May 5, 2021, Adv. Build. Energy Res. 7 (2013) 66–119, https://hal.archives-ouvertes.fr/hal-01052828.
[4] K. Sergei, C. Shen, Y. Jiang, A review of the current work potential of a trombe wall, Renew. Sustain. Energy Rev. 130 (2020) 109947, https://doi.org/10.1016/j.rser.2020.109947.
[5] M.M. Farid, A.M. Khudhair, S.A.K. Razack, S. Al-Hallaj, A review on phase change energy storage: Materials and applications, Energy Convers. Manage. 45 (2004) 1597–1615, https://doi.org/10.1016/j.enconman.2003.09.015.
[6] M. Jafaripour, S.M. Sadrameli, H. Pahlavanzadeh, S.A.H.S. Mousavi, Fabrication and optimization of kaolin/stearic acid composite as a form-stable phase change material for application in the thermal energy storage systems, J. Storage Mater. 33 (2021) 102155, https://doi.org/10.1016/j.est.2020.102155.
[7] P.K.S. Rathore, S.K. Shukla, Enhanced thermophysical properties of organic PCM through shape stabilization for thermal energy storage in buildings: A state of the art review, Energy Build. 236 (2021) 110799, https://doi.org/10.1016/j.enbuild.2021.110799.
[8] S.R.L. da Cunha, J.L.B. de Aguiar, Phase change materials and energy efficiency of buildings: A review of knowledge, J. Storage Mater. 27 (2020) 101083, https://doi.org/10.1016/j.est.2019.101083.
[9] R. Baetens, B.P. Jelle, A. Gustavsen, Phase change materials for building applications: A state-of-the-art review, Energy Build. 42 (2010) 1361–1368, https://doi.org/10.1016/j.enbuild.2010.03.026.
[10] B. Lamrani, K. Johannes, F. Kuznik, Phase change materials integrated into building walls: An updated review, Renew. Sustain. Energy Rev. 140 (2021) 110751, https://doi.org/10.1016/j.rser.2021.110751.
[11] T. Silva, R. Vicente, F. Rodrigues, A. Samagaio, C. Cardoso, Performance of a window shutter with phase change material under summer Mediterranean climate conditions, Appl. Therm. Eng. 84 (2015) 246–256, https://doi.org/10.1016/j.applthermaleng.2015.03.059.
[12] K.O. Lee, M.A. Medina, X. Sun, X. Jin, Thermal performance of phase change materials (PCM)-enhanced cellulose insulation in passive solar residential building walls, Sol. Energy 163 (2018) 113–121, https://doi.org/10.1016/j.solener.2018.01.086.
[13] U. Berardi, S. Soudian, Experimental investigation of latent heat thermal energy storage using PCMs with different melting temperatures for building retrofit, Energy Build. 185 (2019) 180–195, https://doi.org/10.1016/j.enbuild.2018.12.016.
[14] J. Yu, Q. Yang, H. Ye, Y. Luo, J. Huang, X. Xu, W. Gang, J. Wang, Thermal performance evaluation and optimal design of building roof with outer-layer shape-stabilized PCM, Renewable Energy 145 (2020) 2538–2549, https://doi.org/10.1016/j.renene.2019.08.026.
[15] A.A.A.A. Al-Rashed, A.A. Alnaqi, J. Alsarraf, Energy-saving of building envelope using passive PCM technique: A case study of Kuwait City climate conditions, Sustainable Energy Technol. Assess. 46 (2021) 101254, https://doi.org/10.1016/j.seta.2021.101254.
[16] E. Meng, H. Yu, B. Zhou, Study of the thermal behavior of the composite phase change material (PCM) room in summer and winter, Appl. Therm. Eng. 126 (2017) 212–225, https://doi.org/10.1016/j.applthermaleng.2017.07.110.
[17] H. Akeiber, P. Nejat, M.Z. Abd, M.A. Majid, F. Wahid, I.Z. Jomehzadeh, J. K. Famileh, B.R. Calautit, S.A.Z. Hughes, A review on phase change material (PCM) for sustainable passive cooling in building envelopes, Renew. Sustain. Energy Rev. 60 (2016) 1470–1497, https://doi.org/10.1016/j.rser.2016.03.036.
[18] S. Ali Memon, T. Yiu Lo, X. Shi, S. Barbhuiya, H. Cui, Preparation, characterization and thermal properties of Lauryl alcohol/Kaolin as novel form-stable composite phase change material for thermal energy storage in buildings, Appl. Therm. Eng. 59 (2013) 336–347, https://doi.org/10.1016/j.applthermaleng.2013.05.015.
[19] M.M. Umair, Y. Zhang, K. Iqbal, S. Zhang, B. Tang, Novel strategies and supporting materials applied to shape-stabilize organic phase change materials for thermal energy storage–A review, Appl. Energy 235 (2019) 846–873, https://doi.org/10.1016/j.apenergy.2018.11.017.

[20] M. Sawadogo, M. Duquesne, R. Belarbi, A.E.A. Hamami, A. Godin, Review on the Integration of Phase Change Materials in Building Envelopes for Passive Latent Heat Storage, Appl. Sci. 11 (2021) 9305, https://doi.org/10.3390/app11199305.
[21] A. Abhat, Low temperature latent heat thermal energy storage: Heat storage materials, Sol. Energy 30 (1983) 313–332, https://doi.org/10.1016/0038-092X(83)90186-X.
[22] D. Feldman, M.M. Shapiro, D. Banu, C.J. Fuks, Fatty acids and their mixtures as phase-change materials for thermal energy storage, Sol. Energy Mater. 18 (1989) 201–216, https://doi.org/10.1016/0165-1633(89)90054-3.
[23] J. Liang, L. Zhimeng, Y. Ye, W. Yanjun, L. Jingxin, Z. Changlin, Fabrication and characterization of fatty acid/wood-flour composites as novel form-stable phase change materials for thermal energy storage, Energy Build. 171 (2018) 88–99, https://doi.org/10.1016/j.enbuild.2018.04.044.
[24] M. Duquesne, C. Mailhé, S. Doppiu, J.-L. Dauvergne, S. Santos-Moreno, A. Godin, G. Fleury, F. Rouault, E. Palomo del Barrio, Characterization of Fatty Acids as Biobased Organic Materials for Latent Heat Storage, Materials 14 (2021) 4707, https://doi.org/10.3390/ma14164707.
[25] A. Karaipekli, A. Sarı, Preparation, thermal properties and thermal reliability of eutectic mixtures of fatty acids/expanded vermiculite as novel form-stable composites for energy storage, J. Ind. Eng. Chem. 16 (2010) 767–773, https://doi.org/10.1016/j.jiec.2010.07.003.
[26] S. Ben Romdhane, A. Amamou, R. Ben Khalifa, N.M. Saïd, Z. Younsi, A. Jemni, A review on thermal energy storage using phase change materials in passive building applications, J. Build. Eng. 32 (2020) 101563, https://doi.org/10.1016/j.jobe.2020.101563.
[27] L. Boussaba, A. Foufa, S. Makhlouf, G. Lefebvre, L. Royon, Elaboration and properties of a composite bio-based PCM for an application in building envelopes, Constr. Build. Mater. 185 (2018) 156–165, https://doi.org/10.1016/j.conbuildmat.2018.07.098.
[28] M. Duquesne, C. Mailhé, K. Ruiz-Onofre, F. Achchaq, Biosourced organic materials for latent heat storage: An economic and eco-friendly alternative, Energy. 188 (2019) 116067, https://doi.org/10.1016/j.energy.2019.116067.
[29] H. Ke, Phase diagrams, eutectic mass ratios and thermal energy storage properties of multiple fatty acid eutectics as novel solid-liquid phase change materials for storage and retrieval of thermal energy, Appl. Therm. Eng. 113 (2017) 1319–1331, https://doi.org/10.1016/j.applthermaleng.2016.11.158.
[30] F. Benmahiddine, R. Cherif, F. Bennai, R. Belarbi, A. Tahakourt, K. Abahri, Effect of flax shives content and size on the hygrothermal and mechanical properties of flax concrete, Constr. Build. Mater. 262 (2020) 120077, https://doi.org/10.1016/j.conbuildmat.2020.120077.
[31] G. Delannoy, S. Marceau, P. Glé, E. Gourlay, M. Guéguen-Minerbe, D. Diafi, I. Nour, S. Amziane, F. Farcas, Aging of hemp shiv used for concrete, Mater. Des. 160 (2018) 752–762, https://doi.org/10.1016/j.matdes.2018.10.016.
[32] B. Seng, S. Lorente, C. Magniont, Scale analysis of heat and moisture transfer through bio-based materials — Application to hemp concrete, Energy Build. 155 (2017) 546–558, https://doi.org/10.1016/j.enbuild.2017.09.026.
[33] K. Abahri, C. El Hachem, F. Bennai, N. Toan, R. Belarbi, Prediction of hemp concrete morphological deformation by X-ray tomography, 2017, pp. 616–625.
[34] J. Schröder, K. Gawron, Latent heat storage, Int. J. Energy Res. 5 (1981) 103–109, https://doi.org/10.1002/er.4440050202.
[35] H. Wang, W. Lu, Z. Wu, G. Zhang, Parametric analysis of applying PCM wallboards for energy saving in high-rise lightweight buildings in Shanghai, Renewable Energy 145 (2020) 52–64, https://doi.org/10.1016/j.renene.2019.05.124.
[36] Y. Jiang, M. Lawrence, M.P. Ansell, A. Hussain, Cell wall microstructure, pore size distribution and absolute density of hemp shiv, R. Soc. Open Sci. 5 (4) (2018) 171945.
[37] W. Zhang, X. Zhang, X. Zhang, Z. Yin, Y. Liu, M. Fang, X. Wu, X. Min, Z. Huang, Lauric-stearic acid eutectic mixture/carbonized biomass waste corn cob composite phase change materials: Preparation and thermal characterization, Thermochim. Acta 674 (2019) 21–27, https://doi.org/10.1016/j.tca.2019.01.022.
[38] T. Dong, W. jiang, Y.e. liu, Y. Wu, Y. Qi, J. Li, Y. Ma, H. Ben, G. Han, A phase change material embedded composite consisting of kapok and hollow PET fibers for dynamic thermal comfort regulation, Ind. Crops Prod. 158 (2020) 112945.
[39] A. Sarı, G. Hekimoğlu, V.V. Tyagi, Low cost and eco-friendly wood fiber-based composite phase change material: Development, characterization and lab-scale thermoregulation performance for thermal energy storage, Energy 195 (2020) 116983, https://doi.org/10.1016/j.energy.2020.116983.
[40] G. Hekimoğlu, A. Sarı, T. Kar, S. Keleş, K. Kaygusuz, V.V. Tyagi, R.K. Sharma, A. Al-Ahmed, F.A. Al-Sulaiman, T.A. Saleh, Walnut shell derived bio-carbon/methyl palmitate as novel composite phase change material with enhanced thermal energy storage properties, J. Storage Mater. 35 (2021) 102288, https://doi.org/10.1016/j.est.2021.102288.
[41] I. Gómez-Arriaran, I. Sellens-Fernández, M. Odriozola-Maritorena, A. Erkoreka-González, A PC-tool to calculate the Moisture Buffer Value, Energy Proc. 133 (2017) 68–75, https://doi.org/10.1016/j.egypro.2017.09.373.
[42] C. Rode, R. Peuhkuri, B. Time, K. Svennberg, T. Ojanen, Moisture Buffer Value of Building Materials, Heat-Air-Moisture Transport: Measurements on Building Materials, 2007. Doi: 10.1520/STP45403S.
[43] NF EN 12664, Afnor EDITIONS. (n.d.). https://www.boutique.afnor.org/fr-fr/norme/nf-en-12664/performance-thermique-des-materiaux-et-produits-pour-le-batiment-determinat/fa045168/18797 (accessed November 10, 2021).
[44] Norme NF EN 12667 Performance thermique des matériaux et produits pour le bâtiment. Détermination de la résistance thermique par la méthode de la plaque chaude gardée et la méthode fluxmétrique - Produits de haute et moyenne résistance thermique - AFNOR, n.d. https://www.decitre.fr/livres/norme-nf-en-12667-performance-thermique-des-materiaux-et-produits-pour-le-batiment-5552120005762.html (accessed November 10, 2021).
[45] E. Günther, S. Hiebler, H. Mehling, R. Redlich, Enthalpy of Phase Change Materials as a Function of Temperature: Required Accuracy and Suitable Measurement Methods, Int. J. Thermophys. 30 (2009) 1257–1269, https://doi.org/10.1007/s10765-009-0641-z.
[46] I. Petsagkourakis, E. Pavlopoulou, E. Cloutet, Y.F. Chen, X. Liu, M. Fahlman, M. Berggren, X. Crispin, S. Dilhaire, G. Fleury, G. Hadziioannou, Correlating the Seebeck coefficient of thermoelectric polymer thin films to their charge transport mechanism, Org. Electron. 52 (2018) 335–341, https://doi.org/10.1016/j.orgel.2017.11.018.
[47] A.B. Kaiser, V. Skákalová, Electronic conduction in polymers, carbon nanotubes and graphene, Chem. Soc. Rev. 40 (2011) 3786–3801, https://doi.org/10.1039/C0CS00103A.
[48] O. Chung, S.-G. Jeong, S. Kim, Preparation of energy efficient paraffinic PCMs/expanded vermiculite and perlite composites for energy saving in buildings, Sol. Energy Mater. Sol. Cells 137 (2015) 107–112, https://doi.org/10.1016/j.solmat.2014.11.001.
[49] C. Barreneche, J. Vecstaudza, D. Bajare, A.I. Fernandez, PCM/wood composite to store thermal energy in passive building envelopes, 2017. Doi: 10.1088/1757-899X/251/1/012111.
[50] X. Jingchen, Y. Keyan, Z. Yucheng, Y. Yuxiang, C. Jianmin, C. Liping, S.Q. Sheldon, Form-stable phase change material based on fatty acid/wood flour composite and PVC used for thermal energy storage, Energy Build. 209 (2020) 109663, https://doi.org/10.1016/j.enbuild.2019.109663.
[51] T. Kar, A. Samanta, H. Sinnur, Studies on Effect of Application of Capric Acid and Stearic Acid based Reactive Phase Change Materials (rPCM) with PHAMS Binder on Thermal Comfort of Cotton Khadi Fabric as Thermo-tropic Smart Textiles, J. Nat. Fibers (2021) 1–20, https://doi.org/10.1080/15440478.2021.1880517.
[52] E. Terpakova, L. Kidalová, A. Estokova, J. Čigášová, N. Stevulova, Chemical Modification of Hemp Shives and their Characterization, Proc. Eng. 42 (2012) 931–941, https://doi.org/10.1016/j.proeng.2012.07.486.
[53] P. Bouloc, S. Allegret, L. Arnaud (Eds.), Hemp: Industrial Production and Uses, CABI, Wallingford, 2013.
[54] L. Boussaba, G. Lefebvre, S. Makhlouf, A. Grados, L. Royon, Investigation and properties of a novel composite bio-PCM to reduce summer energy consumptions in buildings of hot and dry climates, Sol. Energy 214 (2021) 119–130, https://doi.org/10.1016/j.solener.2020.11.060.
[55] M. Dehmous, E. Franquet, N. Lamrous, Mechanical and thermal characterizations of various thermal energy storage concretes including low-cost bio-sourced PCM, Energy Build. 241 (2021) 110878, https://doi.org/10.1016/j.enbuild.2021.110878.
[56] D.G. Atinafu, W. Dong, X. Huang, H. Gao, G. Wang, Introduction of organic-organic eutectic PCM in mesoporous N-doped carbons for enhanced thermal conductivity and energy storage capacity, Appl. Energy 211 (2018) 1203–1215, https://doi.org/10.1016/j.apenergy.2017.12.025.
[57] M. Asli, F. Brachelet, E. Sassine, E. Antczak, Thermal and hygroscopic study of hemp concrete in real ambient conditions, J. Build. Eng. 44 (2021) 102612, https://doi.org/10.1016/j.jobe.2021.102612.
[58] A. Sarı, A. Bicer, A. Karaipekli, F.A. Al-Sulaiman, Preparation, characterization and thermal regulation performance of cement based-composite phase change material, Sol. Energy Mater. Sol. Cells 174 (2018) 523–529, https://doi.org/10.1016/j.solmat.2017.09.049.

Article 5

Building and Environment 245 (2023) 110841

Contents lists available at ScienceDirect

Building and Environment

journal homepage: www.elsevier.com/locate/buildenv

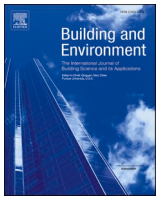

Development and hygrothermal performance analysis of a novel eco-friendly insulating wall under various climatic conditions

M. Sawadogo [a,b,*], F. Benmahiddine [c], A. Godin [a,b], M. Duquesne [a], R. Belarbi [a,d], A. Hamami [a]

[a] La Rochelle Université, LaSIE UMR CNRS 7356, Avenue Michel Crépeau, CEDEX 1, 17042, La Rochelle, France
[b] 4ev Lab, EDF R&D, CNRS, LaSIE, La Rochelle University, Avenue Michel Crépeau, CEDEX 1, 17042, La Rochelle, France
[c] Builders Lab, Builders Ecole d'Ingénieurs, ComUE NU, 1 rue Pierre et Marie Curie, 146110, Epron, France
[d] Canadian University Dubaï, City Walk Dubaï, United Arab Emirates

ARTICLE INFO

Keywords:
Phase change materials
Shape stabilization
Eco-friendly insulators
Thermal inertia and hygrothermal modelling

ABSTRACT

This work proposes the development, characterization and modelling of new eco-friendly building walls integrating stabilized forms of phase change materials. The aim is to enhance the hygrothermal and energy performances of buildings by improving their management of thermal energy throughout the year and meeting users' thermal comfort requirements. These are essential axes to help decarbonize heating and cooling, to rehabilitate buildings and to contribute to the energy transition. The experimental and numerical hygrothermal performances of two different building walls are assessed and compared under realistic weather conditions. The maximum temperature inside the wall is reduced by 2 °C for the phase change material hemp concrete compared to the reference hemp concrete in a context of typical summer heatwaves day. Both phase change material hemp concrete and reference hemp concrete showed good moisture regulation capability by dampening cyclic variations in outdoor humidity. The developed numerical model exhibited a good agreement with the experimental results with a maximum root mean square error between experimental and numerical results of about 0.6 °C and 6% for temperature and relative humidity, respectively.

1. Introduction

Buildings are a particularly energy-consuming sector, with an ageing stock of buildings that requires an improvement of the envelopes to limit heating and cooling needs. In fact, it is responsible for about 40% of the overall energy consumption and CO_2 emissions [1,2]. When considering embodied carbon and embodied energy are taken into account, these percentages rise to about 50% [3]. In the new climate change context, it is crucial to develop strategies to reduce the high energy and carbon requirements of the building sector in order to make it more sustainable and to reduce its environmental impact.

This work proposes the development, characterization and modelling of new eco-friendly walls made of composite materials, more precisely conventional materials and stabilized forms containing a biobased phase change material. These walls will play an active role in heat and cold charge/discharge and will provide walls with a high inertia that will allow limiting the use of heating or air-conditioning (or, depending on the weather conditions, to delay it in time). In addition to the scientific interest of this research field and the many locks to be lift, its ultimate objective is to contribute to increase the performances of buildings by improving the management of thermal energy and integrating the needs of users (thermal comfort). These are essential axes to contribute to decarbonize heating and cooling, to rehabilitate buildings and to achieve the energy transition.

Moreover, in a building, it is preferable to avoid the presence of liquid water in the air or brought by the air and to know if the water vapor is about to condense [4,5]. Indeed, condensation leads to various pathologies such as the deterioration of coatings and window seals, unhealthy air related to mold, decreased durability of building components, increased thermal conductivity etc [6,7]. These undesirable consequences affect heat transfer, comfort within the building and the energy performance of the building.

Faced with the imminent facts, researchers have initiated experiments with biomass products as potential building materials [8–11]. One of the materials considered is the hemp concrete which is a new sustainable building material composed of hemp shives as bio-aggregates and lime as binder [12]. The high porosity of the material provides it with a low thermal conductivity classifying it as a good insulator [13–16]. This material has also a high moisture regulation

* Corresponding author. La Rochelle Université, LaSIE UMR CNRS 7356, Avenue Michel Crépeau, CEDEX 1, 17042, La Rochelle, France.
E-mail address: mohamed.sawadogo@univ-lr.fr (M. Sawadogo).

https://doi.org/10.1016/j.buildenv.2023.110841
Received 27 June 2023; Received in revised form 9 September 2023; Accepted 13 September 2023
Available online 20 September 2023
0360-1323/© 2023 Elsevier Ltd. All rights reserved.

Nomenclature

Properties and variable

C_p	specific heat capacity (J.kg^{-1}.K^{-1})
m	mass (g)
T	temperature (°C)
u	water content of mass ratio (%)
C_m	moisture storage capacity (−)
P	pressure (Pa)
k_T	liquid water conductivity due to a thermal gradient (kg.m^{-1}.s^{-1}.K^{-1})
R	ideal gas constant (J.mol^{-1}.K^{-1})
M_w	molar mass of water (g.mol^{-1})
C_p^*	total heat capacity (J.kg^{-1}.K^{-1})
h	specific enthalpy (J.kg^{-1})
k_l	liquid water permeability (kg.s^{-1}.m^{-1}.Pa^{-1})
k_m	total moisture diffusivity coefficient (kg.s^{-1}.m^{-1}.Pa^{-1})
L_v	latent heat of vaporization of liquid water (J.kg^{-1})
h_c	convective heat transfer coefficient (W.m^{-2}.K^{-1})
h_m	convective mass transfer coefficient (s.m^{-1})
D_v	water vapor diffusivity coefficient (kg.s^{-1}.m^{-1})
D_l	liquid water diffusivity coefficient (kg.s^{-1}.m^{-1})

Subscripts

s	solid
l	liquid
v	vapor
sat	saturation
ref	reference
ext	exterior

Greek symbols

φ	relative humidity (%)
ρ	density (kg.m^{-3})
λ	thermal conductivity (W.m^{-1}.K^{-1})
λ^*	effective thermal conductivity (W.m^{-1}.K^{-1})
δ	water vapor permeability (kg.s^{-1}.m^{-1}.Pa^{-1})
γ	heat transfer by convection due to the vapor pressure gradient coefficient (W.m^{-1}.Pa^{-1})
σ	phase change criterion (−)

Acronyms

HC	hemp concrete
PCM	phase change materials

capacity (with a moisture buffer value (MBV) higher than 1) [17,18]. Despite these many advantages, the thermal capacity of the material is moderate which considerably reduces the thermal regulation capacity.

In a recent study [19], a new composite made of a phase change material (PCM) and hemp concrete (HC), namely PCMHC, was fabricated in order to increase the energy storage capacity of hemp concrete. Indeed, many studies have shown that the incorporation of PCMs in building materials can increase the thermal capacity, energy efficiency and comfort of buildings [20–22]. To that end, the hemp shives were first impregnated with capric acid, which is a biobased PCM [23,24], and then mixed with water and lime to make PCM-based hemp concrete. The thermal properties and performance of this new material were characterized and compared to the reference hemp concrete (without PCM). The results show an improvement of the thermal properties of the HC with the incorporation of the PCM [19].

Composites incorporating PCMs have been the subject of numerous experimental and numerical studies [25–31]. However, only few studies combine numerical and experimental aspects, with a low percentage of 12.5% compared to 52.5% for numerical and 35% for experimental studies [32].

Compared to the state of the art, the originality of this study lies in the following points:

- Development and characterization of an innovative building wall made with hemp concrete incorporating PCMs.
- This work is multidisciplinary and transverse, at the interface of several disciplines and expertises (energy, civil engineering, thermal engineering, experimental and numerical approaches, etc.) and integrates numerical and experimental research activities at several scales (from the materials' one to the walls' one),
- This paper proposes a numerical model simulating the dynamic behavior of building walls incorporating PCMs under realistic weather conditions. The numerical model is provided by the data of a throughout experimental characterization.

The objective of this work is to investigate the experimental and numerical hygrothermal behavior of PCMHC and HC under real weather conditions.

2. Experimental design

2.1. Fabrication of the PCM hemp concrete wall

In this study, two materials are investigated: a reference hemp concrete and PCM hemp concrete. The reference hemp concrete wall has been build in the frame of a previous study focusing on the hysteresis effect [33]. The formulation of hemp concrete consists of mixing by weight 16% hemp shives, 34% Tradical® PF70 (lime) used as a binder and 50% water. The hemp shives used are the Chanvribat provided by Ecohabitat (Ecological Materials for Habitat) with an average density of about 100 kg/m^3. The maximum, minimum and average dimensions of the hemp shives used are summarized in Table A-1 (Appendix A) [34]. The procedure for placing and compacting the mixture unfolded as follows: Initially, the mixture was poured incrementally into the mold and uniformly spread out. Subsequently, manual compaction was executed by hand in a direction perpendicular to the surface of the mixture layer, employing a wooden compactor. This action continued until the mixture layer achieved its final thickness of 10 cm. The dimensions of the walls are 90 × 90 × 10 cm^3. This wall will be used as a reference wall. Thus, the wall developed in this work will have the same dimensions in order to make a comparative study of the hygrothermal performances of these two walls in a biclimatic chamber.

The fabrication of our PCM hemp concrete follows three steps. The first step concerns the selection of the PCM. In a previous study [35], it has been shown that capric acid (CA) and lauric acid (LA) are suitable for the fabrication of PCM hemp shives composites. Based on thermal requirements, which are high latent heat, low undercooling temperature of melting between 15 and 45 °C, capric acid (CA), a fatty acid, supplied from Alfa Aesar with a purity of 99% has been chosen as PCM in this study. The general information of the CA are presented in Table A-2. The PCM has purchase at a price of 31.2 €.kg^{-1} form Alfa Aesar. The impregnation process is used to fabricate the PCM hemp shives following the procedure decribed in Refs. [19,35]. After undergoing a leakage test, the incorporation rate of PCM in hemps shives is found to be 50%. Afterwards, the form stabilized PCM hemp shives are used to fabricate the so-called PCMHC using the same formulation as for the reference hemp concrete and taking into account the impregnation rate. Therefore the mass of hemp shives is double in the PCMHC formulation in order to take into account the PCM. As previously mentioned, the

dimensions of the PCM hemp concrete are similar to that of the reference hemp concrete ($90 \times 90 \times 10$ cm^3) as presented in Figure A-1. The final mass of the considering the dry density is 47.5 kg with 6.5 kg of PCM that corresponds to a fraction of 13.8%. Considering the cost of all the raw material, the total cost of the PCMHC and HC wall are respectively 270 €.kg^{-1} and 20 €.kg^{-1} for a thickness of 10 cm.

2.2. Sensors and data acquisition

In order to ensure a unidirectional heat and moisture transfer, the lateral faces of the two hemp concrete materials are wrapped in aluminium foil. In order to evaluate and compare the thermal and hydric performances of the two walls, Ahlborn FHA 646 R type temperature and relative humidity sensors has been placed at different depths in the walls: 2.5, 5 and 7.5 cm and on the two faces (internal and external as shown in Figure A-1) following the same configuration of the reference HC wall. Therefore, twelve sensors are placed at 4 different positions (Figure A-2) of the wall in order to verify the 1D hypothesis and calculate the uncertainty of the measurements. The number of sensors is high enough to ensure a good reproducibility without disturbing the transfer phenomenon. In addition, the sensor are placed in the diagonal (Figure A-2. Top view) to avoid interaction between each other. The sensors were pre-calibrated by the manufacturer. They are connected to the ALMEMO data acquisition system that records the data every minute. The technical specifications of the sensors are presented in Table 1.

In addition, heat flux sensors (Figure A-2) are placed on the interior and exterior faces of the walls and connected to a Campbell Scientific datalogger. The thermal flux sensitivity of the fluxmeter is 60 μV W^{-1} m^{-2}, with a flux range of 1500 W m^{-2} and an accuracy of 5%.

2.3. Climatic conditions

After instrumentation, the walls are placed between the two compartments of a bi-climatic chamber composed by a C-40/1000/S and C-20/1000/S cambers from CTS GmbH (Figure A-3) in order to evaluate the hygrothermal performance. The two chambers have a test space volume of about 1 m^3. This climatic chamber allows the regulation of the temperature and the RH in the working range specified in Table A-3. In addition, the design of the climatic enables wall in 1D heat and mass transfer conditions.

One compartment of the biclimatic chamber is used to set the indoor conditions while the other compartment simulates outdoor conditions. The indoor condition is fixed at 20 °C and 50% relative humidity for the whole duration of the test. However, the exterior condition is set to vary as presented in Figure A-4. The program used in this study is inspired by the weather of the city of La Rochelle, France in 2022 and taken from the weather station data of the city [36].

The exterior temperature and humidity program are divided in four parts:

- The wall is conditioned for 3 days at 20 °C and 50% (step I).
- Then, for 7 days, the temperature is set at 40 °C and 10% relative humidity to simulate harsh summer conditions (step II).
- Afterwards, a second program where the temperature is set 10 °C and the humidity at 90% for 7 days is started and correspond to a moderate winter conditions (step III).
- Next, the wall is subjected to 7 days of daily cyclic conditions, with a temperature ranging from 18 to 40 °C and a relative humidity varying from 80 to 40%, which represents a typical summer day in the city of La Rochelle, France (step IV).
- Finally, a typical winter condition with temperature varying from −2 to 12 °C within 24 h is set. For sub-zero temperatures, it is not possible to set the relative humidity, so it has been fixed at 50% only for positive temperatures and remains free when the temperature is negative. As for the typical summer day, this program is cycled for 7 days (step V).

Table 1
Technical specifications of the Ahlborn FHA 646 R type RH and T sensors.

RH measurement range	**0 to100% RH**
T measurement range	−20–100 °C
RH accuracy	±2%
T accuracy	−20 to 0 °C: ±0.4 °C 0–70 °C: ±0.2 °C 70–100 °C: ±0.6 °C
Maximum response time	10 s

3. Characterization and material properties

This section is dedicated to the characterization of the properties of the PCM-based hemp concrete (PCMHC) and reference hemp concrete (HC), including dry density, thermal conductivity, specific heat capacity, isotherms of adsorption/desorption isotherms and liquid and water vapor permeability.

3.1. Dry density

The apparent dry density of HC and PCMHC is measured on samples of dimensions $15 \times 15 \times 3$ cm in dry state (conditioning for 14 days in a ventilated oven at 45 °C). The samples mass and volume are measured after the conditioning period and the dry density is obtained by dividing the mass of the dry sample by the total volume ($\rho = m/V$). The apparent density of the HC and PCMHC is 507.1 ± 15.5 kg m^{-3} and 582.2 ± 15.5 kg m^{-3} respectively. The density increase is 13% that is close to the amount of PCM incorporated in the total mixture of hemp concrete.

3.2. Heat capacity

The heat capacity or specific heat capacity is a property that expresses the ability of a material to store heat. This information is essential to complete the thermal characterization of the material. For this purpose, the Calvet calorimeter was used in accordance with the NF EN 821-3 standard [37]. It is equipped with two 3D thermopiles that respectively surround a measuring cell containing a sample of the studied material and a reference cell containing a thermally inert product. The specific feature of the Calvet allows the use of relatively large samples (~1 g), which improves the accuracy of the measurement. The test is performed with a temperature ramp between 0 and 45 °C with a heating rate of 0.1 °C/min and two stabilization steps (12 h at 0 °C and 3 h at 45 °C).

The measurement is made for HC and the PCM only as presented in Fig. 1. The specific heat capacity of HC varies between 1000 and 1100 J kg^{-1} K^{-1} over the considered temperature range. The solid and liquid heat capacity of the PCM varies between 2000 and 2500 J kg^{-1} K^{-1} with a peak value of 45,000 J kg^{-1} K^{-1} at the solid-liquid transition zone. The heat capacity of the eco-friendly composite (PMCHC) is obtained by combining the heat capacity of HC and PCM using the equivalent heat capacity method where the percentage of PCM (capric acid) can be accounted for in the heat capacity of HC as presented in Equation (1).

$$C_{p,PCMHC} = (1-f) * C_{p,HC} + f * C_{p,PCM} \quad (1)$$

where $C_{p,PCM}$ is the heat capacity of pure PCM, f is the mass fraction of PCM in PCMHC (Equation (2)), $C_{p,HC}$ and $C_{p,PCMHC}$ the heat capacity of HC and PCMHC respectively. The value of the mass fraction is 13.6%.

$$f = \left(1 - \frac{mass\ without\ PCM}{mass\ with\ PCM}\right) * 100 \quad (2)$$

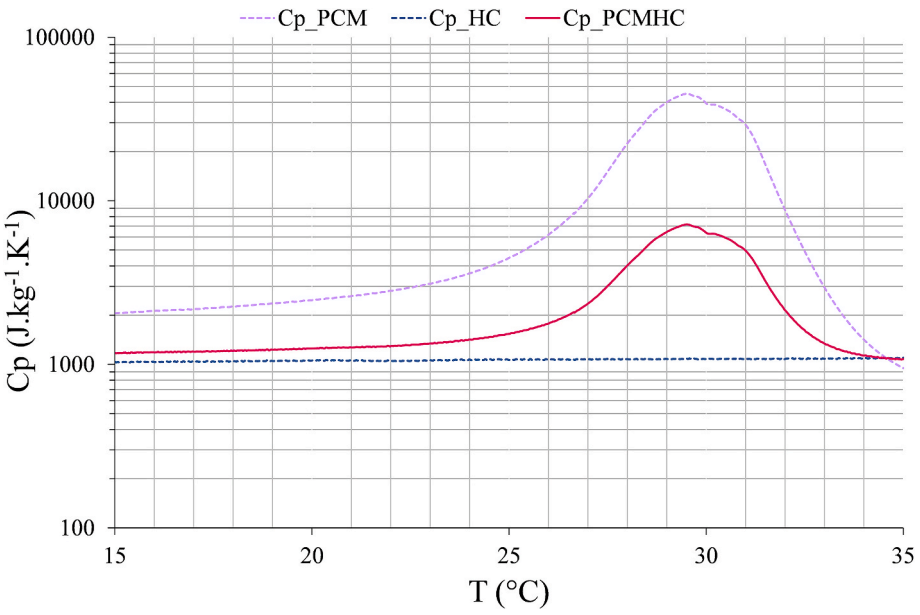

Fig. 1. Heat capacity curve of the pure PCM, HC and PCMHC.

3.3. Thermal conductivity

Thermal conductivity measurement of the materials is conducted using the λ-Meter Ep500e® device based on the guarded hot plate method under stationary conditions at three different temperatures: 10, 23 and 40 °C according to the standard NF EN 12664 [38] and NF EN 12667 [39]. The dimensions of the hemp concrete samples are 15 × 15 × 5 cm^3 and the measurements are performed for both HC and PCMHC and repeated three times to verify the repeatability. The results of the thermal conductivity of HC and PCMHC are shown in Fig. 2. As can be seen, the thermal conductivity of hemp concrete increases with the addition of CA. This result was expected according to the literature of shape-stabilized PCMs where the thermal conductivity of the porous support is enhanced by the impregnation with PCMs [27,40–43]. The reason is that the thermal conductivity of the composite PCM is higher than that of the corresponding support matrix, because CA has replaced air in the hemp shives/CA composites. The thermal conductivity of CA (about 0.21 W m^{-1} K^{-1} at ambient temperature [24]) is 10 times higher than that of air (about 0.02 W $m^{-1}K^{-1}$).

3.4. Sorption isotherms and moisture storage capacity

The sorption isotherm determines the capacity of the material to capture or release water as a function of the relative humidity of the external environment at constant temperature. The experimental determination of this curve is essential for the prediction of the hydric behavior of porous building materials. This test indicates the water content of the mass ratio of a material as a function of the relative humidity. The measurement of the sorption isotherms of HC and PCMHC was performed using the SPS vapor sorption analyzer from ProUmid GmbH, which is based on a gravimetric method. The large temperature range of the SPS enables to conduct vapor sorption analysis at extreme conditions from cool 5 °C to hot 60 °C. Relative humidity can be precisely set and adjusted over the whole range from completely dry 0% up

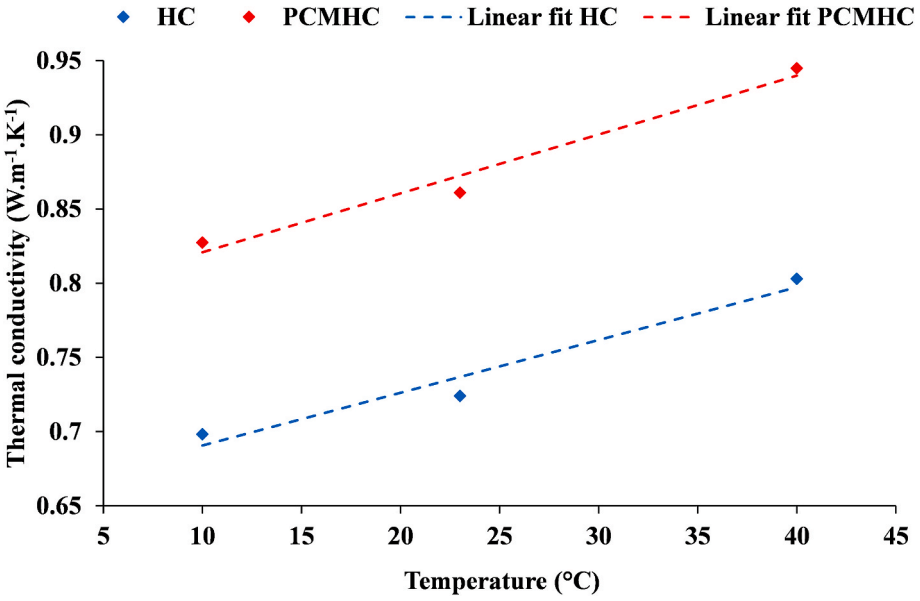

Fig. 2. Thermal conductivity of HC and PCMHC as a function of temperature and linear fit.

to 98% RH close to condensation. Adsorption and desorption isotherm curves are usually modelled using prediction models that exist in the literature such as the Guggenheim-Anderson-de Boer (GAB) model. This type of modelling allows the construction of functions used as inputs for hygrothermal models (Equation (3)).

$$w(\varphi) = \frac{m \bullet C \bullet K \bullet \varphi}{(1 - K\varphi) * (1 - K\varphi + KC\varphi)} \quad (3)$$

where w is the water content (%), φ the relative humidity (%), m is the monolayer capacity, C is the kinetic constant relating to the sorption in the first layer, and K is the kinetic constant relating to multilayer sorption. m, C and K represent the fitting parameters of the GAB model to match the experimental values.

Fig. 3 shows the adsorption isotherms of HC and PCMHC between 0 and 90% relative humidity. In this work, only the adsorption curve is presented since no hysteresis effects are considered that could justify a presentation of the desorption curve. HC has the highest moisture content compared to PCMHC with a maximum value of 0.14%. This decrease in adsorption capacity is due to the incorporation of PCM into the hemp shives that limits the pores available for water adsorption. The sorption isotherms were modelled by the GAB method and the coefficients of the modelling as well as the mean square error between the model and the experimental data are reported in Table 2.

The results of the sorption isotherms are used to calculate the moisture storage capacity (Fig. 4), which is defined as the slope of the sorption isotherm curves ($C_m = \frac{\partial w}{\partial \varphi}$) obtained with the GAB modelling that is continuous. The latter is an important input parameter for coupled heat, air and moisture models. It represents the ability of the material to adsorb and release moisture when environmental moisture conditions change [13]. The moisture storage of HC is higher than that of PCMHC, which is a direct consequence of the isotherm curves. The decrease observed in the water vapor adsorption capacity of the composite material can reduce its hydric properties (hydric buffering capacity and water vapor permeability) as well as its thermal properties (thermal conductivity and specific heat).

3.5. Water vapor permeability

The water vapor permeability coefficient is determined by the cup method described in the standard NF EN ISO 12572 [44] using the GINTRONIC® Gravitest 6400. This device consists of a climatic chamber with 6 cups and automatic weighing. The maximum capacity of the balance is 400 g with a precision of 0.1 mg. A gradient of vapor pressure is applied between two faces of the sample. This gradient is ensured while applying two different humidities (φ = 3% inside the cup and φ = 50% in the ambiance of the climatic chamber). The mass change of the specimen (m) is monitored up to steady state (constant vapor flow through the specimen) and mass equilibrium. Once stabilized, the water vapor flow is calculated. Based on the boundary conditions of the specimen, the water vapor permeance is deduced. The vapor permeability is determined by assuming that the material is homogeneous. The test is performed on three cylindrical specimens of 8 cm diameter and 2 cm thickness.

The vapor permeability of PCMHC and HC is $(1.8 \pm 0.2)\bullet10^{-11}$ (Kg m^{-1} $Pa^{-1}.s^{-1}$) and $(2.7 \pm 0.062)\bullet10^{-11}$ (Kg m^{-1} $Pa^{-1}.s^{-1}$), respectively. There is a decrease in the water vapor permeability of the material with the addition of the PCM in the hemp shives. This result, similar to that observed with the MBV measurement [14], is due to the reduction in the adsorption of the hemp shives with the incorporation of PCM. The water vapor permeability value of HC is consistent with that found in the literature [17,45].

Table 2
Coefficients of the GAB modelling and sum of square error (SSE).

	m	C	K	SSE
HC	0.02245	54.0309	0.93899	$5.55\bullet10^{-5}$
PCMHC	0.02227	20.9271	0.87663	$7.76\bullet10^{-5}$

3.6. Liquid diffusivity

The hydraulic conductivity is a quantity that expresses the ability of a porous medium to transmit a fluid under the effect of a pressure gradient. It depends on the properties of the porous medium where the flow takes place (granulometry, grain shape, intergranular porosity, distribution and shape of the pores), on the properties of the flowing fluid (viscosity, density) and on the degree of saturation of the porous medium.

For porous building materials, there is no device to measure the hydraulic conductivity. The latter is generally estimated by inverse methods. An inverse method has been developed in Ref. [46] that has allow the identification of the liquid and vapor diffusivity of HC and

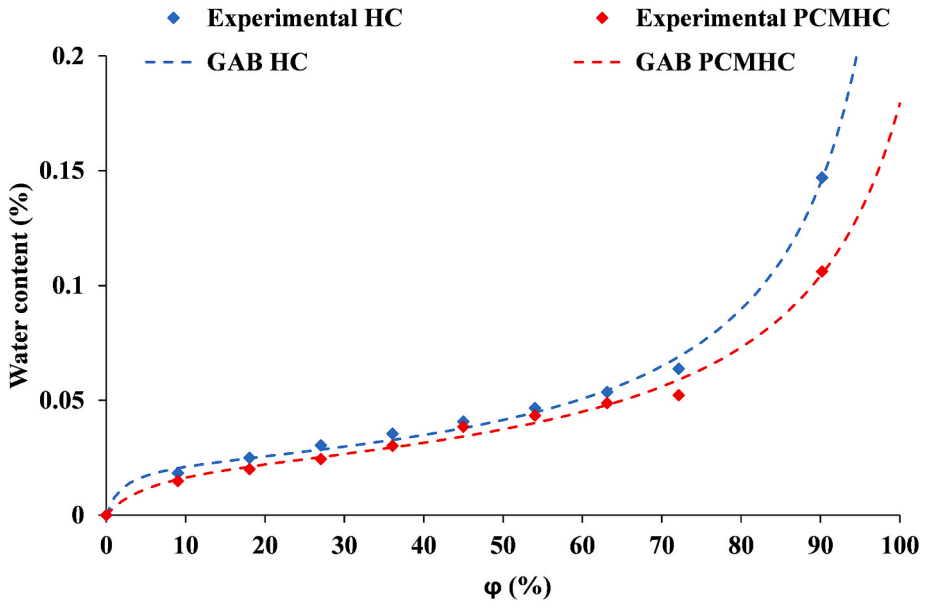

Fig. 3. Adsorption isotherms and GAB modelling of HC and PCMHC.

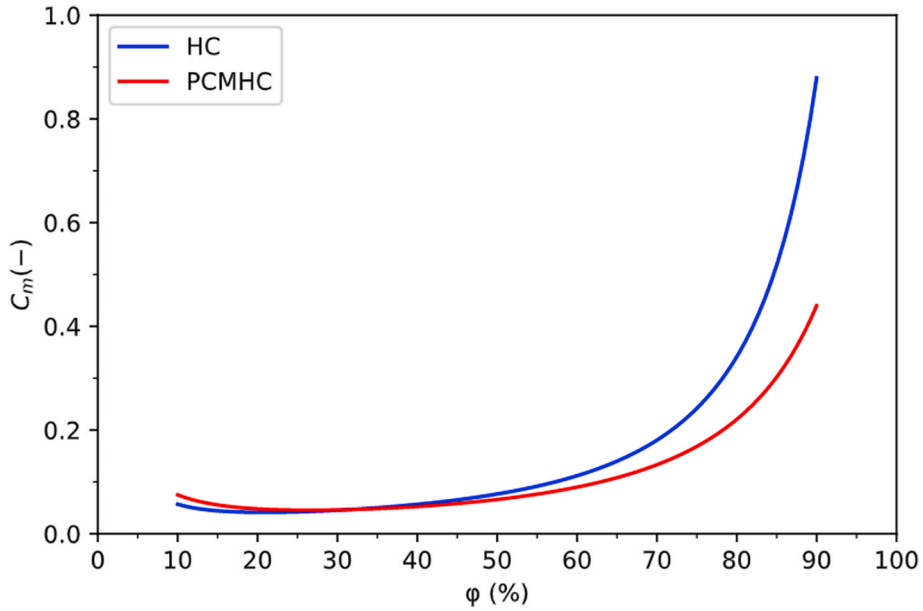

Fig. 4. Moisture storage capacity of HC and PCMHC.

PCMHC. The identification method was based on minimizing the quadratic difference between numerical and experimental values of relative humidity. The liquid and water diffusivity are modelled as exponential functions with two parameters (Equation (4)).

$$\begin{cases} D_v(\varphi) = D_{v0} * e^{a*\varphi} \\ D_l(\varphi) = D_{l0} * e^{b*\varphi} \end{cases} \quad (4)$$

with D_{v0}, D_{l0}, a, b the parameters to be estimated by minimizing the cost function.

The estimated parameters are gathered in Table 3 and Fig. 5 shows the vapor and liquid diffusivity curves obtained by inverse methods. We notice that the vapor diffusivity curve decreases with relative humidity while the liquid diffusivity curve increases with humidity. The vapor diffusivity coefficient of the three materials are very close. The maximum value, around 10^{-6} is reached for low humidities before decreasing when the humidity increases.

The opposite trend is observed with the liquid diffusivity coefficient, which increases with relative humidity. The value of the coefficient is higher for the HC compared to PCMHC. This difference can be explained by the incorporation of PCM in the hemp shives, which decreases its absorption capacity.

3.7. Summary of all measured input data required for the model

The properties required to model hemp concrete and the eco-friendly composite (PCMHC) are summarized in Table 4. All the properties are defined in the nomenclature section.

4. Experimental study

This section focuses on the comparison of the thermal performances of the HC and PCMHC walls in a climatic chamber. Figure A-5 shows the evolution of the surface temperature and relative humidity at the interior and exterior side of each wall. Compared to the temperature and relative humidity program of Figure A-4, one can notice that stabilizing humidity is more difficult for the climatic chamber compared to temperature. The interior humidity that was set to 50% is seen to fluctuate around this mean value. This observation is essential specifically while setting the boundary condition in numerical model, to allow better comparison with the experimental results.

In order to ensure the unidirectional heat and moisture transfer, four sensors have been placed at each depth (2.5, 5 and 7.5 cm), so the total number of sensors is twelve. The temperature and relative humidity at each depth is the average value of four sensors. Figure A-6 shows the mean absolute temperature and relative humidity deviation (MAD (Equation (5))) of the four sensors at each depth. Regarding temperature, greater variances arise from the sensor placed in proximity to external conditions, amounting to approximately 0.4 °C. It's important to highlight that these discrepancies are more pronounced with elevated temperatures and diminish as temperatures decrease. Conversely, the highest relative humidity deviation is found at the material's center, around 2%. Similar to temperature, this deviation correlates with relative humidity. Consequently, deviations peak at higher humidity levels and minimize at lower humidity levels. The fluctuations are lower for the deeper sensors exhibiting the damping effect of the material. For all the positions, the mean absolute deviation of the temperature and relative humidity is below 0.4 °C and 2%, respectively that is in the uncertainty of the sensor. Based on these results, one can easily state the validity of the unidirectional heat and moisture transfer assumption.

$$MAD = \frac{\sum(x_i - \overline{X})}{n} \quad (5)$$

where x_i is the value of the ith sensor, $\overline{X}$ the mean value and n the number of sensors.

Figures A-7 and A-8 show the evolution of the temperature and relative humidity at different positions for HC and PCMHC as a function of time. For analysis purposes, the temperature and relative humidity evolution will be divided into three zones. A region of static conditions on 17 days, a region of typical summer days between day 17 and 24, and finally a typical winter day from day 24–31.

Table 3
Parameters of the water vapor and liquid diffusivity from the minimization.

	D_{v0}	a	D_{l0}	b
HC	$1.2733 \bullet 10^{-6}$	−4.1899	$5.7893 \bullet 10^{-9}$	8.1002
PCMHC	$1.2998 \bullet 10^{-6}$	−4.3631	$7.5511 \bullet 10^{-8}$	4.7225

4.1. Static conditions

Fig. 6 show the evolution of the temperature inside the PCMHC and

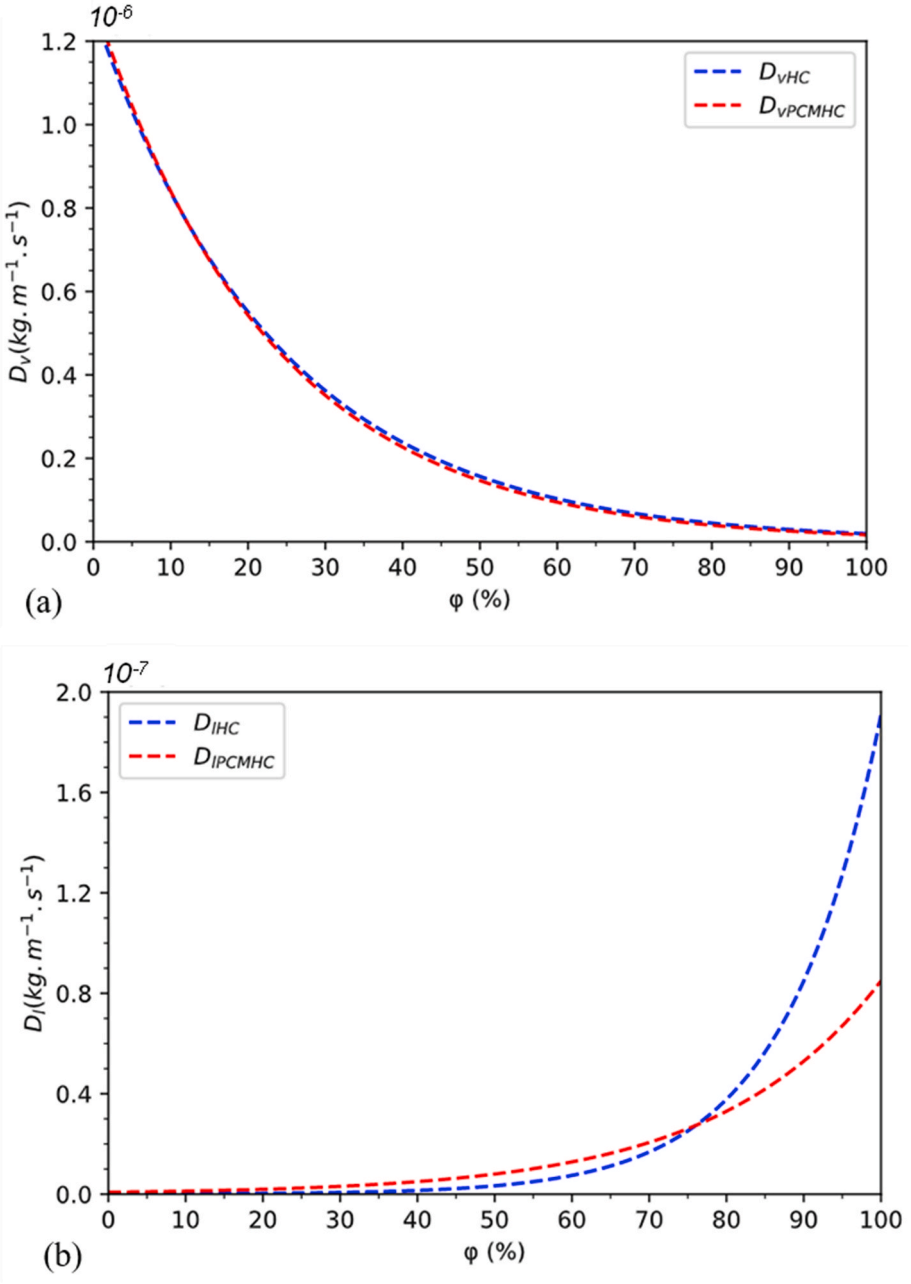

Fig. 5. Water vapor (a) and liquid diffusivity (b) of HC and PCMHC as a function of relative humidity.

HC at 2.5, 5 and 7.5 cm respectively under static weather conditions: conditioning (step I) summer (step II) and winter (step III) (as represented in Figure A-4). The maximum temperature, when the exterior temperature is set at 40 °C, is reduced by 2 °C and 1 °C with the incorporation of the PCM for 2.5 and 5 cm, respectively. However, for the sensor at 7.5 cm, which is close to the indoor conditions, no temperature reduction is observed. This is explained by the fact that this point does not reach the melting temperature of the PCM composite, which is around 30 °C. Therefore, the latent heat effect of the PCMHC is not activated at this depth (7.5 cm).

When the temperature is set at 10 °C, both materials PMCHC and HC show the same behavior with a little advantage for HC that shows better performance at lower temperature. The difference is significant at 7.5 cm with a value around 1 °C. This is explained by the higher thermal conductivity of PCMHC compared to HC considering that both materials act as sensible storage materials for this temperature range.

Fig. 7 shows the evolution of the relative humidity of PCMHC and HC at different position under static weather conditions (steps I, II and III). At the beginning of the test, the HC that was dryer than the PCMHC reached the 50% of relative humidity relatively faster than PCMHC where the 3 days of conditioning was insufficient to reach an equilibrium at 50%. This difference of initial conditions explains partially the fact that the humidity profile of the HC is always below that of PCMHC in the drying phase (humidity fixed at 10%). In fact, the reference wall was stored for several months at room temperature (around 20 °C and internal RH close to 50%), which may have contributed to greater stability of temperature and relative humidity. However, the difference of relative humidity inside the two materials is reduced at the wetting phase (humidity set at 90%) and even negligible for the sensor closed to the boundary conditions (at 2.5 cm). The difference of relative humidity profile between HC and PCMHC is reduced with time and the same humidity profile is obtained at day 10. For the deeper positions (5 cm

Table 4
Hygrothermal properties of the PCM and reference hemp concrete.

Parameters	Value/expressions
w (%)	$\frac{m \bullet C \bullet K \bullet \varphi}{(1-K\varphi)*(1-K\varphi+KC\varphi)}$ Where : $\begin{cases} m = 0.02245, C = 54.0309 \text{ and } K = 0.93899 \text{ (HC)} \\ m = 0.02227, C = 20.9271 \text{ and } K = 0.87663 \text{ (PCMHC)} \end{cases}$
C_m (−)	$\frac{\partial w}{\partial \varphi}$
λ (W.m^{-1}.K^{-1})	$\begin{cases} 0.0003 \bullet T + 0.063 \ (HC) \\ 0.0004 \bullet T + 0.0805 \ (PCMHC) \end{cases}$
D_v (Kg.m^{-1}.s^{-1})	$D_{v0} * e^{a*\varphi}$ Where : $\begin{cases} D_{v0} = 1.2733 \bullet 10^{-6} \text{ and } a = -4.1899 \ (HC) \\ D_{v0} = 1.2998 \bullet 10^{-6} \text{ and } a = -4.3631 \ (PCMHC) \end{cases}$
$C_{p,s}$ (J. kg^{-1}. K^{-1})	$\begin{cases} 1000 - 1100 \ (HC) \\ 1200 - 4500 \ (PCMHC) \end{cases}$
ρ_s (kg.m^{-3})	507.1 (*HC*) 582.2 (*PCMHC*)
L_v (J.kg^{-1})	$2.44 \bullet 10^6$
D_l (Kg.m^{-1}.s^{-1})	$D_{l0} * e^{b*\varphi}$ Where : $\begin{cases} K_{l0} = 5.7893 \bullet 10^{-9} \text{ and } b = 8.1002 \ (HC) \\ K_{l0} = 7.5511 \bullet 10^{-8} \text{ and } b = 4.7225 \ (PCMHC) \end{cases}$

and 7.5 cm), the deviations are less reduced throughout the steps due to a lack of stability from the initial condition; the initial shift is conserved up to day 10. In general, the kinetic is fast for the HC compared to the PCMHC. This observation could be explained by the value of the liquid and vapor permeabilities, and moisture storage capacity of HC higher than those of PCMHC due to the incorporation of capric acid in hemp shives.

4.2. Dynamic conditions: cycling

4.2.1. Typical summer day (step IV)

The evolution of the temperature of PCMHC and HC at different positions under typical summer day cyclic conditions is presented in Fig. 8. PCMHC presented better performances in the reduction of the maximum temperature. In fact, the maximum temperature is reduced by 2 °C for the sensor close to the exterior condition. The reduction is about 1 °C for the sensor at 5 cm and negligible for the sensor at 7.5 cm. These results indicated that the performances of the PCMHC depend on the outdoor conditions, which should be above the melting temperature of the PCM that is around 30 °C. This condition is achieved for the sensor close to the exterior conditions that justify the temperature reduction at 2.5 and 5 cm. The PCMHC exhibited the same performances after seven melting/solidification cycles, which confirms the efficiency of the encapsulation. It should be mentioned that the tests of HC and PCMHC were not conducted at the same time and small discrepancies in the outdoor conditions for the two tests. For instance, for HC at the 6th cycle, the exterior temperature drops by 2 °C that induced a reduction of the maximum temperature of HC at each depth as presented in Fig. 8. This reduction is more visible at 2.5 cm because it is close to exterior condition.

Fig. 9 shows the evolution of the relative humidity of PCMHC and HC at different position under typical summer day weather. In general, the kinetic is fast for the HC compared to the PCMHC. This observation has been explained previously by the value of the liquid and vapor permeabilities, and moisture storage capacity of HC higher than those of PCMHC due to the incorporation of capric acid in hemp shives. The maximum difference is about 4% and obtained at the center of the wall (sensor at 5 cm). This difference is lower for the sensors near the boundary conditions (sensors at 2.5 cm and 7.5 cm) with maximum difference of about 2%.

4.2.2. Typical winter day (step V)

The evolution of the temperature inside of PCMHC and HC wall at different positions for the typical weather condition is shown in Fig. 10. The temperature profile of the two materials shows the same tendency with the temperature slightly higher for the HC that is a better insulator

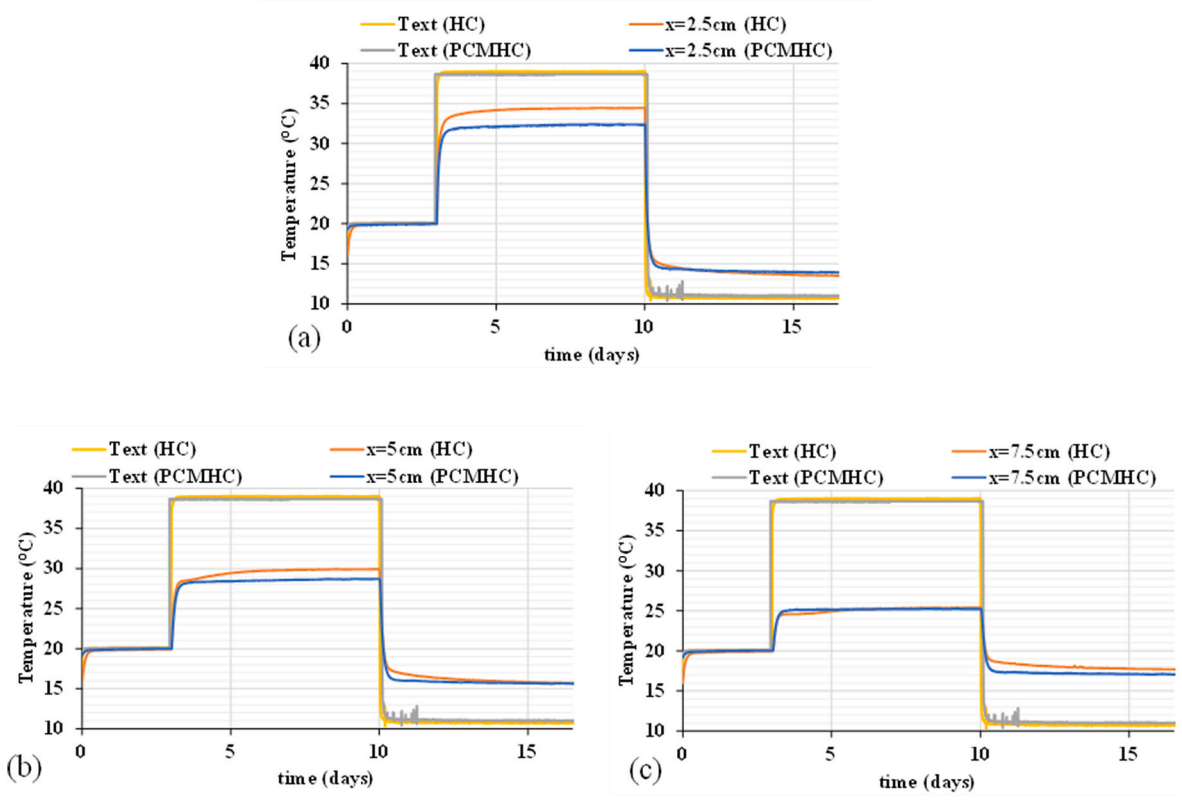

Fig. 6. Evolution of the temperature for HC and PCMHC at x = 2.5 cm (a), 5 cm (b), 7.5 cm (c) under static conditions (Steps I, II and III).

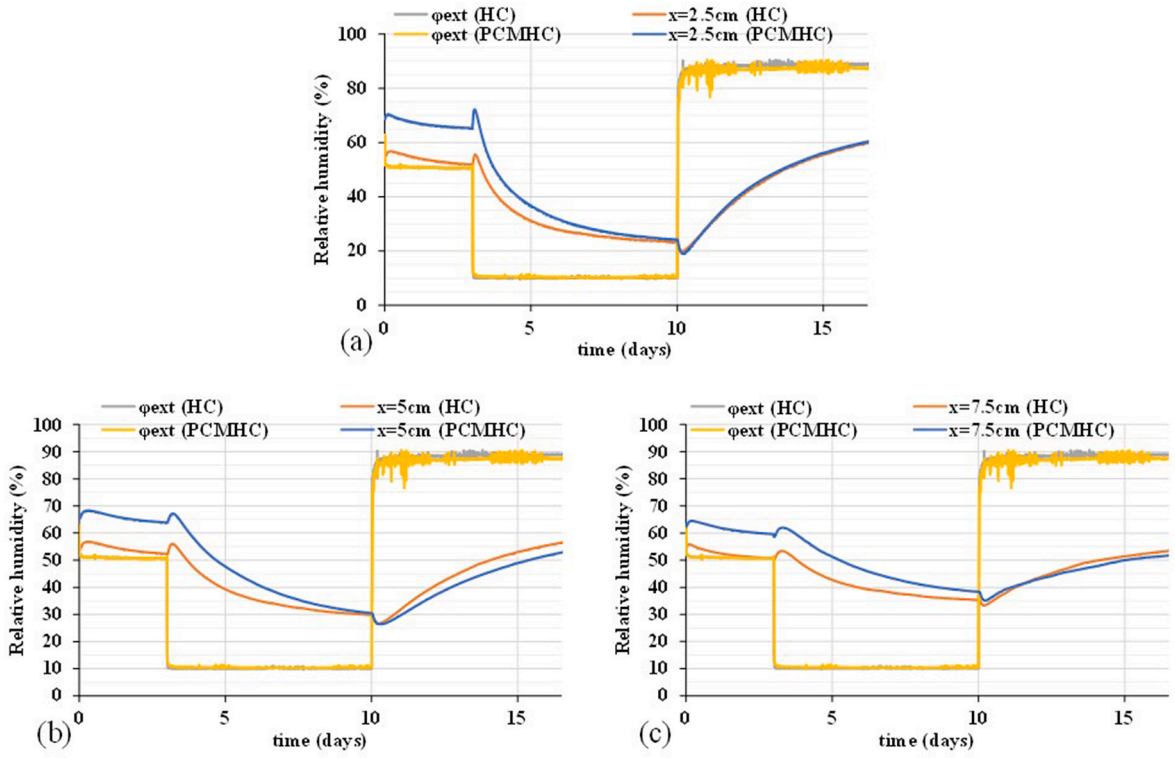

Fig. 7. Evolution of the relative humidity for HC and PCMHC at x = 2.5 (a), 5 (b), 7.5 cm (c) static conditions (Steps I, II and III).

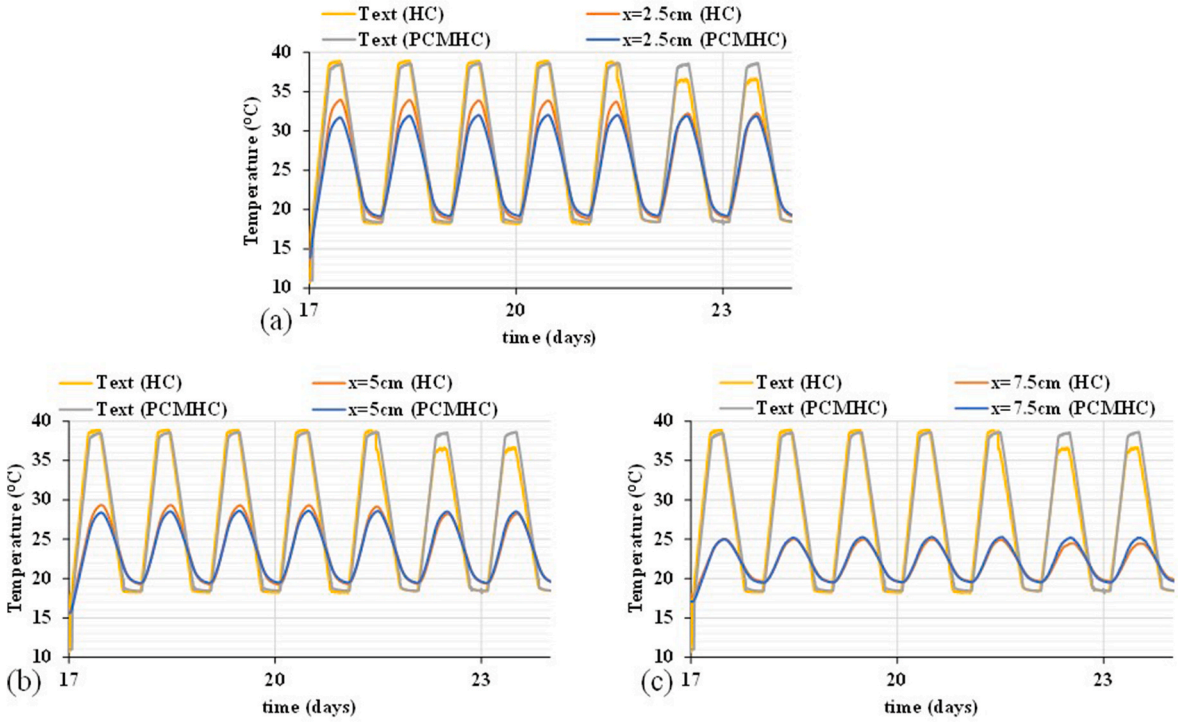

Fig. 8. Evolution of the temperature for HC and PCMHC at x = 2.5 (a), 5 (b), 7.5 cm (c) under typical summer day scenario (step IV).

than PCMHC for cold climate. In fact, for the temperature range experienced by the two walls in winter conditions, the thermal conductivity and the thermal diffusivity of HC are lower than that of the PCMHC. This could explain the better insulation of HC for cold climate. This result was expected due to the melting temperature of capric acid selected as PCM, which is about 30 °C and therefore suitable for hot climate. Below that melting temperature, the latent heat effect is not activated.

Fig. 11 shows the evolution of the relative humidity of PCMHC and HC at different position under typical winter day weather. The two materials showed almost the same behavior at x = 2.5 cm, with a maximum difference of about 2% of relative humidity. However, at the other positions (5 cm and 7.5 cm), the kinetic is faster for the HC

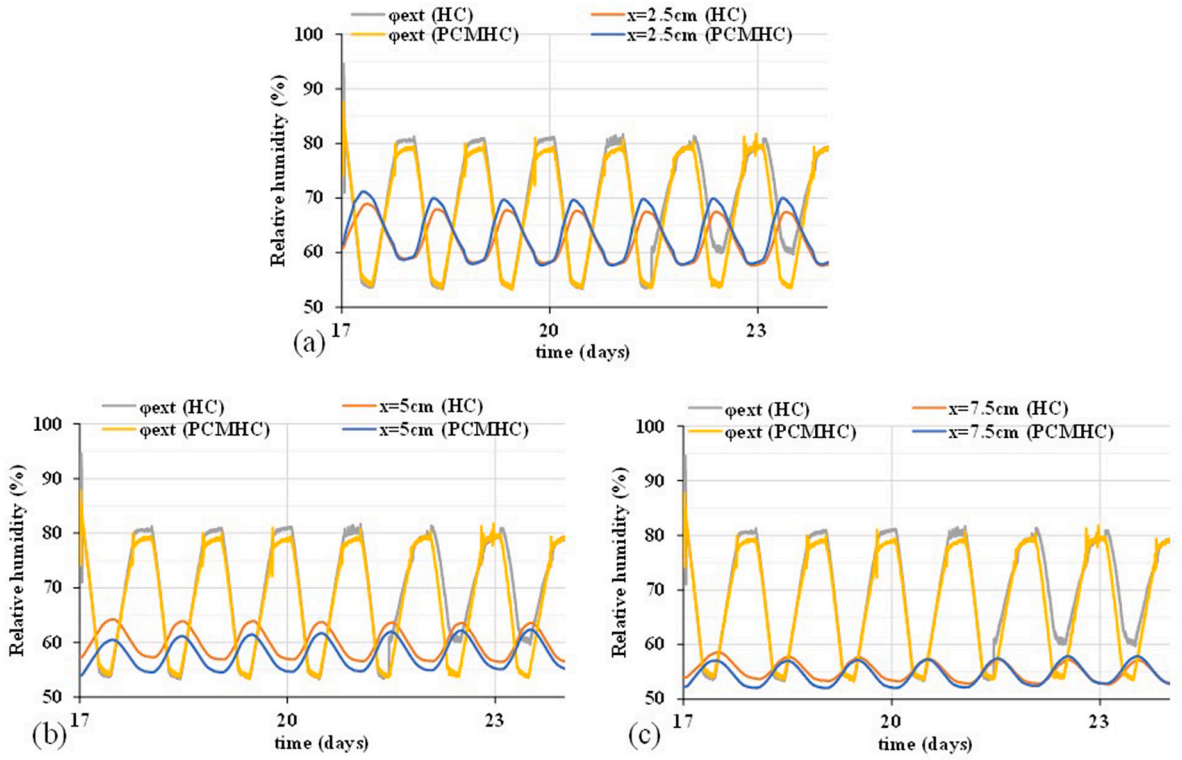

Fig. 9. Evolution the relative humidity for HC and PCMHC at x = 2.5 (a), 5 (b), 7.5 cm (c) under typical summer day scenario (step IV).

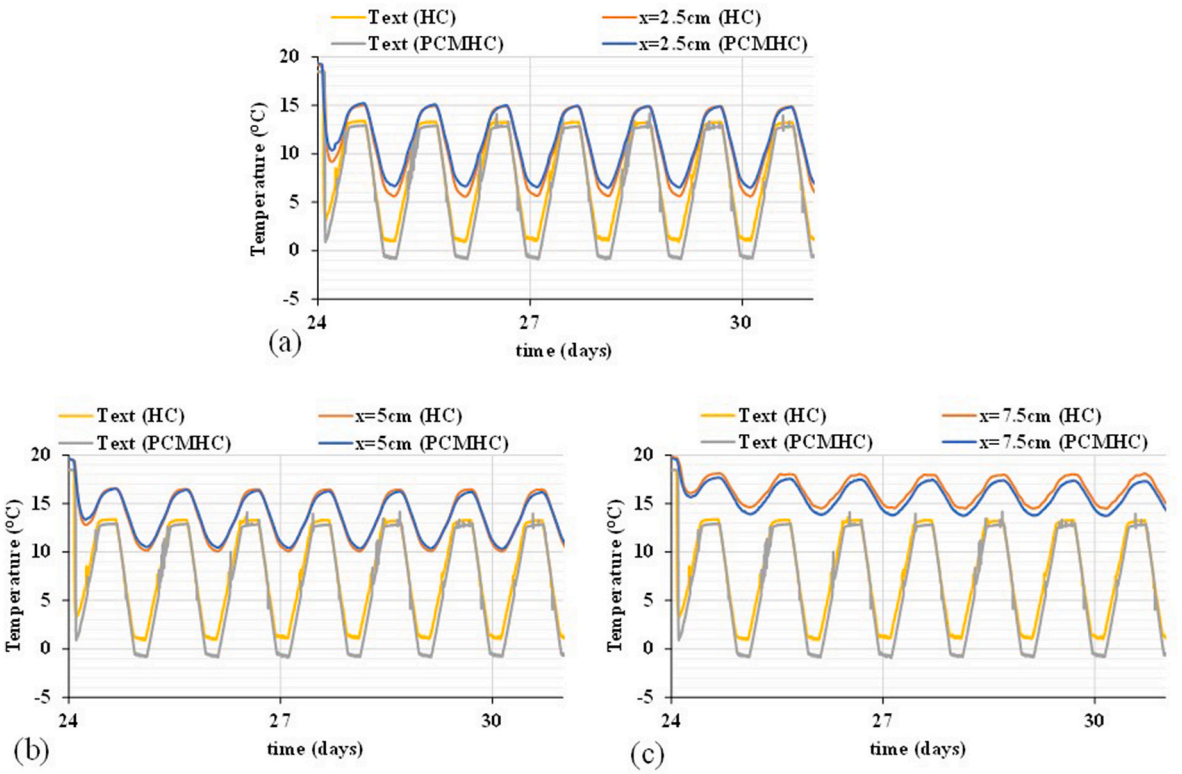

Fig. 10. Evolution of the temperature for HC and PCMHC at x = 2.5 cm (a), 5 cm (b), 7.5 cm (c) under typical winter day scenario (step V).

compared to the PCMHC and the difference is above 1%. In all the weather conditions, both HC and PCMHC showed good moisture dampening capacity with a maximum fluctuation of less than 10% while the outdoor relative humidity varies with an amplitude of 40% (summer-step IV and winter-step V typical day, see Figure A-4). The dampening effect is higher for HC because of higher value of the liquid and vapor permeabilities, and moisture storage capacity compared to HC.

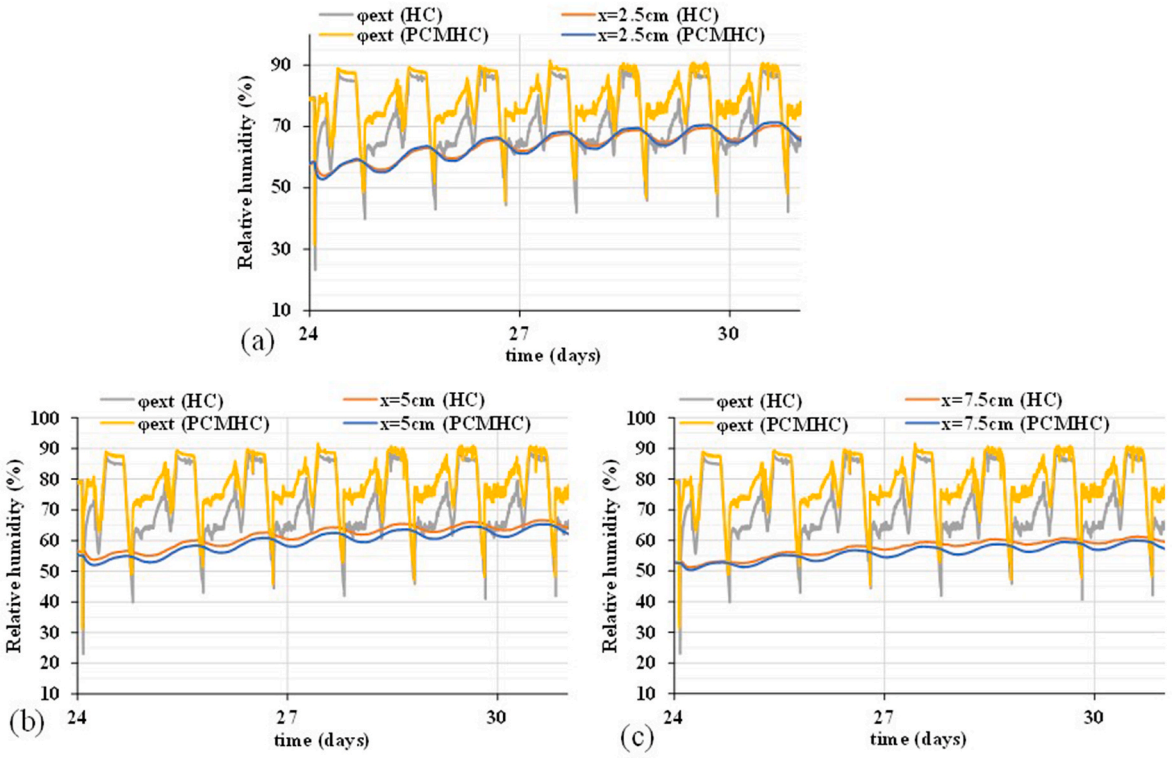

Fig. 11. Evolution of the relative humidity for HC and PCMHC at x = 2.5 cm (a), 5 cm (b), 7.5 cm (c) under typical winter day scenario (step V).

Figure A-9 presents the evolution of the interior and exterior heat fluxes measured at the surface of the walls. The heat flux is positive for negative temperature value and negative when the temperature becomes positive meaning that the direction of the heat flux changes with the temperature gradient according to Fourier law. For the static conditions, the interior heat flux is about 200 W m^{-2} and 100 W m^{-2} when the temperature is set at 40 °C and 10 °C, respectively. The heat flux is stabilized quickly after few hours leading to a steady state region. The heat flux varies between −800 and 300 W m^{-2} for the typical summer day against −200 and 800 W m^{-2} for the typical winter scenario. The exterior heat flux changes drastically at the end of each cycle. This can be explained by the peaks observed in the evolution of outdoor relative humidity, which directly affects the latent heat flux (of water), and therefore the total heat flux. The interior heat flux is inferior to the exterior one that is subjected to continuous change of the climatic condition.

5. Numerical investigation

Experimental studies allow evaluating performances of building materials under real climatic conditions. Such a study is necessary to predict the behavior of these materials once integrated into buildings. However, experimental studies are time consuming and limit the range of investigation. To remedy this, a hygrothermal model has been developed to have more flexibility than the experiment and to test several configurations and climatic conditions.

5.1. Modelling assumptions

In order to model the non-linear coupled heat, air and moisture transfer phenomena, the mathematical formulation of the studied physical problem is based on the following assumptions:

- macroscopically homogeneous, isotropic and rigid solid phase,
- gas phase at constant and uniform pressure,
- thermodynamic equilibrium between all phases present,
- no chemical reaction between the phases,
- no heat transfer by radiation,
- no energy dissipation during flow,
- wetting heat neglected,
- total pressure assumed constant ($\nabla P = 0$).
- There is no hysteresis between the adsorption and desorption phases of water vapor.

5.2. Modelling equations

The hygrothermal model used is based on the model of Philip and de Vries et al. [47,48], the work of Ferroukhi et al. [49], and Remki et al. [50]. The conservation of mass and energy equations are described for all phases considered (liquid, vapor). Then, they are defined according to the transfer drivers given by the vapor pressure and the temperature. The relative humidity is then calculated a posteriori.

The space and time evolutions of the variables (temperature and vapor pressure) have been modelled to analyze the dynamic behavior of innovative eco-friendly walls. The non-linear coupled heat and moisture transfer equation system, after developing the energy and mass conservation equations (see details in Appendix B), is obtained as follows (Equations (6) and (7)):

$$\rho_s \frac{C_m}{P_{v,sat}} \frac{\partial P_v}{\partial t} = div(-k_T \nabla T - k_m \nabla P_v) \tag{6}$$

$$\rho_s C_p^* \frac{\partial T}{\partial t} = div(\lambda^* \nabla T + \gamma \nabla P_v) + \rho_s C_m \sigma L_v \frac{\partial P_v}{\partial t} \tag{7}$$

The boundary conditions on the exterior sides of the wall are set by taking into account the convective heat and mass exchanges related to the indoor and outdoor conditions, mainly the air temperature and humidity. The boundary conditions are summarized in Equations (8) and (9) [49]:

$$(-k_T \nabla T - k_m \nabla P_v)|_{x=0} = h_m \left(P_{v,ext} - P_v(x=0)\right) \tag{8}$$

$$(\lambda^{*}\nabla T+\gamma\nabla P_v)|_{x=0}=h_c(T_{ext}-T(x=0))+(1-\sigma)L_v h_m\left(P_{v,ext}-P_v(x=0)\right) \quad (9)$$

with h_c (W.m^{-2}.K^{-1}) the convective heat transfer coefficient at the surface of the material, h_m (s.m^{-1}) the convective mass transfer coefficient, $P_{v,ext}$ and T_{ext} exterior pressure and temperature, respectively.

The hygrothermal properties of the material are the input parameters from the characterization of the materials (Table 4). These properties and the links with the model coefficients are presented in Figure A-10.

5.3. Experimental validation

The experimental data of the PCMHC is used to validate the numerical model. The simulations are conducted with the software COMSOL Multiphysics. Dirichlet boundary condition assumption is considered by using the surface temperature and relative humidity as interior and exterior boundary conditions for the numerical model.

5.3.1. Thermal performances

Fig. 12 shows the evolution of experimental and numerical temperature within the PCMHC. The numerical simulation showed a good agreement with the experimental data and the evolution of the temperature is accurately reproduced. The temperature difference (Fig. 13) is maximum at the transition zone between the two static zones (steps II and III) (40 and 10 °C) and reached 2.5 °C. Apart from this transition zone, the temperature difference between experimental and numerical simulation fluctuates between ±1 °C which is a good approximation considering the 1D assumption of the model. However, the root mean square error (RMSE) between experience and numerical result is 0.64 °C, 0.38 °C and 0.28 °C for 2.5, 5 and 7.5 cm respectively. The precision increases with the depth and the best estimates are obtained for 7.5 cm that is less sensible to the cyclic exterior condition. These uncertainties are essentially due to the 1D assumption, the uncertainty in characterizing material properties, measurement uncertainty and the uncertainty on the sensor's position. Despite the discrepancies, the numerical model describes with a good accuracy the thermal behavior of the PCMHC.

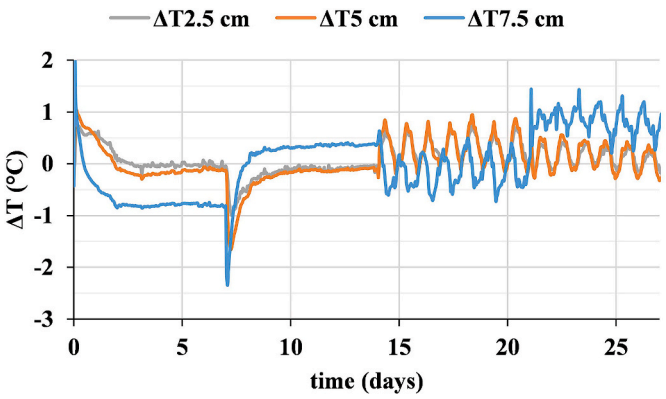

Fig. 13. Evolution of the temperature difference between experimental and numerical simulation for PCMHC at x = 2.5, 5 and 7.5 cm.

5.3.2. Hydric performances

Fig. 14 shows the evolution of the numerical and experimental relative humidity at 7.5 cm. The numerical simulations are performed with and without the total liquid and vapor transfer coefficient due to a temperature gradient (k_T) to assess the effect on the relative humidity profile [51,52]. We can distinguish two regimes: the first one corresponding to the static conditions (steps I, II and III) where the simulation without k_T fit better with the experimental data and a second regime in the dynamic conditions (steps IV and V) where the simulation with k_T shows better agreement. A simulation with k_T overestimate the moisture in static regions whereas a simulation without k_T underestimate the relative humidity in dynamic regions and is enable to reproduce the cyclic behavior. Therefore, the simulations of static conditions are conducted without k_T and the effect of the later is only integrated for dynamic conditions.

The numerical relative humidity is calculated using the procedure described above and compared to the experimental values (see Fig. 15).

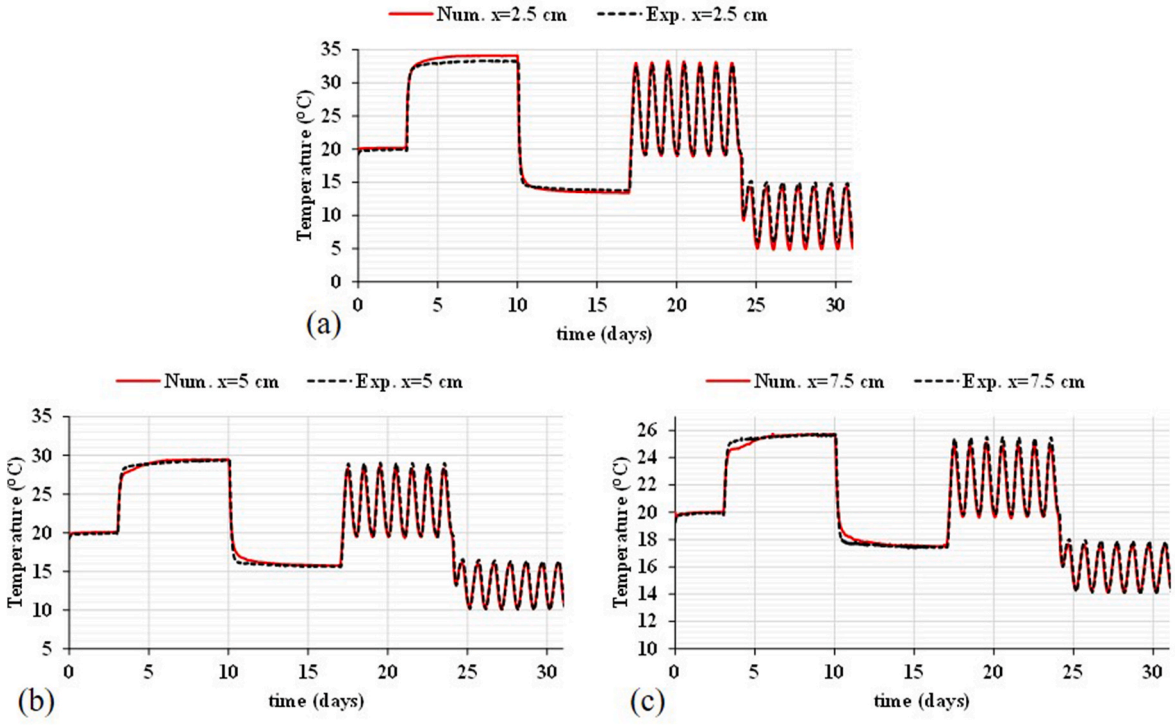

Fig. 12. Comparison between experimental and numerical temperature within PCMHC at x = 2.5 cm (a), 5 cm (b), 7.5 cm (c).

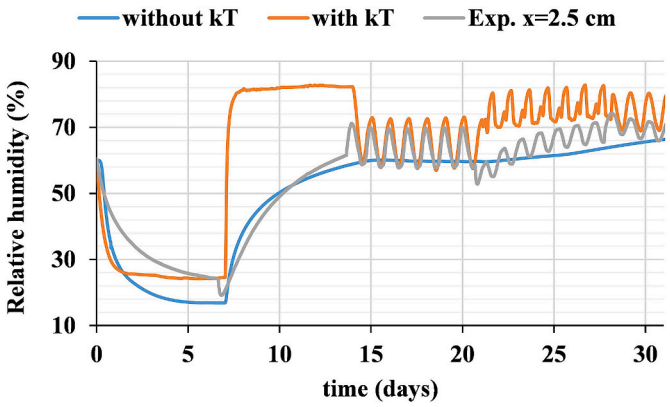

Fig. 14. Comparison of the experimental and numerical relative humidity evolution with and without the total liquid and vapor transfer coefficient due to a temperature gradient (kT).

The experimental and numerical agreement is good. In fact, the RMSE is about 6.02%, 4.69% and 3.81% for 2.5 cm, 5 and 7.5 cm respectively. As for the temperature profile, the precision of the simulation increases with the depth. In addition, the best agreement are observed for the humidification stage (static condition with humidity fixed at 90%) and for typical summer day. The lack of precision for the typical winter day scenario could be attributed to the drastic drop of humidity in the climatic chamber at the beginning of the cycle that the model failed to reproduce. However, the agreement is still good and the numerical model could be used to simulate the hydrothermal behavior of hemp concrete in different climatic conditions.

6. Conclusion

This work focused on the development and evaluation of the experimental and numerical hygrothermal behavior of an innovative building wall made with hemp concrete and incorporating PCMs. HC and PCMHC walls are fabricated in order to test their hygrothermal behavior under various climate conditions: static condition, typical weather day and typical summer day. The following conclusion can be drawn:

- For static weather conditions simulating heat waves periods, the maximum temperature is reduced by 2 °C and 1 °C with the incorporation of the PCM for 2.5 and 5 cm, respectively compared to the reference HC. Under typical summer day conditions, the maximum temperature is reduced by 2 °C for the sensor close to the exterior condition. The reduction is about 1 °C for the sensor at 5 cm and negligible for the sensor at 7.5 cm. The reduction of the maximum temperature by 2 °C under summer heatwaves is due to the raise of the thermal inertia resulting in the incorporation of PCMs. This result is promising for the reduction of cooling needs in buildings. However, for typical winter day scenario, the temperature profile of the two materials shows the same tendency with the temperature slightly higher for the HC that is a better insulator than PCMHC for cold climate.
- Regarding the humidity profile, the kinetic is fast for the HC compared to the PCMHC with a maximum difference of 5% occurring during the drying phase. This observation could be explain by the value of the higher liquid and vapor permeability of HC compared to PCMHC. This reduction was explained by the incorporation of capric acid in hemp shives, which reduces their moisture storage capacity. Both materials showed good moisture regulation capability by dampening cyclic variations in outdoor humidity.
- The numerical model developed showed a good agreement with the experimental results in particular for the thermal behavior. The maximum RMSE between experimental and numerical results is about 0.62 °C and 6.02% for temperature and relative humidity, respectively. The discrepancies are essentially attributed to several factors, including the 1D assumption, the uncertainty of the characterization of the material properties, the uncertainty of the measure and the uncertainty on the position of the sensor.

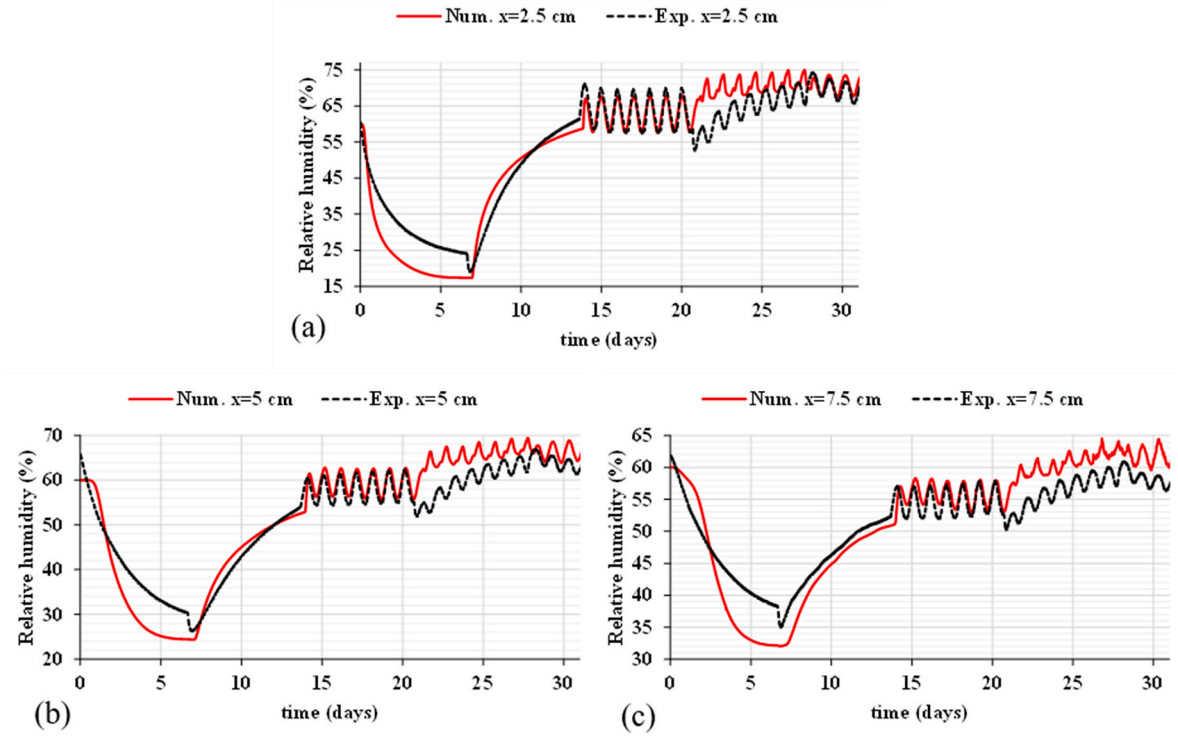

Fig. 15. Comparison between experimental and numerical relative humidity within PCMHC at x = 2.5 cm (a), 5 cm (b), 7.5 cm (c).

Future work will aim at assessing the effect of the PCMHC on the reduction of the cooling and heat loads at a building scale. The hysteresis effect on the accuracy of the numerical model will be assessed. Different configurations of multilayer building walls integrating the PMCHC could be investigated. Finally, a parametric study on the thickness of the layers of the wall and the melting temperature of the phase change material will be carried out in order to optimize the overall system.

Featured application

Passive latent heat storage for building applications, thermal comfort, eco-friendly building materials, high thermal inertia.

CRediT authorship contribution statement

M. Sawadogo: Writing – review & editing, Writing – original draft, Validation, Software, Methodology, Investigation, Formal analysis, Data curation, Conceptualization. **F. Benmahiddine:** Writing – review & editing, Visualization, Validation, Supervision, Methodology, Investigation, Formal analysis, Conceptualization. **A. Godin:** Writing – review & editing, Visualization, Validation, Supervision, Methodology, Investigation, Formal analysis, Conceptualization. **M. Duquesne:** Writing – review & editing, Validation, Supervision, Resources, Project administration, Methodology, Funding acquisition, Formal analysis. **R. Belarbi:** Writing – review & editing, Visualization, Validation, Supervision, Resources, Project administration, Methodology, Funding acquisition, Formal analysis, Conceptualization. **A. Hamami:** Writing – review & editing, Visualization, Validation, Supervision, Project administration, Methodology, Funding acquisition, Formal analysis, Conceptualization.

Declaration of competing interest

The authors declare that they have no known competing financial interests or personal relationships that could have appeared to influence the work reported in this paper

Data availability

Data will be made available on request.

Acknowledgments

This work is carried out in the frame of Region Nouvelle Aquitaine for subsidizing BioMCP project (Project-2017-1R10209-13023) and in the frame of the Laboratory for Energy and Environmental Efficiency of Envelopes and Cities, 4ev Lab, the joint Laboratory between EDF R&D, CNRS, LaSIE conducting research to improve the energy and environmental performance of buildings and the quality of life of the inhabitants of urban spaces.

Appendix A

Table A-1
Minimum, maximum and average length and width of the hemp shives used

	Minimum	Maximum	Average
Length (mm)	4.06	32.45	11.99
Width (mm)	1.69	7.62	4.06
Length/width (−)	1.28	9.13	2.98

Table A-2
General information about capric acid (CA). * Purity as given by the supplier.

Fatty Acid	Acronym	CAS Number	Formula	Supplier	**Price (€/kg)**	Purity * (%)	**Melting Temperature (°C)** [24,53]
Capric acid (Decanoic acid)	CA	334-48-5	$C_{10}H_{20}O_2$	Alfa Aesar	75.1	99	29–33

Table A-3
Temperature, heating rate and RH ranges of the climatic chamber.

Climatic Chamber	Temperature range (°C)	Heating rate range (°C.min^{-1})	RH range (%)
C-40	−40 to 50	0.5 to 35	+10 to +98
C-20	−20 to 70	0.5 to 35	+10 to +98

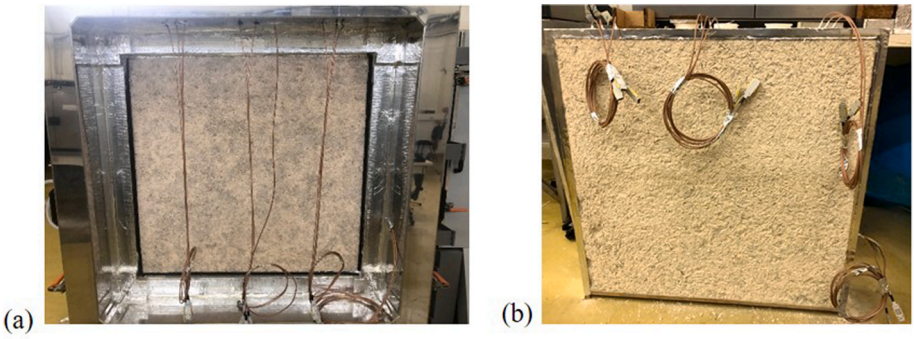

Figure A-1. *90 × 90 × 10 cm^3 insulating walls: Reference hemp concrete (a) and PCM hemp concrete (b).*

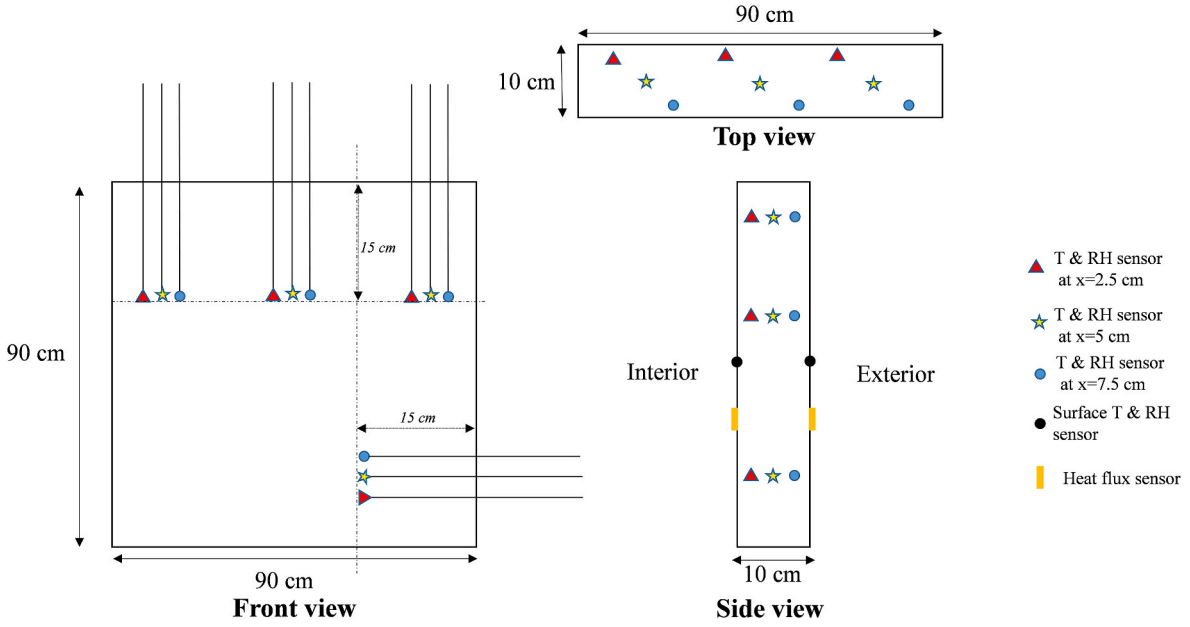

Figure A-2. Position of the temperature and relative humidity sensors, and heat flux sensors.

Figure A-3. C-40/1000/S – C-20/1000/S bi-climatic chamber from CTS GmbH for the hygrothermal test.

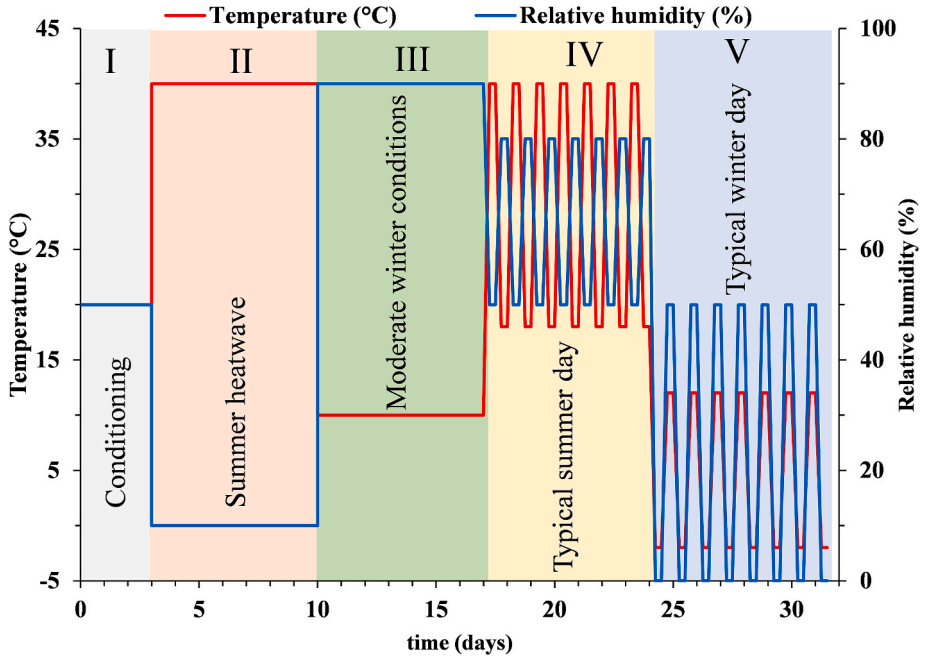

Figure A-4. Temperature and relative humidity program for the hygrothermal test in the climatic chamber.

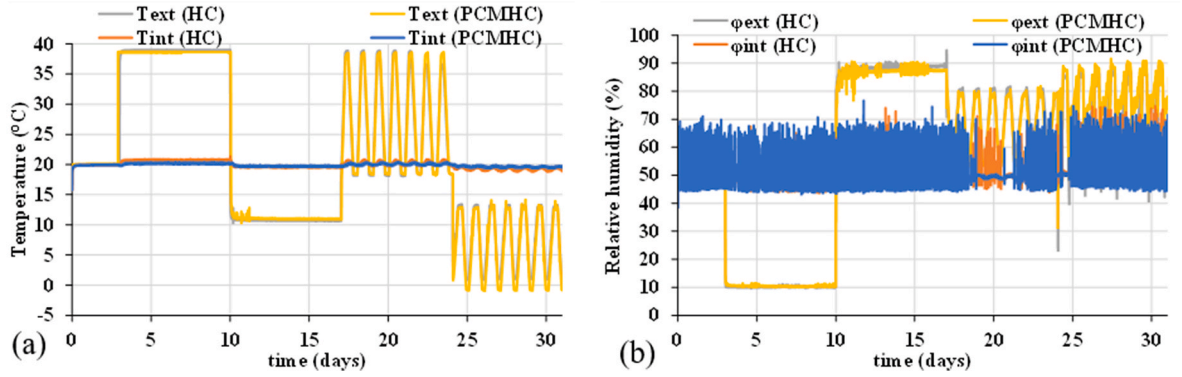

Figure A-5. Interior and exterior temperature (a), relative humidity (b) for the hygrothermal performances test.

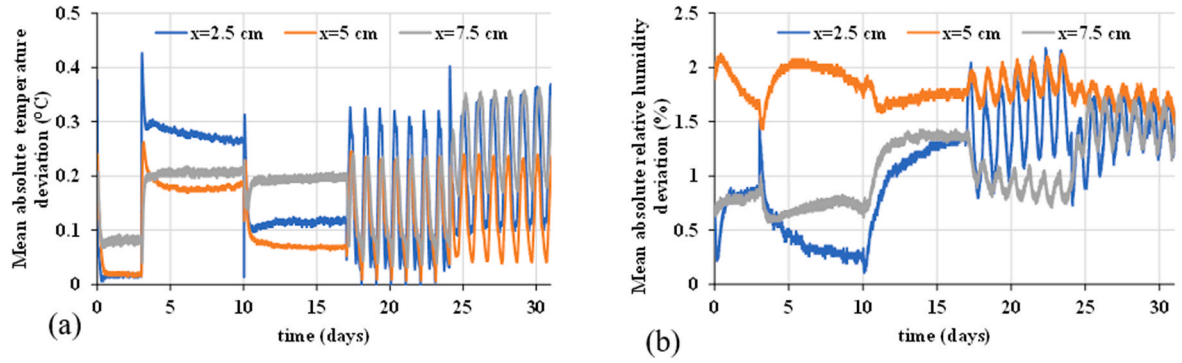

Figure A-6. Mean absolute temperature deviation (a), relative humidity deviation (b) of sensors at x = 2.5, 5 and 7.5 cm.

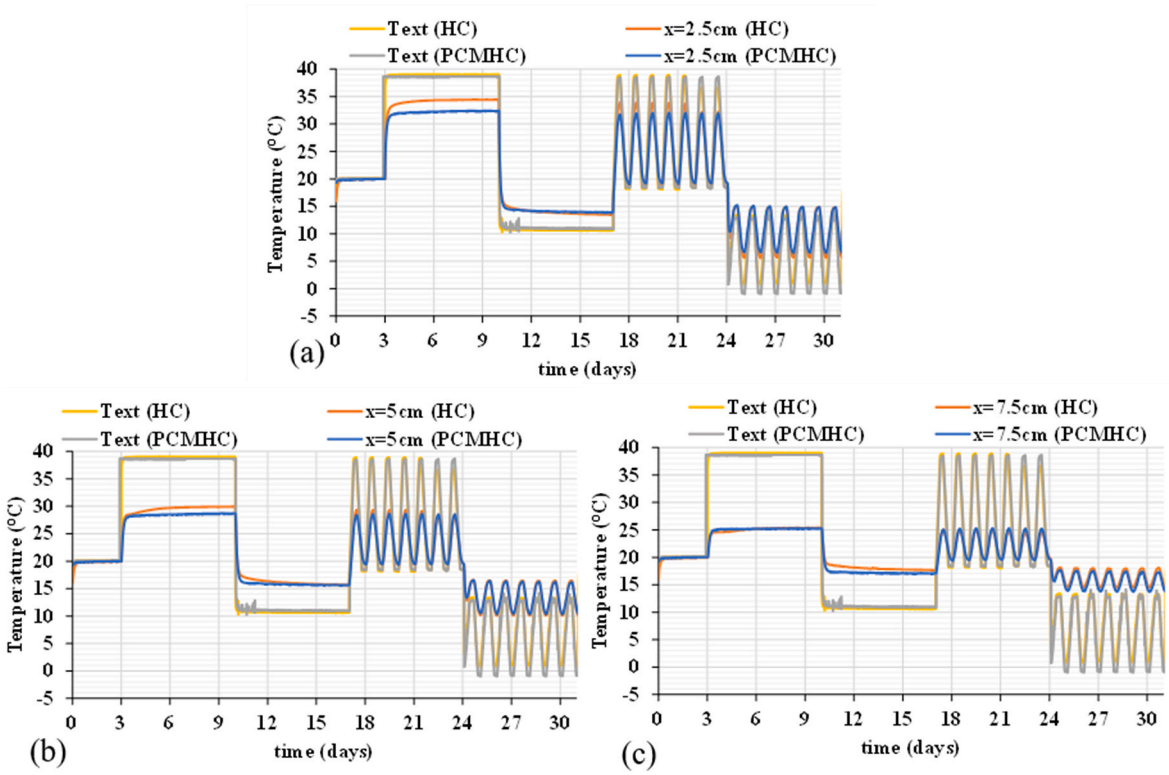

Figure A-7. Evolution of the temperature for HC and PCMHC at x = 2.5 (a), 5 (b), 7.5 cm (c) for the whole duration of the test.

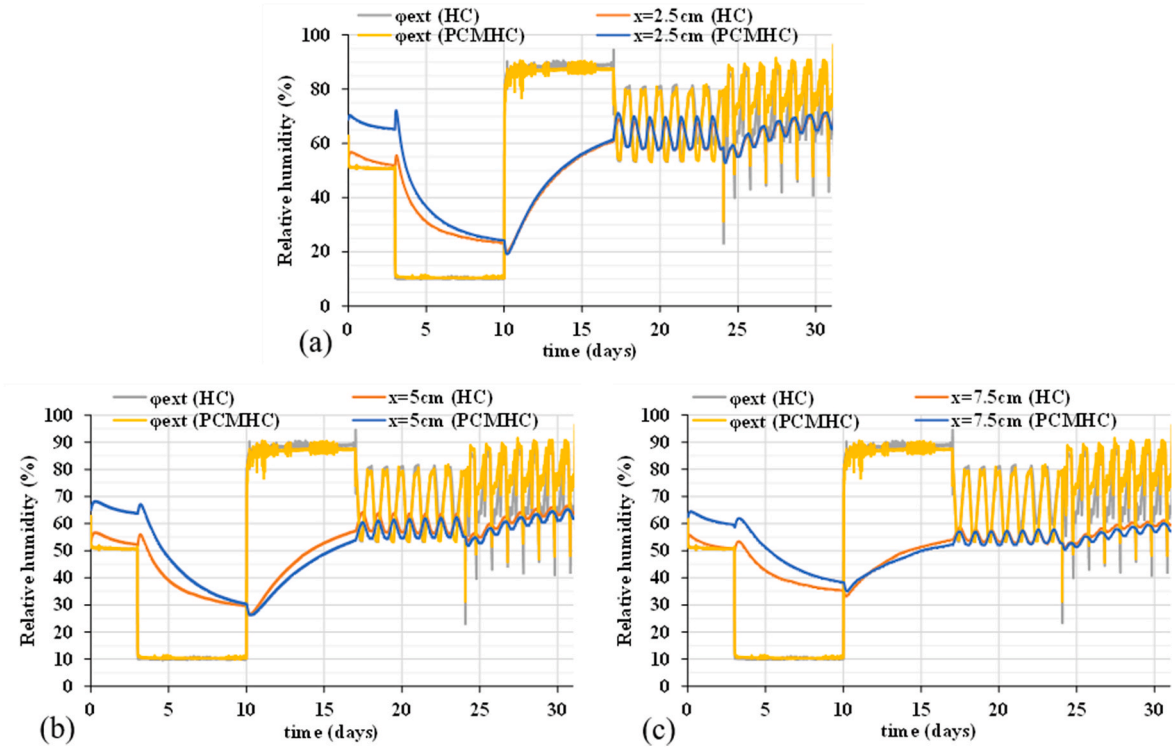

Figure A-8. Evolution of the relative humidity for HC and PCMHC at x = 2.5 cm (b), 5 cm (b), 7.5 cm (c) for the whole duration of the test.

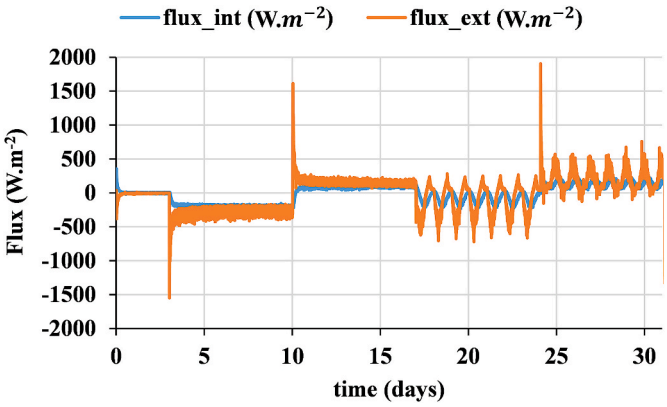

Figure A-9. Interior and exterior heat flux densities at the surface of the walls.

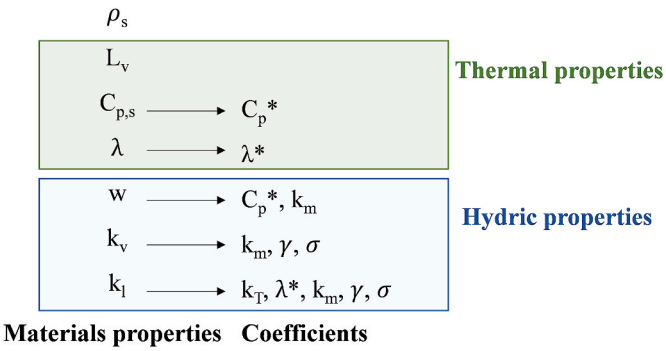

Figure A-10. Material hygrothermal properties and the links with the coefficients of the model.

Appendix B

The mass and energy balance equations are written for each phase (liquid and vapor) and presented in their conservative form under the assumptions mentioned in section 5.1:

$$\frac{\partial w_v}{\partial t} = -div(j_v) + \dot{m} \tag{B1}$$

$$\frac{\partial w_l}{\partial t} = -div(j_l) - \dot{m} \tag{B2}$$

$$\frac{\partial(\rho_s h)}{\partial t} = -div(j_q) \tag{B3}$$

where w_v (kg/m^3) is the water vapor content, w_l (kg/m^3) liquid water content, ρ_s (kg/m^3) the dry density of the material, j_v, j_l and j_q water vapor, liquid and heat flux, respectively, and $\dot{m}$ (kg/(s.m^3)) a source term for the liquid-vapor transition of water.

Vapor phase transport

The transport of the vapor phase is a diffusion process governed by Fick's law that is expressed in porous media as follows:

$$j_v = -\alpha a D \frac{P}{P - P_v} \nabla \rho_v \tag{B4}$$

where a is the gas phase volume content, P (Pa) is the total pressure, P_v is the partial pressure of water vapor, ρ_v (kg.m^{-3}) is its density, D (m^2.s^{-1}) is the binary diffusion coefficient of water vapor in air, and α is a dimensionless factor that reflects the geometric influence of the porous medium on vapor diffusion.

By considering the vapor phase as a perfect gas and using the relationship between P_v, saturation pressure $P_{v,sat}$ (Pa) and relative humidity φ (%), it is possible to express the vapor flow as a function of vapor pressure and temperature, which are the two drivers of interest in this study. Thus, we obtain:

$$j_v = -\delta_v \nabla P_v - k_{T,v} \nabla T \tag{B5}$$

where δ_v (kg.m^{-1}.s^{-1}.Pa^{-1})) is the water vapor permeability and k_v^T (kg.m^{-1}.s^{-1}.K^{-1}) is the vapor transfer coefficient due to a temperature gradient.

Liquid phase transport

Non-isothermal liquid flow in unsaturated porous materials is induced by the capillary suction pressure gradient. By neglecting the Gravity-driven moisture flow, the liquid water flux is as follows:

$$j_l = -k_l \nabla P_c \tag{B6}$$

where k_l (kg.m^{-1}.s^{-1}.Pa^{-1}) is the liquid water permeability coefficient.

Considering the hypothesis of local equilibrium between liquid water and its vapor, Kelvin's law allows us to write the flow of liquid as a function of vapor pressure and temperature, in the same way as with the vapor phase.

$$P_c = \frac{RT\rho_l}{M}\ln(\varphi) = \frac{RT\rho_l}{M}\ln\left(\frac{P_v}{P_{v,sat}}\right) \tag{B7}$$

$$j_l = -k_{T,l}\nabla T - k_{l,P_v}\nabla P_v \tag{B8}$$

with P_c (Pa) the capillary pressure, φ (%) relative humidity, ρ_l (kg.m^{-3}) the density of liquid water, R (J.mol^{-1}.K^{-1}) the ideal gas constant, M (kg.mol^{-1}) the molar mass of water, T (K) the temperature, $P_{v,sat}$ (Pa) the saturation vapor pressure, $k_{T,l} = k_l\frac{R\rho_l}{M}\left[\ln\left(\frac{P_v}{P_{v,sat}}\right) + \frac{T}{P_{v,sat}}\frac{\partial P_{v,sat}}{\partial T}\right]$ (kg.m^{-1}.s^{-1}.K^{-1}) is the liquid phase coefficient governed by a temperature gradient and $k_{l,P_v} = k_l\frac{RT\rho_l}{MP_v}$ (kg.m^{-1}.s^{-1}.Pa^{-1}) the liquid phase transfer coefficient, governed by a water vapor pressure gradient.

Total moisture transport

The total moisture transport equation is obtained by adding the mass conservation equations of the liquid and vapor phase. This yield:

$$\frac{\partial w}{\partial t} = -div(j_m) \tag{B9}$$

with $w = w_v + w_l$, the total moisture content and $j_m = j_v + j_l$, the total moisture flux.

$$j_m = -k_T\nabla T - k_m\nabla P_v \tag{B10}$$

where $k_T = k_{T,l} + k_{T,v}$ and $k_m = \delta_v + k_{l,P_v}$.

The left-hand side of Equation (B9) is now modified to show the vapor pressure instead of the total humidity and yields to equation A11.

$$\frac{\partial w}{\partial t} = \frac{\partial \rho_s u}{\partial t} = \rho_s\frac{\partial u}{\partial \varphi}\frac{\partial \varphi}{\partial t} = \rho_s\frac{C_m}{P_{v,sat}}\frac{\partial P_v}{\partial t} \tag{B11}$$

with $C_m = \frac{\partial u}{\partial \varphi}$ (−) the moisture storage capacity of the material.

The final total moisture transport equation is written as:

$$\rho_s\frac{C_m}{P_{v,sat}}\frac{\partial P_v}{\partial t} = div(-k_T\nabla T - k_m\nabla P_v) \tag{B12}$$

Heat transfer equation

Heat transfer in porous media occurs by conduction under a thermal gradient by application of Fourier's law, by convection through the displacement of the liquid and vapor phase and through phase change phenomena. The heat flux density and the total enthalpy are written as follows:

$$j_q = -\lambda\nabla T + h_l j_l + h_v j_v \tag{B13}$$

$$h = h_s + w_l h_l + w_v h_v \tag{B14}$$

with λ (W.m^{-1}.K^{-1}) the heat conductivity of the material, $h_l = C_{p,l}(T - T_{ref})$,$h_v = C_{p,l}(T - T_{ref}) + L_v$ and $h_s = C_{p,s}(T - T_{ref})$, $C_{p,l}$ (J.kg^{-1}.K^{-1}) and $C_{p,s}$ (J.kg^{-1}.K^{-1}) the specific heat of liquid water and solid material respectively, L_v (J.kg^{-1}) the latent heat of vaporization of water and $T_{ref}(K)$ the reference temperature.

By replacing the expressions for the vapor and liquid flux into Equation (B13), we get:

$$j_q = -\lambda^*\nabla T - \gamma\nabla P_v \tag{B15}$$

where $\lambda^* = \lambda + h_l k_{T,l}$ (W.m^{-1}.K^{-1}) and $\gamma = k_v L_v + h_l k_m$ (W.m^{-1}.Pa^{-1}).

Transferring Equations B13-B15 into Equation (B3), we obtain:

$$\frac{\partial(\rho_s(h_s + w_l h_l + w_v h_v))}{\partial t} = -div(-\lambda\nabla T + h_l j_l + h_v j_v) \tag{B16}$$

By modifying the equation to show the temperature explicitly, we have:

$$\rho_s\left(C_{p,s}+w_l C_{p,l}+w_v C_{p,l}\right)\frac{\partial T}{\partial t}+\rho_s h_l\frac{\partial w_l}{\partial t}+\rho_s h_l\frac{\partial w_v}{\partial t}+\rho_s L_v\frac{\partial w_v}{\partial t}=-div(-\lambda^*\nabla T-\gamma\nabla P_v) \tag{B17}$$

An analysis of the order of magnitude shows that it is possible to neglect the convective transfer by sensible heat compared to the latent heat terms [38]. The heat transfer equation is therefore simplified as follows:

$$\rho_s C_p^*\frac{\partial T}{\partial t}=div(\lambda^*\nabla T+\gamma\nabla P_v)+\rho_s C_m\sigma L_v\frac{\partial P_v}{\partial t} \tag{B18}$$

where $\sigma=\frac{\partial w_v}{\partial w}=\frac{j_v}{j_m}$ defines the proportion of vapor transferred in a body in relation to the total flow of vapor and liquid also called phase change criterion (PCC), $C_p^*=C_{p,s}+uC_{p,l}$.

Finally, the system of coupled transfer equations is as follows (Equations (3) and (4) in the paper):

$$\rho_s\frac{C_m}{P_{v,sat}}\frac{\partial P_v}{\partial t}=div(-k_T\nabla T-k_m\nabla P_v) \tag{B19}$$

$$\rho_s C_p^*\frac{\partial T}{\partial t}=div(\lambda^*\nabla T+\gamma\nabla P_v)+\rho_s C_m\sigma L_v\frac{\partial P_v}{\partial t} \tag{B20}$$

References

[1] Global Status Report for Buildings and Construction 2019 – Analysis, IEA. (n.d.). https://www.iea.org/reports/global-status-report-for-buildings-and-construction-2019 (accessed June 21, 2023).

[2] H. Gabay, I.A. Meir, M. Schwartz, E. Werzberger, Cost-benefit analysis of green buildings: an Israeli office buildings case study, Energy Build. 76 (2014) 558–564, https://doi.org/10.1016/j.enbuild.2014.02.027.

[3] Y. Shang, F. Tariku, Hempcrete building performance in mild and cold climates: integrated analysis of carbon footprint, energy, and indoor thermal and moisture buffering, Build. Environ. 206 (2021), 108377, https://doi.org/10.1016/j.buildenv.2021.108377.

[4] R. Ramirez, B. Ghiassi, P. Pineda, P.B. Lourenço, Simulation of moisture transport in fired-clay brick masonry structures accounting for interfacial phenomena, Build. Environ. 228 (2023), 109838, https://doi.org/10.1016/j.buildenv.2022.109838.

[5] M.S. Rahman, T. Chauvin-Bossé, A. Akbarzadeh, A. Guerini, J. Chapelat, M. Lefsrud, Experimental investigation of heat and moisture transfer with ventilation through porous concrete with embedded coils for air conditioning, Build. Environ. 222 (2022), 109370, https://doi.org/10.1016/j.buildenv.2022.109370.

[6] W. Yu, Y. Zhang, B. Li, Y. Zhang, C. Du, Z. Zhao, et al., Increased risk of respiratory and allergic diseases in preschoolers from building envelope dampness exposure: repeated cross-sectional surveys in multicity China, Build. Environ. 241 (2023), 110433, https://doi.org/10.1016/j.buildenv.2023.110433.

[7] J. Wang, Y. Zhang, B. Li, Z. Zhao, C. Huang, X. Zhang, et al., Effects of mold, water damage and window pane condensation on adult rhinitis and asthma partly mediated by different odors, Build. Environ. 227 (2023), 109814, https://doi.org/10.1016/j.buildenv.2022.109814.

[8] G.M. Amantino, N.P. Hasparyk, F. Tiecher, R.D. Toledo Filho, Assessment of bio-aggregate concretes' properties with rice residue, J. Build. Eng. 52 (2022), 104348, https://doi.org/10.1016/j.jobe.2022.104348.

[9] M. Yadav, M. Agarwal, Biobased building materials for sustainable future: an overview, Mater. Today: Proc. 43 (2021) 2895–2902, https://doi.org/10.1016/j.matpr.2021.01.165.

[10] P. Tyagi, S. Ahmed, C.W. Lai, in: S. Ahmed, Annu (Eds.), Chapter 32 - future prospects of biobased materials, Advanced Applications of Biobased Materials, Elsevier, 2023, pp. 749–764, https://doi.org/10.1016/B978-0-323-91677-6.00013-1.

[11] M. Yadav, M. Agarwal, Biobased building materials for sustainable future: an overview, Mater. Today: Proc. 43 (2021) 2895–2902, https://doi.org/10.1016/j.matpr.2021.01.165.

[12] S. Amziane, F. Collet, Bio-aggregates Based Building Materials: State-Of-The-Art Report of the RILEM Technical Committee 236-BBM, Springer, 2017.

[13] F. Benmahiddine, R. Cherif, F. Bennai, R. Belarbi, A. Tahakourt, K. Abahri, Effect of flax shives content and size on the hygrothermal and mechanical properties of flax concrete, Construct. Build. Mater. 262 (2020), 120077, https://doi.org/10.1016/j.conbuildmat.2020.120077.

[14] M.P. Sáez-Pérez, M. Brümmer, J.A. Durán-Suárez, A review of the factors affecting the properties and performance of hemp aggregate concretes, J. Build. Eng. 31 (2020), 101323, https://doi.org/10.1016/j.jobe.2020.101323.

[15] S. Barbhuiya, B. Bhusan Das, A comprehensive review on the use of hemp in concrete, Construct. Build. Mater. 341 (2022), 127857, https://doi.org/10.1016/j.conbuildmat.2022.127857.

[16] A.T.M.F. Ahmed, M.Z. Islam, M.S. Mahmud, M.E. Sarker, M.R. Islam, Hemp as a potential raw material toward a sustainable world: a review, Heliyon 8 (2022), e08753, https://doi.org/10.1016/j.heliyon.2022.e08753.

[17] F. Benmahiddine, F. Bennai, R. Cherif, R. Belarbi, A. Tahakourt, K. Abahri, Experimental investigation on the influence of immersion/drying cycles on the hygrothermal and mechanical properties of hemp concrete, J. Build. Eng. 32 (2020), 101758, https://doi.org/10.1016/j.jobe.2020.101758.

[18] E. Latif, M. Lawrence, A. Shea, P. Walker, Moisture buffer potential of experimental wall assemblies incorporating formulated hemp-lime, Build. Environ. 93 (2015) 199–209, https://doi.org/10.1016/j.buildenv.2015.07.011.

[19] M. Sawadogo, F. Benmahiddine, A.E.A. Hamami, R. Belarbi, A. Godin, M. Duquesne, Investigation of a novel bio-based phase change material hemp concrete for passive energy storage in buildings, Appl. Therm. Eng. 212 (2022), 118620, https://doi.org/10.1016/j.applthermaleng.2022.118620.

[20] M. Saffari, C. Roe, D.P. Finn, Improving the building energy flexibility using PCM-enhanced envelopes, Appl. Therm. Eng. 217 (2022), 119092, https://doi.org/10.1016/j.applthermaleng.2022.119092.

[21] Y. Abdellatef, M. Kavgic, Thermal, microstructural and numerical analysis of hempcrete-microencapsulated phase change material composites, Appl. Therm. Eng. 178 (2020), 115520, https://doi.org/10.1016/j.applthermaleng.2020.115520.

[22] A. Al-Janabi, M. Kavgic, Application and sensitivity analysis of the phase change material hysteresis method in EnergyPlus: a case study, Appl. Therm. Eng. 162 (2019), 114222, https://doi.org/10.1016/j.applthermaleng.2019.114222.

[23] M. Duquesne, C. Mailhé, K. Ruiz-Onofre, F. Achchaq, Biosourced organic materials for latent heat storage: an economic and eco-friendly alternative, Energy 188 (2019), 116067, https://doi.org/10.1016/j.energy.2019.116067.

[24] M. Duquesne, C. Mailhé, S. Doppiu, J.-L. Dauvergne, S. Santos-Moreno, A. Godin, et al., Characterization of fatty acids as biobased organic materials for latent heat storage, Materials 14 (2021) 4707, https://doi.org/10.3390/ma14164707.

[25] K. Sergei, C. Shen, Y. Jiang, A review of the current work potential of a trombe wall, Renew. Sustain. Energy Rev. 130 (2020), 109947, https://doi.org/10.1016/j.rser.2020.109947.

[26] M. Jafaripour, S.M. Sadrameli, H. Pahlavanzadeh, S.A.H.S. Mousavi, Fabrication and optimization of kaolin/stearic acid composite as a form-stable phase change material for application in the thermal energy storage systems, J. Energy Storage 33 (2021), 102155, https://doi.org/10.1016/j.est.2020.102155.

[27] P.K.S. Rathore, S.K. Shukla, Enhanced thermophysical properties of organic PCM through shape stabilization for thermal energy storage in buildings: a state of the art review, Energy Build. 236 (2021), 110799, https://doi.org/10.1016/j.enbuild.2021.110799.

[28] S.R.L. da Cunha, J.L.B. de Aguiar, Phase change materials and energy efficiency of buildings: a review of knowledge, J. Energy Storage 27 (2020), 101083, https://doi.org/10.1016/j.est.2019.101083.

[29] M. Sawadogo, M. Duquesne, R. Belarbi, A.E.A. Hamami, A. Godin, Review on the integration of phase change materials in building envelopes for passive latent heat storage, Appl. Sci. 11 (2021) 9305, https://doi.org/10.3390/app11199305.

[30] T. Yang, Y. Ding, B. Li, A.K. Athienitis, A review of climate adaptation of phase change material incorporated in building envelopes for passive energy conservation, Build. Environ. (2023), 110711, https://doi.org/10.1016/j.buildenv.2023.110711.

[31] S. Zhang, D. Feng, L. Shi, L. Wang, Y. Jin, L. Tian, et al., A review of phase change heat transfer in shape-stabilized phase change materials (ss-PCMs) based on porous supports for thermal energy storage, Renew. Sustain. Energy Rev. 135 (2021), 110127, https://doi.org/10.1016/j.rser.2020.110127.

[32] B. Lamrani, K. Johannes, F. Kuznik, Phase change materials integrated into building walls: an updated review, Renew. Sustain. Energy Rev. 140 (2021), 110751, https://doi.org/10.1016/j.rser.2021.110751.

[33] F. Benmahiddine, Études des transferts couplés de chaleur, d'air et d'humidité par des techniques de changement d'échelle (microscopique-macroscopique) : application à l'évaluation de la performance énergétique et la durabilité des

matériaux de construction, These de doctorat, La Rochelle, https://www.theses.fr/2020LAROS029, 2020. (Accessed 5 April 2023).
[34] F. Benmahiddine, Études des transferts couplés de chaleur, d'air et d'humidité par des techniques de changement d'échelle (microscopique-macroscopique) : Application à l'évaluation de la performance énergétique et la durabilité des matériaux de construction, Université de La Rochelle ; Université Abderrahmane Mira, Bejaïa (Bejaïa, Algérie), 2020 phd thesis, https://theses.hal.science/tel-03516072. (Accessed 15 August 2023).
[35] M. Sawadogo, A. Godin, M. Duquesne, E. Lacroix, A. Veillère, A.E.A. Hamami, et al., Investigation of eco-friendly and economic shape-stabilized composites for building walls and thermal comfort, Build. Environ. 231 (2023), 110026, https://doi.org/10.1016/j.buildenv.2023.110026.
[36] D.C. Nomades, Météo à La Rochelle en 2022, Historique Météo. (n.d.). https://www.historique-meteo.net/france/charentes/la-rochelle/2022/(accessed August 15, 2023).
[37] NF EN 821-3:2005, Céramiques techniques avancées - Céramiques monolithiques - Propriétés thermophysiques - Partie 3 : détermination de la chaleur spécifique, 2005.
[38] NF EN 12664:2001, Performance thermique des matériaux et produits pour le bâtiment - Détermination de la résistance thermique par la méthode de la plaque chaude gardée et la méthode fluxmétrique - Produits secs et humides de moyenne et basse résistance thermique, 2001.
[39] NF EN 12667:2001, Performance thermique des matériaux et produits pour le bâtiment - Détermination de la résistance thermique par la méthode de la plaque chaude gardée et la méthode fluxmétrique - Produits de haute et moyenne résistance thermique, 2001.
[40] M.M. Umair, Y. Zhang, K. Iqbal, S. Zhang, B. Tang, Novel strategies and supporting materials applied to shape-stabilize organic phase change materials for thermal energy storage–A review, Appl. Energy 235 (2019) 846–873, https://doi.org/10.1016/j.apenergy.2018.11.017.
[41] L. Boussaba, G. Lefebvre, S. Makhlouf, A. Grados, L. Royon, Investigation and properties of a novel composite bio-PCM to reduce summer energy consumptions in buildings of hot and dry climates, Sol. Energy 214 (2021) 119–130, https://doi.org/10.1016/j.solener.2020.11.060.
[42] M. Dehmous, E. Franquet, N. Lamrous, Mechanical and thermal characterizations of various thermal energy storage concretes including low-cost bio-sourced PCM, Energy Build. 241 (2021), 110878, https://doi.org/10.1016/j.enbuild.2021.110878.
[43] D.G. Atinafu, W. Dong, X. Huang, H. Gao, G. Wang, Introduction of organic-organic eutectic PCM in mesoporous N-doped carbons for enhanced thermal conductivity and energy storage capacity, Appl. Energy 211 (2018) 1203–1215, https://doi.org/10.1016/j.apenergy.2017.12.025.
[44] European Standard ISO 12572 Building Materials – Determination of Water Vapor Transmission Properties (ISO/DIS 12572:1997) PrEN ISO 12572, 1997.
[45] T. Jami, S.R. Karade, L.P. Singh, A review of the properties of hemp concrete for green building applications, J. Clean. Prod. 239 (2019), 117852, https://doi.org/10.1016/j.jclepro.2019.117852.
[46] M. Sawadogo, A. Godin, M. Duquesne, R. Belarbi, A. Hamami, An inverse method for the estimation of the vapor and liquid diffusivity coefficient of hemp concrete and phase change material-based hemp concrete materials, Construct. Build. Mater.
[47] J.R. Philip, D.A. De Vries, Moisture movement in porous materials under temperature gradients, Eos, Trans. Am. Geophys. Union 38 (1957) 222–232.
[48] P. Crausse, J.P. Laurent, B. Perrin, Influence des phénomènes d'hystérésis sur les propriétés hydriques de matériaux poreux: comparaison de deux modèles de simulation du comportement thermohydrique de parois de bâtiment, Rev. Gen. Therm. 35 (1996) 95–106, https://doi.org/10.1016/S0035-3159(96)80002-X.
[49] Y. Ferroukhi, R. Djedjig, K. Limam, R. Belarbi, Hygrothermal behavior modeling of the hygroscopic envelopes of buildings: a dynamic co-simulation approach, Build. Simulat. 9 (2016), https://doi.org/10.1007/s12273-016-0292-5.
[50] B. Remki, K. Abahri, M. Tahlaiti, R. Belarbi, Hygrothermal transfer in wood drying under the atmospheric pressure gradient, Int. J. Therm. Sci. 57 (2012) 135–141, https://doi.org/10.1016/j.ijthermalsci.2012.02.005.
[51] X. Wang, X. Jin, Y. Yin, X. Shi, X. Zhou, A transient heat and moisture transfer model for building materials based on phase change criterion under isothermal and non-isothermal conditions, Energy 224 (2021), 120112, https://doi.org/10.1016/j.energy.2021.120112.
[52] A. Trabelsi, R. Belarbi, K. Abahri, M. Qin, Assessment of temperature gradient effects on moisture transfer through thermogradient coefficient, Build. Simulat. 5 (2012) 107–115, https://doi.org/10.1007/s12273-012-0063-x.
[53] H. Ke, Phase diagrams, eutectic mass ratios and thermal energy storage properties of multiple fatty acid eutectics as novel solid-liquid phase change materials for storage and retrieval of thermal energy, Appl. Therm. Eng. 113 (2017) 1319–1331, https://doi.org/10.1016/j.applthermaleng.2016.11.158.

Article 6

buildings

MDPI

Article

Experimental Characterization of Raw Earth Properties for Modeling Their Hygrothermal Behavior

Yassine Elias Belarbi [1], Mohamed Sawadogo [2], Philippe Poullain [1], Nabil Issaadi [1], Ameur El Amine Hamami [2], Stéphanie Bonnet [1] and Rafik Belarbi [2,3,*]

[1] GeM UMR CNRS 6183, Université de Nantes, 52 Rue Michel Ange, CEDEX, F-44606 Saint-Nazaire, France; yassine.belarbi1@etu.univ-nantes.fr (Y.E.B.); philippe.poullain@univ-nantes.fr (P.P.); nabil.issaadi@univ-nantes.fr (N.I.); stephanie.bonnet@univ-nantes.fr (S.B.)
[2] LaSIE UMR 7356 CNRS, La Rochelle Université, Avenue Michel Crépeau, CEDEX 01, F-17042 La Rochelle, France; mohamed.sawadogo@univ-lr.fr (M.S.); ahamami@univ-lr.fr (A.E.A.H.)
[3] Department of Civil and Building Engineering, Université de Sherbrooke, 2500 Bd de l'Université, Sherbrooke, QC J1K 2R1, Canada
* Correspondence: rbelarbi@univ-lr.fr; Tel.: +33-(0)5-46-45-86-25

Abstract: Raw earth is one of the oldest building materials of mankind. Almost a third of the world's population is living in an earth-based house. However, their use remains low compared to conventional materials such as concrete, steel, and wood. Although these geosourced materials are abundant, recyclable, and have a low environmental footprint, their use is very limited in the construction sector. This can be explained by the lack of data regarding their hygrothermal behavior. In this context, the present work aims to highlight the properties of cob construction material with straw addition. An experimental characterization of hygrothermal and microstructural properties has been carried out. Thermal conductivity, specific heat, sorption isotherms, moisture storage capacity, moisture buffer value (MBV), and water vapor permeability are obtained experimentally. Then, the collected data are used as input parameters of a numerical prediction model to numerically assess the thermal and hygric behavior. Cob is then compared to other more commonly used materials to highlight the benefits of its use within the context of the energetic and environmental transition. Our results will allow better understanding of the behavior of the new geosourced material thanks to experimental and numerical investigation.

Keywords: raw earth; hygrothermal characterization; microstructure; moisture buffer capacity

check for updates

Citation: Belarbi, Y.E.; Sawadogo, M.; Poullain, P.; Issaadi, N.; Hamami, A.E.A.; Bonnet, S.; Belarbi, R. Experimental Characterization of Raw Earth Properties for Modeling Their Hygrothermal Behavior. *Buildings* **2022**, *12*, 648. https://doi.org/10.3390/buildings12050648

Academic Editors: Luís Filipe Almeida Bernardo and Miguel Nepomuceno

Received: 31 March 2022
Accepted: 9 May 2022
Published: 12 May 2022

Publisher's Note: MDPI stays neutral with regard to jurisdictional claims in published maps and institutional affiliations.

Copyright: © 2022 by the authors. Licensee MDPI, Basel, Switzerland. This article is an open access article distributed under the terms and conditions of the Creative Commons Attribution (CC BY) license (https://creativecommons.org/licenses/by/4.0/).

1. Introduction

The 19th century marked the beginning of the first Industrial Revolution in the British Empire. During this time, the negative impact of humans on the environment was observed. Overexploitation of various natural resources and the large emission of harmful gases, especially carbon dioxide (CO_2), are the main causes of this problem.

The major activity sectors with an important environmental footprint are intensive agriculture, transportation, and industry. However, the building industry remains the sector with the most negative impact on our planet. It represents 44% of the energy consumed in France [1] and is responsible for 37% of the CO_2 emission [2] as well as 13 to 30% of the waste produced worldwide [3]. This high environmental footprint is broadly caused by concrete. Concrete is the world's most used construction material, with 10 billion cubic meters poured per year [4]. Cement is the main component of concrete. It represents 8% of the total CO_2 emission [5]. Hence, reducing this impact for both existing and new constructions is one of the major societal issues related to the energy and environmental transition. Actually, several approaches can be studied to address this issue while improving the energy and environmental performance of buildings. In France, the new thermal and environmental regulation (RE2020) [6] requires (i) constructing hermetic

buildings with high thermal insulation, (ii) establishing harmonious relationships between the building and its environment, (iii) creating a comfortable and healthy environment for its users, and (iv) preserving natural resources by optimizing their use and by polluting less. To sum up, reducing the carbon footprint of buildings, pursuing the improvement of their energy performance, and ensuring their coolness during hot summers are the major objectives of the RE2020. Thus, one of the approaches that has been considered to achieve these objectives is developing less energy-intensive, more energy-efficient, and environment-friendly materials by using geosourced materials.

Raw earth has been used since the beginning of the sedentarization of mankind around 15,000 BC. However, it was not popular until the 9th millennium when raw earth was used to build cities, particularly in Mesopotamia. Besides, the establishment of cities at that time was not only based on the need to settle near waterways. It was also based on the availability and the quality of raw earth [7]. This material is known to be abundant and reusable. Additionally, raw earth behaves as a thermal and hygrometric regulator, allowing a very comfortable atmosphere during all seasons [8]. However, the growth of the concrete industry has led to lesser use of raw earth, even though almost one third of the world's population lives in a raw earth house [9]. This marginalization is due to the lack of awareness of this material's properties.

There are several construction methods related to raw earth. We can notably find compressed earth block (CEB), rammed earth, wattle and daub, and adobe. Compressed earth blocks (CEB) are a type of adobe brick, made in presses that compress wet, powdered earth. Rammed earth is a process that consists of building monolithic and load-bearing walls of more than 40 cm thickness. The material is compacted in successive layers in a formwork, traditionally made of wood. The loamy earth is worked in a loose state with limited water and may contain stones to increase the mechanical strength. Rammed earth does not contain any fiber. Wattle and daub is a mixture of clay and straw or vegetable fibers. It is only used to fill walls whose structure is wood-framed, or with wooden racks. The adobe construction method is defined by the use of earth bricks that have been air-dried without having been fired in a kiln. A clay soil is used, to which vegetable fibers can be added. The bricks are traditionally hand-molded in a wooden mold and then dried at an indoor air temperature (the bricks are not pressed as for CEB). Within the framework of our study, we are interested in the cob as our construction method. This very old process consists of mixing raw earth with water and sometimes adding vegetable fibers. This mixture is then used in a plastic state and shaped into balls in order to build monolithic walls. This technique has been used for thousands of years in all types of climates. The cob construction method is very resistant to very rainy weather thanks to its porosity. It can even withstand rain for long periods of time [10,11]. Not to mention, it has two major advantages: the effortless construction and the freedom of design compared to other construction methods, such as adobe, compressed earth blocks, or rammed earth, whereas the production of cob requires 18 to 38% of the energy needed for conventional materials. Furthermore, the use of cob reduces the impact of global climate change by 75 to 82% [12]. The term cob comes from England, but we also have the terms of Bauge (France), Lehmweller (Germany), Pahsa (Turkey), Atterati (Italy), and Zabour (Yemen) [13–17].

To the best of our knowledge, except for the few studies presented above, cob building is not well described in the literature [18]. This leads to its low use in current construction. Moreover, its behavior in response to climatic solicitations is rarely modeled. For a remedy, this paper proposes to solve this problem and to overcome the limits of cob building by enriching literature databases. Our aim is to get a better understanding of the behavior of cob mixtures in order to develop its use in our sector. The investigations include microstructure observations, characterization of the compressive strength, thermal conductivity, specific heat, moisture buffer value (MBV), sorption isotherms, water vapor permeability, and numerical simulations. In addition to the experimental characterization, numerical simulation was carried out. The latter is based on the model of Philip and de Vries [19] and the work of [20] and [21]. The aim is to predict the hygrothermal behavior

(water content profile, relative humidity, etc.) of the cob. The estimated properties of the cob are compared to those of other materials such as hemp concrete, glass powder concrete, and clay brick. The aim is to position the cob regarding its utilization as a building envelope material. The experimental measured properties are used as input data to feed the numerical modeling proposed.

2. Materials and Methods

2.1. Raw Earth

The material being studied is a soil excavated in the eco-district of Guerande (city located near Nantes, France). This is a local material chosen to reduce the carbon footprint compared to conventional materials. The granulometric analysis is an important tool for soil classification. Based on the NF EN ISO 17892-4 standard [22], the particle size composition of the Guerande soil was determined by wet sieving for the part of the soil larger than 80 µm and by using sedimentation for elements smaller. It was deduced that the studied soil is a sandy loam type. The latter is composed of 8% clay, 47% silt, and 45% sand. It is specified in the literature that the optimal quantity of clay for the cob construction mode is around 20% [14]. Earth-based materials for buildings are often represented using triangular texture diagram [23]. In France, a classification based on the French soil research organization "GEPPA" is often used [24]. Note that in the GEPPA diagram, the top dimension of the silt is 50 µm, which is different from NF EN ISO 17892-4. Indeed, the silt content based on this system is 44% and the sand content is 48%. The average value of raw earth density is 1878 $kg{\cdot}m^{-3}$ [25]. Furthermore, the Atterberg limits were reached using the NF EN ISO 17892-12 standard [26]. The plastic limit Wp is 17%, while the liquid limit is Wl 34%. The plasticity index Ip is equal to 17. Finally, the blue methylene value was obtained from the standard NF EN 933-9 and is 1.9 [27].

2.2. Straw

An amount of 3% by mass of vegetable fibers was added in the mix. This rate was previously found in the literature for cob [28–30]. The addition of vegetable fibers accelerates the drying process, reduces shrinkage cracks, and improves the cohesion and the ductility of the material [14].

For this purpose, we have valorized a vegetable by-product and integrated it into our material. A by-product means a material that is unavoidably created to produce another desired material [31,32]. Our choice was straw fibers. Straw is a by-product of industrial agriculture, which is made from dry stems of cereal plants, like wheat, barley, spelt, and spurge [33]. For a particle length of 50.8mm, the average density is about 93 $kg{\cdot}m^{-3}$ [34]. Contrary to hay, straw is not very nutritious and is therefore less often used for the feeding of livestock. However, straw is used for litter. Chemically speaking, straw is composed mainly of cellulose and lignin, the same main components as wood [35]. In addition, the incorporation of straw fibers improves the hygrothermal properties of the earth because of their low thermal conductivity, between 0.06 and 0.08 $W{\cdot}m^{-1}{\cdot}K^{-1}$ [36]. This value is slightly lower for hay with values ranging from 0.0284 to 0.0605 $W{\cdot}m^{-1}{\cdot}K^{-1}$, obtained, respectively, at a temperature of −17.8 °C and 60.1 °C. Thermal conductivity had been characterized for different initial mean hay temperatures of hay, moisture contents, and bulk densities [37].

The straw fibers were evenly cut to a size of 50 ± 5 mm before manufacturing the earth-based composites. Afterwards, the average water content of the used soil was measured in order to reach the prescribed water content. According to [29,38,39], the water content of the cob should be between 10 and 28%. Thus, average water content of 21% was chosen for our formulation. In accordance with the literature [40,41], a mass percentage of 3% of fibers in relation to the dry mass of raw earth was retained. Besides, to avoid the absorption of water by the straw fibers that reduces the workability of the composite at the fresh state, the straw fibers were immersed in water for 5 min. Then, the fibers were drained for 5 min.

2.3. Mixing

The manufacturing process was carried out with a mixer and a kneading machine as follows:

- Mixing the raw earth alone for 5 min at 120 rpm
- Adding water and mixing for 5 min at 120 rpm
- Adding half the amount of fiber and kneading for 5 min at 120 rpm
- Adding the remaining fibers and kneading for 5 min at 120 rpm

We then filled hermetic bags with our mixture. We waited for 24 h to make specimens with our cob formulation, giving time for the clay to rehydrate [42]. After that, samples were manufactured with 3D printed molds designed especially for the devices used during our investigation. Prior to the hygrothermal characterization, dry density was measured. The latter has a value of $\rho_s = 1654$ kg·m^{-3}. Moreover, compressive strength has been determined with a value of 2.9 ± 0.1 MPa.

2.4. Microstructure Observations

The microstructure observations have been carried out with the CMOS-based digital microscope VHX 7000 (Keyence) that achieves a typical magnification of ×6000 in the optical wavelength range. Viewed at a resolution of 2880 × 2160 pixels, the physical size of the pixels varies between 0.7 µm and 5 µm depending on the magnification. The following magnifications were used to capture the information: E20 × 20, E20 × 80, E100 × 100, E100 × 300.

2.5. Thermal Conductivity

Thermal conductivity is a property that has the most significant impact on the thermal performance of a building. It describes the insulation capacity (or conductivity) of a material. The thermal conductivity was measured with the Lambda-meter EP500e device for different temperatures 10 °C, 23 °C, and 40 °C (Figure 1). This device is based on the technique of the guarded hot plate which exploits the Fourier's law in steady state according to standards [43,44]. The measurements are performed under a temperature gradient of 15 °C by fixing the hot surface of the device at a reference temperature. The parallelepipedal specimens have the following dimensions: 15 × 15 × 3 cm^3. They were preconditioned in an oven at 40 °C until the mass was stabilized. Finally, the thermal conductivity was calculated using Fourier's law with the unidirectional heat flux through the sample. This is equivalent to the electrical heating power.

$$\lambda = \frac{Q \cdot e}{\Delta T \cdot A} = \frac{U \cdot I \cdot e}{\Delta T \cdot A} \quad (1)$$

where:

e: thickness of the specimen (m);
A: the surface area perpendicular to the heat flux (m^2);
Q: the unidirectional heat flow (W);
ΔT: the temperature gradient (°C);
$U \cdot I$: electrical heating power (W).

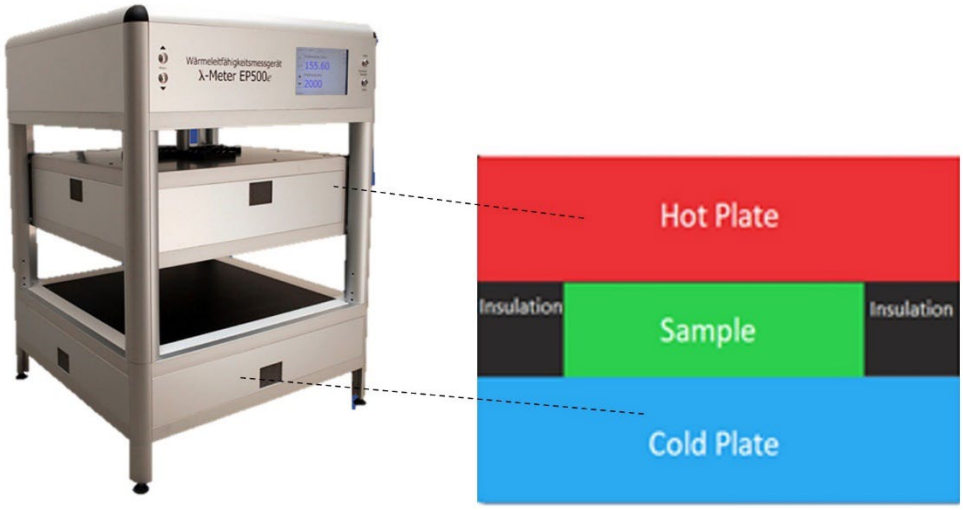

Figure 1. Picture and scheme of the Lambda-meter EP500e.

2.6. Specific Heat Capacity

Thermal capacity or specific heat capacity is a property expressing the capacity of a material to store heat. Knowledge of the thermal capacity of materials is essential to complete the thermal characterization. For this, the Calvet calorimeter was used in accordance with the NF EN 821-3 standard [45]. The Calvet calorimeter shown in Figure 2 is a differential device. It is equipped with two 3D thermopiles that respectively surround a measurement cell in which a sample of the studied material is placed and a reference cell containing a thermally inert product. A larger sample size gives more accurate results, which makes the Calvet method more accurate compared to the traditional DSC equipment. The tested samples are cylindrical with a diameter of 1 cm and a length of about 4 cm. Samples were preconditioned in an oven at 40 °C until the mass was stabilized.

Figure 2. Image of the BT 2.15 Calvet calorimeter.

2.7. Sorption Isotherms

Adsorption and desorption isotherms of the water vapor were determined. It allows us to evaluate the activity of water at the microscopic scale (modes of fixing of the water molecules at the pore scale). This test indicates the water content of the mass ratio of a material according to the relative humidity (RH). The used device is the "Pro-Umid of SPS" which is based on a gravimetric method. The "SPS Pro-Umid" is fully automated. This

device has a gravimetric resolution ranging from 0.1 µg to 10 µg. An internal reference compensates for any drift of the microbalance and offers excellent balance stability, even for long-term measurements (>>24 h). The wide dynamic load range of the microbalances enables accurate and reproducible weighing results at full scale. We measured the isotherms at a temperature of 23 °C with humidity ranging from 0% to 90% of Relative Humidity.

2.8. Moisture Buffer Value (MBV)

The moisture buffering capacity represents the ability of a material to moderate changes in relative humidity in the ambient air. This parameter was measured using the Nordtest method [46]. The principle of the MBV test protocol is to expose the specimens to daily cycles of relative humidity similar to the cycles observed in the building. The samples were then exposed to a cycle of 8 h at 75% RH and 16 h at 33% RH. Prior to measurements, the specimens were pre-conditioned at 23 °C and 50% RH. The dimensions of the cubic specimens are 10 × 10 × 5 cm^3. Figure 3 shows a classification of the materials according to their ability to store moisture from the Nordtest project.

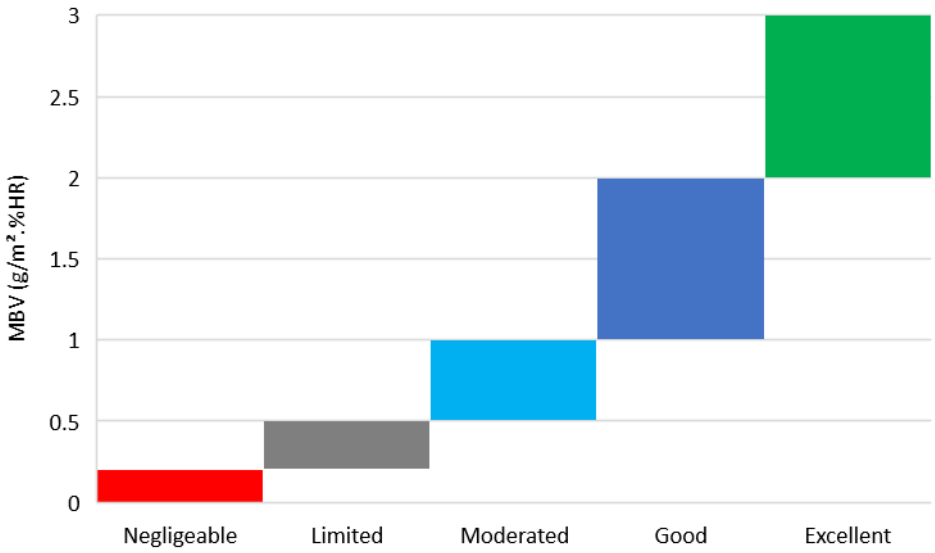

Figure 3. Nordtest project classification of materials versus Moisture Buffer Value.

Finally, the masses were tracked at the end of each cycle to deduce the MBV from the following equation:

$$\mathrm{MBV} = \frac{\Delta m}{A(RH_{max} - RH_{min})} \quad (2)$$

In this equation, Δm is the amplitude of the mass variation during the cycles (g), A is the contact surface between the specimen and the ambient air (m^2), RH_{max} is the relative humidity during the adsorption phase (%), RH_{min} is the relative humidity during the desorption phase (%).

2.9. Water Vapor Permeability

Water vapor permeability characterizes the ability of a material to transfer moisture under a vapor pressure gradient. The measurements were carried out using the Gravitest® device, which is based on the dry cup method according to ISO 12572 [47]. The cup method consists of applying a relative humidity gradient between two surfaces of a specimen under constant and homogeneous temperature. To do so, the specimen was sealed at the top of a cup containing silica gel. The cup was then placed into a climate chamber with a relative humidity of 50% and a temperature of 23 °C. The mass variation of the specimen was

measured until it reached the steady state (constant vapor flux through the specimen) and mass equilibrium during 48 h defined by this criterion:

$$\frac{m(t) - m(t + 48\text{ h})}{m(t + 48\text{ h})} \leq 0.1\% \quad (3)$$

As soon as the vapor flux was stabilized, the latter was calculated. Depending on the boundary conditions of the specimen, permeance to water vapor was deduced. Therefore, the vapor permeability was determined by the assumption that the material is homogeneous. The test was performed on three cylindrical specimens of 8 cm in diameter and 2 cm in thickness.

3. Results and Discussions

3.1. Experimental Characterization

3.1.1. Microstructure Observations

An observation of the cross section of the straw fiber is shown in Figure 4a. It is observed that the microstructure is constituted of multilayers with a tubular structure organized toward the growth of the plant. Many pores are observed at this cross-section. The pore sizes are more or less important with an average diameter of 40 µm. In Figure 4b it appears that the external structure of the straw used in our formulation is smooth with very few irregularities. Figure 5 represents the interface of our material. This shows a good general cohesion of the composite earth/straw. However, in some areas there is poor cohesion between the two materials. This is due to an inter-granular porosity which can be important in case of bad cohesion. This type of porosity could improve the hydric and thermal properties in addition to the intrinsic properties of the straw.

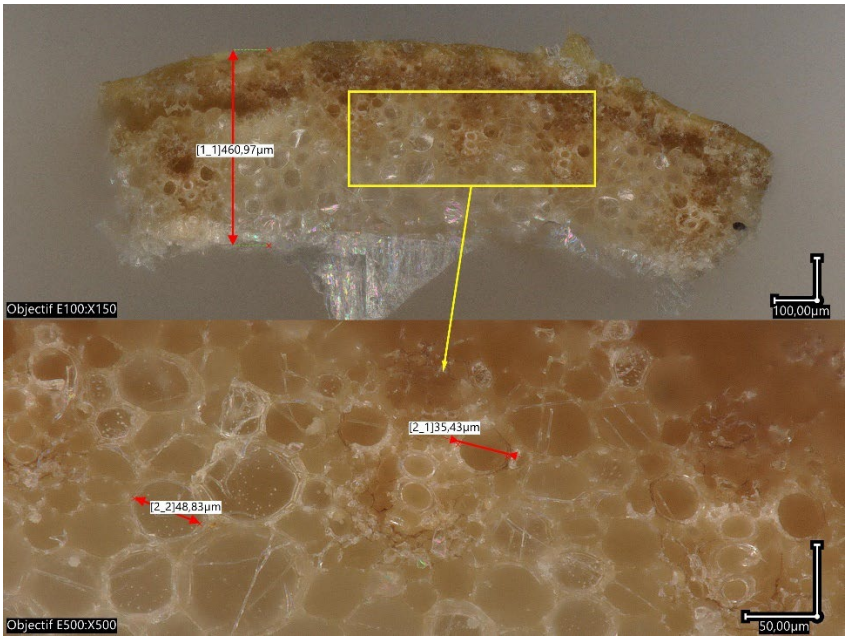

(**a**)

Figure 4. *Cont.*

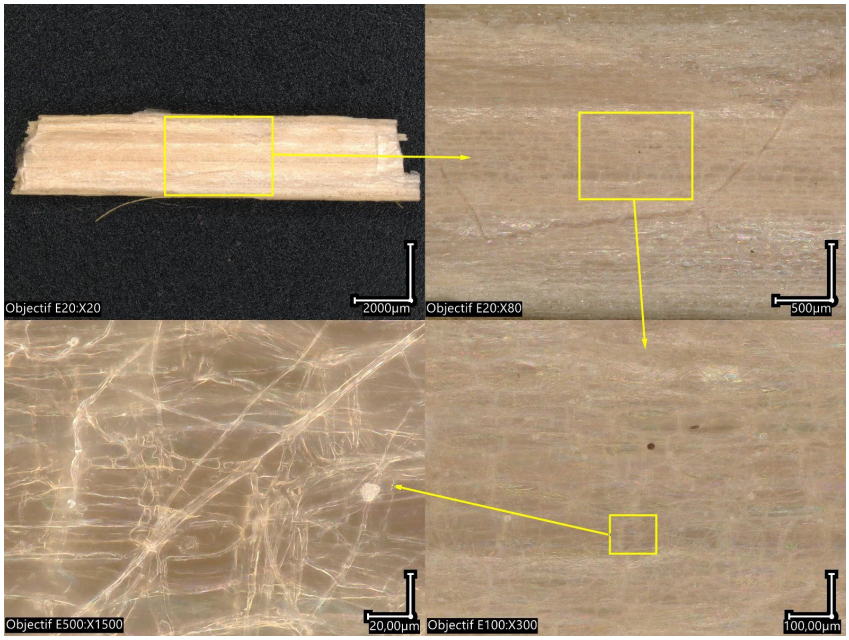

(**b**)

Figure 4. Cross section (**a**) and longitudinal (**b**) microsopic observations of a straw fiber.

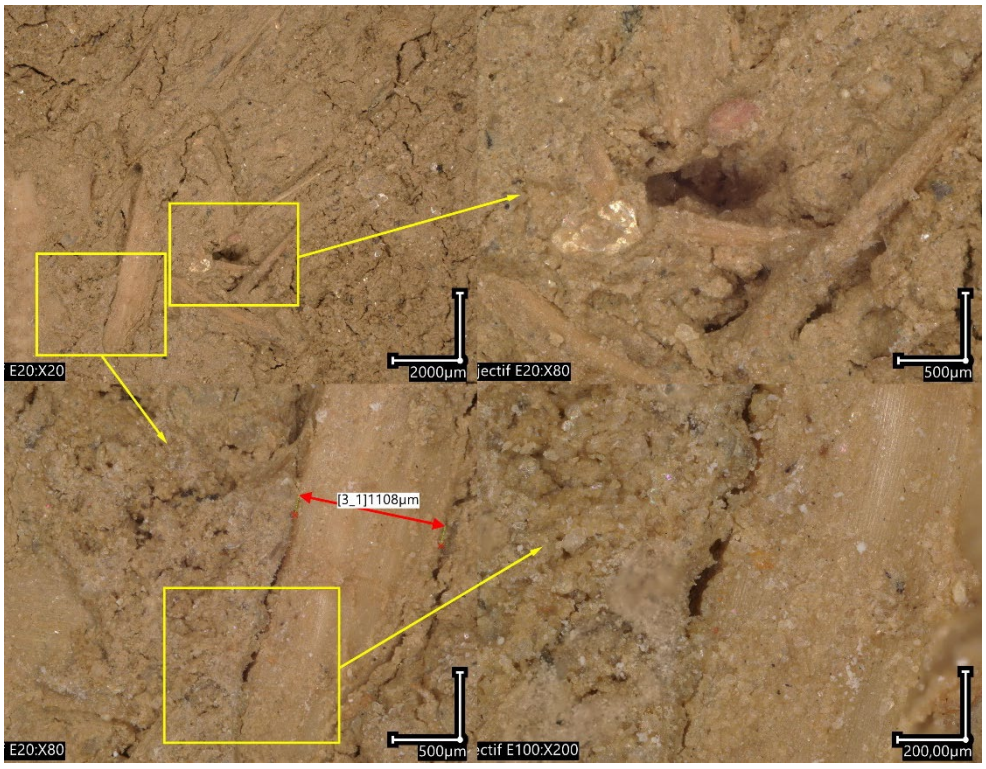

Figure 5. Microscopic observation of the composite raw earth/straw.

3.1.2. Thermal Conductivity

Thermal conductivity is an important property to characterize the thermal behavior of materials. To ensure good reproducibility of the results, three specimens were tested for our formulation. This property was measured at 3 different temperatures, respectively: 10 °C, 23 °C, and 40 °C. The average thermal conductivities for each temperature and their standard deviations are shown in Figure 6. At a temperature of 23 °C, cob has a thermal

conductivity of 0.180 $W \cdot m^{-1} \cdot K^{-1}$. This value is lower than that of other conventional construction materials, such as cementitious concrete. Indeed, this kind of material can reach a thermal conductivity of 1.20 $W \cdot m^{-1} \cdot K^{-1}$ [48–50]. In Figure 7, the thermal conductivity at 23 °C of cob is compared to other materials:

- hemp concrete, an insulating material [51],
- glass powder concrete [52],
- conventional concrete, structural materials [52],
- clay brick [53].

The thermal conductivity of cob is close to hemp concrete and clay brick values. Thus, we can consider our formulation of cob a good insulating material for construction. Its thermal conductivity is about 7 times lower than glass powder concrete. Otherwise, the thermal conductivity of conventional concrete is almost 8 times higher than cob. Moreover, the thermal conductivities assessed on cob correspond to the one measured for unfired earth blocks with a mass straw content of 6% (0.14 ± 0.01 $W \cdot m^{-1} \cdot K^{-1}$). The value is obtained by the same testing method, which is the Guarded Hot Plate GHP [54].

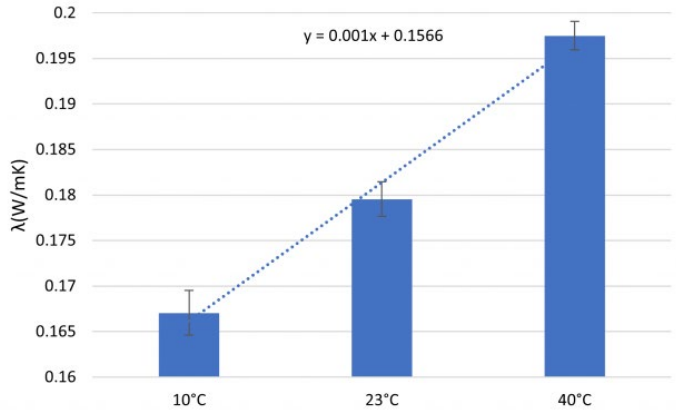

Figure 6. Cob samples' thermal conductivity at different temperatures.

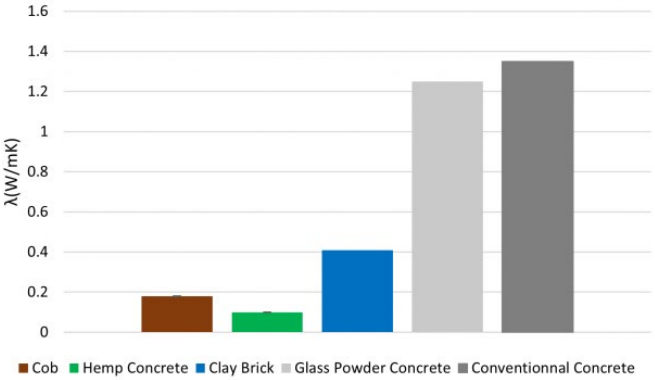

Figure 7. Comparison of thermal conductivity of different materials.

3.1.3. Specific Heat Capacity

The specific heat capacity of cob was measured to quantify its heat storage capacity. It is an essential parameter, as well as the thermal conductivity, to evaluate the decrement factor and the time lag of a wall. Figure 8 presents the evolution of the specific heat capacity as a function of the temperature. The measurement range extended from −10 to 45 °C. Nevertheless, the range exploited is from 0 to 35 °C (Figure 9). This is due to the very strong thermal inertia inside the device. Indeed, this thermal inertia leads to a delay in the transmission of heat, shortening the exploitable range of the data (0 to 35 °C). The specific heat capacity measured for cob is between 800 and 900 $J \cdot kg^{-1} \cdot K^{-1}$. This value is in

accordance with the values found in the literature for raw earth materials (between 800 and 950 J·kg^{-1}·K^{-1} [55,56]). The cob specific heat capacity at 23 °C was compared to the values of hemp concrete [57], glass powder concrete, conventional concrete, and clay brick. In Figure 10 we can observe that the specific heat of cob is 24% lower than that of hemp concrete, 4% higher than glass powder concrete, and 14% higher than clay brick. Besides, the gap between conventional concrete and cob is significantly lower. The trend remains the same for the volumetric heat capacity (Figure 11) with the exception of hemp concrete, which has seen its value fall significantly due to its low density.

To provide hygrothermal models, it is necessary to represent the evolution of the specific heat capacity as a function of temperature in the form of a polynomial of variable degree. Hence, its evolution as a function of temperature (T) is modeled by the linear function $C_P(T) = aT + b$. The coefficients are adjusted by minimizing the difference with the measured values. The fitted coefficients a, b of the linear function are shown in Figure 10 with a residual close to 1 (0.9819).

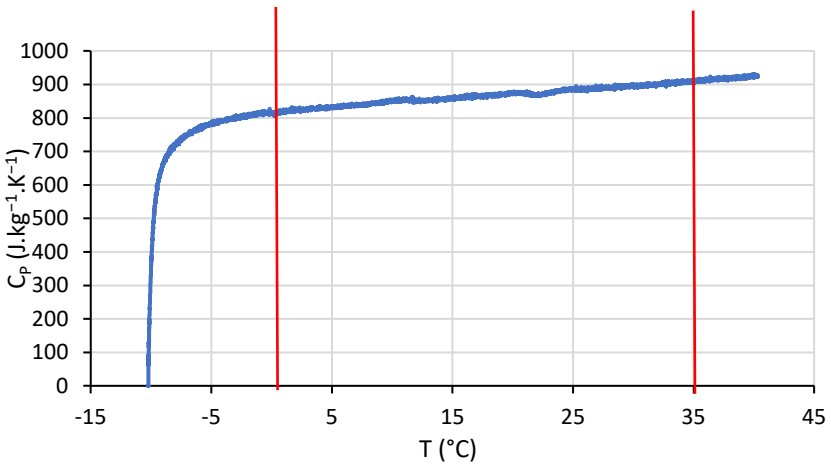

Figure 8. Specific heat capacity cob as a function of temperature.

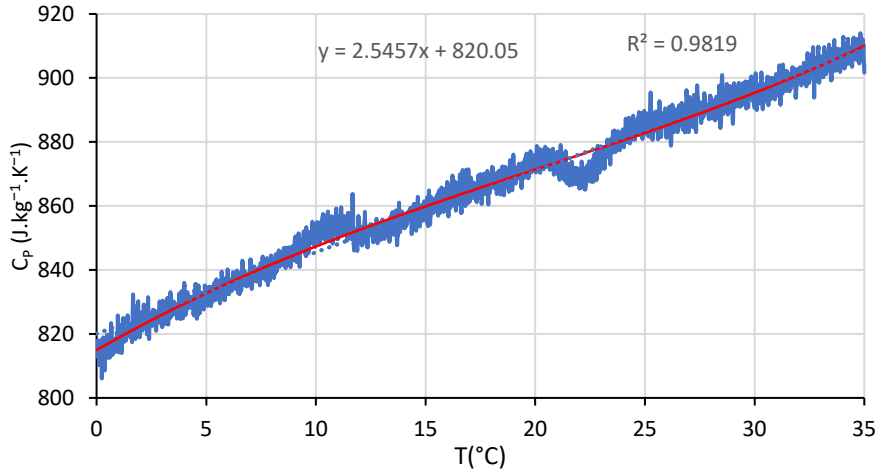

Figure 9. Specific heat capacity of cob in the range temperature exploited and linear fitting.

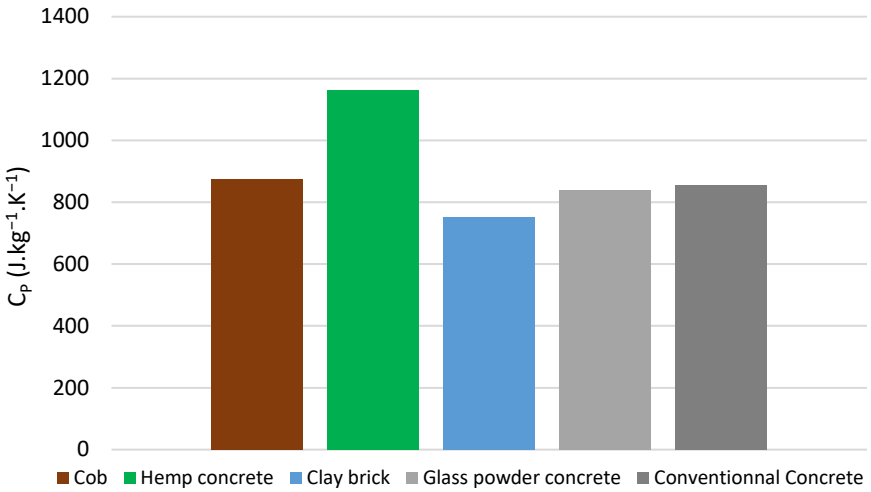

Figure 10. Comparison of cob's specific heat with different materials.

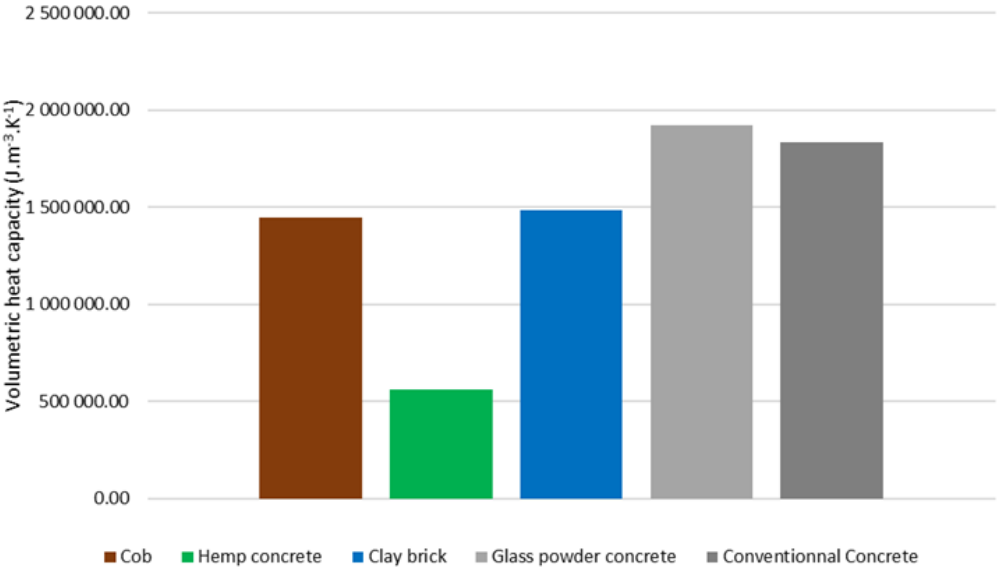

Figure 11. Comparison of cob's volumetric heat capacity with different materials.

3.1.4. Sorption Isotherms

In order to show the advantage of incorporating straw in raw earth, we have measured the adsorption and desorption isotherms at 23 °C on raw earth (RE), straw (S), and raw earth/straw composite (RES). The obtained results are presented in Figure 12.

As can be observed in Figure 12a, the evolution of water content as a function of the relative humidity is showed. It appears that the water content (w) is less significant in the raw earth specimens (RE) compared to the raw earth/straw composite (RES). An increase of about 18% in the maximum water content was noticed in the saturation region after the incorporation of straw in raw earth. This is due to the adsorption capacity of the straw plant (25%), which is one of highest (Figure 12b). By comparing these results with those of other materials (Figure 13a), it is noticed that the glass power and reference concrete have the highest values of water content, that reach 117 and 93 kg·m^{-3}, respectively. Hemp concrete and RES have similar values (between 60 and 80 kg·m^{-3}). In order to better analyze the hygroscopic behavior of the materials, moisture content is plotted in terms of mass ratio (Figure 13b). The maximum mass ratio of the RES and hemp concrete are compared. A higher value for hemp concrete compared to our formulation of raw earth with straw is highlighted. Actually, hemp concrete's value can reach 12–16% depending on

the formulation. Concerning glass powder concrete and conventional concrete, the values of the maximum mass ratio are 4 and 5%, respectively. These values are almost equal to our formulation's one. Thus, it appears that the hysteresis phenomenon is very significant for comparative materials (Figure 13). For clay brick, the maximum water content reaches a very low value of 0.1%. Moisture storage capacity (C_m) is defined as the slope of isotherms sorption curves. It is expressed by:

$$C_m = \frac{\partial w}{\partial \mathrm{RH}} \tag{4}$$

where w (kg·m^{-3}) is the water content and RH is the relative humidity (%).

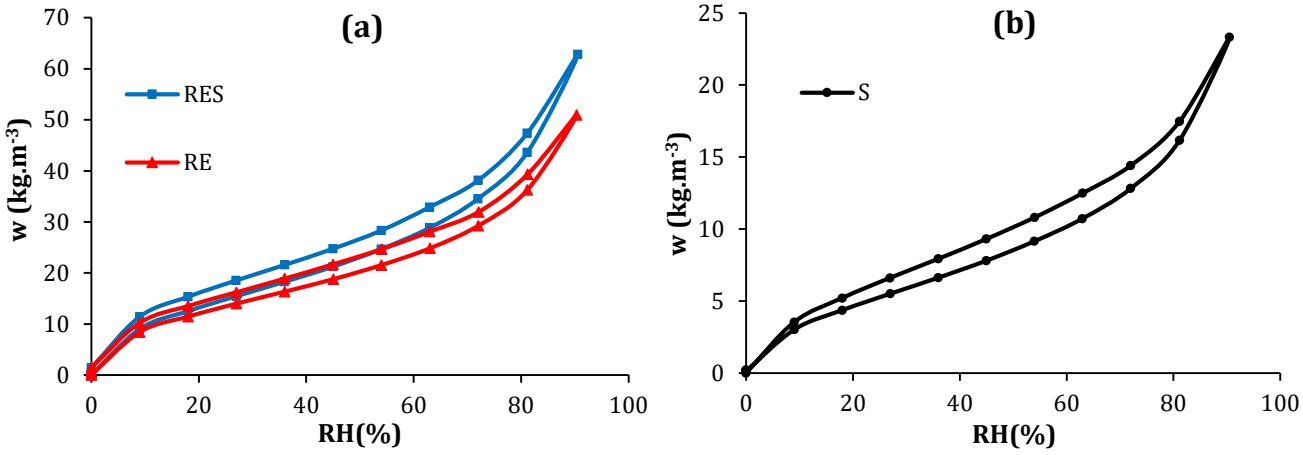

Figure 12. Sorption isotherms of raw earth (RE), raw earth/straw composite (RES) (**a**) and straw (S) (**b**); the lower curve for each formulation corresponds to the adsorption isotherm, while the upper curve corresponds to the desorption isotherm.

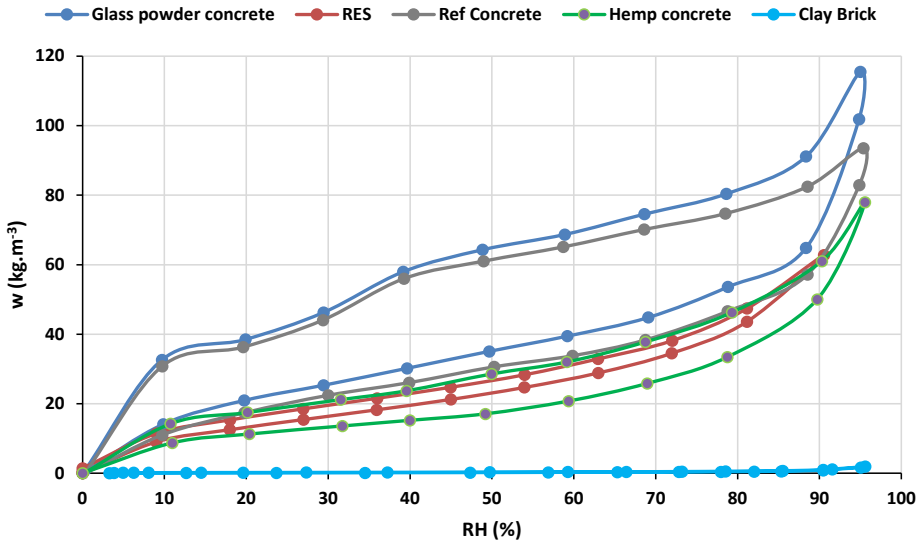

(**a**)

Figure 13. *Cont.*

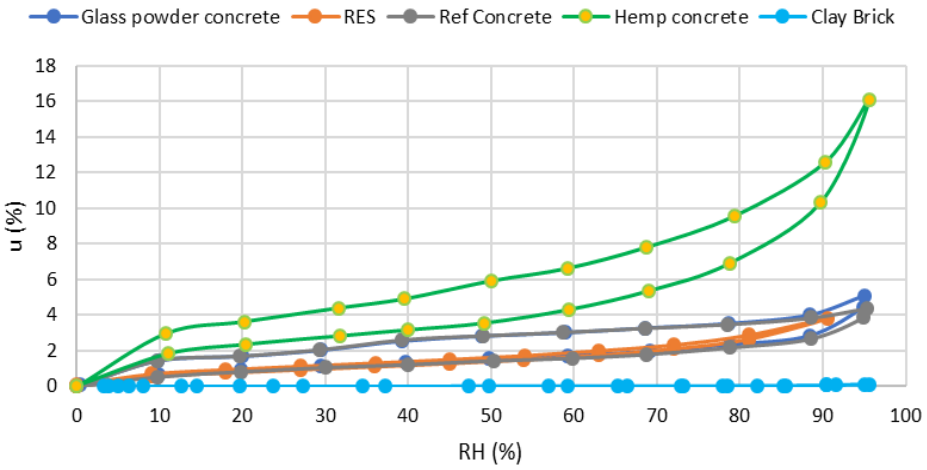

(**b**)

Figure 13. Comparison of sorption isotherms of concrete, glass powder concrete, hemp concrete, clay brick, and raw earth/straw (RES) in terms of water content (**a**) and mass ratio (**b**).

The incorporation of plant fibers within raw earth has increased the moisture storage capacity of the RES samples (Figure 14). This value was compared with those of hemp concrete and concrete. Moisture storage capacity of RES specimens is the highest of materials being studied, reaching a value of 203 kg·m^{-3} at 78% of RH against 151, 117, and 108 kg·m^{-3} for hemp concrete, glass concrete, and conventional concrete, respectively.

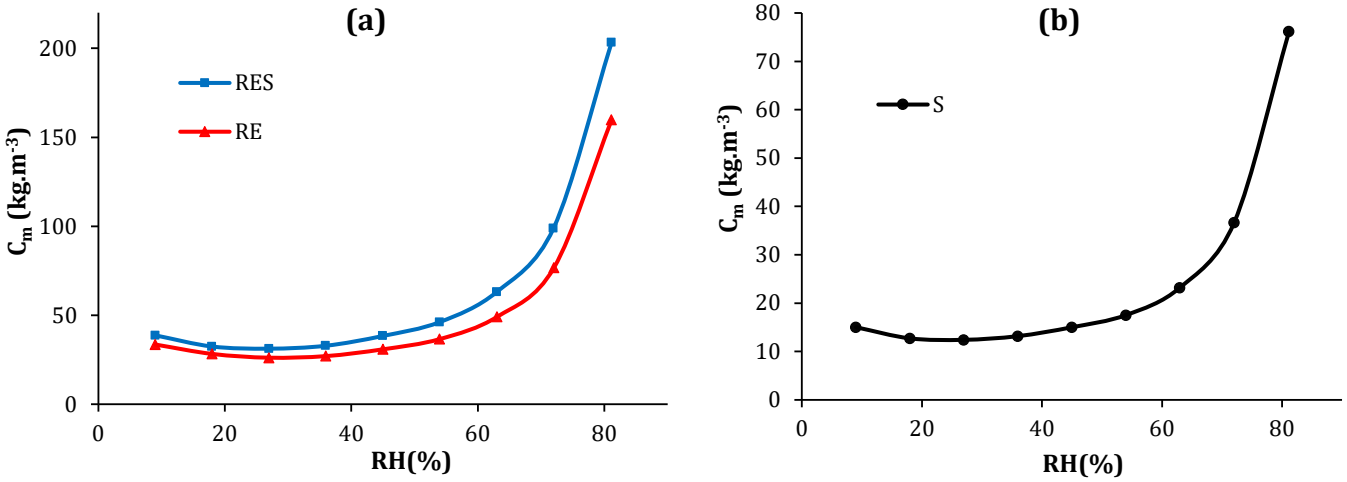

Figure 14. Moisture storage capacity of raw earth, raw earth/straw (**a**), and straw (**b**).

Indeed, the increase observed in the water vapor adsorption capacity of the composite material can improve its hydric properties (hydric buffering capacity and water vapor permeability) as well as its thermal properties (thermal conductivity and specific heat).

3.1.5. Moisture Buffer Value (MBV)

The MBV is used to estimate the dynamic hygrothermal behavior of the material when it is exposed to an indoor environment. It indicates the average amount of water that is exchanged by adsorption or desorption when the surfaces of the material are subjected to changes in the relative humidity for a given time. The tests were performed on four specimens and the mass change was measured for a week to ensure repeatability of the experiment and calculation of the associated uncertainties.

At the end of the tests, the value of MBV measured for the cob formulation was 1.4 g/(m^2·%RH) with associated uncertainty of 0.1. This value is in accordance with the

values referenced in the literature. In reference [58], the MBV of raw earth covered values between 1.13 and 3.73 g/(m^2·%RH). This wide range is explained by the type of soil and some additions such as lime, cement, or geopolymers (NaOH). Moreover, according to the Nordtest project classification, raw earth with straw addition can be considered a good moisture regulator. MBV is compared with values found for other materials (Figure 15). Hemp concrete has an MBV of 2.27 g/(m^2·%RH) which makes it an excellent moisture regulator [51]. Structural materials like concrete or brick have a lower MBV of 0.37 and 0.4 g/(m^2·%RH), respectively [59]. Thus, they are considered a limited (or a weak) moisture regulator.

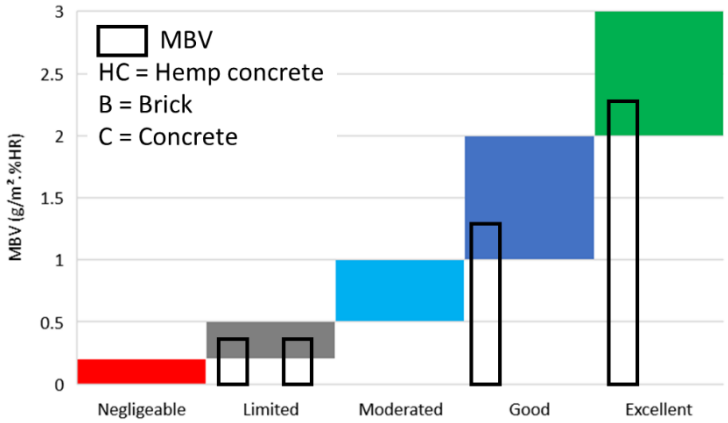

Figure 15. Comparison of cob MBV with other materials.

3.1.6. Water Vapor Permeability

Finally, the water vapor permeability was measured on 3 specimens. The average value obtained is $\delta = 1.08 \times 10^{-11} \pm 6.5 \times 10^{-13}$ kg·s^{-1}·m^{-1}·Pa^{-1}. This result is in accordance with values found in the literature. For adobe, the water vapor permeability has a value ranging from 1.0 to 2.7 $\times$ 10^{-11} kg·s^{-1}·m^{-1}·Pa^{-1} [56]. Besides, for adobe with 3% of straw, water vapor permeability was worth 3.8 $\pm$ 0.3 $\times$ 10^{-11} kg·s^{-1}·m^{-1}·Pa^{-1} [60]. Our cob formulation value is of the same order of magnitude as hemp concrete (Figure 16). Indeed, the latter is equal to 2.85 $\times$ 10^{-11} kg·s^{-1}·m^{-1}·Pa^{-1} [51]. Clay brick water vapor permeability has a value very close to cob, with $\delta = 1.63 \times 10^{-11}$ kg·s^{-1}·m^{-1}·Pa^{-1}. However, the average value for glass powder concrete is around 2.47 $\times$ 10^{-12} kg·s^{-1}·m^{-1}·Pa^{-1}, which is not of the same order of magnitude. This gap is more important for the concrete. The latter has a water vapor permeability of 9.51 $\times$ 10^{-13} kg·m^{-1}·s·$^{-1}$·Pa^{-1} [61]. We can deduce that necessary vapor flux through cob specimens is more important than for concrete specimens. This may be due to a lower porosity or tortuosity of our studied materials.

In addition to water vapor permeability, the water vapour resistance factor (μ), which is usually used in the calculation of interstitial condensation (EN ISO 13788 [62]), has been calculated (Equation (5)) at ambient temperature and atmospheric pressure (p_a).

$$\mu = {}^{\delta_a}/_{\delta} \quad (5)$$

where $\delta_a = \frac{2 \times 10^{-7} T^{0.81}}{p_a}$ is the water vapor diffusion coefficient in the air.

The water vapor resistance factor of the studied materials is presented in Table 1. The tendency is reversed for μ compared to δ. This can be explained by the inversely proportional relationship that links them. Indeed, materials with low value of δ possess a high value μ. Therefore, GPC and REF have the highest water vapor resistance factor due to their low water vapor permeability. The water vapor resistance factor of cob and clay brick are similar to that of bricks and stones. Hemp concrete, which has the lowest μ, due to the high water vapor diffusion, is comparable to materials like platers [63].

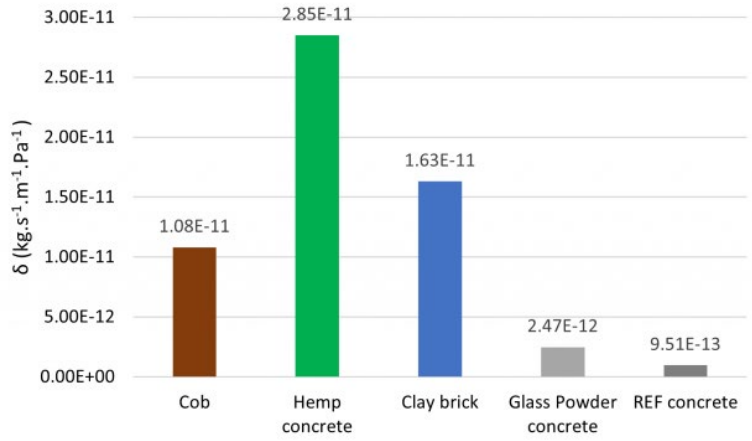

Figure 16. Comparison of water vapor permeability of concrete, glass powder concrete, hemp concrete, clay brick, and raw earth/straw (RES).

Table 1. Water vapor resistance factor of concrete, glass powder concrete, hemp concrete, clay brick, and cob.

Materials	Water Vapor Resistance Factor
Cob	18.52
Hemp concrete	7.02
Clay brick	12.27
Glass powder concrete	80.97
REF concrete	210.30

3.2. Numerical Simulation

3.2.1. Mathematical Model

In order to analyze the hygrothermal behavior of the Cob and compare it with other materials such hemp concrete and glass powder concrete, a numerical simulation was conducted. The used hygrothermal used is based on the model of Philip and de Vries et al. [19] and the work of Ferroukhi et al. [20] and Remki et al. [21], as mentioned in the introduction. Because of the continuity problem for the water content, we have opted for vapor pressure (p_v) and temperature as the driving forces for transport. For more details about the model, the reader is referred to [64]. The equations are developed under the following assumptions:

- Macroscopically homogeneous, isotropic and rigid solid phase;
- Gas phase at constant and uniform pressure;
- Thermodynamic equilibrium between all phases present;
- No chemical reaction between phases;
- No heat transfer by radiation;
- No energy dissipation during flow;
- Wetting heat neglected.

The resulting equations for vapor pressure and temperature are presented as follows:

$$\rho_s \frac{C_m}{P_{v,sat}} \frac{\partial p_v}{\partial t} = -div(-k_T \nabla T - k_m \nabla p_v) \quad (6)$$

$$\rho_s C_p^* \frac{\partial T}{\partial t} = -div(-\lambda^* \nabla T - \gamma \nabla p_v) \quad (7)$$

$p_{v,sat} = 610.5 \cdot \exp((17.269 \cdot T - 4717.03)/(T - 35.85))$ is the saturation pressure;

$k_T = k_l \frac{R\rho_l}{M}\left[\ln\left(\frac{p_v}{P_{v,sat}}\right) + \frac{T}{P_{v,sat}}\frac{\partial p_{v,sat}}{\partial T}\right]$ (kg·m^{-1}·s^{-1}·K^{-1}) is the liquid water conductivity due to a thermal gradient. With k_l the hydraulic liquid conductivity, R ideal gas constant, M the molar mass of water;

$k_m = \delta_v + k_l \frac{RT\rho_l}{Mp_v}$ (kg·m^{-1}·s^{-1}·Pa^{-1}) represents the total moisture diffusivity coefficient with k_v the water vapour permeability;

$C_p^* = C_{p,s} + u \cdot C_{p,l}$ (J·kg^{-1}·K^{-1}) is the total heat capacity, where $C_{p,s}$ and $C_{p,l}$ are respectively the dry and liquid specific heat capacity;

$\lambda^* = \lambda + h_l k_T$ (W·m^{-1}·K^{-1}) is the effective thermal conductivity with λ the dry thermal conductivity, $h_l = C_{p,l}(T - T_0)$ (J·kg^{-1}) the liquid enthalpy;

Finally, $\gamma = \delta_v L_v + h_l k_m$ (W·m^{-1}·Pa^{-1}) where L_v (J·kg^{-1}) is the latent heat of vaporization of liquid water.

The symbols and their units are gathered in the Nomenclature.

3.2.2. Model Validation

The reference test defined in the EN 15026 standard [65] for the validation of a software calculating moisture transfer by numerical simulation is used to validate the model. The model geometry consists of a single segment for the building component. Its size is large enough to represent a semi-infinite region for the time scale of the simulation. A relative humidity of 50% and a temperature of 20 °C are set as initial conditions, while on the left boundary the relative humidity is set to 95% and the temperature is 30 °C. The time study is performed over a year, with temperature and relative humidity distributions checked at 7, 30, and 365 days.

The temperature and moisture content profile (w) of the numerical simulation and experiments at 7, 40, and 365 days are presented in Figure 17. The results showed a good accordance between numerical simulation and experiments.

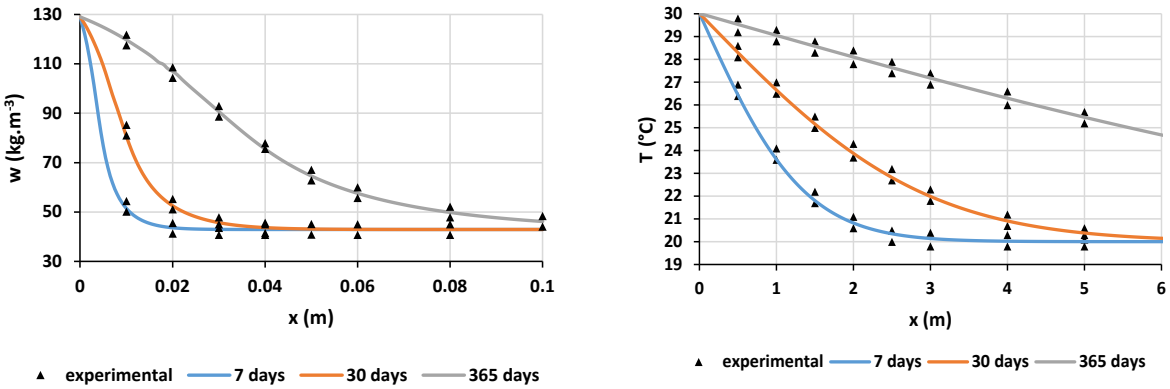

(**a**) (**b**)

Figure 17. Comparison of the water content (**a**) and temperature profiles (**b**) obtained numerically (continuous lines) with those of the EN 15026 standard (triangles).

3.2.3. Results

The numerical simulations are performed for three different types of walls with 20 cm of thickness made of hemp concrete, RES, and clay brick. The main objective is to compare the hydrothermal behavior of the above-mentioned materials with that of cob. The hygrothermal properties of the materials, which are the input parameters of the model, are presented in Table 2. The water content and the moisture storage capacity of each material are obtained from the sorption isotherms presented in the characterization section.

Table 2. Hygrothermal properties of the studied materials.

Materials	Thermal Conductivity ($W \cdot m^{-1} \cdot K^{-1}$)	Water Vapor Permeability ($kg \cdot s^{-1} \cdot m^{-1} \cdot Pa^{-1}$)	Heat Capacity ($J \cdot kg^{-1} \cdot K^{-1}$)	Dry Density ($kg \cdot m^{-3}$)
Hemp concrete [56,63]	0.1	2.85×10^{-11}	1150	484.56
Clay brick [53]	0.41	1.63×10^{-11}	750	1980
Glass powder concrete [52]	$1.29 + 0.607 \cdot w/1000$	$3.38 \times 10^{-11} \cdot \exp(-5.998 \cdot RH)$	850	2290
RES	0.18	1.08×10^{-11}	870	1654

Initially, the material is in equilibrium with a constant external environment equal to T = 20 °C and RH = 50%. At the time t = 0, the new external climatic conditions are T = 35 °C and RH = 90% at the left side (x = 0 cm) and the other side is assumed to be adiabatic and impermeable (Figure 18).

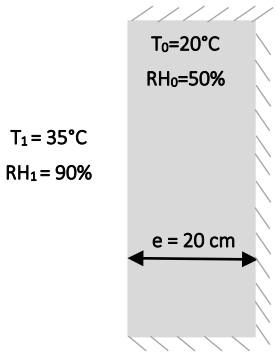

Figure 18. Boundary conditions of the comparison case study.

Due to the difficulty of measuring the hydraulic liquid conductivity, the phase change criterion (PCC) method has been used [66]. This parameter represents the ratio between the vapor flux and the total flux and is expressed as follows:

$$\mathrm{PCC} = \frac{\delta_v \cdot P_v}{k_l \frac{R\rho_l}{M} T + \delta_v \cdot P_{v,sat}} \tag{8}$$

From this expression, a relation between the PCC and the hydraulic liquid conductivity is established:

$$k_l = \left(\frac{1}{\mathrm{PCC}} - 1 \right) \frac{\delta_v \cdot P_v}{\frac{R\rho_l}{M} T} \tag{9}$$

Figure 19 shows the influence of the PCC on the RH profile inside RES. It is noticed that for PCC values less than 0.6, the influence of PCC is not very important, and the mass transfer is essentially vapor transfer and liquid transfer is negligible. For cellulosic wall, Wang et al. [66] have found that if RH is inferior to 60%, the PCC can be set at 1. In this study, it has been arbitrarily set at 0.8 in order to consider the liquid diffusivity that vanishes when PCC is equal to 1. The determination of the hydraulic conductivity could be the purpose of another study.

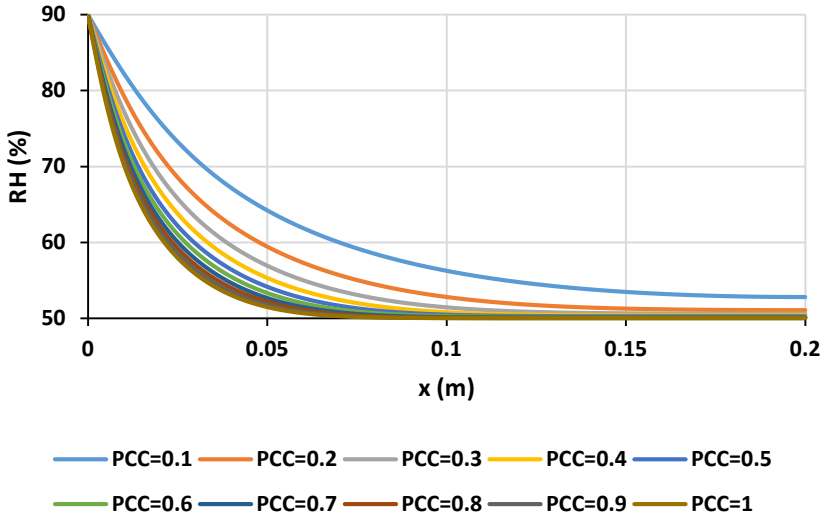

Figure 19. Influence of PCC on the RH profile inside RES.

The temperature and RH profiles in the wall for the three materials are presented in Figure 20. Based on the RH profile, clay brick is the most conductive material for humidity, followed by hemp concrete, RES, and GPC at the latter position. This result is due to the value of the water vapor diffusivity, which is relatively higher for hemp concrete, moderate for RES and clay brick, and low for GPC. In addition, the moisture storage capacity of clay brick is very low (around 7 kg·m^{-3}) compared to the higher values for hemp concrete (280 kg·m^{-3}) and RES (950 kg·m^{-3}). This low moisture storage capacity of clay brick combined with the moderate water vapor diffusivity explains the rapid diffusion of moisture in clay brick. The high moisture storage capacity of RES and GPC delays the moisture transfer in the wall.

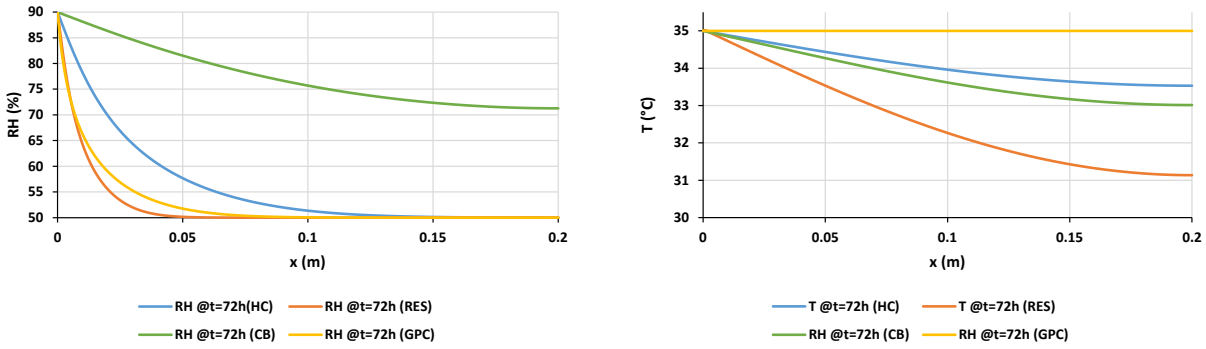

(**a**) (**b**)

Figure 20. Relative humidity (**a**) and temperature profiles (**b**) inside the materials (hemp concrete, cob, and GPC) after 72 h.

The tendency is inversed for the temperature profile. In fact, Cob had the best insulation properties of the four materials, followed by clay brick and hemp concrete, then comes GBC. It should be mentioned that despite the very high thermal conductivity of GPC compared to HC, the temperature is only about 1 °C at 0.2 m. The same remark is possible for RES, which has a higher thermal conductivity than HC but presents a lower increase of temperature compared to HC.

In order to better describe the dynamic inside the materials, the evolution of RH and *T* at 5 cm is presented as a function of time (Figure 21). As can be seen, from the temperature curve, the equilibrium is reached after 24 h, 72 h, and 144 h for GPC, HC, RES, and clay

brick, respectively. The response to temperature solicitation is very low for RES and clay brick compared to the two other materials, which is explained by higher thermal inertia.

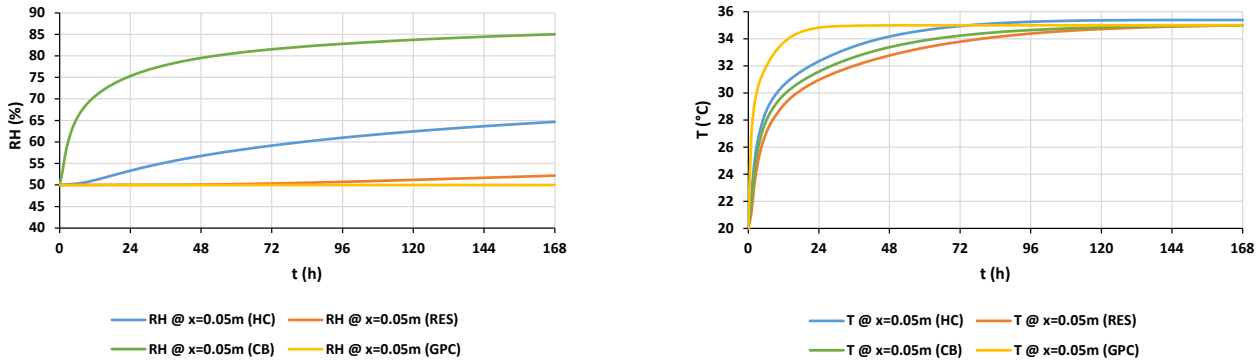

(**a**) (**b**)

Figure 21. Temporal evolution of RH (**a**) and temperature (**b**) at 0.05 m for HC, cob, and GPC.

After 168 h, the RH does not reach equilibrium for any of the three materials. The simulations have been therefore extended to one year in order to have more representative effects (Figure 22). After 3 months, the equilibrium is reached for CB. For HC, the equilibrium is almost reached after 1 year. However, for RES and GPC, the equilibrium is far from being reached, with relative higher value for RES in comparison to GPC.

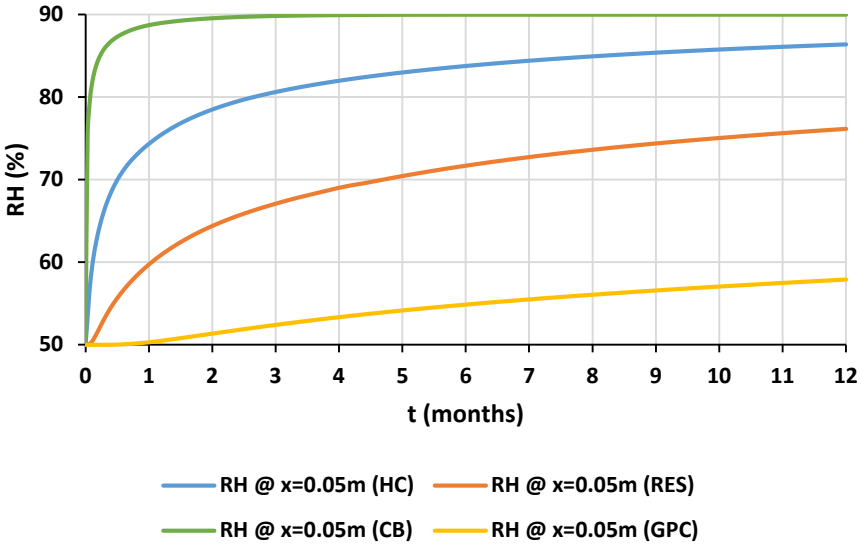

Figure 22. Yearly simulation of the evolution of RH and *T* at x = 0.05 m for HC, cob, and GPC.

From the numerical simulation, it appeared that RES provides the wall with a good thermal inertia with acceptable moisture regulation ability.

4. Conclusions

In this work, a full hygrothermal characterization of cob raw earth material with 3% of straw was presented. Raw earth materials are known for their good thermal inertia. Nevertheless, their hygrothermal properties are not widely dealt within the literature. As an application, we wanted to model the hygrothermal behavior of a building envelope made of the studied material and to compare its behavior to other conventional materials (clay brick, glass powder concrete) and biosourced materials (hemp concrete). The aim was to highlight the advantages to use the studied material. This work therefore provides results that will extend the databases and complete knowledge of the intrinsic properties of

this kind of geosourced materials. Thermal conductivity, specific heat, sorption isotherms, moisture buffer value (MBV), and water vapor permeability were deduced experimentally. Next, the properties were used in a numerical prediction model as input parameters in order to compare cob with other materials used in building sector.

At first it was highlighted that thermal conductivity of the studied formulation is of 0.180 $W \cdot m^{-1} \cdot K^{-1}$. This value is slightly higher than that of hemp concrete, which is about 0.1 $W \cdot m^{-1} \cdot K^{-1}$. Compared to conventional material such as concrete, cob thermal conductivity is eight times lower. Regarding specific heat, a value of 875 $J \cdot kg^{-1} \cdot K^{-1}$ was determined at 23 °C for cob. This value is lower than hemp concrete, which is equal to 1165 $J \cdot kg^{-1} \cdot K^{-1}$. Concrete has a value close to that of cob with a specific heat of 855 $J \cdot kg^{-1} \cdot K^{-1}$. Thanks to sorption isotherms, the maximum adsorbed water was measured. Cob and concrete have values almost equal with 4 and 5%, respectively. Hemp concrete has a value between 12 and 16%. This can be explained by the high amount of hemp shives in the material. Furthermore, hysteresis phenomenon appeared to be more important for concrete and hemp concrete, but not for cob. Additionally, it has been highlighted that moisture storage capacity of cob is approximately 7 times lower than hemp concrete values and twice as low as concrete. MBV tests were carried out for cob and compared with hemp concrete and concrete. A MBV of 1.4 $g/(m^2 \cdot \%RH)$ was obtained, which leads us to consider cob as a good moisture regulator. Hemp concrete has a MBV higher than cob's one. The latter is equal to 2.27 $g/(m^2 \cdot \%RH)$ which defines this material as an excellent moisture regulator. The same statement is not valid for concrete because of this very low MBV that is worth 0.37 $g/(m^2 \cdot \%RH)$. Thus, it is considered as a limited moisture regulator. Finally, water vapor permeability tests were carried out. Cob and hemp concrete have close values with 1.08×10^{-11} $kg \cdot s^{-1} \cdot m^{-1} \cdot Pa^{-1}$ and 2.85×10^{-11} $kg \cdot s^{-1} \cdot m^{-1} \cdot Pa^{-1}$, respectively. Regarding concrete, its water vapor permeability value is much lower with a value of 9.51×10^{-13} $kg \cdot s^{-1} \cdot m^{-1} \cdot Pa^{-1}$.

Thanks to the modeling part, it was highlighted that cob is less conductive for humidity compared to hemp concrete and clay brick but more conductive than glass powder concrete. This tendency is inversed for profile temperature. It was noticed that RES provides the wall with higher thermal inertia than other compared materials. Additionally, it has been shown that the kinetics of moisture transfer is slower for RES and glass powder concrete than hemp concrete and clay brick.

In addition to the very interesting hygrothermal properties of cob, it is important to underline that its environmental and carbon footprint is much lower than other material used in this comparison [12], hence the interest to deepen the research on this theme.

Author Contributions: Conceptualization, P.P., N.I., S.B., A.E.A.H. and R.B.; methodology, Y.E.B.; validation, Y.E.B., M.S., P.P., N.I., S.B., A.E.A.H. and R.B.; formal analysis, Y.E.B. and M.S.; investigation, Y.E.B. and M.S.; resources, A.E.A.H. and R.B.; data curation, Y.E.B. and M.S.; writing—original draft preparation, Y.E.B.; writing—review and editing, P.P., N.I., S.B., A.E.A.H. and R.B.; visualization, M.S.; supervision, P.P., N.I. and S.B.; project administration, R.B.; funding acquisition, A.E.A.H. and R.B. All authors have read and agreed to the published version of the manuscript.

Funding: This research received no external funding.

Institutional Review Board Statement: Not applicable.

Informed Consent Statement: Not applicable.

Data Availability Statement: The data presented in this study are available on request from the corresponding author.

Acknowledgments: Authors are grateful to Ferhat Benmahiddine for his precious help. They thank to ADEME and Pays de la Loire region.

Conflicts of Interest: The authors declare no conflict of interest.

Nomenclature

C_p	Specific heat capacity ($J \cdot kg^{-1} \cdot K^{-1}$)
RH	Relative Humidity (%)
m	Mass (g)
T	Temperature (°C)
u	Water content of mass ratio (%)
w	Water content ($kg \cdot m^{-3}$)
C_m	Moisture storage capacity (%)
p	Pressure (Pa)
k_T	Liquid water conductivity due to a thermal gradient ($kg \cdot m^{-1} \cdot s^{-1} \cdot K^{-1}$)
R	Ideal gas constant ($J \cdot mol^{-1} \cdot K^{-1}$)
M	Molar mass of water ($g \cdot mol^{-1}$)
C_p^*	Total heat capacity ($J \cdot kg^{-1} \cdot K^{-1}$)
h_l	Specific liquid enthalpy ($J \cdot kg^{-1}$)
k_l	Hydraulic liquid conductivity ($kg \cdot s^{-1} \cdot m^{-1} \cdot Pa^{-1}$)
k_m	Total moisture diffusivity coefficient ($kg \cdot m^{-1} \cdot s^{-1} \cdot Pa^{-1}$)
L_v	Latent heat of vaporization of liquid water ($J \cdot kg^{-1}$)
PCC	Phase Change Criterion
Subscripts	
s	solid
l	liquid
v	vapor
sat	saturation
Greek Symbols	
ρ	Density ($kg \cdot m^{-3}$)
λ	Thermal conductivity ($W \cdot m^{-1} \cdot K^{-1}$)
λ^*	Effective thermal conductivity ($W \cdot m^{-1} \cdot K^{-1}$)
δ	Water vapor permeability ($kg \cdot s^{-1} \cdot m^{-1} \cdot Pa^{-1}$)
γ	Heat transfer by convection due to the vapor pressure gradient coefficient ($W \cdot m^{-1} \cdot Pa^{-1}$)

References

1. Climat, Air et Energie. Available online: https://librairie.ademe.fr/changement-climatique-et-energie/1725-climat-air-et-energie-9791029712005.html (accessed on 31 March 2022).
2. The United Nations Environment Programme. *Global Alliance for Buildings and Construction. Global Status Report for Buildings and Construction: Towards a Zero-Emissions, Efficient and Resilient Buildings and Construction Sector—Executive Summary*; The United Nations Environment Programme: Nairobi, Kenya, 2020.
3. Thongkamsuk, P.; Sudasna, K.; Tondee, T. Waste Generated in High-Rise Buildings Construction: A Current Situation in Thailand. *Enrgy Proced.* **2017**, *138*, 411–416. [CrossRef]
4. Meyer, C. Concrete Materials and Sustainable Development in the USA. *Struct. Eng. Int.* **2004**, *14*, 203–207. [CrossRef]
5. CSI: Our Agenda for Action. Available online: https://www.wbcsd.org/jlgbe (accessed on 31 March 2022).
6. Réglementation Environnementale 2020: Réduire l'impact Carbone des Bâtiments Neufs (Dossier RE2020). Available online: http://www.cerema.fr/fr/actualites/RE2020 (accessed on 31 March 2022).
7. Joffroy, T. Les Architectures de Terre Crue: Des Origines à Nos Jours. In *Savoir & Faire: La terre*; Jacquet, H., Ed.; Savoir & Faire: Paris, France, 2016; Volume La terre, pp. 333–347.
8. Minke, G. Building with Earth: Design and Technology of A Sustainable Architecture. Available online: https://vdoc.pub/documents/building-with-earth-design-and-technology-of-a-sustainable-architecture-7n3qjrkm93p0 (accessed on 31 March 2022).
9. Anger, R.; Fontaine, L. *Grains de Bâtisseurs: La Matière En Grains, de la Géologie à l'Architecture*; CRATerre: Villefontaine, France, 2005.
10. Adams, C.; Lynne, E. *Alternative Construction: Contemporary Natural Building Methods*; John Wiley & Sons: Hoboken, NJ, USA, 2000.
11. Keefe, L. *Earth Building: Methods and Materials, Repair and Conservation*; Routledge: Oxfordshire, UK, 2012; ISBN 978-1-134-35017-9.
12. Ben-Alon, L.; Loftness, V.; Harries, K.A.; DiPietro, G.; Hameen, E.C. Cradle to Site Life Cycle Assessment (LCA) of Natural vs. Conventional Building Materials: A Case Study on Cob Earthen Material. *Build. Environ.* **2019**, *160*, 106150. [CrossRef]
13. Hamard, E.; Cazacliu, B.; Razakamanantsoa, A.; Morel, J.C. Cob, a Vernacular Earth Construction Process in the Context of Modern Sustainable Building. *Build. Environ.* **2016**, *106*, 17. [CrossRef]
14. Niroumand, H.; Zain, M.F.M.; Jamil, M. Various Types of Earth Buildings. *Procedia Soc. Behav. Sci.* **2013**, *89*, 226–230. [CrossRef]
15. Evans, I.; Smiley, L.; Smith, M.G. *The Hand-Sculpted House: A Philosophical and Practical Guide to Building a Cob Cottage*; Chelsea Green Publishing: Chelsea, VT, USA, 2002.
16. Ben-Alon, L.; Loftness, V.; Harries, K.A.; Hameen, E.C.; Bridges, M. Integrating Earthen Building Materials And Methods Into Mainstream Construction. *J. Green Build.* **2020**, *15*, 87–106. [CrossRef]

17. Watson, L.; McCabe, K. The Cob Building Technique. Past, Present and Future. *Inf. Constr.* **2011**, *63*, 59. [CrossRef]
18. Fabbri, A.; Morel, J.C.; Aubert, J.-E.; Bui, Q.-B.; Gallipoli, D.; Ventura, A.; Reddy, V.B.V.; Hamard, E.; Pelé-Peltier, A.; Abhilash, H.N. An Overview of the Remaining Challenges of the RILEM TC 274-TCE, Testing and Characterisation of Earth-Based Building Materials and Elements. *RILEM Tech. Lett.* **2021**, *6*, 150–157. [CrossRef]
19. Moisture Movement in Porous Materials under Temperature Gradients. *Eos Trans. Am. Geophys. Union* **1957**, *38*, 222–232. [CrossRef]
20. Ferroukhi, Y.; Djedjig, R.; Limam, K.; Belarbi, R. Hygrothermal Behavior Modeling of the Hygroscopic Envelopes of Buildings: A Dynamic Co-Simulation Approach. *Build. Simul.* **2016**, *9*, 501–512. [CrossRef]
21. Remki, B.; Abahri, K.; Tahlaiti, M.; Belarbi, R. Hygrothermal Transfer in Wood Drying under the Atmospheric Pressure Gradient. *Int. J. Therm. Sci.* **2012**, *57*, 135–141. [CrossRef]
22. NF EN ISO 17892-4. Available online: https://www.boutique.afnor.org/fr-fr/norme/nf-en-iso-178924/reconnaissance-et-essais-geotechniques-essais-de-laboratoire-sur-les-sols-p/fa166662/80069 (accessed on 31 March 2022).
23. Rojat, F.; Hamard, E.; Fabbri, A.; Carnus, B.; McGregor, F. Towards an Easy Decision Tool to Assess Soil Suitability for Earth Building. *Constr. Build. Mater.* **2020**, *257*, 28. [CrossRef]
24. Baize, D. *Guide Des Analyses En Pédologie*, 3rd ed.; Éditions Quae: Versailles, France, 2018.
25. Barnaure, M.; Bonnet, S.; Poullain, P. Earth Buildings with Local Materials: Assessing the Variability of Properties Measured Using Non-Destructive Methods. *Constr. Build. Mater.* **2021**, *281*, 122613. [CrossRef]
26. NF EN ISO 17892-12. Available online: https://www.boutique.afnor.org/fr-fr/norme/nf-en-iso-1789212/reconnaissance-et-essais-geotechniques-essais-de-laboratoire-sur-les-sols-p/fa187930/84021 (accessed on 31 March 2022).
27. NF EN 933-9+A1. Available online: https://www.boutique.afnor.org/fr-fr/norme/nf-en-9339-a1/essais-pour-determiner-les-caracteristiques-geometriques-des-granulats-part/fa181706/41426 (accessed on 31 March 2022).
28. Snell, C.; Callahan, T. *Building Green: A Complete How-to Guide to Alternative Building Methods: Earth Plaster, Straw Bale, Cordwood, Cob, Living Roofs*; Sterling Publishing Company, Inc.: New York, NY, USA, 2009.
29. Phung, T.A. Formulation et Caractérisation d'un Composite Terre-Fibres Végétales: La Bauge. Ph.D. Thesis, Normandie Université, Caen, France, 2018.
30. Engineering Properties of Cob as a Building Material. Available online: https://scialert.net/abstract/?doi=jas.2006.1882.1885 (accessed on 31 March 2022).
31. Behim, M.; Cyr, M.; Clastres, P. Physical and Chemical Effects of El Hadjar Slag Used as an Additive in Cement-Based Materials. *Eur. J. Environ. Civ. Eng.* **2011**, *15*, 1413–1432. [CrossRef]
32. Hwang, C.; Lin, C. Strength Development of Blended Blast-furnace Slag-cement Mortars. *J. Chin. Inst. Eng.* **1986**, *9*, 233–239. [CrossRef]
33. Spezzani, L. *Valorisation Énergétique Des Cultures Intermédiaires et Coproduits Agricoles*; ValBiom: Gembloux, Belgium, 2014.
34. Lam, P.S.W.; Sokhansanj, S.; Bi, X.; Lim, J.; Naimi, L.; Hoque, M.; Mani, S.; Womac, A.; Ye, X.; Narayan, S. Bulk Density of Wet and Dry Wheat Straw and Switchgrass Particles. *Appl. Eng. Agric.* **2008**, *24*, 351–358. [CrossRef]
35. Koh, C.H.; Kraniotis, D. A Review of Material Properties and Performance of Straw Bale as Building Material. *Constr Build Mater.* **2020**, *259*, 120385. [CrossRef]
36. Costes, J.-P.; Evrard, A.; Biot, B.; Keutgen, G.; Daras, A.; Dubois, S.; Lebeau, F.; Courard, L. Thermal Conductivity of Straw Bales: Full Size Measurements Considering the Direction of the Heat Flow. *Buildings* **2017**, *7*, 11. [CrossRef]
37. Opoku, A.; Tabil, L.G.; Crerar, B.; Shaw, M.D. Thermal Conductivity and Thermal Diffusivity of Timothy Hay. *Can. Biosyst. Eng.* **2006**, *48*, 3.
38. Quagliarini, E.; Stazi, A.; Pasqualini, E.; Fratalocchi, E. Cob Construction in Italy: Some Lessons from the Past. *Sustainability* **2010**, *2*, 3291–3308. [CrossRef]
39. Kouakou, C.; Morel, J.-C. Strength and Elasto-Plastic Properties of Non-Industrial Building Materials Manufactured with Clay as a Natural Binder. *Appl. Clay Sci.* **2009**, *44*, 27–34. [CrossRef]
40. Sangma, S.; Tripura, D.D. Compressive and Shear Strength of Cob Wallettes Reinforced with Bamboo and Steel Mesh. *Proc. Inst. Civil. Eng.—Struct. Build* **2021**, 1–15. [CrossRef]
41. Rizza, M.S.; Böttger, H. Effect of Straw Length and Quantity on Mechanical Properties of Cob. In Proceedings of the 16th International Conference on Non-Conventional Materials and Technologies, Winnipeg, MB, Canada, 10–13 August 2015.
42. Réseau Terre. Guides des Bonnes Pratiques Pour la Construction en Terre Crue. Available online: https://reseauterre.hypotheses.org/748#:~{}:text=Les%20guides%20des%20bonnes%20pratiques,usage%2C%20de%20p%C3%A9rennit%C3%A9%2C%20etc (accessed on 31 March 2022).
43. CSTB NF EN 12664. Available online: http://evaluation.cstb.fr/fr/essais/methode/nf-en-12664/ (accessed on 31 March 2022).
44. NF EN 12667. Available online: https://www.boutique.afnor.org/fr-fr/norme/nf-en-12667/performance-thermique-des-materiaux-et-produits-pour-le-batiment-determinat/fa045167/18796 (accessed on 31 March 2022).
45. NF EN 821-3. Available online: https://m.boutique.afnor.org/fr-fr/norme/nf-en-8213/ceramiques-techniques-avancees-ceramiques-monolithiques-proprietes-thermoph/fa113314/24983 (accessed on 31 March 2022).
46. Rode, C.; Peuhkuri, R.; Time, B.; Svennberg, K.; Ojanen, T. Moisture Buffer Value of Building Materials. *Heat-Air-Moisture Transp. Meas. Build. Mater.* **2007**, *4*, 33–44. [CrossRef]
47. NF EN 12572-2. Available online: https://www.boutique.afnor.org/fr-fr/norme/nf-en-125722/structures-artificielles-descalade-partie-2-exigences-de-securite-et-method/fa182518/58638 (accessed on 31 March 2022).

48. Liu, M.Y.J.; Alengaram, U.J.; Jumaat, M.Z.; Mo, K.H. Evaluation of Thermal Conductivity, Mechanical and Transport Properties of Lightweight Aggregate Foamed Geopolymer Concrete. *Energy Build.* **2014**, *72*, 238–245. [CrossRef]
49. Trechsel, H.R. Moisture Analysis and Condensation Control. In *Building Envelopes*; ASTM: West Conshohocken, PA, USA, 2001.
50. Asadi, I.; Shafigh, P.; Abu Hassan, Z.F.; Mahyuddin, N.B. Thermal Conductivity of Concrete—A Review. *J. Build. Eng.* **2018**, *20*, 81–93. [CrossRef]
51. Benmahiddine, F.; Bennai, F.; Cherif, R.; Belarbi, R.; Tahakourt, A.; Abahri, K. Experimental Investigation on the Influence of Immersion/Drying Cycles on the Hygrothermal and Mechanical Properties of Hemp Concrete. *J. Build. Eng.* **2020**, *32*, 101758. [CrossRef]
52. Boukhelf, F.; Trabelsi, A.; Belarbi, R.; Bachir Bouiadjra, M. Experimental and Numerical Modelling of Hygrothermal Transfer: Application on Building Energy Performance. *Energy Build.* **2022**, *254*, 111633. [CrossRef]
53. Allam, R.; Nabil, I.; Belarbi, R.; El-Meligy, M.; Altahrany, A. Hygrothermal Behavior for a Clay Brick Wall. *Heat Mass Transf.* **2018**, *54*, 1579–1591. [CrossRef]
54. Laborel-Préneron, A.; Aubert, J.E.; Magniont, C.; Bertron, A. Influence of Straw Content on the Mechanical and Thermal Properties of Bio-Based Earth Composites. *Acad. J. Civ. Eng.* **2015**, *33*, 517–522. [CrossRef]
55. Medjelekh, D.; Ulmet, L.; Dubois, F. Characterization of Hygrothermal Transfers in the Unfired Earth. *Energy Procedia* **2017**, *139*, 487–492. [CrossRef]
56. Cagnon, H.; Aubert, J.E.; Coutand, M.; Magniont, C. Hygrothermal Properties of Earth Bricks. *Energy Build.* **2014**, *80*, 208–217. [CrossRef]
57. Bennai, F.; Ferroukhi, M.Y.; Benmahiddine, F.; Belarbi, R.; Nouviaire, A. Assessment of Hygrothermal Performance of Hemp Concrete Compared to Conventional Building Materials at Overall Building Scale. *Constr. Build. Mater.* **2022**, *316*, 126007. [CrossRef]
58. McGregor, F.; Heath, A.; Fodde, E.; Shea, A. Conditions Affecting the Moisture Buffering Measurement Performed on Compressed Earth Blocks. *Build. Environ.* **2014**, *75*, 11–18. [CrossRef]
59. Rode, C.; Peuhkuri, R.H.; Mortensen, L.H.; Hansen, K.K.; Time, B.; Gustavsen, A.; Ojanen, T.; Ahonen, J.; Svennberg, K.; Arfvidsson, J. Moisture Buffering of Building Materials. Ph.D. Thesis, Technical University of Denmark, Department of Civil Engineering, Kongens Lyngby, Denmark, December 2005.
60. Laborel-Préneron, A.; Magniont, C.; Aubert, J.-E. Hygrothermal Properties of Unfired Earth Bricks: Effect of Barley Straw, Hemp Shiv and Corn Cob Addition. *Energy Build.* **2018**, *178*, 265–278. [CrossRef]
61. Boukhelf, F.; Cherif, R.; Trabelsi, A.; Belarbi, R.; Bachir Bouiadjra, M. On the Hygrothermal Behavior of Concrete Containing Glass Powder and Silica Fume. *J. Clean. Prod.* **2021**, *318*, 128647. [CrossRef]
62. EN ISO 13788:2012—Hygrothermal Performance of Building Components and Building Elements—Internal Surface Temperature to Avoid Critical Surface Humidity and Interstitial Condensation—Calculation Methods (ISO 13788:2012). Available online: https://standards.iteh.ai/catalog/standards/cen/a22bcdec-871a-464e-a5f2-fc717b608aeb/en-iso-13788-2012 (accessed on 3 May 2022).
63. Togkalidou, T.; Karoglou, M.; Bakolas, A.; Giakoumaki, A.; Moropoulou, A. Correlation of Water Vapor Permeability with Microstructure Characteristics of Building Materials Using Robust Chemometrics. *Transport. Porous Media* **2013**, *99*, 273–295. [CrossRef]
64. Benmahiddine, F.; Belarbi, R.; Berger, J.; Bennai, F.; Tahakourt, A. Accelerated Aging Effects on the Hygrothermal Behaviour of Hemp Concrete: Experimental and Numerical Investigations. *Energies* **2021**, *14*, 7005. [CrossRef]
65. NF EN 15026. Available online: https://www.boutique.afnor.org/fr-fr/norme/nf-en-15026/performance-hygrothermique-des-composants-et-parois-de-batiments-evaluation/fa119083/31029 (accessed on 31 March 2022).
66. Wang, X.; Jin, X.; Yin, Y.; Shi, X.; Zhou, X. A Transient Heat and Moisture Transfer Model for Building Materials Based on Phase Change Criterion under Isothermal and Non-Isothermal Conditions. *Energy* **2021**, *224*, 120112. [CrossRef]

Article 7

Construction and Building Materials 422 (2024) 135804

Contents lists available at ScienceDirect

Construction and Building Materials

journal homepage: www.elsevier.com/locate/conbuildmat

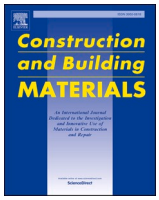

An inverse method for the estimation of the vapor and liquid diffusivity coefficient of conventional and phase change material based hemp concrete

M. Sawadogo [a,b,*], A. Godin [a,b], M. Duquesne [a], R. Belarbi [a,c], A. Hamami [a]

[a] La Rochelle Université, LaSIE UMR CNRS 7356, Avenue Michel Crépeau, CEDEX 1, La Rochelle 17042, France
[b] 4ev Lab, EDF R&D, CNRS, LaSIE, La Rochelle University, Avenue Michel Crépeau, CEDEX 1, La Rochelle 17042, France
[c] Canadian University Dubaï, City Walk Dubaï, United Arab Emirates

ARTICLE INFO

Keywords:
Inverse methods
Mass transfer
Optimization
Liquid diffusivity
Vapor diffusivity
Hemp concrete
Composites with phase change materials

ABSTRACT

This study proposes a method for fast estimation of the hydric properties, including liquid and vapor diffusivities, of three distinct materials: a conventional biosourced insulating material (hemp concrete) and two innovative hybrid composites (hemp concrete with capric acid and hemp concrete with lauric acid). To estimate these parameters, an approach based on an inverse method has been developed. It involves minimizing the quadratic difference between numerical and experimental values of relative humidity, using the Nelder-Mead algorithm by assuming an exponential evolution of the liquid and vapor diffusivities. An unsteady-state experiment has been conducted in a climatic chamber during 18 days to provide experimental data for parameters' estimation. The obtained maximum root mean square error (RMSE) for all the samples is 4.4% that is a satisfactory approximation given the model assumptions and the experimental uncertainties (±2%). The estimated parameters allow calculating all investigated materials' liquid and vapor diffusivities. The validation of the approach is achieved by comparing its results with those from the existing literature.

1. Introduction

The building sector is a major contributor to climate change issues, accounting for more than 40% of energy consumption [1]. As a result, the requirements for building insulation, and consequently the demand for insulation materials, are increasing. The trend is particularly strong for natural, eco-friendly insulation materials with improved energy performance [2]. Among the biobased materials, hemp concrete is presented in many studies as an efficient solution for thermal insulation of buildings due to its low thermal conductivity [3–8]. Moreover, hemp concrete is a material with high water vapor permeability making it a natural moisture regulator [9].

The characterization of the hygrothermal properties of hemp concrete allows a better understanding of the material, obtaining its thermal and hydric properties, which are used as input data of the various hygrothermal models. The thermal properties of interest are the thermal conductivity and the heat capacity. The thermal conductivity is measured through the guarded hot plate method [10,11]. The thermal capacity is measured using calorimetry methods such as differential scanning calorimetry (DSC).

The hydric properties are the moisture storage capacity, the vapor and liquid permeabilities. The moisture storage capacity is obtained through sorption/desorption isotherms. The vapor permeability is measured by the cup method [12,13]. However, the literature is lacking a method for determining the liquid permeability of building materials. Unlike thermal properties (thermal conductivity, heat capacity) which can be determined after relatively fast characterization campaigns (a few days), the characterization of water properties (moisture storage capacity, vapor and liquid permeability) can be very long (few months).

To overcome these constraints, an alternative solution is to use inverse methods to fastly estimate these hydric parameters (liquid and vapor diffusivities) [14–19]. This method consists in estimating parameters of a problem from experimental observations [19–24]. In practice, this is done by calculating the sum of the mean square error between the numerical solution obtained from a mathematical model and the observed data using a minimization algorithm. Zaknoune et al. [25] evaluated moisture transport coefficients in hygroscopic porous materials in buildings using inverse methods. The developed parameter identification method is based on the minimization of the quadratic difference between numerical and experimental values of relative humidity. Busser et al. [26] developed a method for estimating the vapor permeability and sorption curves using the trust-region algorithm. They

* Corresponding author at: La Rochelle Université, LaSIE UMR CNRS 7356, Avenue Michel Crépeau, CEDEX 1, La Rochelle 17042, France.
E-mail address: mohamed.sawadogo@univ-lr.fr (M. Sawadogo).

https://doi.org/10.1016/j.conbuildmat.2024.135804
Received 6 November 2023; Received in revised form 16 February 2024; Accepted 10 March 2024
Available online 18 March 2024
0950-0618/© 2024 Elsevier Ltd. All rights reserved.

showed that simulations using estimated properties accurately represented experimental measurements compared to simulations using properties determined by standard methods.

Except these few studies, the literature is lacking of studies focusing on precise estimation of the hydric properties such liquid and water vapor diffusivities. These proprieties are essential for simulating the hygrothermal behavior of biobased materials [27–31]. Their estimation is therefore a key interest. The present paper aims at estimating the hydric properties of hemp concrete samples incorporating phase change materials in order to provide numerical hygrothermal models with reliable input data.

In the present study, we propose a method for fast and precise estimation of the hydric properties (vapor and liquid diffusivities) of hemp concrete samples: one sample based on hemp concrete serving as reference and two innovative hybrid samples of hemp concrete made from hemp shives impregnated with two phase change materials (PCMs). In order to reduce the number of parameters to be estimated, a characterization campaign was conducted to determine the moisture storage capacity. An unsteady state experimental has been conducted in a climatic chamber to provide experimental data for the parameters' estimation that consists in minimizing the quadratic difference between numerical and experimental values of relative humidity.

2. Methodology

2.1. Problem statement

The purpose of this work is to retrieve the liquid and water vapor permeability of PCM-based hemp concrete. Due to the lack of experimental devices to measure these properties, the inverse method approach was used. An experimental design has been proposed where the samples are submitted to a relative humidity gradient. The mass transfer inside the sample are modelled using the one-dimensional mass transfer equation defined by Fick law for vapor diffusion and Darcy law for the liquid diffusion. This assumption is made possible by the experimental set-up, which only allows moisture to flow in one direction, by efficient insulation of all other faces of the sample. Knowing the material properties and the boundary conditions, it is possible to compute the relative humidity profile inside the material. This is called the direct problem. Another possibility is to use the relative humidity profile to estimate the unknown material properties. This approach is known as inverse method and is the focus of the present study that aim at estimating the liquid and water vapor permeabilities of biobased porous materials. In the next section, the general definition and the equation describing the direct and inverse methods will be presented in details.

2.2. The direct problem

2.2.1. Equations of the direct problem

The direct problem is described by the mass transfer equation under the isothermal assumption. The transfer of dry air is neglected and only the vapor and liquid phases are considered. The transfer drivers considered in this study is the relative humidity.

$$\frac{\partial w}{\partial t} = -div(j_m) \tag{1}$$

with $w = w_v + w_l$ the total water content (kg.m^{-3})and $j_m = j_v + j_l$, the total mass flux (kg.m^{-2}.s^{-1}).

$j_v = -k_v \quad P_{v,sat} \nabla\varphi$ (kg.m^{-2}.s^{-1}) represents the vapor flux density and is governed by Fick's law; with k_v (kg.m^{-1}.s^{-1}.Pa^{-1}) the water vapor permeability, $P_{v,sat}$ (Pa) the saturation vapor pressure and $\nabla\varphi$ the gradient of the relative humidity φ (%).

$j_l = -k_l \frac{RT\rho_l}{M\varphi} \nabla\varphi$ (kg.m^{-2}.s^{-1}) is the induced liquid water mass flow density (obtained from generalized Darcy's law); with k_l (kg.m^{-1}.s^{-1}.Pa^{-1}) the hydraulic conductivity, R (J.mol^{-1}.K^{-1}) the ideal gas constant, T (K) the temperature, ρ_l the liquid water density et M (kg.mol^{-1}) the molar mass of water.

The left-hand side of Eq. 1 is modified to make appear the relative humidity instead of total water content:

$$\frac{\partial w}{\partial t} = \rho_s \frac{\partial u}{\partial t} = \rho_s \frac{\partial u}{\partial \varphi} \frac{\partial \varphi}{\partial t} \tag{2}$$

with $C_m = \frac{\partial u}{\partial \varphi}$ (-) the moisture storage capacity of the material, ρ_s the dry density of the material and u (-) the water content of mass ratio.

We finally obtain:

$$\rho_s C_m(\varphi) \frac{\partial \varphi}{\partial t} = div((D_v(\varphi) + D_l(\varphi))\nabla\varphi) \tag{3}$$

with $D_v(\varphi) = k_v \quad P_{v,sat}$ and $D_l(\varphi) = k_l \frac{RT\rho_l}{M\varphi}$ respectively the vapor and liquid diffusion coefficients expressed kg.m^{-1}.s^{-1}.

In order to reduce the number of parameters of the problem the moisture storage capacity C_m is determined experimentally through the sorption/desorption isotherm curves. Therefore, D_v and D_l are the only parameters to be estimated.

2.2.2. Solving the direct problem and validating the calculation code

The validation of the modelling of the direct problem is an essential step in the optimization strategy. The mass transfer assumed unidirectional becomes:

$$\rho_s C_m(\varphi) \frac{\partial \varphi}{\partial t} = \frac{\partial}{\partial x}\left((D_v(\varphi) + D_l(\varphi)) \frac{\partial \varphi}{\partial x} \right) \tag{4}$$

First, the time dependent term is discretized with an implicit scheme of index n ∈[1, N$_t$] as follows (Eq. 8):

$$\rho_s C_m\left(\varphi_i^{n+1}\right) \frac{\varphi_i^{n+1} - \varphi_i^n}{\Delta t} = \frac{\partial}{\partial x}\left(\left(D_v\left(\varphi_i^{n+1}\right) + D_l(\varphi_i^{n+1})\right) \frac{\partial \varphi_i^{n+1}}{\partial x} \right) \tag{5}$$

where $\Delta t = t_{n+1} - t_n$ is the time step.

The spatial discretization uses a second-order finite difference scheme with a mesh of N elements of index i. The flows are evaluated at the i+1/2 indexes, i.e. at the border of the meshes and not at the nodal points (Eq. (6)).

$$\rho_s C_m\left(\varphi_i^{n+1}\right) \frac{\varphi_i^{n+1} - \varphi_i^n}{\Delta t} = \frac{1}{\Delta x}\left((D_v(\varphi) + D_l(\varphi))|_{i+1/2} \frac{\partial \varphi}{\partial x}|_{i+1/2} - (D_v(\varphi) + D_l(\varphi))|_{i-1/2} \frac{\partial \varphi}{\partial x}|_{i-1/2} \right) \tag{6}$$

where $\Delta x = x_{i+1/2} - x_{i-1/2}$ is the grid size.

The discretized mass transfer equation is therefore written as follows:

$$\begin{aligned} \rho_s C_m\left(\varphi_i^{n+1}\right) \frac{\varphi_i^{n+1} - \varphi_i^n}{\Delta t} = \frac{1}{4 * \Delta x^2} \Big(& \left(D_v\left(\varphi_{i+1}^{n+1}\right) + D_l(\varphi_{i+1}^{n+1})\right) * (\varphi_{i+1}^{n+1} - \varphi_{i-1}^{n+1}) - 4 \\ & * \left(D_v\left(\varphi_i^{n+1}\right) + D_l(\varphi_i^{n+1})\right) * (\varphi_{i+1}^{n+1} - 2 \\ & * \varphi_i^{n+1} + \varphi_{i-1}^{n+1}) - \left(D_v\left(\varphi_{i-1}^{n+1}\right) + D_l(\varphi_{i-1}^{n+1})\right) \\ & * (\varphi_{i-1}^{n+1} - \varphi_{i+1}^{n+1}) \Big) \end{aligned} \tag{7}$$

Table 1
Hygrothermal properties of the monolithic wall [32].

Parameters	Properties
D_m [$m^2.s^{-1}$]	6.10^{-10}
k_v [$kg.m^{-1}.s^{-1}.Pa^{-1}$]	10^{-15}
$P_{v,sat}$ [Pa]	$610.5 * \exp\left(\frac{17.269 * T - 4717.03}{T - 35.85}\right)$ (for T>273.15 K)
w [$kg.m^{-3}$]	$\frac{116}{(1 - \frac{\log(\varphi)}{0.118})^{0.869}}$
D_v [$kg.m^{-2}.s^{-1}$]	$k_v * P_{v,sat}$

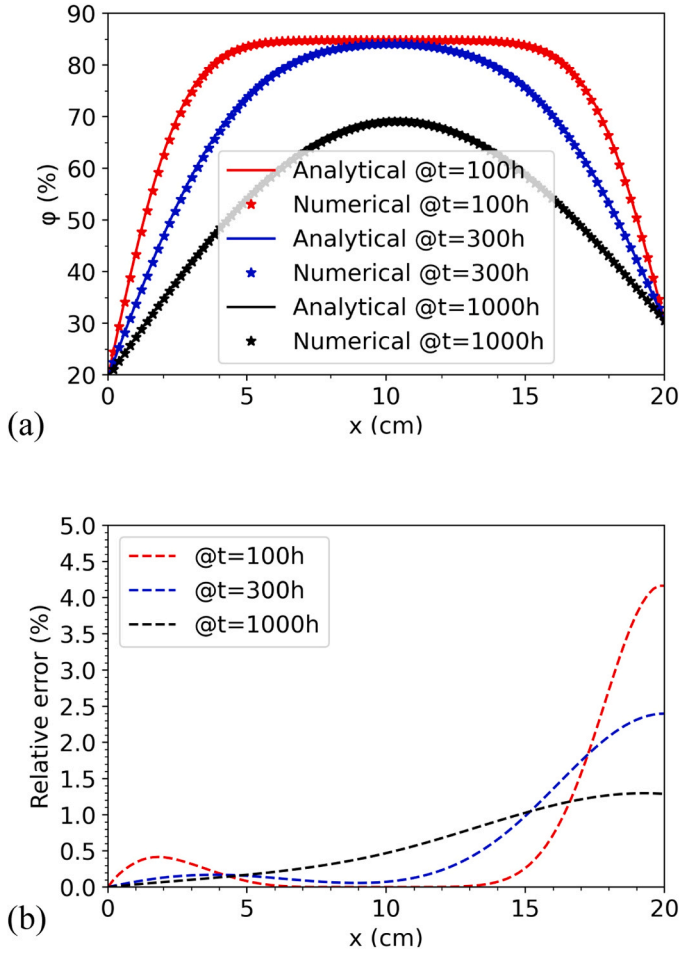

Fig. 1. (a) Comparison of simulation results of the present study vs. analytical solution (b) Relative error between simulation results of the present study and analytical solution.

The solution of the system of algebraic equations (Eq.7) is obtained using a developed Python code based on Thomas' Tri Diagonal Matrix Algrithm "TDMA". In order to ensure the validity of the code before using it to estimate the parameters, a validation case study has been conducted to ensure the accuracy of the methodology.

The validation case is an isothermal drying process defined in the HAMSTAD Benchmark [32]. A 0.2 m thick panel made from a homogeneous building material (monolithic wall) was used in this test. Initial temperature and relative humidity were 20°C and 95% respectively. The relative humidity of the air on the outer and inner surfaces of the panel were 45% and 65% respectively (dirichlet boundary conditions), while the temperature of the entire panel was maintained at a constant value of 20°C throughout the test in order to consider the isothermal drying hypothesis (∇T=0). The choice of this validation case study is motivated by the fact that sseveral authors has used this analytical to efficiently validate their modelling [33–37]. The hydric properties of the studied material are presented in Table 1.

The duration of the simulation is 1000 hours with a fixed time step of 10 s and a space step of 0.2 cm. The convergence criterion is set at 10^{-3}. Fig. 1.a compares the analytic moisture profile with the numerical profiles obtained with the code we developed based on the TDMA method. It can be seen that the two curves are almost overlapping. The plot of the relative error (Fig. 1.b) between the two profiles shows a maximum deviation of only 4%.

The numerical code for solving the direct problem being validated, we proceed to the estimation of the liquid and vapor diffusivities in the next section.

2.3. Inverse methods

2.3.1. Generalities

An inverse problem, as opposed to a direct problem, is a problem in which one tries to determine the causes of a phenomenon from experimental observations of its effects. The resolution of an inverse problem supposes a knowledge of the direct problem resulting from the modelling of the physical phenomenon. Thus, knowing the evolution of the system, it is possible to recover the parameters of the system defined in the direct problem.

In our study, the function of interest, i.e. the observable is the relative humidity φ, which depends on space, time and a set of unknown parameters **p**, defined as follows:

$$\begin{aligned} \varphi : \Omega_x \times \Omega_t \times \Omega_p &\rightarrow [0,1] \\ x \times t \times p &\rightarrow \varphi(x,t,p) \end{aligned} \tag{8}$$

where Ω_x is the spatial domain, Ω_t the time horizon of the observations and Ω_p the set of unknown parameters.

The inverse problem consists in finding the parameters $\mathbf{p}^{\mathbf{est}}$, from a priori parameters $\mathbf{p}^{\mathbf{0}}$, minimizing the difference between the experimental data $\boldsymbol{\varphi}^{\boldsymbol{obs}}$ and the estimated numerical values. The optimization problem to solve is written as follows:

$$\min_{p \in \Omega_p} J(x,t,p) \tag{9}$$

where $J(x,t,p) = \left\| \varphi(x,t,p) - \varphi^{obs} \right\|^2$ is the objective function to be minimized defined as the sum of square error between experimental measurements and estimated values. The minimization parameters are obtained as follows (Eq.10):

$$p^{est} = \underset{p \in \Omega_p}{\operatorname{argmin}} J(x,t,p) \tag{10}$$

Different optimization algorithms have been developed to achieve a reliable solution. Among these algorithms, we can distinguish the gradient-based methods and the derivative-free methods. The optimization of the objective function is performed on Python using an algorithm based on the Nelder-Mead method which is a model search optimization algorithm [38]. The numerical solution of the direct problem is also built on Python using the tridiagonal matrix algorithm (TDMA) after discretizing the differential equation system by the finite difference method.

Nevertheless, before proceeding with the optimization, it is crucial to study whether the parameters are identifiable independently of the experimental measurements. The identification analysis is necessary to create accurate models that can describe the data and whose parameters and predictions are well assessed. With respect to identification, a distinction is made between structural identification, which refers to parameters that are inherently indeterminable due to the structure of the model itself, and practical identification, which refers to measurements that are insufficiently informative to determine the parameters with adequate accuracy [39].

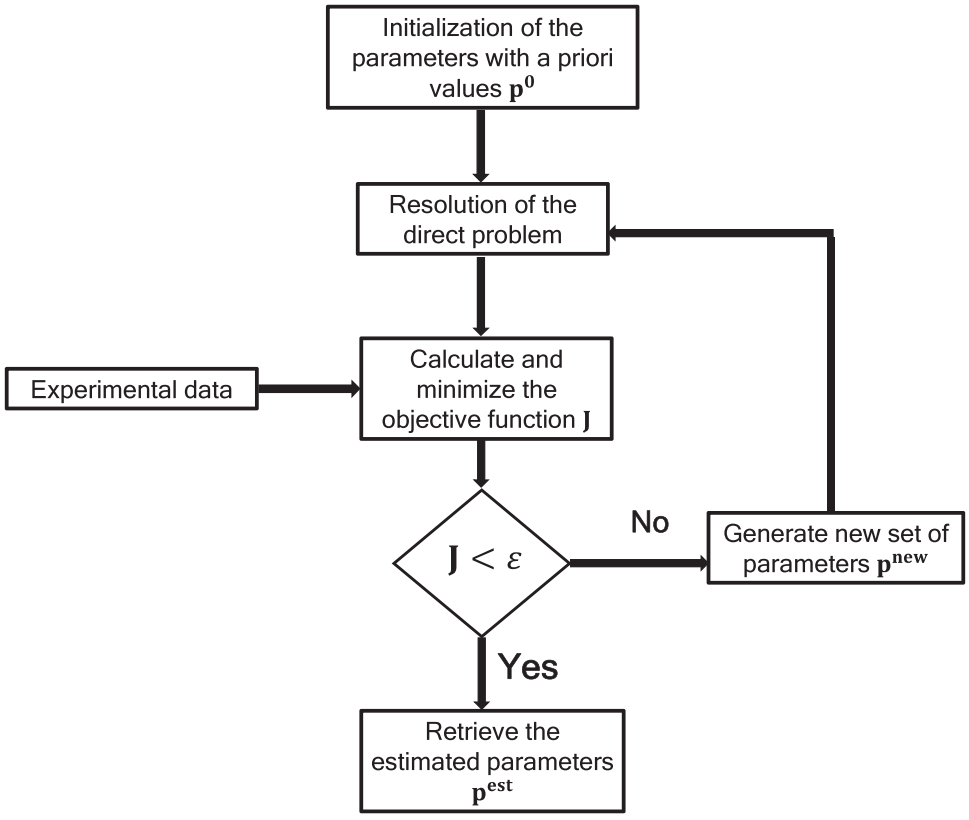

Fig. 2. Minimization strategy for parameter estimation.

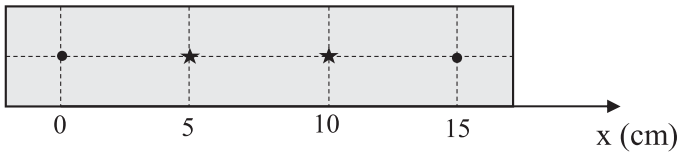

Fig. 3. Schematic representation of the hemp concrete samples and the position of the sensors.

2.3.2. *Implementation strategy*

The first step in the parameter estimation process is the numerical resolution of the one-dimensional mass transfer equation. The numerical resolution of the problem is done following the discretization principle as explained in Section 2.2.2. The system of equations is solved using TDMA algorithm that is a simplified form of Gaussian elimination used to solve tridiagonal systems of equations.

First, the experimental humidity profiles as a function of the time are loaded in the Python code. Then the algorithm of the numerical solution is coupled with a minimization algorithm to minimize the sum of square errors between the numerical solution and the experimental data by varying the parameters. The minimization method based on the Nelder-Mead algorithm, contained in PYTHON's **Scipy.optimize** minimize function is used for the minimization of the objective function. The strength of this method is that it does not require or use function gradient information and is suitable for optimization problems where the function gradient is unknown or cannot be reasonably calculated. The algorithm receives a starting point which can be the end point of another global optimization algorithm or a random point drawn from the domain noted $\mathbf{p}^0$ and referred as a priori value. The parameters minimizing this objective function are the solutions of the inverse problem, $\mathbf{p}^{est}$. These parameters are therefore used to compute the liquid and vapor diffusivities. A summary of the implementation strategy is presented in Fig. 2.

3. Experimental setup

3.1. *Description of the experimental campaign*

The present work focuses on the estimation of the hydric properties of three insulating materials considered in this work, as previously mentioned. The first material is a reference hemp concrete (HC_REF) made from 50% water, 16% hemp shives and 34% binder. In addition to reference hemp concrete, two other materials are fabricated by replacing hemp shives with shives impregnated with two phase change materials: capric acid (CA) and lauric acid (LA) with an impregnation rate of 50% according to the procedure described in [40]. In the rest of this work, HC_CA and HC_LA will be used to describe the samples made from CA and LA impregnated hemp shives respectively.

For each of these three materials, two cylindrical samples of 8 cm diameter and 20 cm height are fabricated. Samples surrounded by moisture-tight aluminum foil in order to insulate them radially, one circular faces is kept free in order to achieve unidirectional mass transfer conditions. In order to avoid constraints related to the boundary conditions, the whole domain will not be considered in the simulations. A retraction of 2.5 cm will be considered on each edge. The domain considered in the simulations is 15 cm long (Fig. 3). Therefore, four Ahlborn temperature and relative humidity (RH) sensors, of type FHA 646 R (5 mm of diameter), are placed inside each sample at different depths: 0 cm, 5 cm, 10 cm and 15 cm. The sensors placed at 0 cm and 15 cm will be considered as left and right boundary conditions. The sensor's accuracy is ±2% over the relative humidity range investigated in this study.

All the faces of the samples are insulated except for one of the circular faces, which is exposed to the environment. The samples are placed in a climatic chamber Excal 2211-HA from Climats (Fig. 4.a and b) are conditioned period of 3 days to ensure that all the materials are the same initial state. Afterwards, they are subjected to a humidity program varying from 10% to 90% and a constant temperature of 23°C

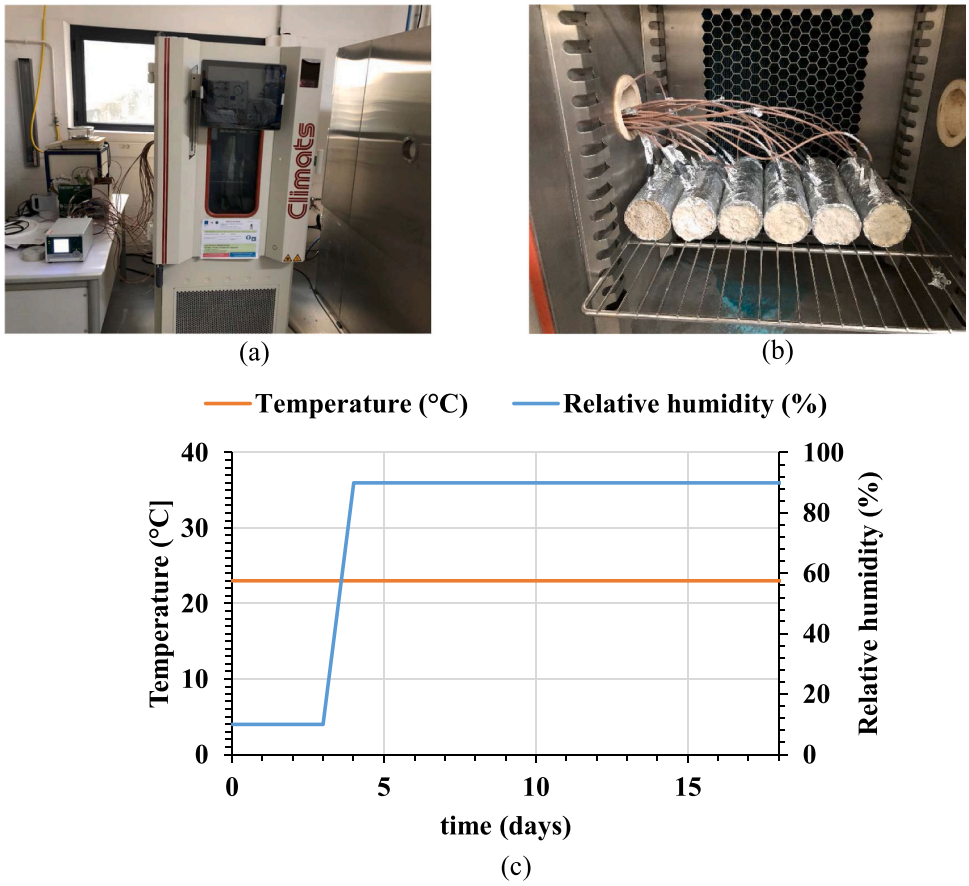

Fig. 4. Experimental setup for the unsteady state case study: (a) Excal 2211-HA climatic chamber from Climats, (b) cylindrical samples with insulated faces and sensors location, (c) temperature and relative humidity program for the unsteady state case study.

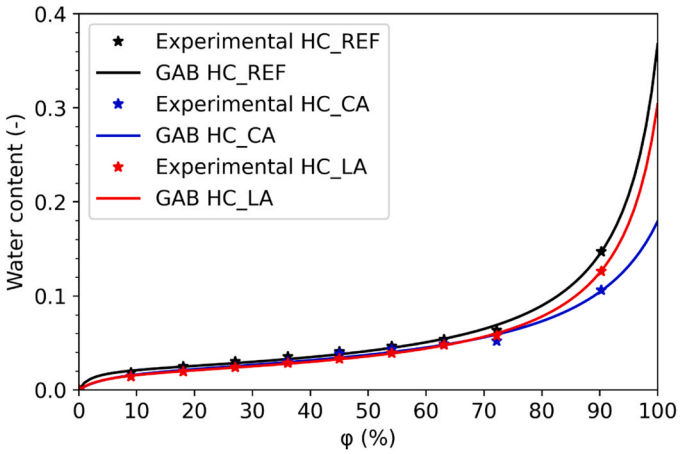

Fig. 5. Sorption isotherms and GAB modelling of HC_REF, HC_CA and HC_LA samples.

Table 2
Coefficients from the GAB modelling for each of the samples along with the mean square error.

	m	*C*	*K*	*RMSE*
HC_REF	0.0224	54.0309	0.9389	0.0027
HC_CA	0.0222	20.9271	0.8766	0.0028
HC_LA	0.0199	24.2531	0.9344	0.0008

(Fig. 4.c) during two weeks. The total duration of the test is 18 days. This case is presented as the unsteady state case study and will allow the identification of the parameters that are liquid and vapor diffusivities.

3.2. Characterization of the moisture storage capacity

In order to reduce the number of parameters to be estimated by inverse methods, a characterization campaign was conducted to determine the moisture storage capacity. This property is defined as the derivative of the sorption isotherm. The sorption isotherm determines the capacity of the material to capture or release water as a function of the relative humidity of the external environment at constant temperature. The experimental determination of this curve is essential for the prediction of the water behavior of porous building materials.

The measurement of the sorption isotherms of the three materials of this study (HC_REF, HC_CA and HC_LA) was performed using the SPS vapor sorption analyzer from ProUmid GmbH, which is based on a gravimetric method. The large temperature range of the SPS enables to conduct vapor sorption analysis at extreme conditions from cool 5°C to hot 60°C. Relative humidity can be precisely set and adjusted over the whole range from completely dry 0% up to 98% RH close to condensation. The advantage of this device lies in the fact that it allows the characterization of up to 23 samples at a time in a very short time. Before starting the characterization, cubic samples (1 cm^3) were dried in a ventilated oven at 40°C.

Sorption and desorption isotherm curves are generally modelled using existing prediction models in the literature such as the Guggenheim-Anderson-de Boer (GAB) model [41] (Eq. (11)). This type of modelling allows the construction of functions used as inputs in hygrothermal models.

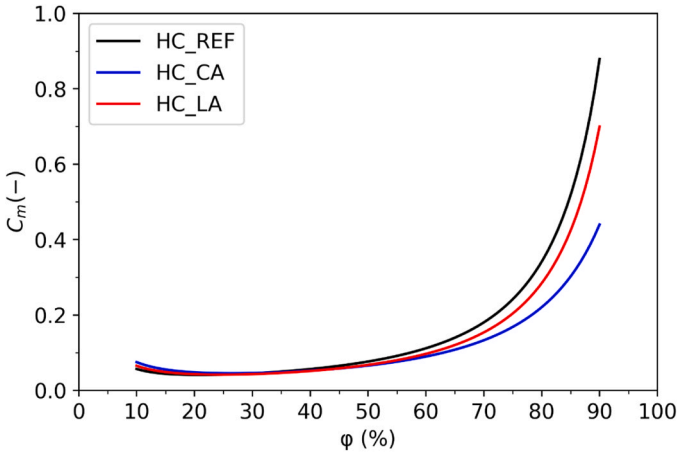

Fig. 6. Moisture storage capacity of the three materials: HC_REF, HC_CA and HC_LA.

$$u(\varphi) = \frac{m \bullet C \bullet K \bullet \varphi}{(1 - K\varphi) * (1 - K\varphi + KC\varphi)} \tag{11}$$

where u is the water content (%), φ the relative humidity (%), m, C, and K the parameters of the GAB model.

Fig. 5.a, b and c show the adsorption isotherms of the three samples between 0% and 90% relative humidity. In this work, only the adsorption curve is presented since no hysteresis effects are considered that could justify a presentation of the desorption curve. HC_REF (Fig. 5.a) has the highest moisture content compared to both HC_CA (Fig. 5.b) and HC_LA (Fig. 5.c), with a maximum value of 0.14%. This decrease in absorption capacity is due to the incorporation of PCM into the hemp shives that fill the pores and limits the spaces available for water adsorption. The adsorption isotherms were modelled by the GAB method and the coefficients of the modelling as well as root mean square errors (RMSE (Eq. 12)) between the model and the experimental data are reported in Table 2. There is a very good agreement between the GAB modelling and the experimental data.

$$RMSE = \sqrt{\frac{\sum_{i=0}^{N} (\widehat{y}_i - y_{\exp,i})^2}{N}} \tag{12}$$

Where $\widehat{y}_i$ is the predicted value and $y_{exp,i}$ the experimental value at the ith measured data and N the number of measurements.

The results of the sorption isotherms are used to calculate the water storage, which is defined as the slope of the sorption isotherm curves. Fig. 6 shows the evolution of the water storage capacity of the three materials. HC_REF has the highest water storage capacity, followed by HC_LA. HC_CA has the lowest water capacity of the three materials.

4. Results of the unsteady case study

This section concerns the estimation of the liquid and the vapor diffusivities in the case of unsteady regime. Both parameters are moisture dependent. The main difficulty is the definition of the evolution function of these two properties with the relative humidity. We consider here that these functions evolve exponentially (Eq. (13)):

$$\begin{cases} D_v(\varphi) = D_{v0} * e^{a*\varphi} \\ D_l(\varphi) = D_{l0} * e^{b*\varphi} \end{cases} \tag{13}$$

with D_{v0}, D_{l0}, a, b the parameters to be estimated by minimizing the objective function.

The assumption of exponential evolution is based on the literature, which shows an exponential trend for these two properties [19,25,42,43].

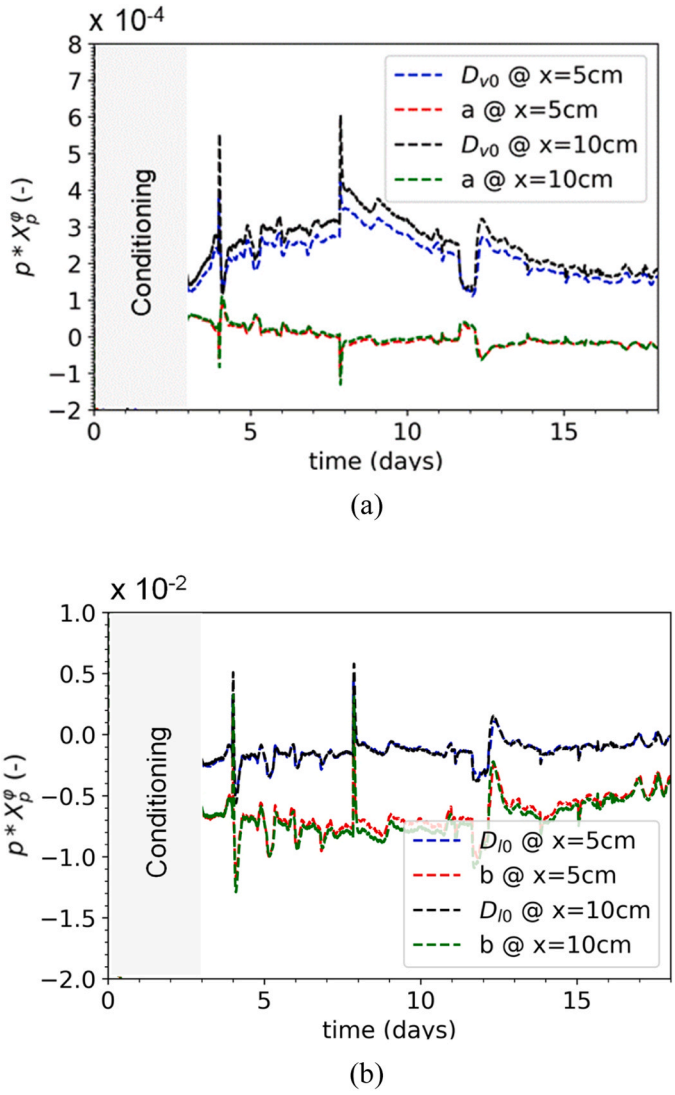

Fig. 7. Sensitivity coefficient of the parameters D_{v0}, a (a) and D_{l0}, b (b) at x=5 cm and x=10 cm.

4.1. Sensitivity study of the parameters

Let analyze the identifiability of parameter sets {D_{v0}, a, D_{l0}, b} from the observations. The sensitivity of the system with respect to the model parameters is verified by differentiating Eq. (4) with respect to each of the four parameters [44,45]. The system of sensitivity equations with respect to the parameter set is as follows (Eqs. (14–17)):

$$\rho_s C_m(\varphi) \frac{\partial X_{D_{v0}}^{\varphi}}{\partial t} = \frac{\partial}{\partial x}\left((D_v(\varphi) + D_l(\varphi)) \frac{\partial X_{D_{v0}}^{\varphi}}{\partial x} \right) + S_{D_{v0}}(\varphi) \tag{14}$$

$$\rho_s C_m(\varphi) \frac{\partial X_{a}^{\varphi}}{\partial t} = \frac{\partial}{\partial x}\left((D_v(\varphi) + D_l(\varphi)) \frac{\partial X_{a}^{\varphi}}{\partial x} \right) + S_{a}(\varphi) \tag{15}$$

$$\rho_s C_m(\varphi) \frac{\partial X_{D_{l0}}^{\varphi}}{\partial t} = \frac{\partial}{\partial x}\left((D_v(\varphi) + D_l(\varphi)) \frac{\partial X_{D_{l0}}^{\varphi}}{\partial x} \right) + S_{D_{l0}}(\varphi) \tag{16}$$

$$\rho_s C_m(\varphi) \frac{\partial X_{b}^{\varphi}}{\partial t} = \frac{\partial}{\partial x}\left((D_v(\varphi) + D_l(\varphi)) \frac{\partial X_{b}^{\varphi}}{\partial x} \right) + S_{b}(\varphi) \tag{17}$$

where $X_{D_{v0}}^{\varphi} = \frac{\partial \varphi}{\partial D_{v0}}$, $X_a^{\varphi} = \frac{\partial \varphi}{\partial a}$, $X_{D_{l0}}^{\varphi} = \frac{\partial \varphi}{\partial D_{l0}}$ and $X_b^{\varphi} = \frac{\partial \varphi}{\partial b}$ are the sensitivity coefficients with respect to D_{v0}, a, D_{l0}, b respectively.

$S_{D_{v0}}(\varphi)$, $S_a(\varphi)$, $S_{D_{l0}}(\varphi)$ and $S_b(\varphi)$ are the source terms related to each

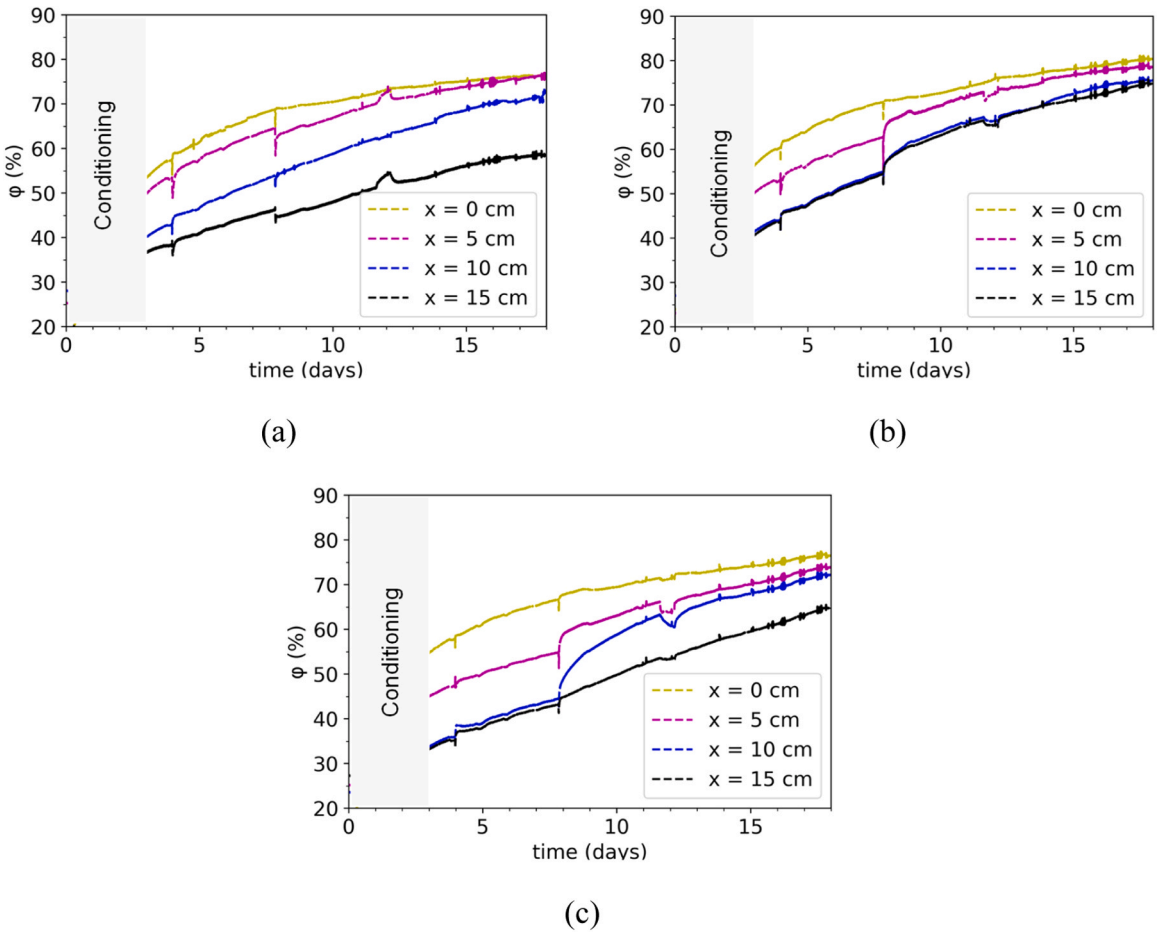

Fig. 8. Evolution of relative humidity in each material at different positions over time: (a) HC_REF, (b) HC_CA and (c) HC_LA.

of the sensitivity equations.

The sensitivity equation system is solved together with the direct problem equation. The solution of the sensitivity equation requires the initialization of the parameters with values close enough to the true solution to accelerate the convergence. The values of the vapor permeability of hemp concrete measured using the cup method are about 10^{-11} kg.m^{-1}.s^{-1}.Pa^{-1} [46,47]. Based on these results, the initialization values of the parameters are chosen in order to have the same order of magnitude as the previous experimental one. The relation between the vapor diffusion coefficient and the vapor permeability is as follows:

$$D_v = k_v * P_{v,sat} \tag{18}$$

The vapor and liquid permeabilities are supposed to have the same order of magnitude (10^{-11} kg.m^{-1}.s^{-1}.Pa^{-1}) and by using Eq. 18, the a priori values of the different parameters of the vapor and liquid diffusivity are:

$D_{v0} = 10^{-6}$kg.m^{-1}.s^{-1}, $D_{l0} = 10^{-6}$kg.m^{-1}.s^{-1}, a = 1, b = 1.

Fig. 7.a and b shows the evolution of the sensitivity coefficients of each of the four parameters to be estimated at x= 5 cm (Fig. 7.a) and x= 10 cm (Fig. 7.b). The relative humidity data of sensors at x= 0 cm and x= 15 cm are used as dirichlet boundary conditions for the sensitivity analysis as well as for the parameter estimation. We notice a predominance of the sensitivity coefficients of the parameters related to the liquid diffusivity, notably K_{l0} and b. This result reflects the preponderance of the liquid diffusivity compared to the vapor diffusivity over the range of humidity considered. Moreover, the sensitivity coefficients vary very little with the position except for a slight shift in time and a reduction in amplitude.

The sensitivity coefficients of the parameters are linearly independent with high magnitudes; therefore, these values can be estimated using the parameter estimation problem.

4.2. Results of the parameter estimation

Fig. 8.a-c shows the evolution of relative humidity inside each sample as a function of time at four different positions. The humidity varies between 20% and 80% for each sample and the evolution with time follows the same trend. After day 4, where the relative humidity is increased to 90%, the humidity sensor shows higher value for the x=0 cm followed by x=5 cm, 10 cm, and 15 cm, as expected. For the first three days, especially the first two days, this order is not observed because the initial hydric state profile is not constant within the samples. For instance, for HC_REF the extremity layer are close to 20% relative humidity where the inside sensors are at 25% and 28% for x=5 cm and x=10 cm, respectively.

However, we note that for the sample HC _CA, the curves of the sensors placed at 10 cm and 15 cm are almost identical. This result may be explained by the proximity of these two sensors. This observation shows the need to estimate the uncertainty of the measurements. We also observed a discontinuity of the measurement at day 8, which is attributable to a momentary interruption of the climatic chamber for 30 minutes. This discontinuity is more pronounced for the samples HC_CA (Fig. 8.b) and HC_LA (Fig. 8.c) and is much more visible on the inner layers (between 5 and 15 cm).

Measurement uncertainties can be of various forms but in this work, we are interested in two types: the measurement uncertainty of the sensor (σ_m) and the uncertainty on its position (σ_X). The total uncertainty on the relative humidity is given by the uncertainty propagation

Table 3
Parameters from the minimization.

	D_{v0} [kg.m^{-1}.s^{-1}]	a	D_{l0} [kg.m^{-1}.s^{-1}]	b	*RMSE (x=5 cm)*	*RMSE (x=10 cm)*
HC_REF	$1.27\bullet10^{-6}$	-4.19	$5.78\bullet10^{-9}$	8.10	2.28%	4.4%
HC_CA	$1.29\bullet10^{-6}$	-4.36	$7.55\bullet10^{-8}$	4.72	1.6%	3.5%
HC_LA	$1.27\bullet10^{-6}$	-4.66	$6.03\bullet10^{-8}$	5.02	4%	2.8%

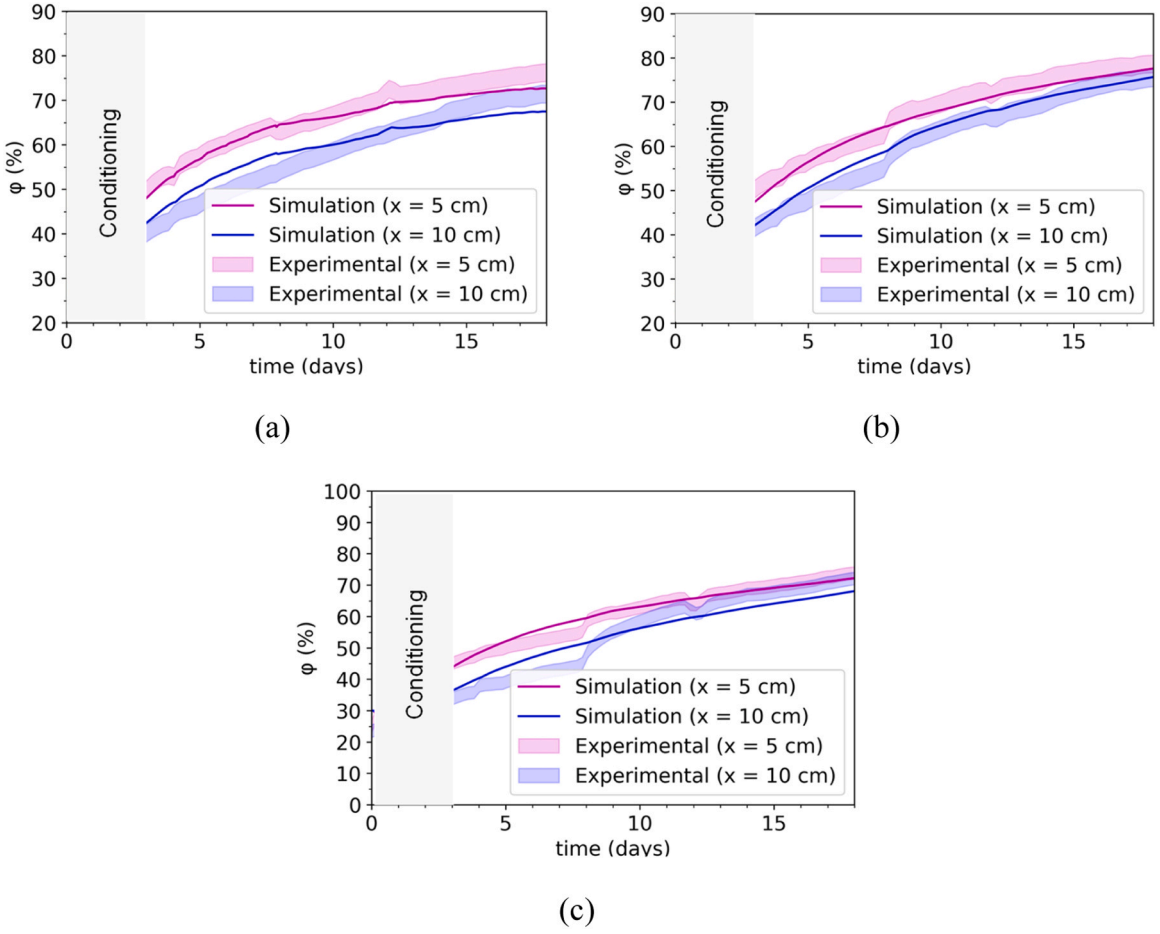

Fig. 9. Comparison between experimental and numerical curves for each material at x= 5 cm and x=10 cm: (a) HC_REF, (b) HC_CA and (c) HC_LA.

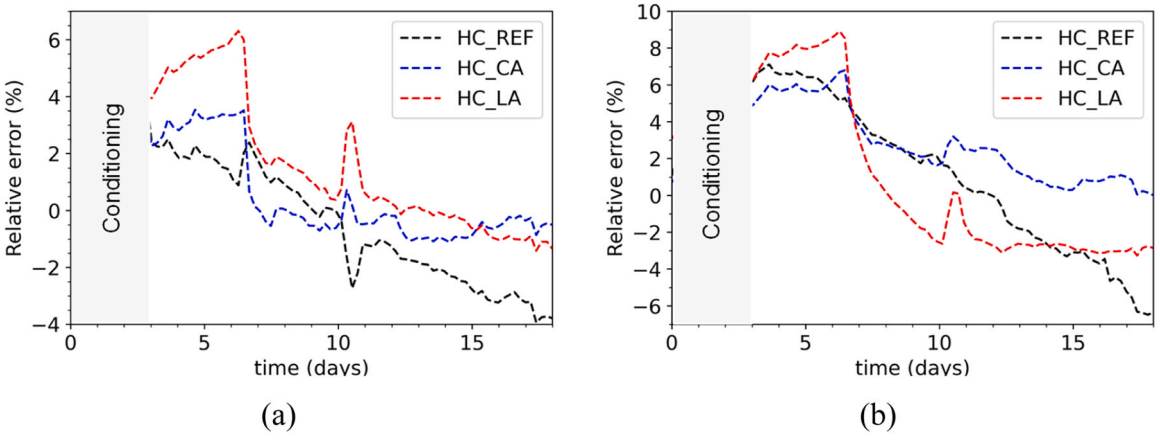

Fig. 10. Relative error between experimental and simulated relative humidity profile for HC_REF, HC_CA and HC_LA samples at x=5 cm (a) and x=10 cm (b).

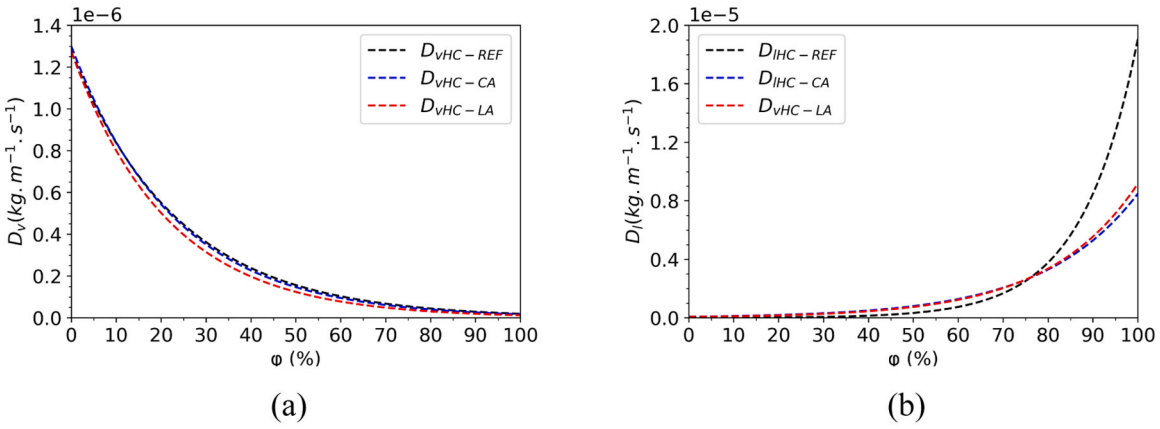

Fig. 11. Vapor (a) and liquid (b) diffusivity coefficients of each material obtained from the estimated parameters.

formula (Eq. 19) [48]:

$$\sigma_\varphi = \sqrt{(\sigma_m)^2 + (\sigma_X)^2} \tag{19}$$

The measurement uncertainty of σ_m of the Ahlborn sensors is 2% over the relative humidity range.

$\sigma_X = \frac{\partial \varphi}{\partial x} dx$ is the measurement uncertainty on the position. The term $\frac{\partial \varphi}{\partial x}$ is calculated from the finite differences and the a priori parameters and dx is taken equal to twice the diameter of the sensor (i.e. 1 cm). These uncertainties are reported on the experimental curves when compared to the simulated ones.

As mentioned earlier (Fig. 3), the sensors placed at the positions x = 0 cm and x = 15 cm will serve as boundary conditions in the minimization procedure and the points x=5 cm and x=10 cm are the points in the domain serving as reference points for the minimization. This procedure is valid for all samples except for HC_CA for which the results at x =10 cm and x = 15 cm are overlapped. For this material, only the point x = 5 cm is retained as reference point for the minimization.

Thus, by applying the procedure described in Fig. 2, the parameters that allow minimizing the objective function are presented in Table 3.

The comparison of the experimental curves, including the measurement uncertainties, with the numerical simulations carried out with the optimized parameters shows a good agreement that justifies the effectiveness of the estimation procedure (Fig. 9.a-c). In general, the estimation is more accurate on the sensor placed at x = 5 cm compared to the one at x = 10 cm. To ensure that, the RMSE of all the estimations are calculated and presented in Table 3.

In fact, the RMSE for the sensor at x=5 cm are 2.28%, 1.6% and 4% for HC_REF, HC_CA and HC_LA, respectively. At x=10 cm the RMSE are 4.4%, 3.5% and 2.8% for HC_REF, HC_CA and HC_LA, respectively. This can be explained by a loss of the exponential curve on the internal layers. Indeed, when we observe the experimental curves at the position x = 10 cm and x = 15 cm, the curves have a quasi-linear trend. This tendency to lose the exponential curve leads to an increase in the error between the experimental data and the numerical simulation, since the assumption of exponential evolution of the properties is made. However, this observation is not true for HC_LA where the opposite trend is observed and showed better accuracy at x=10 cm than for the sensor at x= 5 cm.

In addition, a better accuracy is observed for HC_CA compared to HC_REF and HC_CA. This difference is due to the discontinuity in the experimental curve at day 8 much more visible on the HC_LA samples. In order to confirm this hypothesis, the relative error between experimental and simulated relative humidity using the estimated parameter is presented in Fig. 10 for all the samples. As stated, the maximum error is around day 8 that confirms the assumption made on the discontinuity in the experimental curve at that moment. In addition, one can notice that

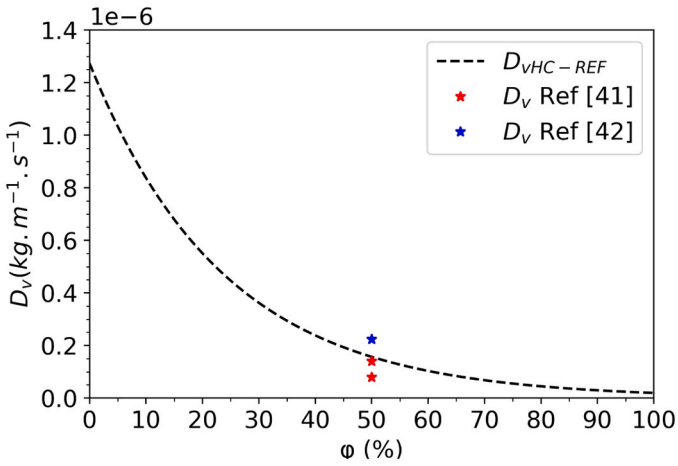

Fig. 12. Comparison between the estimated vapor diffusivity with the literature [46,47].

the maximum error occurred for HC_LA samples that was also visible in Fig. 9.c with maximum relative errors of 7% and 9% at x=5 cm and x=10 cm, respectively.

Fig. 11.a and b show the vapor and liquid diffusivity curves obtained from the estimated parameters. We notice that the vapor diffusivity curve decreases with relative humidity while the liquid diffusivity curve increases with relative humidity. The increase in liquid diffusivity with relative humidity is due to the enhancement of macroscopic moisture transport induced by the microscopic transfer of liquid into the water-filled pores (due to capillary condensation) [46].

The vapor diffusivity coefficients of the three materials are very close. The maximum value, around 10^{-6} is reached for low humidities before decreasing when the relative humidity increases.

The opposite trend is observed with the liquid diffusivity coefficient, which increases with relative humidity. The value of the coefficient is higher for the reference hemp concrete HC_REF compared to the other two materials (HC_CA and HC_LA). This difference can be explained by the incorporation of PCM in the hemp shives, which decreases its adsorption capacity.

Finally, the vapor diffusivity curve is compared with data extracted from literature on the characterization of hemp concrete (Fig. 12). The curve obtained by the inverse method reproduces the results of the literature quite closely.

The disparities of the experimental data from the literature are due to the difference in experimental conditions. Indeed, the two value of liquid diffusivities of reference [41] are obtained using dry and wet cup methods. The estimation strategy constitutes a good approximation of

these properties within a relatively short period.

5. Conclusion

The present work focuses on the determination of the hydric properties that are moisture storage capacity, liquid and vapor diffusivity of three materials comprising hemp concrete, and capric and lauric acid hemp concrete. Therefore, an inverse method coupled with a sum of square error minimization algorithm between experimental data and simulation to estimate the parameters has been developed. This method helps the fast estimation of hydric parameters and solve the problem of the absence of experimental device for the measurement of the liquid diffusivity. In order to reduce the number of parameters, the moisture storage has been determined experimentally. The results show that the moisture storage capacity is higher for reference hemp concrete with a maximum value of about 14% at 90% of relative humidity.

An unsteady state experiments have been used to estimate the hydric parameters that are the liquid and vapor diffusivities using an inverse method. The developed parameter identification method is based on the minimization of the quadratic difference between numerical and experimental values of relative humidity using the Nelder Mead Algorithm. An exponential evolution of the two properties. The results showed a good agreement between experimental and numerical results. The maximum RMSE is 4.4%, 3.5% and 4% for HC_REF, HC_CA and HC_LA, respectively that is a good approximation considering the assumption of the model. Errors could be reduced by considering a different function to describe the evolution of liquid and vapor diffusivities, such as a polynomial function or the exponential of a polynomial. However, even if the results match the experimental data perfectly, the estimated parameters must be feasible. Additionally, different optimization algorithms could be used and compared with the Nelder Mead algorithm used in this study. The assessed parameters are used to determine the liquid and vapor diffusivity curves that reproduce with a good accuracy the results of the literature. These properties should be used in hygrothermal model to simulate the behavior of the materials under different weather conditions in future studies.

CRediT authorship contribution statement

Marie Duquesne: Writing – review & editing, Visualization, Validation, Supervision, Resources, Project administration, Methodology, Funding acquisition, Conceptualization. **Alexandre Godin**: Writing – review & editing, Visualization, Validation, Supervision, Investigation, Formal analysis. **Mohamed Sawadogo**: Writing – review & editing, Writing – original draft, Visualization, Validation, Software, Methodology, Investigation, Formal analysis, Data curation, Conceptualization. **Ameur Hamami**: Writing – review & editing, Visualization, Validation, Supervision, Project administration, Methodology, Investigation. **Rafik Belarbi**: Writing – review & editing, Visualization, Validation, Supervision, Resources, Project administration, Funding acquisition, Conceptualization.

Declaration of Competing Interest

The authors declare that they have no known competing financial interests or personal relationships that could have appeared to influence the work reported in this paper.

Data availability

Data will be made available on request.

Acknowledgments

This work is carried out in the frame of Region Nouvelle Aquitaine for subsidizing BioMCP project (Project-2017–1R10209–13023) and in the frame of the Laboratory for Energy and Environmental Efficiency of Envelopes and Cities, 4ev Lab, the joint Laboratory between EDF R&D, CNRS, LaSIE conducting research to improve the energy and environmental performance of buildings and the quality of life of the inhabitants of urban spaces.

References

[1] Buildings – Topics, IEA (n.d.). https://www.iea.org/topics/buildings (accessed April 30, 2021).
[2] V. Lekavicius, P. Shipkovs, S. Ivanovs, A. Rucins, Thermo-insulation properties of hemp-based products, Latv. J. Phys. Tech. Sci. 52 (2015) 38–51, https://doi.org/10.1515/lpts-2015-0004.
[3] F. Benmahiddine, R. Cherif, F. Bennai, R. Belarbi, A. Tahakourt, K. Abahri, Effect of flax shives content and size on the hygrothermal and mechanical properties of flax concrete, Constr. Build. Mater. 262 (2020) 120077, https://doi.org/10.1016/j.conbuildmat.2020.120077.
[4] G. Delannoy, S. Marceau, P. Glé, E. Gourlay, M. Guéguen-Minerbe, D. Diafi, I. Nour, S. Amziane, F. Farcas, Aging of hemp shiv used for concrete, Mater. Des. 160 (2018) 752–762, https://doi.org/10.1016/j.matdes.2018.10.016.
[5] B. Seng, S. Lorente, C. Magniont, Scale analysis of heat and moisture transfer through bio-based materials — application to hemp concrete, Energy Build. 155 (2017) 546–558, https://doi.org/10.1016/j.enbuild.2017.09.026.
[6] K. Abahri, C. El Hachem, F. Bennai, N. Toan, R. Belarbi, Prediction of hemp concrete morphological deformation by x-ray tomography, in: 2017: pp. 616–625.
[7] S. Barbhuiya, B. Bhusan Das, A comprehensive review on the use of hemp in concrete, Constr. Build. Mater. 341 (2022) 127857, https://doi.org/10.1016/j.conbuildmat.2022.127857.
[8] F. Collet, S. Pretot, Thermal conductivity of hemp concretes: variation with formulation, density and water content, Constr. Build. Mater. 65 (2014) 612–619, https://doi.org/10.1016/j.conbuildmat.2014.05.039.
[9] F. Benmahiddine, F. Bennai, R. Cherif, R. Belarbi, A. Tahakourt, K. Abahri, Experimental investigation on the influence of immersion/drying cycles on the hygrothermal and mechanical properties of hemp concrete, J. Build. Eng. 32 (2020) 101758, https://doi.org/10.1016/j.jobe.2020.101758.
[10] CSTB, NF EN 12664, CSTB Évaluation (n.d.). http://evaluation.cstb.fr/fr/essais/methode/nf-en-12664/ (accessed March 31, 2022).
[11] NF EN 12667, Afnor EDITIONS (n.d.). https://www.boutique.afnor.org/fr-fr/norme/nf-en-12667/performance-thermique-des-materiaux-et-produits-pour-le-batiment-determinat/fa045167/18796 (accessed March 31, 2022)..
[12] NF EN 12572–2, Afnor EDITIONS (n.d.). https://www.boutique.afnor.org/fr-fr/norme/nf-en-125722/structures-artificielles-descalade-partie-2-exigences-de-securite-et-method/fa182518/58638 (accessed March 31, 2022).
[13] T. Duforestel, I. Oubrahim, R. Belarbi, H. El Hardouz, M. Colmet Daâge, Assessment of the water vapor permeability: effect of the total pressure, Int. J. Heat. Mass Transf. 196 (2022) 123210, https://doi.org/10.1016/j.ijheatmasstransfer.2022.123210.
[14] J. Berger, D. Dutykh, N. Mendes, On the optimal experiment design for heat and moisture parameter estimation, Exp. Therm. Fluid Sci. 81 (2017) 109–122, https://doi.org/10.1016/j.expthermflusci.2016.10.008.
[15] J.-L. Dauvergne, Á. Serrano, E. Palomo Del Barrio, Fast estimation of the enthalpy–temperature function of phase change materials, Exp. Therm. Fluid Sci. 122 (2021) 110317, https://doi.org/10.1016/j.expthermflusci.2020.110317.
[16] E. Berrich, F. Aloui, J. Legrand, Experimental validation and critical analysis of inverse method in mass transfer using electrochemical sensor, Exp. Therm. Fluid Sci. 44 (2013) 253–263, https://doi.org/10.1016/j.expthermflusci.2012.07.001.
[17] F. Bozzoli, A. Mocerino, S. Rainieri, P. Vocale, Inverse heat transfer modeling applied to the estimation of the apparent thermal conductivity of an intumescent fire retardant paint, Exp. Therm. Fluid Sci. 90 (2018) 143–152, https://doi.org/10.1016/j.expthermflusci.2017.09.006.
[18] A. Challansonnex, F. Pierre, J. Casalinho, P. Lv, P. Perré, Mass diffusivity determination of various building materials based on inverse analysis of relative humidity evolution at the back face of a sample, Constr. Build. Mater. 193 (2018) 539–546, https://doi.org/10.1016/j.conbuildmat.2018.10.219.
[19] F. Boukhelf, Proposition d'une nouvelle formulation mathématique pour l'analyse du comportement hydro thermo mécanique des structures fonctionnellement graduées, These de doctorat, La Rochelle, 2020. https://www.theses.fr/2020LAROS030 (accessed May 29, 2023).
[20] L.B. Dantas, H.R.B. Orlande, R.M. Cotta, An inverse problem of parameter estimation for heat and mass transfer in capillary porous media, Int. J. Heat. Mass Transf. 46 (2003) 1587–1598, https://doi.org/10.1016/S0017-9310(02)00424-6.
[21] S. Mercier, B. Marcos, C. Moresoli, M. Mondor, S. Villeneuve, Effect of the water content measurements on the estimation and identifiability of water diffusion and convection mass transfer coefficients, Int. J. Heat. Mass Transf. 90 (2015) 480–490, https://doi.org/10.1016/j.ijheatmasstransfer.2015.06.082.
[22] Y. Jannot, H.M. Bal, A. Degiovanni, C. Moyne, Influence of heat transfer on the estimation of water vapor diffusion coefficient in transient regime, Int. J. Heat. Mass Transf. 177 (2021) 121558, https://doi.org/10.1016/j.ijheatmasstransfer.2021.121558.
[23] E. Agoua, S. Zohoun, P. Perré, Utilisation d'une double enceinte pour déterminer le coefficient de diffusion d'eau liée dans le bois en régime transitoire: recours à la simulation numérique pour valider la méthode d'identification: a double climatic chamber used to measure the diffusion coefficient of water in wood in unsteady-state conditions: determination of the best fitting method by numerical simulation,

Int. J. Heat. Mass Transf. 44 (2001) 3731–3744, https://doi.org/10.1016/S0017-9310(01)00022-9.
[24] J. Berger, T. Busser, D. Dutykh, N. Mendes, An efficient method to estimate sorption isotherm curve coefficients, Inverse Probl. Sci. Eng. 27 (2019) 735–772, https://doi.org/10.1080/17415977.2018.1495720.
[25] A. Zaknoune, P. Glouannec, P. Salagnac, Identification of the liquid and vapour transport parameters of an ecological building material in its early stages, Transp. Porous Med 98 (2013) 589–613, https://doi.org/10.1007/s11242-013-0162-x.
[26] T. Busser, J. Berger, A. Piot, M. Pailha, M. Woloszyn, Dynamic experimental method for identification of hygric parameters of a hygroscopic material, Build. Environ. 131 (2018) 197–209, https://doi.org/10.1016/j.buildenv.2018.01.002.
[27] A.V. LuikovHeat and Mass Transfer in Capillary-Porous Bodies Elsevier , Advances in Heat Transfer , 1964, , 123–184, 10.1016/S0065-2717(08)70098-4.
[28] J.R. Philip, D.A. De Vries, Moisture movement in porous materials under temperature gradients, Eos Trans. Am. Geophys. Union 38 (1957) 222–232.
[29] M.Y. Ferroukhi, R. Djedjig, R. Belarbi, K. Limam, K. Abahri, Effect of coupled heat, air and moisture transfers modeling in the wall on the hygrothermal behavior of buildings, Energy Procedia 78 (2015) 2584–2589, https://doi.org/10.1016/j.egypro.2015.11.293.
[30] M. Sawadogo, F. Benmahiddine, A. Godin, M. Duquesne, R. Belarbi, A. Hamami, Development and hygrothermal performance analysis of a novel eco-friendly insulating wall under various climatic conditions, Build. Environ. (2023) 110841, https://doi.org/10.1016/j.buildenv.2023.110841.
[31] R. Belarbi, M. Qin, A. Aït-Mokhtar, L.-O. Nilsson, Experimental and theoretical investigation of non-isothermal transfer in hygroscopic building materials, Build. Environ. 43 (2008) 2154–2162, https://doi.org/10.1016/j.buildenv.2007.12.014.
[32] Assessment Method of Numerical Prediction Models for Combined Heat, Air and Moisture Transfer in Building Components: Benchmarks for One-dimensional Cases - Carl-Eric Hagentoft, Angela Sasic Kalagasidis, Bijan Adl-Zarrabi, Staf Roels, Jan Carmeliet, Hugo Hens, John Grunewald, Max Funk, Rachel Becker, Dina Shamir, Olaf Adan, Harold Brocken, Kumar Kumaran, Reda Djebbar, 2004, (n.d.). https://journals.sagepub.com/doi/10.1177/1097196304042436 (accessed July 31, 2023).
[33] X. Wang, X. Jin, Y. Yin, X. Shi, X. Zhou, A transient heat and moisture transfer model for building materials based on phase change criterion under isothermal and non-isothermal conditions, Energy 224 (2021) 120112, https://doi.org/10.1016/j.energy.2021.120112.
[34] A.W.M. van Schijndel, S. Goesten, H.L. Schellen, Simulating the complete HAMSTAD benchmark using a single model implemented in Comsol, Energy Procedia 132 (2017) 429–434, https://doi.org/10.1016/j.egypro.2017.09.651.
[35] X. Shen, L. Li, W. Cui, Y. Feng, Coupled heat and moisture transfer in building material with freezing and thawing process, J. Build. Eng. 20 (2018) 609–615, https://doi.org/10.1016/j.jobe.2018.07.026.
[36] G. Chen, Q. Luo, X. Guo, X. Liu, M. Tu, Y. He, Study on mould germination risk in hydroscopic building wall, Procedia Eng. 205 (2017) 2712–2719, https://doi.org/10.1016/j.proeng.2017.10.193.
[37] J.I. Knarud, S. Geving, Implementation and benchmarking of a 3D hygrothermal model in the COMSOL multiphysics software, Energy Procedia 78 (2015) 3440–3445, https://doi.org/10.1016/j.egypro.2015.12.327.
[38] J.A. Nelder, R. Mead, A simplex method for function minimization, Comput. J. 7 (1965) 308–313, https://doi.org/10.1093/comjnl/7.4.308.
[39] F.-G. Wieland, A.L. Hauber, M. Rosenblatt, C. Tönsing, J. Timmer, On structural and practical identifiability, Curr. Opin. Syst. Biol. 25 (2021) 60–69, https://doi.org/10.1016/j.coisb.2021.03.005.
[40] M. Sawadogo, F. Benmahiddine, A.E.A. Hamami, R. Belarbi, A. Godin, M. Duquesne, Investigation of a novel bio-based phase change material hemp concrete for passive energy storage in buildings, Appl. Therm. Eng. 212 (2022) 118620, https://doi.org/10.1016/j.applthermaleng.2022.118620.
[41] Z.B. Maroulis, E. Tsami, D. Marinos-Kouris, G.D. Saravacos, Application of the GAB model to the moisture sorption isotherms for dried fruits, J. Food Eng. 7 (1988) 63–78, https://doi.org/10.1016/0260-8774(88)90069-6.
[42] A.A.J. Ketelaars, L. Pel, W.J. Coumans, P.J.A.M. Kerkhof, Drying kinetics: a comparison of diffusion coefficients from moisture concentration profiles and drying curves, Chem. Eng. Sci. 50 (1995) 1187–1191, https://doi.org/10.1016/0009-2509(94)00494-C.
[43] K. Koumbogle, F. Gitzhofer, N. Abatzoglou, Moisture transport coefficients determination on a model pharmaceutical tablet, Processes 10 (2022) 254, https://doi.org/10.3390/pr10020254.
[44] A. Jumabekova, J. Berger, A. Foucquier, G.S. Dulikravich, Searching an optimal experiment observation sequence to estimate the thermal properties of a multilayer wall under real climate conditions, Int. J. Heat. Mass Transf. 155 (2020) 119810, https://doi.org/10.1016/j.ijheatmasstransfer.2020.119810.
[45] J. Berger, T. Busser, S. Reddy, G.S. Dulikravich, Evaluation of the reliability of a heat and mass transfer model in hygroscopic material, Int. J. Heat. Mass Transf. 142 (2019) 118258, https://doi.org/10.1016/j.ijheatmasstransfer.2019.06.014.
[46] F. Collet, J. Chamoin, S. Prétot, C. Lanos, Comparison of the hygric behaviour of three hemp concretes, Energy Build. 62 (2013) 294–303, https://doi.org/10.1016/j.enbuild.2013.03.010.
[47] F. Bennai, M.Y. Ferroukhi, F. Benmahiddine, R. Belarbi, A. Nouviaire, Assessment of hygrothermal performance of hemp concrete compared to conventional building materials at overall building scale, Constr. Build. Mater. 316 (2022) 126007, https://doi.org/10.1016/j.conbuildmat.2021.126007.
[48] J. Taylor, Introduction to Error Analysis, the Study of Uncertainties in Physical Measurements, 2nd Edition, 1997. https://ui.adsabs.harvard.edu/abs/1997ieas.book….T (accessed March 31, 2023).

Article 8

Numerical investigation of innovative and sustainable multilayer walls with increased thermal inertia

M. Sawadogo[1,2*], A. Godin[1,2], R. Belarbi[1,2], A. Hamami[1], A. Perro[3], M. Duquesne[1]

[1]*La Rochelle Université, LaSIE UMR CNRS 7356, Avenue Michel Crépeau, CEDEX 1, 17042 La Rochelle, France*
[2]*4ev Lab, EDF R&D, CNRS, LaSIE, La Rochelle University, Avenue Michel Crépeau, CEDEX 1, 17042 La Rochelle, France*
[3]*Univ. Bordeaux, CNRS, Bordeaux INP, ISM, UMR 5255, 16 avenue Pey Berland, 33607 Pessac, France*

[*] Corresponding author: mohamed.sawadogo@univ-lr.fr

Abstract: *This work focuses on the investigation of multilayer walls' performances and their hygrothermal behavior under realistic unfavourable weather conditions. Humid climates favour surface condensation within walls, which in turn degrades building walls, reducing their durability and increasing energy consumption. Five multilayer walls configuration are tested. They all consist of 10 cm of exterior insulating material, 20 cm of brick and 2 cm of plaster for the finishing layer. The hygrothermal performance of four walls containing conventional insulating layers and one innovative hybrid wall integrating the PCM-biocomposite under real-life climatic conditions in two cities: New Delhi (very hot and humid climate) and Caracas (moderately hot and very humid climate) are investigated. The hybrid wall demonstrated that it could delay temperature peaks by around 28.5 hours in hot and humid climate when exterior temperatures exceed the PCM's melting point. For the city of Caracas, the biobased hybrid wall was more efficient than the hemp concrete one, with a heat transmission load reduced by 20 kW.m^{-2}. A parametric study was carried out to evaluate the influence of the thickness of the bio-composite layer and the fraction of PCM composing it. The fraction of PCM has a significant impact on reducing the heat transfer load, eclipsing the effect of increasing thickness, resulting in more compact, and higher-performance building materials. One of the hybrid innovative walls submitted to New Delhi weather conditions achieves up to 40% heat transfer load reduction.*

Keywords: innovative and sustainable hybrid walls, stabilized forms of phase change materials, increased thermal inertia, hygrothermal modelling.

Nomenclature

Properties and variables

C_p	specific heat capacity (J.kg^{-1}.K^{-1})
T	temperature (°C)
u	water content of mass ratio (%)
C_m	moisture storage capacity (-)
P	pressure (Pa)
k_T	liquid water conductivity due to a thermal gradient (kg.m^{-1}.s^{-1}.K^{-1})
C_p^*	total heat capacity (J.kg^{-1}.K^{-1})
h	specific enthalpy (J.kg^{-1})
k_l	liquid water permeability (kg.s^{-1}.m^{-1}.Pa^{-1})
k_m	total moisture diffusivity coefficient (kg.s^{-1}.m^{-1}.Pa^{-1})
h_c	convective heat transfer coefficient (W.m^{-2}.K^{-1})
h_m	convective mass transfer coefficient (s.m^{-1})

Subscripts

s	solid
v	vapor
l	liquid
sat	saturation
ref	reference
ext	exterior

Greek Symbols

φ	relative humidity (%)
ρ	density (kg.m^{-3})
λ^*	effective thermal conductivity (W.m^{-1}.K^{-1})
δ	water vapor permeability (kg.s^{-1}.m^{-1}.Pa^{-1})
γ	heat transfer by convection due to the vapor pressure gradient coefficient (W.m^{-1}.Pa^{-1})

T_mean	mean daily temperature
φ_mean	mean relative humidity
σ	phase change criterion (-)

Acronyms

BPCM	bio-composite PCM
PCM	phase change material
AFTR	average temperature fluctuation reduction

1 Introduction

In today's context of climate change mitigation and sustainable construction, there is a growing need to develop creative building solutions that reduce environmental impact while optimizing energy efficiency. As a major contributor to global greenhouse gas emissions, the construction industry is playing a leading role in efforts to address these issues [1]. Besides, thermal comfort in a building requires that the indoor temperature remains relatively constant (approximately 19°C in winter and 24°C in summer). This is primarily achieved through thermal inertia, which is mainly attributed to the building's walls. The thermal inertia of the walls also influences buildings' energy consumption. In addition, it is important to also consider the hydric transfer because they have an impact on the deterioration of materials, and therefore on the durability of structures. By accurately predicting the hygrothermal behavior of building envelopes and characterizing material properties (hydric, thermal, microstructural), we can assess moisture-related risks and increase the lifespan of structures (important in the life-cycle analysis of materials, which consequently perform better in the long term).

The incorporation of phase-change materials (PCMs) in building walls is a promising solution in the sake of developing efficient and sustainable building solutions [2–7]. Indeed, the use of PCMs into building envelopes increases thermal comfort by lowering peak and variable indoor temperatures as a result of a storage density 5-10 times that of normal walls [4]. Furthermore, because of the high thermal inertia, the temperature peak is delayed in time, resulting in a lower peak temperature and the ability to benefit from lower electricity costs. The incorporation of PCMs in building walls has been extensively studied both numerically and experimentally over various climatic conditions. They all demonstrated the efficiency of PCMs in indoor temperature regulation. For instance, Al-saadi et al [8] developed and validated a new TRNSYS type for simulating PCM-enhanced multilayer walls. Using the validated module, it was discovered that placing the PCM in direct contact with the interior controlled environment results in the optimal PCM setup. Furthermore, a wide range of PCM thermal properties (latent heat, melting temperature and melting temperature range) were simulated in common US regions to evaluate thermal performance and determine ideal thermal values. Depending on the climatic conditions, the results suggested a maximum savings of 0.8-15.8% on annual cooling load. These maximum cooling loads are obtained for a PCM melting temperature between 26–27°C for cooling dominated climate with a melting range in the range of 0.1–2°C depending on climate. Al-Yasiri et al [9] have demonstrated the effectiveness of a petroleum-based PCM (paraffin wax with a melting temperature of between 40 and 44°C) in stabilizing indoor temperatures in severe hot climates. The PCM was macroencapsulated using metal containers and incorporated into the roof and walls of the PCM room (dipped within the concrete bricks). The results showed an average indoor temperature reduction of 2°C during the day and a maximum thermal load levelling reduction of 8.7 %. The study concluded that the PCM is more effective in the roof than walls, and the PCM amount should vary in walls considering their orientation and peak outdoor conditions.

With the recent development of the bio-based materials [10–12], PCMs are expected to play more role in sustainable buildings construction. Indeed, PCMs and hygroscopic materials such as hemp concrete can be combined to improve the performance of building walls [13,14]. Energy efficiency, temperature regulation and moisture control can all be improved at once by combining the thermal inertia of PCMs with the moisture inertia of hygroscopic materials. Zhu et al [15] studied the effects of Phase Change Humidity Controlling Materials (PCHCM) wallboards on building energy consumption and indoor hygrothermal environment for Wuhan city in China, which has hot and humid summers and cold winters. The simulation results based on EnergyPlus showed that the PCHCM wallboard was able to both reduce energy consumption (energy consumption reduced by 8.3% in summer and 24.9% in winter) and improve indoor hygrothermal environment for the case study building significantly. Similar results were obtained by Wu et al. [14], Shi et al [16] and Chang et al. [17].

Only a few number of researchers have thus thoroughly investigated numerically both thermal and hygroscopic behavior of such materials. Nethertheless, buildings are subjected to a variety of interior and exterior solicitations, which influence their performances, their hygrothermal behavior, the energy consumptions and the building's lifespan. Besides, these solicitations have significant effects on both occupant comfort and indoor air quality, with temperature and moisture playing a critical role [18,19]. To quantify the influence of the solicitation on building performances, a precise modeling of the heat, air and moisture transport phenomena is required [20–28].

The literature shows a lack of specific numerical models capable of dealing with both the phase change and hygroscopic behavior of composite materials, a lack that is even more marked at the building wall scale [29]. One of the innovative contributions of the work presented is to propose a numerical model to simulate the actual behavior of conventional multilayer walls (without PCM) on the one hand, and to compare them with the behavior of the proposed hybrid and sustainable multilayer walls capable of controlling both temperature and humidity.

In order to contribute to this research topic, recently, a new composite made of a biosourced PCM and hemp concrete, namely bio-composite PCM, was fabricated in order to increase the energy storage capacity of hemp concrete and improve its hygrothermal behavior. In addition, the bio-composite PCM possesses a promising moisture storage capacity. These properties allow the regulation of both humidity and temperature. To that end, after a selection step of fibers and PCM [30], the microporosity of the hemp shives was first impregnated with capric acid, which is a biobased PCM with a melting temperature of 30°C, and then mixed with water and lime to fabricate a PCM-based hemp concrete monolayer wall [31,32]. The hygrothermal properties and performances of this new bio-composite wall was characterized and compared to the reference hemp concrete (without PCM). In addition, a heat and moisture model allowing the simulation of this innovative monolayer wall’s behavior under moderate realistic climatic conditions and its comparison to the reference one has been developed and validated against experimental data with a good agreement.

In the continuity of the mentioned previous studies, the present work proposes the development of a numerical strategy to evaluate the hygrothermal behavior of multilayer building walls incorporating PCM under the hot and humid weather conditions of Caracas and New Delhi using the commercial software COMSOL MULTIPHYSICS. These climatic conditions are selected because that are particularly unfavorable to the durability of structures and should highlight the crucial importance of moisture transfer, as it has a harmful impact on both the

building and its energy consumption The multilayer wall is composed of an insulating layer, brick as structural material and plaster as finishing layer. The hygrothermal performances of five insulating layers are compared including the developed bio-composite PCM wall, a reference hemp concrete, a cellulose insulation and two conventional insulators that are expanded polystyrene and glass wool. The cooling transmission loads are calculated in order to evaluate the energy savings that these materials could achieve during hot periods. Finally, the influence of the fraction of PCM and the insulation layer is assessed and the optimum amount of PCM necessary to achieve tangible energy savings that could help to improve the hybrid innovative wall and the material development stage is discussed.

2 Description of the building envelope

This study analyses the hygrothermal performance of five insulating materials: hemp concrete, glass wool, expanded polystyrene, cellulose insulation and the developed bio-composite PCM. The study cases assessed are multilayer walls configurations consisting of 10 cm of exterior insulating material, 20 cm of conventional building material chosen to be brick in our study and 2 cm of plaster for the finishing layer as depicted in Figure 1.

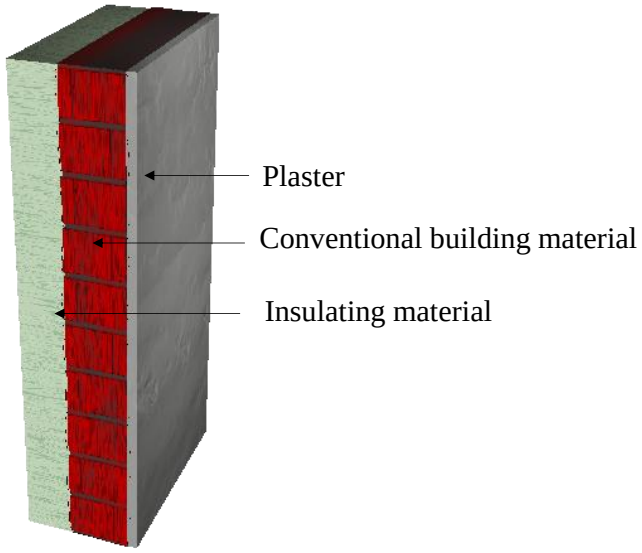

Figure 1. Studied multilayer wall configurations made of an insulation layer (green), a conventional structural building layer always made of brick in this work (red) and finishing layer, always made of plaster in this work (grey).

The multilayer wall is subjected to real unfavorable climatic conditions (temperature and humidity) of two cities: New Delhi for very hot and humid weather and Caracas for moderate hot and very humid weather Figure 2. These cities with hot weathers have been selected (temperature mostly higher than 30°C) in order to fully exhibit the latent heat effect of the bio-composite PCM that undergoes phase transition around 30°C. In fact, the mean daily temperature (T_mean) of the two cities varies between 5 and 50°C for New Delhi city and between 20 and 36°C for Caracas that should allow efficient energy charge and discharge of the bio-composite PCM (Figure 2.a). In addition, the exterior mean relative humidity (φ_mean) of the cities oscillates between 20 and 100% for New Delhi and between 60 and 100% for Caracas (Figure 2.b) and constitutes an interesting case study to evaluate the hydric performances of the different multilayer configurations.

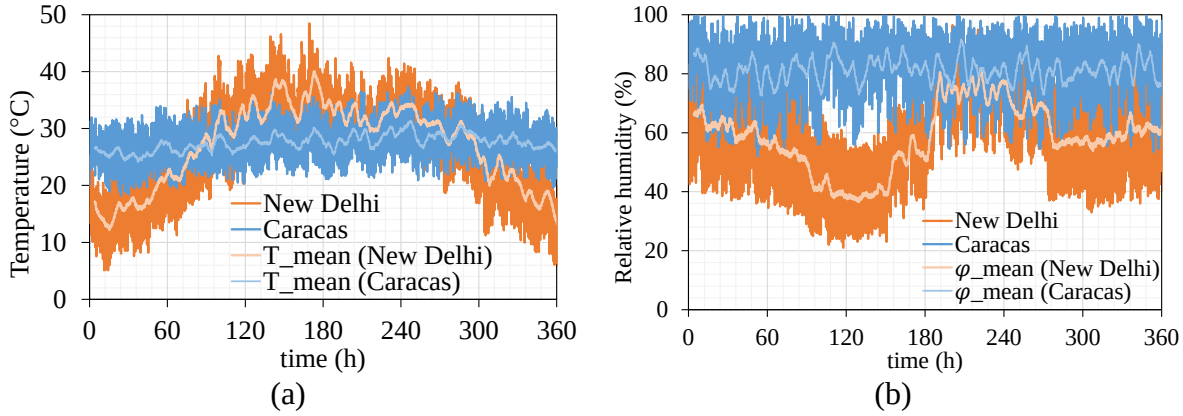

Figure 2. Hourly year and mean temperature (a) and relative humidity (b) of the New Delhi and Caracas city (from TRNSYS software [33]).

3 Problem Statement and modelling

3.1 Schematic 2D-representation

A schematic 2D-representation of the multilayer wall with exterior insulation including the initial conditions, the interior and exterior conditions of the problem is presented in Figure 3. In this study, we will consider a 1D assumption for the numerical simulations and the direction of interest is along the x-axis. This assumption is made possible by the configuration of the biclimatic chamber that allows moisture to flow in one direction. In addition, all the properties of the materials are given for a homogeneous with no variation in space. For these reasons, the 1D assumption is considered a good approximation for the present study.

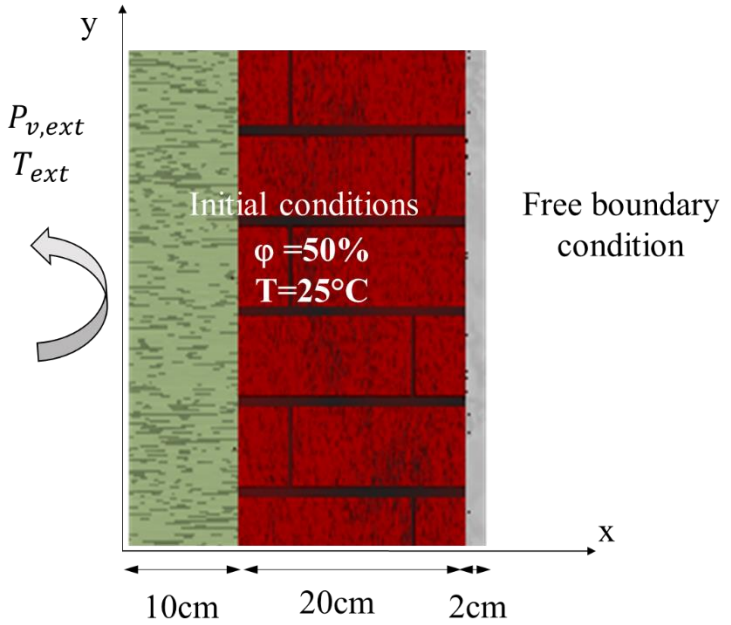

Figure 3. Schematic 2D representation of the multilayer wall configuration with an insulation layer (green), a brick layer (red) and a plaster layer (grey).

The boundary conditions on the exterior sides of the wall are set by taking into account the convective heat and mass exchanges related to the exterior conditions, mainly the air temperature and humidity. These Neumann boundary conditions are summarized in Equations 1 and 2 [34]:

$$(-k_T \nabla T - k_m \nabla P_v)|_{x=0} = h_{m,ext}\left(P_{v,ext} - P_v(x=0)\right) \quad (1)$$

$$(-\lambda^* \nabla T - \gamma \nabla P_v)|_{x=0} = h_{c,ext}\left(T_{ext} - T(x=0)\right) \quad (2)$$

with $h_{c,ext}$ (W.m^{-2}.K^{-1}) the exterior convective heat transfer coefficient at the surface of the material, $h_{m,ext}$ (s.m^{-1}) the exterior convective mass transfer coefficient, $P_{v,ext}$ and T_{ext} the exterior vapor pressure and temperature, respectively.

The free boundary interior conditions are handled by setting the inside air temperature and relative humidity equal to the previous iteration solution of the interior wall surface temperature and relative humidity using the *nojac* function of COMSOL Multiphysics software. After computing the indoor air temperature and relative humidity, the same convective heat and mass transfer conditions utilized for the exterior conditions are applied to the indoor environment (Equation 3-4).

$$(-k_T \nabla T - k_m \nabla P_v)|_{x=\mathrm{L}} = h_{m,int}\left(P_{v,surf}(t-dt) - P_{v,surf}(t)\right) \quad (3)$$

$$(\lambda^* \nabla T + \gamma \nabla P_v)|_{x=\mathrm{L}} = h_{c,int}\left(T_{surf}(t-dt) - T_{surf}(t)\right) \quad (4)$$

with $h_{c,int}$ (W.m^{-2}.K^{-1}) the interior convective heat transfer coefficient at the surface of the material, $h_{m,int}$ (s.m^{-1}) the interior convective mass transfer coefficient, P_v the vapor pressure, $P_{v,surf}$ and T_{surf} the surface vapor pressure and temperature, respectively, dt [s] the time step, k_T [kg.m^{-1}.s^{-1}.K^{-1}] the moisture transfer coefficient due to a temperature gradient, k_m [kg.m^{-1}.s^{-1}.Pa^{-1}] the total moisture diffusion coefficient, λ^* [W.m^{-1}.K^{-1}] he effective thermal conductivity, γ [W.m^{-1}.Pa^{-1}] the convective heat transfer coefficient due to a vapour pressure gradient.

The interior and exterior heat transfer coefficients are set 8 and 18 W.m^{-1}.K^{-1}, respectively [35] whereas the interior and exterior convective mass transfer coefficient are $1.85 \cdot 10^{-8}$ s.m^{-1} and $9.25 \cdot 10^{-8}$ s.m^{-1} [36].

3.2 Modelling equations

The hygrothermal model is based on the model of Philip and de Vries et al [37,38], the work of Ferroukhi et al [34], and Remki et al [39]. The conservation of mass and energy equations are described for all phases considered (liquid, vapor). Then, they are defined according to the transfer drivers given by: the relative humidity and the temperature. Due to the continuity problem for relative humidity in the case of multilayer walls, we have opted for pressure (capillary, vapor and total) and temperature as driving potentials. The relative humidity of the air is calculated a posteriori.

The space and time variations of the variables (temperature and vapor pressure) have been modeled to examine the dynamic behavior of multilayer walls. The system of non-linear coupled heat and moisture transfer equations, derived from the development of energy and mass conservation equations, is expressed as follows (Equations 5 and 6):

$$\rho_s \frac{C_m}{P_{v,sat}} \frac{\partial P_v}{\partial t} = div(k_T \nabla T + k_m \nabla P_v) \quad (5)$$

$$\rho_s C_p^* \frac{\partial T}{\partial t} = div(\lambda^* \nabla T + \gamma \nabla P_v) + \rho_s C_m \sigma L_v \frac{\partial P_v}{\partial t} \quad (6)$$

with σ [-] the ratio between vapour flow and total moisture flow, L_v [J.kg^{-1}] the latent heat of vaporization of liquid water, C_m [-] the moisture storage capacity, C_p^* [J.kg^{-1}.K^{-1}] the effective heat capacity, ρ_s [kg.m^{-3}] the effective heat capacity, $p_{v,sat}$ [Pa] the saturation vapour pressure.

The model has been validated against EN 15026 standard [40], experimental data from the literature [41] and experimental data in a previous study conducted in a climatic chamber [31]. For more details about the model, the authors are referred to [31].

3.3 Input parameters and numerical strategy

Five insulating materials are considered in this work as mentioned previously. The first material is the one integrating the bio-composite (with PCM) that was investigated in previous studies at the material and the monolayer scales [31,32]. The material was manufactured using hemp shives impregnated with capric acid (PCM) with 50 wt% of incorporation rate. The formulation of hemp concrete consists of 50% water, 16% hemp shives (with or without PCM) and 34% binder (Tradical® PF70 (lime)). Based on this formulation, an incorporation rate of 50 wt% in the hemp shives corresponds to a PCM mass fraction of 14 wt% in the bio-composite. The bio-composite PCM and reference hemp concrete will be compared to four conventional insulators namely glass wool, expanded polystyrene, hemp concrete and a cellulose insulation.

The hygrothermal properties of the material, extensively measured in [31] are the input parameters of the model and must be finely characterized in order to have a reliable model describing the real kinetics of the material and therefore of the walls made of them. The properties of all the materials including brick, plaster and the insulating materials are presented in the appendix (Table A 1 and Table A 2).

The numerical computation is conducted using COMSOL Multiphysics. The spatial discretization is performed using finite elements method. An extremely fine mesh has been chosen corresponding to an element size of 3.2 ·10^{-3} m, fine enough to ensure the convergence of the numerical scheme. The system integration is achieved using the Backward Differentiation Formula (BDF) that is a method of time integration based on the algebraic differential formulation [42]. In fact, the BDF solver is an implicit solver that uses backward differentiation formulas with order of accuracy varying from one (also known as the backward Euler method) to five. Due to the strong coupling between the set of differential equations, a fully coupled approached has been used in COMSOL Multiphysics. After an optimization process, a time step of 30 minutes was used and the tolerance is set as physics controlled. Finally, the PCM model is implemented using the equivalent heat capacity method.

4 Results and discussion

4.1 Comparison of the hygrothermal performances of insulating materials

Figure 4.a shows the evolution of the inside surface temperature during the year for all the five studied materials under Caracas weather conditions. For relatively low temperatures (below 28 °C), the glass wool insulation shows the best performances with lower indoor temperature. The bio-composite PCM, hemp concrete and expanded polystyrene have a similar behavior with indoor surface temperatures varying between 25 and 30 °C for the city of Caracas. However,

among these three materials, the lowest temperatures are obtained for the bio-composite PCM followed by expanded polystyrene and hemp concrete. These results show the importance of incorporating PCMs in the regulation of interior temperature in buildings. At very high temperatures and relative humidity, high temperatures were observed for cellulose insulation and glass wool, indicating the importance of the coupled heat and moisture transfer for these materials.

With regard to relative humidity (Figure 4.b), hemp concrete, bio-composite PCM and glass wool respond similarly to exterior solicitations. Indeed, due to the water storage capacity, as well as liquid and vapor permeability of these materials, moisture transfer is faster and stabilizes a relative humidity of around 85%. The kinetics are slightly slower for expanded polystyrene and cellulose insulation, stabilizing at around 80%, which is an average of relative outdoor humidity.

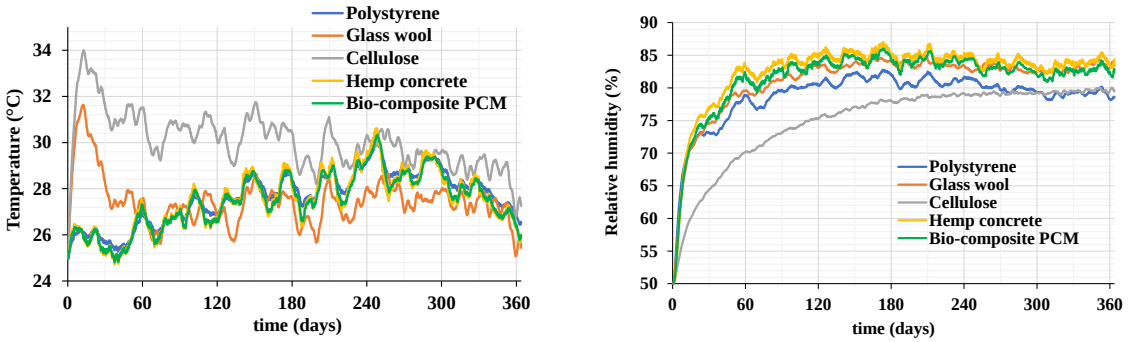

Figure 4. Yearly evolution of the interior surface temperature (a) and relative humidity (b) for the city of Caracas with the tested multilayer wall integrating different insulating layers.

In New Delhi's very hot and humid climate, when humidity levels are below 65%, i.e. before 180 days, cellulose insulation and glass wool are the most effective, with lower interior surface temperature curves than other insulating materials (Figure 5.a). However, at high humidity, the insulating efficiency of these insulation materials drops considerably in favor of hemp concrete, bio-composite PCM and expanded polystyrene. The effect of incorporating PCM into hemp concrete is barely noticeable, due to outdoor temperatures well above the melting point of PCM (around 30°C).

Figure 5.b shows the evolution of indoor humidity over the year for each of the four insulating materials. Interior humidity varies between 40% and 75% for all insulations, with the exception of cellulose insulation, where maximum humidity is slightly below 70%, due to its lower water vapor permeability (Table A 1) compared to the other insulations, resulting in much lower kinetics.

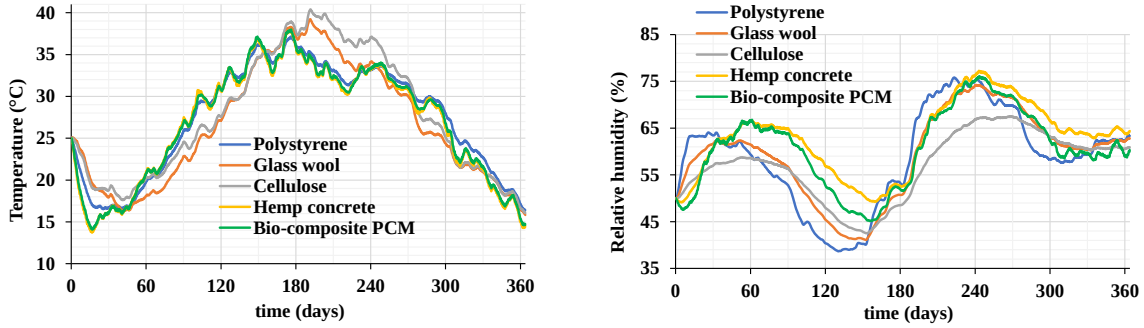

(a) (b)

Figure 5. Yearly evolution of the inside temperature (a) and relative humidity (b) for the city of New Delhi for the multilayer walls integrating different insulating layers.

In order to accurately assess and compare the overall performance of different types of insulation, the heat transmission load that is an indicator of the amount of heat transmitted to the interior environment has been calculated. The more efficient the insulation, the less heat is transmitted. The cooling and heating transmission loads ($Q_{cool/heat}$) were calculated for a thermal comfort range between 20 and 25°C (Equation 7). When the temperature is higher than 25°C, it is accounted as cooling needs and as heating needs if it is inferior to 20°C. The integration is made all over the year and the calculated heat transmission load is an addition of both heating and cooling loads.

$$Q_{cool/heat} = \sum_i h_{m,int} * \Delta T_i \tag{7}$$

With $\Delta T = T - 25$ [°C] for cooling needs and $\Delta T = 20 - T$ [°C] for heating needs, i is the time step index.

Figure 6 shows the heat transmission load for the multilayer walls integrating each of the five insulations under Caracas and New Delhi climatic conditions. Regardless of climatic conditions, glass wool insulation has the best energy performance with the lowest heat transmission load. The performance of other insulating layers is highly dependent on climatic conditions. For New Delhi's very hot and humid climate, hemp concrete and bio-composite PCM perform almost identically, although hemp concrete is slightly more efficient. This could be explained by the exterior temperature profile of the city that is very high compared to the PCM melting temperature. Therefore, the PCM is in liquid state for most of the time without any latent heat contribution. Expanded polystyrene and cellulose insulation have the highest heat transfer loads due to their lower thermal inertia (compared to hemp concrete and bio-composite PCM) combined with their slightly lower thermal conductivity than other insulating materials (glass wool) (Table A 2).

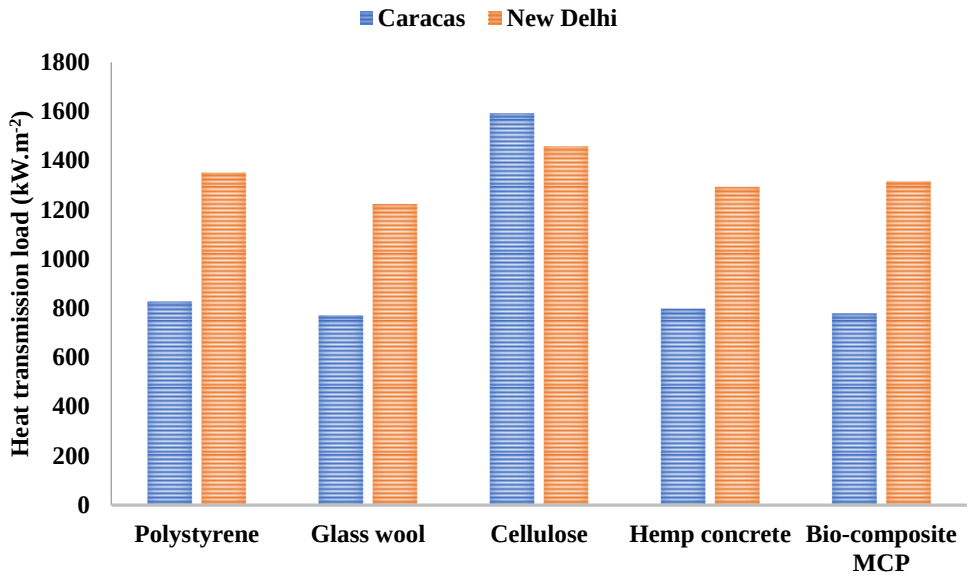

Figure 6. Heat transmission loads of the five multilayer walls integrating different insulating materials submitted to New Delhi and Caracas' weather conditions.

For the hot and very humid climate of the city of Caracas, cellulose insulation proves to be ineffective, with a very high heat transmission load compared to other insulations. Glass wool insulation remains the most efficient, with a heat transmission load below 800 $kW.m^{-2}$. The bio-composite PCM was more efficient in the Caracas climate and shows improved performances compared to hemp concrete. In fact, the city's temperature oscillates around 30°C, the melting point of PCM, enabling the material to be used efficiently. This translates into a difference of 20 $kW.m^{-2}$ between bio-composite PCM and hemp concrete. Finally, expanded polystyrene has comparable performances to bio-composite PCM, hemp concrete and glass wool, even if the heat transmission load is higher than that of the other insulations.

4.2 Parametric study

The incorporation of PCM improved the performance of hemp concrete in the climate of the city of Caracas. However, no significant effect was observed in the hot, humid climate of New Delhi. This lower performance can be explained by the low amount of PCM in the proposed insulation. Indeed, the performance of bio-composite PCM is highly dependent on two factors: the fraction of PCM and the thickness of the material layer. In order to assess the importance of these two parameters, a parametric study was carried out. In addition to bio-composite PCM with 14 wt% PCM, two other formulations with PCM mass percentages of 20 wt% and 30 wt%, were investigated. For each mass fraction, three insulation thicknesses are considered: 10 cm, 20 cm and 30 cm. The different configurations of materials studied are gathered in Table 1.

Table 1. Tested configurations with PCM fractions (14 wt%, 20 wt% and 30 wt%) and insulation thicknesses (10 cm, 20 cm and 30 cm) for the parametric study. The materials are named XPCML where X stands for the fraction of PCM and L the thickness of the layer (for instance 20%PCM20cm means 20 cm of the bio-composite with 20% of PCM.

Thickness (cm)	Fraction of PCM (%)	Material name
10	14%	14%PCM10cm
	20	20%PCM10cm
	30	30%PCM10cm
20	14	14%PCM20cm
	20	20%PCM20cm
	30	30%PCM20cm
30	14	14%PCM30cm
	20	20%PCM30cm
	30	30%PCM30cm

In order to assess the effect of the PCM fraction and the thickness, different performances indicators are used: the maximum temperature reduction, the time shift, the monthly temperature difference and the maximum energy savings potential.

4.2.1 Maximum temperature reduction and time shift

For the city of Caracas, Figure 7 shows that at constant thicknesses, the increase in PCM fraction leads to a reduction in maximum interior surface temperature compared with hemp concrete (layer of reference, referred as REF). Thus, for 10 cm of insulation (Figure 7.a), we note a decrease in temperature throughout the year, with maximum values of 0.4, 0.5 and 0.7°C for 14 wt%, 20 wt % and 30wt% of PCM, respectively (Table 2), at around 230 days. In addition to the temperature reduction, peak temperature delays of up to 36 hours are observed for the composite with 30 wt% of PCM, as a direct consequence of the increased inertia. By increasing the thickness to 20 cm, the temperature reduction becomes 0.6, 0.7 and 0.9°C for 14 wt%, 20 wt% and 30 wt% of PCM, respectively (Figure 7.b). In addition, these temperature peaks are delayed by 70, 76 and 111 hours compared to hemp concrete (Table 2). For a thickness of 30 cm, we obtain a temperature reduction and a maximum time shift of 1°C and 198 hours, respectively for PCM fraction of 14 wt% (Figure 7.c). These temperature reductions occur in the phase change range of the PCM (28-32°C).

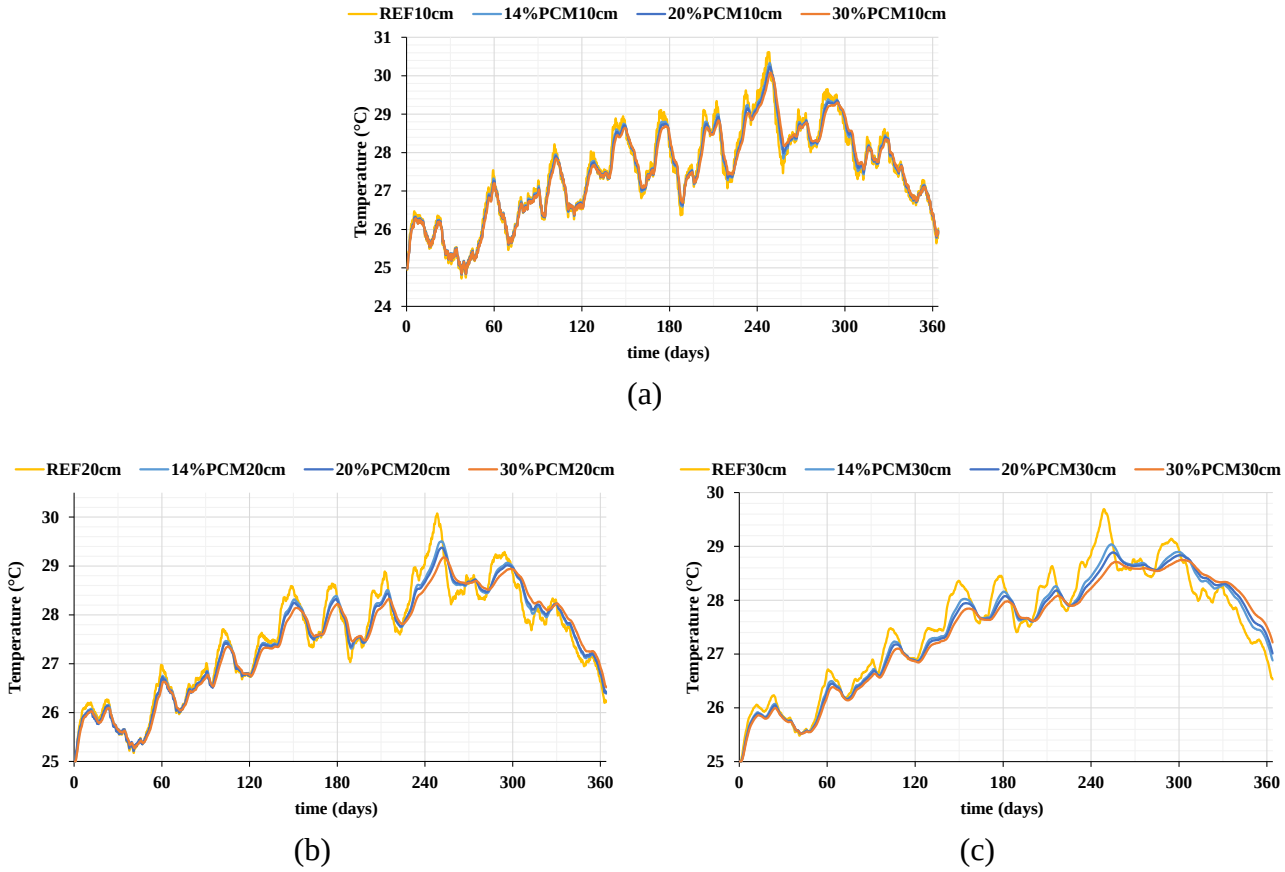

Figure 7. . Evolution of the interior surface temperature in case of multilayer walls integrating the hemp concrete layer (referred as REF followed by the thickness), the bio-composite PCM layer (14%), the bio-composite PCM layer (20%) and the bio-composite PCM layer (30%) with 10 cm (a), 20 cm (b) and 30 cm (c) of thicknesses for walls submitted to the climatic conditions of the city of Caracas. Each configuration is described by the acronym XPCML (in the legend) where X stands for the fraction of PCM and L the thickness of the layer (for instance 20%PCM20cm means 20 cm of the bio-composite with 20% of PCM).

Table 2. Maximum temperature reduction and time shift investigating multilayer hybrid walls integrating different PCM fractions (14 wt%, 20 wt% and 30 wt%) and insulation thickness (10 cm, 20 cm and 30 cm) under Caracas climatic conditions.

Thickness (cm)	Fraction of PCM (wt%)	Maximum temperature reduction (°C)	Delay in time (hours)
10	14	0.4	28.5
	20	0.5	31
	30	0.6	36
20	14	0.6	70
	20	0.7	76.5
	30	0.9	111
30	14	0.7	118
	20	0.8	151.5
	30	1	198

Under the very hot and humid climate of New Delhi, the results show that using PCM as insulation significantly reduces maximum temperatures compared to reference insulation (integrating hemp concrete) and this reduction increases proportionally with insulation thickness (Figure 8.a-c). For a 10 cm insulation thickness, maximum temperatures are reduced by 0.6°C, 0.7°C and 0.9°C for 14 wt%, 20 wt% and 30 wt% of PCM, respectively compared to

hemp concrete (Table 3). These temperature reductions are accompanied by time shifts of 73, 76.5 and 84 hours for each PCM fraction, respectively. By increasing the insulation thickness up to 20 cm, the maximum temperature reductions increase considerably, reaching 1.7°C, with time shifts of up to 69.5 hours for the hybrid multilayer wall integrating the bio-composite layer with 30 wt% of PCM compared to the multilayer wall integrating the reference insulation. At a thickness of 30 cm, the PCM maintains a maximum temperature reduction of around 2.5°C but with a maximum peak temperature delay of 137.5 hours. As in the case of Caracas, for New Delhi also, the peak temperature reduction occurs within the phase change range of PCM. These results highlight the potential of PCMs to mitigate high temperatures in hot environments such as New Delhi, while inducing beneficial delays in the thermal response. However, the very high time lag values, particularly for the hybrid multilayer wall incorporating the bio-composite layer with 30 wt% of PCM, may be explained by the fact that the maximum value is spread over a very long period, making it difficult to detect the peak.

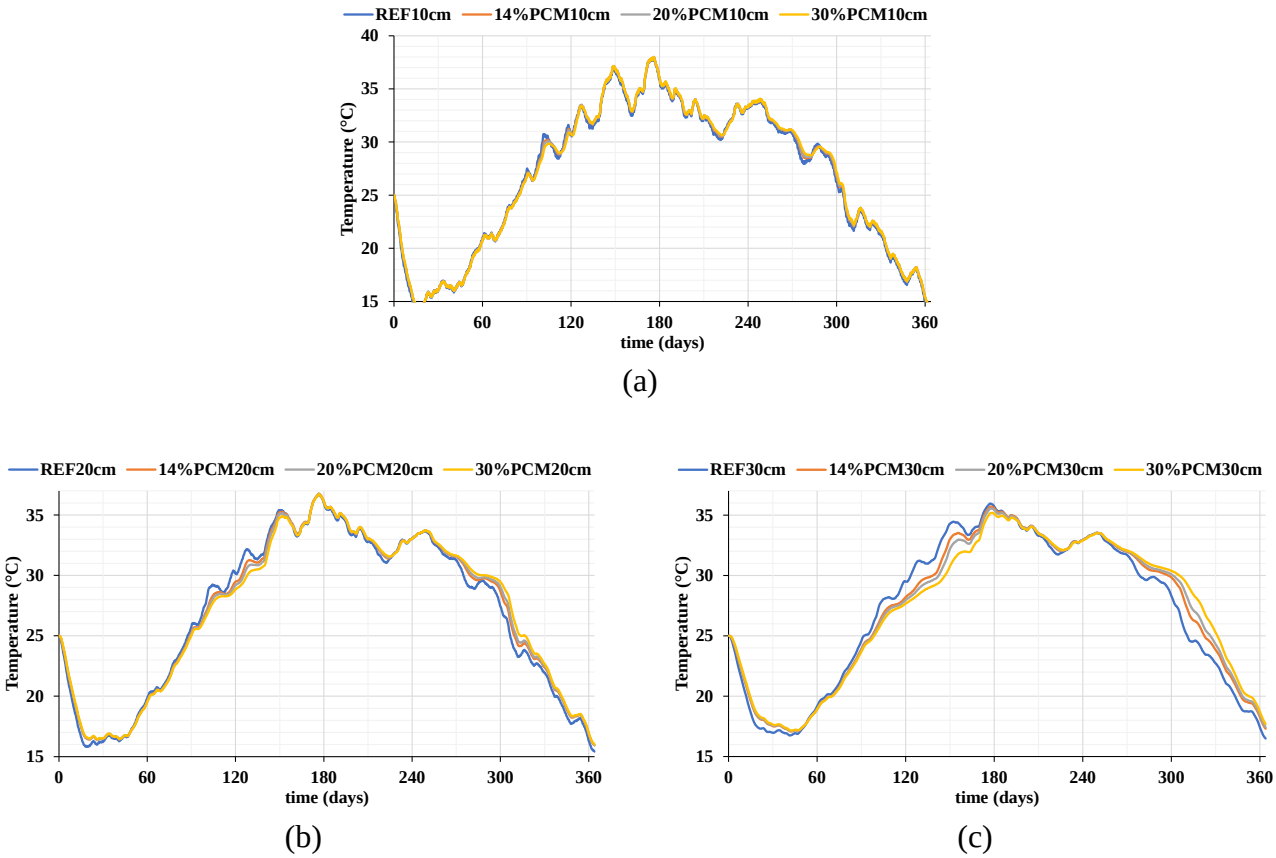

Figure 8. Evolution of the interior surface temperature in case of multilayer walls integrating the hemp concrete layer (referred as REF followed by the thickness), the bio-composite PCM layer (14%), the bio-composite PCM layer (20%) and the bio-composite PCM layer (30%) with 10 cm (a), 20 cm (b) and 30 cm (c) of thicknesses for walls submitted to the climatic conditions of the city of New Delhi. Each configuration is described by the acronym XPCML (in the legend) where X stands for the fraction of PCM and L the thickness of the layer (for instance 20%PCM20cm means 20 cm of the bio-composite with 20% of PCM).

Table 3. Maximum temperature reduction and time shift obtained investigating multilayer hybrid walls integrating different PCM fractions (14 wt%, 20 wt% and 30 wt%) and insulation thickness (10 cm, 20 cm and 30 cm) for New Delhi climatic conditions.

Thickness (cm)	Fraction of PCM (wt%)	Maximum temperature reduction (°C)	Delay in time (hours)
10	14	0.6	73
	20	0.7	76.5
	30	0.9	84
20	14	0.9	33.5
	20	1.3	57
	30	1.7	69.5
30	14	1	72
	20	1.5	80
	30	2.5	137.5

4.2.2 Monthly temperature difference

Another way to assess the effect of the PCM fraction is to investigate the average temperature fluctuation reduction (ATFR) that represents the sum of the average decrease in the daytime zone air temperature and the average increase in the night-time zone air temperature [43]. However, due to the smoothing of the temperature induced by the PCM, it was not possible to calculate the AFTR in a daily basic. Instead, the monthly temperature difference between the hybrid multilayer wall integrating the bio-composite PCM and the reference multilayer wall integrating the hemp concrete is computed for each configuration. This calculation allows us to estimate the monthly performance of PCM and identify the periods during which it performed optimally. A positive value for this difference indicates a favorable impact of the PCM during the month and vice versa. Figure 9.a-c show the monthly temperature difference between the hybrid multilayer wall integrating each fraction of PCM and the reference wall for each thickness for the city of New Delhi. In addition, the exterior monthly temperature is plotted to assess its effect on the PCM performances. The results show that the PCM perform well when the monthly temperature is above 25°C in the ascending phase (March, April, May and June) except for the case with 10 cm. When the monthly temperature starts decreasing, the positive effect vanishes exhibiting the negative effect of the increased inertia. The maximum monthly temperature difference are 0.4, 1.3 and 2.6°C for 10 cm (Figure 9.a), 20 cm (Figure 9.b) and 30 cm (Figure 9.c) respectively. However, the overall performances show negative effect for the incorporation of PCM in New Delhi weather condition. As an alternative solution, it is possible to consider another bio-composite with higher PCM melting temperature such as lauric acid that melts between 41-45.3°C [44,45]. A parametric study of the PCM temperature of fusion should be conducted in future studies in order to select the suitable PCM for a specific weather.

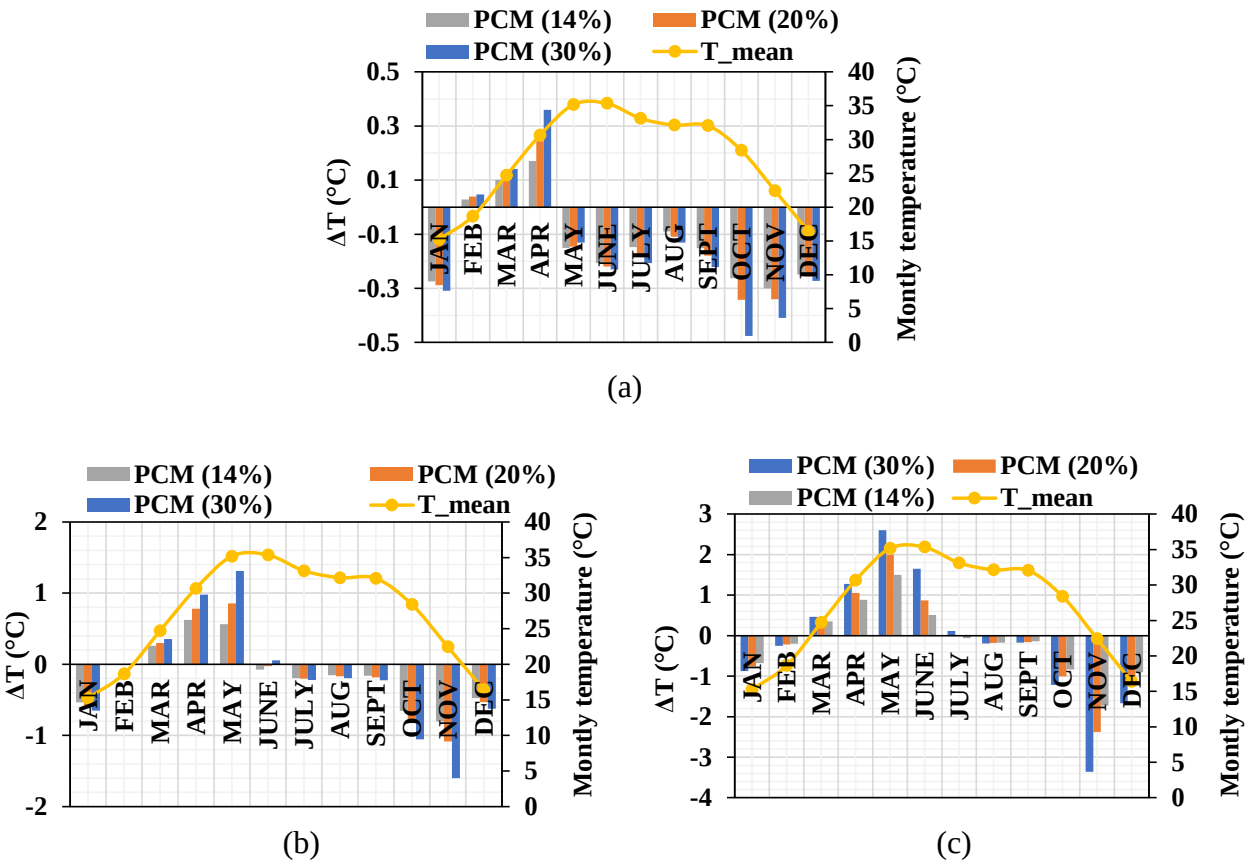

Figure 9. Monthly average exterior temperature (yellow) and temperature difference between each fraction of PCM and the reference hemp concrete with 10 cm (a), 20 cm (b) and 30 cm (c) under New Delhi's climatic conditions.

Figure 10.a-c illustrates the monthly temperature and temperature difference between the hybrid multilayer wall integrating the bio-composite PCM and the reference multilayer wall integrating the hemp concrete is computed for each configuration for the city of Caracas. Except November and December (and September for 10 cm), the difference temperature is positive for all the year independently of the thickness. The maximum temperature differences are obtained when the exterior monthly temperature is between 28 and 29°C (May, June and September) reaching values of 0.2 °C, 0.3 °C and 0.4°C for 10 cm (Figure 10.a), 20 cm (Figure 10.b) and 30 cm (Figure 10.c), respectively for the hybrid multilayer wall bio-composite with 30 wt% of PCM. The melting temperature of the PCM selected for this study is suitable for Caracas weather conditions where the average temperature oscillates between 25 and 30°C.

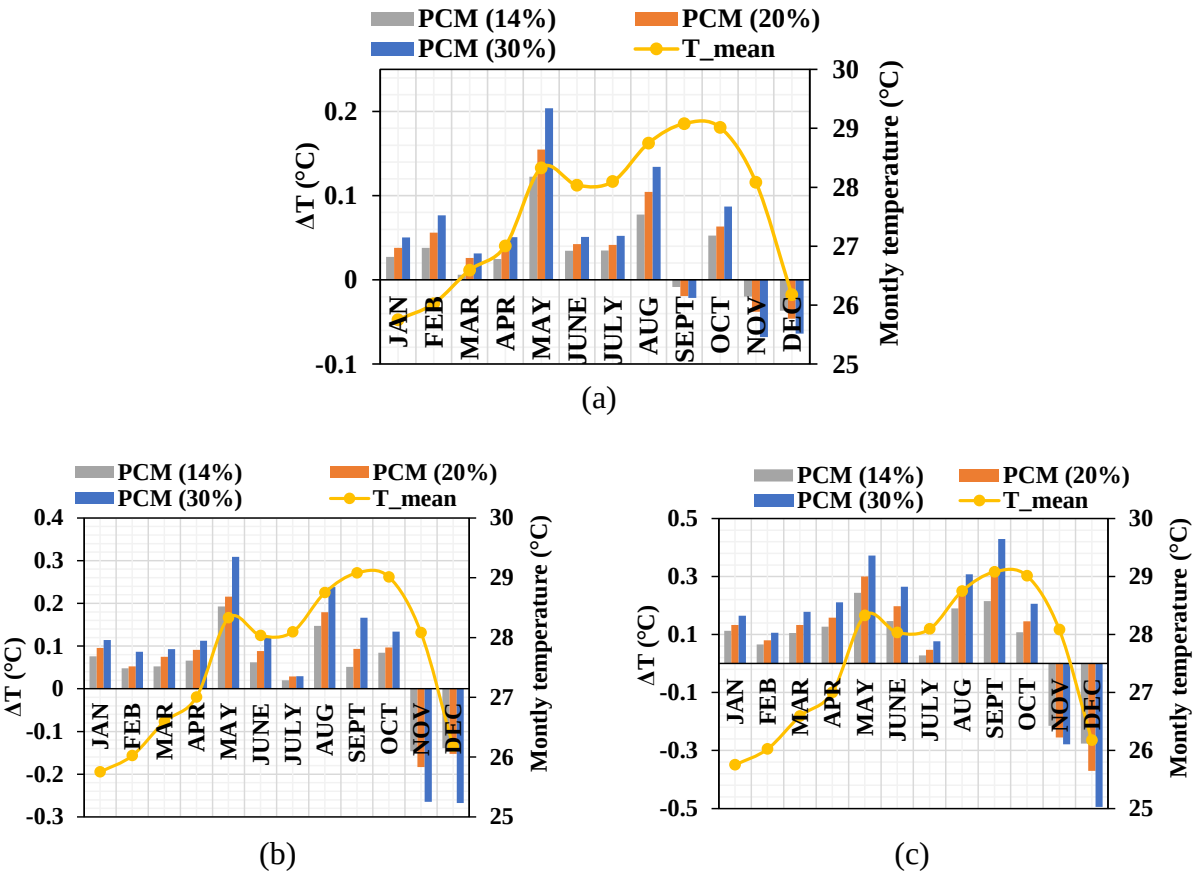

Figure 10. Monthly average exterior temperature (yellow) and temperature difference between each fraction of PCM and the reference hemp concrete with 10 cm (a), 20 cm (b) and 30 cm (c) under Caracas' climatic conditions.

4.2.3 Maximum energy savings potential

To further assess the effect of PCM fraction and insulation layer thickness, the maximum percentage reduction in heat transfer load was calculated for each configuration and under the climatic conditions of New Delhi (Figure 11.a) and Caracas (Figure 11.b). For the city of New Delhi (Figure 11.a), increasing the PCM fraction from 14 wt% to 30 wt% integrated in the hybrid multilayer wall enables a reduction from 15% to over 30% for a thickness of 10 cm. At a thickness of 20 cm, the heat transmission load is reduced by a maximum of 33%, which corresponds to a PCM fraction of 30 wt%. For lower fractions, specifically 14 wt% and 20 wt%, the reduction in heat transmission load is 19% and 25%, respectively for the same thickness of 20 cm. The greatest reductions are obtained for a thickness of 30 cm, with values of 22%, 26% and 40% corresponding to PCM fraction of 14 wt%, 20 wt%, 30 wt%, respectively. These results show that increasing the PCM fraction has more decisive impact on reducing the heat transmission load than increasing the thickness. Indeed, for a given fraction, let's say 14 wt%, going from 10 cm to 30 cm delivers a gain of 5%, whereas increasing the fraction to 30 wt% for a thickness of 10 cm delivers almost twice as much reduction in heat transmission load. As

a result, it is possible to design much more compact insulating materials with higher performance simply by increasing the amount of PCM.

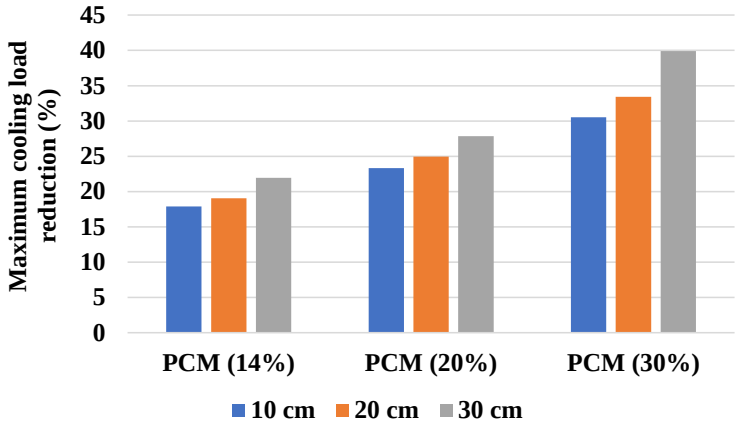

(a)

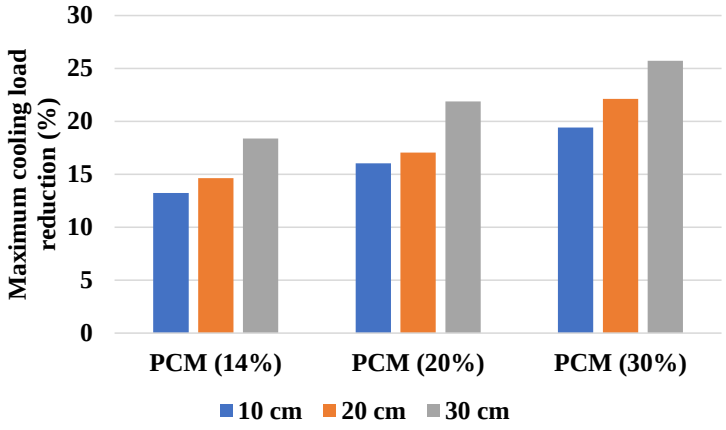

(b)

Figure 11. Effect of the PCM fraction and insulation thickness on the maximum cooling load reduction for the climatic conditions of city New Delhi (a) and Caracas (b).

For the city of Caracas, we can make the same observations as for the city of New Delhi concerning the effect of the PCM fraction and the thickness of the material layer composing the multilayer walls. However, the reductions in heat transfer load are lower than in the very hot climate of New Delhi. Nevertheless, reductions of up to 25% are noted for the bio-composite with 30% PCM and 30 cm of thickness. For a thickness of 10 cm, the reductions are 13%, 16% and 19% for PCM fraction of 14 wt%, 20 wt%, 30 wt%, respectively. Increasing the thickness to 20 cm slightly increases these load reductions to a maximum value of 22% for a PCM fraction of 30 wt%.

This analysis shows that to obtain the maximum benefit from PCM, 30 wt% incorporation should be achieved independently of the thickness of the insulating layer integrated in the hybrid multilayer walls. In such situation, the proposed bio-composite PCM exhibited similar or even better performances compared to glass wool that is considered as an excellent insulator. However, the money savings due to cooling loads reduction should be evaluated and compared to the price of the bio-composite insulation at different PCM fractions and thicknesses to assess

the effectiveness of the proposed solution. This should allow also evaluating the effect of the time shift in the money saving. In fact, the cost of energy being different according to the periods of the day, in particular between the day and the night, the passage to the off-peak periods presents an obvious economic advantage for the users of the building, by reducing the energy bill.

4.2.4 Hydric performances

Figure 12 illustrates the impact of the hemp concrete and bio-composite PCM insulation layers integrating the studied multilayer walls on the interior surface relative humidity. As previously demonstrated, the kinetics are faster for hemp concrete layer at higher humidity levels compared to the bio-composite PCM layer. This can be attributed to the incorporation of PCM, which reduces the material's water vapor permeability. Increasing the thickness has two significant effects: it slows down the kinetics and smoothens the relative humidity curve, making it less responsive to changes in external relative humidity. The immediate result of the slower kinetics is a delay in reaching equilibrium. The effect of the thickness is more visible for the weather of New Delhi, where the maximum relative humidity is reduced by 5% and 10% for 20 cm and 30 cm compared to a thickness of 10 cm. Both resulting multilayer walls showed excellent moisture regulation capacity that increased with the insulating layer thickness.

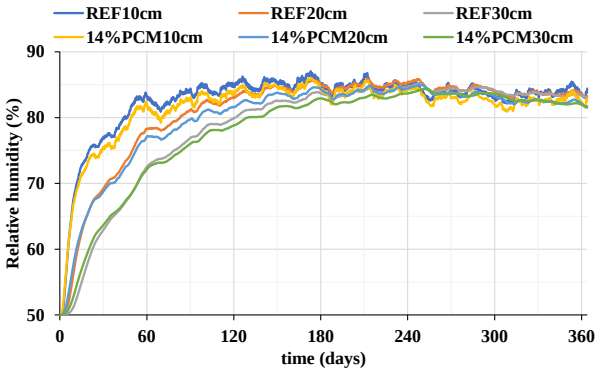

(a)

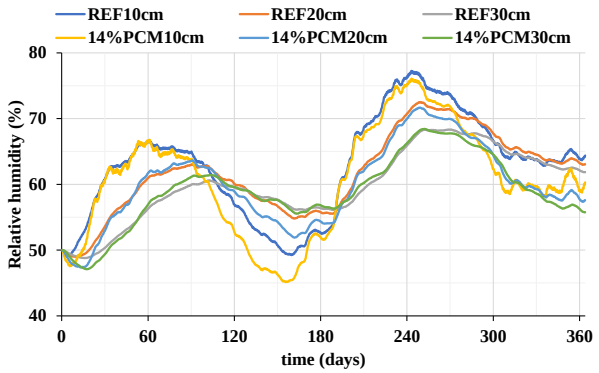

(b)

Figure 12. Effect of the thickness of hemp concrete and bio-composite PCM on the yearly evolution of the inside surface relative humidity of the city of Caracas (a) and New Delhi (b).

4.3 Extension of the study

The model we developed was used to assess the hygrothermal performances of different insulating layers integrated in multilayer walls, including those incorporating phase-change materials (PCMs) in the hot and humid climates of the cities of Caracas and New Delhi. In addition, it enabled us to examine the impact of PCM fractions and insulation thicknesses using several indicators. However, its main limitation lies in its consideration of internal boundary conditions. Indeed, the model assumes that the air temperature is equal to the interior wall surface temperature at the previous iteration and does not take into account air renewal or moisture production. These effects could be taken into account by coupling the hygrothermal model with a Building Energy Simulation software such as TRNSYS. In addition, this approach could enable more accurate calculation of heating and cooling requirements. Our next studies will focus on developing an approach that integrates this model with a Building Energy Simulation software.

5 Conclusion

This study investigates the hygrothermal behavior of multilayer building walls consisting of a layer of insulation, conventional building materials (brick) and plasters under realistic unfavourable weather conditions. Multilayer walls integrating five different insulators including an innovative biobased insulator fabricated with hemp shives impregnated with a phase change material (capric acid), hemp concrete, glass wool, expanded polystyrene and cellulose insulation were compared considering external insulation under the weather condition of Caracas and New Delhi.

In the very hot, humid climate of New Delhi, the multilayer walls integrating hemp concrete and the bio-composite PCM performed similarly, with hemp concrete having a slight advantage due to temperatures above the melting point of PCM. For better results in very hot weather, a promising alternative is to use a PCM with a higher melting temperature than capric acid. The bio-composite PCM showed promise in delaying temperature peaks by about 28.5 hours, when the exterior temperature is above the melting point of PCM. This result is mainly the consequence of the increased thermal inertia of the sustainable hybrid multilayer wall due to the incorporation of the PCM. Expanded polystyrene and cellulose insulation showed higher heat transmission loads, attributed to lower thermal inertia (compared to hemp concrete and bio-composite PCM) and slightly lower thermal conductivity. In the hot, humid conditions of Caracas the bio-composite PCM allows more efficient multilayer walls than the one integrating hemp concrete, with a heat transmission load reduced by 20 $kW.m^{-2}$.

Internal humidity levels were constant for most insulations, ranging from 40% to 75%, with the exception of cellulose insulation, which remained slightly below 70% due to its lower water vapor permeability. Relative humidity responses were similar for the multilayer walls integrating hemp concrete, bio-composite PCM and glass wool, stabilizing around 85% due to their water storage capacity and permeability. The multilayer walls integrating expanded polystyrene and cellulose insulation showed slightly slower kinetics, stabilizing at around 80%, corresponding to the average outdoor relative humidity.

PCM fraction has a significant impact on reducing heat transfer load, overshadowing the effect of thickness increase, enabling more compact, high-performance insulation materials, therefore for more efficient multilayer walls. Indeed, the hybrid multilayer wall integrating the bio-composite with 30 wt% of PCM demonstrates substantial heat transfer load reduction in New

Delhi, with up to 40% decrease in maximum heat transfer load at 30 cm thickness, emphasizing the important role of fraction over thickness for designing efficient insulating layers. Caracas observes similar trends, with up to 25% reductions in heat transfer load for the same material (bio-composite with 30 wt% of PCM) at 30 cm thickness. Therefore, the hybrid multilayer walls integrating the bio-composite PCM insulations show promising performances in hot and humid climates, particularly those corresponding to PCM melting point.

Further works will aim at increasing the fraction of PCM in the developed bio-composite PCM to achieve the expected performances. The effect of the PCM temperature will be assed also to find the optimum melting temperature for specific weather conditions. It is worth mentioning that this study focuses on the energy performances of the multilayer walls without considering the mechanical performance of the structural layer. The latter is assumed to guarantee sufficient mechanical resistance to ensure the mechanical stability of the wall. Finally, a comparative study will be conducted at the building scale in a building energy simulation to evaluate the performances of the proposed solution.

Author Contributions: Conceptualization, all authors; methodology, all authors; formal analysis, all authors; investigation, all authors; resources, all authors; data curation, all authors; writing—original draft preparation, M.S.; writing—review and editing, all authors; visualization, all authors; supervision, R.B., M.D., A.G. and A.H.; project administration, R.B. and M.D.; funding acquisition, R.B., M.D. All authors have read and agreed to the published version of the manuscript.

Declaration of Competing Interest: The authors declare that they have no known competing financial interests or personal relationships that could have appeared to influence the work reported in this paper.

Acknowledgments: This work is carried out in the frame of Region Nouvelle Aquitaine for subsidizing BioMCP project (Project-2017-1R10209-13023) and in the frame of the Laboratory for Energy and Environmental Efficiency of Envelopes and Cities, 4ev Lab, the joint Laboratory between EDF R&D, CNRS, LaSIE conducting research to improve the energy and environmental performance of buildings and the quality of life of the inhabitants of urban spaces.

References

[1] Buildings - Energy System, IEA. (n.d.). https://www.iea.org/energy-system/buildings (accessed October 25, 2023).
[2] V. Basecq, G. Michaux, P. Blondeau, C. Inard, Short term storage systems of the thermal energy for buildings: a review, Advances in Building Energy Research. 7 (2013) 66–119. https://hal.archives-ouvertes.fr/hal-01052828 (accessed May 5, 2021).
[3] S. Ben Romdhane, A. Amamou, R. Ben Khalifa, N.M. Saïd, Z. Younsi, A. Jemni, A review on thermal energy storage using phase change materials in passive building applications, Journal of Building Engineering. 32 (2020) 101563. https://doi.org/10.1016/j.jobe.2020.101563.
[4] B. Lamrani, K. Johannes, F. Kuznik, Phase change materials integrated into building walls: An updated review, Renewable and Sustainable Energy Reviews. 140 (2021) 110751. https://doi.org/10.1016/j.rser.2021.110751.
[5] A.A.A.A. Al-Rashed, A.A. Alnaqi, J. Alsarraf, Energy-saving of building envelope using passive PCM technique: A case study of Kuwait City climate conditions, Sustainable

Energy Technologies and Assessments. 46 (2021) 101254. https://doi.org/10.1016/j.seta.2021.101254.
[6] J. Bohórquez-Órdenes, A. Tapia-Calderón, D.A. Vasco, O. Estuardo-Flores, A.N. Haddad, Methodology to reduce cooling energy consumption by incorporating PCM envelopes: A case study of a dwelling in Chile, Building and Environment. 206 (2021) 108373. https://doi.org/10.1016/j.buildenv.2021.108373.
[7] Y.K. Yang, I.S. Kang, M.H. Chung, S. Kim, J.C. Park, Effect of PCM cool roof system on the reduction in urban heat island phenomenon, Building and Environment. 122 (2017) 411–421. https://doi.org/10.1016/j.buildenv.2017.06.015.
[8] S.N. Al-Saadi, Z. Zhai, A new validated TRNSYS module for simulating latent heat storage walls, Energy and Buildings. 109 (2015) 274–290. https://doi.org/10.1016/j.enbuild.2015.10.013.
[9] Q. Al-Yasiri, M. Szabó, Experimental study of PCM-enhanced building envelope towards energy-saving and decarbonisation in a severe hot climate, Energy and Buildings. 279 (2023) 112680. https://doi.org/10.1016/j.enbuild.2022.112680.
[10] T. Ashour, H. Georg, W. Wu, An experimental investigation on equilibrium moisture content of earth plaster with natural reinforcement fibres for straw bale buildings, Applied Thermal Engineering. 31 (2011) 293–303. https://doi.org/10.1016/j.applthermaleng.2010.09.009.
[11] G.M. Amantino, N.P. Hasparyk, F. Tiecher, R.D. Toledo Filho, Assessment of bio-aggregate concretes' properties with rice residue, Journal of Building Engineering. 52 (2022) 104348. https://doi.org/10.1016/j.jobe.2022.104348.
[12] M. Yadav, M. Agarwal, Biobased building materials for sustainable future: An overview, Materials Today: Proceedings. 43 (2021) 2895–2902. https://doi.org/10.1016/j.matpr.2021.01.165.
[13] Y. Fraine, C. Seladji, A. Aït-Mokhtar, Effect of microencapsulation phase change material and diatomite composite filling on hygrothermal performance of sintered hollow bricks, Building and Environment. 154 (2019) 145–154. https://doi.org/10.1016/j.buildenv.2019.02.036.
[14] D. Wu, M. Rahim, M. El Ganaoui, R. Bennacer, B. Liu, Multilayer assembly of phase change material and bio-based concrete: A passive envelope to improve the energy and hygrothermal performance of buildings, Energy Conversion and Management. 257 (2022) 115454. https://doi.org/10.1016/j.enconman.2022.115454.
[15] N. Zhu, X. Li, P. Hu, F. Lei, S. Wei, W. Wang, An exploration on the performance of using phase change humidity control material wallboards in office buildings, Energy. 239 (2022) 122433. https://doi.org/10.1016/j.energy.2021.122433.
[16] X. Shi, S.A. Memon, W. Tang, H. Cui, F. Xing, Experimental assessment of position of macro encapsulated phase change material in concrete walls on indoor temperatures and humidity levels, Energy and Buildings. 71 (2014) 80–87. https://doi.org/10.1016/j.enbuild.2013.12.001.
[17] S.J. Chang, Y. Kang, S. Wi, S.-G. Jeong, S. Kim, Hygrothermal performance improvement of the Korean wood frame walls using macro-packed phase change materials (MPPCM), Applied Thermal Engineering. 114 (2017) 457–465. https://doi.org/10.1016/j.applthermaleng.2016.11.188.
[18] S. Liu, Y.-T. Kwok, K. Lau, E. Ng, Applicability of different extreme weather datasets for assessing indoor overheating risks of residential buildings in a subtropical high-density city, Building and Environment. 194 (2021) 107711. https://doi.org/10.1016/j.buildenv.2021.107711.
[19] D. Xia, Z. Zhong, Y. Huang, Y. Zou, S. Lou, Q. Zhan, J. Guo, J. Yang, T. Guo, Impact of coupled heat and moisture transfer on indoor comfort and energy demand for residential

buildings in hot-humid regions, Energy and Buildings. 288 (2023) 113029. https://doi.org/10.1016/j.enbuild.2023.113029.
[20] C. Recart, C. Sturts Dossick, Hygrothermal behavior of post-retrofit housing: A review of the impacts of the energy efficiency upgrade strategies, Energy and Buildings. 262 (2022) 112001. https://doi.org/10.1016/j.enbuild.2022.112001.
[21] R. Wang, H. Ge, D. Baril, Moisture-safe attic design in extremely cold climate: Hygrothermal simulations, Building and Environment. 182 (2020) 107166. https://doi.org/10.1016/j.buildenv.2020.107166.
[22] D. Bastien, M. Winther-Gaasvig, Influence of driving rain and vapour diffusion on the hygrothermal performance of a hygroscopic and permeable building envelope, Energy. 164 (2018) 288–297. https://doi.org/10.1016/j.energy.2018.07.195.
[23] Y. Liu, Y. Wang, D. Wang, J. Liu, Effect of moisture transfer on internal surface temperature, Energy and Buildings. 60 (2013) 83–91. https://doi.org/10.1016/j.enbuild.2013.01.019.
[24] R. Belarbi, M. Qin, A. Aït-Mokhtar, L.-O. Nilsson, Experimental and theoretical investigation of non-isothermal transfer in hygroscopic building materials, Building and Environment. 43 (2008) 2154–2162. https://doi.org/10.1016/j.buildenv.2007.12.014.
[25] M. Qin, A. Aït-Mokhtar, R. Belarbi, Two-dimensional hygrothermal transfer in porous building materials, Applied Thermal Engineering. 30 (2010) 2555–2562. https://doi.org/10.1016/j.applthermaleng.2010.07.006.
[26] F. Bennai, M.Y. Ferroukhi, F. Benmahiddine, R. Belarbi, A. Nouviaire, Assessment of hygrothermal performance of hemp concrete compared to conventional building materials at overall building scale, Construction and Building Materials. 316 (2022) 126007. https://doi.org/10.1016/j.conbuildmat.2021.126007.
[27] A. Trabelsi, R. Belarbi, K. Abahri, M. Qin, Assessment of temperature gradient effects on moisture transfer through thermogradient coefficient, Build. Simul. 5 (2012) 107–115. https://doi.org/10.1007/s12273-012-0063-x.
[28] T. Busser, J. Berger, A. Piot, M. Pailha, M. Woloszyn, Comparison of model numerical predictions of heat and moisture transfer in porous media with experimental observations at material and wall scales: An analysis of recent trends, Drying Technology. 37 (2019) 1363–1395. https://doi.org/10.1080/07373937.2018.1502195.
[29] M. Sawadogo, M. Duquesne, R. Belarbi, A.E.A. Hamami, A. Godin, Review on the Integration of Phase Change Materials in Building Envelopes for Passive Latent Heat Storage, Applied Sciences. 11 (2021) 9305. https://doi.org/10.3390/app11199305.
[30] M. Sawadogo, A. Godin, M. Duquesne, E. Lacroix, A. Veillère, A.E.A. Hamami, R. Belarbi, Investigation of eco-friendly and economic shape-stabilized composites for building walls and thermal comfort, Building and Environment. 231 (2023) 110026. https://doi.org/10.1016/j.buildenv.2023.110026.
[31] M. Sawadogo, F. Benmahiddine, A. Godin, M. Duquesne, R. Belarbi, A. Hamami, Development and hygrothermal performance analysis of a novel eco-friendly insulating wall under various climatic conditions, Building and Environment. (2023) 110841. https://doi.org/10.1016/j.buildenv.2023.110841.
[32] M. Sawadogo, F. Benmahiddine, A.E.A. Hamami, R. Belarbi, A. Godin, M. Duquesne, Investigation of a novel bio-based phase change material hemp concrete for passive energy storage in buildings, Applied Thermal Engineering. 212 (2022) 118620. https://doi.org/10.1016/j.applthermaleng.2022.118620.
[33] Welcome | TRNSYS : Transient System Simulation Tool, (n.d.). https://www.trnsys.com/ (accessed August 8, 2023).
[34] Y. Ferroukhi, R. Djedjig, K. Limam, R. Belarbi, Hygrothermal behavior modeling of the hygroscopic envelopes of buildings: A dynamic co-simulation approach, Building Simulation. 9 (2016). https://doi.org/10.1007/s12273-016-0292-5.

[35] J. Uyttenbroeck, Building heat loss calculations: Choice of internal temperature and of heat exchange coefficient hi, Building Services Engineering Research and Technology. 11 (1990) 49–56. https://doi.org/10.1177/014362449001100202.
[36] L. Ayres de Mello, L.M. Moura, N. Mendes, A model for assessment of heat and moisture transfer through hollow porous buildings elements, Case Studies in Thermal Engineering. 14 (2019) 100446. https://doi.org/10.1016/j.csite.2019.100446.
[37] J.R. Philip, D.A. De Vries, Moisture movement in porous materials under temperature gradients, Eos, Transactions American Geophysical Union. 38 (1957) 222–232.
[38] P. Crausse, J.P. Laurent, B. Perrin, Influence des phénomènes d'hystérésis sur les propriétés hydriques de matériaux poreux: Comparaison de deux modèles de simulation du comportement thermohydrique de parois de bâtiment, Revue Générale de Thermique. 35 (1996) 95–106. https://doi.org/10.1016/S0035-3159(96)80002-X.
[39] B. Remki, K. Abahri, M. Tahlaiti, R. Belarbi, Hygrothermal transfer in wood drying under the atmospheric pressure gradient, International Journal of Thermal Sciences. 57 (2012) 135–141. https://doi.org/10.1016/j.ijthermalsci.2012.02.005.
[40] NF EN 15026, Afnor EDITIONS. (n.d.). https://www.boutique.afnor.org/fr-fr/norme/nf-en-15026/performance-hygrothermique-des-composants-et-parois-de-batiments-evaluation/fa119083/31029 (accessed March 31, 2023).
[41] S.O. Olutimayin, C.J. Simonson, Measuring and modeling vapor boundary layer growth during transient diffusion heat and moisture transfer in cellulose insulation, International Journal of Heat and Mass Transfer. 48 (2005) 3319–3330. https://doi.org/10.1016/j.ijheatmasstransfer.2005.02.024.
[42] S. Dokos, Numerical Integration of Ordinary Differential Equations, in: S. Dokos (Ed.), Modelling Organs, Tissues, Cells and Devices: Using MATLAB and COMSOL Multiphysics, Springer, Berlin, Heidelberg, 2017: pp. 55–104. https://doi.org/10.1007/978-3-642-54801-7_3.
[43] S. Kenzhekhanov, S.A. Memon, I. Adilkhanova, Quantitative evaluation of thermal performance and energy saving potential of the building integrated with PCM in a subarctic climate, Energy. 192 (2020) 116607. https://doi.org/10.1016/j.energy.2019.116607.
[44] M. Duquesne, C. Mailhé, K. Ruiz-Onofre, F. Achchaq, Biosourced organic materials for latent heat storage: An economic and eco-friendly alternative, Energy. 188 (2019) 116067. https://doi.org/10.1016/j.energy.2019.116067.
[45] M. Duquesne, C. Mailhé, S. Doppiu, J.-L. Dauvergne, S. Santos-Moreno, A. Godin, G. Fleury, F. Rouault, E. Palomo del Barrio, Characterization of Fatty Acids as Biobased Organic Materials for Latent Heat Storage, Materials. 14 (2021) 4707. https://doi.org/10.3390/ma14164707.
[46] X. Wang, X. Jin, Y. Yin, X. Shi, X. Zhou, A transient heat and moisture transfer model for building materials based on phase change criterion under isothermal and non-isothermal conditions, Energy. 224 (2021) 120112. https://doi.org/10.1016/j.energy.2021.120112.

Appendix

Table A 1. Hygrothermal properties of hemp concrete (HC), bio-composite PCM (BPCM), cellulose insulation and expanded polystyrene.

Parameters	Hemp concrete/bio-composite PCM	Cellulose insulation [41,46]	Expanded Polystyrene
u (%)	$\frac{m \cdot C \cdot K \cdot \varphi}{(1-K\varphi) * (1-K\varphi+KC\varphi)}$ Where : $\begin{cases} m = 0.02245, C = 54.0309 \text{ and } K = 0.93899 \text{ (REF)} \\ m = 0.02227, C = 20.9271 \text{ and } K = 0.87663 \text{ (BPCM)} \end{cases}$	$exp(-8.96 + 18.68\varphi - 10.85\varphi^2 + -11.4\varphi^3 + 12.47\varphi^4)$	$\frac{m \cdot C \cdot K \cdot \varphi}{(1-K\varphi) * (1-K\varphi+KC\varphi)}$ Where: $m = 0.5231, C = 0.6231$ and $K = 0.0133$
C_m $(-)$	$\frac{\partial w}{\partial \varphi}$		
λ (W.m^{-1}.K^{-1})	$\begin{cases} 0.0003 \cdot T + 0.063 \ (REF) \\ 0.0004 \cdot T + 0.0805 \ (BPCM) \end{cases}$	$-0.092 + 0.15\varphi - 0.06\,\varphi^{1.5} + 0.129\exp(-\varphi)$	0.04 $0.0003 \cdot T + 0.0305$
δ_v (Kg.m^{-1}.Pa^{-1}.s^{-1})	$D_{v0} * e^{a*\varphi}/p_{v,sat}$ Where : $\begin{cases} D_{v0} = 1.2733 \cdot 10^{-6} \ and \ a = -4.1899 \ (REF) \\ D_{v0} = 1.2998 \cdot 10^{-6} \ and \ a = -4.3631 \text{ (BPCM)} \end{cases}$	$\frac{1}{1.35 \cdot 10^{10} - 4.36 \cdot 10^{9}\varphi}$	$5.34 \cdot 10^{-12}$
$C_{p,s}$ (J. kg^{-1}.K^{-1})	$\begin{cases} 1000 - 1100 \ (HC) \\ 1200 - 4500 \text{ (BPCM)} \end{cases}$	1400	1568
ρ_s (kg.m^{-3})	507.1 (HC) 582.2 $(BPCM)$	50	30
L_v (J.kg^{-1})	$2.44 \cdot 10^6$		
k_l (Kg.m^{-1}.Pa^{-1}.s^{-1})	$D_{l0} * e^{b*\varphi}/p_{v,sat}$ Where : $\begin{cases} K_{l0} = 5.7893 \cdot 10^{-9} \ and \ b = 8.1002 \ (REF) \\ K_{l0} = 7.5511 \cdot 10^{-8} \ and \ b = 4.7225 \text{ (BPCM)} \end{cases}$	$\frac{\rho_s C_m \varphi(-0.032 + 13.078\,\varphi) \cdot 10^{-10}}{4.62 \cdot 10^5 T(1 - 0.91\,\varphi + 0.42)}$	$\frac{\rho_s C_m \varphi}{4.62 \cdot 10^5 T} * (\frac{A_w}{w_{sat}})^2$ where $A_w = 0.02\ kg/(m^2 s^{\frac{1}{2}})$ et $w_{sat} = 3\ kg/m^3$

Table A 2. Hygrothermal properties of plaster, glass wool and brick.

Parameters	Plaster	Glass wool	Brick
u (%)	$\frac{m \cdot C \cdot K \cdot \varphi}{(1-K\phi) * (1-K\varphi+KC\varphi)}$ where $m = 0.0207008$, $C = 0.25951629$ and $K = 0.79967109$.	$\frac{m \cdot C \cdot K \cdot \varphi}{(1-K\phi) * (1-K\varphi+KC\varphi)}$ where $m = 4.9998$, $C = 1.883 \cdot 10^{-3}$ and $K = 0.71132$	$\frac{m \cdot C \cdot K \cdot \varphi}{(1-K\phi) * (1-K\varphi+KC\varphi)}$ where $m = 0.0137$, $C = 157.71$ and $K = 0.9196$
C_m $(-)$	$\frac{\partial w}{\rho_s \partial \varphi}$		
λ (W.m^{-1}.K^{-1})	0.8	$0.0002 \cdot T + 0.0254$	0.684
δ_v (Kg.m^{-1}.Pa^{-1}.s^{-1})	$1.64 \cdot 10^{-11}$	$9.35 \cdot 10^{-11}$	$5 \cdot 10^{-11}\varphi^3 - 4 \cdot 10^{-11}\varphi^2 + 10^{-11}\varphi + 10^{-11}$
$C_{p,s}$ (J. kg^{-1}.K^{-1})	863.9	928	867.32
ρ_s (kg.m^{-3})	1820	32.7	1791.02
L_v (J.kg^{-1})	$2.44 \cdot 10^6$		
k_l (Kg.m^{-1}.Pa^{-1}.s^{-1})	$\frac{\rho_s C_m \varphi}{4.62 \cdot 10^5 T} * (\frac{A_w}{w_{sat}})^2$ where $A_w = 0.152\ kg/(m^2 s^{\frac{1}{2}})$ and $w_{sat} = 91\ kg/m^3$	$\frac{\rho_s C_m \varphi}{4.62 \cdot 10^5 T} * (\frac{A_w}{w_{sat}})^2$ where $A_w = 4.7 \cdot 10^{-4}\ kg/(m^2 s^{\frac{1}{2}})$ and $w_{sat} = 0.02\ kg/m^3$	$2 \cdot 10^{-8} \cdot \exp(31.48 \cdot \varphi)$